

Brain projects come
together pp. 11 & 42

The hidden force behind
this year's El Niño p. 22

Reducing fuel fire
hazards pp. 32 & 72

Science

\$10
2 OCTOBER 2015
sciencemag.org

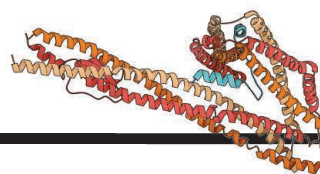
AAAS

Brain neurons diverge

Mutations reveal
developmental
pathways pp. 37 & 94



CONTENTS



33, 56, & 106

Stability in the nuclear pore

2 OCTOBER 2015 • VOLUME 350 • ISSUE 6256



26

NEWS

IN BRIEF

12 Roundup of the week's news

IN DEPTH

16 NEW PROTEINS MAY EXPAND, IMPROVE GENOME EDITING

Mining bacterial immune systems yields two new editing tools and has the potential to contribute many more *By E. Pennisi*

17 TALKING SCIENCE AND GOD WITH THE POPE'S NEW ASTRONOMER

Guy Consolmagno, director of the Vatican Observatory, wants to show the world that religion supports astronomy *By E. Carlidge*

18 EUROPE'S RIFTS OVER TRANSGENIC CROPS DEEPEN AT KEY DEADLINE

Policy differences among 28 E.U. member states come into sharper focus in the wake of major reform *By T. Rabesandratana*

20 HAVE PHYSICISTS SEEN THE DYING FLASH OF DARK MATTER?

Dark particle decays could explain tantalizing x-ray signal seen in multiple galaxies, including our own Milky Way *By E. Carlidge*

21 HOLLAND'S GIANT WAVEMAKER HAS SPLASHY DEBUT

Delta Flume will allow researchers to study how coastal defenses fare against powerful surf *By M. Enserink*

FEATURES

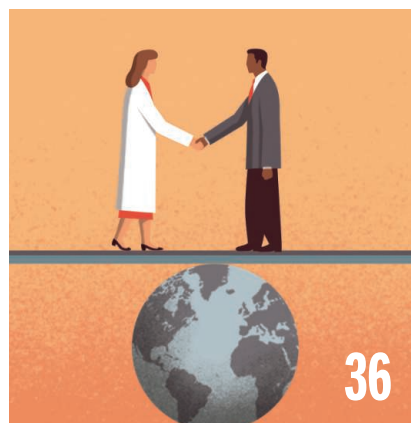
22 THE STORM KING

A mysterious tropical weather pattern called the Madden-Julian oscillation fuels El Niños and triggers rain, heat waves, and hurricanes around the globe *By E. Hand*

..... **25 Taking the pulse of the tropics**
By E. Hand

26 POOLING RESOURCES

Ecologist Aram Calhoun forges creative alliances in her quest to protect ephemeral vernal pools *By J. U. Adams*



36

INSIGHTS

LETTERS

30 NEXTGEN VOICES

PERSPECTIVES

32 SAFER FUELS BY INTEGRATING POLYMER THEORY INTO DESIGN

Jet fuels are stabilized with polymers assembling in solution *By M. Jaffe and S. Allam*

► REPORT P. 72

33 LOCKING DOWN THE CORE OF THE PORE

A highly stable heterotrimeric protein complex lines the central channel of the nuclear pore *By K. S. Ullman and M. A. Powers*

► RESEARCH ARTICLE P. 56; REPORT P. 106

34 THE IPCC AT A CROSSROADS: OPPORTUNITIES FOR REFORM

Increase focus on policy-relevant research *By C. Carraro et al.*

36 ADDED VALUE FROM IPCC APPROVAL SESSIONS

Flexible, creative author teams are critical *By C. B. Field and V. R. Barros*

37 A TREE OF THE HUMAN BRAIN

Genomes of single neurons trace the developmental and mutational history of the brain *By S. Linnarsson*

► REPORT P. 94

38 HOW STABLE ARE FOOD WEBS DURING A MASS EXTINCTION?

Fossil data provide a detailed view of how food webs changed across the Permian-Triassic mass extinction *By C. R. Marshall*

► REPORT P. 90

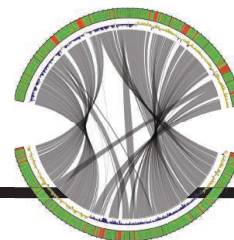
39 EYEING UP A JUPITER-LIKE EXOPLANET

Extreme adaptive optics systems enable the direct imaging of exoplanetary systems *By D. Marwet*

► REPORT P. 64

Science Staff	8
New Products	114
Science Careers	116

CONTENTS



55

An experimental
gut microbiota

2 OCTOBER 2015 • VOLUME 350 • ISSUE 6256

40 CLOUDS RESOLVED

Clouds are puffy to the finest scale

By E. Bodenschatz

► REPORT P. 87

42 IT TAKES THE WORLD TO UNDERSTAND THE BRAIN

International brain projects discuss how to coordinate efforts By Z. J. Huang and L. Luo

► EDITORIAL P. 11

SCIENCE PRIZE ESSAY

46 SLOW OR FAST? A TALE OF SYNAPTIC VESICLE RECYCLING

A new model accounts for synaptic transmission speed By S. Watanabe

BOOKS ET AL.

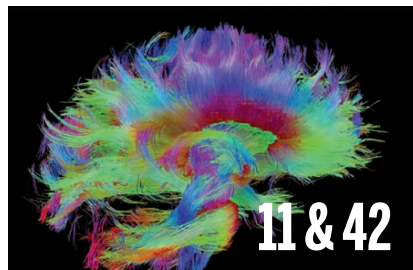
49 THE GRADUATE SCHOOL MESS

By L. Cassuto, reviewed by J. Gutlerner

50 SECRET

I. Brunswick et al., curators,

reviewed by G. Frazzetto



11 & 42

RESEARCH

IN BRIEF

52 From *Science* and other journals

RESEARCH ARTICLES

55 GUT MICROBIOTA

Genetic determinants of in vivo fitness and diet responsiveness in multiple human gut *Bacteroides* M. Wu et al.

RESEARCH ARTICLE SUMMARY; FOR FULL TEXT:

dx.doi.org/10.1126/science.aac5992

56 STRUCTURAL BIOLOGY

Architecture of the fungal nuclear pore inner ring complex T. Stuwe et al.

► PERSPECTIVE P. 33; REPORT P. 106

REPORTS

64 PLANETARY SCIENCE

Discovery and spectroscopy of the young jovian planet 51 Eri b with the Gemini Planet Imager B. Macintosh et al.

► PERSPECTIVE P. 39

68 NANOELECTRONICS

End-bonded contacts for carbon nanotube transistors with low, size-independent resistance Q. Cao et al.

72 POLYMER CHEMISTRY

Megasupramolecules for safer, cleaner fuel by end association of long telechelic polymers M.-H. Wei et al.

► PERSPECTIVE P. 32; PODCAST

76 EARTH HISTORY

State shift in Deccan volcanism at the Cretaceous-Paleogene boundary, possibly induced by impact

P. R. Renne et al.

78 WATER STRUCTURE

Ultrafast 2D IR spectroscopy of the excess proton in liquid water

M. Thämer et al.

82 MEMORY MECHANISMS

Multiple repressive mechanisms in the hippocampus during memory formation J. Cho et al.

87 CLOUDS

Holographic measurements of inhomogeneous cloud mixing at the centimeter scale M. J. Beals et al.

► PERSPECTIVE P. 40

90 PALEOECOLOGY

Community stability and selective extinction during the Permian-Triassic mass extinction P. D. Roopnarine and K. D. Angielczyk

► PERSPECTIVE P. 38

94 NEURODEVELOPMENT

Somatic mutation in single human neurons tracks developmental and transcriptional history

M. A. Lodato et al.

► PERSPECTIVE P. 37

98 INJURY RECOVERY

Function of the nucleus accumbens in motor control during recovery after spinal cord injury M. Sawada et al.

102 NEUROTRANSMISSION

Aldehyde dehydrogenase 1a1 mediates a GABA synthesis pathway in midbrain dopaminergic neurons J.-I. Kim et al.

106 STRUCTURAL BIOLOGY

Crystal structure of the metazoan Nup62•Nup58•Nup54 nucleoporin complex H. Chug et al.

► PERSPECTIVE P. 33; RESEARCH ARTICLE P. 56

DEPARTMENTS

11 EDITORIAL

The promise of neurotechnology

By Andrew Schwartz

► PERSPECTIVE P. 42

130 WORKING LIFE

After the bombs By Elisabeth Pain

ON THE COVER



Illustration of projection neurons from the human cerebral cortex, with nuclei colored to reflect distinct sets of somatic DNA mutations. When a mutation occurs in a dividing cell, it marks

all of the cell's descendants. Identification of clones marked by mutation enables reconstruction of human brain development. Because developmental defects lie at the heart of many neurological diseases, understanding development is a primary goal of neuroscience. See pages 37 and 94. Illustration: C. Bickel/Science

SCIENCE (ISSN 0036-8075) is published weekly on Friday, except the last week in December, by the American Association for the Advancement of Science, 1200 New York Avenue, NW, Washington, DC 20005. Periodicals mail postage (publication No. 484460) paid at Washington, DC, and additional mailing offices. Copyright © 2015 by the American Association for the Advancement of Science. The title SCIENCE is a registered trademark of the AAAS. Domestic individual membership and subscription (51 issues): \$153 (\$74 allocated to subscription). Domestic institutional subscription (51 issues): \$1282. Foreign postage extra: Mexico, Caribbean (surface mail) \$55; other countries (air assist delivery) \$85. First class, airmail, student, and emeritus rates on request. Canadian rates with GST available upon request. GST #R1254 88122. Publications Mail Agreement Number 1069624. Printed in the U.S.A. Change of address: Allow 4 weeks, giving old and new addresses and 8-digit account number. Postmaster: Send change of address to AAAS, P.O. Box 96178, Washington, DC 20090-6178. Single-copy sales: \$10.00 current issue, \$15.00 back issue prepaid includes surface postage; bulk rates on request. Authorization to photocopy material for internal or personal use under circumstances not falling within the fair use provisions of the Copyright Act is granted by AAAS to libraries and other users registered with the Copyright Clearance Center (CCC) Transactional Reporting Service, provided that \$30.00 per article is paid directly to CCC, 222 Rosewood Drive, Danvers, MA 01923. The identification code for Science is 0036-8075. Science is indexed in the Reader's Guide to Periodical Literature and in several specialized indexes.

Editor-in-Chief Marcia McNutt

Executive Editor Monica M. Bradford **News Editor** Tim Appenzeller

Managing Editor, Research Journals Katrina L. Kelner

Deputy Editors Barbara R. Jasny, Andrew M. Sugden(UK), Valda J. Vinson, Jake S. Yeston

Research and Insights

SR. EDITORS Caroline Ash(UK), Gilbert J. Chin, Lisa D. Chong, Julia Fahrenkamp-Uppenbrink(UK), Pamela J. Hines, Stella M. Hurlty(UK), Paula A. Kiberstis, Marc S. Lavine(Canada), Kristen L. Mueller, Ian S. Osborne(UK), Beverly A. Purnell, L. Bryan Ray, Guy Riddihough, H. Jesse Smith, Jelena Stajic, Peter Stern(UK), Phillip D. Szurmi, Brad Wible, Nicholas S. Wigginton, Laura M. Zahn **ASSOCIATE EDITORS** Brent Grocholski, Keith T. Smith, Sacha Vignieri **ASSOCIATE BOOK REVIEW EDITOR** Valerie B. Thompson **ASSOCIATE LETTERS EDITOR** Jennifer Sills **CHIEF CONTENT PRODUCTION EDITOR** Cara Tate **SR. CONTENT PRODUCTION EDITOR** Harry Jack **CONTENT PRODUCTION EDITORS** Jeffrey E. Cook, Chris Filiatreau, Cynthia Howe, Lauren Kmec, Barbara P. Ordway, Catherine Wolner **SR. EDITORIAL COORDINATORS** Carolyn Kyle, Beverly Shields **EDITORIAL COORDINATORS** Ramatoulaye Diop, Joi S. Granger, Lisa Johnson, Anita Wynn **PUBLICATIONS ASSISTANTS** Aneera Dobbins, Jeffrey Hearn, Dona Mathieu, Le-Toya Mayne Flood, Shannon McMahon, Scott Miller, Jerry Richardson, Rachel Roberts(UK), Alice Whaley(UK), Brian White **EXECUTIVE ASSISTANT** Anna Bashkurova **ADMINISTRATIVE SUPPORT** Janet Clements(UK), Lizanne Newton(UK), Maryrose Madrid, Laura-Nadine Schuhmacher (UK, Intern), Alix Welch (Intern), John Wood(UK)

News

NEWS MANAGING EDITOR John Travis **INTERNATIONAL EDITOR** Richard Stone **DEPUTY NEWS EDITORS** Daniel Clery(UK), Robert Coontz, Elizabeth Culotta, David Grimm, David Malakoff, Leslie Roberts **CONTRIBUTING EDITOR** Martin Enserink(Europe) **SR. CORRESPONDENTS** Jeffrey Mervis, Elizabeth Pennisi **NEWS WRITERS** Adrian Cho, Jon Cohen, Jennifer Couzin-Frankel, Carolyn Gramling, Eric Hand, Jocelyn Kaiser, Catherine Matacic, Kelly Servick, Robert F. Service, Erik Stokstad(Cambridge, UK), Emily Underwood **INTERNS** Hanae Armitage, Emily DeMarco, Annick Laurent, Laura Olivieri, Juan David Romero **CONTRIBUTING CORRESPONDENTS** Michael Balter(Paris), John Bohannon, Ann Gibbons, Mara Hvistendahl, Sam Kean, Eli Kirsch, Kai Kupferschmidt(Berlin), Andrew Lawler, Christina Larson(Beijing), Mitch Leslie, Charles C. Mann, Eliot Marshall, Virginia Morell, Dennis Normile(Tokyo), Heather Pringle, Tania Rabesandratana(London), Gretchen Vogel(Berlin), Lizzie Wade(Mexico City) **CAREERS** Donisha Adams, Rachel Bernstein **COPY EDITORS** Julia Cole, Jennifer Levin (Chief) **ADMINISTRATIVE SUPPORT** Jessica Williams

Executive Publisher Rush D. Holt

Publisher Kent R. Anderson **Chief Digital Media Officer** Rob Covey

BUSINESS OPERATIONS AND PORTFOLIO MANAGEMENT DIRECTOR Sarah Whalen **BUSINESS SYSTEMS AND FINANCIAL ANALYSIS DIRECTOR** Randy Yi **MANAGER OF FULFILLMENT SYSTEMS** Neal Hawkins **SYSTEMS ANALYST** Nicole Mehmedovic **ASSISTANT DIRECTOR, BUSINESS OPERATIONS** Eric Knott **MANAGER, BUSINESS OPERATIONS** Jessica Tierney **BUSINESS ANALYSTS** Cory Lipman, Cooper Tilton, Celeste Troxler **FINANCIAL ANALYST** Robert Clark **RIGHTS AND PERMISSIONS ASSISTANT DIRECTOR** Emilie David **PERMISSIONS ASSOCIATE** Elizabeth Sandler **RIGHTS, CONTRACTS, AND LICENSING ASSOCIATE** Lili Kiser

MARKETING DIRECTOR Ian King **MARKETING MANAGER** Julianne Wielga **MARKETING ASSOCIATE** Elizabeth Sattler **SR. MARKETING EXECUTIVE** Jennifer Reeves **SR. ART ASSOCIATE, PROJECT MANAGER** Tzeitel Sorrosa **ART ASSOCIATE** Seil Lee **SR. ART ASSOCIATE** Kim Huynh **ASSISTANT COMMERCIAL EDITOR** Selby Frame **MARKETING PROJECT MANAGER** Angelissa McArthur **PROGRAM DIRECTOR, AAAS MEMBER CENTRAL** Peggy Mihelich **FULFILLMENT SYSTEMS AND OPERATIONS** membership@aaas.org **MANAGER, MEMBER SERVICES** Pat Butler **SPECIALISTS** LaToya Casteel, Terrance Morrison, Latasha Russell **MANAGER, DATA ENTRY** Mickie Napoleoni **DATA ENTRY SPECIALISTS** JJ Regan, Brenden Aquilino, Fiona Giblin

DIRECTOR, SITE LICENSING Tom Ryan **DIRECTOR, CORPORATE RELATIONS** Eileen Bernadette Moran **SR. PUBLISHER RELATIONS SPECIALIST** Kiki Forsythe **PUBLISHER RELATIONS MANAGER** Catherine Holland **PUBLISHER RELATIONS, EASTERN REGION** Keith Layson **PUBLISHER RELATIONS, WESTERN REGION** Ryan Rexroth **SALES RESEARCH COORDINATOR** Aiesha Marshall **MANAGER, SITE LICENSE OPERATIONS** Iquo Edim **SENIOR PRODUCTION SPECIALIST** Robert Koepke **SENIOR OPERATIONS ANALYST** Lana Guz **FULFILLMENT ANALYST** Judy Lillibridge **ASSOCIATE DIRECTOR, MARKETING** Christina Schlecht **MARKETING ASSOCIATES** Thomas Landreth, Isa Sesay-Bah

DIRECTOR OF WEB TECHNOLOGIES Ahmed Khadr **SR. DEVELOPER** Chris Coleman **DEVELOPERS** Dan Berger, Jimmy Marks **SR. PROJECT MANAGER** Trista Smith **SYSTEMS ENGINEER** Luke Johnson

CREATIVE DIRECTOR, MULTIMEDIA Martyn Green **DIRECTOR OF ANALYTICS** Enrique Gonzales **SR. WEB PRODUCER** Sarah Crespi **WEB PRODUCER** Alison Crawford **VIDEO PRODUCER** Nguyen Nguyen **SOCIAL MEDIA PRODUCER** Meghna Sachdev

DIRECTOR OF OPERATIONS PRINT AND ONLINE Lizabeth Harman **DIGITAL/PRINT STRATEGY MANAGER** Jason Hillman **QUALITY TECHNICAL MANAGER** Marcus Spiegel **PROJECT ACCOUNT MANAGER** Tara Kelly **DIGITAL PRODUCTION MANAGER** Lisa Stanford **ASSISTANT MANAGER DIGITAL/PRINT** Rebecca Doshi **SENIOR CONTENT SPECIALISTS** Steve Forrester, Antoinette Hodal, Lori Murphy, Anthony Rosen **CONTENT SPECIALISTS** Jacob Hedrick, Kimberley Oster

DESIGN DIRECTOR Beth Rakouskas **DESIGN EDITOR** Marcy Atarod **SENIOR DESIGNER** Garvin Grullón **DESIGNER** Chrystal Smith **GRAPHICS MANAGING EDITOR** Alberto Cuadra **SENIOR SCIENTIFIC ILLUSTRATORS** Chris Bickel, Katharine Sutfiff **SCIENTIFIC ILLUSTRATOR** Valerie Altounian **SENIOR ART ASSOCIATES** Holly Bishop, Nathalie Cary, Preston Huey **SENIOR PHOTO EDITOR** William Douthitt **PHOTO EDITORS** Leslie Blizard, Christy Steele

DIRECTOR, GLOBAL COLLABORATION, CUSTOM PUBLICATIONS, ADVERTISING Bill Moran **EDITOR, CUSTOM PUBLISHING** Sean Sanders: 202-326-6430 **ASSISTANT EDITOR, CUSTOM PUBLISHING** Tianna Hicklin: 202-326-6463 **ADVERTISING MARKETING MANAGER** Justin Sawyers: 202-326-7061 science_advertising@aaas.org **ADVERTISING MARKETING ASSOCIATE** Javia Flemmings **ADVERTISING SUPPORT MANAGER** Karen Foote: 202-326-6740 **ADVERTISING PRODUCTION OPERATIONS MANAGER** Deborah Tompkins **SR. PRODUCTION SPECIALIST/GRAPHIC DESIGNER** Amy Hardcastle **PRODUCTION SPECIALIST** Yuse Lajimnuhup **SR. TRAFFIC ASSOCIATE** Christine Hall **SALES COORDINATOR** Shirley Young **ASSOCIATE DIRECTOR, COLLABORATION, CUSTOM PUBLICATIONS/CHINA/TAIWAN/KOREA/SINGAPORE** Ruolei Wu: +86-186 0082 9345, ruwu@aaas.org **COLLABORATION/ CUSTOM PUBLICATIONS/JAPAN** Adarsh Sandhu + 81352-81-5142 asandhu@aaas.org **EAST COAST/E. CANADA** Laurie Faraday: 508-747-9395, FAX 617-507-8189 **WEST COAST/W. CANADA** Lynne Stickrod: 415-931-9782, FAX 415-520-6940 **MIDWEST** Jeffrey Dembski: 847-498-4520 **3005, Steven Loerch**: 847-498-4520 **x3006 UK EUROPE/ASIA** Roger Goncalves: TEL/FAX +41 43 243 1358 **JAPAN** Katsuyoshi Fukamizu(Tokyo): +81-3-3219-5777 kufukamizu@aaas.org **CHINA/TAIWAN** Ruolei Wu: +86-186 0082 9345, ruwu@aaas.org

WORLDWIDE ASSOCIATE DIRECTOR OF SCIENCE CAREERS Tracy Holmes: +44 (0) 1223 326525, FAX +44 (0) 1223 326532 tholmes@science-int.co.uk **CLASSIFIED** advertise@sciencecareers.org **US SALES** Tina Burks: 202-326-6577 **Nancy Toema**: 202-326-6578 **SALES ADMINISTRATOR** Marc Gallun **EUROPE/ROW SALES** Axel Gesatzki, Sarah Leach **SALES ASSISTANT** Kelly Grace **Japan Hiroyuki Mashiki**(Kyoto): +81-75-823-1109 hymashiki@aaas.org **CHINA/TAIWAN** Ruolei Wu: +86-186 0082 9345 ruwu@aaas.org **MARKETING MANAGER** Allison Pritchard **MARKETING ASSOCIATE** Aimee Aponte

AAAS BOARD OF DIRECTORS RETIRING PRESIDENT, CHAIR Gerald R. Fink **PRESIDENT** Geraldine (Geri) Richmond **PRESIDENT-ELECT** Barbara A. Schaaf **TREASURER** David Evans **SHAW CHIEF EXECUTIVE OFFICER** Rush D. Holt **BOARD** Bonnie L. Bassler, May R. Berenbaum, Carlos J. Bustamante, Stephen P.A. Fodor, Claire M. Fraser, Michael S. Gazzaniga, Laura H. Greene, Elizabeth Loftus, Mercedes Pascual

SUBSCRIPTION SERVICES For change of address, missing issues, new orders and renewals, and payment questions: 866-434-AAAS (2227) or 202-326-6417, FAX 202-842-1065. Mailing addresses: AAAS, P.O. Box 96178, Washington, DC 20090-6178 or AAAS Member Services, 1200 New York Avenue, NW, Washington, DC 20005

INSTITUTIONAL SITE LICENSES 202-326-6730 **REPRINTS:** Author Inquiries 800-635-7181 **COMMERCIAL INQUIRIES** 803-359-4578 **PERMISSIONS** 202-326-6765, permissions@aaas.org **AAAS Member Services** 202-326-6417 or <http://membercentral.aaas.org/discounts>

Science serves as a forum for discussion of important issues related to the advancement of science by publishing material on which a consensus has been reached as well as including the presentation of minority or conflicting points of view. Accordingly, all articles published in Science—including editorials, news and comment, and books reviews—are signed and reflect the individual views of the authors and not official points of view adopted by AAAS or the institutions with which the authors are affiliated.

INFORMATION FOR AUTHORS See pages 678 and 679 of the 6 February 2015 issue or access www.sciencemag.org/about/authors

SENIOR EDITORIAL BOARD

Robert H. Grubbs, *California Institute of Technology*, Gary King, *Harvard University*
Susan M. Rosenberg, *Baylor College of Medicine*, Ali Shalatifard, *Northwestern University*
Feinberg School of Medicine, Michael S. Turner, *U. of Chicago*

BOARD OF REVIEWING EDITORS (Statistics board members indicated with \$)

Adriano Aguzzi, *U. Hospital Zurich*
Takuzo Aida, *U. of Tokyo*
Leslie Aiello, *Wenner-Gren Foundation*
Judith Allen, *U. of Edinburgh*
Sonia Altizer, *U. of Georgia*
Sebastian Amigorena, *Institut Curie*
Kathryn Anderson, *Memorial Sloan-Kettering Cancer Center*
Meinrat O. Andreae, *Max-Planck Inst. Mainz*
Paola Ariotti, *Harvard U.*
Johan Auwerx, *EPFL*
David Awschalom, *U. of Chicago*
Clare Baker, *Caltech*
Jordi Bascompte, *Estación Biológica de Doñana CSIC*
Facundo Batista, *London Research Inst.*
Ray H. Baughman, *U. of Texas, Dallas*
David Baum, *U. of Wisconsin*
Carlo Beenakker, *Leiden U.*
Kamran Behnia, *ESPCI-ParisTech*
Yasmine Belkaid, *NIH/NIDH*
Philip Benfey, *Duke U.*
Stephen J. Benkovic, *Penn State U.*
May Berenbaum, *U. of Illinois*
Gabriele Bergers, *U. of California, San Francisco*
Bradley Bernstein, *Massachusetts General Hospital*
Peer Bork, *EMBL*
Bernard Bourdon, *Ecole Normale Supérieure de Lyon*
Chris Bowler, *Ecole Normale Supérieure*
Ian Boyd, *U. of St. Andrews*
Emily Brodsky, *U. of California, Santa Cruz*
Ron Brookmeyer, *U. of California Los Angeles (\$)*
Christian Büchel, *Hamburg-Eppendorf*
Joseph A. Burns, *Cornell U.*
Carter Tribble Butts, *U. of California, Irvine*
Gyorgy Buzsaki, *New York U. School of Medicine*
Blanche Capel, *Duke U.*
Mats Carlsson, *U. of Oslo*
Ib Chorkendorff, *U. of Denmark*
David Clapham, *Children's Hospital Boston*
David Clary, *U. of Oxford*
Joel Cohen, *Rockefeller U., Columbia U.*
James Collins, *Boston U.*
Robert Cook-Deegan, *Duke U.*
Alan Cowman, *Walter & Eliza Hall Inst.*
Robert H. Crabtree, *Yale U.*
Roberta Croce, *Vrije Universiteit*
Janet Currie, *Princeton U.*
Jeff L. Dangel, *U. of North Carolina*
Tom Daniel, *U. of Washington*
Frans de Waal, *Emory U.*
Stanislas Dehaene, *Collège de France*
Robert Desimone, *MIT*
Claude Desplan, *New York U.*
Ap Dijksterhuis, *Radboud U. of Nijmegen*
Dennis Discher, *U. of Pennsylvania*
Gerald W. Dorn II, *Washington U. School of Medicine*
Jennifer A. Doudna, *U. of California, Berkeley*
Bruce Dunn, *U. of California, Los Angeles*
William Dunphy, *Caltech*
Christopher Dye, *WHO*
Todd Ehlers, *U. of Tuebingen*
David Ehrhardt, *Carnegie Inst. of Washington*
Tim Elston, *U. of North Carolina at Chapel Hill*
Gerhard Ertl, *Fritz-Haber-Institut, Berlin*
Barry Everitt, *U. of Cambridge*
Ernst Fehr, *U. of Zurich*
Anne C. Ferguson-Smith, *U. of Cambridge*
Michael Feuer, *The George Washington U.*
Toren Finkel, *NHLBI, NIH*
Kate Fitzgerald, *U. of Massachusetts*
Peter Fratzl, *Max-Planck Inst.*
Elaine Fuchs, *Rockefeller U.*
Daniel Geschwind, *UCLA*
Karl-Heinz Glassmeier, *TU Braunschweig*
Ramon Gonzalez, *Rice U.*
Julia R. Greer, *Caltech*
Elizabeth Grove, *U. of Chicago*
Nicolas Gruber, *ETH Zurich*
Kip Guy, *St. Jude's Children's Research Hospital*
Taekjip Ha, *U. of Illinois at Urbana-Champaign*
Christian Haass, *Ludwig Maximilians U.*
Michael Hasselmo, *Boston U.*
Martin Heimann, *Max-Planck Inst. Jena*
Yka Helariutta, *U. of Cambridge*
James A. Hendler, *Rensselaer Polytechnic Inst.*
Janet G. Hering, *Swiss Fed. Inst. of Aquatic Science & Technology*
Kai-Uwe Hinrichs, *U. of Bremen*
Kei Hirose, *Tokyo Inst. of Technology*
David Hodell, *U. of Cambridge*
David Holden, *Imperial College*
Lora Hooper, *UT Southwestern Medical Ctr. at Dallas*
Raymond Huey, *U. of Washington*
Auke IJsspeert, *Swiss Fed. Inst. of Tech*
Steven Jacobsen, *U. of California, Los Angeles*
Kai Johnsson, *EPFL Lausanne*
Peter Jonas, *Inst. of Science & Technology (IST) Austria*
Matt Kaeberlein, *U. of Washington*
William Kaelin Jr., *Dana-Farber Cancer Inst.*
Daniel Kahne, *Harvard U.*
Daniel Kammen, *U. of California, Berkeley*
Masashi Kawasaki, *U. of Tokyo*
V. N. Karym, *Seoul National U.*
Joel Kingsolver, *U. of North Carolina at Chapel Hill*
Robert Kingston, *Harvard Medical School*
Etienne Kochlin, *Ecole Normale Supérieure*
Alexander Koldkin, *Johns Hopkins U.*
Leonid Kruglyak, *UCLA*
Thomas Langer, *U. of Cologne*
Mitchell A. Lazar, *U. of Pennsylvania*
David Lazer, *Harvard U.*
Thomas Lecuit, *IDM*
Virginia Lee, *U. of Pennsylvania*
Stanley Lemon, *U. of North Carolina at Chapel Hill*
Ottoline Leyser, *Cambridge U.*
Marcia C. Linn, *U. of California, Berkeley*
Jianglu Liu, *Michigan State U.*
Luis Liz-Marzan, *CIC biomaGUNE*
Jonathan Losos, *Harvard U.*
Ke Lu, *Chinese Acad. of Sciences*
Christian Lüscher, *U. of Geneva*
Laura Machesky, *CRUK Beatson Inst. for Cancer Research*
Anne Magurran, *U. of St. Andrews*
Oscar Marin, *CSIC & U. Miguel Hernández*
Charles Marshall, *U. of California, Berkeley*
C. Robertson McClung, *Dartmouth College*
Graham Medley, *U. of Warwick*
Tom Mistl, *NCI*
Yasushi Miyashita, *U. of Tokyo*
Mary Ann Moran, *U. of Georgia*
Richard Morris, *U. of Edinburgh*
Alison Murray-Reif, *NC State U. (\$)*
Thomas Murray, *The Hastings Center*
James Nelson, *Stanford U. School of Med.*
Daniel Neumark, *U. of California, Berkeley*
Kitty Nijmeijer, *U. of Twente*
Pär Nordlund, *Karolinska Inst.*
Helga Nowotny, *European Research Advisory Board*
Ben Olken, *MIT*
Joe Orenstein, *U. of California Berkeley & Lawrence Berkeley National Lab*
Harry Orr, *U. of Minnesota*
Andrew Oswald, *U. of Warwick*
Steve Palumbi, *Stanford U.*
Jane Parker, *Max-Planck Inst. of Plant Breeding Research*
Giovanni Parmigiani, *Dana-Farber Cancer Inst. (\$)*
Donald R. Paul, *U. of Texas, Austin*
John H. J. Petrini, *Memorial Sloan-Kettering Cancer Center*
Joshua Plotkin, *U. of Pennsylvania*
Albert Polman, *FOM Institute AMOLF*
Philippe Poulin, *CNRS*
Jonathan Pritchard, *Stanford U.*
David Randall, *Colorado State U.*
Colin Renfrew, *U. of Cambridge*
Felix Rey, *Institut Pasteur*
Trevor Robbins, *U. of Cambridge*
Jim Roberts, *Fred Hutchinson Cancer Research Ctr.*
Barbara A. Romanowicz, *U. of California, Berkeley*
Amy Rosenzweig, *Northwestern University*
Jens Rostrop-Nielsen, *Haldor Topsøe*
Mike Ryan, *U. of Texas, Austin*
Mitinori Saitou, *Kyoto U.*
Shimon Sakaguchi, *Kyoto U.*
Miquel Salmeron, *Lawrence Berkeley National Lab*
Jürgen Sandkühler, *Medical U. of Vienna*
Alexander Schier, *Harvard U.*
Randy Seeley, *U. of Cincinnati*
Vladimir Shalae, *Purdue U.*
Robert Siliciano, *Johns Hopkins School of Medicine*
Denis Simon, *Arizona State U.*
Uri Simonsohn, *U. of Pennsylvania*
Alison Smith, *John Innes Centre*
Richard Smith, *U. of North Carolina (\$)*
John Speakman, *U. of Aberdeen*
Allan C. Spradling, *Carnegie Institution of Washington*
Jonathan Sprent, *Garvan Inst. of Medical Research*
Eric Steig, *U. of Washington*
Paula Stephan, *Georgia State U. and National Bureau of Economic Research*
Molly Stevens, *Imperial College London*
V. S. Subrahmanian, *U. of Maryland*
Ira Tabas, *Columbia U.*
Sarah Teichmann, *Cambridge U.*
John Thomas, *North Carolina State U.*
Shubha Tole, *Tata Institute of Fundamental Research*
Christopher Tyler-Smith, *The Wellcome Trust Sanger Inst.*
Herbert Virgin, *Washington U.*
Bert Vogelstein, *Johns Hopkins U.*
Cynthia Volkert, *U. of Göttingen*
Douglas Wallace, *Dalhousie U.*
David Wallace, *Weizmann Inst. of Science*
Ian Walmsey, *U. of Oxford*
Jane-Ling Wang, *U. of California, Davis*
David A. Wardle, *Swedish U. of Agric. Sciences*
David Waxman, *Fudan U.*
Jonathan Weissman, *U. of California, San Francisco*
Chris Wikle, *U. of Missouri (\$)*
Ian A. Wilson, *The Scripps Res. Inst. (\$)*
Timothy D. Wilson, *U. of Virginia*
Rosemary Wyse, *Johns Hopkins U.*
Jan Zaenen, *Leiden U.*
Kenneth Zaret, *U. of Pennsylvania School of Medicine*
Jonathan Zehr, *U. of California, Santa Cruz*
Len Zon, *Children's Hospital Boston*
Maria Zuber, *MIT*

BOOK REVIEW BOARD

David Bloom, *Harvard U.*, Samuel Bowring, *MIT*, Angela Creager, *Princeton U.*, Richard Sweder, *U. of Chicago*, Ed Wasserman, *DuPont*

The promise of neurotechnology

The various brain initiatives for producing new tools, with the goal of advancing neurological therapies, have led to widespread attention on neurotechnology. Perhaps the most exciting aspect of this rapidly expanding field is the prospect of propelling experiments beyond scientific dogma to discover how the brain generates behavior.

A sharper focus on this challenge will help direct the development of tools that can elucidate fundamental operations of the brain.

Generally, contemporary brain research views anatomical connectivity as critical for understanding how the brain works. But there is a growing appreciation that identifying and characterizing structural minutiae cannot, by itself, explain brain function. It is unlikely that the nervous system has modular design principles analogous to those of machines, in which each component performs a discrete operation. When a machine malfunctions, the failed component can be diagnosed because its missing function has clear causal consequences. The rules governing communication between neurons are based on statistics with unknown probabilities, thus invalidating simple causality. Every neuron has multiple functional roles, with each function carried out by many neurons in ways that vary over time. With a system of this complexity, comfortable assumptions about brain mechanisms based simply on brain structure are misplaced. Effective investigation of brain function necessitates moving beyond the structure-function concept in the brain-machine analogy.

This shift in perspective underlies recent progress in neural prosthetics, achieved largely when complexity is not only recognized but used to advantage. These devices are predicated on the idea that individual neurons encode multiple parameters with different strengths, and that movement intention can be decoded from populations of neurons. Population algorithms enable the robust extraction of movement parameters from brain activity, even though they may be poorly encoded by individual neurons. The elucidation of this population

principle, combined with technology for large-scale recordings of single-neuron activity patterns, has led to demonstrations of paralyzed people operating prosthetic devices to replace their lost capabilities. This exciting success, which has now advanced to intentionally driven movement of the arm, wrist, and fingers, is based on a description of how movement parameters are encoded. Still, this description is not enough to truly understand

how the brain controls behavior. For this, we must address the complexity of neuronal interaction that leads to encoding and the way signals converge to generate action.

There can be little doubt that new computational approaches (tools), backed by an increasing capability for recording ever-larger populations of neural signals, will revolutionize neuroscience. Examination of correlated firing within a recorded sample of neurons can help scientists define groups of functionally interacting neurons as well as the so-called latent drivers that induce the correlation. These drivers might arise, for instance, from stimulation acting simultaneously on neurons that work together to begin

a behavior, or they could result from neurons firing in harmony within a specific brain location. Such glimmers of the functional network are exciting to contemplate, because they require no a priori assumption of putative function or assignment to anatomical structure. Rather, studies can begin to describe the joint and conditional probabilities that characterize the fundamental operations of the nervous system.

After the human genome sequence was revealed, researchers found that the nebulous causality between genes and molecular action needed to be addressed before revolutionary disease treatments could be developed. By now directing neuroscience research and technology efforts toward understanding the systematic interactions between neurons and the conditions necessary for these to take place, we can fulfill the promise of new neurological therapies in a timely manner.

— Andrew Schwartz



“... new computational approaches...will revolutionize neuroscience.”



Andrew Schwartz is Distinguished Professor in the Department of Neurobiology and Endowed Chair in Systems Neuroscience at the University of Pittsburgh, Pittsburgh, PA. E-mail: abs21@pitt.edu

“Any scientist or dietitian who is willing to take Coca-Cola funding gets it.”

Marion Nestle, professor of nutrition, food studies, and public health at New York University, to *The New York Times*, on Coca-Cola's release last week of obesity-related research it funds. <http://scim.ag/CokeFunds>

IN BRIEF



The Syrian conflict has prompted the first withdrawal from the Svalbard seed vault.

Syrian researchers to make first seed bank withdrawal

Researchers from the International Center for Agricultural Research In The Dry Areas (ICARDA), formerly based in Aleppo, Syria, will make the first withdrawal from the Svalbard Global Seed Vault, officials for the Global Crop Diversity Trust, which oversees the Svalbard vault, said on 21 September. The Svalbard vault, located on the remote Norwegian island of Spitsbergen, contains a wide variety of plant seeds that are duplicates of seeds in other gene banks, in order to insure against the loss of

those seeds during regional or global crises. The Syrian conflict forced much of ICARDA's staff to flee the country, and the Svalbard seeds will help the center generate material for new seed banks in Lebanon and Morocco, focusing on crops including wheat, barley, and their wild relatives. “It is [ICARDA's] mandate to allow this material to be accessed by scientists, breeders, and farmers,” says the trust's Brian Lainoff. “With no foreseeable future in which there is peace [in Syria], it was important to reestablish collections so they can continue to work.”

AROUND THE WORLD

Unveiling China's nuclear past

HUAIROU, CHINA | A slice of modern China's scientific history that was concealed for 6 decades is now on display to the public for the first time, revealing details of the country's atom bomb program. What was once a top-secret satellite and nuclear weapons R&D facility on the outskirts of Beijing is now a museum run by the Chinese Academy of Sciences. At its peak, more than 17,000 Chinese researchers toiled at the nuclear lab, established in 1958. However, the site was not widely known before it was unveiled this fall,

coinciding with the start of classes at the academy's sprawling Huairou campus. The “two bombs, one satellite” project museum, as it's called, includes documents, photos, and even the names of some key scientists.

Cancer test draws FDA warning

SILVER SPRING, MARYLAND | The U.S. Food and Drug Administration (FDA) has called out genetic testing company Pathway Genomics for failing to seek its approval before marketing a blood test to screen for various cancers in healthy people. Pathway's CancerIntercept Detect service, which costs between \$299 and \$699, relies

on liquid biopsy, a relatively new screening approach that identifies DNA from circulating tumor cells in blood. The company maintains that the test can be legally marketed under separate regulations governing laboratory-developed tests, because a physician must agree to order the test, and Pathway returns any positive results indicating the presence of cancer through a person's doctor. But in a 21 September warning letter, FDA told the company that the test's blood collection tubes constitute a medical device, and called the product “a high risk test that has not received adequate clinical validation and may harm the public health.”

Spacetime ripple hunt resumes

LIVINGSTON, LOUISIANA | The quest for gravitational waves—ripples in space and time that emanate from stellar sources—is once again underway. Last week, physicists working with the Laser Interferometer Gravitational-Wave Observatory (LIGO) began their first observing run since they rebuilt their instrument in Livingston, and its twin in Hanford, Washington. Although the original LIGO, which ran from 2002 to 2010, could detect a pair of neutron stars spiraling into each other from 65 million light-years away, advanced LIGO should eventually detect such sources out to 650 million light-years, researchers say. Right now, however, the LIGO interferometers are sensitive enough to see such binary neutron stars to just between 200 million and 260 million light-years—already a factor of three improvements over the original LIGO. Even so, there's only a small chance that it will spot anything in this first 3-month data-collection run. <http://scim.ag/LIGOhunt>

Shell abandons Arctic offshore

WAINWRIGHT, ALASKA | Oil giant Royal Dutch Shell has announced that it will abandon oil drilling in the Arctic's Chukchi Sea “for the foreseeable future,” citing “the high costs associated with the project, and the challenging and unpredictable federal regulatory environment in offshore Alaska.” The exploratory well the company drilled this summer, Shell says, did not yield sufficient oil and gas to justify its \$7 billion price tag. Supporters of offshore Arctic drilling are disappointed, whereas environmentalists say Shell's decision is a win for the region and the global climate. Shell has also spent some \$15 million since 2010 on environmental studies managed by native governments



Shell's Polar Pioneer drilling rig (in Seattle in May).



Scientists have found a new species of hadrosaur that lived in the Arctic (here in an artist's impression).

Duck-billed dino thrived in Arctic

Scientists have discovered the fossilized bones of a new dinosaur species that apparently flourished in what is now northern Alaska. The creature, a type of duck-billed dinosaur, or hadrosaur, was abundant in the region about 70 million years ago. More than 6000 bones from the species—more than any other Alaska dinosaur—were collected from a site called the Prince Creek Formation, and have been excavated and categorized, the study's authors reported in *Acta Palaeontologica Polonica*. The team named the new species *Ugrunaaluk kuukpikensis*, which means “ancient grazer” in Inupiaq, the language of Alaska Inupiat Eskimos. Although the creatures would have experienced periods of winter darkness and possibly snow, temperatures in the region were warmer than they are today, averaging in the low 40s, and fossilized pollen evidence suggest the dinosaurs lived in a conifer forest. The find builds support for the idea that some dinosaurs were adapted to the cooler temperatures of the Arctic, the researchers say.

in Alaska (*Science*, 21 August, p. 778). The fate of those programs is not known, said Alex Whiting, an environmental official with the native village of Kotzebue, which has received funding under the Northwest Arctic Borough's partnership with Shell. “I wouldn't be surprised, though, if they kept it going just in case they decided to return to the region,” he says.

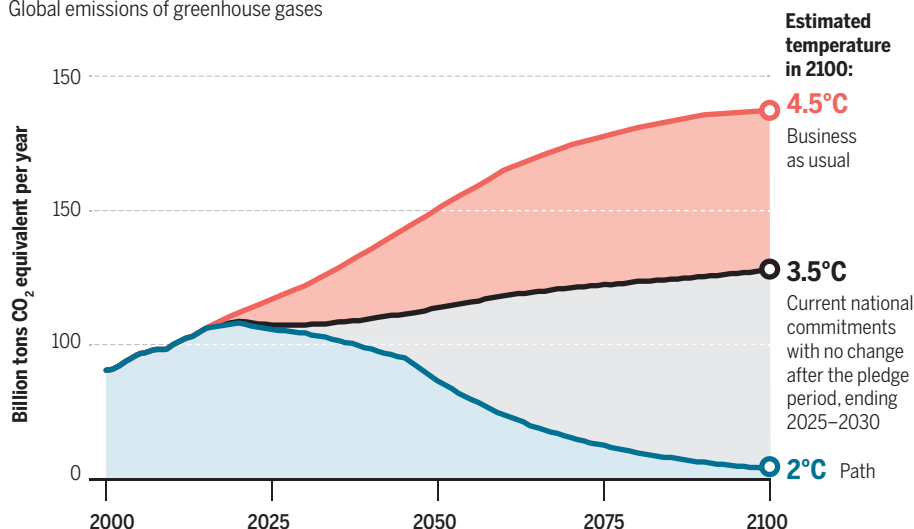
\$100 million in new BRAIN funds

WASHINGTON, D.C. | The Kavli Foundation and several university partners announced \$100 million in new funding for neuroscience research this week, including three new institutes at Johns Hopkins University, The Rockefeller University, and the University of California, San Francisco. Each institute will receive a

\$20 million endowment supported equally by their universities and the foundation, along with startup funding, to pursue projects in areas such as brain plasticity and tool development. The new funding, geared at providing stable support for high-risk, interdisciplinary research, “more than meets the commitment” of \$40 million made by the Kavli Foundation to the national Brain Research through Advancing Innovative Neurotechnologies Initiative, launched by President Barack Obama in 2013, Robert Conn, president and CEO of the Kavli Foundation, said in a press release. “The establishment of three new institutes, along with the added investment in our existing neuroscience institutes, will further empower great scientists to help write the next chapter in neuroscience.”

How much warming by 2100?

Global emissions of greenhouse gases



Climate pledges not enough to curb warming

Current national commitments to cut greenhouse gases would likely allow average global temperatures to rise by 3.5°C by 2100, suggests a new analysis conducted by the nonprofit group Climate Interactive and released this week. That is well above the 2°C rise deemed safe by many policymakers and researchers. The analysis, appearing roughly 2 months ahead of a United Nations meeting in Paris intended to finalize a new global climate deal, focuses on emissions targets pledged to date by more than 70 nations, which are together responsible for about 65% of the world's emissions. The new model assumes annual emissions will remain flat for the remainder of the century after 2025 to 2030; nations will neither do more to clamp down on annual emissions, nor allow them to rise. But that would translate to steadily rising temperatures as carbon pollution continues to accumulate in the atmosphere (red curve), and failure to reach the goal of holding warming to 2°C (blue curve). <http://scim.ag/warmpledge>

China debuts new launch vehicle

XINZHOU, CHINA | China has debuted its latest rocket: the Long March 6. Designed primarily to take microsatellites to low-Earth orbit, the rocket blasted off on 20 September from Taiyuan Satellite

Launch Center in northeastern China with a payload of 20 small satellites, some of which were student-built technology demonstrations. The success of Long March 6 sets the stage for China's largest planned rocket, the Long March 5, which is expected to debut next year using the



same core engine as the Long March 6. The Long March 5 is considered pivotal for China's plans for planetary exploration; the Chang'e 5 lunar sample return mission, for instance, is expected to be launched aboard a Long March 5 in 2017.

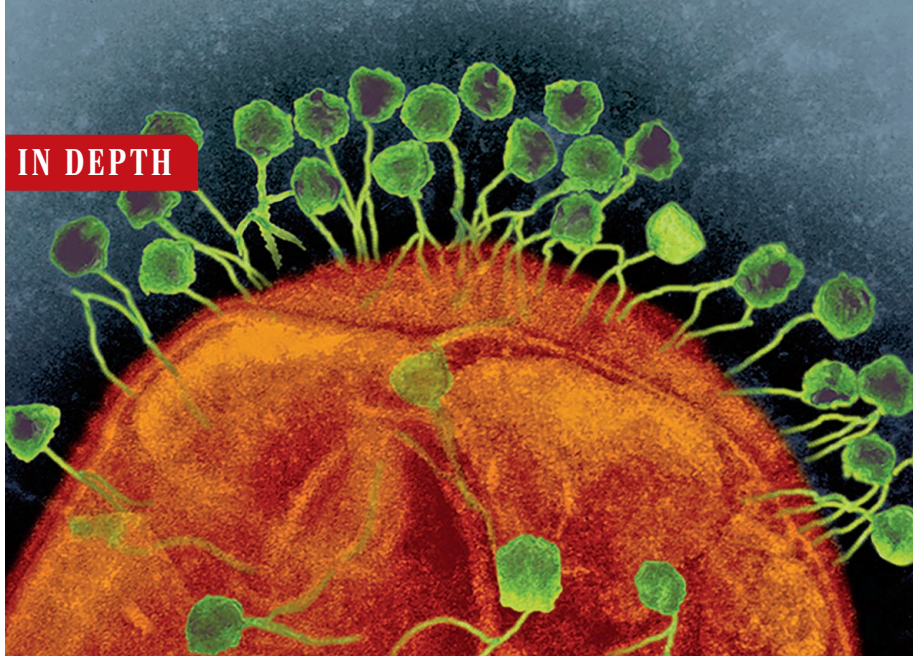
NEWSMAKERS

Novartis taps new R&D head

The world's largest drug company by sales has chosen a prominent Harvard physician-scientist to head its research and development operation. Hematologist and cancer researcher **James Bradner** of Dana-Farber Cancer Institute and Harvard Medical School will take over as president of the Novartis Institutes for BioMedical Research next March, the company announced last week. Bradner has investigated new drug candidates that target cancer gene pathways with a focus on blood cancers, and has been a strong proponent of open-source drug discovery. He gained attention in 2010 by deciding not to patent his discovery of a compound called JQ1, which inhibits proteins known as bromodomains that are known to malfunction in some cancers. Bradner will replace Mark Fishman, who has held the position for 13 years but has reached the company's mandatory retirement age.

Minister accused of plagiarism

A cabinet member often tagged as German Chancellor Angela Merkel's heir apparent is the latest politician to be tripped up by the country's plagiarism sleuths. Last week, the website VroniPlag Wiki published an analysis of German defense minister **Ursula von der Leyen's** 1990 dissertation on the diagnosis of infections in pregnant women. The group found plagiarized passages on 27 of the dissertation's 62 pages. Von der Leyen, who practiced as a gynecologist before entering politics, told the German press that she rejected the accusation of plagiarism, and had already asked the Hannover Medical School, which awarded her medical degree, to examine the publication. The university confirmed in a statement that it has begun a formal inquiry by the school's commission for good scientific practice. Since 2011, at least a dozen German politicians have had their degrees reviewed, and often revoked, following plagiarism accusations. Two of Merkel's previous cabinet members resigned in the face of plagiarism scandals: defense minister Karl-Theodor zu Guttenberg and minister of education and research Annette Schavan. <http://scim.ag/vonderLeyen>



A bacterium (red) defends against DNA inserted by viruses (green) with a RNA-enzyme complex that scientists have turned into a genome-editing tool.

BIOLOGY

New proteins may expand, improve genome editing

Mining bacterial immune systems yields two new editing tools and has the potential to contribute many more

By Elizabeth Pennisi

Three years ago, bioinformatics expert Daniel Haft was slogging through databases of microbial DNA sequences when he and his colleagues identified what appeared to be a group of genes with no clear function. They gave one of these genes the uninspired name *Cpf1*. “I was not thinking, ‘And here is the next great tool for custom editing eukaryotic genomes!’” recalls Haft, now at the National Center for Biotechnology Information in Bethesda, Maryland.

But that’s just what *Cpf1* may prove to be, according to one of the pioneers of CRISPR, a fast-developing technology for deleting, adding, or altering stretches of DNA. At a meeting last week, and in the 24 September issue of *Cell*, Feng Zhang, a molecular biologist from the Broad Institute and the McGovern Institute for Brain Research at the Massachusetts Institute of Technology in Cambridge, offered data suggesting that the DNA-cutting enzyme

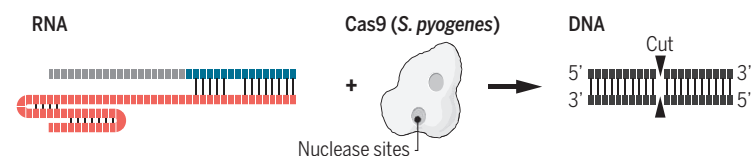
encoded by the gene Haft’s group identified could make CRISPR simpler, more effective, and more powerful.

Researchers believe the enzyme is a harbinger of a wave of other genome-surgery molecules waiting to be identified in bacteria. “There are hundreds of variations of CRISPR,” says David Weiss, a microbiologist at Emory University in Atlanta, and each “may offer unique advantages that could be harnessed for genome editing.”

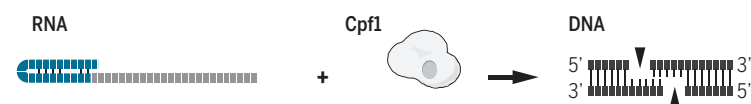
CRISPR 2.0

The CRISPR genome-editing system typically combines a DNA-cutting enzyme called Cas9 with a long RNA molecule, but a protein called Cpf1 requires less RNA and slices DNA differently.

Standard CRISPR-Cas9



CRISPR-Cpf1



Indeed, at the same Cold Spring Harbor Laboratory conference Zhang attended, another scientist described a different bacterial protein that could also expand CRISPR’s capabilities.

Standing for Clustered Regularly Interspaced Short Palindromic Repeats, CRISPR exploits a natural process by which bacteria defend themselves against foreign DNA—from invading viruses, for example. The bacteria create protein-RNA complexes in which the RNA serves to recognize the DNA, and the protein, an enzyme called a nuclease, excises the interloper genetic material, often with the help of other molecules. Researchers once thought the system was too complicated to harness for genome editing, but they eventually discovered a simple nuclease called Cas9 didn’t need much help beyond some RNAs (*Science*, 23 August 2013, p. 833). Already that tool, CRISPR-Cas9, has given researchers faster or easier ways to modify the DNA of crops and animals, conduct biomedical experiments, and most controversially, genetically engineer human embryos.

But CRISPR-Cas9 “is not perfect,” says Rotem Sorek, a microbiologist at the Weizmann Institute of Science in Rehovot, Israel. Among other problems, the nuclease, Cas9, can make mistakes, altering genes other than its target. And the standard Cas9 used in CRISPR is a relatively large protein, which makes it challenging to put into the cells being modified. “Looking for alternatives is important,” says Shiraz Shah, a bioinformatician at the University of Copenhagen.

That’s what Zhang and his colleagues did. Led by Eugene Koonin, a bioinformatician at the National Center for Biotechnology Information, the team combed through GenBank, the popular archive of DNA sequences, and concluded that bacteria wield as many as five different forms of CRISPR, each with a distinctive family of nucleases. Koonin and Zhang suspected that one of those, the Cpf1 family, might need even less RNA to edit genes than does the Cas9 enzyme family.

Koonin, Zhang, and their colleagues initially identified 46 different Cpf1 genes in GenBank. Zhang’s team went on to demonstrate that two worked in human cells,

cutting every gene they were targeted to. Cpf1 “is another breakthrough,” for genome editing, says Stan Brouns of Wageningen University in the Netherlands, who studies CRISPR systems.

Cpf1 differs from Cas9 in a few key ways, Zhang’s team showed. For either protein to start cutting DNA, the target DNA needs to be flanked on one end by a so-called PAM sequence. Cas9 requires a PAM that contains guanine and cytosine bases; in contrast, Cpf1 prefers two thymines in a row. Thus, a CRISPR system using Cpf1 could expand the overall number of modifiable genes. “There is a need for a collection of different proteins so that cuts can be placed anywhere,” says George Church, a Harvard University geneticist. Cpf1 could be particularly useful in manipulating the genomes of organisms—including humans and the malaria parasite *Plasmodium falciparum*—that are rich in thymines.

In addition, Cpf1 requires RNA half as long as that needed by Cas9. That’s a “clear advance,” says Rodolphe Barrangou, a molecular biologist at North Carolina State University in Raleigh, because it eases the task of synthesizing the gene-editing complex. And while Cas9 cuts straight across double-stranded DNA, Cpf1 makes a “staggered cut,” such that one strand of the double helix is five bases longer than the other one (see diagram, p. 16). The effect of this jagged end is unclear: It may enable more accurate editing, particularly in the nondividing cells common in the body and the brain, but it could also alter the ratio of the two types of DNA repair mechanisms involved, leading to a less precise repair, Barrangou says.

Don’t count out Cas9 just yet. The protein comes in many versions, and at least one, from a bacterium that can cause meningitis, can also work without a long guide RNA, says Erik Sontheimer, a molecular biologist from the University of Massachusetts Medical School in Worcester. At the meeting, he reported that this Cas9 also cut DNA attached to RNA, an unusual ability that may prove useful for some types of editing. (The work will appear later this month in *Molecular Cell*.)

“Time will tell” how useful these latest nucleases will become for genome editing, says Jennifer Doudna, a biochemist and CRISPR pioneer at the University of California, Berkeley. For example, Cpf1’s target specificity remains unclear. Eventually, Barrangou predicts, each one will carve out its own genome-editing niche. Further probing of the weapons used by bacterial immune systems is sure to yield still other instruments, Sontheimer says. “Some as-yet-undiscovered defense strategies may provide molecular tools that we can’t even envision.” ■

Q&A

Talking science and God with the pope’s new astronomer

Guy Consolmagno, director of the Vatican Observatory, wants to show that religion can support astronomy

By Edwin Cartledge, in Rome

On 18 September, Pope Francis appointed Jesuit brother Guy Consolmagno as the new director of the Vatican Observatory, which employs a dozen astronomers to study asteroids, meteorites, extrasolar planets, stellar evolution, and cosmology. The observatory is based at the pope’s summer residence south of Rome and operates a 1.8-meter telescope in Arizona, where the skies are clearer.

Consolmagno, 63, grew up in the Detroit, Michigan, area and has a Ph.D. in planetary science. He carried out postdoctoral research

starving. I didn’t have an answer so I went off to Africa with the U.S. Peace Corps. Then I discovered that as soon as I said I was an astronomer, people wanted to know more. They didn’t have running water but they wanted to look through a telescope.

Being able to see the sky is something that makes us human. Our souls have to be fed every bit as much as our stomachs. That realization made me come back and teach astronomy. To my mind, the Vatican supports astronomy because it is an important part of being human. Indeed, we have summer outreach programs every 2 years to take astronomy to people in the developing world who don’t usually get to experience it.

Q: When was the observatory created?

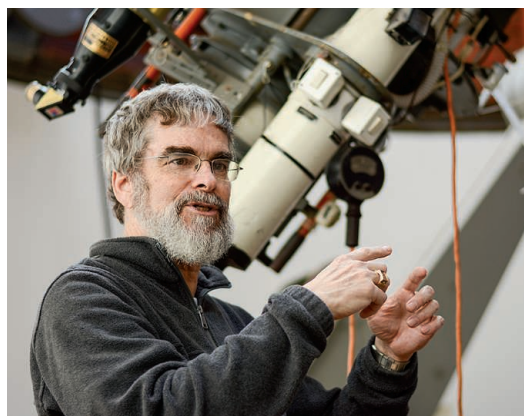
A: Its roots go back to Pope Gregory XIII’s reform of the calendar in the 16th century, which needed input from astronomers. But it was in the 1890s that Leo XIII founded the institution, to show that science and religion were not opposed to one another, unlike the popular impression given by the Galileo affair. It was also intended to underline the Vatican’s status as an independent country. So its creation came down to a little bit of politics and a little

bit of church teaching.

You have to remember that the geneticist Gregor Mendel was a monk, while the reigning Big Bang theory of cosmology was devised by a Catholic priest named Georges Lemaître. As scholars, we are open to go wherever the science leads us. Indeed, my job is simply to do good science. We have no agenda beyond that.

Q: How much interest does the current pope take in science?

A: The previous director of the Vatican Observatory, José Funes, was Argentinian. When thinking of becoming a Jesuit, he asked a senior member of the order whether he should join then or complete his studies in astronomy first; he was advised to finish studying. The Jesuit who gave that



“My job is simply to do good science,” Consolmagno says.

and taught astronomy before becoming a Jesuit in 1989. Four years later, he joined the Vatican Observatory, where he studies meteorites and asteroids. “Guy is a true all-around scientist,” says Daniel Britt, an astronomer at the University of Central Florida in Orlando, who has worked with Consolmagno. “He is always willing to learn, and willing to take the risks associated with breaking new ground. On top of all that he is one of the best public speakers I have ever seen.”

This interview has been edited for clarity and brevity.

Q: Why does the Vatican do astronomy?

A: Years ago, when I was a postdoctoral researcher at the Massachusetts Institute of Technology [in Cambridge], I asked myself why I was doing astronomy when people are

advice was Jorge Bergoglio, who is now Pope Francis. Francis, who has a background in chemistry, was encouraging Jesuits to be astronomers 30 years ago.

Q: Have Vatican astronomers made major contributions to science?

A: I think so, but those contributions are a little bit different to those of other scientists. It's not that we have an ideology or are getting things through divine inspiration, but we don't have a 3-year grant cycle to worry about. Typically, we do survey work, which is painstaking and sometimes tedious. For example, in the 1930s the observatory opened a laboratory to measure the spectral lines of metals, and the data it produced are used to interpret stellar spectra to this day.

We also have one of the world's largest collections of meteorites. We catalog their physical and chemical properties and study how small bodies in the solar system form and evolve. It isn't going to make the front page but it provides data that everybody else uses.

Q: Does God get in the way of doing good astronomy?

A: Just the opposite. He is the reason we do astronomy. I would say that is true even if you don't believe in God. We do it first of all because we can, because the universe acts according to laws. That is a religious idea. The Romans, on the other hand, believed in nature gods that intervene according to whim—but if you believe in that you can't be a scientist. Believing in a supernatural god is different.

You also have to believe that the universe is real and not an illusion. You have to believe that the universe is so good that it is worth spending your life studying it, even if you don't become rich or famous. That sense that gets you up every morning is the presence of God.

Q: What do you hope to achieve as director of the Vatican Observatory?

A: First of all, I want to provide space for other astronomers to do their work. And I also want to show the world that religion supports astronomy. It is often religious people who most need to see that; they need to know that astronomy is wonderful and that they shouldn't be afraid of it. I often quote John Paul II, when he said [of evolution] that "truth cannot contradict truth." If you think you already know everything about the world, you are not a good scientist, and if you think you know all there is to know about God, then your religious faith is at fault. ■

Edwin Cartlidge is a science writer in Rome.



BIOTECHNOLOGY

Europe's rifts over transgenic crops deepen at key deadline

Policy differences among 28 E.U. member states come into sharper focus in the wake of major reform

By **Tania Rabesandratana**

reece's fiscal problems and a massive refugee crisis have laid bare deep rifts in the European Union, leading to bitter policy disputes and the reappearance of border controls eliminated years ago. A quieter rift is deepening on the issue of genetically modified (GM) crops, which many Europeans reject. An E.U. directive that took force in April essentially allows countries to bypass E.U.-wide authorizations for these crops and set their own rules. This week marks the deadline for countries to file their first plans to keep GM crops out—an exercise that has brought the fractures between pro- and anti-GM governments into full view.

The new directive has "split the E.U. policy landscape, with a great number of countries completely out" against GM plants, says Franziska Achterberg, an E.U. food policy director at Greenpeace in Brussels, a staunch opponent of genetic modification in agriculture. But by ending years of deadlock, some hope it could also smooth the way for more research and commercialization of GM crops.

Under the new rules, individual countries can reject particular GM crops for cultivation on their land—even if they have been judged safe by the European Food Safety Authority (EFSA) and approved by the European Commission (*Science*, 12 December 2014, p. 1280). One route—Option 1, in E.U. parlance—is to ask seed manufacturers not to seek authorization to sell specific seeds in their territories. Member states have until 3 October to send such demands through the European Commission for four GM crops that are either already on the market, or have received EFSA's green light but are still pending. (All are GM maize products; only one of them, Monsanto's MON810, is currently grown in the European Union.)

As *Science* went to press, nine member states out of 28, plus the regional government of Wallonia in Belgium, had submitted Option 1 requests (see map, p. 19). In a sign of the depth of their opposition to GM crops, these countries also asked the companies to exempt them from another four types of GM maize products that haven't even been reviewed by EFSA yet. "They are including crops that are far from being approved, say-

PHOTO: © JIM RICHARDSON/CORBIS

Downloaded from www.sciencemag.org on October 30, 2015



Many E.U. countries want to nothing to do with GM crops such as this maize variety bred in a Monsanto lab.

ing ‘we want none of that,’” Achterberg says. “Our position is very strict: We would like to keep our territory free from [GM crops],” says Juris Zinārs, a representative of the Ministry of Agriculture of Latvia.

Other countries that generally shun GM crops, such as Germany and Italy, might still use Option 1 by this week’s deadline. They could also take another route, Option 2: introducing national bans, either for individual crops or for groups of products, on all or part of their country’s territory. This route doesn’t come with a deadline attached, but it does require a country to invoke “compelling grounds” that do not contradict EFSA’s scientific risk assessment.

A government could pursue Option 2, for instance, by arguing that it wants to develop its organic farming sector, or that the measures recommended by EFSA to reduce the exposure of sensitive insects to a GM maize’s pollen are impractical. Companies would be free to challenge those arguments in court; France, for one, lost several court cases after it tried to ban GM crops before the current reform.

Option 1 is “easy and quick,” says Zinārs of Latvia, one of the first countries to use it. Seed manufacturers have 30 days to respond, and in Latvia’s case they have already agreed to honor the country’s requests, either explicitly or tacitly. But Greenpeace advises EU states to use Option 2, because it does not rely on manufacturers’ decisions to eliminate GM crops and might provide farmers, beekeepers, and others with more certainty.

Advocates of GM crops have described this year’s reform as a blow to science-based regulation in the European Union, but some

hope that it will have a positive side effect. Until now, the bickering between member states often meant that authorization procedures at the European level were blocked for years. Now that countries can opt out, pan-European approvals might happen more quickly. “We hope that the new rules will speed up the decision-making process,” says a diplomatic source at Spain’s permanent representation to the European Union in Brussels. (Spain is one of the few European countries that grows GM maize.)

The reform might also make it easier for GM research to be carried out in Europe. “In Spain’s case, the difficulty to make decisions at the European level has meant a significant drop in field trials and research on GM plants in our country,” the Spanish diplomat says. Indeed, Europe’s broad rejection of GM crops has been “deadening” for applied GM research, says Mike Bevan, a plant biologist and deputy director of the John Innes Centre in Norwich in the UK. Europe is a “marvelous [place] to do basic research; there is a reasonable level of funding and [researchers] are well connected to each other,” says Bevan, who

comes from New Zealand. But “ultimately, it’s frustrating” that this work doesn’t find an outlet in Europe, he adds.

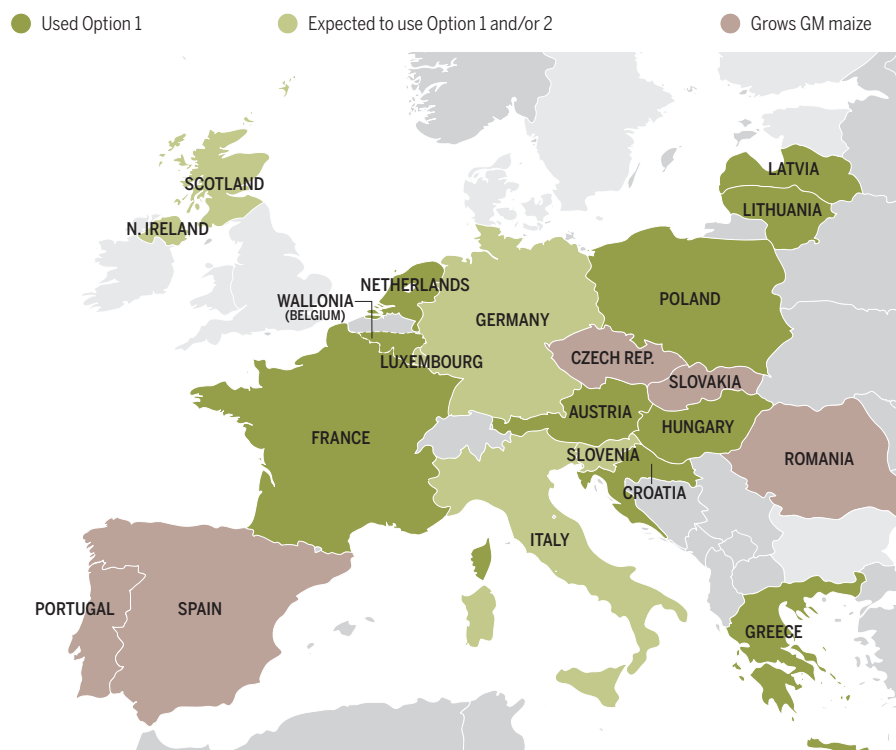
It may be too late for a turnaround, however. Several agricultural biotech firms have already given up on developing GM crops for Europe. “Our business is focused almost entirely on traditional seeds,” says Mark Buckingham from Monsanto UK. Some European scientists are still doing interesting GM science, Buckingham adds, but any new crops based on it would be marketed elsewhere in the world, he predicts.

Meanwhile, the European Commission is trying to extend the “renationalization” approach to another, much bigger GM business: food and animal feed imports. Earlier this year, the Commission proposed similar opt-out options for the authorization of these products, which are currently regulated at the European level. Although consumers and governments widely reject GM cultivation, the European Union imports about 60 kilograms of GM soybean products per person per year, mainly to feed livestock, says EuropaBio, an industry group in Brussels.

The European Parliament is expected to vote on this subject later this month. If the proposal passes, it would be yet another recognition that some chasms on the continent are simply too wide to bridge. ■

A fractured continent

As *Science* went to press, 10 governments had asked seed manufacturers to keep GM crops out. Others were considering the same, or Option 2, a national ban.





A fog of x-ray emitting gas fills the center of our galaxy, where physicists have sought a dark-matter signal.

PARTICLE PHYSICS

Have physicists seen the dying flash of dark matter?

Dark particle decays could explain tantalizing x-ray signal seen in multiple galaxies, including our own Milky Way

By Edwin Cartlidge

Dark matter, by definition, can't be seen directly—except perhaps when it dies. For years, scientists have scanned the skies for signals given off by the decay or mutual annihilation of these elusive particles, which make up fully 80% of the matter in the universe. They've seen nothing definitive, but physicists are now reporting a new candidate: a peak in x-ray emission at an energy of 3.5 thousand electron volts (keV).

After many inconclusive claims, this one may be testable, they and other researchers say, by an upcoming satellite mission. "The 3.5-keV x-ray signal has a real chance of being definitively confirmed as dark matter in a few years, unlike other putative signals currently on the market," says Jonathan Feng, a particle theorist at the University of California (UC), Irvine. If it is from dark matter, the signal will give physicists their first direct handle on what the elusive stuff might consist of.

To date, theorists' leading dark matter candidate has been so-called weakly interacting massive particles (WIMPs)—hypothetical massive particles that don't interact with light and other electromagnetism but do respond to gravity and the weak nuclear force. Laboratory experiments haven't spotted WIMPs, however, and the gamma rays that some scientists believe could be coming from the annihilation

of WIMPs in the centers of galaxies might simply be the radiation given off by more prosaic sources, such as hot gas.

Particle physicist Alexey Boyarsky of Leiden University in the Netherlands and colleagues went after a different quarry: x-ray signals from the decay of hypothetical particles that would be much lighter than WIMPs. They scoured data from the European Space Agency's XMM-Newton orbiting x-ray observatory for signs of particles weighing a few keV—a millionth of the mass of WIMPs. The group started its search in 2005, and last year they finally got lucky, finding the 3.5-keV peak in the x-ray spectrum from both the Milky Way's nearest neighbor, the Andromeda Galaxy, and the Perseus galaxy cluster. Another group—physicist Esra Bulbul of the Harvard-Smithsonian Center for Astrophysics in Cambridge, Massachusetts, and colleagues—also reported finding an emission line at about 3.5 keV in the combined spectra from 73 galaxy clusters.

Now, in a paper accepted for publication in *Physical Review Letters*, Boyarsky's group reports a similar peak in x-rays from the core of the Milky Way. The intensity of the peak lies in the right range to be produced by dark matter reactions, the researchers say: It implies a density of dark matter higher than a lower limit inferred from measurements of galaxy clusters, but lower than a ceiling calculated from studies of the Milky Way's outer regions. "The

signal passes a very nontrivial consistency check," Boyarsky says.

Some other researchers are skeptical. Physicist Ondrej Urban of the Kavli Institute for Particle Astrophysics and Cosmology at Stanford University in Palo Alto, California, and his colleagues say they don't see any real evidence of the 3.5-keV signal in spectra of four galaxy clusters, including Perseus, from the NASA/Japanese space agency Suzaku x-ray satellite. And physicists Tesla Jeltema and Stefano Profumo of UC Santa Cruz say that even if the 3.5-keV line is real, it could easily come from something less exotic than dark matter: the x-rays given off when ions of potassium and other elements blasted into space by supernovae collide, exciting their remaining electrons.

To try and settle the matter, Boyarsky and his colleagues have booked observing time on XMM-Newton, which will let them study the x-ray spectrum of a dwarf galaxy thought to harbor lots of dark matter but very little normal matter. "If we see the signal there, it would be very hard to interpret it in terms of normal astrophysics," he says. "That would constitute very solid proof of dark matter." The ultimate test, however, could come from a new x-ray satellite called ASTRO-H, which Japan plans to launch next year. ASTRO-H will be able to plot the shape of the 3.5-keV peak in much more detail than current satellites can, Feng says. A relatively broad line, he explains, would imply that the x-rays are due to dark matter, because the emissions from the fast-moving particles are expected to be Doppler-shifted. A narrower line, in contrast, would point to normal matter as the source.

If dark matter is the cause, physicists will still need to pin down its identity. Feng says the energy and intensity of the 3.5-keV line are "just as would be expected" from sterile neutrinos: hypothetical ultraelusive cousins of ordinary neutrinos that would give off x-rays when decaying into normal neutrinos.

Cosmologist Kevork Abazajian at UC Irvine says that sterile neutrinos are plausible but that other hypothetical particles could also produce the signal. He says that ground-based measurements of β -decay—the same radioactive process that yielded the first hints that neutrinos exist—could settle whether keV-scale sterile neutrinos really exist, and whether astronomers may be seeing their dying light. ■

Edwin Cartlidge is a science writer in Rome.

Holland's giant wavemaker has splashy debut

Delta Flume will allow researchers to study how coastal defenses fare against powerful surf

By **Martin Enserink** in Delft, the Netherlands

Dutch scientists are making waves—big ones. A new experimental facility at Deltares, a research institute here, has begun producing the largest manmade waves in the world. Like kids building sand castles below the tideline, scientists will let the walls of water crash on dikes of different designs and other structures—sometimes until they're destroyed.

The Delta Flume, which officials will inaugurate on 5 October, is a 300-meter-long water-filled trough that's 9.5 meters high and 5 meters wide. At one end sits a gigantic metal plate called a wave board; four pistons move it back and forth to whip up the kind of waves that the sea can unleash. The waves travel along the flume and crash on to whatever researchers have built at the other end—which could include a novel type of dike, an artificial sand dune or gravel beach, or a pylon used to hold up an offshore wind turbine.

More than half of the Netherlands is below sea level and a 1953 flood killed more than 1800 people, which is why this small country is obsessed with keeping its 3000 kilometers of primary flood defenses up to date. But Deltares hopes that foreign researchers, governments, and private contractors will also find their way to the Delta Flume, says Marcel van Gent, who heads a team of 35 scientists and consultants at the institute.

"It's a very nice facility," says Javier López Lara, a coastal engineer at the Environmental Hydraulics Institute "IH Cantabria" in Santander, Spain. He predicts that the wavemaker will be "of great importance in our field for many reasons." Coastal defenses are becoming more important as sea levels rise, he notes, and the flume will also provide new insights into natural processes such as sediment transport along

shorelines, and the mechanical properties of coastal soils, López Lara says.

Other countries have large wave facilities as well, although the exact design differs from one to the next. Japan's Port and Airport Research Institute, for instance, has a flume to mimic tsunamis, built to generate one wall of water instead of a steady onslaught of waves.

The new Dutch flume replaces an older, smaller version that will be retired after 35 years of service. The Delta Flume boasts bigger waves; the maximum significant wave height—a measure of a storm's intensity—is 2.2 meters, but individual waves may top out

at 4.5 meters. There are other innovations as well, such as radar and laser systems to measure wave heights at any location.

The facility needs to be so big because in hydraulic engineering, small-scale models often aren't good enough. A few structures, such as breakwaters built of rock, can be studied using miniature versions, but materials such as sand, clay, and grass behave differently in small-scale models than in the real world, Van

Gent says. The flume will allow researchers to build realistic, 1:1 scale models of 85% of Dutch coastal defenses.

Plenty of studies are on the drawing board, Van Gent says. Engineers have begun developing so-called nature-based coastal protection, such as willow forests. Such "living shorelines" have been shown to do well under many circumstances, but an experiment in the Delta Flume might be the only way to show how they behave during very rare and very powerful storms. Another area that has not been studied much is how dikes behave after their coverings have eroded away. The dike's core—often made of sand and clay—may still withstand the water for some time. That means "you might have a damaged dike, but not a flood," Van Gent says. "That's important to know." ■



The new facility is 300 meters long and boasts waves as high as 4.5 meters.



THE STORM KING

A mysterious tropical weather pattern called the Madden-Julian oscillation fuels El Niños and triggers rain, heat waves, and hurricanes around the globe

By Eric Hand

The clouds swelled over the Indian Ocean, forming a herd that lumbered east along the equator, bringing days of wind and rain wherever it went. By March, the clouds had reached the Pacific, east of New Guinea, and piled up to the stratosphere in a mass thousands of kilometers across.

Westerly gusts, nearing the force of tropical storm winds, swept warm water into a mound that barely rose above the surface but jutted deeply into cold waters 100 meters down. The enormous bulge of tropical water rolled eastward toward South America, like an upside-down tidal wave.

In May, a second rain and wind event plowed into the western Pacific, shouldering another massive slug of warm water eastward. In July, yet another disturbance thundered through.

When this trio of weather events began early last spring, warm waters were already gathering on the far side of the Pacific, off the coast of Peru—the beginnings of the global weather phenomenon known as El Niño. But it was a weak start. The three extra pulses of warm water turned this El Niño into a beast: It is now the strongest since 1997 and may end up being the most severe on record. It has already boosted hurricane activity in the Pacific Ocean, tamped it down in the Atlan-

tic, and set the stage for torrential rain in southern California and the U.S. South.

Yet, although everyone is bracing for a monster El Niño this winter, few know much about the phenomenon that triggered it. Fewer still know its name: the Madden-Julian oscillation (MJO). The bouts of tropical storminess that the MJO brings not only play an important role in fueling El Niño events, but also have striking weather effects in their own right. The MJO is the single biggest driver of weather in the tropics, and at higher latitudes it can lead to cold snaps, heat waves, rainy seasons, and hurricanes—just about everything El Niño does, says Adam Sobel, an atmospheric sci-



Clouds grow in the early stages of a 2011 Madden-Julian oscillation event in the Indian Ocean.

entist at Columbia University. “The MJO is the most important [oscillation] about which we understand as little as we do,” he says. Yet “people have never heard of it.”

But scientists are making progress in understanding this hidden force in weather and climate. Computer models are finally mimicking the MJO, after decades of failure. That is allowing weather forecasters to push their predictions further into the future than ever before, while climate scientists are exploring how the MJO will behave in a warmer world. And after an intense field campaign in the Indian Ocean involving dozens of nations, researchers are starting to answer some of the most fundamental questions of all: Why does the MJO exist, and how does it form?

“I saw someone refer to it as the madden-Julian oscillation,” says Tony Del Genio, a climate modeler at NASA’s Goddard Institute for Space Studies in New York City. “We’ve been frustrated for so long. I think we’re taking steps in the right direction. But I also think the story is not over yet.”

SOME YEARS, no MJO events occur. Other years, there are more than half a dozen. Most often they form over the Indian Ocean during the northern winter, as tall rain-clouds coalesce into clusters. This “active phase” of rain and wind is preceded by a zone of clear skies, the “suppression phase.”

The two phases march eastward in tandem at about 5 meters per second and cross Indonesia into the Pacific. There, the storms lose strength, but the system speeds up to as much as 15 meters per second. Some MJO events die when they hit the mountain wall of the Andes, but the seeds of others continue across South America, the Atlantic, and Africa. A few even circumnavigate the globe, winding up in the Indian Ocean 30 to 60 days after they started.

As the MJO’s active phase proceeds around the equator, it shapes weather in distant latitudes. In the Indian Ocean, it can trigger and enhance the Indian and Australian monsoons. When it is over the Pacific, atmospheric ripples can peel off from the MJO and tilt the jet stream, sending humid air from the vicinity of Hawaii up to drench the Pacific Northwest in “Pineapple Express” events. Other “teleconnections” in the atmosphere lead to cold snaps and heat waves in North America and Europe. And when the MJO persists into the Atlantic basin, it can affect cyclone formation: A 2000 study found that hurricanes are four times more likely to form during an active MJO phase than during a suppressed one. In 2012, for instance, Hurricane Sandy formed just after a strong MJO passed through.

It took keen insight and one of the most powerful punch card computers of its time for Roland Madden and Paul Julian to dis-

cover the MJO in 1971, working with data from a scattering of island weather stations (see sidebar, p. 25). Soon the MJO was unmistakable in images from weather satellites, which revealed throngs of cumulonimbus clouds regularly circling Earth’s belly. Yet the computer models that climate scientists and weather forecasters rely on could not reproduce the MJO, to the modelers’ embarrassment. “We’re not happy when something that shows up in the real world does not show up in our models,” Del Genio says.

Those models work by dividing Earth’s atmosphere up into millions of boxes. Weather observations provide the starting conditions of temperature, humidity, wind speed, and other variables for each box. Then the model is set in motion, evolving according to the laws of physics. Making the boxes smaller to sharpen the model’s resolution quickly raises the computational cost to prohibitive levels. One of the best forecast models in the world, at the European Centre for Medium-Range Weather Forecasts (ECMWF) in Reading, U.K., uses boxes that are 16 kilometers on a side. That is still too coarse to model local phenomena, such as the billowing evolution of individual storm clouds; it will be a decade before computers will be capable of running global cloud-resolving models for daily forecasts.

In the meantime, modelers cheat: They apply “parameterizations,” semiempirical

computational shortcuts applied within grid boxes for processes such as cloud formations. These parameterizations were somehow fouling up the formation and movement of MJO events. The models did show storms gathering over the equatorial ocean, but they grew too fast in too many places, dumping their moisture as rain and preventing the formation of squadrons of small- and medium-sized rain clouds needed to assemble an MJO event.

A breakthrough came with a study published in 2008 and led by Peter Bechtold, a principal scientist at ECMWF. Bechtold realized that the parameterizations in the ECMWF model were not accounting for the turbulence along the edges of rising, moist cloud columns. With more turbulence, dry air can mix into the cloud, effectively stopping its rise—a process researchers call

entrainment. Entrainment could slow the formation of the biggest storm clouds, keeping the MJO events from aborting themselves early. Bechtold showed that once cloud parameterization in the ECMWF model was altered to include more entrainment, MJO events began to appear.

Other major weather forecasting models in Europe, Japan, and the United States soon followed ECMWF's lead—and because MJOs have such far-reaching effects on weather, the models gained new forecasting power. ECMWF weather forecasts now have some predictive skill out to a world-leading 25 days. Other forecasters are finding new customers. Earlier this year, WSI, a division of The Weather Company, launched an MJO-based forecast that helps predict cold snaps and heat waves in North America and Europe up to 5 weeks in advance. So far, most of Ventrice's

customers are hedge funds and traders who want to make bets on energy supplies such as heating oil or natural gas, says Michael Ventrice, a WSI scientist in Andover, Massachusetts. He says retailers are using MJO forecasts from other modelers to tweak the timing of seasonal clothing lineups.

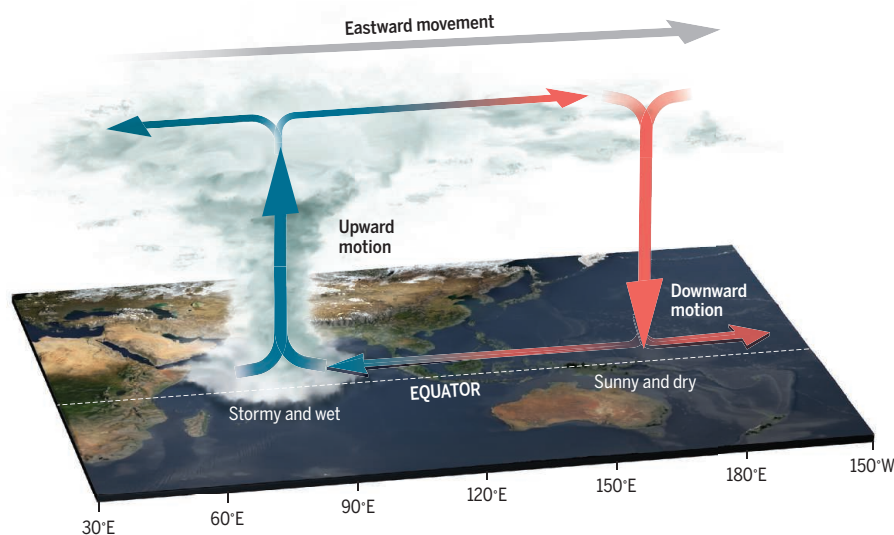
Climate researchers have made less progress than weather forecasters in simulating the MJO. In a 2006 study, just two of 14 global climate models produced a reasonable MJO. Part of the problem was that the fix that worked so well for weather forecasters produced unwanted side effects for the overall long-term climate. Upping entrainment, which dries out the biggest storm clouds, left more moisture for medium-sized rainstorms around the globe, making the overall climate too wet. "Entrainment is the medicine to make the MJO, but it made the rest of the climate have an upset stomach," Del Genio says.

Some climate modelers are starting to find workarounds—either with further tweaks to parameterizations or with models that simulate clouds explicitly for small areas. But a study published in May found that even now, only eight of 27 global climate models produce good MJO events. Some poor performers even made MJOs that moved backward, from east to west.

Still, the models are already offering glimpses of how the MJO could change in a warmer world. A study published in July found that, if global temperatures rise 4°C by the end of the century—the likely outcome if greenhouse gas emissions continue to grow unabated—the MJO would increase in both frequency and intensity. That's both good news and bad, says Eric Maloney, an atmospheric scientist at Colorado State University, Fort Collins. "A stronger MJO in future climate is potentially going to exacerbate some [weather] extremes, but possibly allow us to better predict them on seasonal time frames," he says.

Around the world in 30-60 days

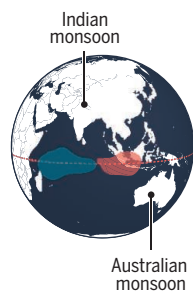
The Madden-Julian oscillation (MJO) forms in the Indian Ocean as a pair of related wet and dry phases. In tandem, the system moves eastward at about 5 meters per second, circling the globe in 1 or 2 months.



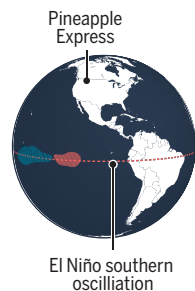
Regional effects

The MJO not only drives weather in the tropics but can also trigger and strengthen phenomena such as monsoons and hurricanes elsewhere in the world.

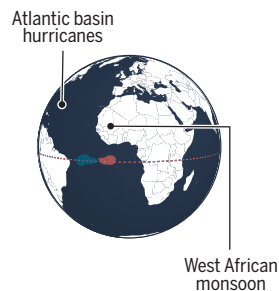
MJO forms



MJO loses some rain but speeds up



Depleted of rain, MJO continues as a low-high pressure system



WHILE MODELERS STRUGGLE to predict MJOs, field researchers recently mounted a massive campaign to understand what gives birth to them in the first place.

The approximately \$60 million campaign, called CINDY/DYNAMO, was led by Japan and the United States and concentrated on the place where the MJO begins. "We simply cannot explain why MJO would start from the Indian Ocean," says Chidong Zhang, who studies ocean-atmosphere interactions at the University of Miami in Florida and is the principal investigator for the U.S. portion of the project, which included universities and other research institutions from 14 countries.

From October 2011 to March 2012—a winter season in which they could reasonably expect to catch a couple of MJOs in the

act—the CINDY/DYNAMO partners flooded the zone. Satellites can look down on the cloud tops that mark an MJO event. But to watch one take shape, researchers needed a vertical picture of all the cloud layers. They got it from radars operating at different frequencies from sites on land and ships, ocean measurements from ships and buoys, and atmospheric readings from more than 23,000 weather balloons and two dedicated aircraft.

All that data did not pin down the reason for the MJO's existence, but it did elevate a new candidate. For years, some theorists thought the MJO was a variation on a much swifter eastward-moving wave of atmospheric pressure called a Kelvin wave. But a Kelvin wave can exist in a dried-out atmosphere. Maloney says the CINDY/DYNAMO results suggest that the MJO owes its existence to moisture. He says the MJO is an example of a "moisture mode" that develops when humid air rises and circulates inside storm clouds.

Del Genio, who has followed the debates as an outsider, says that the moisture mode theory "seems to be gaining traction." But Zhang, who in 2005 wrote a review that identified a half-dozen explanatory theories, isn't quite ready to anoint it as the winner, although he says it is appealing.

Even if the MJO is a moisture mode, there remains the question of what mechanism brings the moist air to the Indian Ocean at the critical time. The CINDY/DYNAMO campaign appears to have stumbled on at least one answer. The Intertropical Convergence Zone (ITCZ) is a band of low pressure where the two hemispheres' trade winds collide, forming a pool of moist, hot air. In the Northern Hemisphere's winter, in the Indian Ocean, that band sits 500 to 1000 kilometers south of the equator. The field campaign found that, just before an MJO kicks off, the ITCZ shifts northward into the MJO's cauldron of formation, supplying it with moisture.

What pushes the ITCZ toward the equator, Zhang says, may be dry air moving in from the southern latitudes of the Indian Ocean. Maloney suggests that just as the MJO affects weather in higher latitudes through teleconnections, phenomena in the higher latitudes of the Indian Ocean exert the same kind of remote control over the MJO.

Even as it hinted at answers, the DYNAMO campaign underscored the mysteries that remain. For example, Zhang says, team members aren't even sure how many MJOs they saw. Everyone agrees that there were at least two. But a third event, which satisfied some criteria for an MJO but not others, left them divided. "I often joke that we wanted to find out how MJO initiates," Zhang says. "When we came out of the field, we did not how to define MJO. That's progress." ■

How two pioneers took the tropics' pulse

By Eric Hand

It was 1970, and two young scientists were hoping that their thick stacks of computer punch cards contained clues to the hidden rhythms of tropical weather.

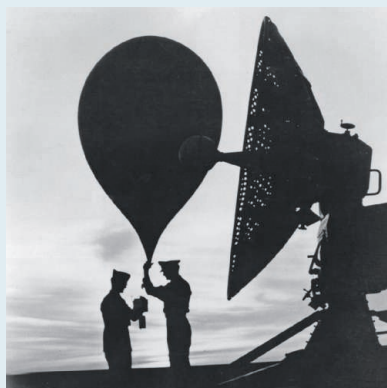
Roland Madden, a former forecaster for the U.S. Air Force, was working at the National Center for Atmospheric Research (NCAR) in Boulder, Colorado, alongside Paul Julian, a scientist nearly 10 years his senior and an expert on a new computer-aided technique for finding patterns in data.

In the wake of World War II, island weather stations dotting the Pacific began to accumulate long-term data sets. Analysis of them revealed not just the obvious daily and seasonal changes, but, in 1960, a 26-month cycle of shifting stratospheric winds called the quasi-biennial oscillation. The discovery showed that tropical weather, long ignored for its seeming dullness, held more than balmy, blue skies.

At NCAR, Madden and Julian wanted to probe further. They had a fancy new computer to work with: a CDC (Control Data Corporation) 6600, with 64 kilobits of memory and a 10-megahertz clock. They also had a new way to sift that data

for temporal patterns in wind speeds, temperature, or pressure: the fast Fourier transform, a technique invented by mathematicians in 1965. What they needed was a big data set.

It would come from a lonely spit in the Pacific Ocean called Kanton Island. The coral lagoon sits about halfway between Hawaii and Fiji, close to the crosshairs of the International Date Line and the equator. An operator would release a weather balloon at 1 p.m. local time. A radio dish antenna, tracking the rising sphere, would gather temperature, humidity, and pressure data. Geometric calculations yielded the wind speed.



Studies on Kanton Island yielded crucial data.

By 1970, that data had wound up on

magnetic tapes at NCAR. Madden converted the tape into decks of computer punch cards that were fed into the maw of the CDC 6600. (Today, thousands of the cards sit in boxes in Madden's garage. "I use them for shopping lists," says Madden, now 77. "I suppose now they're museum pieces.")

The CDC 6600 churned through its punch card decks. The Fourier analysis showed that air pressures fell and winds peaked roughly every 44 days. Madden and Julian began to imagine a giant storm system passing over Kanton Island every month and a half. In a 1971 publication of the *Journal of the Atmospheric Sciences*, they called it the "40-50 day oscillation." But they did not yet have a mental picture of what it really was. "We only had that one station," Madden recalls. "Was this thing moving, or locally pulsing, or what?"

They accumulated data from other weather stations, islands with names like Eniwetok, Wake, and Yap. They folded in surface pressure data collected by ships crisscrossing the ocean during the International Geophysical Year, 1957–58. A piece-meal geography emerged. First, they confirmed that the oscillation was confined to the tropics—it didn't extend beyond 10° north and south latitude. But Madden still wanted to visualize its movement.

One night in 1971, he took home printouts of a data set: surface pressures for various longitudes, over time. He spread them out on his couch and set to work. By hand, he subtracted out the long-term mean, and found that each day, negative pressure anomalies popped out at a particular longitude. A day or two later, those anomalies shifted east. It was a "eureka" moment, the first glimpse of how the disturbance that would eventually bear his name marched along the equator. "All of a sudden, I saw this beautiful eastward movement," he recalls. "I remember telling my kids, 'We're going to be famous.'" ■

POOLING RESOURCES

Ecologist Aram Calhoun forges creative alliances in her quest to protect ephemeral vernal pools

By Jill U. Adams, in Topsham, Maine

As a kid growing up in rural Rhode Island, Aram Calhoun ran the frog patrol. When she caught neighborhood boys throwing frogs into traffic, she'd chase the offenders and beat them up. Then she'd persuade her adversaries to become allies. "I recruited two of the worst ones to my team," the ecologist recalls. "We'd go find frogs and save them."

These days, Calhoun takes a similar though less pugilistic approach to her work. But the University of Maine, Orono (UMO), academic is tackling a more difficult task than persuading kids to stop squashing frogs. She's leading an innovative effort here to overcome two of the tougher challenges in conservation biology in the United States: protecting small, ephemeral waterbodies called vernal pools that are critical to the survival of many amphibians

and other organisms, and making conservation work on privately held lands.

It's a decades-old endeavor that has taken Calhoun, trained as a microbial ecologist, far beyond basic research. She has helped recruit citizen scientists to collect key field data. She has assembled teams of scientists, economists, town planners, and developers to develop economically viable plans for balancing conservation and development. And she has grown accustomed to dealing with people who—at first—see her as the enemy. "People screaming at me," she says, recalling contentious town meetings. "The police had to come once."

As with those frog squashers, however, Calhoun has won over some of her foes. She earns people's respect by being respectful of them. And now her work in two Maine communities is on the verge of setting a precedent for how local communities can work with developers and private land-

owners to protect sensitive ecosystems—instead of fighting.

"I'll admit I was a little skeptical" about Calhoun's effort, says Ruth Ladd of the U.S. Army Corps of Engineers in Concord, Massachusetts, a federal agency that plays a major role in protecting wetlands and has been monitoring Calhoun's work. But she has been "tenacious. ... As complicated as things were, she always behaved as if it could be done."

CALHOUN, 56, grew up in Rhode Island's Hope Valley, "or hopeless valley as the locals called it," she says. She planned to become a teacher and pursue her interests in wildlife and conservation in her free time. But her older brother, who worked for an environmental group, encouraged Calhoun to put her passion first. After earning her doctorate at UMO in 1996, she won a prestigious Switzer Fellowship, which allowed her to

Downloaded from www.sciencemag.org on October 8, 2015

PHOTO: TRISTAN SPINSKI



Aram Calhoun looks for frogs in a vernal pool behind her home in Maine.

split her time between a UMO laboratory and Maine Audubon, a nonprofit group heavily involved in state environmental policy discussions.

The sometimes alarmist rhetoric Calhoun heard during those policy fights annoyed her. “I hated it when environmentalists would say, ‘All the frogs in Maine are dying,’” she recalls. But the experience “really shaped my research, by showing me the gaps in policy.”

One big gap involved vernal pools. These small, scattered, temporary ponds, often fed by spring rains and snowmelt, are sometimes treated as an afterthought in environmental regulations, which tend to focus on protecting bigger, more permanent wetlands. Yet in New England’s forests, they are vital breeding grounds for frogs and salamanders; because the pools typically dry up each summer, they harbor no fish that would eat amphibian eggs. The wetlands also support

threatened species of turtles and dragonflies and are fertile oases for woodland birds and mammals.

Vernal pools are particularly vulnerable in the northeastern United States. One reason is that there is relatively little publicly owned land in the region, so most pools are on private property, where land use can be harder to regulate. Another is that many regulators don’t even know where the pools are located. In Maine, Calhoun discovered that the state needed “a basic inventory. We were starting from square one.” In 1999, she began organizing citizen scientists to conduct surveys to help fill in the map. Volunteers got a bit of training and then headed into the field, collecting data on the location and size of vernal pools, as well as the presence of key amphibian species.

CALHOUN WAS ALSO LEARNING the political landscape, which was marked by bitter conflicts over efforts to protect wetlands. Not far from her office in Orono, a riverside town of some 10,000 residents in central Maine, town planners had approved building 57 homes on a 16-hectare plot of undeveloped land. But the project stalled when officials with the federal Army Corps, which must review any project that would disturb certain types of wetlands, ruled against letting the builder fill a vernal pool. The decision effectively cut in half the number of allowed homes, and “ultimately killed the project,” says Evan Richert, Orono’s town planner.

Some might view the development’s failure as a conservation success, but Richert says it’s not that simple. The project was consistent with planners’ efforts to promote “smart growth” in Orono, he says, avoiding sprawl by concentrating development in compact, walkable areas. And its failure meant developers might “just hopscotch a mile out of town and develop there,” potentially fragmenting open space that might have higher ecological value than the in-town wetlands.

Richert eventually shared his frustrations with Calhoun, who had called him to discuss mapping Orono’s vernal pools. Both believed the existing rules, which Maine instituted in 2007 and were stricter than federal regulations, were still shortsighted and didn’t help meet larger goals. They wondered: How can better compromises be struck between conservation and development?

TO FIND ANSWERS, Calhoun teamed up with UMO economist Kathleen Bell and others on a range of basic and applied research projects. One challenge was ecological: better understanding how much development vernal pool habitats could

withstand before becoming too fragmented to support genetically diverse amphibian populations or cycle nutrients. Another was economic: understanding the cost and local impact of placing some pool-rich lands off-limits to development.

The researchers soon focused their work on two towns where surveyors had already mapped vernal pools: Orono and Topsham, a town of 8000 people 150 kilometers to the southwest. They created computer simulations that fused ecological and economic data, including amphibian abundance, the conservation value of surrounding landscapes, land values, zoning classifications, and growth projections. And they started running scenarios that examined various trade-offs: What might different levels of development or conservation mean for vernal pool connectivity and economic growth? How much would it cost to pay some landowners to place protective easements on their pools, in order to make up for allowing development on other parcels?

In 2013, the work got a major boost in the form of a 5-year, \$1.5 million grant from the National Science Foundation, and last year Calhoun, Bell, and two co-authors laid out their approach in the *Proceedings of the National Academy of Sciences*. They envisioned allowing developers to build on pools within town-defined “growth zones” if they paid fees that then would be used to compensate rural landowners for protecting pools on their properties.

In the same spirit of give-and-take, Calhoun invited developers to join the meetings of an informal working group she had organized of scientists, regulators, and others interested in developing better ways of protecting Maine’s vernal pools.

ONE INVITEE WAS JIM HOWARD, a native Mainer and owner of the Priority Real Estate Group in Topsham. When he accepted Calhoun’s invitation, he knew exactly what vernal pools were: a headache. “Not just a headache, but a hurdle, an obstacle, red tape, and battles,” he says. He had learned the hard way; vernal pools once scuttled one of his firm’s potential development projects.

At first, Howard says he was wary—a feeling that only grew when the working group began discussing Calhoun and Bell’s fees-for-development strategy. “Fees!” Howard says, remembering his reaction. “They want me to pay more?”

But after Howard went back to his office and did some calculations, he realized the approach—known as an in lieu fee program—could pay off. It would allow him to develop higher value properties that, under existing regulations, were off-limits because of vernal pools.



Temporary vernal pools are a favorite egg laying spot for frogs and other amphibians.

Using in lieu fees to conserve wetlands wasn't a new idea; many regulatory programs require builders to mitigate their impact on wetlands with payments to third parties, who then use the funds to preserve, restore, or build new wetlands somewhere else—often hundreds of kilometers away from the impact site. (It's a controversial practice, however; critics argue that mitigation can't really replace what's lost.) What made Calhoun and Bell's approach different was its local scale: The researchers envisioned conservation happening nearby, within the same town as the development. And the program would be voluntary, potentially reducing political resistance and creating incentives. "We're adding an option ... not overturning anything," Calhoun argued.

Going local was easier said than done, however. State and federal wetland regulators would have to let towns bend rules that would otherwise prevent such tradeoffs. And to get the ecology and economics right, the researchers needed detailed data that would help them determine specific, workable fee structures. Still, Calhoun and Bell were optimistic.

AS THE RESEARCHERS ran their refined models for Topsham this past winter, however, their hearts sank. The economic analysis showed the development fee they'd been working with wouldn't pay for the conservation side of the equation. And that meant broaching the sensitive topic of higher fees at a working group meeting

with Howard and other developers and planners. "It had the potential to be a disaster," Calhoun recalls.

It wasn't, thanks to Howard. The economic analysis was flawed, the developer informed the researchers, because it used property values that were too low. (They had been drawn from tax assessments.) Once Howard did recalculations "with the market value, ... all the numbers worked," he says.

And as the plan began to take final form, state and federal regulators signaled that they would be willing to take the un-

leagues with enabling the improbable.

Calhoun "used her scientific enterprise to inform the discussion," says Elizabeth Hertz, who directs Maine's municipal planning programs. When new questions came up, for example, Calhoun would task her graduate students with finding concrete answers.

It was "a blessing to have a professor take the lead on this," the U.S. Army Corps's Ladd says. "Having a university involved means research grants and graduate students. If the Corps was leading, I'm not sure we could pull it off." And Calhoun and her collaborators say their economic-ecological approach should be applicable to a whole host of other small natural features, such as bat caves, prairie potholes, desert springs, and rocky outcrops.

For Calhoun, the lesson is the same one she learned as a kid on frog patrol: Be open to the idea that apparent foes could be potential allies. And "don't go to people *with* solutions," she says. "Go to them *for* solutions."

You might even change some perspectives along the way, she says. Howard recalls the day his wife shouted into the house, "There are lizards in the pool!" He went to investigate. "Those aren't lizards," he pronounced, drawing on what he'd learned in his vernal pool meetings. "They're yellow-spotted salamanders!" And he released them back into the wild where they belonged. ■

Jill Adams is a freelance writer in Albany.

Vernal pools were "not just a headache, but a hurdle, an obstacle, red tape, and battles."

Jim Howard, owner of Priority Real Estate Group, in Topsham, Maine

usual step of endorsing the experiment—assuming town governments went along.

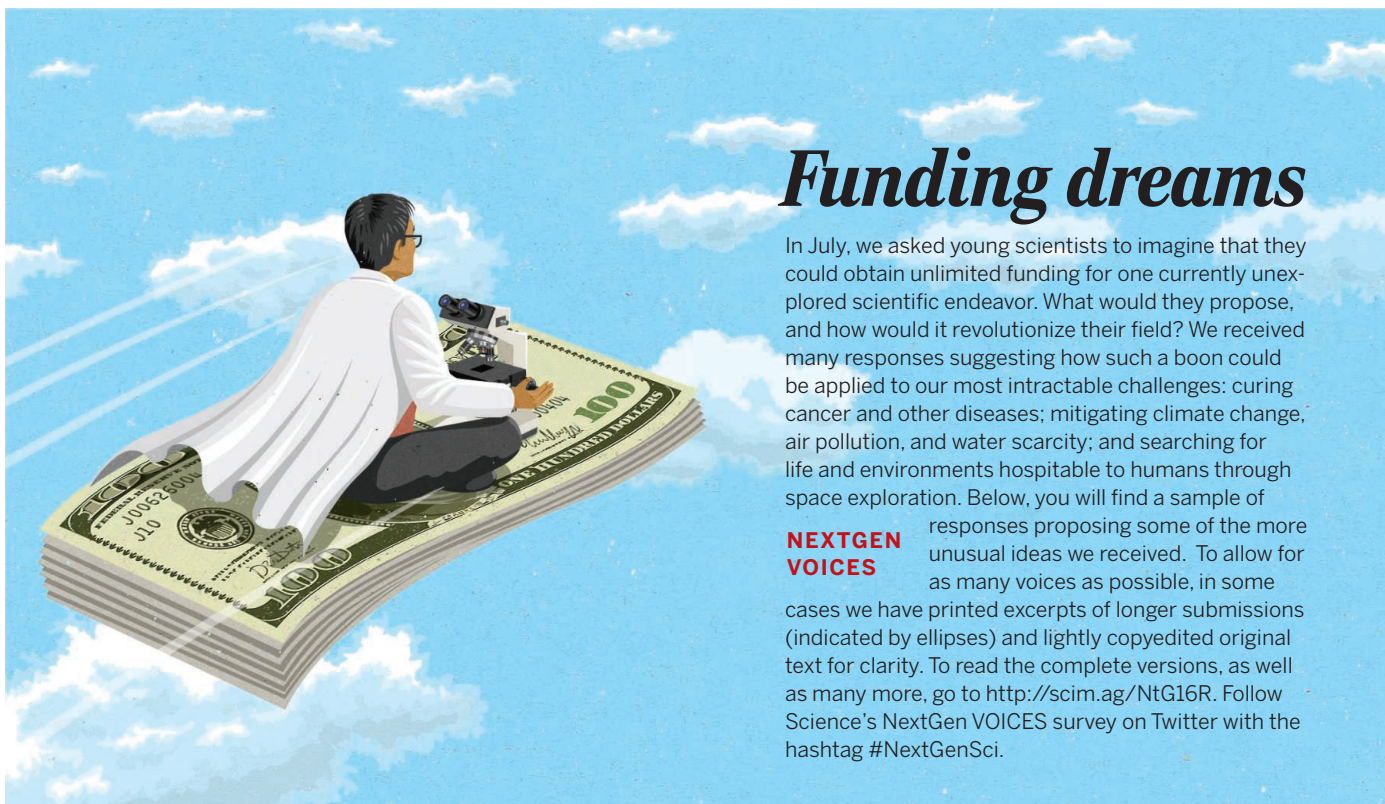
CALHOUN'S TEAM LEAPT THAT hurdle earlier this year, as town councils in Orono and Topsham approved ordinances that take effect this fall. The plans, as written, protect at least two vernal pools for every one that is compromised.

It will take time to figure out whether the ordinances are working and whether other towns and states could adopt similar approaches. Still, many observers are already crediting Calhoun and her col-



LETTERS

Edited by Jennifer Sills



Funding dreams

In July, we asked young scientists to imagine that they could obtain unlimited funding for one currently unexplored scientific endeavor. What would they propose, and how would it revolutionize their field? We received many responses suggesting how such a boon could be applied to our most intractable challenges: curing cancer and other diseases; mitigating climate change, air pollution, and water scarcity; and searching for life and environments hospitable to humans through space exploration. Below, you will find a sample of

NEXTGEN VOICES

responses proposing some of the more unusual ideas we received. To allow for as many voices as possible, in some cases we have printed excerpts of longer submissions (indicated by ellipses) and lightly copyedited original text for clarity. To read the complete versions, as well as many more, go to <http://scim.ag/NtG16R>. Follow Science's NextGen VOICES survey on Twitter with the hashtag #NextGenSci.



IF I HAD unlimited funding, I would put it all toward funding the human resource needs of science. The days of applying for contracts to cover salary would be over. Postdocs would

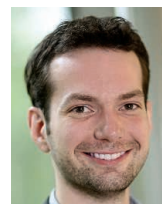
have job security and benefits, and students would not pay tuition. Adjuncts would be compensated for their work at fair market rates. Childcare would be provided, free of charge, to parents in scientific careers. In short, the basic economic needs of scientists would be met....Universal funding would completely change the scientific system, as people from all over the world and from all backgrounds would be empowered to take on science careers. Those of us privileged enough to have jobs in the field would take on riskier questions if we knew that a failed experiment would not threaten our ability to

feed our families, and more scientists would tackle questions that people in power do not want asked. The most worthy global science project is a project that opens science to all. Nothing would be more revolutionary.

Brett Favaro

School of Fisheries, Fisheries and Marine Institute of Memorial University of Newfoundland, St. John's, NL, A1C 5R3, Canada and Department of Ocean Sciences, Memorial University of Newfoundland, Marine Lab Road, Logy Bay, NL, A1K 3E6, Canada. E-mail: brett.favaro@mi.mun.ca

IF I HAD unlimited funding, I would build a state-of-the-art, free, open-source case-management system for law enforcement. Along with a case-management system, I would provide free computer equipment, support, and training to every country.... Such a system would help reduce certain types of corruption and improve police auditing. The global community would benefit from

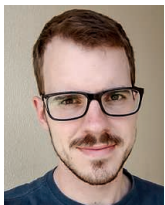


more accurate, more standardized crime data being made available from every participating country. I would use this global crime data to better understand trends and motivations for

human trafficking and child exploitation. I would explore why countries favor the investigation of certain crimes while essentially ignoring others. I would also investigate what police strategies are most effective in fighting trafficking and exploitation, and the relation between the reduction of crime in one country and the increase of the same crime in other countries. This would let us create an organized global strategy.

Joshua I. James

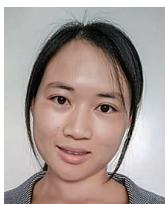
Digital Forensic Investigation Research (DFIRE) Laboratory, College of International Studies, Hallym University, Chuncheon, Gangwon-do, 200-702, South Korea. E-mail: Joshua@cybercrimetechnology.com



I WOULD LIKE to explore the limits between living and nonliving systems.... With unlimited funding (and supposing that this could also acquire an unlimited powerful computational tool), I would like to start simulations with very simple collections of molecules needed for life and continuously increase the complexity of the system until the "living" behavior (such as self-replication or metabolism) arise from the nonliving parts. This could give us new information about the origin of the life in the universe and in our planet, as well as tell us the limits of free will in a chain of biochemical reactions.

Wagner E. Richter

Institute of Chemistry, University of Campinas, Campinas, São Paulo, 13.083-970, Brazil.
E-mail: wagner.richter@iqm.unicamp.br



...I WANT TO build a glacier chamber in which to study huge artificial glaciers. The environment in the chamber would be similar to a real glacier's surroundings.

The difference is that we could control the factors influencing the glaciers and install sensors detecting variation in the chamber. This would help us to learn about the contribution from different factors affecting glacier melting and develop some control measures to slow down or stop the melting of the glaciers.

Xin Wan

Key Laboratory of Tibetan Environment Changes and Land Surface Processes, Institute of Tibetan Plateau Research, Chinese Academy of Sciences, Beijing, 100101, China. E-mail: xin.wan@itpcas.ac.cn



I WOULD identify a global patient cohort with familial Alzheimer's disease (AD) mutations but no dementia over 5-year periods....I would collect biomarkers from this set to identify poten-

tial neuroprotective molecules. Neuronal iPS cells from this group would be generated and analyzed at proteomic as well as transcriptomic levels, to be compared with an age-matched, gender-matched, ethnicity-matched control set. The iPS cell study would yield mRNA and protein molecular drug targets that provide neuroprotection to the donor individuals of these cells in spite of their genetic background, which

makes them susceptible to developing AD. Functional overexpression or inhibition studies of these molecular targets with animal models of AD would follow to give more mechanistic insights....

Sachin S. Tiwari

Institute for Integrated Cell-Material Sciences, Kyoto University, Kyoto, 606-8501, Japan.
E-mail: sactiw@gmail.com



...BIOLOGY has been entirely based on what life could be on Earth, simply because this is the only environment where we know life exists.... In an unprecedented era where synthetic biology is

becoming increasingly practical to implement and we are becoming more aware of the environments of our solar system and beyond, I would propose a project to engineer unicellular life forms that can withstand various environments that would likely never occur on Earth. Human-driven evolution would unveil a host of surprising processes that may lead us to completely redefine what life itself means.

Tommy Vo

Department of Molecular Biology and Genetics, Cornell University, Ithaca, NY 14850, USA.
E-mail: tvv3@cornell.edu



WITH unlimited funding, I would endeavor to close the knowledge gap on biodiversity by discovering, cataloging, and describing all life on Earth. Current estimations on the number of

species on Earth carry great uncertainty. This is a major issue for conservation, as we cannot conserve what we don't know, and a potentially significant number of species may go extinct before we even know of their existence. To complete the species list, I would organize extensive biodiversity sampling in yet-unexplored or difficult-to-reach areas and in environments that require expensive specialized equipment. These include ocean floors, forest canopy, soils, and underground caves and streams. The complete list of species on Earth will reveal the true scale of biodiversity loss. It will also help to detect all endangered species and allow the establishment of adapted conservation programs. New species discovery will also greatly benefit pharmacological research. Finally, taxonomic description of all species on Earth will provide an invaluable

resource for the field of evolutionary biology and would help in reconstructing the complete tree of life.

Marie-Caroline Lefort

Department of Natural Sciences, Unitec Institute of Technology, Mt. Albert, Auckland, 1025, New Zealand and Bio-Protection Research Centre, Lincoln University, Christchurch, 7647, New Zealand.
E-mail: Marie-Caroline.Lefort@lincolnuni.ac.nz



A CURRENTLY unexplored avenue in the field of stem cell biology is the clinical relevance of niche biology. Ever since Schofield coined the term "niche" in 1978, great strides have been

made to discover molecular signals and cellular support systems that maintain stem cell functionality in flies, worms, and mammals. The practical implication of this voluminous information would be to create "stem cell niche biobanks," wherein data that has been rigorously tested and verified in the requirements for specific factors for the maintenance of stem cells of all tissue types can be consolidated. These banks would have little pockets of tissue-specific niches that allow for the maintenance of an individual's stem cells from his brain, muscle, blood, or kidney that can be harvested on demand and continue to be maintained even after repeated usage. This endeavor would not only serve as a personalized repository of all types of stem cells, but would represent the next level in implementing the studies being conducted in niche biology....

Suchitra D. Gopinath

Translational Health Science and Technology Institute, NCR Biotech Science Cluster, Faridabad, 121001, India. E-mail: sgopinath@thsti.res.in

SUBMIT NOW: POLITICAL SCIENCE

Add your voice to *Science*! Our new NextGen VOICES survey is now open:

How do political priorities (or political sensitivities to particular groups) affect your ability to do or communicate science?

To submit, go to http://scim.ag/NG_17

Deadline for submissions is 13 November. A selection of the best responses will be published in the 1 January 2016 issue of *Science*. Submissions should be 200 words or less. *Science* will withhold your name from publication upon request.

PERSPECTIVES



POLYMER CHEMISTRY

Safer fuels by integrating polymer theory into design

Jet fuels are stabilized with polymers assembling in solution

By Michael Jaffe and Sahitya Allam

For the past few decades, the civil aviation industry has increased its efforts to prevent fuel fires initiated by aviation crashes by improving fuel safety and handling. These fires are estimated to be responsible for 40% of fatalities, corresponding to approximately 500 to 1000 deaths that could be minimized annually with improved fire-safe fuel (1). Fuel fires are also increasingly becoming a hazard to homeland security, as seen in the example of the September 11, 2001 attacks on the World Trade Centers (2). The mist is much more flammable than the liquid, and antimisting kerosene (AMK) interferes with mist formation by incorporating a low concentration (<0.3 weight percent) of high molecular weight polymer; (FM-9) into Jet-A fuel (3). However, routine handling (e.g., passage through pumps) (see the photo) breaks the polymer chain through hydrodynamic tension, and it becomes inadequate for mist suppression (4). The challenge is to find a mist-control polymer that is stable at handling conditions. On page 72 of this issue, Wei *et al.* (5) show how telechelic polymers that break and reassemble can be effective mist suppressors under real handling and fuel-injection conditions.

Department of Biomedical Engineering, New Jersey Institute of Technology, Newark, NJ 07102, USA.
E-mail: michael.jaffe@njit.edu

Low concentrations (≤ 100 parts per million) of long-chain polymers (molecular weight $\geq 5 \times 10^6$) in solution lower drag in liquids and control fuel misting (6, 7). The problem is that very long chain polymers tend to be unstable in shear and difficult to polymerize (8). Also, misting is critical for jet engines—the polymer cannot inhibit the desirable mist formation that affects combustion properties like flash point. Using statistical mechanics, Wei *et al.* predicted that low concentrations of telechelic chains, with molecular masses between 400 and 1000 kg/mol and end-group associative strengths in the narrow range of 16 to $18 k_B T$ (9), will self-assemble to form mega-supramolecules that would impart antimisting and flow control to fuels while overcoming the tendency of long molecules to fracture during shear. Outside of the predictive parameter range, the chains are either unstable in shear (if too long), or form cyclic structures (if too short).

If the chain end-association energy is too weak, long-chain formation is inadequate; if too strong, few linear species form. To test the theory, the authors used ring-opening metathesis polymerization to produce polyolefin chains within the desired molecular weight range. They covalently attached tertiary amine and carboxylic acid end groups onto the chains to produce longer telechelic chains with associative energies in the desired 16 to $18 k_B T$ range. Light scattering and shear viscosity measurements confirmed that the telechelics do associate to form the

Safer travels. The polymer developed by Wei *et al.* can stabilize jet fuel if an accident ruptures fuel tanks.

desired supramolecules with the desired effects on liquid-fuel viscosity. Further experimentation showed that the molecules produced are stable under engine usage conditions (fuel pump experiments) and reduce drag in turbulent flow (behavior similar to the known behavior of ultralong linear polybutylene chains). The fuel still supports combustion (in diesel test engines) but decreases mist particle size and lowers its flammability when the fuel is dispersed by impact.

The most exciting aspect of these results is the demonstration of continuity between basic theory and applied science and the recognition that an important commercial application can be derived directly from a quantitative theoretical prediction. Computational materials science can be a cost-effective way to identify new materials with potentially superior properties, thus avoiding the time-consuming empirical or serial process of experimentally evaluating numerous variants. Well-tested materials are often retested and modified to be suitable for a wide range of applications, but few materials are developed or discovered *de novo* with exceptional properties.

Modeling and computer simulations can address this issue by enabling the prediction of the properties of complex materials, narrowing the range of promising candidates and increasing the probability of success. To be useful, these models and simulations must be consistent with theory and take into account relevant size scales, from nanoscale through macroscopic scales. Fortunately, the availability of software to perform these calculations has reduced the need to simplify models for computational convenience, but more needs to be done to improve computational and experimental convergence. By bridging theory and experimentation through computation, testing and development can be better rationalized to allow for improved allocation of resources, as well as greater creativity and novelty, in designing materials. ■

REFERENCES AND NOTES

1. M.-H. Wei, J. Kornfield, R. L. A. David, Associate polymers for mist-control, European Patent EP2419496A1 (2010).
2. T. W. Eager, C. Musso, *JOM* **53**, 8 (2001).
3. R. J. Mannheimer, "Real-time quality control of antimisting kerosene (AMK)" (Southwest Research Institute, San Antonio, TX, 1985).
4. W. Brostow, *Polymer* **24**, 631 (1983).
5. M.-H. Wei *et al.*, *Science* **350**, 72 (2015).
6. J. F. Motier, Hydrocarbon fuels containing antimisting agents, European Patent 0177649 (1986).
7. K. K. Chao *et al.*, *AIChE J.* **30**, 111 (1984).
8. S. Malik, R. A. Mashelkar, *Chem. Eng. Sci.* **50**, 105 (1995).
9. The thermal energy is the product of the Boltzmann constant k_B and temperature T , about 0.6 kcal/mol at room temperature.

10.1126/science.aac9827

Locking down the core of the pore

A highly stable heterotrimeric protein complex lines the central channel of the nuclear pore

By **Katharine S. Ullman**¹
and **Maureen A. Powers**²

Nuclear pore complexes (NPCs), first observed by electron microscopy 65 years ago, mediate selective transport of macromolecules between the nucleus and cytoplasm of eukaryotic cells. Although the exact size and protein composition of NPCs can vary between species, these massive and complex machines are highly conserved in their overall organization, which consists of multiple copies of ~30 nuclear pore proteins, or nucleoporins (Nups), in a symmetrical eightfold radial arrangement. Deciphering the structure of this immense complex has required ongoing multifaceted approaches (1). On page 106 and 56 in this issue, Chug *et al.* (2) and Stuwe *et al.* (3), respectively, have employed parallel approaches in very distant species and arrived at remarkably similar and informative structures of an essential subcomplex of the NPC.

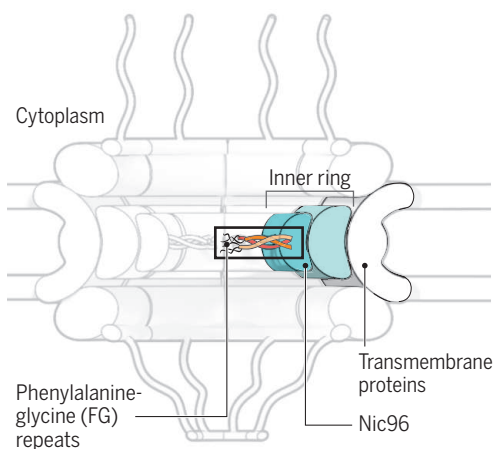
The mechanism by which nuclear transport receptors (NTRs) selectively carry cargo through the NPC has been much debated. Models are focused on the phenylalanine-glycine (FG) repeat domains found in a subset of Nups and, in particular, how the FG domains of the central channel are anchored within the NPC core (see the figure). Discrimination between models has been complicated by the surprising lack of a definitive picture of the Nup62/Nsp1 (4) subcomplex found in the central channel of the NPC. Nup62/Nsp1 and its subcomplex partners Nup58/Nup49 and Nup54/Nup57 were among the first Nups identified more than 20 years ago and are crucial for nuclear import (5, 6). Nonetheless, even the stoichiometry of this subcomplex has been controversial (7), and a structure encompassing the full ordered domains of all members has proven elusive.

Chug *et al.* tackled the metazoan NPC by reconstituting proteins from the frog *Xenopus laevis*, whereas Stuwe *et al.* capitalized on a thermophilic fungus (*Chaetomium thermophilum*) pioneered for improved protein stability and crystallization (8). Both studies began with proteins lacking the FG domains and then trimmed additional residues, testing many versions to obtain the largest fragments that assembled a single homogeneous complex. Structures were stabilized by inclusion of single-chain antibodies. Chug *et al.* show that an antibody that recognizes only the assembled complex could isolate the en-

creasing overall stability through contacts to each domain. This configuration is consistent with the finding of both studies that all members of the Nup62/Nsp1 subcomplex are required for Nup93/Nic96 binding. An unexpected feature is a distinct α/β domain in Nup54/Nup57. A role for this module remains to be determined, as potential interaction partners are as yet unknown.

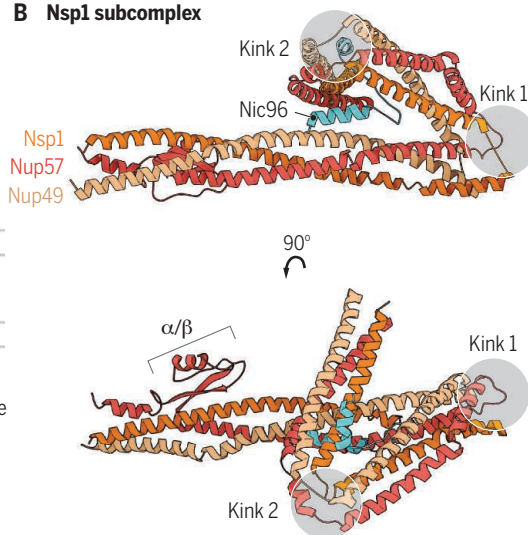
A key feature of many current models of the transport mechanism is the self-association of hydrophobic FG domains to form a permeability barrier. NTRs traverse this barrier by transiently competing for

A Nuclear pore complex



The NPC core. (A) Cross-sectional arrangement of the core nucleoporin subcomplexes is shown. For brevity, only *C. thermophilum* nomenclature is shown. Transmembrane proteins, inner ring structures, and the coiled and FG domains of the Nsp1 subcomplex are shown. (B) Structure of the *C. thermophilum* Nsp1 subcomplex coiled-coil domain. [Adapted from (3)]

B Nsp1 subcomplex



dogenous Nup62 subcomplex from *Xenopus* egg extract, confirming the physiological relevance of these structures.

Both structures reveal a 1:1:1 heterotrimeric parallel coiled coil. There are multiple contacts between the three intertwined chains, and the interactions extend further throughout the domain than previously appreciated. Toward the carboxyl termini, all three chains bend back sharply, producing a kink that is stabilized by interactions between the post-kink coil and the main coiled domain. A second kink in all three chains leads to the third coil segment, solved in the fungal structure, which binds to the adapter Nup, Nic96. The Nic96 helix lies in close proximity to all three coiled segments,

interaction with the FG repeats (9, 10). Recently, an alternate mechanism emerged in which NTR binding to FG domains triggers a dramatic rearrangement (or "ring cycle") of the Nsp62 subcomplex within the NPC central channel to enable passage of NTR-cargo complexes (11, 12). The trimeric structure presented by Chug *et al.* and Stuwe *et al.*, however, is highly stable, with multiple interactions between each of the three members in an equimolar ratio. This configuration is seemingly incompatible with the ring-cycle model, which was inferred from smaller fragments of structure that may have been atypical lower-affinity partnerships formed when protein regions interact out of context.

¹Department of Oncological Sciences, Huntsman Cancer Institute, University of Utah, Salt Lake City, UT 84112, USA. ²Department of Cell Biology, Emory University School of Medicine, Atlanta, GA 30322, USA. E-mail: mpowers@emory.edu

Stuwe *et al.* additionally addressed the interactions that anchor the Nsp1 subcomplex to the inner ring complex of the NPC. Binding of the Nsp1 heterotrimer to Nic96 was essential to target the heterotrimer to the NPC, and disruption of this binding decreased nuclear export and had severe effects on growth in the yeast *Saccharomyces cerevisiae*. Interaction between Nic96 and Nup192 of the inner ring complex was also defined and structurally characterized. Unexpectedly, disruption of the binding interface through mutation of either Nup192 or Nic96 did not displace the heterotrimer from the yeast NPC, although it led to severe growth and export phenotypes. These results suggest that additional connections will be identified between Nic96 and other nucleoporins of the inner ring, and, overall, that gaps remain in our knowledge of how these proteins make vital contributions at the NPC core.

The new structural information from Chug *et al.* and Stuwe *et al.* is a launching pad for elucidating many aspects of pore function. In particular, there is now a context for considering posttranslational modifications and processing, which occur under various circumstances ranging from progression of the cell division cycle to viral infection. These structures may also illuminate a familial mutation of Nup62 that is associated with a neurological disorder (13). The highly conserved heterotrimeric structure provides a point of reference against which new information can be compared, such as the structural basis for Nup62/Nsp1's participation in a second, independent subcomplex of the NPC (14, 15). Overall, structural information for this central subunit of the nuclear pore and new insights into its connections to other pore components represent an important stride forward in deciphering the NPC, both its architecture and its fundamental functions. ■

REFERENCES AND NOTES

1. E. Hurt, M. Beck, *Curr. Opin. Cell Biol.* **34**, 31 (2015).
2. H. Chug *et al.*, *Science* **350**, 106 (2015).
3. T. Stuwe *et al.*, *Science* **350**, 56 (2015).
4. Orthologous nucleoporins are designated with the metazoan/fungal name, e.g., Nup62/Nsp1.
5. D. R. Finlay *et al.*, *J. Cell Biol.* **114**, 169 (1991).
6. E. C. Hurt, *EMBO J.* **7**, 4323 (1988).
7. A. Ulrich *et al.*, *Mol. Biol. Cell* **25**, 1484 (2014).
8. S. Amlacher *et al.*, *Cell* **146**, 277 (2011).
9. J. Yamada *et al.*, *Mol. Cell. Proteomics* **9**, 2205 (2010).
10. S. Frey, D. Gorlich, *EMBO J.* **28**, 2554 (2009).
11. S. R. Solmaz *et al.*, *Proc. Natl. Acad. Sci. U.S.A.* **110**, 5858 (2013).
12. J. Koh, G. Blobel, *Cell* **161**, 1361 (2015).
13. L. Basel-Vanagaite *et al.*, *Ann. Neurol.* **60**, 214 (2006).
14. C. Macaulay *et al.*, *J. Biol. Chem.* **270**, 254 (1995).
15. S. M. Bailer *et al.*, *Mol. Cell. Biol.* **21**, 7944 (2001).

ACKNOWLEDGMENTS

We thank X. Cheng (Emory University) for assistance with figures.

10.1126/science.aad3797



CLIMATE CHANGE

The IPCC at a crossroads: Opportunities for reform

Increase focus on policy-relevant research

By Carlo Carraro,^{1,2} Ottmar Edenhofer,^{3,4,5*} Christian Flachsland,^{3,6} Charles Kolstad,⁷ Robert Stavins,⁸ and Robert Stowe⁸

The Intergovernmental Panel on Climate Change (IPCC) has proven its value as an institution for large-scale scientific collaboration to synthesize and assess large volumes of climate research for use by policy-makers, as well as for establishing credibility of findings among diverse national governments. But the IPCC has received considerable criticism of both its substance and process. The new IPCC leadership to be elected in October could help guide the IPCC to a clear, shared understanding of future objectives and could shape procedural reforms. We identify key opportunities for reform by addressing two related questions: Is the IPCC doing the right things? Is the IPCC doing things right?

DOING THE RIGHT THINGS? To remain policy-relevant, the IPCC needs to shift focus and increasingly address response options to climate change. The informa-

tion base for making decisions on climate stabilization and related public policies is fragmented. Providing clear and integrated information regarding climate impacts and policy options for mitigation and adaptation at various scales (subnational, national, and international) along alternative climate stabilization pathways—and about their respective costs, benefits, and risks—would better inform decision-makers and societies about consequences associated with alternative policy choices. This does not mean that the IPCC should choose among policy options but rather provide the information to facilitate choices by policy-makers.

A major reason for this fragmentation of key information is that IPCC Assessment Reports (ARs) are organized by Working Groups (WGs) focused on the physical science of climate change (WGI), adaptation and impacts (WGII), and mitigation options (WGIII). A different organization might achieve more integrated analysis of policies. For example, one WG could focus on natural-science aspects of climate change, and a second could provide a more integrated perspective on mitigation, adaptation, and the

socioeconomic implications of impacts.

IPCC reports could also develop better understanding and assessment of climate impacts, drivers of greenhouse gas emissions, and policy options at subglobal levels. However, the approval session of the WGIII summary for policy-makers (SPM) in Berlin in 2014 revealed that such geographically specific assessments can be difficult for governments to accept (1–3).

The architecture of the climate agreement to be concluded at the United Nations Framework Convention on Climate Change (UNFCCC) conference in Paris in December will consist of voluntary pledges by governments that might be compared with one another to provide incentives for increasing levels of ambition over time. In this context, increasing the IPCC's focus on policy assessment, capitalizing on emerging literature in this area [e.g., (4–6)], would offer two advantages. First, it would facilitate learning and diffusion of lessons from climate policy experiments worldwide. Second, credible ex post empirical analysis of policies and comparison with ex ante forecasts are critical to building trust between countries continuously involved in policy negotiations (7). Also, more consideration could be given to alternative options for defining and measuring equity and efficiency in a voluntary, “bottom-up” climate regime—again building trust and possibly prompting increased mitigation ambition over time.

Increased focus on alternative public policies may bring potential for controversy between governments and researchers (1–3, 8). Governments hesitate to have their policy programs publicly scrutinized by an intergovernmental panel, and researchers may not be aware of or sensitive to value-laden and politicized questions. Governments and researchers need to carefully execute their roles at the science-policy interface in recognizing and carefully managing diverse viewpoints, without compromising scientific rigor and objectivity (3, 9).

If the IPCC shifts focus along these lines, it will need to actively encourage targeted research on selected topics for which evidence is still lacking. The next leadership of the IPCC should enhance engagement with policy researchers and modelers to help build the necessary knowledge base.

DOING THINGS RIGHT? In addition to building a clear, common understanding of its future focus, the IPCC must address practical and procedural problems. The Fifth AR pushed author teams and technical support units (TSUs) to their management limits. Operating single TSUs from multiple geographical locations should be avoided so as not to further complicate management tasks. Also, the high costs of time and travel commitments put at risk the participation of the best researchers. At the least, the IPCC should consider reducing the number and length of lead author meetings and making greater use of remote collaboration.

Focusing the initial scoping process on identifying policy-maker questions that the

“Governments and researchers need to carefully execute their roles at the science-policy interface...”

AR will respond to (rather than unspecified broad topics) could increase its relevance and usefulness. IPCC rules enable direct interaction between policy-makers, scientists, and other stakeholders only at the start and end of the multiyear assessment process. This limits opportunities to maximize the AR's policy relevance and address potential conflicts between researchers and government representatives. This could be improved by adding a round of interactions during the writing process. Lessons might be learned from the Structured Expert Dialogues organized during the UNFCCC's 2013–2015 review of the 2°C goal, in which government representatives held interactive question-and-answer sessions with experts from the IPCC and other organizations.

The IPCC could strengthen its process of selecting lead authors. Developing-country perspectives must be adequately represented, although scientific skills, capability, and international reputation should remain paramount. These dual goals of quality and diversity can be better achieved by more actively recruiting from the many distinguished scholars from developing countries who are working in the developed world but, nevertheless, can represent developing-country perspectives. This has sometimes been a challenge in the past. New partnerships, including with national and international academies of sciences, could support the author-nomination process.

The SPMs are the most widely referenced element of each WG report, largely because their text is negotiated and formally

approved by IPCC-member governments. The politically negotiated nature of the government-approval process at the end of each AR can lead to a dilution of key messages. Yet it would be difficult and possibly undesirable to change the SPM production process; IPCC reports are treated as authoritative partly because governments have formally accepted the SPM text. Instead of trying to change the SPM process and format, increasing the prominence of technical summaries (written solely by lead authors) would be useful. Renaming them “executive summaries” and engaging expert communicators could make them more accessible to policy-makers and the public. More clearly distinguishing between these two types of summaries could facilitate explicit acknowledgment and acceptance of divergent views that sometimes prevail between scientists and governments.

As the IPCC considered in its recent round of self-evaluation, the panel could also emphasize shorter, more-targeted reports that focus on recent research and that respond quickly and flexibly to the expressed needs of policy-makers.

OVERCOMING INERTIA. The new IPCC leadership will require support from governments to ensure success. The lack of government interest in major IPCC reform in the past can suggest satisfaction with its performance, but also reflects resistance to change in an organization prone to bureaucratic inertia. With its current substantive focus and procedural rules, the IPCC will have a difficult time meeting future challenges. After the UNFCCC Paris talks conclude in December, governments may have more appetite—and reason—to reconsider the IPCC's role in light of a new global climate-policy regime based on national implementation of highly heterogeneous, domestically determined policies. ■

REFERENCES

1. D. G. Victor, R. Gerlagh, G. Baiocchi, *Science* **345**, 34 (2014).
2. N. K. Dubash, M. Fleurbaey, S. Kartha, *Science* **345**, 36 (2014).
3. O. Edenhofer, J. Minx, *Science* **345**, 37 (2014).
4. N. Koch, S. Fuss, G. Grosjean, O. Edenhofer, *Environ. Policy* **73**, 676 (2014).
5. C. Böhringer, *Rev. Environ. Econ. Policy* **8**, 1 (2014).
6. M. Ranson, R. N. Stavins, *Clim. Policy* **10**, 1080/14693062.2014.997658 (2014).
7. J. Aldy, *Clim. Change* **126**, 279 (2014).
8. R. N. Stavins, *Environ. Forum (Washington D.C.)* **31**, 14 (2014).
9. O. Edenhofer, M. Kowarsch, *Environ. Sci. Policy* **51**, 56 (2015).

ACKNOWLEDGMENTS

The authors acknowledge the Alfred P. Sloan Foundation, the Fondazione Eni Enrico Mattei, and the Mercator Research Institute on Global Commons and Climate Change for sponsoring a workshop in Berlin, Germany, 18 to 20 February 2015, where these ideas were discussed. We appreciate contributions made by participants.

¹Fondazione Eni Enrico Mattei, 30124 Venice, Italy. ²Ca' Foscari University of Venice, 30123 Venice, Italy. ³Mercator Research Institute on Global Commons and Climate Change, 10829 Berlin, Germany. ⁴Potsdam Institute for Climate Research, 14473 Potsdam, Germany. ⁵Technische Universität Berlin, 10623 Berlin, Germany. ⁶Hertie School of Governance, 10117 Berlin, Germany. ⁷Stanford University, Stanford, CA 94305, USA. ⁸Harvard University, Cambridge, MA 02138, USA. ^{*}Corresponding author. E-mail: ottmar.edenhofer@pik-potsdam.de

CLIMATE CHANGE

Added value from IPCC approval sessions

Flexible, creative author teams are critical

By Christopher B. Field^{1,3*} and Vicente R. Barros^{2,3}

Approval sessions of the Intergovernmental Panel on Climate Change (IPCC) generate broadly shared ownership of scientific knowledge on climate change—a key contribution to the influence of IPCC reports (1, 2). Yet several recent essays have highlighted weaknesses of the approval process (3, 4). We draw on our experience cochairing Working Group II to provide some balance and to characterize important strengths. Although the governmental approval process can be cumbersome, sleep-depriving, and tinged with risk of political influence (5), successful approval sessions sharpen policy-relevant findings to make them more clear and useful (6).

IPCC summaries for policy-makers (SPMs) are approved line by line, by consensus of all participating governments. Typically, approval sessions involve 100 to 150 countries, plus senior representatives of the IPCC author team (1, 7). Given the high stakes and wide attention, it is hard to imagine approval sessions getting beyond the first few lines. Yet SPMs, many pages in length, get approved, usually with only minor changes to most content, cementing the status of the SPM and entire report as the definitive assessment of the state of knowledge on climate-change science. No other products of the scientific community achieve anything similar.

Extensive involvement of governments in approving SPMs can create the risk of political tinkering with the scientific findings. But this risk can be managed. The key is flexible author teams focused on the essence of each issue, interacting creatively with country delegates to craft solutions that address concerns while maintaining accuracy, rigor, and balance. Commentators have critiqued the sometimes inelegant or jargon-laden

wording of IPCC findings (8). It is difficult to phrase complex, subtle findings in a way that is accessible, crisp, and not susceptible to misinterpretation. That is where the approval process almost always helps.

Approval sessions are efficient for identifying text or figures that cause problems. The hard part is identifying improvements that work. Issues often arise because material is unclear, hard to put into context, seemingly inconsistent with the underlying evidence,



or subject to alternative interpretations. For concerns like these, approval sessions reliably lead to text and graphics with better precision and clarity. Of course, the results are not always entirely positive, especially if author teams too narrowly circumscribe a definition of the “correct” scientific expression. In the process, authors and country delegates must be willing to stretch to find common solutions.

Other times, issues arise based not on accuracy but on potential implications for upcoming negotiations. The dynamics of an approval session can help keep this risk of politicization in check, but it has been a challenge, especially for some topics in the economic and political sciences (3, 4). Failure to find common ground can result in limited coverage of particular issues in an SPM, and it can lead to legitimate questions about the effectiveness of the IPCC in highlighting specific assessment topics.

There are many examples of the approval process leading to dramatic improvements. One example concerns the relationship between a change in the mean of some climate

variable (e.g., temperature or precipitation) and the risk of extremes. This is a core concept for the IPCC special report, *Managing the Risks of Extreme Events and Disasters to Advance Climate Change Adaptation* (9). The draft SPM did not have a conceptual figure illustrating possible relations between means and extremes, although there was a figure in the report itself. In crafting the draft SPM, the author team felt that the concept was too simple to require a figure. Through the approval process, countries emphasized the importance of strengthening the presentation of key concepts. Eventually, persuasive arguments from several countries made it clear that, without the figure, the report's other findings became too confusing for many users.

What are lessons for the future? There are many other issues that are large in scale and extended in time, that integrate a range of interacting natural and human processes, and that involve values, priorities, and attitudes about risk as well as scientific information. An IPCC-like process applied to such topics could help create shared ownership and strengthen the foundations for good decisions. The Intergovernmental Platform on Biodiversity and Ecosystem Services (10), explicitly designed to build on some key features of the IPCC, will provide a test of the model's replicability.

IPCC approval sessions add value to the science-policy interface. Still, SPMs are legitimately criticized for being too long (8), difficult to understand (8), and selective in their coverage (4). Some level of this may be an unavoidable consequence of an inclusive process that addresses complex issues. But past successes point to creative approaches for clearly communicating robust science, increasing its relevance for society. ■

REFERENCES

1. B. Bolin, *A History of the Science and Politics of Climate Change: The Role of the Intergovernmental Panel on Climate Change* (Cambridge Univ. Press, New York, 2007).
2. E. Vasileiadou, G. Heimeriks, A. C. Petersen, *Environ. Sci. Policy* **14**, 1052 (2011).
3. O. Edenhofer, J. Minx, *Science* **345**, 37 (2014).
4. D. G. Victor, *Nature* **520**, 27 (2015).
5. M. Hulme, M. Mahoney, *Prog. Phys. Geogr.* **10.1177/030913310373719** (2010).
6. D. W. Cash et al., *Proc. Natl. Acad. Sci. U.S.A.* **100**, 8086 (2003).
7. IPCC, Appendix A of “The principles governing IPCC work” (IPCC, Geneva, 2013).
8. R. Black, *Nat. Clim. Change* **5**, 282 (2015).
9. IPCC, *Managing the Risks of Extreme Events and Disasters to Advance Climate Change Adaptation: A Special Report of Working Groups I and II of the Intergovernmental Panel on Climate Change*, C. B. Field et al., Eds. (Cambridge University Press, Cambridge and New York, 2012).
10. C. Perrings, A. Duraiappah, A. Larigauderie, H. Mooney, *Science* **331**, 1139 (2011).

¹Carnegie Institution for Science, Stanford, CA 94305, USA.

²University of Buenos Aires, Buenos Aires, Argentina. ³Cochair, Working Group II, Intergovernmental Panel on Climate Change.

*Corresponding author. E-mail: cfield@ciw.edu

A tree of the human brain

Genomes of single neurons trace the developmental and mutational history of the brain

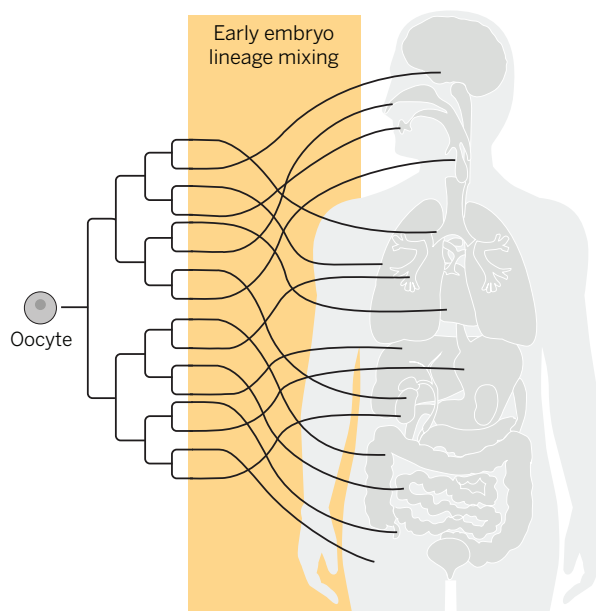
By Sten Linnarsson

Every cell of your body was generated by cell division, forming a lineage tree that goes back to the fertilized egg. Mutations are introduced by errors in DNA replication at every cell division, as well as by mutational processes that operate continuously, such as exposure to ultraviolet light. As a consequence, every cell may have its own unique genome, with potentially distinct gains and losses of function. Furthermore, these mutations create a record of the developmental ancestry of each cell, which can be used to reconstruct their lineage tree. Now, on page 94 of this issue, Lodato *et al.* use single-cell whole-genome sequencing to show these processes at work in the human brain (1). This is important because many unresolved questions in human biology and medicine are in fact questions about the human cell lineage tree in development and disease (2). Charles Darwin famously drew the first phylogenetic tree in 1837. This was only a month after he had started his first notebook on evolution, but the idea had already gelled in his mind that all species are linked like the branches on a tree. A few years later, around the time he was completing *On the Origin of Species*, a similarly remarkable insight was forming among a small group of scientists in Germany. Theodor Schwann and Matthias Schleiden had realized that both plants and animals are made of nothing but cells, but it was Robert Remak who showed that new cells arise through binary fission. These insights lead to the conclusion that every individual is also a tree—a cell lineage tree.

More than 150 years later, in 2005, Frumkin *et al.* showed that somatic mutations occur at cell division, in sufficient numbers that they can in principle be used to reconstruct complete human cell lineages (3). More recently, single-cell whole-genome

sequencing was used to reveal patterns of clonal evolution in breast cancer (4). Last year, Behjati *et al.* used organoid culture to amplify the genomes of individual mouse cells for whole-genome sequencing (5). They found that lineages could be reconstructed back to the early embryo, revealing that the earliest cells contribute to all tissues, but in highly skewed proportions.

Lodato *et al.* now extend the study of naturally occurring somatic mutations to the human brain. Sequencing 36 single neu-



Mutation trees. Lineages found in the prefrontal cortex were also often found in peripheral organs, showing that there must have been extensive mixing of lineages in the pre-gastrulation embryo.

rons from human prefrontal cortex, they found more than a thousand mutations per cell, the majority of which were unique to that cell. They noted that mutation rates at transcribed loci and at DNase I hypersensitivity sites were elevated, which suggests that RNA transcription and histone dissociation make DNA vulnerable in nondividing cells. This is in contrast to cancer, where errors related to DNA replication are more prevalent.

Although most mutations were intergenic, some occurred in coding regions. For example, a mutation in a voltage-gated sodium channel gene (*SCN1A*) was found, which would likely have caused epileptic seizures

if more widespread in the lineage. Remarkably, a quick calculation shows that it's likely that every coding nucleotide of every gene is mutated somewhere in the brain. If mutations accumulate with age, they may potentially contribute to disease. For instance, α -synuclein and β -amyloid are hypothesized to have prion-like properties (6), where misfolded proteins aggregate, spread, and catalyze the misfolding of further copies of native protein (causing, respectively, Parkinson's disease and Alzheimer's disease). This raises the question of how such a cascade could be initiated. But if every gene is mutated somewhere in the brain—and probably many times in many cells—it seems possible that a prion-like disease could be seeded by the rare occurrence of mutations that cause protein misfolding.

The authors used droplet digital polymerase chain reactions to analyze their catalog of prefrontal cortex mutations in other tissues of the body. This revealed a nested pattern across the brain, exactly as would be expected of mutations that accumulate during embryonic development. Even within a few millimeters of prefrontal cortex, multiple lineages were intermingled and were also found in heart, lung, and other peripheral organs, showing that lineages must have become physically mixed in the early embryo (see the figure). Indeed, any given neuron in the prefrontal cortex was more closely related to a cardiomyocyte than to 75% of its neighboring neurons.

These findings were enabled by recent advances in sequencing technology, single-cell sample preparation, and computational analysis. In the coming years, we can expect additional lineage trees of individual humans to deepen our understanding of embryogenesis as well as of how somatic

mutations may contribute to brain disease. In this way, the first small tree that Lodato *et al.* have drawn is a glimpse of the scientific and medical rewards that lie ahead as we begin exploring the human cell lineage tree in full. ■

REFERENCES

1. M. A. Lodato *et al.*, *Science* **350**, 94 (2015).
2. E. Shapiro, T. Biezuner, S. Linnarsson, *Nat. Rev. Genet.* **14**, 618 (2013).
3. D. Frumkin, A. Wasserstrom, S. Kaplan, U. Feige, E. Shapiro, *PLOS Comput. Biol.* **1**, e50 (2005).
4. Y. Wang *et al.*, *Nature* **512**, 155 (2014).
5. S. Behjati *et al.*, *Nature* **513**, 422 (2014).
6. M. Goedert, *Science* **349**, 1255555 (2015).

Division of Molecular Neurobiology, Department of Medical Biochemistry and Biophysics, Karolinska Institutet, S-171 77 Stockholm, Sweden. E-mail: sten.linnarsson@ki.se

ECOLOGY/PALEONTOLOGY

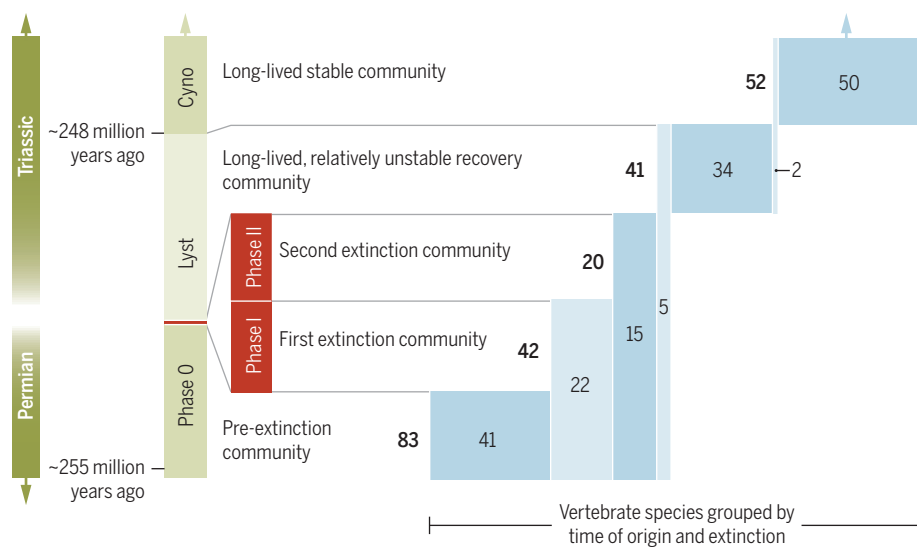
How stable are food webs during a mass extinction?

Fossil data provide a detailed view of how food webs changed across the Permian-Triassic mass extinction

By Charles R. Marshall

As we confront the reality of the ongoing human-driven mass extinction (1), attention often focuses on the response of individual species to environmental change. However, species survival also depends on other species in the food web: Changing population numbers or extinction of one species can propagate through the food web to cause further perturbation or extinction. Although this has long been appreciated (2), it is hard to test predictions of how food webs of living ecosystems will be affected by disturbance. The fossil record provides a window into how past food webs have responded to mass extinction. On page 90 of this issue, Roopnarine and Angielczyk (3) assess food web stability of the remarkably well-preserved terrestrial communities of the Karoo Basin in South Africa across the largest past mass extinction, the Permian-Triassic event (~252 million years ago).

Department of Integrative Biology, University of California Museum of Paleontology, University of California, Berkeley, CA 94720, USA. E-mail: crmarshall@berkeley.edu



Changing food webs. Roopnarine and Angielczyk have analyzed the stability of fossil terrestrial communities that span the end-Permian mass extinction (3). Two very short-lived extinction communities (red) predated the final extinction. The durations of the phase I and II communities and their position with respect to the Permian-Triassic boundary (~252 million years ago) are not well understood. Numbers give the total number of species in each community.

assic boundary and that represent successive decimations of the phase 0 community, a bizarre Early Triassic recovery community (LAZ/Lyst), and the Middle Triassic post-recovery community (Cyno).

Reconstructing the exact configuration of the species' linkages in fossil food webs is difficult without the capacity to observe species interactions directly. To circumvent this problem, for each community the authors constructed 100 plausible food webs, each with a different linkage pattern between the species that is consistent with the ecological properties of the species and with the general properties of food webs.

Roopnarine and Angielczyk then compared the local stability of each plausible food web with four randomized variants of each web. Food webs consist of guilds (groups of species that exploit the same resource, e.g., large carnivores or small herbivores). These are organized into networks that dictate which guilds interact. An actual food web consists of the set of realized species links among the interacting guilds, typically a subset of all the possible species links among those guilds (e.g., which large carnivores prey upon which small herbivores). The variant food webs were created by either randomly reassigning the species to the feeding guilds, randomly reorganizing the guild network, removing the guild network altogether, or changing the frequency distribution of the number of links between species.

The stability of the pre-extinction community (phase 0), which lasted about 3 million years, generally exceeded that of its variant food webs. Its stability was thus similar to that of modern food webs. That community was then successively decimated in two extinction phases over an interval of ~120,000 years (6) or possibly much longer (7). The stabilities of these surviving communities also generally exceeded that of their variant food webs. This elevated stability stemmed, in part, from the initial preferential extinction of small-bodied amniotes (all vertebrates excluding fish and amphibians).

The higher extinction rate for small-bodied species is unexpected given that, in the modern world, extinction rates rise with body size. However, there are fundamental differences between Permian and present-day ecosystems. Today many large mammals feed on grasses. As small plants with shallow roots, grasses are likely to be harder hit by aridification and acidification, both of which are thought to have been major drivers of the end-Permian terrestrial extinctions (8, 9). Because there were no grasses in the Permian, there was a stronger correlation between plant size and the size of the species that fed on them than exists

today (6). As the end-Permian environmental crisis unfolded, it appears to have preferentially affected small plants, and thus small herbivores and their predators (6).

Although the initial decimation of the Permian community did not seem to adversely affect food web stability, the Early Triassic recovery community (Lyst/LAZ) was no more stable than the variant food webs. This community consisted of a few mass extinction survivors and a large number of new species, including an unusual diversity of amphibians and small insectivores. The inferred instability is consistent with previous work showing that this community is much more sensitive to extinction introduced at the base of its food web than are the Permian communities (10).

After ~4 million years, the relatively unstable recovery ecosystem was replaced with the Middle Triassic community (Cyno), which inherited just two of its 52 vertebrate species from the initial recovery community. This latter community had a stability similar to that of the robust pre-extinction community (phase 0).

The study raises some fundamental questions. Was the Triassic recovery community less stable simply because of its unusual taxonomic composition, or did its lack of stability reflect unusual properties, perhaps a fundamental instability of the abiotic environment in the Early Triassic (11)? Alternatively, is food web stability a property that increases with evolutionary time as taxa are replaced, with the Early Triassic representing a “standard” founding community? In general, what is the relationship between evolutionary change and food web stability? This question is particularly pertinent given our current perturbation of Earth’s ecosystems (12). Similar dissection of fossil food webs as they traverse major evolutionary transitions will help illuminate the fundamental question of how food web structure evolves and how it affects the resilience of the biosphere to perturbation. ■

REFERENCES AND NOTES

1. A. D. Barnosky *et al.*, *Nature* **471**, 51 (2011).
2. R. M. May, *Stability and Complexity in Model Ecosystems* (Princeton Univ. Press, Princeton, NJ, 1973).
3. P. D. Roopnarine, K. D. Angielczyk, *Science* **350**, 90 (2015).
4. J. A. Dunne *et al.*, *PLoS Biol.* **6**, e102 (2008).
5. J. A. Dunne, C. C. Labandeira, R. J. Williams, *Proc. R. Soc. B* **281**, 20133280 (2014).
6. R. M. H. Smith, J. Bothe-Brink, *Palaeogeogr. Palaeoclimatol. Palaeoecol.* **396**, 99 (2014).
7. R. A. Gastaldo, *Geology* **43**, 939 (2015).
8. M. J. Benton, A. J. Newell, *Gondwana Res.* **25**, 1308 (2014).
9. M. A. Sephton *et al.*, *Geology* **43**, 159 (2015).
10. P. D. Roopnarine *et al.*, *Proc. R. Soc. B* **274**, 2077 (2007).
11. J. L. Payne *et al.*, *Science* **305**, 506 (2004).
12. A. D. Barnosky *et al.*, *Nature* **486**, 52 (2012).

ACKNOWLEDGMENTS

Thanks to S. P. Quek for her critical reviews of the manuscript.

10.1126/science.aad2729

PLANETARY SCIENCE

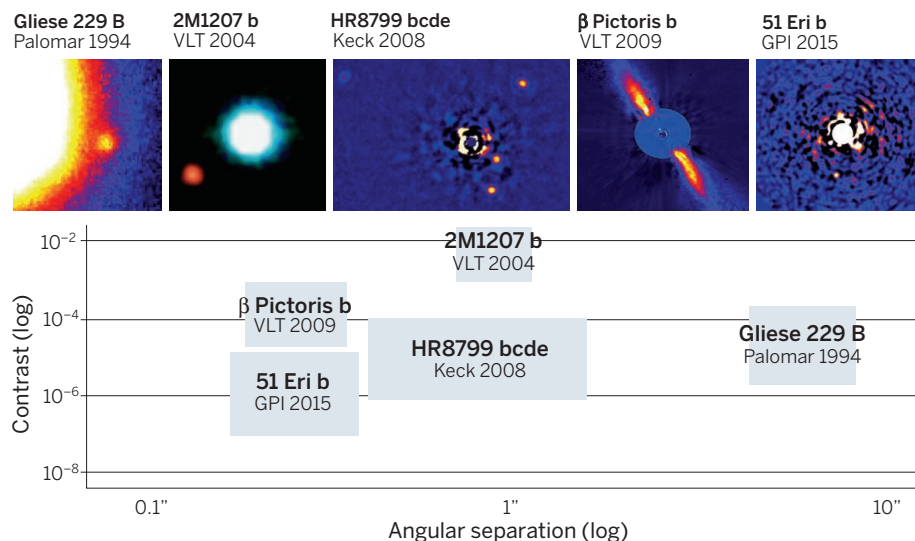
Eyeing up a Jupiter-like exoplanet

Extreme adaptive optics systems enable the direct imaging of exoplanetary systems

By Dimitri Mawet

With thousands of exoplanets having been discovered over the past 20 years, the solar system is recognized as presenting just one example among a mind-boggling variety of system architectures: from circumbinary exoplanets (1), systems with tightly packed inner planets (2), water-worlds

capabilities, yet have ushered in an entirely new branch of astrophysics called comparative exoplanetology, putting the solar system and its planets into a universal perspective. On page 64 of this issue, Macintosh *et al.* (9) present the discovery of a young giant exoplanet with the Gemini Planet Imager (GPI) and a technique called high-contrast imaging. Beyond taking striking pictures (see the figure), the technique promises to yield



Coming into view. Evolution of contrast versus angular separation illustrated by representative scientific discoveries in the infrared. Discovery of the brown dwarf companion around Gliese 229 at Palomar (12); the planetary mass companion around brown dwarf 2M1207 with the first-generation adaptive optics infrared camera of the Very Large Telescope (13); the four giant planets around A-type star HR8799 with the Keck adaptive optics system (15); the discovery of giant planet β Pictoris (14); and the new GPI discovery of 51 Eri b by Macintosh *et al.* (9).

(3), potential Earth twins (4), super-Earths (5), sub- and super-Neptunes (6), evaporating comet-like planets (7), giant rings (8), and hazy hot Jupiters all the way to extremely long-period lonely massive objects looking more like failed stars than giant planets. So far, the vast majority of these planetary systems have been discovered indirectly by techniques looking at tiny variations in their host star’s motion and/or brightness. These techniques have limited remote-sensing ca-

the most detailed measurements of whole distant planetary systems, including spectroscopy of planet atmospheres and time-resolved astrometry of their orbital motion.

The first exoplanet around a solar-type star was detected indirectly 20 years ago with the Doppler technique, which measures variations in the radial velocity of a star due to the gravitational pull of one or several orbiting planets, and thus the orbital periods and planetary masses by virtue of the laws of gravitation. Bolstered by NASA’s highly successful space telescope Kepler, the transit method measures the dimming of starlight as a planet passes in front of it,

Department of Astronomy, Jet Propulsion Laboratory, California Institute of Technology, Pasadena, CA 91125, USA.
E-mail: dmawet@astro.caltech.edu

yielding the planet's radius. Combining both the transit and Doppler techniques, when possible, is extremely powerful, allowing average densities to be inferred and thereby informing atmospheric and planetary interior models. For instance, the ability to distinguish between iron-, silicate-, or volatile-rich planets revealed that most planets exceeding 1.6 Earth radii are likely not rocky and that Neptune-like and sub-neptunes are common (6). Some favorable transiting cases are amenable to spectroscopic analysis, which can determine the molecular composition of the upper layers of planetary atmospheres—if the local weather, and thus cloud coverage, cooperates (10).

Direct imaging of exoplanets requires separating the signal of a relatively small, faint, and cooler object seemingly very close to a huge, overwhelmingly bright ball of fiery gas. Imaging an object at the angular separation and contrast of the planet discovered by Macintosh *et al.* is equivalent to spotting a tiny ember flying off a blazing campfire 200 km away, while looking through a window battered by heavy rain. Macintosh *et al.* and other similar projects address these difficulties by a four-pronged approach: Take the biggest available optical telescope; use a device called a coronagraph to reject the blinding starlight; correct the blurring effect of Earth's turbulent atmosphere as much as possible by using an extreme adaptive optics system; and, finally, target young planetary systems where forming giant planets still generate enough internal heat from their contraction and glow in the infrared.

Adaptive optics is a sophisticated technique that effectively removes the twinkle from the stars. By means of a dedicated sensor, it measures the corrugation of the incoming waves of starlight upon propagation through the 100 km of Earth's turbulent atmosphere more than 100 times per second. Almost simultaneously, the adaptive optics system imposes the inverse corrugation on a small deformable mirror with a few hundred actuators, flattening the wavefront and restoring the image quality and finesse of the scope in real time. Adaptive optics systems have been used on ground-based telescopes for more than 20 years. The performance of GPI, and other extreme adaptive optics systems, relies on the 10-fold increase in speed and actuator density, which results in much better image quality, a prerequisite to efficient starlight suppression, and thus high-contrast imaging.

What makes the first exoplanet discovery of GPI so interesting is its timing and nature. 51 Eridani b (Eri b) was the GPI "object of interest" number 2, so either Macintosh *et al.* were extremely lucky, or we are on the verge of a great harvest of planets by second-

generation high-contrast imaging surveys. The first generation of direct imaging surveys started more than 10 years ago indeed turned up very few giant planets. Limited in contrast and inner working angle, these first attempts nevertheless found that long-period giant planets, orbiting at several tens of astronomical units (an AU is the distance from the Sun to Earth), are rare around all spectral types (11), and that the handful of planets imaged so far have weak or nonexistent methane absorption features, with a spectral energy distribution resembling that of the more massive cloudy field brown dwarfs. One plausible reason for the dearth of long-period giant planets is that high-entropy gravitational instability and core collapse, both star-formation mechanisms, are becoming less efficient processes.

An alternative explanation is that giant planets formed in situ through core accretion closer to the ice lines, stay nearby, and do not scatter or migrate outward to much larger orbits. High-contrast imaging and spectroscopy could rapidly confirm the latter scenario. Indeed, 51 Eridani b is the first directly imaged planet showing a spectrum similar to those of other brown dwarf classifications, with a textbook methane absorption feature reminiscent of Jupiter's. As we work our way through the inner reaches of extrasolar planetary systems with spectro-imagers like GPI and subsequent generations on the 30-m class of extremely large ground-based telescopes, we will be able to refine our understanding of the formation of giant planets, bridging the gap between field brown dwarfs and Jupiter-like planets. The results presented by Macintosh *et al.* mark the beginning of a new era in the quest for our planetary system's origins and the prospect of life outside our solar system. All the technological ingredients are now in place for major breakthroughs in the field of high-contrast imaging, aided by a suite of projects exploiting the largest ground- and space-based telescopes. ■

REFERENCES

1. W. F. Welsh *et al.*, *Astrophys. J.* **809**, 26 (2015).
2. W. J. Borucki *et al.*, *Science* **340**, 587 (2013).
3. L. Kaltenegger *et al.*, *Astrophys. J.* **775**, L47 (2013).
4. L. A. Rogers, K. Deck, J. Lissauer, J. Carter, IAU General Assembly, Meeting 29, 2257697 (2015).
5. J. M. Jenkins *et al.*, *Astron. J.* **150**, 56 (2015).
6. F. Fressin *et al.*, *Astrophys. J.* **766**, 81 (2013).
7. D. Ehrenreich *et al.*, *Nature* **522**, 459 (2015).
8. M. A. Kenworthy, E. E. Mamajek, *Astrophys. J.* **800**, 126 (2015).
9. B. Macintosh *et al.*, *Science* **350**, 64 (2015).
10. D. K. Sing *et al.*, *Mon. Not. R. Astron. Soc.* **416**, 1443 (2011).
11. B. P. Bowler, M. C. Liu, E. L. Shkolnik, M. Tamura, *Astrophys. J. Suppl. Ser.* **216**, 7 (2015).
12. T. Nakajima *et al.*, *Nature* **378**, 463 (1995).
13. G. Chauvin *et al.*, *Astron. Astrophys.* **425**, 29 (2004).
14. C. Marois *et al.*, *Science* **322**, 1348 (2008).
15. A.-M. Lagrange *et al.*, *Astron. Astrophys.* **493**, 21 (2009).

10.1126/science.aad0904



ATMOSPHERIC SCIENCE

Clouds resolved

Clouds are puffy to the finest scale

By Eberhard Bodenschatz

The pillowing structure and filamentary detail of clouds has inspired many paintings as well as associations to down pillows. Turbulence is at the source of this beauty. It affects aerosol-cloud droplet interaction, cloud particle collisions and merging, and entrainment and mixing of environmental air with clouds (1, 2). These microphysical processes are important for predicting weather and climate (3). Yet it has remained very difficult to observe clouds at the temporal and spatial scales required to gain understanding of these processes. On page 87 of this issue, Beals *et al.* (4) show that the filamentary structure of entrainment and mixing reaches to the centimeter scale in a cloud.

The authors used a sophisticated holographic imaging system that allowed them

Max Planck Institute for Dynamics and Self-Organization,
Am Faßberg, 37077 Göttingen, Germany.
E-mail: eberhard.bodenschatz@ds.mpg.de



to measure both the locations and the sizes of the micrometer-size water droplets in three dimensions while flying through warm cumulus clouds with an airplane. Their findings are a breakthrough in the measurement of microphysical processes in clouds. They show that state-of-the-art imaging technologies enable quantitative measurements of cloud microphysical processes at unprecedented precision, resulting in the discovery of unexpected phenomena. Data like those presented in this report promise to guide the development of more accurate parameterizations of cloud microphysics in weather and climate models (1–3).

Micrometer-sized droplets and ice crystals that are carried by very turbulent flows give a cloud its appearance. Details of these highly dynamical processes are very hard to observe in a real cloud. An impression of the rapid and complex dynamics give the cloud-like pillows coming from hydrothermal vents at Iceland (see the first figure and video). Within a cloud, turbulent winds carry droplets, and mix them with moist and dry air, cold and warm air, and also aerosols that are needed for cloud condensation nucleation. Cloud microphysical processes include (2) evaporation, condensation, freezing, melting, sublimation, deposition and merging, and inertial particle dynamics (5).

One way to visualize the inhomogeneity and intermittency of a cloud is to illuminate a cloud with a laser sheet and observe the scattering from the cloud droplets (see the second figure) (6, 7). This method demonstrates the inhomogeneous, filamentous distribution of cloud droplets at the centimeter scale (inset, second figure). It thus provides evidence that clouds have features reminiscent of turbulent mixing at the smallest scales (8).

Beals *et al.* now succeed in showing quantitatively that warm clouds are inho-

Cloud-like dynamics. The fast and intermittent dynamics of clouds, their filamentous structure, and the multiscale, highly dynamical structure of the turbulence can be observed closely at the blow holes of the hydrothermal plants at Iceland. There, overheated steam blows rapidly from exit pipes into the surrounding air (see also the video at http://scim.ag/aad1386_mov2), generating a turbulent jet of condensing air that is carried away by the prevailing wind and mixed with the surrounding dry air. These processes are very reminiscent of a boundary between a cloud and clear air.

mogeneous at the smallest scales of turbulence. They found that droplets cluster in filaments of droplet-filled air surrounded by clear air. Within a filament, particles had approximately equal sizes. As also pointed out by the authors, their observations have important consequences for understanding cloud optical depth, cloud top circulation, cloud life cycle, and large droplet production. As recently summarized by Bony *et al.* (3), more accurate microphysical cloud parameterizations are much needed for predicting large-scale circulation patterns and climate sensitivity. Cloud microdynamics can also be regarded as a simple form of combustion (9). Insights into cloud microphysical processes can therefore also help engineers concerned with combustion processes.

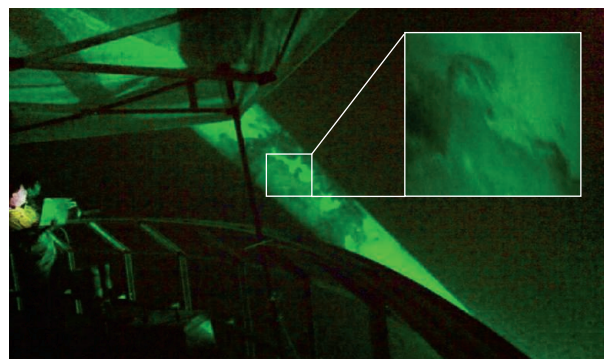
With further development of this and other direct imaging techniques (5, 10), it soon will be possible not only to observe the spatial distribution and size of droplets but also to follow individual droplets or ice particles and to measure particle-particle interactions like collisions, coalescence efficiencies, ice aggregation, and drop- or ice-breakup. These data are much needed to better our understanding of cloud microphysics and its consequences for weather and climate. ■

REFERENCES AND NOTES

1. A. P. Khain, *Environ. Res. Lett.* **4**, 015004 (2008).
2. B. Stevens, *Nature* **503**, 47 (2013).
3. S. Bony *et al.*, *Nat. Geosci.* **8**, 261 (2015).
4. M. J. Beals *et al.*, *Science* **350**, 87 (2015).
5. G. P. Bewley *et al.*, *New J. Phys.* **15**, 083051 (2013).
6. S. Risius *et al.*, *Atmos. Meas. Tech.* **8**, 3209 (2015).
7. H. Siebert *et al.*, *Atmos. Meas. Tech.* **8**, 3219 (2015).
8. Z. Warhaft, *Annu. Rev. Fluid Mech.* **32**, 203 (2000).
9. A. Majda, P. Sauganidis, *Comm. Pure Appl. Math.* **53**, 1284 (2000).
10. A. Schroeder *et al.*, *Flow Turbulence Combust.* 10.1007/s10494-015-9616-2 (2015).

ACKNOWLEDGMENTS

The image shown in the second figure was taken during a measurement campaign at the Environmental Research Station Schneefernerhaus. I am thankful to J. F. Bodenschatz, S. Risius, H. Xi, H. Xu, who conducted the light sheet experiments with me, and to S. Malinowski, T. Schmeissner, R. A. Shaw, and H. Siebert, who participated in all aspects of the measurement campaign. Support of the research from the Max Planck Society and the Bavarian Ministry of the Environment and Consumer Protection is acknowledged.



Fine-scale structure. Dynamics of a warm convective cloud observed at 21:50 CEST on 29 August 2011 at the Environmental Research Station Schneefernerhaus at ~2700 m (2, 3). The cloud was illuminated with a 48-W green laser sheet, with the plane perpendicular to the observer. The laser sheet was slightly divergent and at the observation site was ~1.5 m wide and ~3 cm thick (see also the video at http://scim.ag/aad1386_mov1). High (low) concentration of droplets scatter much (little) light. (Inset) A region ~30 cm in diameter reflects the fine-scale structure of the droplet distribution within the turbulent cloud.

PHOTO: EBERHARD BODENSCHATZ

NEUROSCIENCE

It takes the world to understand the brain

International brain projects discuss how to coordinate efforts

By Z. Josh Huang¹ and Liqun Luo²

We are on the verge of a fundamental leap toward understanding the human brain, and the implications for health and society are profound. Large-scale brain projects have been launched or are being planned in multiple continents and countries (1–4). In June, about 50 leading scientists from the United States, Europe, Japan, Korea, and China gathered in Suzhou, China (organized by Cold Spring Harbor Asia) to discuss the opportunities and challenges in brain research (5). The benefits of international coordination and collaboration were recognized, and the discussions laid a foundation for future meetings aimed at fleshing out details related to specific goals.

COMPLEXITY. The human brain is arguably the most complex entity in the known universe, and this complexity is best reflected by the fact that the brain strives to understand itself—how its molecules, cells, circuits, and systems enable perception, cognition, memory, emotion, thought, language, art, and contemplation of humanity's place in the natural world. Inquiry into the origins of mental faculties and disorders in the brain dates back to antiquity (6). Since the formulation of the neuron doctrine and detailed structural studies by Ramón y Cajal more than a century ago (7), there has been great progress in understanding the cellular basis of brain organization and function. In the past decade, technological advances in multiple disciplines have accelerated that progress. New tools for visualizing, recording, and manipulating neurons and neural circuits are enabling deeper insight into how the brain processes information and guides behavior. Advances in computer science have exponentially boosted the capacity for analyzing, cu-

rating, and sharing enormous data sets. And genome-wide mapping has identified genetic variants that contribute to a wide spectrum of human brain disorders.

To better appreciate the challenges of understanding the brain, it is informative to compare the brain projects with the first large-scale international bioscience collaboration launched in late 1980s—the Human Genome Project. The Human Genome Project aimed to determine the complete sequence of

to, thousands of other neurons distributed over local and distant brain space, delineating the wiring diagram of these neurons (the connectome) alone is an immense challenge. Moreover, the connectome is not a static network; both the connectivity pattern and connection strengths change across life stages and are modified by an individual's experience and learning. Furthermore, mapping the connectome is only one step toward understanding the brain—it is the dynamic firing of neuronal ensembles and their communication across local and global networks, which are layered onto the structural framework of the connectome, that generate perception, cognition, and action.

SIX FRONTS. Neuroscientists largely agree that to achieve a deep understanding of how the brain processes information and orchestrates mental functions, substantial progress is needed on at least six fronts: (i) identifying the basic components of brain circuits—classes of neurons that share similar properties and perform similar functions (belong to the same cell types); (ii) deciphering the neuronal wiring diagrams integrated across multiple scales, from individual synapses (microscopic) to the entire brain (macroscopic); (iii) recording the firing patterns—the common vocabulary of neuronal communication—of large numbers of neurons across different brain regions while an animal or human subject performs well-characterized behavioral or cognitive tasks; (iv) manipulating neuronal firing patterns with spatiotemporal

precision so as to establish the causality between neuronal activity and circuit function that contributes to behavior; (v) inventing computational tools for integrating and analyzing large and complex data sets; and (vi) formulating overarching brain theories that transcend levels and scales, conceptualize experimental findings, and predict novel circuit properties that underlie brain function. In addition, because most experiments are performed in animal models, knowledge gleaned from animal experiments must be integrated with insights gained from recording,

Brain projects summary

BRAIN PROJECTS	MAJOR GOALS AND FOCUS
U.S. BRAIN Initiative	<ul style="list-style-type: none"> • Tools to enable a brain cell census and for recording/modulating brain circuit activity linked to behavior • Multilevel brain data • New computational models and theory
Japan Brain/MINDS	<ul style="list-style-type: none"> • Nonhuman primate brain • Collaboration between clinicians and researchers toward knowledge-based diagnosis and treatment of brain disorders
Europe HBP (Human Brain Project)	<ul style="list-style-type: none"> • Big data integration and analysis • Computational modeling
Allen Institute for Brain Science	<ul style="list-style-type: none"> • Mouse visual system • Human cortex • Open, public, shared database and tools
Korea Brain Project	<ul style="list-style-type: none"> • Systems neuroscience of cognition and brain disorders • Neural circuits and brain imaging
China Brain Science Project (in planning)	<ul style="list-style-type: none"> • Neural circuitry of cognition • Brain disorders • Brain-inspired intelligence technologies
Brain Canada	<ul style="list-style-type: none"> • Increased brain research funding • Collaboration related to brain disorders
Taiwan	<ul style="list-style-type: none"> • Neurodegeneration • Chronic pain
Australia	<ul style="list-style-type: none"> • Collaboration with U.S. BRAIN

the human genetic blueprint encrypted in ~3 billion nucleotides organized along 23 chromosomes. The genome is a largely static linear sequence composed of just four discrete nucleotides; the ~20,500 protein-encoding genes constitute 1 to 2% of this sequence. The project provided the foundation for an explosion of biomedical research.

The human brain can be considered vastly more complex in multiple aspects. It contains ~10¹¹ neurons, linked by ~10¹⁴ synaptic connections. As any one neuron on average receives inputs from, and delivers outputs

¹Cold Spring Harbor Laboratory, Cold Spring Harbor, NY 11724, USA. ²HHMI/Department of Biology, Stanford University, Stanford, CA 94305, USA. E-mail: huangj@csih.edu; lluo@stanford.edu

stimulating, and imaging the human brain to understand human mental functions and to treat brain disorders.

OVERVIEW OF PROJECTS. The current brain projects launched or planned in different countries have different emphases (see the table and figure). The U.S. BRAIN (Brain Research through Advancing Innovative Neurotechnologies) Initiative is now in the second year of a 12-year plan. Its initial phase emphasizes developing new tools that are expected to catalyze discoveries in later phases about neural circuit function in health and disease (*1, 2*). The European Union's Human Brain Project (*3*), started in 2013 and financed by the Future Emerging Technologies Program of the European Community, focuses on large-scale computational modeling and building neuroinformatics standards for brain databases, and could benefit from data acquired from brain projects around the globe. Japan's Brain/MINDS (Brain Mapping by Integrated Neurotechnologies for Disease Studies) project (*4*), launched at the end of 2014, features primates—in particular, the marmoset, a relatively new genetic primate model—for basic research and for modeling human brain disorders. Brain Canada was announced this year, supporting collaborative, multidisciplinary, multi-institutional neuroscience research. Korea also just started its brain project on the systems neuroscience of cognition and brain disorders, with emphasis on neural circuits and brain imaging. China has yet to officially announce its brain project, but discussions are well under way, and its scope will likely include neural circuits of cognition, brain disorders, and brain-inspired intelligence technologies. Nonhuman primate studies including the macaque monkey, a long-standing model for neuroscience research, are likely to be part of China's brain project. Taiwan is planning a modest-scale brain project on neurodegeneration and chronic pain, with emphasis on interdisciplinary studies and development of novel neurotechnologies. This year, Australia established a collaborative effort with the U.S. BRAIN Initiative. In addition to these government-funded brain projects, the Seattle-based, privately funded Allen Institute for Brain Science launched a 10-year brain circuit project that intends to create a system of publicly shared data and tools to study mouse and human visual systems.

STANDARDIZATION. No single country or brain project alone is equipped with the collective intellectual, technological, financial, and human power needed to achieve

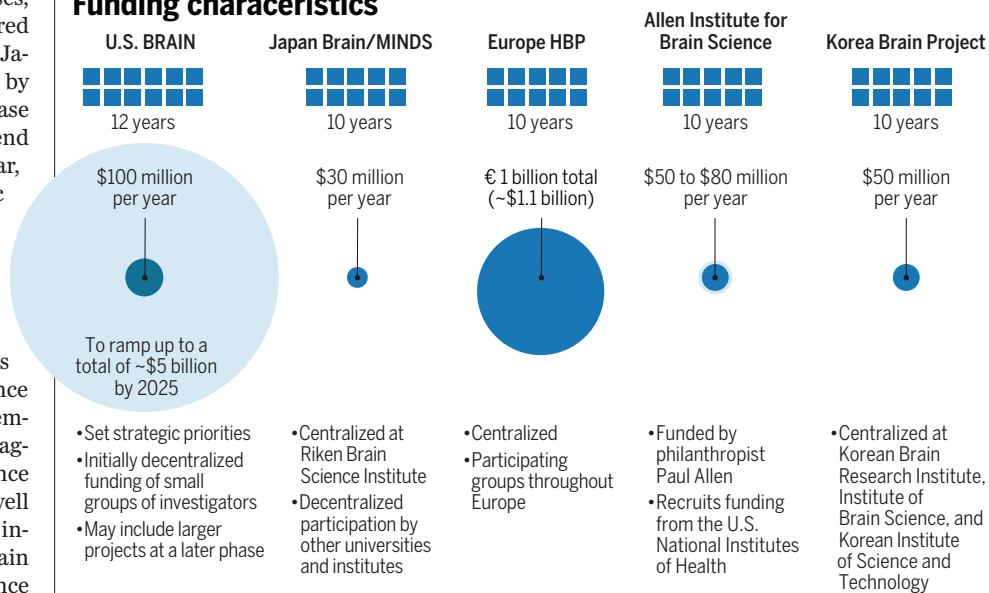
the task of understanding the brain. The Suzhou discussions identified several areas where the needs for international coordination are particularly acute but likely to be high-yielding if particular strengths of the different brain projects are leveraged and standardization is implemented.

Take the problem of cell type as an example. The brain consists of a large diversity of nerve cell types that serve as working units of widely distributed neural networks. Systematic identification and classification of this parts list is a prerequisite to mapping the wiring diagram, recording and manipulating cell type-specific activity, and deciphering circuit operations that underlie information processing and behavior. The recent convergence of neural developmental studies from invertebrates to mammals, as well as genetic

cell types across multiple model organisms, including humans, should reveal common principles as well as key differences concerning the organization of the brain's working units. With this parts list in hand, scientists can systematically establish experimental access to specific cell types, which will greatly facilitate and integrate multiple levels of neural circuit studies.

Coordination and standardization of data (not to mention metadata acquisition, curation, and analysis) are more challenging in certain domains of neuroscience research such as neurophysiology and brain imaging. An extreme example is behavior, the final output of neural circuit operation and ultimate manifestation of brain function. Because behavior results from the integration of sensory inputs, brain states, and cogni-

Funding characteristics



and genomic technologies, has made it possible to systematically identify distinct cell types. Single-cell transcriptome profiling (quantitative determination of the expression levels of all genes) promises to refine cell type definition and enhance precision of genetic access to individual cell types (using genetic tools to label, record, and manipulate activity in a cell type-specific manner). Thus, the cell type problem is fundamental and challenging, yet well-defined and solvable by leveraging the collective power of individual brain projects.

What should be standardized in this context? Cell transcriptomes can be acquired with a defined format, deposited into a common database, and analyzed similarly to the genome data. Data sets on cell location, morphology, and projection patterns (locations in the brain where cells send information) can also be standardized. Comparisons of

active decision-making, and because it manifests as high-dimensional motor output, it is inherently complex and variable even in highly constrained experimental conditions, let alone more naturalistic paradigms. To understand the neural basis of behavior, scientists use many different and often highly specialized experimental designs to record and manipulate neuronal activities in different brain regions while animals or human subjects perform tasks of varying sophistication. Thus, not only the behavioral data themselves but also simultaneous recording and manipulation of neural activity can be difficult to standardize. Indeed, the Suzhou discussions included vigorous debate as to whether it is possible, or even beneficial, to standardize a few sets of agreed-upon behavioral paradigms for data acquisition and comparison across different labs, and for comparison across species.

SHARING. There is pressing need for an infrastructure that makes sharing data among the brain projects feasible. But creating such a system is a formidable task, and funding and personnel requirements are often underestimated. However, the benefits of data sharing make this an important issue. For example, genetic data from human patients suffering from brain disorders can be shared around the globe; such data sharing thus far has spurred the identification of genetic variants contributing to disorders such as schizophrenia and autism (8–10). In 2005, the International Neuroinformatics Coordinating Facility (INCF) was initiated by the Global Science Forum of the Organization for Economic Cooperation and Development to help advance data reuse and reproducibility in brain research through the development of global standards, best practices, tools, and infrastructure (11). INCF and other similar organizations may be best positioned to support data sharing (as well as draw partnerships among scientific, clinical, technical, industrial, and funding arms).

Another need is for resource sharing. For example, nonhuman primate research is highly valuable for disease biology but is expensive and time-consuming, with associated ethical issues. Genetic engineering and genetic modeling of human brain disorders in nonhuman primate models could greatly benefit from coordinating research on shared experimental animals. Establishing international primate centers as hubs for such collaborations could move this forward.

TRAINING. In response to the avalanche of big data on multiple scales, and in recognition of the extraordinary complexity of neural circuits endowed with an abundance of feedback loops, there is a need to expand the field of theory and computational modeling. Computational neuroscience provides a necessary bridge between neurobiology and brain-inspired intelligence. In particular, the Suzhou discussions noted the importance of equipping a new generation of scientists with the knowledge and tools of multiple disciplines for exploring the brain. In particular, a consensus emerged that analyzing and conceptualizing large data sets from brain projects will require talents that can better integrate experimental neuroscience with computational analyses, modeling, and theory. To leverage brain projects at the international scale, “hybrid” interdisciplinary degree programs and training centers across

different nations are needed that offer theoretical, computational, and experimental courses. Another useful mechanism is to support sustained programs of exchange students among collaborating research groups to learn specific experimental techniques or data analysis tools.

FUNDING. Even in nations where brain projects are already ongoing, steady support is not guaranteed. For example, although the working group of the U.S. BRAIN Initiative has made specific, conservative budget recommendations for 12 years, the actual funding requires congressional approval each year and is subject to short-term fluctuations of the political process. All brain projects at present are organized to primarily fund research groups within individual countries or a continent. Thus, innovative funding strategies and mechanisms are needed to support international collaboration. Here, support from private organizations and philanthropists can boost the brain projects. For example, the Allen Institute for Brain Science, launched ~10 years ago, has generated large data sets (such as murine gene



expression and neuronal projection maps) that have benefited the neuroscience community worldwide. Likewise, the Janelia Farm Research Campus of the Howard Hughes Medical Institute, also established ~10 years ago (focused on information-processing principles in neural circuits and developing new tools), has made key contributions to the foundation of brain projects. The Simons Foundation launched a “Global Brain” collaboration for studies of population neural data at cellular resolution and advanced statistical modeling, and the Kavli Foundation has supported neuroscience centers and the initial discussion of the U.S. BRAIN project. Strategic collaborations that capitalize on the unique expertise of small research groups on the one hand, and the high-throughput, large data capacity of private research institutes on the other, may achieve milestone advances that are not possible by working separately. Of course, continued and effective engagement with the public is critical to gathering and maintaining support for brain projects.

NEXT STEPS. The most important outcome of the Suzhou discussions is the unanimous agreement and enthusiasm that coordination of the world’s multiple brain projects is necessary and feasible, even though specific implementation mechanisms remain to be worked out. In the formative period of genome se-

quencing, a series of meetings including those organized by Cold Spring Harbor Laboratory profoundly shaped the foundation and international collaboration of the Human Genome Project. The success of this project has revolutionized biology and medicine and has produced exceptionally high returns on the investment (12). Unlike this and other large-scale national or international physics (e.g., CERN) and engineering programs (e.g., space programs), all characterized by well-defined goals and more definable strategies, a unique challenge for the brain projects is that the overarching goal may only be achieved by solving a large set of multifaceted and interrelated problems in multiple organisms (including humans), with highly interdisciplinary approaches carried out in many laboratories across the globe. There are few precedents for such a large-scale and highly sophisticated scientific endeavor. We envision that the discussions initiated in Suzhou will continue in future meetings as the national brain projects evolve. The collective success of these projects will be enormous: It will yield greater insight into the inner working of the human brain, often considered the last frontier of scientific inquiry; help to treat devastating brain disorders that are major burdens on current and future society; inspire brain-like computer design and intelligence technologies; spawn new industries and stimulate new economies; build foundational links from science to the humanities; and ultimately achieve a deeper understanding of what makes us human. ■

REFERENCES AND NOTES

1. L. A. Jorgenson *et al.*, *Philos. Trans. R. Soc. London Ser. B* **370**, 20140164 (2015).
2. www.braininitiative.nih.gov/2025/BRAIN2025.pdf
3. www.humanbrainproject.eu/
4. <http://brainminds.jp/en/overview/organization>
5. Cold Spring Harbor Asia Conference on International Brain Projects, 19 to 22 June 2015, Suzhou, China (see the supplement).
6. Hippocrates, *On the Sacred Disease* (~400 C.E.); <http://classics.mit.edu/Hippocrates/sacred.html>.
7. S. Ramón y Cajal, *Histology of the Nervous System of Man and Vertebrates* (Oxford Univ. Press, Oxford, 1995; translation of 1911 French version).
8. Schizophrenia Working Group of the Psychiatric Genomics Consortium, *Nature* **511**, 421 (2014).
9. S. De Rubeis *et al.*, *Nature* **515**, 209 (2014).
10. I. Iossifov *et al.*, *Nature* **515**, 216 (2014).
11. www.incf.org
12. http://battelle.org/docs/default-document-library/economic_impact_of_the_human_genome_project.pdf

ACKNOWLEDGMENTS

We thank all meeting participants (see the supplement) for their contributions to the discussion, and W. Newsome, T. Bonhoeffer, W. Koroshetz, S. Hyman, G. Buzsaki, and Y. Fregnac for comments. We acknowledge Suzhou Industrial Park for generously supporting the meeting.

SUPPLEMENTARY MATERIALS

www.sciencemag.org/content/350/6256/42/suppl/DC1
Supplementary Text

ESSAY

NEUROSCIENCE

Slow or fast? A tale of synaptic vesicle recycling

A new model accounts for synaptic transmission speed

By Shigeki Watanabe*

Whether resting on a couch, walking in a park, or running in a race, our nervous system must sustain an activity commensurate with physical and mental demands. Neuronal communication is carried out by chemical signals that are released from one nerve terminal and received by another. These chemical signals, or neurotransmitters, are packaged in vesicles. When neurons are activated, some of these vesicles fuse with the cell membrane—releasing the neurotransmitters to be detected by interconnected neurons.

During sustained neuronal activity, this process is repeated over and over, which imposes three major challenges on neurons. First, vesicle membrane is continuously added to the cell surface. Second, vesicle proteins become lodged at the site of fusion. Third, the supply of synaptic vesicles in the terminal becomes scarce. To counteract these changes,

eppendorf
& Science
PRIZE FOR
NEURO
BIOLOGY

synaptic vesicle membrane and proteins are rapidly removed from the plasma membrane by local recycling. This local recycling generates the new synaptic vesicles that are then loaded with neurotransmitter for further rounds of fusion and release.

TWO MODELS FOR SYNAPTIC VESICLE RECYCLING. In the early 1970s, two models were put forward for synaptic vesicle recycling that were based on the analysis

of frog neuromuscular junctions by electron microscopy: “kiss and run” (1, 2) and clathrin-mediated endocytosis (3, 4). These two models resemble two methods used in the recycling of glass bottles. The kiss-and-run mechanism is like refilling the same bottle: The same vesicle that has just undergone fusion is retrieved and refilled (see the figure, panel A). The clathrin-mediated mechanism is like molding a new bottle from a used one: the old vesicle is resorbed into the plasma membrane and must be subsequently remolded (figure, panel B).

Speed is a factor that distinguishes these two models. The kiss-and-run pathway is fast, requiring only 1 to 2 s (5). By contrast, in the clathrin model, the remodeling of a

new vesicle requires ~10 to 20 s (3, 4, 6–8). Given the importance of speed to neuronal communication, the kiss-and-run model may seem more plausible, yet many studies have pointed to the essential function of clathrin and clathrin-associated proteins in synaptic vesicle recycling (9, 10). Does clathrin function suffice under all conditions? Or does kiss-and-run recycling predominate in some conditions—perhaps during periods of prolonged stimulation? Despite extensive research in the last 40 years, there are no definitive answers to these questions.

A TECHNIQUE THAT CAPTURES MEMBRANE DYNAMICS. One problem with previous studies is that they used intense stimulation to guarantee the observation of endocytic structures. To observe synaptic vesicle recycling after a single stimulus or a short burst of stimuli, we used lentivirus to express the light-sensitive channelrhodopsin ChetaTC in mouse hippocampal neurons. These channels act like a switch for neuronal activity: A short flash of light activates the channelrhodopsin, which switches the neurons “on” and causes fusion of synaptic vesicles at the terminals. The neurons were then frozen at defined time points after stimulation. By controlling the interval between the stimulation and freezing, we were able to capture snapshots of the events at different time points—in effect, generating a “flip-book” of membrane movement during synaptic transmission with millisecond temporal resolution (11).

RAPID REMOVAL OF VESICLE MEMBRANE. According to both the clathrin and the kiss-and-run models, membrane invaginations equal to the size of a synaptic vesicle

Charité Universitätsmedizin Berlin, 10117 Berlin, Germany.
*E-mail: shigekixx@gmail.com



GRAND PRIZE WINNER: Shigeki Watanabe

Shigeki Watanabe received his undergraduate and Ph.D. degrees from University of Utah. For his Ph.D. and postdoctoral work, he has been studying

the mechanisms underlying synaptic vesicle cycle in *Caenorhabditis elegans* neuromuscular junctions and mouse hippocampal neurons. In January 2016, he will begin his own laboratory at Johns Hopkins University, where he will study the membrane and protein dynamics that mediate synaptic plasticity.



FINALIST: Julija Krupic

Julija Krupic received her undergraduate degree from Vilnius University and a Ph.D. from University College London (UCL). She is currently a Sir Henry Wellcome Fel-

low at UCL, where she conducts research on how place cell activity guides animal behavior. In 2016, Julija will move to the Salk Institute where she will study how connectivity affects the functional properties of place cells.

www.sciencemag.org/content/350/6256/46.2

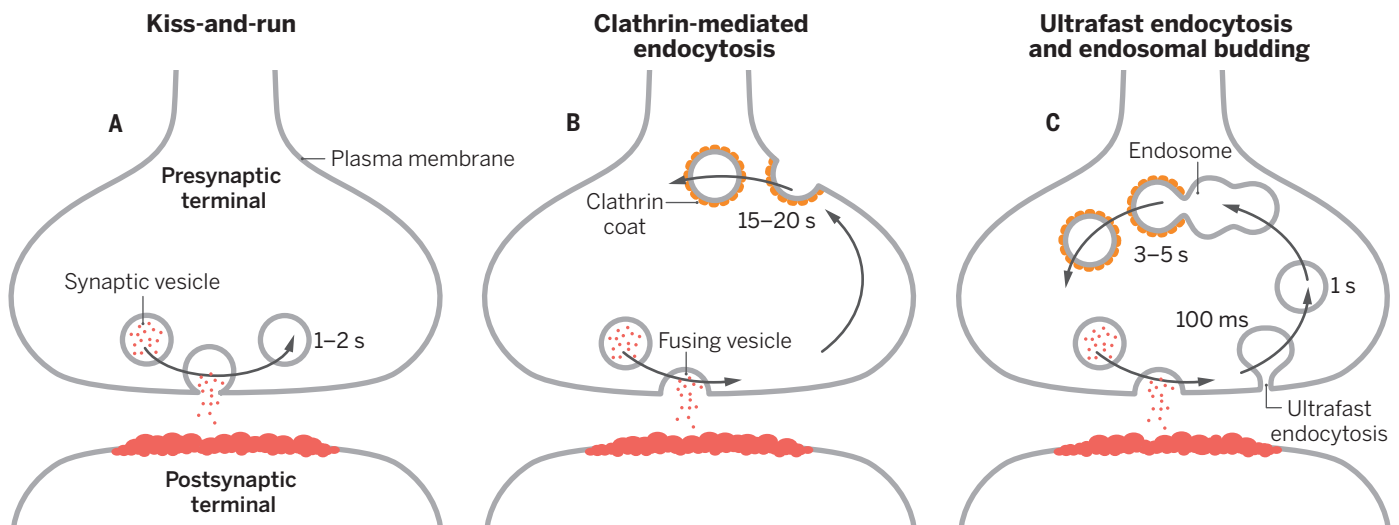


FINALIST: Jeremiah Cohen

Jeremiah Cohen received his undergraduate degree from Brandeis University, a Ph.D. in neuroscience from Vanderbilt University, and completed his

postdoctoral work at Harvard University. His laboratory in the Solomon H. Snyder Department of Neuroscience at Johns Hopkins University investigates the neural circuits underlying reward, mood, and decision-making.

www.sciencemag.org/content/350/6256/46.3



Models of synaptic recycling. (A) The kiss-and-run model. Vesicles transiently fuse with the plasma membrane. After the neurotransmitter release, the fusion pore is closed and the vesicles are recovered. (B) The clathrin-mediated endocytosis model. A synaptic vesicle fuses and collapses into the membrane. A new vesicle is formed in a region distant from the fusion site. (C) A new model of synaptic vesicle recycling. After a rapid internalization of the membrane via ultrafast endocytosis, the vesicle membrane is delivered to an endosome. Clathrin-mediated regeneration of synaptic vesicles occurs at the endosome.

would be expected to form on the plasma membrane after fusion of synaptic vesicles. However, we observed invaginations roughly twice as large as a synaptic vesicle in the region immediately lateral to the site of the fusion (12, 13). This process was initiated 50 ms after stimulation and was completed within 100 ms, far faster than either the kiss-and-run or clathrin-mediated mechanisms. Unlike what would have been expected on the basis of the clathrin or kiss-and-run models, however, we observed that a large portion of membrane is taken into the terminal, and synaptic vesicles are not recovered directly from the plasma membrane (figure, panel C).

REMOLDING VESICLES FROM ENDOSOMES. To determine how vesicles are regenerated, we followed the fate of the internalized membrane using ferritin as a tracer (14). About 1 s after stimulation, the endocytosed membrane was delivered to another organelle, an endosome. Clathrin-coated buds about the size of a synaptic vesicle formed on these endosomes 1 to 3 s after stimulation. Synaptic vesicles containing ferritin molecules accumulated in the terminal after 5 to 6 s. When clathrin function was genetically or pharmacologically blocked, ferritin molecules were retained in endosomes. These results suggested that synaptic vesicles are reconstituted at endosomes and that this process is dependent on the clathrin function (14). Thus, the vesicles are molded anew; however, the molding takes place within the cell rather than at the cell surface (figure, panel C).

TOWARD A UNIFIED MODEL? The recycling mechanism seems to have an ultrafast component followed by a slower component (figure, panel C). The ultrafast mechanism rapidly clears the fusion sites of excess membrane (and presumably of vesicle proteins). The slower mechanism, a clathrin-dependent process, reconstitutes vesicles at a more leisurely pace from endosomes. Our research suggests that the ultrafast component of vesicle recycling is not a kiss-and-run method and that the

“These results suggested that...the vesicles are molded anew; however, the molding takes place within the cell rather than at the cell surface.”

slow mechanism does not operate at the plasma membrane. What could account for the disagreement between our data and data reported in previous publications?

The answer to this question may lie in the experimental conditions. Mice are endotherms, yet many of the previous experiments were conducted with tissue kept at room temperature. When we repeated our experiments at room temperature, synaptic vesicles were regenerated directly from the plasma membrane in a clathrin-dependent fashion (14).

What about kiss-and-run? Although we

did not observe kiss-and-run structures, these results do not rule out that this process may be occurring at the nerve terminals, because our technique is not sensitive enough to determine whether the fusion pore of a particular vesicle is stable over time. It is also possible that synapses have adapted different mechanisms to meet specific demands for recycling.

Ultrafast endocytosis comes as a bit of a surprise. Why do synapses need to remove membrane from the surface so rapidly? One possibility is that the immediate role for endocytosis is not to restore vesicle numbers but rather to clear the fusion site so that another vesicle can fuse in rapid succession.

REFERENCES

1. B. Ceccarelli, W. P. Hurlbut, A. Mauro, *J. Cell Biol.* **54**, 30 (1972).
2. R. Fesce, F. Grohovaz, F. Valtorta, J. Meldolesi, *Trends Cell Biol.* **4**, 1 (1994).
3. J. E. Heuser, T. S. Reese, *J. Cell Biol.* **57**, 315 (1973).
4. T. M. Miller, J. E. Heuser, *J. Cell Biol.* **98**, 685 (1984).
5. A. A. Alabi, R. W. Tsien, *Annu. Rev. Physiol.* **75**, 393 (2013).
6. J. Balaji, T. A. Ryan, *Proc. Natl. Acad. Sci. U.S.A.* **104**, 20576 (2007).
7. B. Granseth, B. Odermatt, S. J. Royle, L. Lagnado, *Neuron* **51**, 773 (2006).
8. M. Armbruster, M. Messa, S. M. Ferguson, P. De Camilli, T. A. Ryan, *eLife* **2**, e00845 (2013).
9. J. Dittman, T. A. Ryan, *Annu. Rev. Cell Dev. Biol.* **25**, 133 (2009).
10. Y. Saheki, P. De Camilli, *Cold Spring Harb. Perspect. Biol.* **4**, a005645 (2012).
11. S. Watanabe, M. W. Davis, E. M. Jorgensen, in *Nanoscale Imaging of Synapses*, U. V. Nägerl, A. Triller, Eds. (Springer New York, 2014), pp. 43–57.
12. S. Watanabe et al., *eLife* **2**, e00723 (2013).
13. S. Watanabe et al., *Nature* **504**, 242 (2013).
14. S. Watanabe et al., *Nature* **515**, 228 (2014).

ESSAY

NEUROSCIENCE

Brain crystals

Our brains may perceive distance differently in environments with polarized geometry

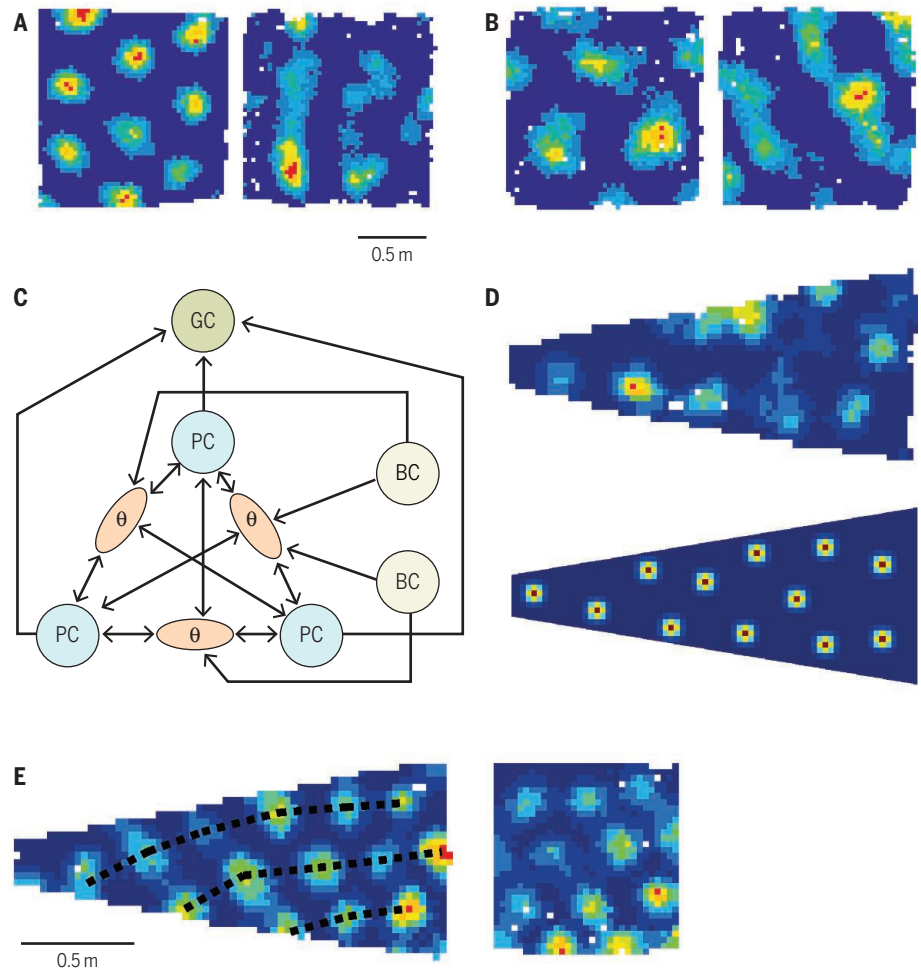
By Julija Krupic*

I have been enthralled with crystals ever since I was a child. Growing up, I was fortunate enough to have a neighbor who was a geologist with a mesmerizing collection of colorful minerals. My first personal exploration of crystal formation came with watching icicles growing on the eaves of our roof. They came in different shapes and sizes and made me wonder: “How?” Later, I was surprised to discover that there was a whole field of “icicle physics” that dealt with precisely this question (1, 2).

Imagine my renewed excitement when, as a budding neuroscientist at university, I learned that there was crystal-like neural activity in the brain. There is a group of neurons in the parahippocampal formation named “grid cells” that fire in hexagonal symmetry (3) (see the figure, panel A, left). Grid neurons themselves are not necessarily arranged in a crystal-like pattern in the brain [although some argue this could be the case (4)]. Rather, each cell acts as a crystal “generator,” where the fundamental blocks are fields of neural activity.

Grid cell firing appears to be invariant to properties of the enclosure (e.g., size, shape), as well as an animal’s behavior (e.g., running speed, grooming), which prompts the suggestion that they represent an internally generated path integration system for navigation (3). The universal metric of space had been found (3, 5, 6)!

I became curious as to whether the hexagonal grid was the only crystal structure in the brain. For instance, engineers and architects often prefer a square grid for constructing space—it is the periodicity rather than a particular symmetry that is a key prerequisite for a metric system to work. I recorded



Breaking grid symmetry. (A) Firing-rate maps of a grid cell (left) and a bandlike spatially periodic cell (right). (B) Occasionally, cell firing altered for grid (left) and non-grid (right) patterns between trials. (C) A schematic of the force-boundary interaction model. Place cells (blue, PC) and border cells (tan, BC) are interconnected via an inhibitory theta interneuron network (orange, θ). The place cells drive the firing pattern of the grid cell (light brown, GC). (D) Recorded (top) and predicted (bottom) grid cell in a trapezoidal enclosure. (E) An example of right-to-left grid expansion and rotation in a trapezoid (left). Such transformation was not observed in a square environment (right).

from neurons in the rat parahippocampal region to see if cells with other firing patterns could be found there. To my delight, I found another class of spatially tuned cells that fired in response to multiple discrete locations in the environment. The pattern was not random but failed to exhibit the hexagonal symmetry observed in grid cells (figure, panel A, right) (7).

I developed an analysis method based on the two-dimensional Fourier transform to quantify the properties of all spatial cells in the parahippocampal region (including grid cells) and proposed a possible underlying mechanism for grid cell formation. Our results suggest that grid cells form the most stable subset of a larger continuum of locational cells whose firing properties can be described as a weighted sum of a small number (from 1 to 4) of periodic, bandlike

inputs. We noticed that under certain circumstances grid cells lost their hexagonal symmetry and became more irregular, on some occasions even acquiring a bandlike firing pattern (figure, panel B). The geometry of the enclosure in which the rat was tested seemed to play a major role in facilitating such pattern transitions.

The geometry of an enclosure is defined by the arrangement of its boundaries. Indeed, “border cells” located in close anatomical proximity to grid cells are active along the boundaries of the enclosure (8, 9). We thought that perhaps border cells could play an important role in shaping grid cell pattern. We tested this idea by developing a model in which a grid cell firing pattern was generated by interacting place cells (cells in the hippocampus that are active in a particular place of the enclosure) and border cells (10). We called this a field-boundary interaction model (figure,

Department of Cell and Developmental Biology, University College London, London WC1E 6BT, UK. *E-mail: j.krupic@ucl.ac.uk

panel C). We postulated that the strength of interaction of individual place fields would be proportional to the distance between the grid cells in a winner-take-all manner and that the role of border cells is to “push” the fields away. The model predicted that grid cells would exhibit hexagonal symmetry in square and circular enclosures but that this pattern would break down in more polarized enclosures, such as trapezoids. It also indicated that the grid orientations would

be aligned to the walls of the enclosure.

We went on to test this model experimentally by recording grid cells in rats that were placed in square, circular, hexagonal, and trapezoidal enclosures (11). Our results confirmed both predictions: grid cell orientations were clustered in square, but not circular, enclosures, and the perfect grid pattern seen in the square enclosures did not exist in trapezoidal enclosures. In trapezoids, the grid became more elliptical and nonhomogeneous: It was larger and rotated toward the narrower part of the trapezoid compared with the wider part (figure, panels D and E). Such profound distortions were not observed in the square or circular enclosures where the symmetrical and consistent pattern was similar to those observed in most previous studies. The results challenge the idea that the grid cell system can act as a universal spatial metric for the cognitive map, as grid patterns changed remarkably between enclosures and even within the same enclosure. It is possible that grid cells may still be measuring distance in trapezoids, albeit in a distorted fashion, and this finding leads to the intriguing idea that our brains perceive distance differently in environments with polarized geometry.

These results made us wonder what the grid cell system is really used for: Is it a metric system with some limitations or is it a matrix of locations, and has the metric property emerged as a side effect?

REFERENCES

1. A. S.-H. Chen, S. W. Morris, *Phys. Rev. E Stat. Nonlin. Soft Matter Phys.* **83**, 026307 (2011). Medline doi:10.1103/PhysRevE.83.026307
2. The Iccicle Atlas (Univ. of Toronto); www.physics.utoronto.ca/Iccicle_Atlas/.
3. T. Hafting, M. Fyhn, S. Molden, M.-B. Moser, E. I. Moser, *Nature* **436**, 801 (2005). Medline doi:10.1038/nature03721
4. S. Ray *et al.*, *Science* **343**, 891 (2014). Medline doi:10.1126/science.1243028
5. E. I. Moser, M.-B. Moser, *Hippocampus* **18**, 1142 (2008). Medline doi:10.1002/hipo.20483
6. G. Buzsáki, E. I. Moser, *Nat. Neurosci.* **16**, 130 (2013). Medline doi:10.1038/nn.3304
7. J. Krupic, N. Burgess, J. O'Keefe, *Science* **337**, 853 (2012). Medline doi:10.1126/science.1222403
8. T. Solstad, C. N. Boccara, E. Kropff, M.-B. Moser, E. I. Moser, *Science* **322**, 1865 (2008). Medline doi:10.1126/science.1166466
9. C. N. Boccara *et al.*, *Nat. Neurosci.* **13**, 987 (2010). Medline doi:10.1038/nn.2602
10. J. Krupic, M. Bauza, S. Burton, C. Lever, J. O'Keefe, *Philos. Trans. R. Soc. London B Biol. Sci.* **369**, 20130188 (2014). doi:10.1098/rstb.2013.0188
11. J. Krupic, M. Bauza, S. Burton, C. Barry, J. O'Keefe, *Nature* **518**, 232 (2015). Medline doi:10.1038/nature14153

10.1126/science.aad3002



FINALIST: Julija Krupic

Julija Krupic received her undergraduate degree from Vilnius University and a Ph.D. from University College London (UCL). She is currently a Sir Henry Wellcome Fellow at UCL, where she conducts research on how place cell activity guides animal behavior. In 2016, Julija will move to the Salk Institute where she will study how connectivity affects the functional properties of place cells.

ESSAY

NEUROSCIENCE

Dopamine and serotonin signals for reward across time scales

Neurons that release different neurotransmitters transmit different information about rewards

By **Jeremiah Y. Cohen**

It is one of the peculiar features of most modern neurophysiology that the experimentalist...seldom knows which type of neuron he or she is listening to.... This problem deserves immediate and serious attention.

Francis Crick, 1999 (1)

Neurobiology has thrived on the confluence of multiple fields. For most of the 20th century, this meant combining chemistry and neuroanatomy [“The gains in brain are mainly in the stain” (2)], as well as electronics and neurophysiology (the gains in brain are mainly in the amplifier’s gain, if you like). Recent years have seen the addition of molecular biology to our bag of tricks. We wished to take advantage of tools from different fields to understand the relationship between neurons that release dopamine or serotonin and reward (3, 4).

Beginning with an accidental discovery in 1953, Olds and colleagues found that electrical stimulation of particular brain areas was powerfully rewarding: Rats would compulsively press a lever to obtain stimulation, ignoring naturally rewarding stimuli such as food, water, or mates (5, 6). This discovery inspired researchers to try to determine the neural basis of such reinforcement.

Dopamine is a key neurotransmitter for reward in the brain. In the 1990s, Schultz and colleagues discovered that dopaminergic neurons in the ventral tegmental area (VTA) were excited by unexpected reward, whereas their response to reward was diminished when a sensory cue predicted the reward (7). That is, dopaminergic neurons are excited when the outcome is better than expected, whereas they are inhibited when the outcome is worse than expected.

Solomon H. Snyder Department of Neuroscience, Brain Science Institute, Johns Hopkins University School of Medicine, Baltimore, MD 21205, USA. *E-mail: jeremiah.cohen@jhmi.edu

This suggests that the brain’s reward system is activated only when the brain fails to predict outcomes correctly. Such a signal is called “reward prediction error” (RPE).

These findings changed the way we think about the reward system, but how such calculations are performed in the brain remains unknown. A number of related reinforcement-learning models have suggested that a value-dependent inhibitory signal might counteract the excitatory reward signal to suppress dopaminergic output for expected, but not unexpected, rewards (8). To determine whether this is how the system works in vivo, we aimed to record the signals of different types of neurons in the VTA of mice during a reward-prediction task.

As Crick pointed out in 1999, a challenge from the outset is how to determine what types of neuron are being recorded during such experiments. In classical neurophysiological studies, the experimenter places a microelectrode in an animal’s brain and

compares neuronal activity with the animal’s behavior. We “tagged” dopaminergic neurons (and, in separate experiments, inhibitory GABAergic neurons) with a light-activated protein, channelrhodopsin-2 (9, 10). Using transgenic mice that express

the enzyme Cre recombinase in either dopaminergic or GABAergic neurons, we introduced Cre-dependent viruses carrying channelrhodopsin-2 (9, 10), which created light-sensitive dopaminergic or GABAergic neurons. We then implanted several small electrodes and an optical fiber into the VTA. While recording the activity of randomly sampled neurons, we noted whether each neuron responded to a pulse of light from a laser. If it did, then we knew it was a dopaminergic (or GABAergic) neuron.

We recorded from VTA neurons while mice performed a classical conditioning task, in which odors predicted different rewards or punishments. Our first surprise came when we discovered that every neuron we observed showed one of three distinct types of activity. Type I neurons showed RPE-like activity, firing brief bursts of action potentials when the mouse smelled a reward-predicting odor (or the reward itself). These neurons showed decreases in activity relative to baseline when the reward was unexpectedly omitted. Type II neurons showed reward-expectation-like activity, increasing their firing in a sustained way when the mouse smelled a reward-predicting odor. These neurons fired regardless of whether the reward was delivered as expected or unexpectedly omitted. Type III neurons showed activity that mirrored type II neurons, except that firing rates decreased in anticipation of a reward rather than increased. Our second surprise came when we compared the activity of all neurons to the neurotransmitter they released (dopamine or GABA). We found that dopaminergic neurons were all type I and that GABAergic neurons were all type II. The identity of the type III neurons has yet to be determined.

We next asked whether dopaminergic neurons signaled only the immediate properties of the environment (for example, “I’m about to get a reward”), or whether slower dopaminergic signaling could underlie longer-term emotional states. We varied the amount of reward slowly over time, and were surprised to find no evidence of longer-term reward signaling in

**eppendorf
& Science
PRIZE FOR
NEURO
BIOLOGY**

FINALIST: Jeremiah Cohen



Jeremiah Cohen received his undergraduate degree from Brandeis University, a Ph.D. in neuroscience from Vanderbilt University, and completed his

postdoctoral work at Harvard University. His laboratory in the Solomon H. Snyder Department of Neuroscience at Johns Hopkins University investigates the neural circuits underlying reward, mood, and decision-making.

dopaminergic neurons. How, then, do our enduring mood states arise?

To answer this question, we turned our attention to a different neuromodulator: serotonin. Serotonin is thought to be involved in many behaviors, but its function has been elusive (11). This is due, in part, to the challenges in recording from identified serotonergic neurons during behavior. We took an approach similar to the one described above, tagging serotonergic neurons with channelrhodopsin-2 and establishing criteria for identifying these cells (3). We recorded the activity of these light-identified serotonin neurons as mice participated in a task in which the amount of reward or punishment varied predictably over time. We found that 40% of dorsal raphe serotonergic neurons showed slow variations in the activity that correlated with the amount of reward in

“[N]eurons fired...whether the reward was delivered...or unexpectedly omitted.”

the environment. This was remarkable, particularly given that the VTA dopaminergic neurons did not respond to this information. In addition, many serotonergic neurons signaled short-term information about upcoming rewards and punishments with brief changes in firing rates. This suggests that serotonergic neurons have the ability to signal reward and punishment on both slow and fast time scales and may be involved in generating emotional states like mood.

REFERENCES

1. F. Crick, *Philos. Trans. R. Soc. Lond. B Biol. Sci.* **354**, 2021 (1999).
2. F. E. Bloom, in *The Neurosciences: Paths of Discovery* (MIT Press, Cambridge, MA, 1975), pp. 211–227.
3. J. Y. Cohen, M. W. Amoroso, N. Uchida, *eLife* **4**, e06346 (2015).
4. J. Y. Cohen, S. Haesler, L. Vong, B. B. Lowell, N. Uchida, *Nature* **482**, 85 (2012).
5. J. Olds, *Drives and Reinforcements: Behavioral Studies of Hypothalamic Functions* (Raven Press, New York, 1977).
6. J. Olds, P. Milner, *J. Comp. Physiol. Psychol.* **47**, 419 (1954).
7. W. Schultz, P. Dayan, P. R. Montague, *Science* **275**, 1593 (1997).
8. J. C. Houk, J. L. Adams, A. G. Barto, in *Models of Information Processing in the Basal Ganglia* (MIT Press, Cambridge, MA, 1995), pp. 249–270.
9. E. S. Boyden, F. Zhang, E. Bamberg, G. Nagel, K. Deisseroth, *Nat. Neurosci.* **8**, 1263 (2005).
10. G. Nagelet al., *Proc. Natl. Acad. Sci. U.S.A.* **100**, 13940 (2003).
11. P. Dayan, Q. J. Huys, *Annu. Rev. Neurosci.* **32**, 95 (2009).

10.1126/science.aad3003

BOOKS *et al.*

EDUCATION

Beyond “publish or perish”

A greater emphasis on teaching could improve career prospects for graduate students

By Johanna Gutlerner

As an undergraduate biology major contemplating pursuing a Ph.D., I remember the anxiety I felt when I saw a special issue of *Science* that asked whether we were training too many Ph.D.s for the jobs that existed. That issue was published 20 years ago. As Leonard Cassuto reminds us in his new book, *The Graduate School Mess*, scholars were warning of the overproduction of Ph.D.s even 20 years before that. Yet, for at least the past 40 years, unfounded optimism has prevailed, with graduate school leaders hoping that market forces would offer a correction. In 2013, the proportion of doctoral graduates in science and engineering fields with a secured job or post-doc was lower than it had been in the 15 previous years (1). Meanwhile, Ph.D.s granted in all fields have risen over the past decade, with basic biomedical Ph.D.s rising most sharply. Yet only about 23% of these graduates go on to tenured academic research positions (2). Clearly, the data do not encourage optimism.

Some prominent scholars have suggested that we should slash the number of Ph.D.s that we are training; however, Cassuto argues that this will lead to a lack of diversity of every kind, with graduate schools admitting only the surest bets, breeding elitism and homophily. While acknowledging that some reduction in the number of trainees may be necessary, Cassuto offers a different solution. He believes that we need to focus on how and what we teach, as well as training our students to teach.

Cassuto argues that too many of us do not recognize that teaching can improve one's research and is often at the origins of new research ideas. Nor have we heeded the calls for “scientific teaching,” in which

faculty look to the education or cognitive psychology literature for strategies to transform their curriculum and teaching practices and then test them in their own classrooms (3).

Taking Cassuto's point further, we can no longer afford to consider teaching as a career that anyone with an advanced degree is qualified to do. By not modeling high-quality student-centered teaching and not using evidence-based teaching strategies, we leave our graduate students underprepared to teach undergraduates and communicate their research to a gen-



“... we can no longer afford to consider teaching as a career that anyone with an advanced degree is qualified to do.”

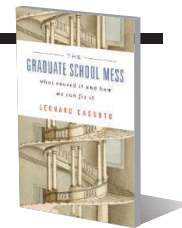
eral audience. We are also denying them skills that would be of benefit in other professions.

At a time when only 16% of U.S. high school seniors are proficient in math and interested in pursuing a degree in science, technology, engineering, and mathematics (STEM), there is an obvious need for better and more inspiring science teaching at all levels of education (4). Yet we find little emphasis in the university on creating pathways for STEM Ph.D.s to go into teaching at the kindergarten to 12th-grade level (K–12). Although Cassuto argues for a renewed focus on teaching as a way to more broadly prepare students for their future careers, he stops short of advocating for the policy and

The Graduate School Mess What Caused It and How We Can Fix It

Leonard Cassuto

Harvard University Press,
2015. 319 pp.



perception changes that could create a new pipeline of K–12 teachers.

The book's most enlightening chapters take a historical look at the challenges that have faced doctoral educators throughout time. For instance, he examines the history of the graduate admissions process, beginning in the late 1800s. In doing so, he shows how admissions policies have been formalized and bureaucratized in a way that supports the narrow goal of admitting and training future research faculty, and he describes how the teaching fellowship has been co-opted to support graduate research. The mandate to “teach less and publish more” has led to “the systematic disrespect of the teaching ranks—and of teaching generally—by graduate schools [which] is not just mendacious but also counterproductive,” he maintains.

Cassuto clearly presents the challenges facing graduate institutions, including antiquated admissions policies; incoherent course offerings; esoteric, gate-keeping qualifying exams; long times to degrees; and failure to prepare students for diverse career outcomes. These have been described well elsewhere, however. The novelty of his treatment is in identifying broader and more encompassing forms of teaching as a solution.

In his final chapter, he urges us to develop a new ethic for the university, in which the priorities of graduate education are better interwoven with those of the university and society as a whole. Today, he argues, a successful doctoral education requires that we learn how to apply our knowledge “throughout society, not just in universities.”

REFERENCES

1. *Doctorate Recipients from U.S. Universities: 2013*, National Science Foundation (NSF), National Center for Science and Engineering Statistics. Special Report NSF 15-304 (NSF, Arlington, VA, 2015); www.nsf.gov/statistics/sed/2013/.
2. *Biomedical Research Workforce Working Group Report* (National Institutes of Health, Washington, DC, 2012); http://acd.od.nih.gov/biomedical_research_wgreport.pdf.
3. J. Handelsman *et al.*, *Science* **304**, 521 (2004).
4. Science, Technology, Engineering and Math: Education for Global Leadership (U.S. Department of Education, Washington, DC, 2015); www.ed.gov/stem.

10.1126/science.aac7868

The reviewer is the co-director of the Curriculum Fellows Program, Harvard Medical School, Boston, MA 02115, USA.
E-mail: johanna_gutlerner@hms.harvard.edu



Pixelated projections of visitors' shadows appear in a light installation created by artist Aram Bartholl.

EXHIBITION

Can you keep a secret?

An interactive exhibition explores the plight of privacy in the digital age

By Giovanni Frazzetto

Gabriel García Márquez once said that all human beings have a public, a private, and a secret life. Today more than ever, fast global communication and advanced digital technology constantly redraw the boundaries between the three. Unprecedented incidents as diverse as the Ashley Madison hacking scandal and Edward Snowden's disclosure of the NSA's global monitoring activities have made it clear that we risk losing confidential information to malicious virtual thieves as well as intrusive governments. Leaving a trace in cyberspace now comes at the cost of total personal exposure.

A coherent and polished exhibition that explores the concept of secrecy in the digital age opened recently at the Science Gallery Dublin, a pioneering institution that pushes limits of inquiry across artists and scientists. *Secret* invites visitors to reflect on timely issues of privacy, espionage, and surveillance with a series of enticing works that unite art, design, and media technology.

For better or worse, our search for technological progress inevitably chases utopian visions. In *The Republic of Privacy*, Soomi Park ingeniously creates a fictional

nation in which extravagant devices provide absolute risk-free privacy. For instance, avoiding the peril of data storage, the security of drawing cash from an ATM is guaranteed through an authentication system in which dogs identify account holders by their unique personal scents. [This scenario is not as unrealistic as it may sound: In a recent study, dogs were able to detect prostate cancer with 90% accuracy by sniffing patients' urine (1).]

Paradoxically, operations that are in place to preserve privacy also have the power to disrupt it. Conjuring a blast waiting to happen, the possibility of uncovering mass data surveillance is astutely visualized in Julian Oliver's *Transparency Grenade*. Subtly disguised as an elegant perfume bottle, a Soviet F1 hand grenade hides a computer, a microphone, and a wireless antenna. When the pin is pulled, the device detects all network traffic and audio signals in the immediate vicinity and streams them to a server where the data can be extracted and analyzed.

The leakage of inconvenient truths becomes a political protest in Matt Kenyon's *Notepad*, a stack of ordinary-looking yellow legal pads in which each ruled line is a microprinted text listing the full names, dates, and sites of every civilian death on record during the first three years of the Iraqi war. The typescript being visible only with a magnifying glass, this "secret memorial" was distributed as regular stationery to United States senators and gov-

Secret

Nothing to See Here
Ian Brunswick, Tad Hirsch,
Julian Oliver, and Marie
Redmond, curators
Science Gallery Dublin,
7 August 2015 to
1 November 2015
www.sciencegallery.com



ernment representatives in 2010.

A hallmark of shows at the Science Gallery is their fun interactive content, and *Secret* is no exception. In Osman Khan's *Net Worth*, visitors have the opportunity to visualize their Internet presence by swiping their credit cards in a card-reader. The device detects their name, Googles it, and then shows the user how they compare to other visitors, as well as famous figures, including Beyoncé, Bono, Michael Jackson, and even Jesus (who ranks at the very top).

Raising issues of censorship and identity protection, an installation by Aram Bartholl makes the process of pixelation a tangible activity for visitors whose shadows are transformed into pixelated silhouettes, at the resolution of 0.16 pixels per inch, as they walk behind a backlit wall.

As it occurs in greetings between freemasons or Mafiosi, a seeming innocent handshake can sanction tacit agreements or facilitate an exchange of secrets by means of distinct grips or touches. Nicolas Myers's playful *Secret Handshake Training Device* consists of a robot-like hand sticking out of a box. When grasped, it delivers a message in the form of a series of subtle vibrations to each finger. Visitors are then asked to play back the message by tapping their own fingers against those of the device in the same order and at the same speed.

In another installation, visitors can check the safety of a 4-digit PIN by tapping it into a keypad. A display shows how many times the same code has been entered since the beginning of the exhibition. (Hint: 0000 and 1234 are not very original.)

After visiting this thought-provoking and eye-opening show, you may decide to reset all your passwords, reduce your online presence, or disappear from the Internet altogether. But remember, "if you want to keep a secret, you must also hide it from yourself (2)."

REFERENCES

1. R. Bahnsen, *J. Urol.* 193, 1083 (2015).
2. G. Orwell, 1984 (Secker and Warburg, London, 1949).

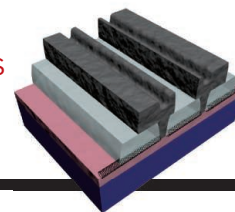
10.1126/science.aac6549

The reviewer is the author of *Joy, Guilt, Anger, Love* (Penguin, 2014) and is a visiting research fellow at Trinity College Dublin. E-mail: gio@giovannifrazzetto.com

RESEARCH

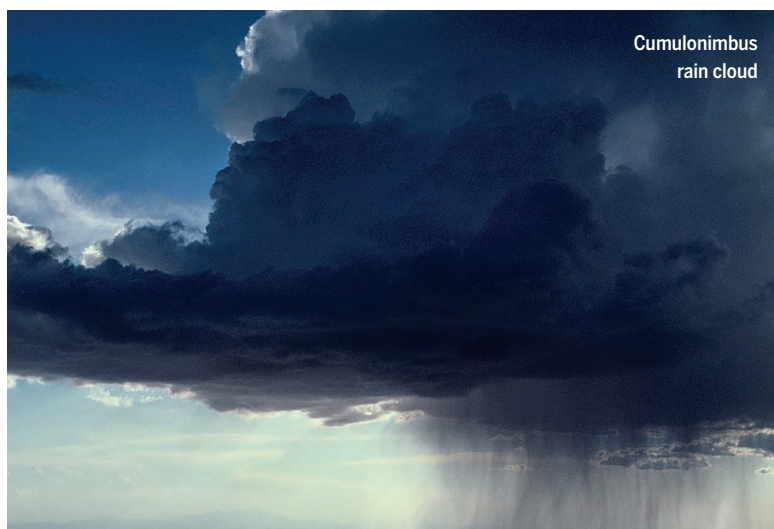
Molybdenum films and carbon nanotubes team up

Cao et al., p. 68



IN SCIENCE JOURNALS

Edited by Stella Hurtley



Cumulonimbus
rain cloud

CLOUDS

Cloud mixing and droplet evolution

When clouds mix with drier air because of atmospheric turbulence, some of the cloud droplets evaporate. Beals *et al.* developed an airborne holographic imaging system to look at changes in the spatial structure and sizes of these droplets (see the Perspective by Bodenschatz). Turbulent mixing of clouds with clear air caused dramatic fluctuations in the number density of water droplets but left their mean diameter essentially unchanged. This finding should help models better represent these hard-to-parameterize cloud processes. — HJS

Science, this issue p. 87; see also p. 40

EARTH HISTORY

Making an impact in more ways than one

Massive eruptions formed the Deccan Traps flood basalts in India at around the same time as the mass extinction event 65 million years ago. Renne *et al.* precisely dated the massive volcanic field, which suggests a simultaneous increase in volcanism associated with the famous Chicxulub impact. Strong ecologic recovery may have been impossible until the volcanism slowed down 500,000 years later. — BG

Science, this issue p. 76

(DOM) is especially important for its role in storing roughly 700 Gt of carbon. Zark *et al.* used large mesocosms suspended in a Swedish fjord to measure DOM response to acidification likely to be experienced in the year 2100. Encouragingly, despite enormously complex system dynamics, DOM in acidified mesocosms rarely differed from that in controls. We're not necessarily off the hook, but at least carbon stored in DOM may withstand the insult of acidification that our excessive generation of CO₂ will create in this century. — SN

SciAdv. 10.1126.sciadv.1500531 (2015).

Permian-Triassic Extinction (see the Perspective by Marshall). The structure and diversity of communities were key predictors of stability through the event. Furthermore, extinctions were not random, with smaller-bodied species being more prone to extinction. This pattern is in direct contradiction to the patterns seen in our current extinction. Thus, the current anthropogenically driven extinction is fundamentally different from previous catastrophic extinctions. — SNV

Science, this issue p. 90; see also p. 38

INJURY RECOVERY

Motivation helps reverse neuronal damage

Motivation plays a fundamental role in mediating recovery after neurological injuries. Sawada *et al.* evaluated the potential contribution of the nucleus accumbens, a brain motivation center, to movement control after spinal cord injury in monkeys. The activity of the nucleus accumbens during the early phase after injury was important for the recovery of motor performance. — PRS

Science, this issue p. 98

OCEAN ACIDIFICATION

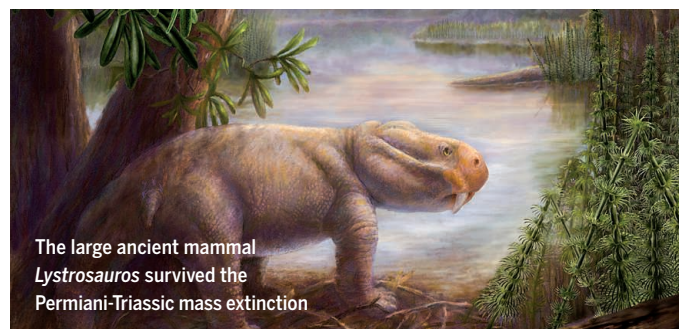
Resilience of the oceans revealed

Earth will witness a massive change in ocean acidification in this century. Ocean acidification adversely affects marine biodiversity and biogeochemistry. Dissolved organic matter

PALEOECOLOGY

No precedent

Human activities are creating a mass extinction event. The intensity of this event is unprecedented during human times, but there have been several comparable events during Earth's history. Roopnarine and Angielczyk examined one of the largest, the



The large ancient mammal
Lystrosaurus survived the
Permian-Triassic mass extinction

STRUCTURAL BIOLOGY

Building a gate to the nucleus

Nuclear pore complexes form a gateway between the cytoplasm and the nucleus (see the Perspective by Ullman and Powers). Stuwe *et al.* combined structural, biochemical, and functional analyses to elucidate the architecture of a six-protein complex that makes up the inner ring of the fungal nuclear pore. This includes a central trimeric complex homologous to the Nup62 complex found in metazoans that is incorporated into the nuclear pore inner-ring complex. Chug *et al.* report the structure of the metazoan trimeric Nup62 complex. Neither study supports a model in which the pore can dilate and constrict. Instead they suggest a rigid pore in which flexible domains called FG repeats fill the channel and form a barrier that can be traversed by receptors that carry cargos across. — VV

Science, this issue pp. 56 and 106; see also p. 33

PLANETARY SCIENCE

An exoplanet extracted from the bright

Direct imaging of Jupiter-like exoplanets around young stars provides a glimpse into how our solar system formed. The brightness of young stars requires the use of next-generation devices such as the Gemini Planet Imager (GPI). Using the GPI, Macintosh *et al.* discovered a Jupiter-like planet orbiting a young star, 51 Eridani (see the Perspective by Mawet). The planet, 51 Eri b, has a methane signature and is probably the smallest exoplanet that has been directly imaged. These findings open the door to understanding solar system origins and herald the dawn of a new era in next-generation planetary imaging. — BG

Science, this issue p. 64; see also p. 39

GENOME EDITING

Improving gene editing in human T cells

Gene editing holds promise for correcting human disease, but has been hampered by low efficiencies. To address this, Sather *et al.* devised a more effective way to disrupt and replace the CCR5 locus in human T cells, a procedure known to improve HIV clearance. Serotype 6 of an adeno-associated viral vector worked particularly well for the delivery of nucleases and repair templates to primary human T cells, achieving efficient gene editing rates and little toxicity. The nuclease they used (megaTAL) generated homology-directed repair (rather than nonhomologous end-joining repair) and so could both delete and replace the target locus. When inserted into the locus, chimeric antigen receptors and an HIV fusion inhibitor ameliorated HIV infection in mice. — KLK

Sci. Transl. Med. **7**, 307ra156 (2015).

POLYMER CHEMISTRY

Transient polymer links are better

Very long polymer molecules elongate in shearing flows. This ordering of the chains lowers the viscosity of small-molecule solvents. The chains also reduce the dangers of misting during explosive spreading of the solvents. However, the long polymer chains degrade during normal fuel handling and clog pumping equipment. Wei *et al.* used telechelic polymers—short chains with reactive end groups—to form extremely long chains in organic solvents (see the Perspective by Jaffe and Allam). These reformable polymers offer the potential for better fuel safety without the drawbacks of covalently bonded long-chain polymers. — MSL

Science, this issue p. 72; see also p. 32

IN OTHER JOURNALS

Edited by Sacha Vignieri and Jesse Smith



Genes recruited during “pregnancy” in male seahorses are homologous to those used by females across taxa

REPRODUCTIVE EVOLUTION

Like mother, like father

Live birth has evolved repeatedly across the major taxonomic groups, but in the vast majority it is the female that does the brooding. The most developed case of gender reversal in brooding occurs among seahorses. In some seahorse species, males not only incubate the eggs internally but develop a pouch structure that is strikingly similar to a uterus in terms of form and function. Whittington *et al.* produced a detailed transcriptome of the genes up-regulated during pregnancy in male *Hippocampus abdominalis* and found that those involved in embryo growth and support functions, such as nutrient transport and waste removal, were generally homologous to those seen in pregnant female mammals and reptiles. Thus, it seems that the pregnancy pathway is much the same whether fish or mammal, female or male. — SNV

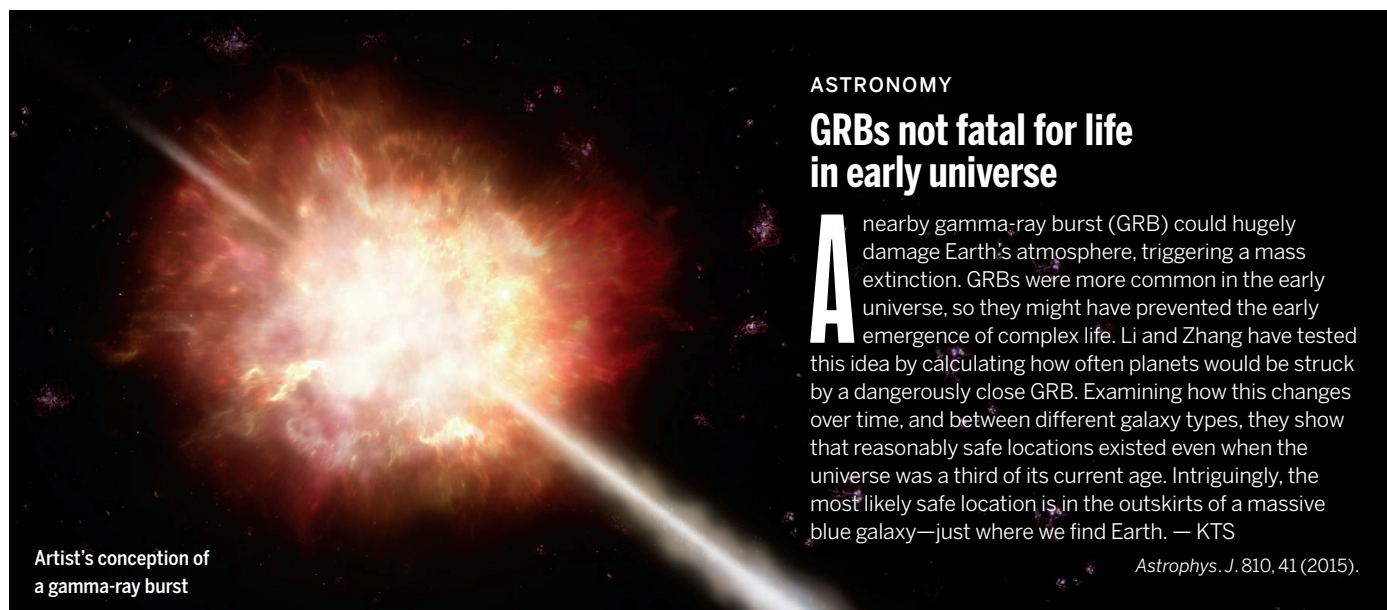
Mol. Biol. Evol. **10.1093/molbev/msv177** (2015).

SUPERCONDUCTION

Building a nanowire superconducting qubit

A major ingredient of a superconducting qubit is a Josephson junction, typically containing an insulator that acts as a bridge (“weak link”) between two superconductors. Larsen *et al.* and de Lange *et al.* fabricated superconducting qubits that,

instead of an insulator, used a semiconducting nanowire as the weak link. Both groups used InAs nanowires, in one case enclosed in a shell of superconducting Al and in the other contacted by superconducting NbTiN. The researchers controlled the frequency of the qubit—a complex operation in the conventional setup—by simply modulating the carrier



Artist's conception of a gamma-ray burst

ASTRONOMY

GRBs not fatal for life in early universe

A nearby gamma-ray burst (GRB) could hugely damage Earth's atmosphere, triggering a mass extinction. GRBs were more common in the early universe, so they might have prevented the early emergence of complex life. Li and Zhang have tested this idea by calculating how often planets would be struck by a dangerously close GRB. Examining how this changes over time, and between different galaxy types, they show that reasonably safe locations existed even when the universe was a third of its current age. Intriguingly, the most likely safe location is in the outskirts of a massive blue galaxy—just where we find Earth. — KTS

Astrophys. J. 810, 41 (2015).

concentration of the nanowire with gate voltage. The new architecture may lead to more-scalable quantum computers and address fundamental issues such as the quantum statistics of Majorana fermions. — JS

Phys. Rev. Lett. **115**, 127001; 127002 (2015).

WATER SPLITTING

A close look at the catalyst interface

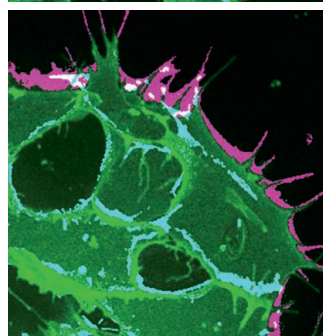
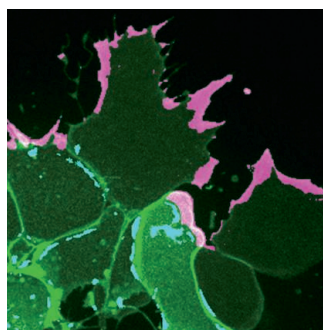
The light-driven splitting of water into hydrogen and oxygen is a widely studied approach toward storing solar energy for use at night and on cloudy days. Hill *et al.* constructed cells in which *n*-doped silicon absorbed the light and a cobalt catalyst on top helped accelerate the oxygen-generating half of the reaction. Their goal was to study how the catalyst/silicon interface influenced the cell's photovoltage. By probing the system in both solution and solid-state environments, they discerned a crucial contribution from an SiO_x oxide layer between the silicon and cobalt. Noncontinuous cobalt coverage also contributed to an enhanced photovoltage. The results could help guide optimization of this and similar device designs. — JSY

Nat. Mater. 10.1038/nmat4408 (2015).

NEURAL CREST

Oh, what places they'll go

Neural crest cells originate from the neuroepithelium, but end up scattered throughout the body, serving as progenitors of a variety of cell types ranging from pigment to bone. Scarpa *et al.* asked how such initially well-behaved cells become individualistic pioneers. The key



Migrating neural crest cells reach for new substrates (magenta) as their cell-cell holds (cyan) decrease

is a switch in the collection of molecules that the cell uses to hold on to its environment. With this switch, the neural crest cell's ability to hold on to neighboring neural crest cells weakens at the same time as its ability to hold on to other substrates strengthens. The shifted balance of power tears apart neighboring cells and favors pathways to new territory. As for adolescents' yearning to leave home, the pull of the horizon weakens anchors at the birthplace. — PJH

Dev. Cell **34**, 421 (2015).

MICROBIOME

The most wanted and most fastidious

Cataloging of the human microbiota is continuing apace, but our functional knowledge of the key organisms is woeful. Ó Cuív *et al.* have exploited bacterial sex, or conjugation, to isolate and genetically manipulate a broad range of the functionally important Firmicute bacteria from mixed human fecal cultures. The recombinant pEHR5 vectors are stably maintained and can be used to fluorescently label some of the *Clostridium*-group bacteria, which are poorly understood organisms, despite several species being earmarked as desirable for a healthy gut

community. This technique will allow the integration of metagenomics with bacterial genetics and paves the way to discovering what these organisms do and where in the gut they do it. — CA

Sci. Rep. 10.1038/srep13282 (2015).

ANTIBIOTICS

Triple threat

Methicillin-resistant *Staphylococcus aureus* (MRSA) is a worldwide threat to human health, because it is resistant to a large class of β -lactams (penicillins) and to second-generation penicillins, including methicillin. However, Gonzales *et al.* report that combining different classes and generations of these drugs could be effective in fighting MRSA. A 1:1:1 mix of three compounds—a β -lactam, a carbapenem, and a β -lactamase inhibitor—synergistically targeted bacterial cell wall synthesis and was bactericidal against 73 different clinical isolates of MRSA. The drug combination prevented MRSA from acquiring resistance to the mix and cleared infection in a mouse model of lethal MRSA. The finding opens the prospect of using already-clinically approved drugs to treat multidrug resistant infections. — LC

Nat. Chem. Biol. 10.1038/nchembio.1911 (2015).

PHOTO: (FROM TOP) ESO/A. ROQUETTE; SCARPA ET AL., DEVELOPMENTAL CELL (24 AUGUST 2015) © 2015 CELL PRESS

ALSO IN SCIENCE JOURNALS

Edited by Stella Hurtley

GUT MICROBIOTA

Diet shapes host and gut microbe fitness

The human gut microbiota is hugely diverse, with many strain variants having a multiplicity of effects on host metabolism and immunity. To define some of these functions, Wu *et al.* made libraries of mutants of *Bacteroides* species known for their capacity to process otherwise intractable dietary fiber. Germ-free mice colonized with defined gut microbiota communities containing the mutants were fed specific diets containing different ratios of fat and fiber. Genes, strains, and species were identified that were associated with specific metabolic pathways. The community responses to dietary shifts were manipulated in an attempt to characterize species for their probiotic or therapeutic potential. — CA

Science, this issue p. 55

WATER STRUCTURE

How well does water share its protons?

Chemists have spent centuries trying to understand what acids look like at the molecular level. It's clear now that water molecules in the liquid accommodate extra protons. Less clear is whether the protons piggyback on individual water molecules (Eigen structure) or find shared accommodation between two at a time (Zundel structure). Thämer *et al.* acquired time-resolved vibrational spectra

across an unusually broad span of the mid-infrared, allowing them to monitor stretches and bends at the same time. Their results imply a more prominent role for the Zundel structure than previously anticipated. — JSY

Science, this issue p. 78

NEURODEVELOPMENT

Individualized neuronal mutations in the human brain

The neurons of the human brain can last for decades, carrying out computational and signaling functions. Lodato *et al.* analyzed the DNA of individual neurons sampled from postmortem human brains and found that individual neurons acquired somatic mutations (see the Perspective by Linnarsson). The mechanism of mutation involved gene transcription rather than DNA replication. Thus, postmitotic neurons would seem to be their own worst enemy: Genes used for neuronal function are the very genes put most at risk of somatic mutation. — PJH

Science, this issue p. 94; see also p. 37

MEMORY MECHANISMS

Memory consolidation by gene suppression

Storing a persistent memory in the brain involves dynamic gene regulation. However, our knowledge of the target genes controlled during memory

formation is limited. Cho *et al.* used RNA sequencing and ribosome profiling to compare transcription and translational levels in the mouse hippocampus before and after memory formation. Under basal conditions, there was an unexpected translational repression of ribosomal protein-coding genes. Early after learning, specific genes were translationally repressed. Later, suppression of a group of genes resulted from the inhibition of estrogen receptor alpha signaling. Thus, suppression mechanisms in the hippocampus appear to play a major role during memory consolidation. — PRS

Science, this issue p. 82

NEUROTRANSMISSION

An alternative way of making GABA

Midbrain dopaminergic neurons release both the inhibitory neurotransmitter GABA and dopamine. In the central nervous system, GABA synthesis is usually mediated by two glutamate decarboxylases (GAD65 and GAD67). Kim *et al.* found that midbrain dopaminergic neurons use a different, evolutionary conserved GABA synthesis pathway that is independent of GAD65 and GAD67. These cells synthesize GABA from putrescine via the enzymes diamine oxidase and aldehyde dehydrogenase 1a1. GABA synthesized by this pathway accounts for approximately 70% of co-released GABA. — PRS

Science, this issue p. 102

CELL BIOLOGY

Increasing the response to TGF- β signals

TGF- β is a cytokine that binds to cell surface receptors and triggers the epithelial-to-mesenchyme transition. This process promotes pathological scarring known as fibrosis and contributes to cancer progression and metastasis. Budi *et al.* found that insulin, which is released in response to high glucose and used to treat diabetes, enhanced the trafficking of TGF- β receptors to the surface of mouse embryonic fibroblasts and epithelial cells. These results may help to explain why diabetics are prone to fibrosis and how hyperglycemia and insulin could enhance cancer progression and metastasis. — WW

Sci. Signal. **8**, ra96 (2015).

NANOELECTRONICS

Making better small contacts

Semiconducting single-walled carbon nanotubes have potential size and conductivity advantages over silicon for making smaller transistors. However, as metal electrical contacts decrease in size, the associated resistance increases to impractical values. Cao *et al.* reacted molybdenum films with semiconducting carbon nanotubes to create a carbide contact. The resistance of these contacts remained low even for 10-nm-scale contacts. — PDS

Science, this issue p. 68

RESEARCH ARTICLE SUMMARY

GUT MICROBIOTA

Genetic determinants of in vivo fitness and diet responsiveness in multiple human gut *Bacteroides*

Meng Wu, Nathan P. McNulty, Dmitry A. Rodionov, Matvei S. Khoroshkin, Nicholas W. Griffin, Jiye Cheng, Phil Latreille, Randall A. Kerstetter, Nicolas Terrapon, Bernard Henrissat, Andrei L. Osterman, Jeffrey I. Gordon*

INTRODUCTION: Relatively little is known about the genetic factors that allow members of the human gut microbiota to occupy their niches. Identification of these factors is important for understanding mechanisms that determine microbiota assembly and perturbation through diet, disease, and clinical treatments. Discovery of these factors should enable new approaches for intervening therapeutically in the functional properties of the human gut microbiota. We present a generalizable approach by which to identify fitness determinants for multiple bacterial strains simultaneously in a model human gut microbiota, obtain gene-level characterization of responses to diet change, and design prebiotics for precision microbiota manipulation.

RATIONALE: We developed a method—multi-taxon INsertion Sequencing (INSeq)—for monitoring the behavior of tens of thousands of transposon (Tn) mutants of multiple bacterial species and strains simultaneously in

the guts of gnotobiotic mice. We focused on four prominent human gut *Bacteroides*: one strain of *B. cellulosilyticus*, one strain of *B. ovatus*, and two strains of *B. thetaiotaomicron*. INSeq libraries, each composed of 87,000 to 167,000 isogenic Tn mutant strains, were produced (single site of Tn insertion per mutant strain; a total of 11 to 26 Tn insertions represented in the library per gene; and 82 to 92% genes covered per genome). The four mutant libraries were introduced into germ-free mice together with 11 wild-type species commonly present in the human gut microbiota. Animals were given a diet rich in fat and simple sugars but devoid of complex polysaccharides [diet 1 (D1)] or one rich in plant polysaccharides and low in fat (D2), either monotonously or in the sequence D1-D2-D1 or D2-D1-D2. We calculated a “fitness index” for each gene on the basis of the relative abundance of its INSeq reads in the fecal or cecal microbiota compared with the input library. In vivo INSeq data were correlated

with INSeq data generated from organisms cultured under defined in vitro conditions; microbial RNA-seq profiling of the community’s metatranscriptome; and reconstructions of metabolic pathways, regulons, and polysaccharide utilization loci. On the basis of the results, we designed a prebiotic intervention.

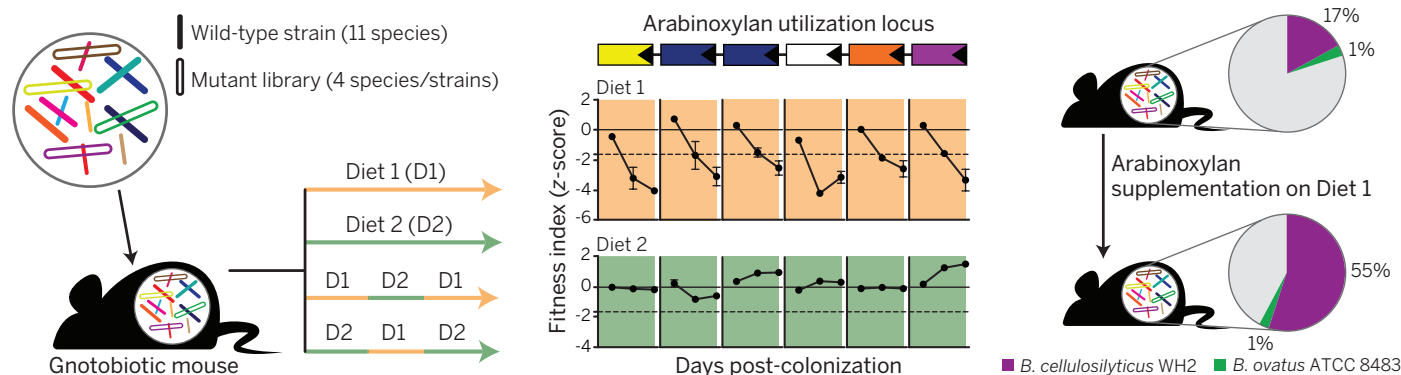
RESULTS: Multi-taxon INSeq (i) provided a digital readout of the remarkably consistent pattern of community assembly; (ii) identified shared as well as species-, strain-, and diet-specific fitness determinants associated with a variety of metabolic or nutrient processing

pathways, including those involving amino acids, carbohydrates, and vitamins/cofactors; (iii) enabled quantitative gene-level measurement of the resilience of the responses to diet perturbations; (iv) revealed that arabinoxylan, the most common hemicellulose in cereals, could be used to deliberately manipulate the representation of *Bacteroides cellulosilyticus*; and (v) defined the niche adjustments of this and the other *Bacteroides* to arabinoxylan supplementation of the high-fat diet.

CONCLUSION: In principle, the approach described can be used to obtain a more comprehensive understanding of how host genotype, diet, physiologic, metabolic, and immune factors, as well as pathologic states, affect niches in gut and nongut habitats, as well as to facilitate development of therapeutic interventions for modifying community structure/function. ■

The list of author affiliations is available in the full article online.

*Corresponding author. E-mail: jgordon@wustl.edu
Cite this article as M. Wu et al., *Science* 350, aac5992 (2015). DOI: 10.1126/science.aac5992



Identification of a prebiotic that specifically increases the abundance of *B. cellulosilyticus*. (Left) The four mutant libraries were pooled together with 11 other phylogenetically diverse wild-type strains, and this consortium, representing an artificial human gut microbiota, was introduced into germ-free mice. Community assembly, the effects of diet, and recovery from diet oscillations were characterized at a community, strain, and gene level in these gnotobiotic animals by use of multi-taxon INSeq. (Middle) Multi-taxon

INSeq revealed an arabinoxylan utilization locus in *B. cellulosilyticus* that is critical for the organism’s fitness in the high-fat/simple-sugar diet (D1) context but not in the D2 context. A homologous arabinoxylan utilization locus in *B. ovatus* was not a fitness determinant with either diet. (Right) Consistent with this finding, supplementation of drinking water with arabinoxylan in mice consuming D1 selectively increased the abundance of *B. cellulosilyticus* but not *B. ovatus*.

RESEARCH ARTICLE

GUT MICROBIOTA

Genetic determinants of in vivo fitness and diet responsiveness in multiple human gut *Bacteroides*

Meng Wu,^{1,2} Nathan P. McNulty,¹ Dmitry A. Rodionov,^{3,4} Matvei S. Khoroshkin,⁴ Nicholas W. Griffin,^{1,2} Jiye Cheng,^{1,2} Phil Latreille,⁵ Randall A. Kerstetter,⁵ Nicolas Terrapon,⁶ Bernard Henrissat,^{6,7} Andrei L. Osterman,³ Jeffrey I. Gordon^{1*}

Libraries of tens of thousands of transposon mutants generated from each of four human gut *Bacteroides* strains, two representing the same species, were introduced simultaneously into gnotobiotic mice together with 11 other wild-type strains to generate a 15-member artificial human gut microbiota. Mice received one of two distinct diets monotonously, or both in different ordered sequences. Quantifying the abundance of mutants in different diet contexts allowed gene-level characterization of fitness determinants, niche, stability, and resilience and yielded a prebiotic (arabinoxylan) that allowed targeted manipulation of the community. The approach described is generalizable and should be useful for defining mechanisms critical for sustaining and/or approaches for deliberately reconfiguring the highly adaptive and durable relationship between the human gut microbiota and host in ways that promote wellness.

The human gut microbiota is highly diverse (1–3). A current view is that strains acquired by an individual early in life persist for decades and that strains are shared among family members. The microbiota can rapidly adapt to changing conditions, but the degree to which given sets of strains share or compete for niche space in the gut ecosystem is poorly understood. Identification of the genetic factors that define an organism's niche is important for understanding the mechanisms that determine community assembly, community responses to and recovery after various perturbations, and the food webs that link microbes to one another and to their host. Discovery of these factors should spawn new approaches for intentional manipulation of the functional properties of the microbiota.

In this Research Article, we describe an approach for simultaneously identifying genetic determinants of fitness for multiple members of a defined artificial human gut microbiota installed in gnotobiotic mice fed distinct diets monotonously or in an ordered sequence. We focus on four human gut *Bacteroides* strains: *B. cellulosilyticus* WH2, *B. ovatus* ATCC 8483, *B. thetaiotaomicron* 7330, and *B. thetaiotaomicron* VPI-5482 [finished

genomes for the first three strains were obtained by combining PacBio and Illumina sequencing (supplementary materials, materials and methods) (4)]. Culture-independent surveys of a number of human populations indicate that all three of these *Bacteroides* species are prominently represented in the guts of healthy individuals (1, 2). All four strains contain numerous genes involved in the recognition and processing of otherwise indigestible dietary polysaccharides (table S1) (4–7). We applied genome-wide transposon mutagenesis to these three prominent human gut-derived *Bacteroides* species and the two strain representatives of one of them, and we colonized singly housed, germ-free mice with all four mutant libraries together with a defined consortium of 11 other wild-type human gut bacterial species representing major phylogenetic lineages present in the microbiota. The microbiome of this 15-member community encodes key metabolic functions identified in anaerobic food webs, including the ability to process polysaccharides to oligosaccharides and simple sugars and to ferment amino acids (7, 8).

This approach not only allowed us to examine assembly of the 15-member artificial community but to characterize responses to dietary perturbations and recovery after these perturbations (stability and resilience) at the community level, the individual species/strain level, and the gene level. We identified shared as well as species- and strain-specific genetic and metabolic features that affect fitness of *Bacteroides* in the gut environment.

Characterizing multiple transposon mutant libraries simultaneously in vivo (multi-taxon INSeq)

Each library we generated from the four bacterial strains was composed of 87,000 to 167,000

isogenic transposon (Tn) mutants. Each mutant contained a single site of insertion of the Tn element. Of the open reading frames (ORFs) in these four *Bacteroides*, 81.5 to 91.8% contained a Tn insertion, allowing us to conclude that disruption of these genes did not preclude growth in the rich medium used to construct the libraries (an analysis of “essential” genes not represented in the various mutant libraries is provided in the supplementary materials, with a focus on those involved in carbohydrate, amino acid, and vitamin/cofactor biosynthesis/catabolism).

Each ORF was covered by an average of 11 to 26 Tn insertions (table S2 and fig. S1, A to D). These Tn mutant libraries were introduced into germ-free mice together with 11 wild-type species that are common constituents of the adult gut microbiota (fig. S2A). To permit simultaneous analysis of multiple mutant libraries in the same recipient gnotobiotic mouse, a *mariner* Tn delivery vector with *MmeI* sites positioned at each end of the Tn (9, 10) was modified so that it contained two taxon-specific barcodes (fig. S2B). *MmeI* digestion of microbial DNA prepared from the gut contents or feces of recipient gnotobiotic mice cleaves genomic DNA at a site 20 or 21 base pairs (bp) distal to the restriction enzyme's recognition site. The site of Tn insertion and the relative abundance of each Tn mutant in the input libraries introduced into mice and in the “output” communities recovered from these animals were defined by using a multi-taxon insertion sequencing (INSeq) protocol. This protocol enables sequencing of the flanking genomic sequence in addition to the taxon-specific barcode positioned within the Tn (fig. S2B). A software package (supplementary materials, materials and methods) was used to assign sequencing reads based on the sample-specific and taxon-specific barcodes. Control experiments, using “mock communities” composed of the 15-member collection of cultured human gut bacteria with different proportions of the mutant libraries (ranging from 0.5 to 40% of the community) revealed that this protocol had high specificity ($91.6 \pm 0.84\%$ of reads mapped to sites of Tn insertion), high sensitivity (a mutant library representing as little as 0.5% of the entire community could be characterized), and good reproducibility [coefficient of determination (R^2) > 0.9; $n = 5$ technical replicates/mock community] (supplementary materials, materials and methods, results, and table S2).

To identify mutations that were deleterious in the gut, we calculated a “fitness index” for each gene based on the relative abundance of its INSeq reads in the output community (for example, fecal microbiota) compared with the input library. We observed that the output-to-input log-ratios for the entire mutant population were bimodally distributed, with the vast majority of mutants (genes) falling in a normal distribution to the right of a much smaller distribution with lower fitness. To statistically distinguish these two populations, we implemented the expectation-maximization (EM) algorithm to iteratively estimate the unknown parameters (mean and variance) for each population using a likelihood function based on observed

¹Center for Genome Sciences and Systems Biology, Washington University School of Medicine, St. Louis, MO 63108, USA. ²Center for Gut Microbiome and Nutrition Research, Washington University School of Medicine, St. Louis, MO 63108, USA. ³Infectious and Inflammatory Disease Center, Sanford-Burnham-Prebys Medical Discovery Institute, La Jolla, 92037 CA, USA. ⁴A. A. Kharkevich Institute for Information Transmission Problems, Russian Academy of Sciences, Moscow 127994, Russia. ⁵Monsanto Company, St. Louis, MO 63167, USA. ⁶Architecture et Fonction des Macromolécules Biologiques, Centre National de la Recherche Scientifique et Aix-Marseille Université 13288 Marseille cedex 9, France. ⁷Department of Biological Sciences, King Abdulaziz University, Jeddah, Saudi Arabia. *Corresponding author. E-mail: jgordon@wustl.edu

data (the log-ratios for each individual gene) (supplementary materials, materials and methods). We calculated a z score (fitness index) for the difference between each gene's log-ratio and the mean of the normal distribution of the population represented by the vast majority of the mutants (fig. S2, C to E). A P value was determined based on a normal distribution by using a Z test, and a q value was assigned after applying a multiple hypothesis testing correction (FDR). To avoid misidentifying genes as significant fitness determinants, we only considered those that, when mutated, were significantly depleted in the output library across biological replicates. In silico simulations revealed that this EM algorithm-based procedure yielded a false positive rate of less than 5% for mutants in genes whose relative abundance was $>0.002\%$ (fig. S3B). These simulations were verified by applying the analysis pipeline to our mock communities (table S2). ORFs satisfying the criteria of having a significant q value in one diet condition and no fitness defects in any biological replicates under another diet condition were defined as “diet-specific fitness factors.”

Community assembly, stability, and resilience in response to different diets

Adult (10 to 12 weeks old) male germ-free C57BL/6J mice were placed on either a low-fat/high-plant polysaccharide (LF/HPP) chow or a diet in which calories were largely derived from hydrogenated vegetable shortening and beef tallow and carbohydrates were limited to sucrose, corn starch, and maltodextrin (plus an indigestible cellulose binder) [high-saturated fat/high-simple sugar (HF/HS) diet]. Diets were introduced 7 days before animals received a single oral gavage of the artificial community containing the four mutagenized strain libraries and 11 wild-type strains (Fig. 1A). In control experiments, we used a 15-member community composed of all wild-type strains, or 15-member communities that only contained a single mutant library (fig. S4A). Groups of singly caged mice were maintained on either the LF/HPP or HF/HS diet for the duration of the experiment, whereas other groups were subjected to a reciprocal set of diet oscillations (LF/HPP→HF/HS→LF/HPP or HF/HS→LF/HPP→HF/HS) ($n = 5$ mice/diet treatment/community type/gnotobiotic isolator) (Fig. 1A). We used short-read shotgun sequencing [community profiling by sequencing (COPRO-seq)] of DNA prepared from fecal samples collected over the course of each experiment to define the relative abundance of each community member.

When considered as a whole, each mutant library acted similarly to the parental wild-type strain in terms of its proportional abundance in the community (fig. S4B and table S3). In both monotonously fed treatment groups, the relative abundance of *B. cellulosilyticus* WH2 was high, although significantly greater in animals fed LF/HPP chow ($36 \pm 1.6\%$ versus $16 \pm 3.1\%$ after 16 days on the diets; $P < 0.01$, Mann-Whitney test). *B. ovatus* ATCC 8483 had a preference for conditions associated with LF/HPP chow feeding ($11 \pm 0.7\%$ versus

$0.8 \pm 0.3\%$; $P < 0.01$, Mann-Whitney test). Strain-specific differences were also evident; *B. thetaiotaomicron* VPI-5482 was more successful in the LF/HPP diet context than was *B. thetaiotaomicron* 7330 ($9 \pm 0.5\%$ versus $0.02 \pm 0.04\%$; $P < 0.05$, Mann-Whitney test), whereas the 7330 strain had significantly higher abundance than the VPI-5482 strain when animals were consuming the HF/HS

diet ($6 \pm 1.4\%$ versus $3 \pm 0.5\%$; $P < 0.05$, Mann-Whitney test) (fig. S5A).

Multi-taxon INSeq allowed us to obtain a genome-wide, gene-level view of the effects of the selective pressures exerted by diets on fitness. Analysis of the relative abundances of all *B. cellulosilyticus* mutants in fecal samples collected at 4, 10, and 16 days after gavage in the two

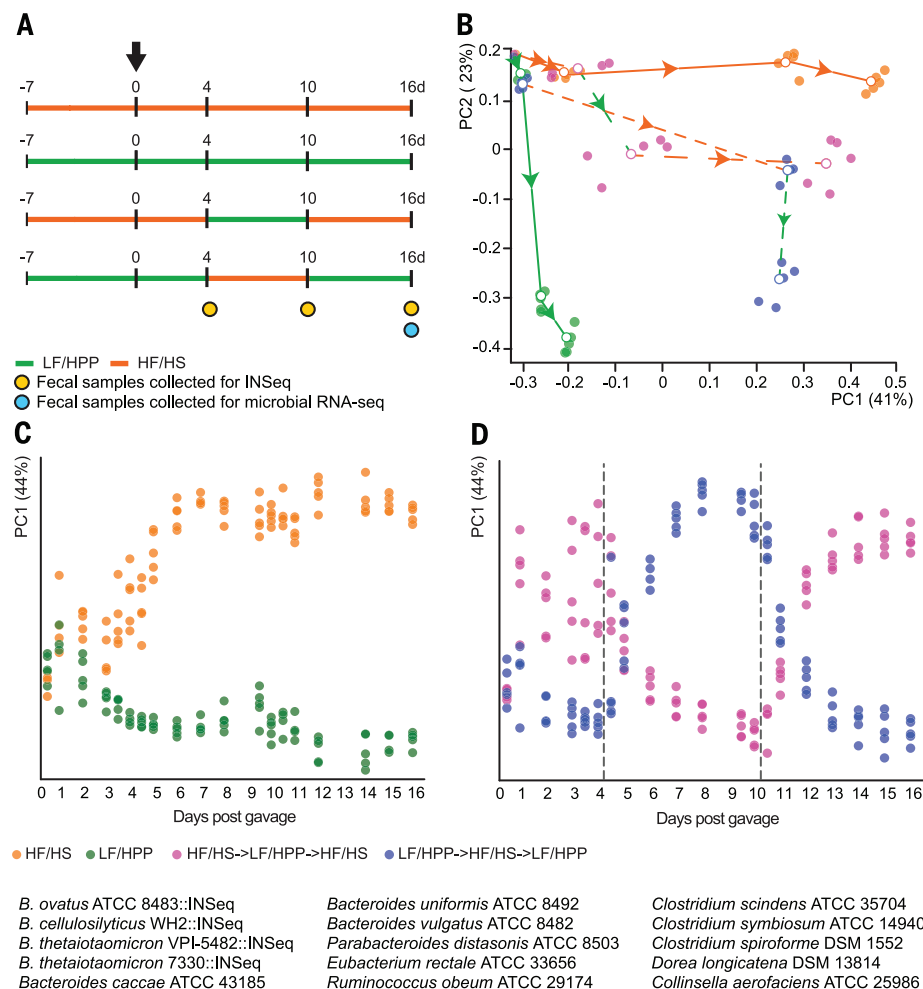


Fig. 1. The effect of diet and diet oscillations on the configuration of the 15-member artificial community containing 11 wild-type strains and the four mutant libraries, including the structure of the population of *B. cellulosilyticus* WH2 mutants. (A) Experimental design. 10- to 12-week-old germ-free male C57BL/6J mice were gavaged with the indicated consortium of 15 strains shown at the bottom of the panel. Animals were given the LF/HPP and/or the HF/HS diet in the order shown. Fecal samples were collected at the indicated time points for INSeq and microbial RNA-seq analyses. (B) Principal coordinates analysis (PCoA) of Hellinger distance measurements based on the relative abundance of *B. cellulosilyticus* WH2 Tn mutants in fecal samples, as defined by multi-taxon INSeq. Each solid circle represents the population of all mutants in *B. cellulosilyticus* WH2 sampled from an individual mouse in the indicated diet treatment group. Circles are color-coded based on the diet treatment group. Each open circle represents the location in the ordination plot of the population of Tn mutants, averaged for all animals in a given treatment group sampled at a given time point [data shown for $T = 0$ (input library before gavage), 4, 10, and 16 days after gavage]. Lines connect open circles for each of the four treatment groups. Dashed lines denote the two different diet oscillation groups. The colors of the lines correspond to the diet being consumed (green, LF/HPP; orange, HF/HS). Arrowheads superimposed on lines indicate the passage of time. (C and D) PCoA of Hellinger distance measurements based on COPRO-seq data. Each solid circle represents a fecal community sampled from an individually caged mouse belonging to the indicated diet treatment group. These circles were ordinated in the same coordinate space but are being shown as two separate panels for clarity. Vertical dashed lines in (D) indicate the time point at which a diet switch occurred.

monotonous diet treatment groups disclosed that by day 4, the mutant population had already manifested diet-specific configurations [permutational multivariate analysis of variance (PERMANOVA) of Bray-Curtis dissimilarities, $R^2 = 0.676$, $P = 0.001$]. The relative abundances of *B. cellulosilyticus* mutants were remarkably consistent between individually caged mice monotonously fed a given diet, including groups of mice housed in different gnotobiotic isolators (Student's unpaired *t* test) (fig. S6A). This within-treatment group consistency was sustained as the configuration of the mutant population evolved during the ensuing 11 days of monotonous diet consumption (Fig. 1B and fig. S6, B and C). [Because we compared an INSeq library of a given single species/strain after in vivo selection under different dietary treatments, we used the nonphylogenetic Hellinger metric (11) to calculate the dissimilarity between the libraries within or between treatment groups.]

Multi-taxon INSeq of fecal samples collected at the end of 16 days of monotonous diet consumption yielded 550 HF/HS diet-specific *B. cellulosilyticus* fitness determinants and 34 LF/HPP diet-specific determinants: 244 of the 550 HF/HS diet-specific genes had Kyoto Encyclopedia of Genes and Genomes (KEGG) Orthology (KO) assignments; among this group, there was a significant enrichment of genes belonging to the KEGG categories “Membrane Transport” (for example, one operon involved in iron transport, another involved in phosphate transport), “Metabolism of Cofactors and Vitamins” [for example, seven genes in the cobalamin biosynthesis pathway, which is consistent with the view that the capacity to synthesize and use cobalamin and other substituted corrins is an important determinant of survival in the gut (9, 12)], and “Protein Folding, Sorting, and Degradation” (the functional annotations and fitness indices of these genes are provided in table S4).

Resilience—the ability of a system to “absorb changes of state variables and parameters, and still persist”—has been differentiated in community ecology from stability, which is “the ability of a system to return to an equilibrium state after a temporary disturbance” (13). The two groups of mice subjected to a reciprocal set of diet oscillations [LF/HPP (4 days)→HF/HS (6 days)→LF/HPP (6 days) or HF/HS (4 days)→LF/HPP (6 days)→HF/HS (6 days)] exhibited consistent and marked diet-specific changes in overall community structure as defined by COPRO-seq (Fig. 1, C and D; also see the patterns of change in relative abundances of *B. cellulosilyticus* and *B. ovatus* in fig. S5A). The 15-member community showed elements of both resilience and stability in the face of brief dietary disturbances. Oscillating the mice between the LF/HPP and HF/HS diets produced substantial changes in the relative proportions of community members, but all persisted through the disturbance (resilience), and perturbed and unperturbed communities converged on very similar states determined by the final diet consumed by the mice. At the end of the experiment, the diets explained 82.6% of the variance between fecal communities (Hellinger distances, PERMANOVA,

$P = 0.001$) (fig. S7A). The interaction between diets and treatment (monotonous diet versus diet oscillation) explained only 8.7% of the variance, which is similar to its explanatory power before the disturbance ($R^2 = 8.7\%$).

Followup INSeq analysis of the same fecal DNA samples used for COPRO-seq afforded an opportunity to simultaneously characterize the degree to which the aggregate collections of *B. cellulosilyticus* and *B. ovatus* mutants were able to persist and recover from a diet disturbance (an INSeq-based definition of resilience and stability) and the variation in such recovery between animals (an INSeq-based measure of stochasticity). The *B. cellulosilyticus* WH2 INSeq library showed high resilience to the brief dietary perturbations in the sense that the library as a whole persisted throughout the experiment, although some individual mutants did not. However, it did not show the same stability that the 15-member community did; in the mice that experienced diet oscillations, Hellinger distances indicate that the library of mutants did not converge to the same state as in monotonously fed mice but rather persisted as a reconfigured population. This can be seen in the Hellinger distances between the libraries at the end of the experiment, when diet explained 38.7% of the variance, but the interaction between diet and treatment explained 35.1% (PERMANOVA, $P = 0.001$) (fig. S7B)—a value much greater than its explanatory power before the diet oscillation ($R^2 = 8.2\%$).

The configuration of the *B. cellulosilyticus* mutant population exhibited diet-specific changes. However, during the “recovery phase,” when these two groups of mice subjected to diet oscillations were returned to the starting diet of the sequence, the *B. cellulosilyticus* mutant library shifted toward a state similar but not identical to that observed in monotonously fed hosts (Fig. 1B). Of the 550 *B. cellulosilyticus* genes identified as HF/HS diet-specific fitness determinants in monotonously fed animals, 251 had significantly higher *z* scores (were less required) in animals that had been switched temporarily to LF/HPP chow and then returned to the HF/HS diet, as compared with mice that had only consumed the HF/HS diet [includes the six genes comprising the only one of its 113 polysaccharide utilization loci (PULs) identified as a HF/HS diet-specific fitness determinant (see table S4A and below)]. Similarly, 21 of the 34 genes designated as LF/HPP diet-specific fitness determinants in monotonously fed mice had significantly higher *z* scores in mice that had been temporarily switched to the HF/HS diet and then returned to LF/HPP chow (table S4A). As with *B. cellulosilyticus*, diet oscillations of the type A to B to A (or B to A to B) led to increased similarity in the overall patterns of fitness in the *B. ovatus* mutant library compared with the patterns of fitness in the library of mutants present in mice fed the diets monotonously (fig. S8 and table S4B). This response to perturbation may represent an important mechanism behind the maintenance of diet-specific traits in a member or members of a microbiota harbored by hosts experiencing more varied diets

(here, we are using mutants as proxies for functional “traits”).

Identifying core in vivo fitness determinants in four *Bacteroides* strains

Genes that are conserved among the four *Bacteroides* strains and that show a significant effect on fitness in all strains in both dietary contexts can be defined as a core set of in vivo fitness determinants for these members of this genus; as such, they inform us about the resource requirements and selective pressures these taxa experience in the gut in this community context and under these two dietary conditions.

In total, 2238 genes are conserved among all four *Bacteroides* strains. Multi-taxon INSeq of fecal samples, collected from mice colonized for 16 days and monotonously fed one or the other diet, revealed 82 conserved genes with significant diet-independent effects on fitness in all four strains (table S5). The fitness indices (*z* scores) for these genes varied as a function of strain but less so across the different diets ($P < 0.001$; two-way ANOVA). Among the 82 core fitness determinants, 15 were components of biosynthesis pathways for arginine (ArgB, ArgC, ArgD, ArgF, ArgE, ArgG, and ArgH), aspartate (AspC1), lysine (LysA), methionine (MetA), aromatic amino acids (AroH-TyrA, TyrA2, and TyrB), branched chain amino acids (LeuB), and histidine (HisI) (fig. S9A, table S6A, and supplementary materials). In follow-up studies, the *B. cellulosilyticus* mutant library was grown to stationary phase in minimal medium lacking amino acids and containing one of several carbon sources [glucose, xylose, arabinose, or wheat arabinoxylan (the most common hemicellulose in cereals)] or in control-rich medium [tryptone-yeast extract-glucose (TYG)] ($n = 6$ replicates/growth condition). INSeq analysis of the input library and stationary phase cultures (table S7) confirmed that Tn mutagenesis of the 15 core fitness determinants annotated as being involved in the biosynthesis of 11 amino acids precluded growth in any of four types of amino acid-depleted minimal media but did not affect growth in the rich medium (supplementary materials). Together, these results emphasize the important contribution of amino acid biosynthesis to the survival of these *Bacteroides* strains in the niches they occupy in the 15-member community in the two diet contexts tested in this study. This is consistent with our previous observation made in gnotobiotic mice that the biomass of a 10-member community composed of all wild-type human gut-derived strains—including the three *Bacteroides* used in the current study (*B. thetaiotaomicron* VPI-5482, *B. ovatus* ATCC 8483, and *B. caccae* ATCC 43185)—correlates with the amount of protein in the diet (8).

Genes related to carbohydrate utilization/metabolism were also prominently represented among the 82 shared in vivo fitness factors (fig. S9B and table S6B). These include (i) members of arabinose, fructose, glucose/galactose, and hexuronate utilization pathways [three inner-membrane monosaccharide transporters—glucose/galactose permease (GlcT), arabinose permease (AraP), and

fructose transporter (FruP)—plus a previously unidentified arabinose-dependent repressor from the NrtR family (AraR), an enzyme from the arabinose catabolic pathway (AraA), two galactose catabolic enzymes (GalM, GalE), and two enzymes from the hexuronate-utilization pathway (KdgK, KdgA)]; (ii) three sugar-responsive transcriptional regulators, including homologs of BT4338, a Crp-like transcription factor that controls a proposed global sugar catabolic regulon (14) encompassing up to 30 genes per genome that participate in the utilization of arabinose, xylose, fucose, galacturonate, pectin, and β -hexosamines; and (iii) cytoplasmic enzymes involved in starch and glycogen synthesis [starch/glycogen synthase (BT1294), glycogen branching enzymes (BT0771 and BT4303), and alpha-glucanotransferases (BT4304 and BT4305)].

Group B vitamins are essential micronutrients that serve as cofactors (or their precursors) used by various enzymes involved in many facets of cellular metabolism. All three *Bacteroides* species are prototrophs for all B vitamins and their respective cofactors except cobalamin (vitamin B12), which is not synthesized by *B. thetaiotaomicron* or *B. ovatus* [application of the metabolic subsystem approach implemented in SEED (15) in order to investigate

the ability of the three *Bacteroides* species to produce and salvage thiamine, riboflavin, niacin, biotin, pyridoxine, cobalamin, pantothenate, and folate is described in the supplementary materials]. All three *Bacteroides* species lack orthologs for all known transporters for B vitamins other than thiamine (vitamin B1) and cobalamin (fig. S9C and table S6C). Our in vivo multi-taxon INSeq analysis revealed that components of B-vitamin biosynthetic pathways as well as thiamine and cobalamin transporters functioned as strain-specific but not core fitness determinants (supplementary materials). This result indicated that in our gnotobiotic model, all three *Bacteroides* species, represented by four strains, have different requirements for B vitamins and/or deploy divergent strategies for acquiring them (for example, through de novo biosynthesis or from the diet, or from other microbes with B vitamin transporters) (detailed analysis of in vitro fitness determinants in vitamin B/cofactor biosynthetic pathways is provided in the supplementary materials).

One approach that has been used to search for genes that act as fitness determinants in vivo is to identify those that exhibit significant differences in their expression in vitro versus in a given body habitat (16). Therefore, we compared

RNA sequencing (RNA-seq) data sets from the four *Bacteroides* strains, generated by using fecal samples collected at the same time as samples for INSeq, with RNA-seq data sets produced from *B. cellulosilyticus* during log phase growth in rich medium or in minimal medium containing single carbon sources such as arabinose, arabinoxyran, xylose, or glucose. The results revealed that only 3 of the 82 core fitness determinants had significantly higher levels of expression in vivo under both diet conditions than under any of the in vitro conditions examined ($n = 4$ mice/diet treatment; $n = 3$ biological replicates/in vitro growth condition) (fig. S10A). The fact that expression of the remaining 79 core fitness determinants, including the regulator of the proposed sugar catabolic regulon (fig. S10B), was not higher in vivo than in vitro highlights one of the benefits of INSeq and provides a cautionary note that sole reliance on differential expression as a criterion may miss genes that are critical for survival in a given environmental context.

Differences in fitness determinants in the two *B. thetaiotaomicron* strains

B. thetaiotaomicron VPI-5482 is one of the most studied human gut *Bacteroides* (4, 5, 14, 17–19).

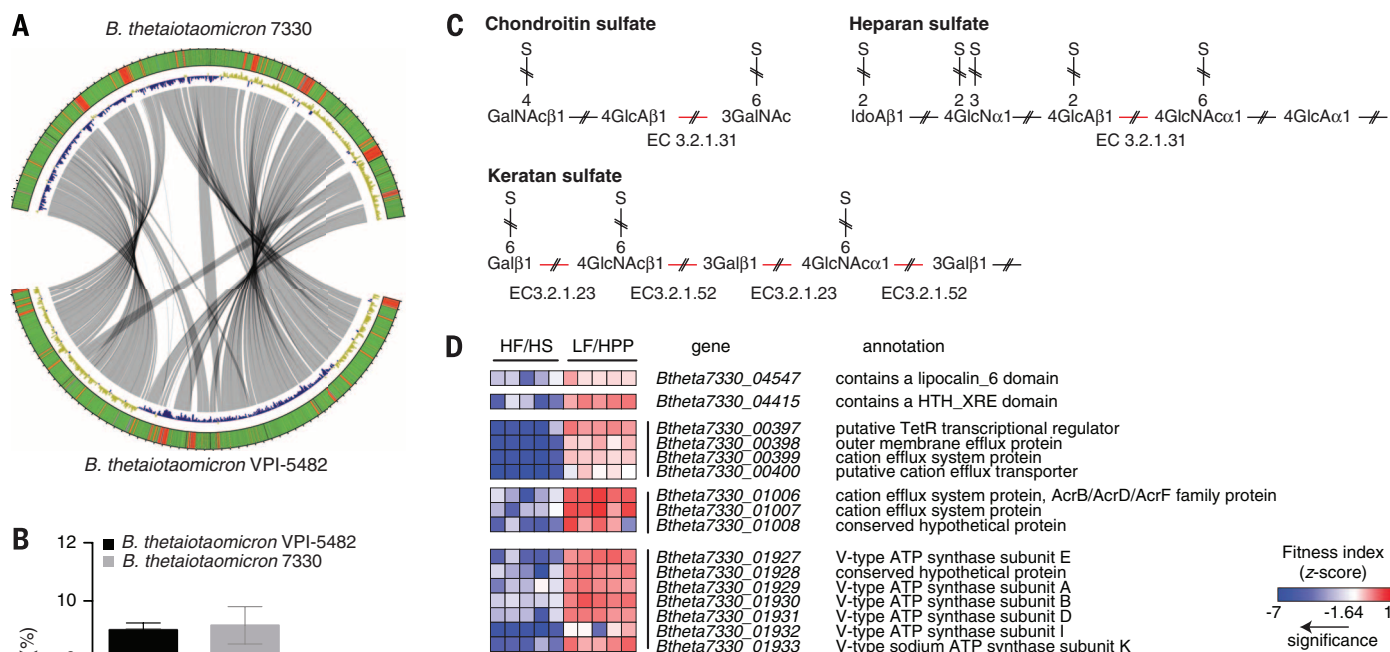


Fig. 2. HF/HS diet-specific fitness determinants in *B. thetaiotaomicron* 7330. (A) Circos-generated alignment of the *B. thetaiotaomicron* VPI-5482 and *B. thetaiotaomicron* 7330 genomes (26). Gray lines connect segments of DNA conserved between these two genomes (these regions were identified through alignment with Mauve) (27). The color-coded outer circle denotes the similarity between their proteins: green, >90% identity (based on Blastp alignment); blue, 70 to 90% identity; red, <70% identity; black, intergenic regions. GC skew was calculated by using a sliding window size of 10kb (yellow, GC skew > 0; purple, GC skew < 0). (B) COPRO-seq analysis of the relative abundance of the two *B. thetaiotaomicron* strains in the fecal microbiota of mice sampled 2 weeks after gavage while consuming the HF/HS or LF/HPP diets. Mean values \pm SEM are shown ($n = 5$ individually caged mice harboring a community consisting of 11 wild-type and the four mutant libraries per treatment group). The summed relative abundance of the two strains remains the same, even though the relative representation of the individual strains is significantly different in the two diet contexts ($P < 0.001$, 2-way ANOVA). (C) HF/HS diet-specific fitness determinants in *B. thetaiotaomicron* 7330 involved in degradation of glycosaminoglycans associated with the intestinal mucosa (genes highlighted with red lines and identified by the EC annotations of their protein products). (D) HF/HS diet-associated changes in the z scores of 7330-strain-specific fitness determinants that are involved in transcription regulation (*Btheta7330_04415*) or are components of operons encoding transport systems (vertical black lines to the left of the gene ID denote individual operons).

B. thetaiotaomicron 7330 is a strain recovered from a healthy adult. Syntenic regions in their genomes are illustrated in Fig. 2A. The representation of genes in KEGG categories and KEGG pathways for the two strains are described in table S8A. Provided in table S8B is a list of the 91 PULs encompassing 808 predicted ORFs in the 7330 strain, 18 of which (136 ORFs) are distinct (their protein products had <90% similarity to any protein in the predicted VPI-5482 proteome).

As noted above, the 7330 strain is more successful in the 15-member community context when mice are consuming the HF/HS diet. Although the relative representation of each *B. thetaiotaomicron* strain in the 15-member community varied by 340-fold depending upon the diet, their total relative abundance in the community was the same across the two diets (Fig. 2B), raising the possibility that the strains compete for a niche in this community and that occupancy of this niche by one strain or the other is highly sensitive to diet. Therefore, we used INSeq to identify factors that define their dietary niches (table S9, which includes the 385 HF/HS diet-specific fitness determinants in *B. thetaiotaomicron* 7330). In the absence of dietary polysaccharides, *B. thetaiotaomicron* VPI-5482 adaptively forages on host mucosal glycans, suggesting that the capacity to consume both dietary- and host-derived glycans is one of the mechanisms by which it is able to survive in the gut (5, 20, 21). The HF/HS diet-specific and 7330 strain-specific fitness factors include genes in two operons specifying components of cation efflux systems plus several glycoside hydrolases predicted to be involved in the catabolism of mucosal glycans (Fig. 2, C and D, and table S9B). The latter include genes (*Btheta7330_01433*, *Btheta7330_02903*, and *Btheta7330_02906*) that encode three members of glycoside hydrolase family GH20 (β -hexosaminidase, EC 3.2.1.52) that likely cleave GlcNAc residues. Their orthologs are also represented in the VPI-5482 genome, but in this strain, they do not convey a significant fitness effect. Thus, one functional distinction between the two strains revealed through multi-taxon INSeq is that they likely use different strategies for adaptive foraging of mucosal glycans in the absence of dietary polysaccharides.

Individual *Bacteroides* species contain multiple capsular polysaccharide biosynthesis (*CPS*) loci, allowing for a large number of combinations of expressed loci in different environmental contexts. We used multi-taxon INSeq to identify *CPS* loci and their component genes that were critical for fitness in vivo within and across species and strains as a function of diet. The two *B. thetaiotaomicron* strains vividly illustrate the different contributions of individual *CPS* loci to survival. *CPS4* was the only one of the VPI-5482 strain's seven *CPS* loci that functioned as a significant fitness determinant in the context of the 15-member community and either of the two diets (as shown in fig. S11B, 20 of its 21 genes, collectively covered by >1200 Tn mutants, were defined as essential). In contrast, *CPS3*—a locus

in the 7330 strain's genome composed of 18 genes not found in the VPI-5482 strain—was the only one among its six *CPS* loci critical for fitness in either diet context (all 18 genes, covered by >850 mutants, had significant fitness indices) (fig. S11C). INSeq established that this strain specificity for *CPS* fitness effects was evident along the length of the gut (table S9C). The importance of these loci is not simply attributable to their levels of expression: Microbial RNA-seq of fecal samples collected at 4 and 16 days after gavage revealed that neither *CPS4* in *B. thetaiotaomicron* VPI-5482 nor *CPS3* in *B. thetaiotaomicron* 7330 is the dominantly expressed locus in either diet context (table S10).

Identifying a diet supplement that can specifically manipulate *B. cellulosilyticus* abundance

B. cellulosilyticus WH2 is equipped with more carbohydrate active enzymes (CAZymes) dedicated to glycan digestion than is any other sequenced *Bacteroidetes* genome reported to date (7). Its 510 CAZymes—comprising glycoside hydrolases, polysaccharide lyases, carbohydrate esterases, and associated noncatalytic carbohydrate binding modules—are distributed among 113 PULs. Only one of the 113 PULs (*BcellWH2_04321-4327*) functioned as a significant fitness determinant in the HF/HS diet context (Fig. 3A). The fitness indices of the 127 Tn mutants that mapped to the six genes in this PUL were remarkably consistent between individually caged animals as a function of their diet. Moreover, as noted above, the relative abundances of these mutants were higher in mice that had undergone an HF/HS-LF/HPP-HF/HS diet oscillation than in mice monotonously fed the HF/HS diet (Fig. 3A). This PUL is contained within a region of the genome spanning *BcellWH2_04292-BcellWH2_04327* that contains three hybrid two-component systems (an analysis of putative HTCS regulons in this genomic region is provided in the supplementary materials) (fig. S12).

The *BcellWH2_04321-4327* PUL consists of a hybrid two-component system (HTCS) transcriptional regulator (a characterization of DNA binding motifs and regulated operons is presented in the supplementary materials) and a xylan utilization system core (22), which consists of a SusC/D pair (*BcellWH2_04325/26*), a hypothetical protein (*BcellWH2_04324*), a predicted xylanase belonging to glycoside hydrolase family 10 (GH10; *BcellWH2_04323*), a predicted β -galactosidase from GH35 (*BcellWH2_04322*), and a predicted feruloyl esterase (*BcellWH2_04321*) (Fig. 3A and fig. S12, A and B). Gas chromatography/mass spectrometry (GC/MS) of the products of acid hydrolysis of the HF/HS diet revealed small amounts of xylose and arabinose (61.2 ± 7.5 μ g/g and 62.8 ± 6.2 μ g/g, respectively). Our previous in vitro growth studies of *B. cellulosilyticus* WH2 cultured in minimal medium supplemented with one of 31 distinct carbohydrate substrates, plus RNA-seq analysis of the bacterium recovered at mid-log phase from those minimal media that supported its growth, revealed that this PUL was induced by xylan and arabinoxylan (7) (fig. S13A). Arabinox-

ylans are made of a xylan backbone with α -L-arabinose side chains. They also contain ferulic acid and other phenolic acids that are covalently linked to them via ester linkages. A likely role for the product of *BcellWH2_04321* in the context of this PUL would be removal of the ferulic esters from arabinoxylan. The GH10 xylanase targets the xylan backbone, whereas the GH35 enzyme likely removes the α -linked L-arabinose side chains (α -L-arabinose is identical to β -D-galactose, except for the C-6 moiety).

B. ovatus, the only other *Bacteroides* strain in the artificial community that could grow in minimal medium containing purified arabinoxylan as the sole carbon source (fig. S13B), contains a PUL (*Boavatus_01723-32*) that is induced when this medium is supplemented with arabinoxylan (or xylan) (6). Multi-taxon INSeq of fecal samples collected from mice harboring the 15-member community showed that unlike the xylan- and arabinoxylan-inducible *B. cellulosilyticus* PUL *BcellWH2_04321-27*, this PUL is not required for survival of *B. ovatus* in the HF/HS diet context (Tn mutants in its SusC and xylanase genes produced no significant fitness defects) (fig. S13C).

Given these results, we examined the effects of consumption of arabinoxylan purified from wheat on the relative abundances of *B. cellulosilyticus* and *B. ovatus* and their fitness determinants. Our rationale was that we could use arabinoxylan to induce expression of the one *B. cellulosilyticus* WH2 PUL that was a key fitness factor in the HF/HS diet context, and that PUL induction would be accompanied by improved fitness. Therefore, before colonization with the 15-member community containing the INSeq libraries, one group of germ-free mice received the HF/HS diet plus drinking water supplemented with wheat-derived arabinoxylan (7.5% w/v) for 7 days. Another group received the same diet but without arabinoxylan in their drinking water. All groups were then gavaged with the artificial community: The group pretreated with arabinoxylan continued to receive the HF/HS diet and supplemented water ad libitum for the next 14 days and then was switched to unsupplemented water. A reciprocal treatment group received unsupplemented water plus the HF/HS diet for 14 days, followed by a switch to arabinoxylan-supplemented water. A third group received unsupplemented water plus the low-fat, high-plant polysaccharide (LF/HPP) diet for 14 days, followed by a switch to supplemented water (while being maintained on the LF/HPP chow); these animals served as a control because the targeted PUL only manifests itself as a fitness determinant in the context of the high-fat, polysaccharide-deficient diet ($n = 5$ individually caged mice per treatment groups A, B, and C in Fig. 3B).

COPRO-seq analysis of fecal samples collected at the end of each 14-day treatment period demonstrated that arabinoxylan produced a significant increase in *B. cellulosilyticus* abundance in mice fed the HF/HS diet (adjusted P value <0.001; Student's t test; comparing group B to group A at the 14-day time point, and the 30-day versus 14-day time points within group A in Fig. 3C) but

no significant effect in the LF/HPP diet context (as seen in the 30-day versus 14-day time points for group C). Consistent with the INSeq results showing that the arabinoxylan utilization PUL in *B. ovatus* is not a fitness determinant in the HF/HS diet context, we observed no significant effects of arabinoxylan treatment on the relative abundance of this community member (Fig. 3C). We confirmed these findings in a separate experiment in which two groups of gnotobiotic mice harboring the 15-member community were treated for 56 days with a HF/HS diet with or without supplementation of their drinking water with 15% (w/v) arabinoxylan. In this higher-dose, longer-duration, monotonous-diet experiment, the abundance of *B. cellulosilyticus* WH2 increased significantly (as did levels of cecal short chain fatty acids and deconjugated bile acids), whereas *B. ovatus* showed no response (fig. S14, A and B). Arabinoxylan treatment did not pro-

duce a statistically significant difference in total body weight (Student's *t* test).

We identified 407 *B. cellulosilyticus* WH2 genes that functioned as fitness determinants when mice consumed the HF/HS diet but not when mice also received arabinoxylan in their drinking water (table S11A). The arabinoxylan- and xylan-inducible PUL *BcellWH2_04321-4327* was included among this group of genes (fig. S15A). *B. cellulosilyticus* contains another PUL encoding a predicted xylanase (*BcellWH2_04296-4307*) that is also induced by xylan and arabinoxylan in vitro. Neither of these two PULs are fitness determinants when *B. cellulosilyticus* is grown in minimal medium containing arabinoxylan as the sole carbon source (table S7). The *BcellWH2_04296-4307* PUL is not a fitness determinant when mice are consuming the HF/HS diet, with or without arabinoxylan, suggesting that together, these two PULs—*BcellWH2_04321-4327* (the HF/HS

diet specific fitness PUL that is no longer required with arabinoxylan supplementation) and *BcellWH2_04296-4307* (not required under either of the two conditions)—provide redundant yet distinguishable functions in the 15-member community context. A recent study of the orthologous PULs in *B. ovatus* ATCC 8483 showed that they are regulated by different xylan structures: All xylans contain a conserved β 1,4-xylose core backbone that is variably decorated with monosaccharide side chains; *Bovatus_01727-01732*, the ortholog of *BcellWH2_04321-4327*, is regulated by simpler xylans, whereas *B. ovatus_03715-03733* is regulated by more complex (decorated) xylans (23). This finding together with our results suggest that (i) the xylan present in the HF/HS diet is a simpler type that is processed by the *BcellWH2_04321-4327* PUL, and (ii) adding a xylan of intermediate complexity (wheat arabinoxylan) induces both of the PULs. We postulate

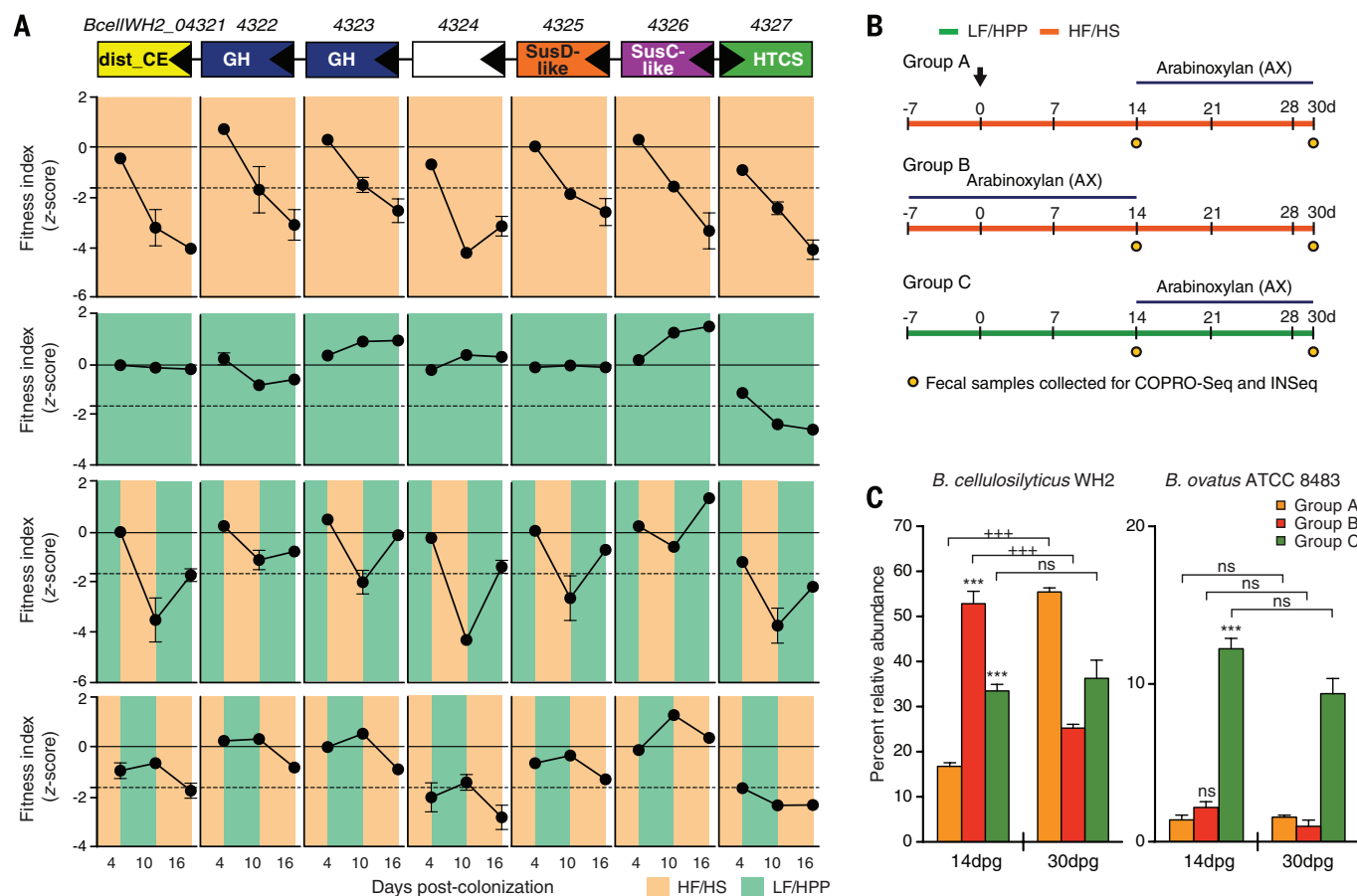


Fig. 3. Arabinoxylan increases the relative abundance of *B. cellulosilyticus* WH2 in vivo. (A) INSeq analysis reveals that all genes in PUL *BcellWH2_04321-4327* have significant fitness indices (z values) in the HF/HS diet context. *BACWH2_04327*, encoding a hybrid two-component system (HTCS) regulator, is the only gene in this PUL that has a significant fitness effect on the LF/HPP diet. Functional annotations for genes in the PUL are shown together with the direction of their transcription. Fitness indices for each gene in the different diet contexts (orange, HF/HS; green, LF/HPP) are plotted as mean values \pm SEM. The horizontal dashed line indicates the cutoff for significance ($P < 0.05$; z test with FDR correction). *dist_CE*, distant relative of carbohydrate esterase; *GH*, glycoside hydrolase; *HTCS*, hybrid two-component system. (B) Experimental design. Adult C57BL/6J germ-free mice were gavaged with a consortium containing

11 wild-type strains plus the four *Bacteroides* INSeq libraries. Animals were fed the HF/HS or LF/HPP diets with or without supplementation of their drinking water with 7.5% arabinoxylan ($n = 5$ individually caged mice per group). (C) The relative abundance of *B. cellulosilyticus* and *B. ovatus* was defined by COPRO-seq analysis of fecal samples collected at the indicated time points. Mean values \pm SEM are plotted. *** $P < 0.001$ compared with the reference group A at 14 days post-gavage (dpg); +++ $P < 0.001$ for within group comparisons of the 30- versus 14-dpg fecal sample (Student's *t* test after FDR correction). *B. ovatus*, the only other *Bacteroides* strain in the community that exhibited significantly increased growth in minimal medium supplemented with arabinoxylan (fig. S13B) did not manifest a significant change in its relative abundance in vivo when arabinoxylan was added to the drinking water. ns, not significant.

that this dual induction creates a functional redundancy with respect to arabinoxylan utilization in *B. cellulosilyticus* WH2 that accounts for our finding that neither PUL alone is required for fitness in the setting of arabinoxylan supplementation of the HF/HS diet. Targeted mutation and complementation of genes in one, the other, or both *BcellWH2_04321-04327* and *BcellWH2_04296-4307* would provide an opportunity to independently validate the roles of these two PULs in different diet contexts. Once genetic tools have been developed to stably express the one or two proteins required to complement the corresponding single- and double-knockout strains in either or both PULs in vivo, these experiments can and should be performed.

There were several transporters that were no longer significant fitness determinants in arabinoxylan-supplemented mice; these include four MFS-type transporters [a nucleoside H⁺ symporter, plus transporters for galactose/glucose (GlcT), fructose (FruP), and di/tri-peptides], iron and zinc transporters, and two ABC-type antimicrobial peptide transporters (a ranking based on their *q* scores is available in fig. S15B). Two MFS-type multidrug transporters and one ABC-type antimicrobial peptide transporter were the only *B. ovatus* genes in the KEGG category “Membrane transport” that lost their significant fitness index scores with arabinoxylan treatment (these transporters are not homologous to those identified in *B. cellulosilyticus*). A number of human gut *Bacteroides*, including *B. ovatus*, are known to be highly resistant to antimicrobial peptides (24). Import of gut mucosal-derived antimicrobial peptides is one strategy gut symbionts use for avoiding destruction of their cell membranes (25). Some *Bacteroides* species are able to turn to gut mucosal glycans as alternative sources of nutrients when polysaccharides are not well represented in the diet. Arabinoxylan supplementation may mitigate this need, and thus, the observed diminished requirement for antimicrobial peptide transporters could reflect alterations in interactions with the mucosa.

A total of 27 genes were identified in the *B. cellulosilyticus* genome that functioned as significant fitness determinants when mice received the HF/HS diet plus arabinoxylan but not when animals received the HF/HS diet alone (table S11A). These include (i) all genes in an operon (*BcellWH2_00893-895*) that includes a sulfate transferase (EC 2.7.7.4), which is consistent with the observed increase in deconjugated bile acids documented by UPLC-MS of cecal contents (fig. S14C), and (ii) several genes that highlight how increases in arabinoxylan availability enhance the importance of ammonium utilization for synthesis of amino acids and proteins in this community and diet context [an ammonium transporter (*BcellWH2_05255*), plus glutamine, and glutamate synthetases (*BcellWH2_5244* and *BcellWH2_05271*, respectively)].

Even though *B. ovatus* did not manifest a significant change in its relative abundance when mice received arabinoxylan supplemented water, multi-taxon INSeq revealed 41 genes that were

not fitness determinants when mice consumed the HF/HS diet alone but “acquired” significant *z* scores when arabinoxylan was introduced (table S11B). These include seven closely linked glycosyltransferase genes (*Bovatus_03504-II*), suggesting that this organism changes its glycan utilization strategies when it encounters arabinoxylan in the gut environment.

Prospectus

We cannot distinguish a direct effect of a given diet or diet oscillation on a given community member from a primary effect of that diet or diet perturbation on one or more other community members that interact with the member/strain exhibiting changes in its abundance. We could have limited ourselves to mono-colonizations in order to establish direct effects of diet on these features, but we would have lost our ability to describe responses to diet changes and ascertain the niches of these organisms in the more “natural” context of a microbial community.

In our study, multi-taxon INSeq is used to provide an operational description of an organism’s niche by determining which sets of genes allow a bacterial strain to coexist with other strains or species under a defined set of habitat conditions (for example, gnotobiotic mice representing a given genetic background, colonized with a given set of sequenced organisms, and fed a given set of diets). In principle, this approach can be applied to gut and nongut habitats in gnotobiotic mice representing different genetic backgrounds, harboring different microbial consortia and manipulated in various ways to obtain a more comprehensive picture of how host genotype influences the niches available. It also offers a way to address a range of questions: from how to functionally discriminate strains when exploring the microbial genetic foundations of opportunism, stochasticity in community assembly, or stability and resilience after perturbations, to the selection of probiotic candidates for bioremediation of perturbed/dysbiotic microbial communities, or identifying compounds that affect the functional configurations of a targeted microbiota, or characterizing of the nutritional effects/value of diets and their ingredients.

REFERENCES AND NOTES

- K. E. Nelson et al., A catalog of reference genomes from the human microbiome. *Science* **328**, 994–999 (2010). doi: [10.1126/science.1183605](https://doi.org/10.1126/science.1183605); pmid: 20489017
- J. Qin et al., MetaHIT Consortium, A human gut microbial gene catalogue established by metagenomic sequencing. *Nature* **464**, 59–65 (2010). doi: [10.1038/nature08821](https://doi.org/10.1038/nature08821); pmid: 20203603
- J. J. Faith et al., The long-term stability of the human gut microbiota. *Science* **341**, 1237439 (2013). doi: [10.1126/science.1237439](https://doi.org/10.1126/science.1237439); pmid: 23828941
- J. Xu et al., A genomic view of the human-*Bacteroides thetaiotaomicron* symbiosis. *Science* **299**, 2074–2076 (2003). doi: [10.1126/science.1080029](https://doi.org/10.1126/science.1080029); pmid: 12663928
- J. L. Sonnenburg et al., Glycan foraging in vivo by an intestine-adapted bacterial symbiont. *Science* **307**, 1955–1959 (2005). doi: [10.1126/science.1109051](https://doi.org/10.1126/science.1109051); pmid: 15790854
- E. C. Martens et al., Recognition and degradation of plant cell wall polysaccharides by two human gut symbionts. *PLOS Biol.* **9**, e1001221 (2011). doi: [10.1371/journal.pbio.1001221](https://doi.org/10.1371/journal.pbio.1001221); pmid: 22205877
- N. P. McNulty et al., Effects of diet on resource utilization by a model human gut microbiota containing *Bacteroides cellulosilyticus* WH2, a symbiont with an extensive glycomiome. *PLOS Biol.* **11**, e1001637 (2013). doi: [10.1371/journal.pbio.1001637](https://doi.org/10.1371/journal.pbio.1001637); pmid: 23976882
- J. J. Faith, N. P. McNulty, F. E. Rey, J. I. Gordon, Predicting a human gut microbiota’s response to diet in gnotobiotic mice. *Science* **333**, 101–104 (2011).pmid: 21596954
- A. L. Goodman et al., Identifying genetic determinants needed to establish a human gut symbiont in its habitat. *Cell Host Microbe* **6**, 279–289 (2009). doi: [10.1016/j.chom.2009.08.003](https://doi.org/10.1016/j.chom.2009.08.003); pmid: 19748469
- A. L. Goodman, M. Wu, J. I. Gordon, Identifying microbial fitness determinants by insertion sequencing using genome-wide transposon mutant libraries. *Nat. Protoc.* **6**, 1969–1980 (2011). doi: [10.1038/nprot.2011.417](https://doi.org/10.1038/nprot.2011.417); pmid: 22094732
- C. R. Rao, in *Multivariate Statistics and Matrices in Statistics*, E.-M. Titt, T. Kollo, H. Niemi, Eds. (VSP, Utrecht, Netherlands, 1995), pp. 143–161.
- P. H. Degnan, N. A. Barry, K. C. Mok, M. E. Taga, A. L. Goodman, Human gut microbes use multiple transporters to distinguish vitamin B₁₂ analogs and compete in the gut. *Cell Host Microbe* **15**, 47–57 (2014). doi: [10.1016/j.chom.2013.12.007](https://doi.org/10.1016/j.chom.2013.12.007); pmid: 24439897
- C. S. Holling, Resilience and stability of ecological systems. *Annu. Rev. Ecol. Syst.* **4**, 1–23 (1973). doi: [10.1146/annurev.es.04.110173.000245](https://doi.org/10.1146/annurev.es.04.110173.000245)
- D. A. Ravcheev, A. Godzik, A. L. Osterman, D. A. Rodionov, Polysaccharides utilization in human gut bacterium *Bacteroides thetaiotaomicron*: Comparative genomics reconstruction of metabolic and regulatory networks. *BMC Genomics* **14**, 873 (2013). doi: [10.1186/1471-2164-14-873](https://doi.org/10.1186/1471-2164-14-873); pmid: 24330590
- R. Overbeek et al., The subsystems approach to genome annotation and its use in the project to annotate 1000 genomes. *Nucleic Acids Res.* **33**, 5691–5702 (2005). doi: [10.1093/nar/gki866](https://doi.org/10.1093/nar/gki866); pmid: 16214803
- A. G. Lindenstraub et al., Transcriptome analysis of *Enterococcus faecalis* toward its adaptation to surviving in the mouse intestinal tract. *Arch. Microbiol.* **196**, 423–433 (2014). doi: [10.1007/s00203-014-0982-2](https://doi.org/10.1007/s00203-014-0982-2); pmid: 24700373
- A. R. Reeves, J. N. D’Elia, J. Frias, A. A. Salyers, A *Bacteroides thetaiotaomicron* outer membrane protein that is essential for utilization of maltotriose and starch. *J. Bacteriol.* **178**, 823–830 (1996). pmid: 8550519
- A. R. Reeves, G. R. Wang, A. A. Salyers, Characterization of four outer membrane proteins that play a role in utilization of starch by *Bacteroides thetaiotaomicron*. *J. Bacteriol.* **179**, 643–649 (1997).pmid: 9006015
- J. A. Shipman, J. E. Berleman, A. A. Salyers, Characterization of four outer membrane proteins involved in binding starch to the cell surface of *Bacteroides thetaiotaomicron*. *J. Bacteriol.* **182**, 5365–5372 (2000). doi: [10.1128/JB.182.19.5365-5372.2000](https://doi.org/10.1128/JB.182.19.5365-5372.2000); pmid: 10986238
- E. C. Martens, H. C. Chiang, J. I. Gordon, Mucosal glycan foraging enhances fitness and transmission of a saccharolytic human gut bacterial symbiont. *Cell Host Microbe* **4**, 447–457 (2008). doi: [10.1016/j.chom.2008.09.007](https://doi.org/10.1016/j.chom.2008.09.007); pmid: 18996345
- P. C. Kashyap et al., Genetically dictated change in host mucus carbohydrate landscape exerts a diet-dependent effect on the gut microbiota. *Proc. Natl. Acad. Sci. U.S.A.* **110**, 17059–17064 (2013). doi: [10.1073/pnas.1306070110](https://doi.org/10.1073/pnas.1306070110); pmid: 24062455
- D. Dodd, R. I. Mackie, I. K. Cann, Xylan degradation, a metabolic property shared by rumen and human colonic *Bacteroidetes*. *Mol. Microbiol.* **79**, 292–304 (2011). doi: [10.1111/j.1365-2958.2010.07473.x](https://doi.org/10.1111/j.1365-2958.2010.07473.x); pmid: 21219452
- A. Rogowski et al., Glycan complexity dictates microbial resource allocation in the large intestine. *Nat. Commun.* **6**, 7481 (2015).pmid: 26112186
- T. W. Cullen et al., Antimicrobial peptide resistance mediates resilience of prominent gut commensals during inflammation. *Science* **347**, 170–175 (2015). doi: [10.1126/science.1260580](https://doi.org/10.1126/science.1260580); pmid: 25574022
- C. L. Shelton, F. K. Raffel, W. L. Beatty, S. M. Johnson, K. M. Mason, Sap transporter mediated import and subsequent degradation of antimicrobial peptides in *Haemophilus*. *PLOS Pathog.* **7**, e1002360 (2011). doi: [10.1371/journal.ppat.1002360](https://doi.org/10.1371/journal.ppat.1002360); pmid: 22072973

26. M. Krzywinski *et al.*, Circos: An information aesthetic for comparative genomics. *Genome Res.* **19**, 1639–1645 (2009). doi: [10.1101/gr.092759.109](https://doi.org/10.1101/gr.092759.109); pmid: [19541911](https://pubmed.ncbi.nlm.nih.gov/19541911/)
27. A. E. Darling, B. Mau, N. T. Perna, progressiveMauve: Multiple genome alignment with gene gain, loss and rearrangement. *PLOS ONE* **5**, e11147 (2010). doi: [10.1371/journal.pone.0011147](https://doi.org/10.1371/journal.pone.0011147); pmid: [20593022](https://pubmed.ncbi.nlm.nih.gov/20593022/)

ACKNOWLEDGMENTS

We thank D. O'Donnell and M. Karlsson for their assistance with gnotobiotic mouse husbandry; X. Zhou and A. Bell for their work on PacBio sequencing; and A. Reyes, M. Charbonneau, P. Ahern, and A. Hsiao for many helpful suggestions. This work was supported in part by grants from the NIH (DK30292, DK70977, DK52574, and GM108527), the Crohn's and Colitis Foundation of America, the European Union's Seventh Framework Program (FP/2007/2013)/

European Research Council (ERC) Grant Agreement 322820 (to B.H.), the Monsanto Company (for PacBio and Illumina sequencing and finishing the *B. thetaiotaomicron* 7330, *B. ovatus* ATCC8483, and *B. cellulosilyticus* WH2 genomes), and the Russian Science Foundation (to D.A.R. and M.S.K.) INSeq, COPRO-seq, and microbial RNA-seq data sets have been deposited in the European Nucleotide Archive (ENA) under accession no. PRJEB9434. The finished and annotated genome sequences of *B. thetaiotaomicron* 7330, *B. ovatus* ATCC 8483, and *B. cellulosilyticus* WH2 have been deposited in the National Center for Biotechnology Information under accession no. PRJNA289334. J.I.G. is cofounder of Matatu, a company characterizing the role of diet-by-microbiota interactions in animal health. N.P.M. is currently an employee of Matatu. A.L.O. is an Adjunct Vice President for Research for Buffalo BioLabs. A U.S. patent application (PCT/US2014/045141) has been filed by

Washington University related to methods for identifying dietary supplements, such as arabinoxylans, that can be used to deliberately manipulate the representation of targeted members of the human gut microbiota.

SUPPLEMENTARY MATERIALS

www.sciencemag.org/content/350/6256/aac5992/suppl/DC1
Materials and Methods
Supplementary Text
Figs. S1 to S17
References (28–44)
Tables S1 to S14

18 May 2015; accepted 21 August 2015
[10.1126/science.aac5992](https://doi.org/10.1126/science.aac5992)

RESEARCH ARTICLE

STRUCTURAL BIOLOGY

Architecture of the fungal nuclear pore inner ring complex

Tobias Stuwe,^{1*} Christopher J. Bley,^{1*} Karsten Thierbach,^{1*} Stefan Petrovic,^{1*} Sandra Schilbach,^{1†} Daniel J. Mayo,¹ Thibaud Perriches,¹ Emily J. Rundlet,¹ Young E. Jeon,¹ Leslie N. Collins,¹ Ferdinand M. Huber,¹ Daniel H. Lin,¹ Marcin Paduch,² Akiko Koide,² Vincent Lu,² Jessica Fischer,³ Ed Hurt,³ Shohei Koide,² Anthony A. Kossiakoff,² André Hoelz^{1‡}

The nuclear pore complex (NPC) constitutes the sole gateway for bidirectional nucleocytoplasmic transport. We present the reconstitution and interdisciplinary analyses of the ~425-kilodalton inner ring complex (IRC), which forms the central transport channel and diffusion barrier of the NPC, revealing its interaction network and equimolar stoichiometry. The Nsp1•Nup49•Nup57 channel nucleoporin heterotrimer (CNT) attaches to the IRC solely through the adaptor nucleoporin Nic96. The CNT•Nic96 structure reveals that Nic96 functions as an assembly sensor that recognizes the three-dimensional architecture of the CNT, thereby mediating the incorporation of a defined CNT state into the NPC. We propose that the IRC adopts a relatively rigid scaffold that recruits the CNT to primarily form the diffusion barrier of the NPC, rather than enabling channel dilation.

One of the hallmarks of eukaryotic evolution is the enclosure of genetic information in the nucleus. The spatial segregation of replication and transcription in the nucleus from translation in the cytoplasm imposes the requirement of transporting thousands of macromolecules between these two compartments. Nuclear pore complexes (NPCs) are massive transport channels that allow bidirectional macromolecular exchange across the nuclear envelope (NE) and thus function as key regulators of the flow of genetic information from DNA to RNA to protein (1).

NPCs are formed by multiple copies of ~34 distinct proteins, termed nucleoporins (nups) (1). The docking of the yeast coat nup complex (CNC) crystal structure into a cryo-electron tomographic (ET) reconstruction of the intact human NPC revealed its organization into two 16-membered CNC rings on the nuclear and cytoplasmic faces of ~100-nm NE pores (Fig. 1A) (2, 3). This arrangement established that the doughnut-shaped inner ring is composed of adaptor and channel nups (3).

Anchoring of the inner ring in the NE pore is mediated by the membrane recruitment complex, composed of adaptor nups Nup53 and Nup170, and transmembrane nup Ndc1 (1, 4–6). Recently, Nup53 was shown to harbor distinct binding sites

for Nic96, Nup170, and Nup192, allowing the Nup53•Nup170 heterodimer to interact with either Nic96•Nup192 or Nic96•Nup188 (7, 8).

The inner ring harbors the central transport channel and diffusion barrier of the NPC, preventing macromolecules larger than ~40 kD from freely diffusing across the NE (1, 9). The channel nups Nsp1, Nup49, and Nup57 constitute part of the central transport channel and form the diffusion barrier with their disordered phenylalanine-glycine (FG) repeats (1, 9–11). Transport factors ferry cargo across the NE by binding to FG repeats in the central transport channel (1, 9). Furthermore, the central transport channel seems to be permanently occupied by transport factors even after biochemical purification of NPCs (10, 12). In addition to their N-terminal FG repeats, the three channel nups are predicted to possess C-terminal coiled-coil regions (13, 14). The knockout of any of the three channel nups is lethal in *Saccharomyces cerevisiae*, whereas the deletion of any two N-terminal FG-repeat regions can be tolerated but reduces transport rates, suggesting an essential function of the coiled-coil regions (13, 15–19).

Arguably, the most important questions about the inner ring architecture pertain to the recruitment and positioning of the channel nups, because of their essential function in forming the diffusion barrier and providing binding sites for transport factors. Native purifications from *S. cerevisiae* and mammalian cells showed that the channel nups copurified with Nic96, suggesting the evolutionary conservation of a heterotetrameric Nsp1•Nup49•Nup57•Nic96 complex (13, 20, 21). Subsequent biochemical reconstitution attempts yielded channel nup complexes with inconsistent stoichiometries that resisted structural analysis (22–24). Reconstitutions employing channel nup

fragments revealed dynamic interactions and generated a series of crystal structures with various homomeric and heteromeric assembly states (22, 25, 26). Biochemical analysis of these structures led to heavily contested models that have resisted physiological validation, including the proposal that the reversible karyopherin-mediated transition between homo- and hetero-oligomers facilitates the constriction and dilation of the central transport channel (25–28).

Despite more than half a century of research, our understanding of the inner ring architecture remains rudimentary. The prevalent assumption is that the inner ring of the NPC is composed of multiple copies of a single NPC subcomplex, but such a complex has remained elusive. Here, we present an in-depth characterization of the NPC's inner ring. Starting with the reconstitution of a ~425-kD heterohexameric inner ring complex (IRC), we demonstrate its scaffolding function by showing that it interacts with additional peripheral nups. In dissecting the underlying protein interaction network of the IRC, we determined an equimolar stoichiometry for its six components and identified Nic96 as the sole NPC attachment site for the channel nup heterotrimer (CNT). Nic96 is essential for CNT recruitment and, through its interaction with Nup192, for proper CNT positioning within the inner ring scaffold *in vivo*. Structural and functional analyses of the intact CNT reveal a defined coiled-coil domain architecture that is specifically recognized by Nic96. Our results differ markedly from previous characterizations of channel nup fragments and an associated model for a flexible transport channel that is capable of constriction and dilation of up to ~400 Å (25–28). We propose a model for the inner ring architecture in which 16 copies of the IRC form a relatively rigid scaffold. In the proposed arrangement, the central transport channel would be filled with the channel nup FG repeats to establish the diffusion barrier of the NPC and to provide binding sites for cargo•transport factor complexes.

Reconstitution and biochemical dissection of the IRC and binding of peripheral nups

To reconstitute and uncover the architectural principles of a putative IRC, we developed expression and purification protocols for the channel, adaptor, and cytoplasmic filament nups from *Chaetomium thermophilum* on the milligram scale. All purified nups lacked FG-repeat regions to facilitate soluble protein expression (Fig. 1A). We refer to all nups in the remainder of the text according to the *C. thermophilum* nomenclature and indicate nups from other species with a prefix.

Using recombinant purified nups, we reconstituted a monodisperse heterohexameric IRC containing the adaptor nups Nup192, Nic96, and Nup145N and the Nsp1•Nup49•Nup57 CNT (Fig. 1, A and B, and fig. S1A). The ~425-kD measured molecular mass of the IRC is consistent with an equimolar stoichiometry (table S1). No higher-order oligomers formed at concentrations up to ~5 μM. Our reconstitution omitted Nup170 because

¹California Institute of Technology, Division of Chemistry and Chemical Engineering, 1200 East California Boulevard, Pasadena, CA 91125, USA. ²Department of Biochemistry and Molecular Biology, The University of Chicago, Chicago, IL 60637, USA. ³Biochemistry Center of Heidelberg University, 69120 Heidelberg, Germany.

*These authors contributed equally to this work.

†Present address: Max-Planck-Institute of Biophysical Chemistry, Molecular Biology, Am Fassberg 11, 37077 Göttingen, Germany.

‡Corresponding author. E-mail: hoelz@caltech.edu

of its low solubility in standard buffer conditions. However, the interaction of Nup170 with a C-terminal region of Nup53, directly adjacent to the membrane-binding motif, established its proximity to the pore membrane (7).

Further analyses showed that the reconstituted IRC is a bona fide NPC scaffold complex, capable of binding the membrane recruiting Nup53 and the peripheral cytoplasmic filament complex (CFC), forming a stable hetero nonamer (Fig. 1C and fig. S1B). The measured masses for both complexes, ~100 kD lower than expected, in-

dicated their dynamic nature at the tested concentrations. The reconstitution and structure determination of a core IRC-CFC attachment complex composed of the CFC nups Nup82^{NTD} and Nup159^T and the autoproteolytic domain (APD) of the IRC component Nup145N revealed the molecular details of this intersubcomplex linkage (Fig. 1J; fig. S2, A and B; and table S2). A structural comparison with its *S. cerevisiae* homolog showed that the interactions of the core CFC•Nup145N^{APD} complex are conserved, despite low sequence conservation (29, 30). This

analysis supports the hypothesis that nup interactions in the NPC are evolutionarily conserved (fig. S3).

Because Nup145N acts as an adaptor that attaches the CFC, we probed its interaction with the other IRC components. Nup145N formed a stoichiometric complex with Nup192, elicited weak CNT association, and barely interacted with the Nic96 solenoid (SOL) (fig. S2, C to E). However, Nup145N was incapable of linking the CNT to Nup192, suggesting mutually exclusive interactions (fig. S2F).

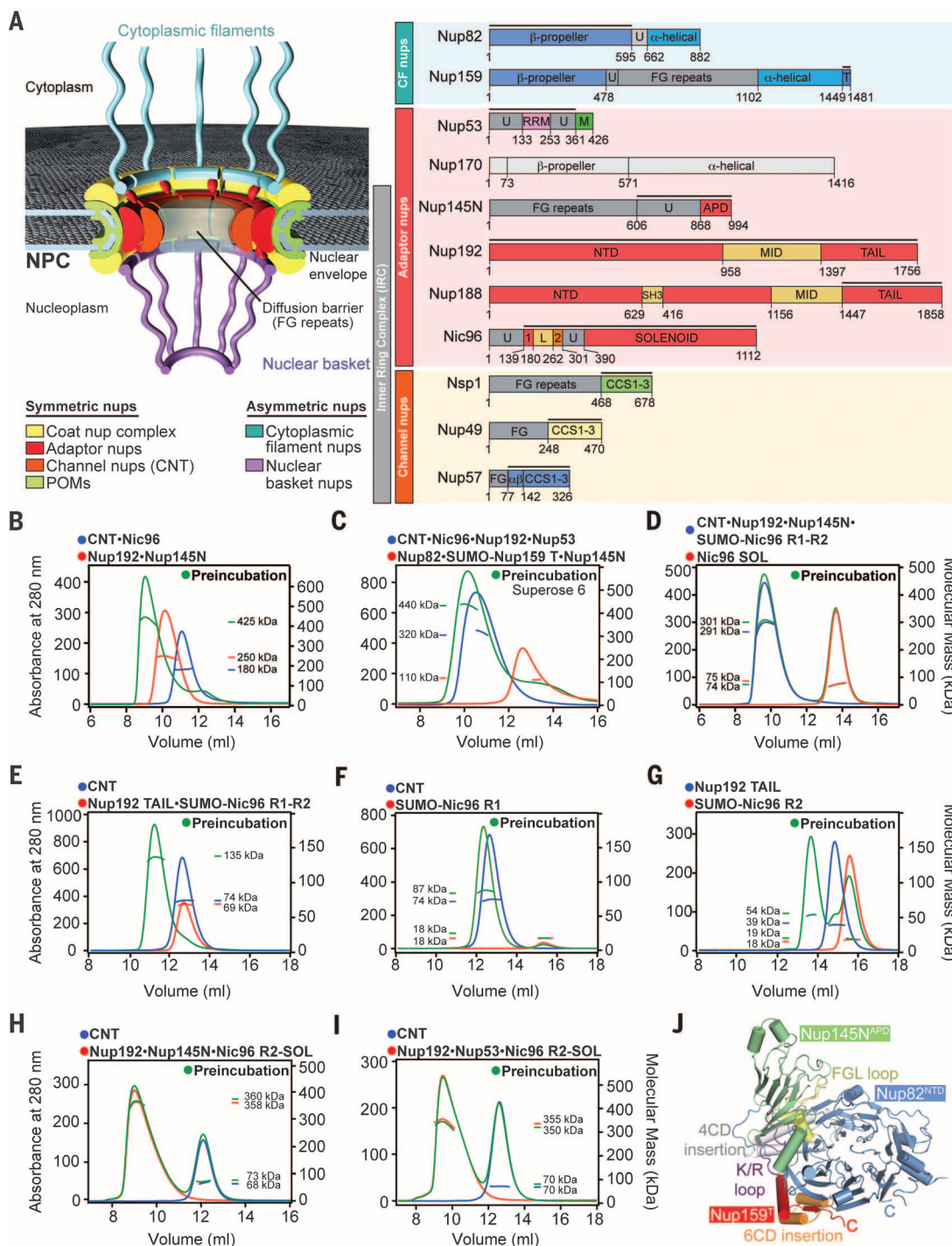


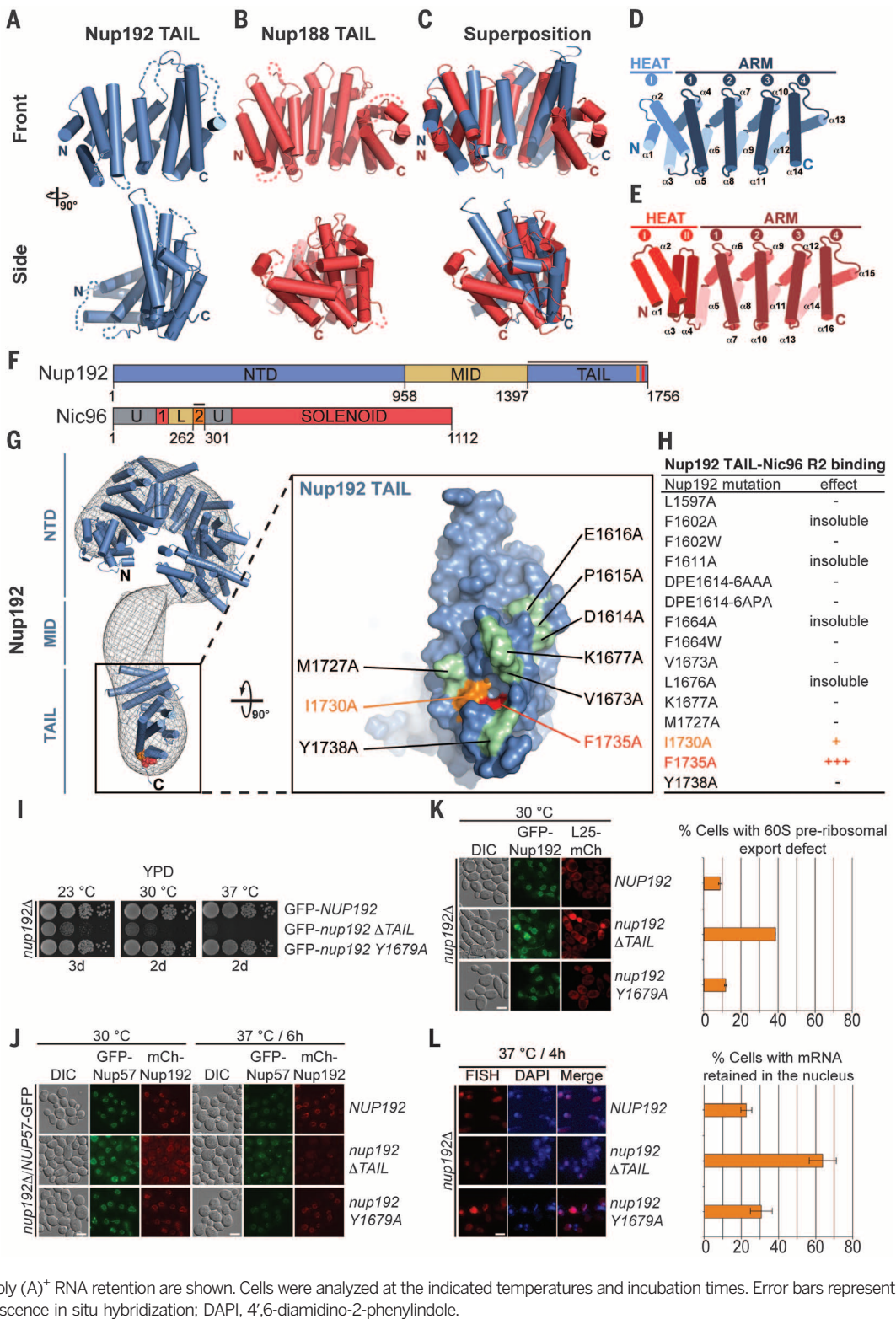
Fig. 1. Reconstitution and analysis of the IRC.

(A) Cross-sectional schematic representation of the NPC and domain structures of the *C. thermophilum* nucleoporins (nups). Black lines indicate regions used for reconstitution. U, unstructured; T, TAIL; NTD, N-terminal domain; MID, middle domain; SH3, Src-homology 3-like domain; L, linker domain; APD, autoproteolytic domain; RRM, RNA recognition motif; M, membrane-binding motif; FG repeats, phenylalanine-glycine repeats; CCS, coiled-coil segment; α/β, α/β insertion domain. (B to I) Pairwise biochemical interaction analyses of various reconstituted nup complexes. SEC-MALS profiles of nup or nup complexes are shown individually (red and blue) and after their preincubation (green). Measured molecular masses (in kilodaltons) are indicated for the peak fractions. (J) Structure of the Nup82^{NTD}•Nup159^T•Nup145N^{APD} cytoplasmic filament nup complex (CFC) is shown in a cartoon representation. Nup145N^{APD} (green), Nup159^T (red), and Nup82^{NTD} (blue); the Nup82^{NTD} helical 4CD (gray) and 6CD (orange) insertions and FGL loop (yellow); and the conserved Nup145N^{APD} K/R loop (purple) are illustrated.

The IRC reconstitution enabled us to identify how the CNT is incorporated into the IRC by defining a minimal CNT attachment complex. We found that Nup145N, Nic96^{SOL}, and the N-terminal and middle domains of Nup192 were dispensable for CNT attachment, because a minimal stoichiometric Nup192^{TAIL}•Nic96^{R1-R2}•CNT attachment complex could be reconstituted (Fig. 1, D and E, and fig. S1, C and D). Nic96^{R1-R2} is an adaptor linking the CNT with Nup192^{TAIL} (Fig. 1, F and G, and figs. S1, E and F, and S4, A and B). Consistently, no interaction between Nup192^{TAIL} and

the C1 NT was observed (fig. S4C). Notably, an IRC lacking Nic96^{R1} failed to incorporate the CNT, demonstrating that Nic96^{R1} is the sole IRC attachment site for the CNT (Fig. 1H and fig. S1G). We tested whether Nup53 could rescue the deletion of Nic96^{R1} by providing an additional CNT binding

Fig. 2. Structural and functional analyses of the TAIL domains of Nup192 and Nup188. Cartoon representations of (A) Nup192^{TAIL} (blue), (B) Nup188^{TAIL} (red), and (C) a superposition of the two structures are shown in two different orientations. (D and E) Schematic representation of Nup192^{TAIL} and Nup188^{TAIL} structures. Positions of HEAT and ARM repeats are indicated. (F) Domain structures of Nup192 and Nic96 are shown; black bars indicate fragments used for interaction studies in (H). (G) Docking of Nup192^{TAIL} and the previously determined Nup192^{NTD} crystal structure into the yeast Nup192 EM envelope (8, 32). The inset illustrates the position of Nup192^{TAIL} and is expanded on the right, rotated by 90°. Surface representation of Nup192^{TAIL} with the location of the analyzed mutations and their effect on Nic96^{R2} binding indicated; no effect (green), decreased binding (orange), abolished binding (red). (H) Summary of tested Nup192^{TAIL} mutants and their effect on SUMO-Nic96^{R2} binding; (–) no effect, (+) decreased binding, (+++) abolished binding. (I) Growth analysis of *S. cerevisiae* strains carrying the indicated GFP-NUP192 variants. Serial dilutions of the respective cells were spotted onto YPD plates and grown for 2 to 3 days. (J) Subcellular localization of mCherry-Nup192 variants (red) and Nup57-GFP (green) in a *nup192Δ*/NUP57-GFP strain. DIC, differential interference contrast. (K) Subcellular localization of the 60S ribosomal export reporter Rpl25-mCherry (red) and GFP-tagged Nup192 variants (green) in a *nup192Δ* strain. Representative images and quantification of nuclear Rpl25-mCherry retention are shown on the right. (L) mRNA export assay in a *nup192Δ* strain carrying GFP-NUP192 variants. Representative images and quantification of nuclear poly (A)⁺ RNA retention are shown. Cells were analyzed at the indicated temperatures and incubation times. Error bars represent the SD. Scale bars: 5 μm. FISH, fluorescence in situ hybridization; DAPI, 4',6-diamidino-2-phenylindole.



site. However, the CNT did not incorporate into the IRC in the presence of Nup53 (Fig. 1I and fig. S1H).

These data established an equimolar stoichiometry of the six different IRC components and demonstrated that the CNT is solely attached

to the adaptor nups through its interaction with Nic96^{R1}.

The Nic96-Nup192 interaction positions the CNT in the central transport channel

Consistent with previous findings that Nup192 and Nup188 form mutually exclusive complexes (7), we were able to reconstitute an architecturally equivalent Nup188^{TAIL}•Nic96^{R1-R2}•CNT heteropentamer (fig. S5, A and B). However, salt stability and competition experiments showed that Nup192^{TAIL} interacts more tightly with Nic96^{R2} than Nup188^{TAIL} does (figs. S5, C and D, and S6, A and B).

To gain insight into the molecular details of the Nic96^{R2} interaction with Nup192 and Nup188, we determined the crystal structures of the TAIL domains of Nup192 and Nup188 (table S2). Nup192^{TAIL} and Nup188^{TAIL} share a similar crescent-shaped architecture, composed of ARM and HEAT repeats with overall similar surface conservation and electrostatic properties. However, Nup188^{TAIL} contains an additional evolutionarily conserved C-terminal ARM repeat (Fig. 2, A to E, and figs. S7 to S11) (31). When docked into the electron microscopy (EM) reconstruction of *S. cerevisiae* Nup192, Nup192^{TAIL} was located at the bottom of the question mark-shaped map (Fig. 2G) (32). Based on the structural and biochemical results and previous findings that Nup192, but not Nup188, is essential for viability in yeast, we focused our further analyses on the IRC containing Nup192 (33, 34).

To identify the Nic96^{R2} interaction surface in Nup192^{TAIL}, we tested alanine mutants of 15 conserved surface residues and identified two adjacent residues, Phe¹⁷³⁵ and Ile¹⁷³⁰, that abolished binding and decreased the interaction with Nic96^{R2}, respectively (Fig. 2, F to H, and figs. S12 and S13). Both residues are located in a hydrophobic pocket at the bottom of the Nup192 molecule (Fig. 2G).

To evaluate the physiological relevance of the identified Nup192-Nic96 interaction for NPC function, we analyzed the identified Nup192 mutants in *S. cerevisiae*. Whereas the F1735A point mutant (Y1679A in yeast) displayed no notable defects in growth and ribosomal or mRNA export, the removal of the entire TAIL domain resulted in a substantial growth defect at all temperatures and substantial mRNA and ribosomal export defects at 30° and 37°C, respectively (Fig. 2, I, K, and L). Despite the severity of the Δ TAIL phenotypes, Nup57-GFP (green fluorescent protein) yielded strong NE staining (Fig. 2J), consistent with our biochemical analyses that Nup192^{TAIL} is expendable for CNT attachment.

These data established that the Nic96-Nup192 interaction is dispensable for CNT incorporation into the NPC but required for proper NPC function, suggesting that the Nic96-Nup192 interaction is required for correct CNT positioning and, in turn, for the proper placement of the FG-repeat meshwork.

Nic96 is the sole NPC attachment site for the CNT in vivo

To characterize the adaptor function of Nic96, we carried out a mutational analysis of the conserved R1 and R2 regions of Nic96, which interact with

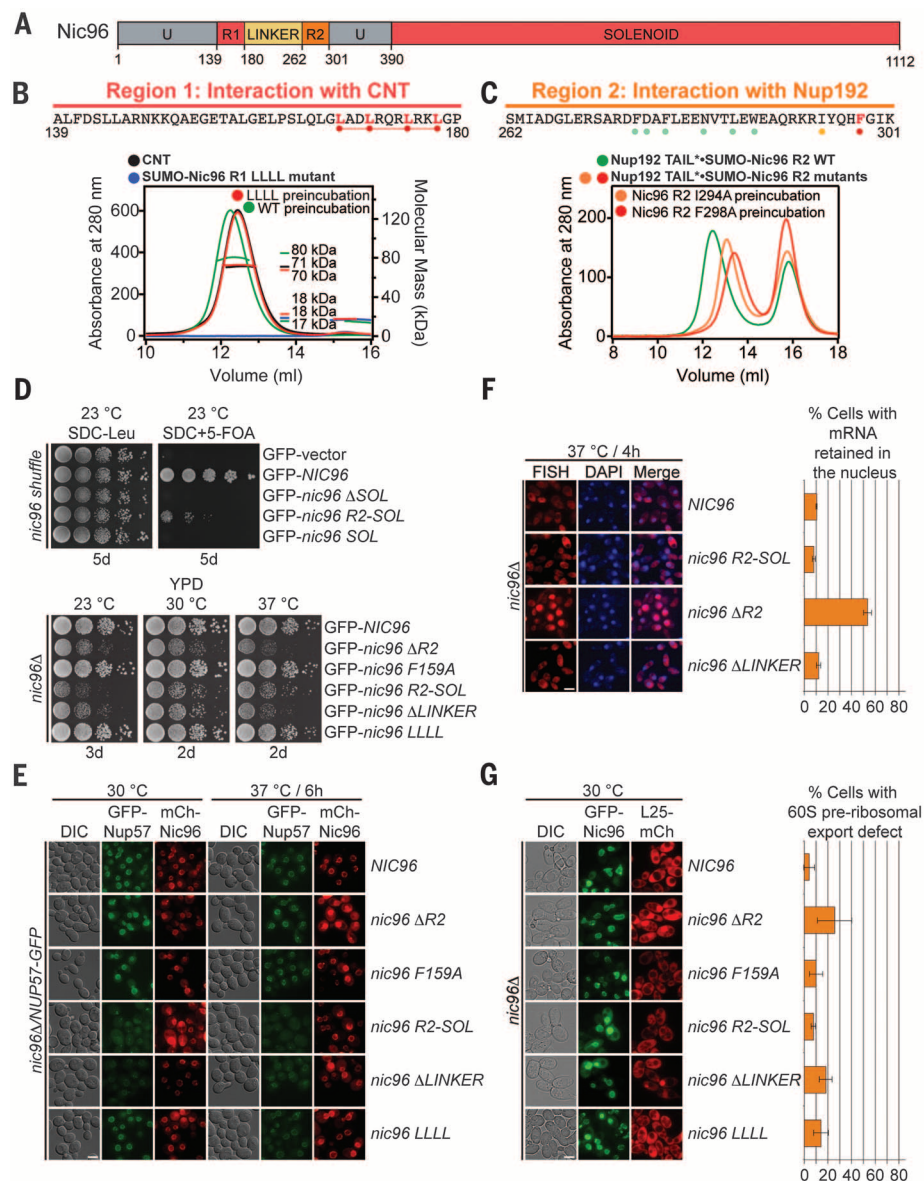


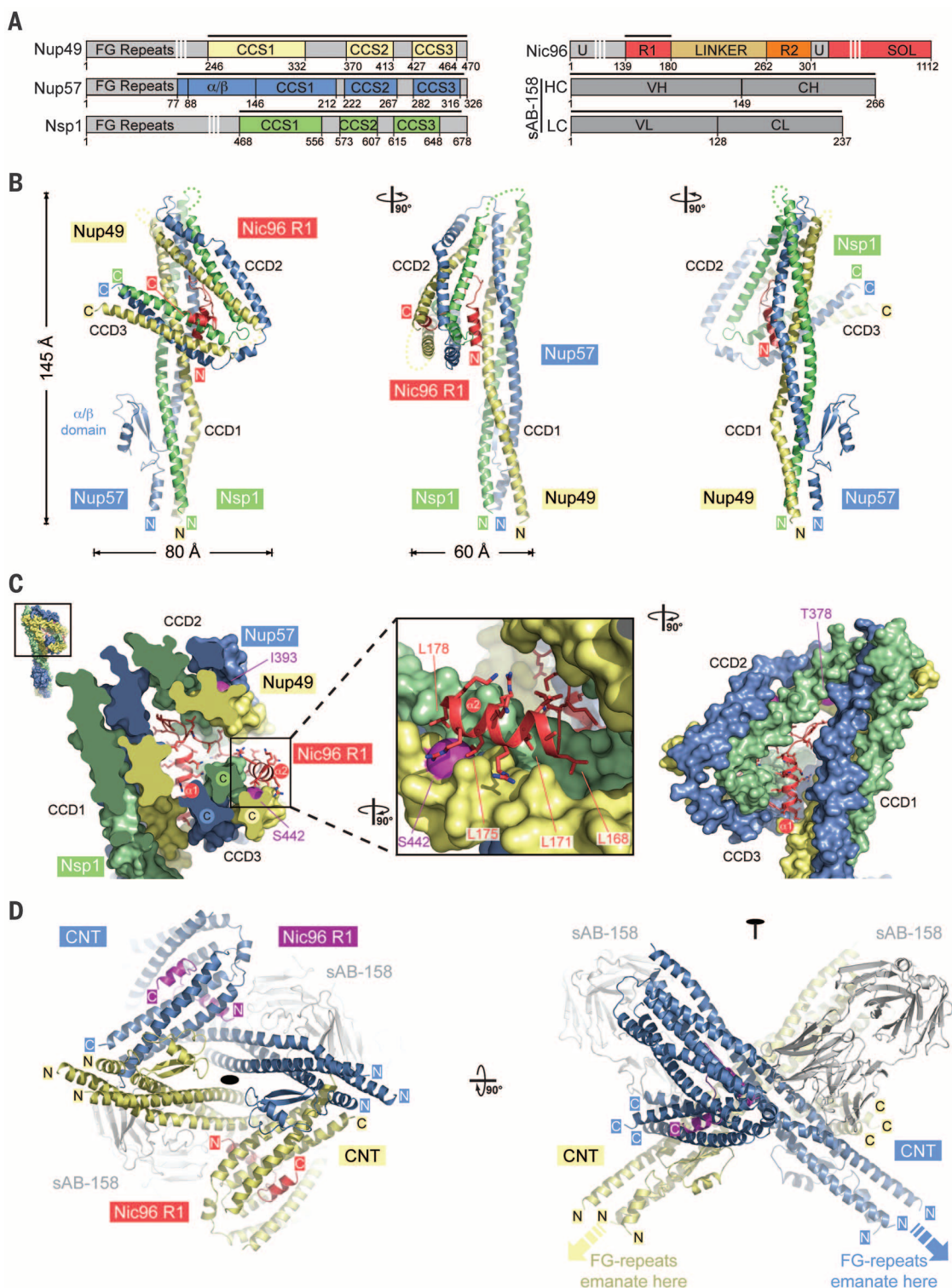
Fig. 3. Nic96 is an adaptor protein that attaches the CNT to Nup192. (A) Domain structure of Nic96 is shown. R1, region 1; R2, region 2. (B) The positions of the mutated leucine residues of the LLLL mutant are indicated below the primary Nic96^{R1} sequence. SEC-MALS profiles of CNT (black), Nic96^{R1} LLLL mutant (blue), and after preincubation of the CNT with wild-type Nic96^{R1} (green) or Nic96^{R1} LLLL (red). Measured molecular masses are indicated for the peak fractions. (C) The positions of the mutated residues are indicated below the primary Nic96^{R2} sequence and colored according to their effect on Nup192^{TAIL} binding; no effect (green), mild effect (orange), abolished binding (red). SEC profiles of Nup192^{TAIL} preincubated with wild-type Nic96^{R2} (green), Nic96^{R2} I294A (orange), and Nic96^{R2} F298A (red). (D) Growth analysis of *S. cerevisiae* strains carrying the indicated GFP-NIC96 variants. Serial dilutions of the respective cells were spotted onto indicated plates and grown for 2 to 5 days at the specified temperatures. FOA, 5-fluoroorotic acid. (E) Subcellular localization of mCherry-Nic96 variants (red) and Nup57-GFP (green) in a *nic96Δ/NUP57-GFP* strain. (F) mRNA export assay in a *nic96Δ/NUP57-GFP* strain carrying GFP-NIC96 variants. Representative images and quantification of nuclear poly(A)⁺ RNA retention are shown. (G) Subcellular localization of the 60S ribosomal export reporter Rpl25-mCherry (red) and GFP-tagged Nup49 variants (green) in a *nic96Δ* strain. Quantification of nuclear Rpl25-mCherry retention is shown on the right. Cells were analyzed at the indicated temperatures and incubation times. Error bars represent the SD. Scale bars: 5 μ m.

the CNT and Nup192, respectively (Fig. 3, A to C, and fig. S13). Because the Nic96^{R1}-CNT interaction is stable at increased salt concentrations but sensitive to C-terminal truncations, we focused our analysis on conserved hydrophobic residues

in the C-terminal region of Nic96^{R1} (figs. S14 and S15A). Indeed, mutating four leucines located at the C-terminal end of R1 to alanines (LLLL mutant) abolished the Nic96^{R1}-CNT interaction (Fig. 3B and figs. S13 and S15B).

Similarly, because the Nic96^{R2}-Nup192^{TAIL} interaction is also salt stable and was disrupted by mutating a hydrophobic pocket on Nup192^{TAIL}, we focused our mutational analysis on evolutionarily conserved hydrophobic residues of Nic96^{R2}

Fig. 4. Crystal structure of the intact Nsp1-Nup49-Nup57 CNT bound to Nic96^{R1} and sAB-158. (A) Domain structures of the *C. thermophilum* channel nups Nsp1, Nup49, and Nup57; the adaptor nup Nic96; and sAB-158. Black lines indicate the construct boundaries of the crystallized CNT•Nic96^{R1}•sAB-158 complex. The constructs of the three channel nups comprise all regions with predicted secondary-structure elements and only lack their unstructured N-terminal FG-repeat regions. VH, heavy-chain variable region; CH, heavy-chain constant region; VL, light-chain variable region; CL, light-chain constant region. (B) Cartoon representation of the Nic96^{R1}•CNT crystal structure viewed from three sides. For clarity, sAB-158 has been omitted. (C) Details of the Nic96^{R1}-CNT interaction, illustrating the three channel nups and Nic96^{R1} in surface and cartoon representation, respectively. The inset marks the region enlarged and 90° rotated in the middle panel. A further 90° rotated view is shown on the right. Nic96^{R1} (red) and Nup49 (magenta) residues that abolish CNT•Nic96^{R1} complex formation upon mutation (Figs. 3 and 5) are indicated. (D) Structure of the CNT•Nic96^{R1}•sAB-158 dimer shown in cartoon representation. The two copies of the CNT, Nic96^{R1}, and sAB-158 are shown in blue/yellow, magenta/red, and gray, respectively. A 90° rotated view is shown on the right. The two CNT•Nic96^{R1}•sAB-158 complexes in the asymmetric unit are related by twofold rotational symmetry (black oval). Notably, the N termini of all channel nups in the dimer point in the same direction, which would permit the FG repeats to project toward the central transport channel of the NPC.



(figs. S5C and S13). We identified two mutations, I294A and F298A, which reduced and abolished Nup192^{TAIL} binding, respectively (Fig. 3C and fig. S16).

Next, we carried out functional analyses of the identified Nic96 mutants in *S. cerevisiae* (fig. S17). Nic96 fragments lacking either Nic96^{SOL} (Δ SOL) or Nic96^{R1-R2} (SOL) were unable to rescue the previously identified lethal *nic96* Δ phenotype and were not analyzed further (Fig. 3D) (35). All remaining mutants were viable and yielded NE

staining, consistent with NPC incorporation (Fig. 3E). A Nic96 mutant lacking the Nup192-interacting region R2 (Δ R2) displayed severe growth and mRNA export defects yet failed to affect Nup57-GFP localization (Fig. 3, D to F). Nic96 mutants lacking the CNT-interacting region R1 (R2-SOL) and R1-R2 linker (Δ LINKER) also had severe growth defects accompanied by a marked decrease and no detectable NE staining for Nup57-GFP, respectively (Fig. 3, D to F). Additionally, Δ R2 and Δ LINKER displayed a mild ribosome

export defect (Fig. 3G). The milder LLLL and F159A mutants failed to yield any notable phenotypes (Fig. 3, D to G).

Together, these experiments demonstrated that the channel nup Nup57 is anchored to the NPC solely through its interaction with Nic96 in vivo, in agreement with our biochemical studies.

Channel nup fragments do not capture the solution behavior of the intact CNT

A secondary-structure analysis revealed that the channel nups Nsp1, Nup49, and Nup57 possessed evolutionarily conserved domain architectures with an N-terminal FG-repeat region of varying length, followed by three predicted α -helical coiled-coil segments, CCS1–3 (fig. S18A). Nup57 contained an additional evolutionarily conserved α/β region, which preceded the three coiled-coil regions.

Lacking a fully assembled CNT structure, we attempted to obtain structural insight from short channel nup fragments. Using fragments of Nic96 and the three channel nups from three different species, we carried out a systematic interaction and crystallization analysis, which led to the structure determination of multiple channel nup fragments (figs. S19 to S21). This approach yielded six different crystal structures of homomeric and heteromeric channel nup assemblies with different stoichiometries (figs. S18B, S22, and S23). Two structures revealed novel assembly states (figs. S18B and S24). The remaining four were almost identical to previously determined *Rattus norvegicus* structures (22, 25, 26). These assembly states constituted the basis for the proposal of a dilating transport channel, whose diameter is modulated by karyopherin-mediated transitioning between these homomeric and heteromeric assembly states (25–28). Despite the very high degree of sequence conservation between human and rat fragments with identical domain boundaries, we observed different assembly states that behaved inconsistently when mutated or further truncated (figs. S25 and S26).

In contrast, only two states were detected for the intact CNT in solution, corresponding to monodisperse equimolar monomeric and dimeric species (fig. S18C). At concentrations up to ~30 mg/ml, the predominant species was the CNT monomer. Both the CNT monomer and dimer were capable of forming monodisperse heterotetrameric complexes with Nic96^{R1} in solution (fig. S18D).

To identify which of the three channel nups form a specific interaction with Nic96^{R1}, we carried out a glutathione S-transferase (GST)-pull-down interaction assay. We found that GST-Nic96^{R1} did not interact with separately purified Nsp1 or Nup49·Nup57 in isolation but formed a complex in the presence of both (fig. S18E).

These data show that the coiled-coil architecture of the intact CNT cannot be elucidated by a reductionist approach that involves channel nup coiled-coil fragments, because of their inconsistent behavior in solution and their inability to capture the correct stoichiometry of the intact CNT.

Crystal structure of CNT·Nic96^{R1}

Our biochemical and in vivo data established that the CNT architecture can only be elucidated

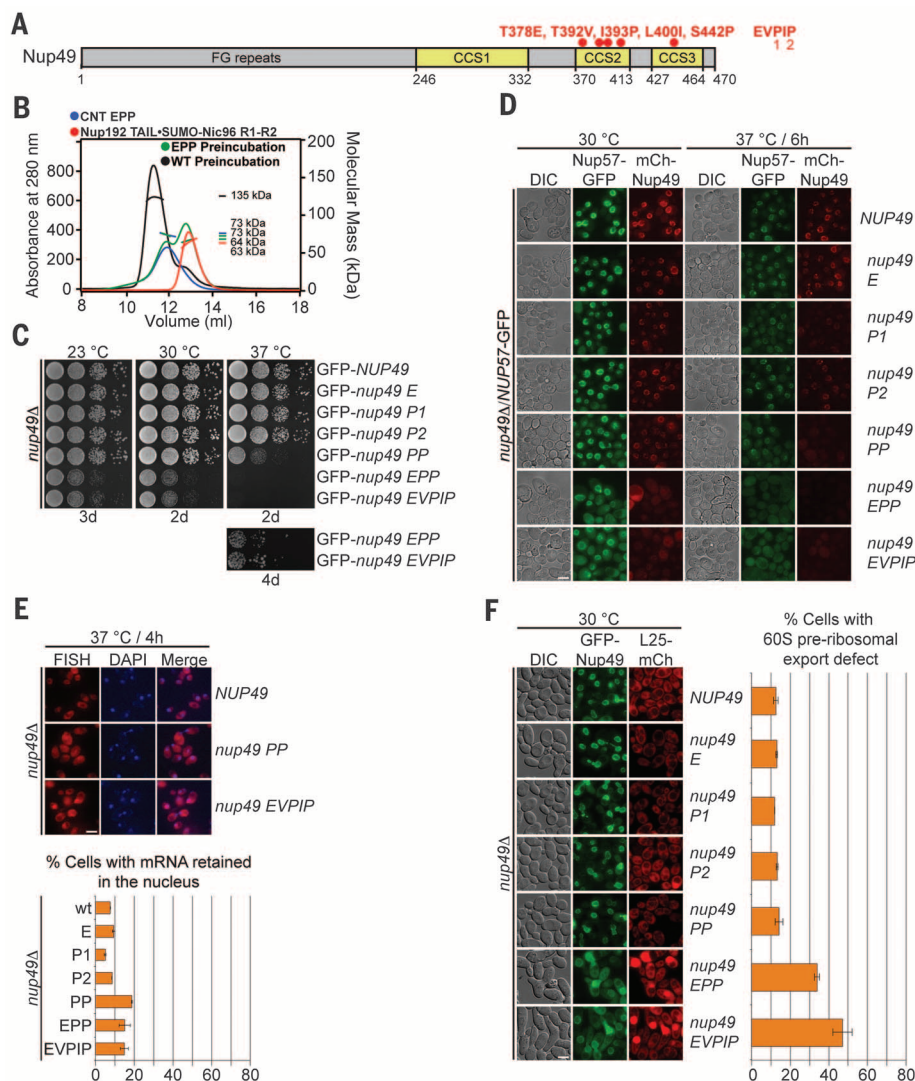


Fig. 5. The intact CNT is recruited to the NPC by its interaction with Nic96. (A) Domain structure of Nup49, indicating the corresponding EVPIP mutations (red) of the *S. cerevisiae* *nup49-313* allele (37). (B) SEC-MALS profiles of the CNT^{EPP} mutant (blue) and Nic96^{R1-R2}·Nup192^{TAIL} (red), and after their preincubation (green). As reference, wild-type CNT·Nic96^{R1-R2}·Nup192^{TAIL} is shown (black). Measured molecular masses (in kilodaltons) are indicated for the peak fractions. (C) Growth analysis of *S. cerevisiae* strains carrying the indicated GFP-NUP49 variants. Serial dilutions of the respective cells were spotted onto YPD plates and grown for 2 to 4 days at the specified temperatures. (D) Subcellular localization of mCherry-Nup49 variants (red) and Nup57-GFP (green) in a *nup49* Δ /NUP57-GFP strain. (E) mRNA export assay in a *nup49* Δ strain carrying GFP-NUP49 variants. Representative images and quantification of nuclear poly(A)⁺ RNA retention are shown. (F) Subcellular localization of the 60S ribosomal export reporter Rpl25-mCherry (red) and GFP-tagged Nup49 variants (green) in a *nup49* Δ strain. Quantification of nuclear Rpl25-mCherry retention is shown on the right. Cells were analyzed at the indicated temperatures and incubation times. Error bars represent the SD. Scale bars: 5 μ m.

by a structure of the intact CNT and that the physiologically relevant state is the CNT•Nic96^{RI} attachment complex. However, extensive crystallization attempts for the CNT•Nic96^{RI} yielded crystals that diffracted to ~10 Å resolution, at best. To improve the diffraction quality, we generated a series of conformation-specific, high-affinity monobodies (MBs) and synthetic antibody Fab fragments (sABs) by phage display selection methods as crystallization chaperones. Up to two different MBs or sABs could bind to the intact IRC and CNT•Nic96^{RI}, forming monodisperse stoichiometric complexes (figs. S27 and S28). These data established that access to the CNT was sterically unrestricted by its incorporation into the IRC, suggesting that the CNT protrudes from the IRC.

Crystals of CNT•Nic96^{RI}•sAB-158 diffracted to a 3.77 Å resolution, facilitating structure determination by single anomalous dispersion (SAD) (fig. S29 and table S4). The crystal contacts were primarily mediated by sAB-158, demonstrating the effectiveness of chaperoning reagents in aiding the crystallization of difficult structural targets (fig. S30). The three channel nups formed a parallel, three-stranded, heterotrimeric coiled-coil structure with two sharp kinks that divided the CNT into three left-handed coiled-coil domains (CCD1–3), with an overall resemblance to the numeral “4” and maximum dimensions of ~145 Å × ~80 Å × ~60 Å (Fig. 4, A and B, and movies S1 and S2). CCD1 formed the ~145 Å long stalk and was composed of the N-terminal coiled-coil segments

(CCS1) of Nsp1, Nup49, and Nup57, each containing 12 heptad repeats. Analogously, CCS2 and CCS3 were each composed of five heptad repeats that were ~70 Å in length. The three CCDs were connected by unstructured linker regions, of varying length, between the three coiled-coil segments of each channel nup. CCS1 of Nup57 was interrupted close to the base of the stalk by a 56-residue insertion forming a novel fold with two parallel β sheets and one α helix, termed the α/β insertion domain (Fig. 4B).

A salient feature of the structure was the extensive interaction of Nic96^{RI} with all three CCDs of the CNT, located in the triangular opening at the apex of the “4” (Fig. 4B and movie S3). Nic96^{RI} formed two 11-residue α helices, α1 and α2, which were linked by a sharply kinked 16-residue connector (Fig. 4C). One face of helix α1 recognized CCD1 by binding the Nup57–Nup49 surface, while the opposite face of helix α1 interacted with the Nsp1–Nup57 surface of CCD3. The kinked loop inserted as a wedge between the top of the long stalk-forming CCD1 and CCD2. Residues at the N and C termini of the loop formed additional electrostatic contacts with the Nup57–Nup49 surface of CCD1 and extensive hydrophobic contacts with the Nup49–Nsp1 surface of CCD2, respectively. Finally, helix α2, which harbors our LLLL mutant, bound exclusively to the hydrophobic Nsp1–Nup49 surface of CCD3. Not only did Nic96^{RI} recognize the proper assembly of all three CCDs by forming specific interactions with composite CCD surfaces that are each formed by two different channel

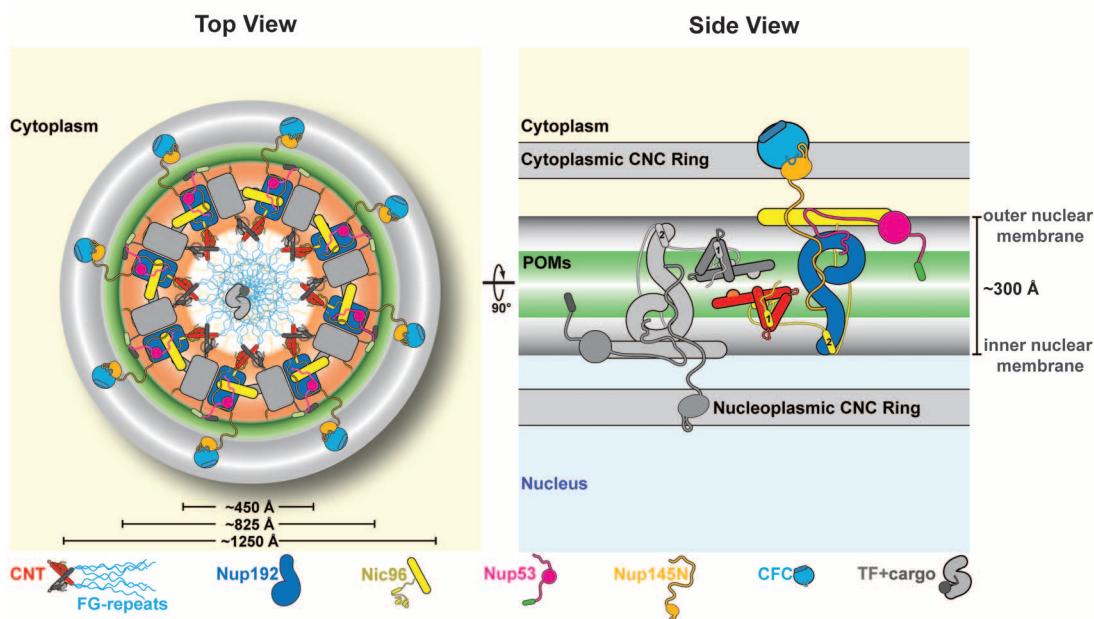
nups, it also locked the CNT into a specific conformation. Overall, ~4150 Å² of surface area are buried in the Nic96^{RI}–CNT interface, involving 38 and 64 residues of Nic96^{RI} and the CNT, respectively. The evolutionary conservation of these interface residues further corroborates the evolutionary conservation of the CNT•Nic96^{RI} architecture (figs. S13 and S31 to S34).

CNT•Nic96^{RI}•sAB-158 forms a cross-handshake dimer in the asymmetric unit of the crystal that is generated by two identical dimerization interfaces, involving the Nup57 α/β insertion domain and CCD3 (Fig. 4D and movie S4). The CNT•Nic96^{RI} dimer buried ~2600 Å² of surface area. The N termini of all channel nups in the dimer point in the same direction, which would permit the FG repeats to be projected toward the central transport channel. Notably, sAB-158 did not participate in CNT•Nic96^{RI} dimer formation, as it recognized a composite Nup57–Nup49 surface in the middle of the CCD1 stalk.

The N-terminal regions of Nsp1, Nup49, and Nup57 in the three-stranded CCD1 stalk appeared to contain seven-residue signature motifs akin to coiled-coil trigger sequences that were previously shown to facilitate proper three-stranded coiled-coil assembly (fig. S35A) (36). An N-terminal truncation of Nup57, Δα/β, which lacked four helical turns of CCS1 and the α/β insertion domain, transformed the equimolar and monodisperse CNT into a polydisperse mixture (fig. S35, B to E). These data provided a molecular explanation for the observed heterogeneous stoichiometries

Fig. 6. Proposed architecture of the NPC inner ring scaffold.

Sixteen copies of the IRC are anchored to the nuclear pore membrane and arranged in a ring-shaped scaffold in an antiparallel fashion to satisfy the established eightfold and twofold symmetry axes of the NPC. Each IRC is composed of the channel nucleoporins Nsp1, Nup49, and Nup57 (CNT, red) and the adaptor nucleoporins Nup192 (blue), Nic96 (yellow), Nup53 (magenta), and Nup145N (orange). The cytoplasmic and nuclear CNC rings (gray), the putative location of the pore membrane proteins (POMs) (green), and the inner ring (red) are shown. On the cytoplasmic side, Nup145N attaches the cytoplasmic filament nucleoporins Nup82 and Nup159 (CFC, cyan). The primarily unstructured adaptor nucleoporins Nup53 and Nup145N mediate the association of various structured IRC components and thus are critical for the IRC scaffold integrity. Nic96 functions as an assembly sensor that recognizes the conformation of the overall 4-shaped three-stranded coiled-coil domain architecture of the CNT, thereby mediating the selective incorporation of a defined CNT state into the NPC. The CNTs are positioned in the equatorial



plane of the inner ring, with the FG repeats of all three channel nups projecting toward the central transport channel. The antiparallel orientation of adjacent IRCs would generate two CNT rings, one at the top and another at the bottom of the central transport channel. This arrangement would allow for the formation of a transport factor–mediated FG repeat meshwork or hydrogel, which would further reinforce the inner ring, scaffold. For size reference, a β-karyopherin•cargo complex is shown in gray.

and dynamic nature of previous mammalian CNT reconstitutions, which also lacked this region (22, 23, 26, 28). In addition to removing the trigger sequence, Nup57 $\Delta\alpha/\beta$ exposed a hydrophobic surface of approximately four unpaired heptad repeats (~50 Å in length). Thus, misfolding and aggregation would be expected.

We conclude that the CNT adopts a robust coiled-coil domain architecture with a single defined assembly state that is specifically recognized by Nic96^{R1} to ensure NPC incorporation of only properly assembled CNT. None of the interactions from previously determined channel nup fragment crystal structures occurred in the intact CNT. Thus, these data strongly disagree with the model in which the CNT undergoes dynamic rearrangements to facilitate NPC constriction and dilation, as previously proposed based on the dynamic nature of various channel nup fragment interactions (25, 26, 28).

Nic96 is an assembly sensor for the properly assembled CNT

Next, we identified channel nup mutants that disrupted the Nic96^{R1}-CNT interaction. As we deemed alanine scanning mutagenesis unlikely to disrupt the extensive CNT-Nic96^{R1} interface, we characterized a previously identified quintuple *S. cerevisiae* Nup49 mutant (EVPIP; K376E, I390V, I391P, V398I, and L449P) (37). The five Nup49 EVPIP mutations mapped to two Nic96^{R1} interfaces located in CCD2 and CCD3 (Figs. 4C and 5A). The corresponding *C. thermophilum* CNT^{EVPIP} mutant failed to interact with the minimal IRC in size-exclusion chromatography–multiangle light scattering (SEC-MALS) experiments (Fig. 5A and fig. S36A). Further analysis showed that CNT^{EPP} was sufficient to abolish binding and CNT^{PP} severely reduced binding, but no single mutant alone affected complex formation (Fig. 5B and fig. S36, B to F). The severity of the required mutations demonstrated the robustness of the CNT-Nic96^{R1} interaction.

Next, we tested the effects of these Nup49 mutations in *S. cerevisiae*. Whereas the single mutants displayed no phenotypes, PP displayed a temperature-sensitive growth defect, which was intensified in EPP and EVPIP, consistent with their decreased thermostability (Fig. 5C and fig. S37). In line with the growth defects, PP showed wild-type levels of mCherry-Nup49 and Nup57-GFP NE staining at 30°C but barely detectable levels at 37°C (Fig. 5D). The temperature-sensitive localization defect for both nups was increased in EPP and EVPIP, which showed severe reduction and complete loss of NE staining at 30° and 37°C, respectively (Fig. 5D). Interestingly, despite an almost complete loss of Nup49 and Nup57 from the NE, we only observed a mild effect on mRNA export (Fig. 5E). Regardless, the EPP and EVPIP mutants resulted in a ribosomal export defect at 30°C (Fig. 5F).

These data established that NE recruitment of Nup57 and NE recruitment of Nup49 are codependent, consistent with our biochemical and structural analyses that Nic96^{R1} only interacts with the intact CNT, validating that the CNT•Nic96^{R1}

structure represents the physiologically relevant state in the assembled NPC.

Conclusions

Through reconstitution and systematic structural and functional analysis of the IRC, we established the equimolar stoichiometry of its six components and uncovered the physiologically relevant underlying interaction network. We showed that Nup53 and the CFC could be attached to the IRC, facilitating membrane attachment and functionalization at the cytoplasmic face, respectively. Surprisingly, none of the previously determined dynamic channel nup fragment assemblies occur in the intact CNT•Nic96^{R1} structure. Indeed, the CNT adopts a robust parallel three-stranded coiled-coil domain architecture resembling the numeral 4. This organization guarantees that the N-terminal FG repeats of the three channel nups emanate from a single site on the CNT surface. Because Nic96 harbors an assembly sensor for this specific CNT state, the NPC incorporation of the three channel nups is codependent and thereby enables the concomitant generation of the diffusion barrier and cargo•transport factor complex docking sites. Additionally, we demonstrated that efficient nucleocytoplasmic transport also requires proper CNT positioning, which is achieved by the Nic96-Nup192 interaction. The conclusion that the inner ring of the NPC adopts a relatively rigid architecture with a transport channel filled with channel nup FG repeats is also supported by a channel nup FG repeat-coated artificial nanopore, which mimicked the NPC's transport selectivity (38).

NPC recruitment of a single robust CNT assembly state rules out the possibility that channel nups dynamically rearrange into different assembly states with various stoichiometries to facilitate karyopherin-assisted dilation and constriction of the central transport channel, as previously proposed (25–28). Indeed, dilation is unnecessary, as the central transport channel of the human NPC can easily accommodate even one of the largest cargoes, the pre-60S ribosomal particle (fig. S38) (2, 39).

Apart from its role in the CNT, Nsp1 forms a mutually exclusive complex with the C-terminal coiled-coil regions of Nup82 and Nup159 at the cytoplasmic face of the NPC (40). The CNT•Nic96^{R1} structure suggests that Nsp1•Nup82•Nup159 might adopt a similar three-stranded coiled-coil domain architecture. More generally, our biochemical and structural studies of the three channel nups demonstrate that utmost caution is required when analyzing heteromeric coiled-coil interactions.

The finding that the IRC and the IRC•CFC•Nup53 heterononamer are monomeric in solution is not unexpected. The CNC is also monomeric in solution, but it organizes into densely packed, 16-membered peripheral rings in the intact NPC (2, 3). The cryo-ET reconstruction of the human NPC suggests that the inner ring is large enough to accommodate 16 copies of the IRC, and we propose that they are recruited to the nuclear pore membrane by their association with the membrane-anchored Nup53•Nup170•Ndc1 complex (Fig. 6)

(5, 41). Stabilization of the inner ring scaffold could occur through multiple weak interactions between adjacent IRCs, including the dimerization of neighboring CNTs, the formation of a FG-repeat hydrogel in the central transport channel (9), and/or transport factor•cargo complex binding to such a FG-repeat meshwork. A 16-membered inner ring scaffold accounts for ~10-MD of the NPC mass. Our results represent a major step forward toward the in vitro reconstitution of the entire NPC, which is essential for the development of in vitro assays to quantitatively characterize nucleocytoplasmic transport.

REFERENCES AND NOTES

1. A. Hoelz, E. W. Debler, G. Blobel, *Annu. Rev. Biochem.* **80**, 613–643 (2011).
2. K. H. Bui et al., *Cell* **155**, 1233–1243 (2013).
3. T. Stuwe et al., *Science* **347**, 1148–1152 (2015).
4. N. Eisenhardt, J. Redolfi, W. Antonin, *J. Cell Sci.* **127**, 908–921 (2014).
5. E. Onischenko, L. H. Stanton, A. S. Madrid, T. Kieselbach, K. Weis, *J. Cell Biol.* **185**, 475–491 (2009).
6. J. M. Mitchell, J. Mansfield, J. Capitanio, U. Kutay, R. W. Wozniak, *J. Cell Biol.* **191**, 505–521 (2010).
7. S. Amlacher et al., *Cell* **146**, 277–289 (2011).
8. T. Stuwe, D. H. Lin, L. N. Collins, E. Hurt, A. Hoelz, *Proc. Natl. Acad. Sci. U.S.A.* **111**, 2530–2535 (2014).
9. A. Cook, F. Bono, M. Jinek, E. Conti, *Annu. Rev. Biochem.* **76**, 647–671 (2007).
10. M. P. Rout et al., *J. Cell Biol.* **148**, 635–651 (2000).
11. S. Frey, R. P. Richter, D. Görlich, *Science* **314**, 815–817 (2006).
12. Q. Yang, M. P. Rout, C. W. Akey, *Mol. Cell* **1**, 223–234 (1998).
13. P. Grandi, N. Schlaich, H. Tekotte, E. C. Hurt, *EMBO J.* **14**, 76–87 (1995).
14. T. Hu, T. Guan, L. Gerace, *J. Cell Biol.* **134**, 589–601 (1996).
15. C. Wimmer, V. Doye, P. Grandi, U. Nehrbass, E. C. Hurt, *EMBO J.* **11**, 5051–5061 (1992).
16. S. R. Wente, M. P. Rout, G. Blobel, *J. Cell Biol.* **119**, 705–723 (1992).
17. U. Nehrbass et al., *Cell* **61**, 979–989 (1990).
18. L. A. Strawn, T. Shen, N. Shulga, D. S. Goldfarb, S. R. Wente, *Nat. Cell Biol.* **6**, 197–206 (2004).
19. E. C. Hurt, *EMBO J.* **7**, 4323–4334 (1988).
20. T. Guan et al., *Mol. Biol. Cell* **6**, 1591–1603 (1995).
21. P. Grandi et al., *Mol. Biol. Cell* **8**, 2017–2038 (1997).
22. I. Melčák, A. Hoelz, G. Blobel, *Science* **315**, 1729–1732 (2007).
23. A. Ulrich, J. R. Partridge, T. U. Schwartz, *Mol. Biol. Cell* **25**, 1484–1492 (2014).
24. N. L. Schlaich, M. Häner, A. Lustig, U. Aebi, E. C. Hurt, *Mol. Biol. Cell* **8**, 33–46 (1997).
25. S. R. Solmaz, G. Blobel, I. Melčák, *Proc. Natl. Acad. Sci. U.S.A.* **110**, 5858–5863 (2013).
26. S. R. Solmaz, R. Chauhan, G. Blobel, I. Melčák, *Cell* **147**, 590–602 (2011).
27. J. Koh, G. Blobel, *Cell* **161**, 1361–1373 (2015).
28. A. Sharma, S. R. Solmaz, G. Blobel, I. Melčák, *J. Biol. Chem.* **290**, 18370–18378 (2015).
29. T. Stuwe, L. S. von Borzyskowski, A. M. Davenport, A. Hoelz, *J. Mol. Biol.* **419**, 330–346 (2012).
30. K. Yoshida, H. S. Seo, E. W. Debler, G. Blobel, A. Hoelz, *Proc. Natl. Acad. Sci. U.S.A.* **108**, 16571–16576 (2011).
31. K. R. Andersen et al., *eLife* **2**, e00745 (2013).
32. P. Sampathkumar et al., *Structure* **21**, 560–571 (2013).
33. B. Kosova, N. Panté, C. Rollenhagen, E. Hurt, *J. Biol. Chem.* **274**, 22646–22651 (1999).
34. J. D. Aitchison, M. P. Rout, M. Marelli, G. Blobel, R. W. Wozniak, *J. Cell Biol.* **131**, 1133–1148 (1995).
35. P. Grandi, V. Doye, E. C. Hurt, *EMBO J.* **12**, 3061–3071 (1993).
36. S. Frank, A. Lustig, T. Schulthess, J. Engel, R. A. Kammerer, *J. Biol. Chem.* **275**, 11672–11677 (2000).
37. V. Doye, R. Wepf, E. C. Hurt, *EMBO J.* **13**, 6062–6075 (1994).
38. T. Jovanovic-Talisman et al., *Nature* **457**, 1023–1027 (2009).
39. B. Bradatsch et al., *Nat. Struct. Mol. Biol.* **19**, 1234–1241 (2012).
40. S. M. Baller, C. Baldus, E. Hurt, *Mol. Cell Biol.* **21**, 7944–7955 (2001).
41. L. A. Hawrylyuk-Gara, E. K. Shibuya, R. W. Wozniak, *Mol. Biol. Cell* **16**, 2382–2394 (2005).

ACKNOWLEDGMENTS

We thank W. M. Clemons, A. Correia, G. Mobbs, A. Patke, D. C. Rees, S. O. Shan, and E. Stuwe for critical reading of the manuscript; M. Budd for help with yeast experiments; J. Herrmann, R. Kunze, and L. Zhang for technical support; and J. Kaiser and the scientific staff of the

Stanford Synchrotron Radiation Lightsource (SSRL) Beamline 12-2, the National Institute of General Medical Sciences and National Cancer Institute Structural Biology Facility (GM/CA) at the Advanced Photon Source (APS), and the Advanced Light Source (ALS) beamline 8.2.1 for support with x-ray diffraction measurements. We acknowledge the Gordon and Betty Moore Foundation, the Beckman Institute, and the Sanofi-Aventis Bioengineering Research Program for support of the Molecular Observatory at the California Institute of Technology (Caltech). The operations at the SSRL, ALS, and APS are supported by the U.S. Department of Energy and the NIH. GM/CA has been funded in whole or in part with federal funds from the National Cancer Institute (ACB-12002) and the National Institute of General Medical Sciences (AGM-12006). T.S. was supported by a Postdoctoral Fellowship of the Deutsche Forschungsgemeinschaft. S.P. and D.H.L. are Amgen Graduate Fellows, supported through the Caltech-Amgen Research Collaboration. F.M.H. was supported by a Ph.D. student fellowship of the Boehringer Ingelheim Fonds. S.K. was supported by NIH Awards

R01-GM090324 and U54-GM087519 and by the University of Chicago Comprehensive Cancer Center (P30-CA014599). A.A.K. was supported by NIH awards U01-GM094588 and U54-GM087519 and by Searle Funds at The Chicago Community Trust. A.H. was supported by Caltech startup funds, the Albert Wyrick V Scholar Award of the V Foundation for Cancer Research, the 54th Mallinckrodt Scholar Award of the Edward Mallinckrodt Jr. Foundation, a Kimmel Scholar Award of the Sidney Kimmel Foundation for Cancer Research, a Camille-Dreyfus Teacher Scholar Award of The Camille and Henry Dreyfus Foundation, and NIH grant R01-GM111461. The coordinates and structure factors have been deposited with the Protein Data Bank with accession codes 5CWV (Nup192^{TAIL}), 5CWU (Nup188^{TAIL}), 4JQ5 (hsNup49^{CCS2+3*}), 4JNV and 4JNU (hsNup57^{CCS3*}), 5CWT (Nup57^{CCS3*}), 4JQ7 (hsNup49^{CCS2+3*}•hsNup57^{CCS3*}; 2:2 stoichiometry), 4JQ9 (hsNup49^{CCS2+3*}•hsNup57^{CCS3*}; 1:2 stoichiometry), 5CWW (Nup82^{NTD}•Nup159^T•Nup145N^{APD}), and 5CWS (CNT•Nic96^{R1}•sAB-158). The authors declare no financial

conflicts of interest. S.K. and A.K. are inventors on a patent application filed by the University of Chicago that covers a design of monoclonal antibodies (US 13/813,409). Monoclonal antibodies are available from S.K. under a material transfer agreement with the University of Chicago.

SUPPLEMENTARY MATERIALS

www.sciencemag.org/content/350/6256/56/suppl/DC1

Materials and Methods

Figs. S1 to S38

Tables S1 to S9

Movies S1 to S4

References (42–65)

29 June 2015; accepted 12 August 2015

Published online 27 August 2015

10.1126/science.aac9176

REPORTS

PLANETARY SCIENCE

Discovery and spectroscopy of the young jovian planet 51 Eri b with the Gemini Planet Imager

B. Macintosh,^{1,2*} J. R. Graham,³ T. Barman,⁴ R. J. De Rosa,³ Q. Konopacky,⁵ M. S. Marley,⁶ C. Marois,^{7,8} E. L. Nielsen,^{9,1} L. Pueyo,¹⁰ A. Rajan,¹¹ J. Rameau,¹² D. Saumon,¹³ J. J. Wang,³ J. Patience,¹¹ M. Ammons,² P. Arriaga,¹⁴ E. Artigau,¹² S. Beckwith,³ J. Brewster,⁹ S. Bruzzone,¹⁵ J. Bulger,^{11,16} B. Burningham,^{6,17} A. S. Burrows,¹⁸ C. Chen,¹⁰ E. Chiang,³ J. K. Chilcote,¹⁹ R. I. Dawson,³ R. Dong,³ R. Doyon,¹² Z. H. Draper,^{8,7} G. Duchêne,^{3,20} T. M. Esposito,¹⁴ D. Fabrycky,²¹ M. P. Fitzgerald,¹⁴ K. B. Follette,¹ J. J. Fortney,²² B. Gerard,^{8,7} S. Goodsell,^{23,24} A. Z. Greenbaum,^{25,10} P. Hibon,²⁴ S. Hinkley,²⁶ T. H. Cotten,²⁷ L.-W. Hung,¹⁴ P. Ingraham,²⁸ M. Johnson-Groh,^{8,7} P. Kalas,^{3,9} D. Lafreniere,¹² J. E. Larkin,¹⁴ J. Lee,²⁷ M. Line,²² D. Long,¹⁰ J. Maire,¹⁹ F. Marchis,⁹ B. C. Matthews,^{7,8} C. E. Max,²² S. Metchev,^{15,29} M. A. Millar-Blanchaer,³⁰ T. Mittal,³ C. V. Morley,²² K. M. Morzinski,³¹ R. Murray-Clay,³² R. Oppenheimer,³³ D. W. Palmer,² R. Patel,²⁹ M. D. Perrin,¹⁰ L. A. Poyneer,² R. R. Rafikov,¹⁸ F. T. Rantakyro,²⁴ E. L. Rice,^{34,33} P. Rojo,³⁵ A. R. Rudy,²² J.-B. Ruffio,^{1,9} M. T. Ruiz,³⁵ N. Sadakuni,^{36,24} L. Saddlemyer,⁷ M. Salama,³ D. Savransky,³⁷ A. C. Schneider,³⁸ A. Sivaramakrishnan,¹⁰ I. Song,²⁷ R. Soummer,¹⁰ S. Thomas,²⁸ G. Vasisht,³⁹ J. K. Wallace,³⁹ K. Ward-Duong,¹¹ S. J. Wiktorowicz,²² S. G. Wolff,^{25,10} B. Zuckerman¹⁴

Directly detecting thermal emission from young extrasolar planets allows measurement of their atmospheric compositions and luminosities, which are influenced by their formation mechanisms. Using the Gemini Planet Imager, we discovered a planet orbiting the ~20-million-year-old star 51 Eridani at a projected separation of 13 astronomical units. Near-infrared observations show a spectrum with strong methane and water-vapor absorption. Modeling of the spectra and photometry yields a luminosity (normalized by the luminosity of the Sun) of 1.6 to 4.0×10^{-6} and an effective temperature of 600 to 750 kelvin. For this age and luminosity, “hot-start” formation models indicate a mass twice that of Jupiter. This planet also has a sufficiently low luminosity to be consistent with the “cold-start” core-accretion process that may have formed Jupiter.

Several young, self-luminous extrasolar planets have been directly imaged at infrared (IR) wavelengths (1–8). The planets directly imaged to date are massive [(estimated at 5 to 13 Jupiter masses (M_J))] and positioned at large separations [9 to 650 astronomical units

(AU)] from their host star, compared with planets in our solar system. Photometry and spectroscopy can be used to probe the atmospheres of these young jovian planets, providing clues about their formation. Several unexpected results have emerged. The near-IR colors of these planets are

mostly red, indicating cloudy atmospheres similar to those of brown dwarfs of spectral type L. Methane absorption features are prominent in the near-IR spectra of T dwarfs [effective temperature (T_{eff}) < 1100 K], as well as in the giant planets of our solar system, but such features are weak or absent in the directly imaged exoplanets (4, 9–11). Most young planets appear to be methane-free, even at temperatures where equivalent brown dwarfs show evidence of methane, suggesting nonequilibrium chemistry and persistent clouds that are probably age- and mass-dependent (1, 12–15).

In spite of uncertainties about their atmospheric properties, the luminosities of these planets are well constrained. Luminosity is a function of age, mass, and initial conditions (16, 17) and hence can provide insights into a planet's formation. Rapid formation (e.g., through global disk instabilities acting on a dynamical time scale) yields high-entropy planets that are bright at young ages (“hot start”). Alternatively, two-stage formation—in which the development of a dense solid core is followed by gas accretion through a shock, as is likely in the case of Jupiter—can produce a range of states, including lower-entropy planets that are cooler and slightly smaller in radius (“cold start”). The young directly imaged planets are almost all too bright for the cold-start model to apply, except for specific accretion shock properties; however, their formation is also difficult to explain by global instability, which should operate preferentially at higher masses and at large semimajor axis separations (18, 19). In addition, these planets are close to the limit of sensitivity for first-generation large-telescope adaptive optics (AO) systems. The goal of the latest generation of surveys, which use dedicated high-contrast AO coronagraphs (20–23) such as the Gemini Planet Imager (GPI) and its counterparts, is to expand the sample of directly imaged planets to include closer separations, lower masses, and lower temperatures, a crucial empirical step toward investigating the above modes of formation.

The Gemini Planet Imager Exoplanet Survey (GPIS) is targeting 600 young nearby stars with the GPI instrument. The star 51 Eridani (51 Eri) was chosen as an early target for the survey because of its youth and proximity. Its stellar properties are given in Table 1. The star exhibits

weak mid- and far-IR excess emission, indicating low-mass inner (5.5 AU) and outer (82 AU) dust belts (24, 25). It also has two distant (~2000 AU) stellar companions, which constitute the 6-AU-separation M-dwarf binary system GJ 3305 (26). 51 Eri and GJ 3305 were classified in 2001 as

¹Kavli Institute for Particle Astrophysics and Cosmology, Stanford University, Stanford, CA 94305, USA.

²Lawrence Livermore National Laboratory, 7000 East Avenue, Livermore, CA 94040, USA. ³Department of

Astronomy, University of California–Berkeley, Berkeley, CA 94720, USA. ⁴Lunar and Planetary Laboratory, University of

Arizona, Tucson, AZ 85721, USA. ⁵Center for Astrophysics and Space Sciences, University of California–San Diego, 9500 Gilman Drive, La Jolla, CA 92093, USA. ⁶NASA Ames

Research Center, MS 245-3, Moffett Field, CA 94035, USA. ⁷National Research Council of Canada, Herzberg Institute of

Astrophysics, 5071 West Saanich Road, Victoria, British Columbia V9E 2E7, Canada. ⁸Department of Physics and

Astronomy, University of Victoria, 3800 Finerty Road, Victoria, British Columbia V8P 5C2, Canada. ⁹Search for

Extraterrestrial Intelligence Institute, Carl Sagan Center, 189 Bernardo Avenue, Mountain View, CA 94043, USA. ¹⁰Space

Telescope Science Institute, 3700 San Martin Drive, Baltimore, MD 21218, USA. ¹¹School of Earth and Space Exploration,

Arizona State University, Post Office Box 871404, Tempe, AZ 85287, USA. ¹²Institut de Recherche sur les Exoplanètes,

Département de Physique, Université de Montréal, Montréal, Québec H3C 3J7, Canada. ¹³Los Alamos National Laboratory,

Post Office Box 1663, MS F663, Los Alamos, NM 87545, USA. ¹⁴Department of Physics and Astronomy, University of

California–Los Angeles, 430 Portola Plaza, Los Angeles, CA 90095, USA. ¹⁵Department of Physics and Astronomy, Centre

for Planetary Science and Exploration, The University of Western Ontario, London, Ontario N6A 3K7, Canada. ¹⁶Subaru

Telescope, 650 North A'ohoku Place, Hilo, HI 96720, USA. ¹⁷Science and Technology Research Institute, University of

Hertfordshire, Hatfield AL10 9AB, UK. ¹⁸Department of Astrophysical Sciences, Princeton University, Princeton, NJ

08544, USA. ¹⁹Dunlap Institute for Astronomy and Astrophysics, University of Toronto, 50 St. George Street,

Toronto, Ontario M5S 3H4, Canada. ²⁰Institut de Planétologie et d'Astrophysique de Grenoble, Université Grenoble Alpes,

Centre National de la Recherche Scientifique, 38000 Grenoble, France. ²¹Department of Astronomy and Astrophysics,

University of Chicago, 5640 South Ellis Avenue, Chicago, IL 60637, USA. ²²Department of Astronomy and Astrophysics,

University of California–Santa Cruz, Santa Cruz, CA 95064, USA. ²³Department of Physics, Durham University, Stockton

Road, Durham DH1, UK. ²⁴Gemini Observatory, Casilla 603, La Serena, Chile. ²⁵Department of Physics and Astronomy, Johns

Hopkins University, 3600 North Charles Street, Baltimore, MD 21218, USA. ²⁶University of Exeter, Astrophysics Group,

Physics Building, Stocker Road, Exeter EX4 4QL, UK. ²⁷Department of Physics and Astronomy, University of Georgia,

Athens, GA 30602, USA. ²⁸Large Synoptic Survey Telescope, 950 North Cherry Avenue, Tucson, AZ 85719, USA.

²⁹Department of Physics and Astronomy, Stony Brook University, 100 Nicolls Road, Stony Brook, NY 11794-3800, USA. ³⁰Department of Astronomy and Astrophysics, University

of Toronto, Toronto, Ontario M5S 3H4, Canada. ³¹Steward Observatory, 933 North Cherry Avenue, University of Arizona,

Tucson, AZ 85721, USA. ³²Department of Physics, University of California–Santa Barbara, Broida Hall, Santa Barbara, CA 93106-9530, USA. ³³Department of Astrophysics, American

Museum of Natural History, New York, NY 10024, USA. ³⁴Department of Engineering Science and Physics, College of

Staten Island, City University of New York, Staten Island, NY 10314, USA. ³⁵Departamento de Astronomía, Universidad de

Chile, Camino El Observatorio 1515, Casilla 36-D, Las Condes, Santiago, Chile. ³⁶Stratospheric Observatory for Infrared

Astronomy, Universities Space Research Association, NASA Armstrong Flight Research Center, 2825 East Avenue P,

Palmdale, CA 93550, USA. ³⁷Sibley School of Mechanical and Aerospace Engineering, Cornell University, Ithaca, NY 14853,

USA. ³⁸Physics and Astronomy, University of Toledo, 2801 West Bancroft Street, Toledo, OH 43606, USA. ³⁹Jet

Propulsion Laboratory, California Institute of Technology, 4800 Oak Grove Drive, Pasadena, CA 91109, USA.

⁴⁰Department of Physics and Astronomy, University of

California–Berkeley, Berkeley, CA 94720, USA. ⁴¹Department of Physics and Astronomy, University of

California–San Diego, San Diego, CA 92093, USA. ⁴²Department of Physics and Astronomy, University of

California–Los Angeles, Los Angeles, CA 90095, USA. ⁴³Department of Physics and Astronomy, University of

California–Santa Cruz, Santa Cruz, CA 95064, USA. ⁴⁴Department of Physics and Astronomy, University of

California–Santa Cruz, Santa Cruz, CA 95064, USA. ⁴⁵Department of Physics and Astronomy, University of

members of the β Pictoris moving group (27), and subsequent measurements support this identification (28). The estimated age of the β Pictoris moving group ranges from 12 to 23 million years (My) (27, 29–32). Giving strong weight to the group's lithium-depletion boundary age, we adopted an age of 20 ± 6 My for all four components of the 51 Eri system (28).

We observed 51 Eri in the H band (1.65 μ m) in December 2014, as the 44th target in the GPIES campaign. GPI observations produce spectroscopic cubes with a spectral-resolving power of 45 over the entire field of view. A companion planet designated 51 Eri b, was apparent after subtraction of the point spread function (PSF). The planet is located at a projected separation of 13 AU, and its spectra exhibit distinctive strong methane and water-vapor absorption (Figs. 1 and 2). We observed 51 Eri again in January 2015 to broaden the wavelength coverage, using GPI (J band, 1.25 μ m) and the W. M. Keck Observatory's Near Infrared Camera 2 (NIRC2; Lp band, 3.8 μ m). The observed spectra are highly similar to those of a field brown dwarf of spectral type T4.5 to T6 (Fig. 2). The J-band spectrum confirmed methane absorption at this wavelength, and the extremely red H-Lp color is similar to that of other cool, low-mass objects (Fig. 3). The signal-to-noise ratio at J-band wavelengths is inferior to that at H-band wavelengths, and extraction introduces additional systematic effects. The J-band detection is reliable ($>6\sigma$), but the fluxes in individual spectral channels are less certain. However, the methane feature was robustly detected at both bands (28).

Demonstrating common proper motion (33), or showing that the probability of a foreground or background contaminant is extremely low, establishes the nature of directly imaged planets. The interval between the December 2014 and January 2015 observations is too brief, given our astrometric accuracy (28), to show that 51 Eri b

and 51 Eri share proper motion and parallax. However, nondetection of 51 Eri b in archival data from 2003 (28) excludes a stationary background source and requires proper motion within ~ 0.1 arc sec/year of 51 Eri. The strong methane absorption that is evident for 51 Eri b is found only in T-type or later brown dwarfs. We determined the probability of finding a T dwarf in our field by merging the observed T-dwarf luminosity functions (27, 28) and adopting the spectral types and absolute magnitudes for T dwarfs (34), from which we calculated a false alarm rate of 1.72×10^{-7} methane objects (i.e., types T0 to T8.5) per GPI field ($>5\sigma$). The proper motion constraint eliminates a further 66% of likely background T-dwarf proper motions. The total false alarm probability after observing 44 targets is the probability of a T-spectrum object appearing in 44 Bernoulli trials, given by the binomial distribution, which yields a final probability of 2.4×10^{-6} . Although the occurrence rate of planetary companions is not known with precision, the detection of planetary objects at similar physical separations to 51 Eri b, such as β Pic b and HR8799 e, indicates that the rate is $>10^{-3}$ per star. Hence, with the high-quality spectrum available to us, it is much more likely that 51 Eri b is a bound planetary companion than a chance alignment.

We used planetary atmosphere and evolution models to estimate the properties of 51 Eri b. We first fitted the observed J- and H-band spectra using standard cloud-free equilibrium-chemistry models, with radii constrained based on mass as given by evolutionary tracks, similar to those in (35). This constrained fit gives an effective temperature of 750 K, with a radius [0.76 Jupiter radius (R_J)] and surface gravity similar to those of an old (10 billion years), high-mass brown dwarf. A similar, though less extreme, result (small radii and hence high masses and old ages) is associated with several model fits to observations of the HR8799 planets (13, 15, 16), even though high

Table 1. Properties of 51 Eridani and 51 Eridani b.

51 Eridani	
Spectral type	FOIV
Mass (solar masses)	1.75 ± 0.05
Luminosity (L/L_\odot)	7.1 ± 1
Distance (pc)	29.4 ± 0.3
Proper motion (milli-arc sec/year)	44.22 ± 0.34 (east), -64.39 ± 0.27 (north) (44)
Age (My)	20 ± 6
Metallicity (metal abundance over hydrogen abundance)	-0.027 (45)
J, H, Ks, Lp (magnitudes)	4.74 ± 0.04 , 4.77 ± 0.08 , 4.54 ± 0.02 , 4.54 ± 0.21
Dust luminosity divided by bolometric luminosity	$\sim 10^{-6}$
51 Eri b	
Projected separation (milli-arc sec)	449 ± 7 (31 January 2015)
Projected separation (AU)	13.2 ± 0.2 (31 January 2015)
Absolute J-band magnitude	16.75 ± 0.40
Absolute H-band magnitude	16.86 ± 0.21
Absolute Lp-band magnitude	13.82 ± 0.27

*Corresponding author. E-mail: bmacintosh@stanford.edu

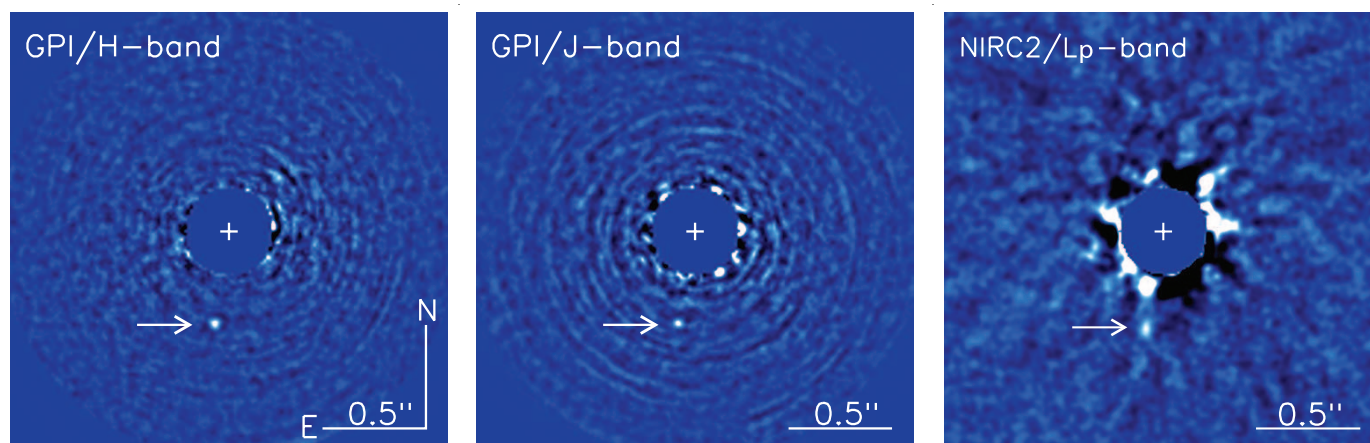


Fig. 1. Images of 51 Eri and 51 Eri b (indicated by the arrow) after PSF subtraction. (A) H-band GPI image from December 2014. **(B)** J-band GPI image from January 2015. **(C)** Lp-band NIRC2 image from January 2015.

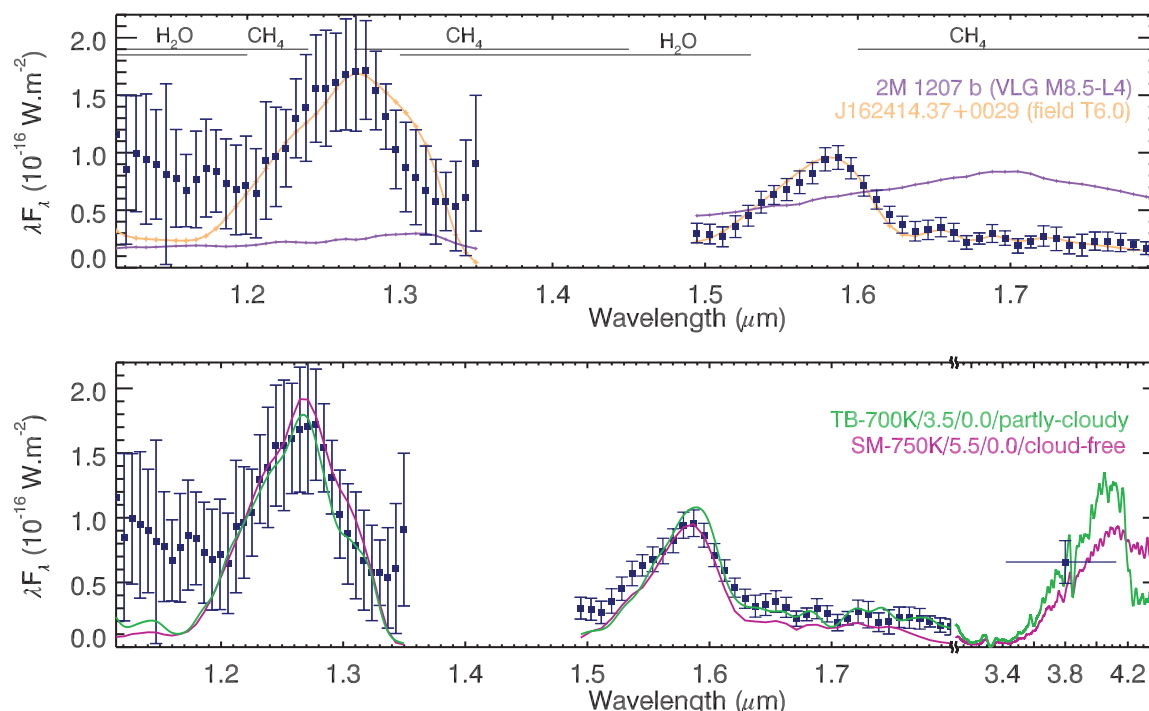


Fig. 2. J- and H-band spectra for 51 Eri b from GPI data, after PSF subtraction. Strong methane absorption, similar to that of Jupiter, is apparent. **(Top)** Spectra for the hotter young planetary object 2M 1207 b (purple) and a high-mass-field T6 brown dwarf from the SpeX library (orange) (43) are overlaid. **(Bottom)** Observed J and H spectra and Lp photometry with two model fits overlaid: a young, low-mass, partly cloudy object (TB-700K, green) and a higher-mass cloud-free object (SM-750K, pink). The main source of error in the extracted spectra is residual speckle artifacts, so errors in neighboring spectral channels are strongly correlated; error estimation is discussed in (28). λF_{λ} flux.

masses are excluded by dynamical stability considerations (36). This model was not constrained to fit the Lp-band observation but does so within 1.6σ .

We next fitted a model to the J-H spectra and Lp photometry using a linear combination of cloudy and cloud-free surfaces and nonequilibrium chemistry, and we allowed the planet's radius to vary independently of the radii given by evolutionary tracks. Models of this type generally produce reasonable fits to other directly imaged planets (11–13, 15, 37, 38). This model produced a slightly lower effective temperature. The spectral shape and colors only weakly constrain gravity but favor lower masses, and the radius ($\sim 1 R_J$) is con-

sistent with evolutionary tracks, given the age of the system. Table 2 summarizes the results of the modeling. With the spectral and atmospheric uncertainties, a wide range of other models (including those with temperatures as high as ~ 1000 K) are also broadly consistent with the observations. The low temperature is supported by the evidence of strong methane absorption that is not observed for other planets of similar age.

The value of $\log(L/L_{\odot})$, -5.4 to -5.8 (where L/L_{\odot} is the planet's luminosity normalized by that of the Sun), is similar in all models, regardless of temperature or clouds. Combined with the age, the luminosity can be used to estimate the mass of

the planet. For a hot-start model, this corresponds to a mass of $\sim 2 (t/20 \text{ My})^{0.65} [(L/2 \times 10^{-6} L_{\odot})^{0.54} M_J$, the lowest-mass self-luminous planet directly imaged to date (t , age of the planet). 51 Eri b, unlike other young (<100 million-year-old) planetary-mass companions, has a low enough luminosity to be consistent with cold-start core-accretion scenarios. In cold-start evolution, luminosity at an age of 20 My is nearly independent of mass, so the mass of 51 Eri b would be between 2 and $12 M_J$.

51 Eri b and the GJ 3305 binary system form a hierarchical triple configuration (28), but the companion pair is far enough away that the planet is expected to be dynamically stable in its current

Fig. 3. Color-magnitude diagram of brown dwarfs (gray and black) and planetary-mass objects (colors). 51 Eri b is indicated with a red star, distinct from most other planets in the methane-dominated T-dwarf region of the diagram. The Lp photometry for field brown dwarfs is taken from (45, 46) or converted from the Wide-field Infrared Survey Explorer W1 band (47) using an Lp-versus-W1 linear fit. Parallaxes are available for all objects plotted (46). M_{Lp} , Lp-band absolute magnitude.

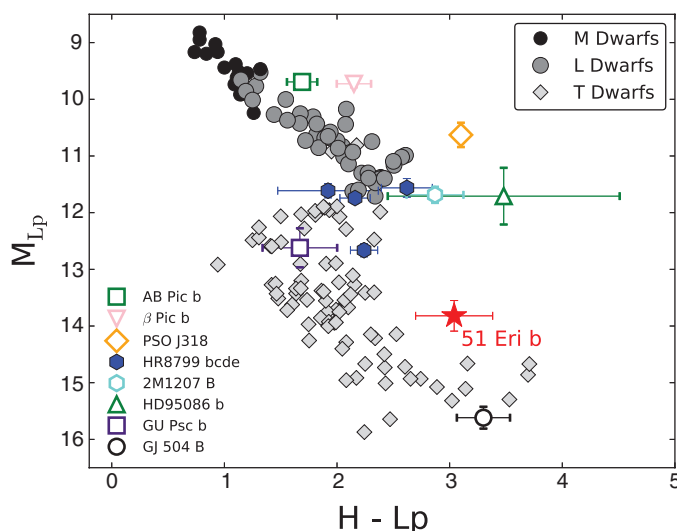


Table 2. Modeling results for 51 Eri b.

	Cloud-free equilibrium model SM-750K	Partial-cloud model TB-700K
Absolute J-band magnitude	16.82	16.64
Absolute H-band magnitude	17.02	16.88
Absolute Lp-band magnitude	14.3	13.96
T_{eff} (K)	750	700
Radius (R_J)	0.76	1
$\log(L/L_\odot)$	-5.8	-5.6
$\log(\text{surface gravity})$	5.5	3.5
Age (My)	10,000	20 (assumed to match stellar age)
Mass (M_J)	67	2 (from luminosity, assuming a high-entropy start)

orbit (26). Moreover, the young age of the system suggests that although long-term dynamical effects, such as secular Lidov-Kozai oscillations, might have altered the planet's eccentricity and inclination, it is unlikely that they have had time to produce the extreme eccentricities required for tidal friction to alter the planet's semimajor axis (39). The formation of a $\sim 2M_J$ planet at an orbital distance of ~ 15 AU around a Sun-like star can be explained by modest extensions to the core-accretion theory. Early versions of the theory found that accretion of the core at larger orbital distances is in danger of taking too long, failing to capture the natal gas before it dissipates (40). 51 Eri b is close enough to the star that this may be less of a problem, and the addition of migration (41) or pebbles that experience gas drag (42) also helps overcome this time-scale difficulty.

The transition from L-type to T-type planets appears to occur over a narrow range of temperatures, between ~ 1000 K (HR8799 b and PSO J318.5-22) (42) and 700 K (51 Eri b). Direct determination of an object's mass, either through spectral surface gravity indicators or reflex astrometry of the primary star, could determine whether

it formed through hot- or cold-start processes. 51 Eri b provides an opportunity to study in detail a planet that is still influenced by the initial conditions of its formation. With a methane-dominated spectrum, low luminosity, and a potentially low-entropy start, 51 Eri b is a bridge between wider-orbit, hotter, more massive planets and planets at Jupiter-like scales.

REFERENCES AND NOTES

- C. Marois *et al.*, *Science* **322**, 1348–1352 (2008).
- P. Kalas *et al.*, *Science* **322**, 1345–1348 (2008).
- A.-M. Lagrange *et al.*, *Science* **329**, 57–59 (2010).
- M. Kuzuhara *et al.*, *Astrophys. J.* **774**, II (2013).
- J. C. Carson *et al.*, *Astrophys. J.* **763**, L32 (2013).
- J. Rameau *et al.*, *Astrophys. J.* **772**, L15 (2013).
- V. Bailey *et al.*, *Astrophys. J.* **780**, L4 (2014).
- D. Lafrenière, R. Jayawardhana, M. H. van Kerkwijk, *Astrophys. J.* **689**, L153–L156 (2008).
- M. Janson *et al.*, *Astrophys. J.* **778**, L4 (2013).
- M.-E. Naud *et al.*, *Astrophys. J.* **787**, 5 (2014).
- T. S. Barman, Q. M. Konopacky, B. Macintosh, C. Marois, Simultaneous detection of water, methane and carbon monoxide in the atmosphere of exoplanet HR8799b, <http://xxx.lanl.gov/abs/1503.03539>.
- T. S. Barman, B. Macintosh, Q. M. Konopacky, C. Marois, *Astrophys. J.* **733**, 65 (2011).
- A. J. Skemer *et al.*, *Astrophys. J.* **792**, 17 (2014).
- M. S. Marley *et al.*, *Astrophys. J.* **754**, 135 (2012).

- N. Madhusudhan, A. Burrows, T. Currie, *Astrophys. J.* **737**, 34 (2011).
- M. S. Marley, J. J. Fortney, O. Hubickyj, P. Bodenheimer, J. J. Lissauer, *Astrophys. J.* **655**, 541–549 (2007).
- D. S. Spiegel, A. Burrows, *Astrophys. J.* **745**, 174 (2012).
- R. R. Rafikov, *Astrophys. J.* **648**, 666–682 (2006).
- K. M. Kratter, R. Murray-Clay, A. N. Youdin, *Astrophys. J.* **710**, 1375–1386 (2010).
- J.-L. Beuzit *et al.*, SPHERE Consortium, paper presented at In the Spirit of Lyot 2010: Direct Detection of Exoplanets and Circumstellar Disks, Paris, 25 to 29 October 2010; abstract available at <http://adsabs.harvard.edu/abs/2010lyot.confE.44B>.
- N. Jovanovic *et al.*, The Subaru Coronagraphic Extreme Adaptive Optics system: Enabling high-contrast imaging on solar-system scales, <http://xxx.lanl.gov/abs/1507.00017>.
- B. R. Oppenheimer *et al.*, *Proc. SPIE* **8447**, 844720 (2012).
- B. Macintosh *et al.*, *Proc. Natl. Acad. Sci. U.S.A.* **111**, 12661–12666 (2014).
- R. I. Patel, S. A. Metchev, A. Heinze, *Astrophys. J. Suppl. Ser.* **212**, 10 (2014).
- P. Riviere-Marichalar *et al.*, *Astron. Astrophys.* **565**, A68 (2014).
- M. Janson *et al.*, *Astrophys. J. Suppl. Ser.* **214**, 17 (2014).
- B. Zuckerman, I. Song, M. S. Bessell, R. A. Webb, *Astrophys. J.* **562**, L87–L90 (2001).
- Material and methods are available as supplementary materials on Science Online.
- M. Simon, G. H. Schaefer, *Astrophys. J.* **743**, 158 (2011).
- A. S. Binns, R. D. Jeffries, *Mon. Not. R. Astron. Soc. Lett.* **438**, L11–L15 (2014).
- E. E. Mamajek, C. P. M. Bell, *Mon. Not. R. Astron. Soc.* **445**, 2169–2180 (2014).
- T. D. Brandt *et al.*, *Astrophys. J.* **786**, 1 (2014).
- G. Chauvin *et al.*, *Astron. Astrophys.* **438**, L25–L28 (2005).
- J. D. Kirkpatrick, *et al.*, *Astrophys. J.* **753**, 156 (2012).
- D. Saumon, M. S. Marley, *Astrophys. J.* **689**, 1327–1344 (2008).
- D. C. Fabrycky, R. A. Murray-Clay, *Astrophys. J.* **710**, 1408–1421 (2010).
- J. Chilcote *et al.*, *Astrophys. J.* **798**, L3 (2015).
- T. Currie *et al.*, *Astrophys. J.* **795**, 133 (2014).
- D. Fabrycky, S. Tremaine, *Astrophys. J.* **669**, 1298–1315 (2007).
- J. B. Pollack *et al.*, *Icarus* **124**, 62–85 (1996).
- Y. Alibert, C. Mordasini, W. Benz, C. Winisdoerffer, *Astron. Astrophys.* **434**, 343–353 (2005).
- M. Lambrechts, A. Johansen, *Astron. Astrophys.* **544**, A32 (2012).
- This research has benefitted from the SpeX Prism Spectral Libraries, maintained by A. Burgasser at <http://pono.ucsd.edu/~adam/browndwarfs/spexprism>.
- F. van Leeuwen, *Astron. Astrophys.* **474**, 653–664 (2007).
- E. R. Houdebine, C. J. Butler, D. Garcia-Alvarez, J. Telting, *Mon. Not. R. Astron. Soc.* **426**, 1591–1605 (2012).
- B. A. Macintosh *et al.*, *Proc. SPIE* **7015**, 701518 (2008).
- J. K. Chilcote *et al.*, *Proc. SPIE* **8446**, 84468W (2012).

ACKNOWLEDGMENTS

This work is based on observations obtained at the Gemini Observatory, which is operated by the Association of Universities for Research in Astronomy under a cooperative agreement with NSF on behalf of the Gemini partnership, whose membership includes: NSF (United States); the National Research Council (Canada); the Comisión Nacional de Investigación Científica y Tecnológica (Chile); the Australian Research Council (Australia); the Ministério da Ciência, Tecnologia e Inovação (Brazil); and Ministerio de Ciencia, Tecnología e Innovación Productiva (Argentina). The research was supported by grants from NSF, including AST-1411868 (B.M., K.F., J.P., and A.R.), AST-0909188 and AST-1313718 (J.R.G., P.K., R.D.R., and J.W.), AST-1413718 (M.P.F. and G.D.), and AST-1405505 (T.B.). Support was also provided by grants from NASA, including NNX14AJ80G (B.M., F.M., E.N., and M.P.), NNX15AZ591 (D.S. and M.M.), NNX15AD95G (J.R.G. and P.K.), NNX11AD21G (J.R.G. and P.K.), and NNX11ZDA001N (S.M. and R.P.). J.R., R.D., and D.L. acknowledge support from the Fonds de Recherche du Québec. Support is acknowledged from NSF fellowships DGE-123825 (A.Z.G.), DGE-131230 (K.W.-D.), DGE-1232825 (S.G.W.), and DGE-1144087 (L.W.H.). Portions of this work were performed under the auspices of the U.S. Department of Energy by Lawrence Livermore National Laboratory under contract DE-AC52-07NA27344. GPI data are archived at the Gemini Science Archive: www.cadc-coda.hia-ihh.nrc-cnrc.gc.ca/en/gsa/.

SUPPLEMENTARY MATERIALS

www.sciencemag.org/content/350/6256/64/suppl/DC1
Materials and Methods
Figs. S1 to S3
Tables S1 to S3
References (48–90)

17 May 2015; accepted 3 August 2015
Published online 13 August 2015
10.1126/science.aac5891

NANO-ELECTRONICS

End-bonded contacts for carbon nanotube transistors with low, size-independent resistance

Qing Cao,* Shu-Jen Han, Jerry Tersoff, Aaron D. Franklin,† Yu Zhu, Zhen Zhang,‡ George S. Tulevski, Jianshi Tang, Wilfried Haensch

Moving beyond the limits of silicon transistors requires both a high-performance channel and high-quality electrical contacts. Carbon nanotubes provide high-performance channels below 10 nanometers, but as with silicon, the increase in contact resistance with decreasing size becomes a major performance roadblock. We report a single-walled carbon nanotube (SWNT) transistor technology with an end-bonded contact scheme that leads to size-independent contact resistance to overcome the scaling limits of conventional side-bonded or planar contact schemes. A high-performance SWNT transistor was fabricated with a sub-10-nanometer contact length, showing a device resistance below 36 kilohms and on-current above 15 microampere per tube. The p-type end-bonded contact, formed through the reaction of molybdenum with the SWNT to form carbide, also exhibited no Schottky barrier. This strategy promises high-performance SWNT transistors, enabling future ultimately scaled device technologies.

After decades of rapidly increasing computer performance, microprocessor clock frequencies have stalled at ~3 to 5 GHz since the early 2000s, as silicon (Si) metal-oxide-semiconductor field-effect transistors (MOSFETs) approach their physical limits (1–3). Two key issues are making high-performance but low-power devices with ultrashort gate pitch (the summary of channel length L_{ch} , the distance between the source and drain electrodes, and the contact length L_c , the length of these contacts)—that is, less than 30 to 40 nm—and lowering the contact resistance between the electrodes and the channel. The problems are interrelated, in that contact resistance increases with decreasing L_c for Si and especially for III-V semiconductors such as GaAs (2, 4). Semiconducting single-walled carbon nanotubes (SWNTs) potentially offer the optimal performance as the channel material for ultrascaled FETs (5–7). The SWNT saturation velocity is several times higher than that of Si, and the intrinsic thinness (~1 nm in diameter) of SWNTs provides the superior electrostatic control needed for devices with ultrashort L_{ch} (6). Indeed, SWNT transistors with 9 nm L_{ch} outperform the best Si MOSFETs with similar L_{ch} (8, 9), and SWNT transistors with advanced self-aligned “gate-all-around” geometry have been fabricated (10, 11) and integrated into complex functional integrated circuits (12, 13).

However, as is the case with Si and III-V semiconductors, a key obstacle to ultrascaled SWNT transistor technology is forming low-resistance and scalable contacts. The total contact resist-

ance $2R_c$ dominates the performance of scaled devices as the channel transport becomes ballistic. Early SWNT transistors were plagued by poor electrical properties of the metal contacts (14, 15). In a major advance, Javey *et al.* achieved low-resistance barrier-free p-type electrical contacts to SWNT using palladium (Pd) (16). As in earlier work, the Pd metal was deposited on top of the SWNT to form so-called side-bonded contacts, in

which electrons are injected along the length of the tube-metal interface (15, 17). However, with such a contact scheme, $2R_c$ is low only for large-area contacts, reflecting the weak Pd-SWNT coupling, and the resistance $2R_c$ increases rapidly as the contact area shrinks (18–20). [The weak metal-SWNT coupling is not well understood and might reflect the nonideal wetting of metals on a curved nanotube surface, or the partial coverage of nanotube surface by insulating impurities such as amorphous carbon (C)]. The contact area is proportional to L_c measured along the SWNT direction. Previous experiments indicate that $2R_c$ will increase from ~5 kilohm for long contacts ($L_c > 200$ nm) to ~65 kilohm at L_c of 9 nm (21), and to much higher values for even smaller contacts, which is unacceptably large for logic transistors beyond the 2020 time frame (22).

Here, we report a contact scheme that allows scaling the contacts to 10 nm and beyond without increasing $2R_c$. An end-bonded contact, in which the SWNT channel abruptly ends at the metal electrodes, is formed through a solid-state reaction between the nanotube and deposited Mo electrodes. Although the carrier injection is limited to an interface of ~2 nm² in size, $2R_c$ was remarkably low, down to 25 to 35 kilohm. No barrier was observed for hole transport, and scaling L_c from 300 nm to below 10 nm did not change the contact resistance; whereas in conventional side-bonded contacts to nanotubes or planar contacts in Si MOSFETs, $2R_c$ shows a characteristic dependence on L_c . Using this end-bonded contact scheme, we successfully demonstrate a p-channel SWNT transistor with an average contact length of merely 9 nm that exhibits on-state

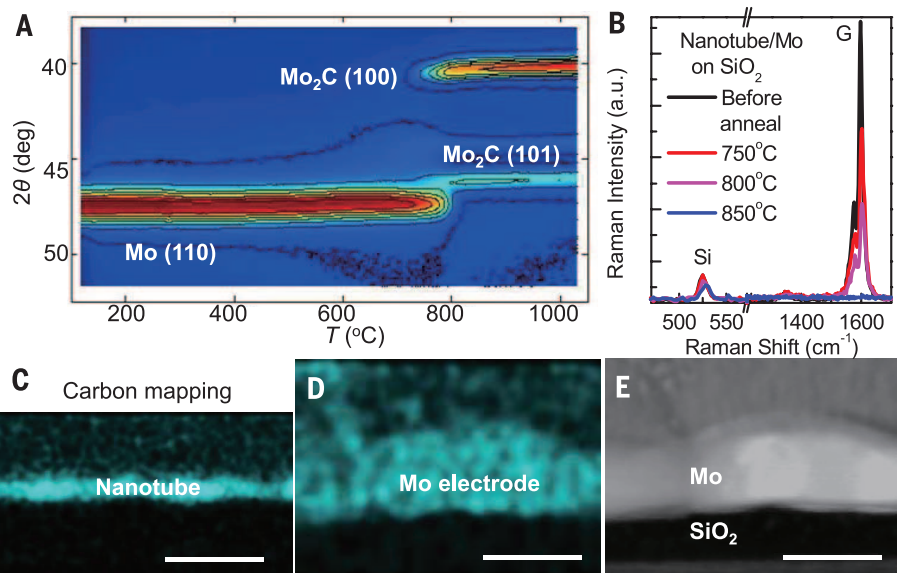


Fig. 1. Reaction of carbon nanotubes with Mo thin film. (A) In situ temperature-variable x-ray diffraction pattern of Mo deposited on a thick nanotube film showing peaks characteristic for Mo and Mo₂C. (B) Raman spectra for double-layered nanotubes covered by 8 nm Mo before and after annealed under different temperatures, showing the characteristic G band of nanotubes and the transverse optical phonon band of crystalline Si substrate. (C and D) False-colored EDX maps of carbon for nanotubes annealed to 850°C without (part C) or with (part D) the Mo film on top. (E) Cross-sectional TEM image showing the profile of the Mo film after annealing as in (D). Scale bars, 20 nm.

IBM Thomas J. Watson Research Center, Yorktown Heights, NY 10598, USA.

*Corresponding author. E-mail: qcao@us.ibm.com †Present address: Department of Electrical and Computer Engineering, Duke University, Durham, NC 27708, USA. ‡Present address: Department of Engineering Sciences, Uppsala University, Uppsala, Sweden.

resistance below 36 kilohm, an on/off current ratio above 10^4 , an on-current above $15\ \mu\text{A}$, and a zero Schottky barrier at contacts.

Ab initio calculations suggest that SWNTs could form good electrical contacts to metals in the end-bonded geometry in which an open tip of the nanotube is directly coupled to metal electrodes through strong covalent bonds (23–25). However, it is very difficult to realize such a structure in experiment. Zhang *et al.* reported the fabrication of SWNT-metal heterostructures through the solid-state carbide formation reaction, in which the C-C bond cleavage and the C-metal bond formation were completed simultaneously (26). The atomically abrupt metal-nanotube junctions have been characterized by means of transmission electron microscopy (TEM) for metals including titanium (Ti) and niobium (Nb) (26), as well as tungsten (W), iron (Fe), and chromium (Cr) (27, 28). However, their successful adoption in transistors as reliable low-resistance contacts has not yet been demonstrated because of integration challenges. The best attempt to date used Ti (29), but Ti is problematic because its low work function leads to a Schottky barrier (29, 30), and destructive reactions with the gate oxide occur at the carbide formation temperature (31). Fifteen metals are known to form stable carbide phases (32), and among these, W, molybdenum (Mo), and Fe exhibit the highest electronegativity or work function

and thus have the strongest tendency to form carbides rather than oxides. Among these three candidates, WC requires formation temperature well above 1000°C , whereas in Fe_3C , a graphite layer is generally observed to segregate atop (32). Thus, we believe that Mo_2C is the best candidate for contacting semiconducting SWNTs.

We confirmed the reaction between carbon nanotubes and the deposited Mo film using time-resolved in situ x-ray diffraction (XRD) (Fig. 1A). To obtain sufficient XRD signal intensity, a thick Mo film (30 nm) was deposited on top of a 200-nm-thick mat of SWNTs sitting on a SiO_2/Si substrate (33). The C atoms from the SWNTs started to react with Mo to form Mo_2C above $\sim 800^\circ\text{C}$, as evidenced by the disappearance of Mo (110) peak around $2\theta \approx 47^\circ$ and the emergence of carbide peaks at $2\theta \approx 40^\circ$ and 46° , which correspond to the (100) and (101) planes of the Mo_2C crystal, respectively. In real devices, the amount of C provided by SWNTs is much smaller than the Mo available in the electrodes. To verify the reaction in this regime, Raman spectroscopy was used to monitor the effect of thermal treatment on a bilayer of SWNTs [$\sim 4\text{ nm}$ thick, assembled with the Langmuir-Schaefer method (34)] covered by a semitransparent 8-nm-thick Mo film. Although the structural integrity of exposed SWNTs was not affected in this temperature range under vacuum (fig. S1), the Raman intensity of the char-

acteristic G band of the nanotubes under Mo started to decrease above 750°C and was completely extinguished in samples annealed at 850°C (Fig. 1B), indicating the occurrence of a reaction destroying the SWNT lattice. Energy-dispersive x-ray (EDX) spectroscopy mapping revealed that under the Mo, the C atoms from the SWNTs dispersed into the Mo (Fig. 1, C to E). In a real device structure in which SWNTs are only covered by Mo in the contact region, this dissolution of C in Mo matrix should lead to an abrupt point-like junction between the three-dimensional (3D) Mo electrode and the 1D SWNT channel (Fig. 2, A to B), considering the low diffusion coefficient of Mo resulting from its high melting temperature (26).

Forming such desired end-bonded structure does not guarantee the good electrical quality of the contacts between Mo and the semiconducting SWNT channel. In order to qualify as a good electrical contact, this pointlike Mo-SWNT end contact must exhibit nearly zero barrier and small contact resistance even with a cross-sectional area down to $\sim 1\text{ nm}^2$. To test this, Mo end-contacted FETs with a nominal L_{ch} of 60 nm were made with individual SWNTs deposited from solution. These devices have rather large Mo electrodes ($\sim 500\text{ nm}$ wide) and were fabricated on a Si substrate covered by 20 nm thermally robust Si nitride gate dielectric. The transfer characteristics of a representative device are shown in Fig. 2C,

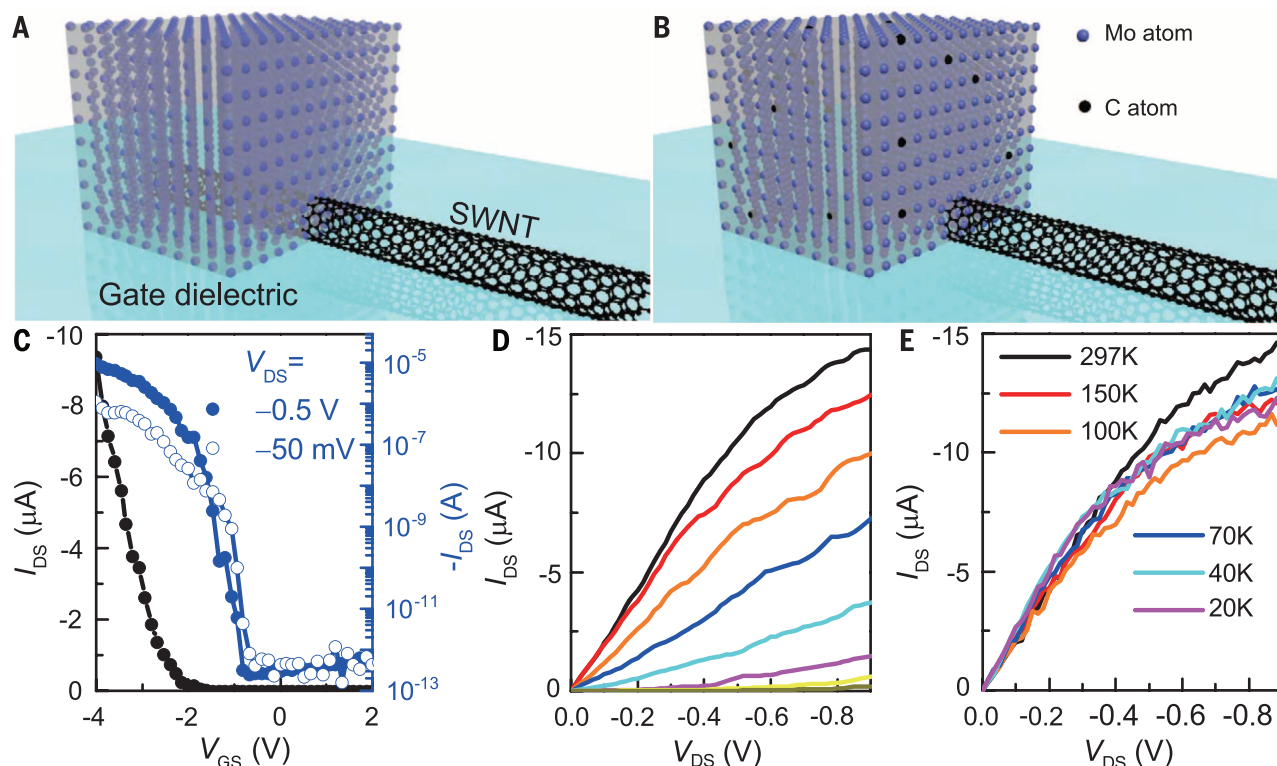


Fig. 2. Mo end-contacted SWNT transistors. (A and B) Schematics showing the conversion from a side-bonded contact (A), where the SWNT is partially covered by Mo, to end-bonded contact (B), where the SWNT is attached to the bulk Mo electrode through carbide bonds while the C atoms from originally covered portion of the SWNT uniformly diffuse out into the Mo electrode. (C) Transfer characteristics of a typical Mo end-contacted single-nanotube transistor built

on 20 nm SiN_x gate dielectric with a nominal L_{ch} of 60 nm plotted in both linear (black, left axis) and logarithmic (blue, right axis) scales with applied V_{DS} of -0.5 V (filled circles) and -0.05 V (hollow circles). I_{DS} , drain-to-source current. (D) Output characteristics of the device at room temperature (V_{GS} changes from -6 V to 1 V in steps of 1 V). (E) Output characteristics for the same device taken at $V_{\text{GS}} = -6\text{ V}$ for different temperatures ranging from 297 to 20 K.

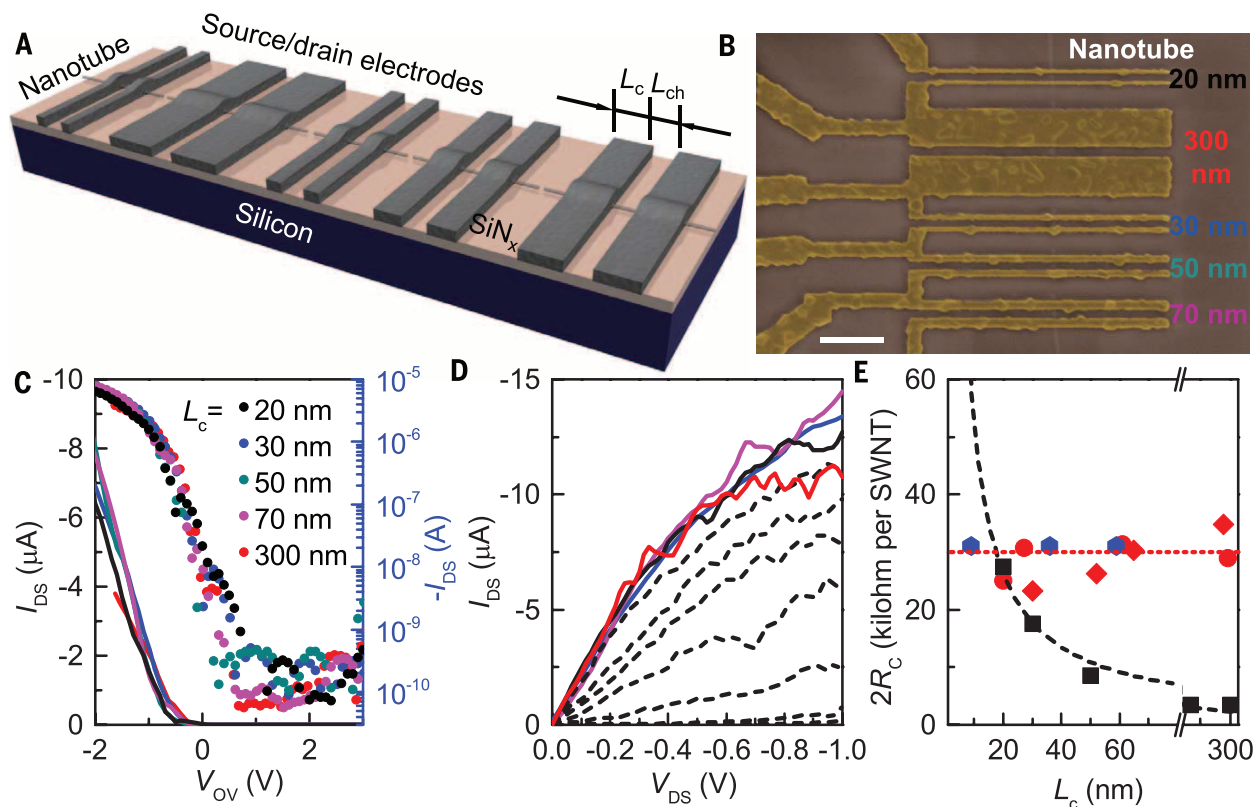


Fig. 3. Contact length scaling of Mo end-contacted quasiballistic SWNT transistors. (A) Schematic and (B) false-colored SEM images of a set of transistors fabricated on the same nanotube, with L_c ranging from 20 to 300 nm. Scale bar, 400 nm. (C) Collection of transfer characteristics from a set of Mo end-contacted single-nanotube transistors with different L_c plotted in both linear (lines, left axis) and logarithmic (symbols, right axis) scales with applied V_{DS} of -0.5 V. (D) Output characteristics of the same devices as in (C) measured at V_{GS} of -6 V. Curves for the device with 20 nm L_c measured with descending V_{GS} at a step of 1 V are also

plotted (dashed lines). (E) Plot of $2R_c$ as a function of L_c for two sets of Mo end-contacted devices (red), with each set on a different nanotube (red circle or diamond represents a set of transistors on the same tube), and the best Pd side-contacted nanotube devices from (21) (black square). Additional Mo end-contacted nanotube devices whose L_c are confined by contact trenches (extracted from Fig. 4F) are shown as blue hexagons. The black dashed curve represents a fitting to the formula of $2R_c = 2\rho_c/L_c$, where ρ_c is the linear contact resistivity. The red dotted line serves as a visual guide highlighting the invariance of $2R_c$ for end-bonded contacts.

with an on/off current ratio up to 10^7 and a small subthreshold swing of ~ 100 mV/decade. Its output characteristics (Fig. 2D) reveal other aspects of the excellent device performance, including on-state resistance ~ 40 kilohm, saturation current near $15 \mu\text{A}$, and nearly linear current-voltage characteristics at small drain-to-source bias (V_{DS}). All of these results suggest that high-quality barrier-free contacts were formed. The absence of Schottky barrier was further confirmed with temperature-dependent measurements. The device output characteristics remain unchanged when measured from room temperature to 20 K (Fig. 2E), indicating nearly zero Schottky barrier for hole injection. Although the real contact area is extremely small, these end-bonded contacts demonstrate excellent electrical reliability, with negligible changes in on-state current or on/off current ratio when the device was electrically cycled more than 400 times, under a peak current density above $4 \times 10^8 \text{ A cm}^{-2}$ (fig. S2), presumably because of the formation of robust metal carbide bonds (28).

For truly end-bonded contacts, $2R_c$ should be independent of contact size. Unlike conventional side contacts, all of the carrier collection should occur at the quasi-0-D interface, with the negli-

gible spreading resistance (fig. S3) (33), so the contact resistance $2R_c$ should be independent of the physical width of the metal contact L_c . We measured devices with a short L_c of 20 nm made on solution-processed SWNTs and found that $\sim 50\%$ of them exhibited low overall device resistance (below 40 kilohm) (fig. S4), which is comparable with the ratio obtained from devices made with wide contacts. To further confirm the invariance of contact resistance with L_c and verify the formation of an end-bonded contact, we needed to control other factors, in particular the dependence of $2R_c$ on the SWNT diameter and band gap (16). To do this, we fabricated a series of devices with different L_c on the same long nanotube grown by means of chemical vapor deposition (Fig. 3, A and B). This approach provided precisely defined device geometries with a constant diameter and band gap among devices. The diameter of this particular SWNT was ~ 1.6 nm (fig. S5) from atomic force microscopy (AFM). The L_{ch} for each device was 60 nm, so that the SWNT channel should be ballistic, and thus the $2R_c$ could be approximated as the total device resistance minus the quantum resistance of the SWNT channel ($R_Q = 6.5$ kilohm) (16).

The transfer characteristics of devices with L_c varying from 20 to 300 nm at the same gate overdrive (V_{OV} , defined as the gate bias V_{GS} applied above the device threshold voltage) (plotted in Fig. 3C) showed no off-state performance difference caused by such wide L_c variation. The values of $2R_c$, extracted from the low-field slope of the output curves at high V_{GS} (Fig. 3D), are all in the range of 25 to 35 kilohm per SWNT. Considering that the junction area is merely $\sim 2 \text{ nm}^2$, this value corresponds to a contact resistivity as low as $3 \times 10^{-10} \text{ ohm cm}^2$, compared with previous best value in the range of 1.5×10^{-9} to $4 \times 10^{-9} \text{ ohm cm}^2$ for metal to Si or SWNT contacts (21, 35). In Fig. 3E, the L_c scaling of our devices is compared with one of the best reported Pd side-bonded contacts (21). For side-bonded contacts, because of the distributed nature of SWNT-metal interface, the $2R_c$ is proportional to the reciprocal of L_c in small contact regime as in the standard transmission line model commonly used for semiconductor devices (19, 36). Mo end-bonded contacts start to outperform Pd side-bonded contacts at dimensions near 20 nm, and we project that the former possesses more than two times the performance advantage for L_c scaled below 10 nm.

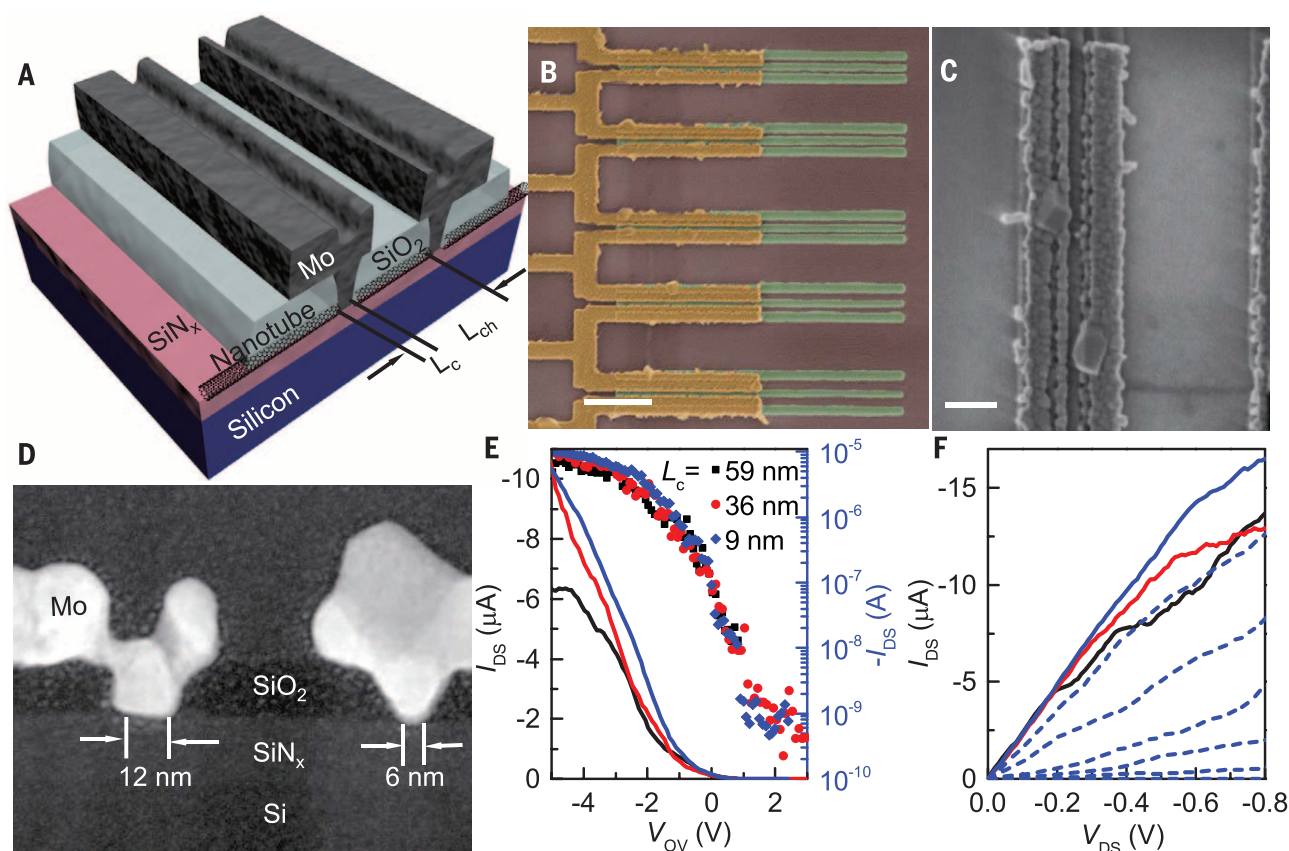


Fig. 4. Mo end-contacted quasiballistic SWNT transistors with L_c defined by contact trenches. (A) Schematic and (B) false-colored SEM image of a set of Mo end-contacted nanotube transistors made on the same nanotube with L_c ranging from ~ 10 to 60 nm defined by SiO_2 contact trenches. The diameter of this particular nanotube is determined to be ~ 1.7 nm by means of AFM (fig. S5). Scale bar, 400 nm. (C) Top-view SEM image of the ~ 9 nm effective L_c nanotube transistor at a higher magnification. Scale bar, 100 nm. (D) Cross-sectional high-

angle annular dark field-STEM of this device showing the trench profile for the accurate determination of L_c . (E) Collection of transfer characteristics from the set of Mo-contacted nanotube transistors as in (B) with different L_c plotted in both linear (lines, left axis) and logarithmic (symbols, right axis) scales under applied V_{DS} of -0.5 V. (F) Output characteristics of the same devices as in (E) measured at V_{OV} of -7 V. Curves for the device with ~ 9 nm effective L_c measured with descending V_{GS} at a step of 1 V are also plotted (dashed lines).

As a final demonstration that a Mo end-bonded contact can maintain its low $2R_c$ and thus serve as the contact scaling solution for future ultimately scaled device technologies, we constructed a SWNT transistor with a physical L_c below 10 nm (a schematic is shown in Fig. 4A; the detailed fabrication flow is depicted in fig. S6). The actual Mo-to-SWNT contacts are confined by the size of SiO_2 trenches, similar to the contact vias in standard Si MOSFETs. The corresponding scanning electron microscopy (SEM) and scanning transmission electron microscopy (STEM) images in Fig. 4, B to D, characterize the geometry of the sub- 10 -nm L_c device, performed after electrical measurements. The cross-sectional STEM image (Fig. 4D) provides information on the sidewall shape of the SiO_2 trenches to give an accurate extraction of the effective device L_c to be ~ 9 nm, which is taken as the average of L_c for source and drain electrodes. Mo nicely filled into these narrow vias. The roughness on the metal top surface is caused by the grain growth induced by this annealing process and can be planarized with a chemical-mechanical polishing process in the real technology integration process flow. Transfer and output characteristics of three devices with effective L_c of 59 , 36 , and 9 nm made on this

SWNT are plotted in Fig. 4, E and F, with their on-current levels consistent with each other, confirming the L_c independence of $2R_c$ (Fig. 3E). The device with 9 nm L_c performs well with an on-current of >10 μA at only -0.5 V V_{DS} , an on/off current ratio of 10^4 , and extracted overall device resistance in low-bias regime less than 36 kilohm. For a realistic SWNT transistor consisting of a nanotube array with a tube pitch of ~ 8 nm (5), the effective device contact resistance per width becomes ~ 240 ohm μm , which satisfies even the most stringent target listed by International Roadmap for Semiconductors up to 1.3 nm technology node in 2028 (37). This end-bonded contact geometry formed through reaction between Mo and nanostructures could readily be extended to improve the L_c scaling behavior of ultrascaled nanoelectronic devices on the basis of other low-dimensional materials including graphene and MoS_2 . We have only demonstrated p-channel SWNT transistors using p-type end contacts. It will be difficult to form end-bonded n-type contacts to SWNTs in which electrons are directly injected into the conduction band of SWNTs with this carbide formation approach, as metals with low enough work function tend to oxidize

first rather than react with C. However, it is still possible to realize n-channel SWNT device operation even with end-bonded contacts to high work function metals through electrostatic doping in the vicinity of the source electrode (10, 38).

REFERENCES AND NOTES

1. T. N. Theis, P. M. Solomon, *Science* **327**, 1600–1601 (2010).
2. W. Haensch et al., *IBM J. Res. Develop.* **50**, 339–361 (2006).
3. R. F. Service, *Science* **323**, 1000–1002 (2009).
4. J. A. del Alamo, *Nature* **479**, 317–323 (2011).
5. G. S. Tulevski et al., *ACS Nano* **8**, 8730–8745 (2014).
6. J. Appenzeller, *Proc. IEEE* **96**, 201–211 (2008).
7. A. D. Franklin, *Nature* **498**, 443–444 (2013).
8. A. D. Franklin et al., *Nano Lett.* **12**, 758–762 (2012).
9. F. Kreupl, *Nature* **484**, 321–322 (2012).
10. A. D. Franklin et al., *Nano Lett.* **13**, 2490–2495 (2013).
11. C. D. Cress, S. Datta, *Science* **341**, 140–141 (2013).
12. Q. Cao et al., *Nature* **454**, 495–500 (2008).
13. M. M. Shulaker et al., *Nature* **501**, 526–530 (2013).
14. J. Appenzeller et al., *Phys. Rev. Lett.* **89**, 126801 (2002).
15. F. Léonard, A. A. Talin, *Nat. Nanotechnol.* **6**, 773–783 (2011).
16. A. Javey, J. Guo, Q. Wang, M. Lundstrom, H. Dai, *Nature* **424**, 654–657 (2003).
17. N. Nemeec, D. Tománek, G. Cuniberti, *Phys. Rev. Lett.* **96**, 076802 (2006).

18. F. Xia, V. Perebeinos, Y. M. Lin, Y. Wu, P. Avouris, *Nat. Nanotechnol.* **6**, 179–184 (2011).
19. P. M. Solomon, *IEEE Electron Device Lett.* **32**, 246–248 (2011).
20. A. D. Franklin, D. B. Farmer, W. Haensch, *ACS Nano* **8**, 7333–7339 (2014).
21. A. D. Franklin, Z. Chen, *Nat. Nanotechnol.* **5**, 858–862 (2010).
22. International technology roadmap for semiconductors (ITRS, www.itrs.net) predicts that the device L_{ch} should shrink to ~10 nm by the 2020 time frame, with length of ~9 nm for contacts. For a realistic carbon nanotube transistor consisting of a nanotube array with a tube pitch of ~8 nm, when scaled to L_c of 9 nm the effective device contact resistance per width for best side-bonded Pd contacts becomes ~520 ohm μ m, which is two to three times higher than that of current silicon MOSFETs.
23. J. J. Palacios, A. J. Pérez-Jiménez, E. Louis, E. Sanfabián, J. A. Vergés, *Phys. Rev. Lett.* **90**, 106801 (2003).
24. V. Vitale, A. Curioni, W. Andreoni, *J. Am. Chem. Soc.* **130**, 5848–5849 (2008).
25. Y. Matsuda, W.-Q. Deng, W. A. Goddard III, *J. Phys. Chem. C* **114**, 17845–17850 (2010).
26. Y. Zhang, T. Ichihashi, E. Landree, F. Nihey, S. Iijima, *Science* **285**, 1719–1722 (1999).
27. J. A. Rodríguez-Manzo et al., *Proc. Natl. Acad. Sci. U.S.A.* **106**, 4591–4595 (2009).
28. M.-S. Wang, D. Golberg, Y. Bando, *Adv. Mater.* **22**, 5350–5355 (2010).
29. R. Martel et al., *Phys. Rev. Lett.* **87**, 256805 (2001).
30. Z. Chen, J. Appenzeller, J. Knoch, Y. M. Lin, P. Avouris, *Nano Lett.* **5**, 1497–1502 (2005).
31. A. E. Morgan, E. K. Broadbent, K. N. Ritz, D. K. Sadana, B. J. Burrow, *J. Appl. Phys.* **64**, 344–353 (1988).
32. W. P. Leroy, C. Detavernier, R. L. Van Meirhaeghe, C. Lavoie, *J. Appl. Phys.* **101**, 053714 (2007).
33. Materials and methods are available as supplementary materials on Science Online.
34. Q. Cao et al., *Nat. Nanotechnol.* **8**, 180–186 (2013).
35. Z. Zhen et al., *IEEE Electron Device Lett.* **34**, 723–725 (2013).
36. K. L. Grosse, M.-H. Bae, F. Lian, E. Pop, W. P. King, *Nat. Nanotechnol.* **6**, 287–290 (2011).
37. ITRS predicts that overall source/drain parasitic resistance per width should be 256 ohm μ m for multigate transistors targeting at high-performance applications at 1.3 nm technol-

ogy node with a L_c less than 4 nm in 2028. However, no manufacturable solutions are known to keep this resistance level upon scaling beyond even a 7-nm node from 2018.

38. J. Zhang, C. Wang, Y. Fu, Y. Che, C. Zhou, *ACS Nano* **5**, 3284–3292 (2011).

ACKNOWLEDGMENTS

We thank J. Bucchignano for technical assistance with electron-beam lithography. Q. C. conceived and designed the experiments. Q. C., S.-J.H., A.D.F., and J.S.T. performed the experiments. Y.Z. performed STEM and EDX analysis. Z.Z. performed in situ XRD. G.S.T. provided carbon nanotubes. Q.C. wrote the manuscript. All authors discussed the results and commented on the manuscript.

SUPPLEMENTARY MATERIALS

www.sciencemag.org/content/350/6256/68/suppl/DC1
Materials and Methods
Figs. S1 to S7
References (39–43)

15 June 2015; accepted 4 August 2015
10.1126/science.aac8006

POLYMER CHEMISTRY

Megasupramolecules for safer, cleaner fuel by end association of long telechelic polymers

Ming-Hsin Wei,^{1*} Boyu Li,^{1*} R. L. Ameri David,¹ Simon C. Jones,² Virendra Sarohia,³ Joel A. Schmitgal,⁴ Julia A. Kornfield^{1†}

We used statistical mechanics to design polymers that defy conventional wisdom by self-assembling into “megasupramolecules” (≥ 5000 kg/mol) at low concentration (≤ 0.3 weight percent). Theoretical treatment of the distribution of individual subunits—end-functional polymers—among cyclic and linear supramolecules (ring-chain equilibrium) predicts that megasupramolecules can form at low total polymer concentration if, and only if, the backbones are long (>400 kg/mol) and end-association strength is optimal. Viscometry and scattering measurements of long telechelic polymers having polycyclooctadiene backbones and acid or amine end groups verify the formation of megasupramolecules. They control misting and reduce drag in the same manner as ultralong covalent polymers. With individual building blocks short enough to avoid hydrodynamic chain scission (weight-average molecular weights of 400 to 1000 kg/mol) and reversible linkages that protect covalent bonds, these megasupramolecules overcome the obstacles of shear degradation and engine incompatibility.

Ultralong polymers (weight-average molecular weight $M_w \geq 5000$ kg/mol) exhibit striking effects on fluid dynamics even at low concentration; for example, polymer concentrations of 100 parts per million (ppm) or less can enable mist control (1, 2) and drag reduction (3). The key to both mist control and drag reduction is the ability of polymers to store energy as they stretch, such that the fluid as a whole resists elongation. The high potency of ultralong linear polymers

is due to the onset of chain stretching at low elongation rates and to the chains' high ultimate conformational elongation (4). For example, increasing M_w from 50 kg/mol to 5000 kg/mol decreases the critical elongation rate by more than three orders of magnitude and increases the ultimate molecular elongation by two orders of magnitude.

Unfortunately, ultralong backbones undergo chain scission during routine handling because hydrodynamic tension builds up along the backbone to a level that breaks covalent bonds; this “shear degradation” continues until the chains shorten to a point that their valuable effects are lost ($M_w < 1000$ kg/mol) (3). Self-assembly of end-associative polymers creates supramolecules that can potentially break and reassociate reversibly, but formation of megasupramolecules ($M_w \geq 5000$ kg/mol) at low concentration has never been realized for two reasons: (i) End-to-end

association at low concentration predominantly leads to rings of a small number of chains (5), and (ii) the size of the building blocks is limited because end association is disfavored when they are larger than 100 kg/mol (6–8).

The current study focuses on megasupramolecules soluble in low-polarity fluids, especially in liquid fuels. Transportation relies on such liquids, presenting the risk of explosive combustion in the event of impact, such as in the 1977 Tenerife airport disaster—an otherwise survivable runway collision that claimed 583 lives in the post-crash fireball. Subsequent tests of ultralong, associative polymers [e.g., ICT's “FM-9,” > 3000 kg/mol copolymer, 5 mole percent (mol %) carboxyl units] in fuel increased the drop diameter in post-impact mist (1, 9), resulting in a relatively cool, short-lived fire. However, these polymers interfered with engine operation (10), and their ultralong backbone—essential for mist control—degraded upon pumping (3).

Our goal is to create megasupramolecules at low concentration that behave like ultralong polymers, exhibiting expanded (“self-avoiding”) conformation at rest and capable of high elongation under flow (Fig. 1A, right). This is in contrast to the collapsed, inextensible supramolecules formed by long chains with associative groups distributed along their backbone (Fig. 1A, left) (11, 12). To mimic ultralong polymers, association must occur at chain ends and be predominantly pairwise. In contrast to multimeric association (6, 8) that leads to flower-like micelles at low concentration (Fig. 1A, center), recent studies have shown that hydrogen bonding can readily achieve pairwise association for short chains with $M_w \leq 50$ kg/mol (7, 13–19). At low concentration, these have no significant rheological effects, consistent with the theory of ring-chain equilibrium (5, 20–23); small rings are the predominant species at low concentration (Fig. 1A, center). We realized that using very long chains as the building blocks would disfavor rings, because the entropy cost of closing a ring increases strongly with chain length.

Despite prior reports indicating that end association becomes difficult as chain length increases

¹Division of Chemistry and Chemical Engineering, California Institute of Technology, Pasadena, CA 91125, USA.

²Electrochemical Technologies Group, Jet Propulsion Laboratory, Pasadena, CA 91109, USA. ³Office of the Chief Technologist, Jet Propulsion Laboratory, Pasadena, CA 91109, USA. ⁴U.S. Army RDECOM TARDEC, 6501 East 11 Mile Road, Warren, MI 48397, USA.

*These authors contributed equally to this work. †Corresponding author. E-mail: jakornfield@cheme.caltech.edu

(6–8), we ventured into the regime of long telechelic polymers (LTPs, Fig. 1A, right; see table S1 for list of polymers) at concentrations below 1%, using theory to guide the selection of molecular structures. To aid material design, we used a lattice model in which the polymer molecular weight simply maps onto the corresponding number of connected lattice sites, each site with a volume equal to that of an effectively freely jointed segment (“Kuhn segment”)—a well-established property tabulated for many polymers (table S2). We chose unsaturated hydrocarbon backbones because of their solubility (remaining in solution down to the freezing point of fuel) and strength (table S3) (24). In addition to the Kuhn segment volume, two additional attributes of the polymer backbone enter into the entropy cost of ring closure: the Kuhn segment length (how short the distance between ends must be for a ring to close) and the excluded volume parameter (how expanded the chain is in solution). The end-association strength (i.e., energy penalty for unpaired ends) enters through the chemical potential of the linear species.

With this treatment, we computed the inventory of all cyclic and linear supramolecules as a function of concentration, backbone length, and end-association strength by solving the system of equilibrium relationships in a population balance model (Fig. 1B). The resulting predictions indicate that an adequate concentration of megasupra-

molecules [e.g., >50 ppm of supramolecules with $M_w \geq 5000$ kg/mol (2)] forms if the concentration of LTPs is 1400 ppm, their backbone has approximately 6000 Kuhn segments [$M_w = 500$ kg/mol for polycyclooctadiene (PCOD)], and their ends associate pairwise with an energy of 16 to 18 kT [modeling after Goldstein (25); figs. S1 to S6]. Furthermore, theory shows that the favorable window of chain lengths and association strengths is relatively narrow. If the backbone is too short (e.g., 200 kg/mol PCOD), the fraction of material that is “lost” to the formation of small cyclics increases, and consequently the concentration of telechelics must be increased. If the backbone is too long (e.g., 1000 kg/mol PCOD), the individual telechelics become susceptible to degradation in strong flows (below). If the association energy is too low (e.g., 14 kT), formation of supramolecules is inadequate. If the association energy is too high (e.g., 20 kT), dangling ends are overly penalized and too few linear species form. Two implications emerge from the computations. One is the need for an unusually strong association strength (because the concentration of end groups, 6 μM , is three orders of magnitude lower than examined previously for supramolecular polymers). The other is the need for an unusually strong backbone to avoid shear degradation of the chains themselves.

The need for end groups that favor pairwise association motivated us to seek hydrogen-bonding

moieties (7, 13–19) that could confer the required association strength. There are several associating supramolecular motifs that offer multidentate hydrogen bond association (7). We tested both a tridentate pair (THY/DAAP) and a hexadentate pair (HR/CA); both failed to produce significant rheological consequences (fig. S7), despite nuclear magnetic resonance (NMR) confirmation that they associate (figs. S8 and S9). In both of these pairs, repulsive secondary electrostatic interactions cut the association strength in half relative to that expected for the number of hydrogen bonds (26), consistent with the association constant of HR/CA, $1.5 \times 10^4 \text{ M}^{-1}$ (corresponding to $\sim 10 \text{ kT}$) (7). Therefore, we turned to charge-assisted hydrogen bonds [CAHBs (27)] that are typically 3 times stronger than ordinary hydrogen bonds (each CAHB provides about 8 to 9 kT binding energy). Simply placing two tertiary amines at each end of the “dibase” chains (DB) and two carboxylic acids at each end of the “diacid” chains (DA) (Fig. 1C) provides an association strength of 16 to 18 kT (27), as recommended by the theoretical results.

To install functional groups at both chain ends with high fidelity (>95%; fig. S10), we use a two-step ring-opening metathesis polymerization (ROMP) protocol (Fig. 1C) (28, 29) in the presence of a chain transfer agent (CTA). Polymers conforming to the theory are synthesized using carefully purified *cis,cis*-1,5-cyclooctadiene (COD; fig. S11) (29, 30) and CTAs bearing functional end groups (COD/CTA ratio > 3000:1, adjusted to give the desired molecular weight). End groups with discrete numbers of hydrogen bonds (difunctional ends, denoted DA or DB; tetrafunctional ends, denoted TA) (Fig. 1C) can be installed after polymerization by conversion of ester- or chloride-ended polymers (which serve as nonassociative controls, NA), with degrees of conversion >95% (figs. S12 to S14). To test predicted effects of backbone length, we also prepared corresponding telechelics with shorter backbones (e.g., Fig. 2A, $M_w \approx 45$, 140, or 300 kg/mol; see table S1).

The formation of megasupramolecules is evident from solution viscosity and multiangle laser light scattering (MALLS) measurements. Shear viscosities show that our longer telechelics do associate into supramolecules [e.g., at 2 mg/ml in cyclohexane, 300k (i.e., 300 kg/mol) DA/DB gives a shear viscosity comparable to 670k NA (Fig. 2A); this holds for tetralin and Jet-A as well (Fig. 2B and fig. S15A)]. Even for telechelics with M_w of 670k—for which the concentration of end groups is less than 10 μM (one-thousandth of previously studied concentrations) (7)—the ends manifestly associate: The viscosity of the 670k DA/DB solution is twice that of the nonassociative control (Fig. 2A), and multimillion-molecular weight supramolecules are confirmed by MALLS (Fig. 2C and fig. S15, C and D). At concentrations as low as 0.22 mg/ml (0.028 wt %), 670k LTPs form supramolecules with an apparent M_w of 2200 kg/mol (Fig. 2C), in accord with the model prediction that M_w corresponds to approximately a three-chain assembly for these conditions, because rings and chains from dimer to tetramer dominate (fig. S16; for 300k DA/DB, fig. S15, C and D). According to

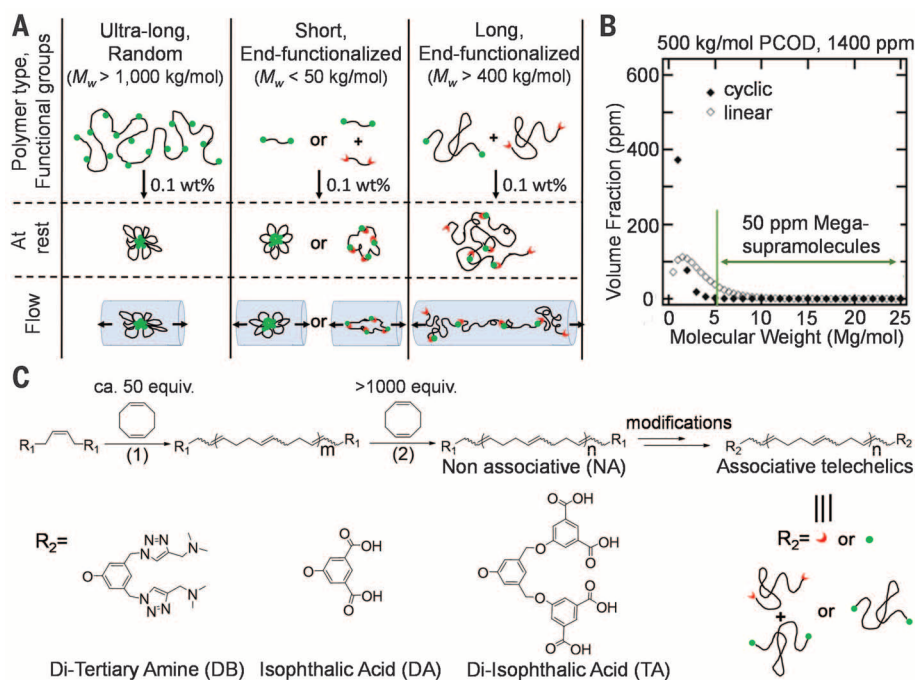


Fig. 1. Design and synthesis of long telechelic polymers (LTPs). (A) Proposed assembly of long telechelic polymers (LTPs) into megasupramolecules (right; only linear species shown) compared to that of randomly functionalized associative polymers (left) and prior end-associative telechelics (center) in terms of degree of polymerization and conformations at rest and in elongational flow. (B) Ring-chain equilibrium distribution of cyclic and linear supramolecules. 1 Mg/mol = 1000 kg/mol. (C) Synthesis of telechelics (nonassociative with R_1 end groups; structures in fig. S12) and postpolymerization conversion to associative telechelics (R_2 end groups, bottom). (1): Grubbs II, dichloromethane (DCM), 40°C, 1 hour; (2): Grubbs II, DCM, 40°C, until stir bar stops (>5 min), equivalents of COD for desired molecular weight. DA, diacid; DB, dibase; TA, tetraacid.

Fig. 2. Evidence of supramolecules in solutions of equimolar mixture of α,ω -di(isophthalic acid) and α,ω -di(di(tertiary amine)) polycyclooctadienes (DA/DB). (A) Effect of size of telechelics ($k = \text{kg/mol}$) on specific viscosity of supramolecular solutions and nonassociative (NA) controls in cyclohexane (CH) at 2 mg/ml (0.25 wt %, 25°C). (B) Effect of solvent on specific viscosity for 2 mg/ml (0.25 wt %) solutions (25°C) of telechelics having $M_w = 670k$ due to both polarity (dielectric constant, table S4) and solvent quality for the backbone (fig. S15A). (C) Static light scattering (35°C) shows that association of $\sim 670k$ DA with DB chains in CH at 0.22 mg/ml (0.028 wt %) produces supramolecules (solid symbols) with an apparent M_w greater than 2000 kg/mol ($2.2M = 2200 \text{ kg/mol}$), which separate into individual building blocks (x) when an excess of a small-molecule tertiary amine is added [open symbols, triethylamine (TEA), 10 $\mu\text{l/ml}$; see fig. S15B for its effect on viscosity]. Curves show predictions of the model for complementary telechelics (1000 kg/mol) in solution at 1400 ppm (solid, supramolecules; dashed, nonassociated telechelics; details in fig. S15C). (D) Concentration-normalized SANS intensities (25°C) for 50k telechelics in d_{12} -cyclohexane at concentrations well below the overlap concentration of NA (2 mg/ml for NA and DB; 0.05 mg/ml for DA and DA/DB) show that DA/DB adopts a relatively open conformation.

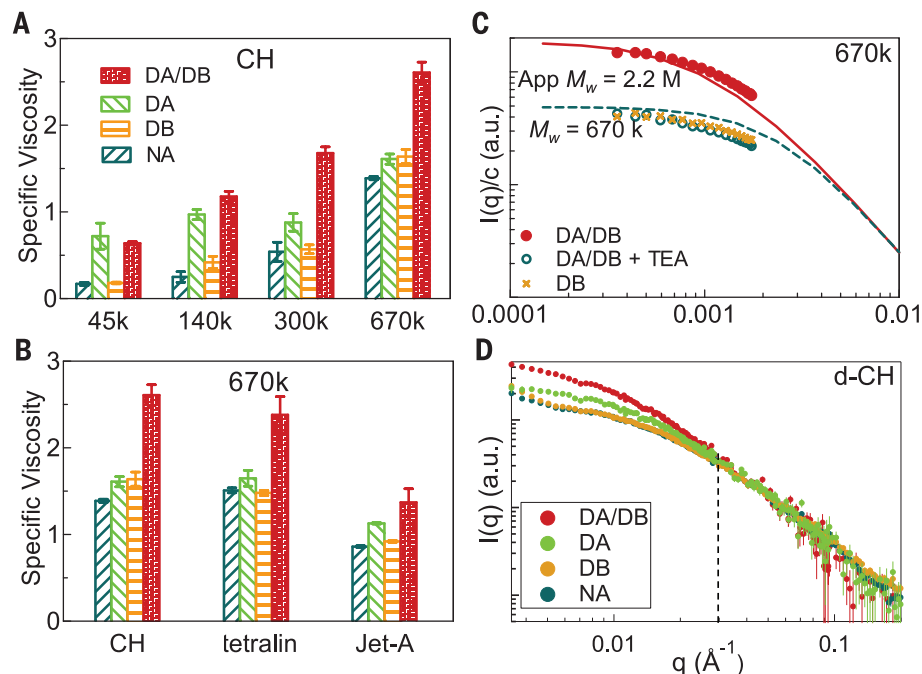
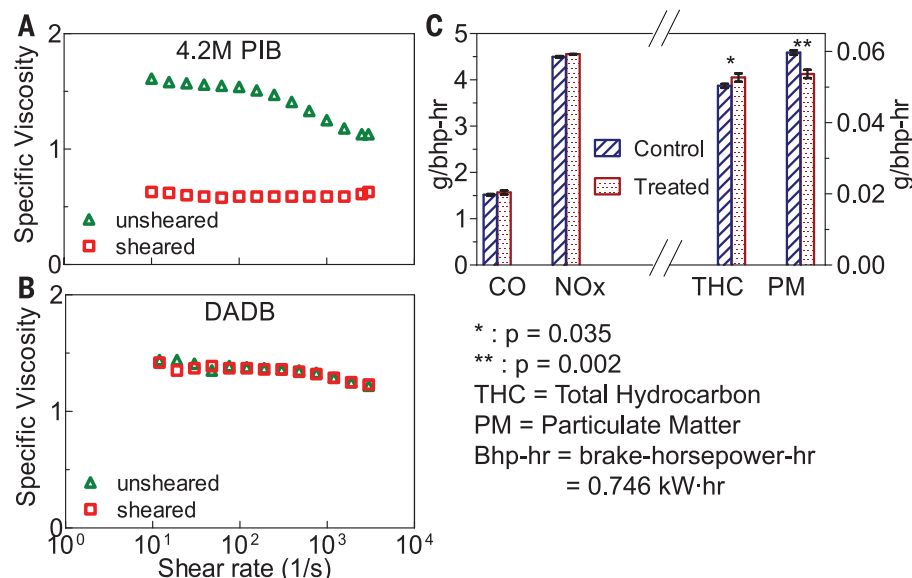


Fig. 3. Shear resistance and engine compatibility of LTPs. (A) The decrease of specific viscosity for 4.2M PIB (1.6 mg/ml, 0.2 wt %) in Jet-A at 25°C after approximately 60 passes through a Bosch fuel pump as shown in fig. S18A (sheared) relative to as-prepared (unsheared) indicates shear degradation. (B) Specific viscosities of 2.4 mg/ml (0.3 wt %) of a 1:1 molar ratio of α,ω -di(isophthalic acid) and α,ω -di(di(tertiary amine)) polycyclooctadienes ($\sim 670k$ DA/DB) in Jet-A at 25°C, sheared versus unsheared. (C) Emission data using an unmodified long-haul diesel engine. Control: untreated diesel. Treated: diesel treated with 0.14 wt % 670k DA/DB (details in fig. S19).



our model, more than one-third of the telechelics are in species with molecular weight greater than the M_w of the supramolecules. Because of the greater strength of CAHB, acid-base pairing dominates over acid-acid pairing (measured by $^1\text{H-NMR}$; fig. S17). Small-angle neutron scattering (SANS) confirms that complementary end-associative polymers avoid the problem of chain collapse. The conformation on length scales up to the radius of gyration (R_g) of the individual chains is just as open for end-associative chains as it is for the corresponding nonassociative chains: at scattering vector $q > 2\pi/R_g \approx 0.03 \text{ \AA}^{-1}$, their

scattering patterns coincide (Fig. 2D). Together, MALLS, NMR, and SANS reveal the molecular basis of the rheological behavior (Fig. 2, A and B)—complementary end association into megasupramolecules with expanded conformations.

Unlike ultralong polyisobutylene (4.2M PIB, 4200 kg/mol) (Fig. 3A), LTPs survive repeated passage through a fuel pump (Fig. 3B and fig. S18) and allow fuel to be filtered easily. The acid number, density, and flash point of the fuel are not affected by megasupramolecules (table S5). Initial tests in diesel engines indicate that fuel treated with LTPs can be used without engine modification (fig. S19);

in a long-haul diesel engine (360HP Detroit Diesel), power and efficiency were not measurably affected (fig. S19B). Additionally, LTPs provided a 12% reduction in diesel soot formation (Fig. 3C).

Experiments under turbulent pipe flow compare the drag reduction effect of ultralong polymers with that of megasupramolecules: For a given pressure drop, the increase of volumetric flow rate with LTPs (670k DA/DB at 0.1 wt %) is comparable to that with ultralong linear polyisobutylene (4200 kg/mol PIB at 0.02 wt %), with the distinction that LTPs retain their efficacy after multiple passes (fig. S20). Similarly, high-speed impact experiments

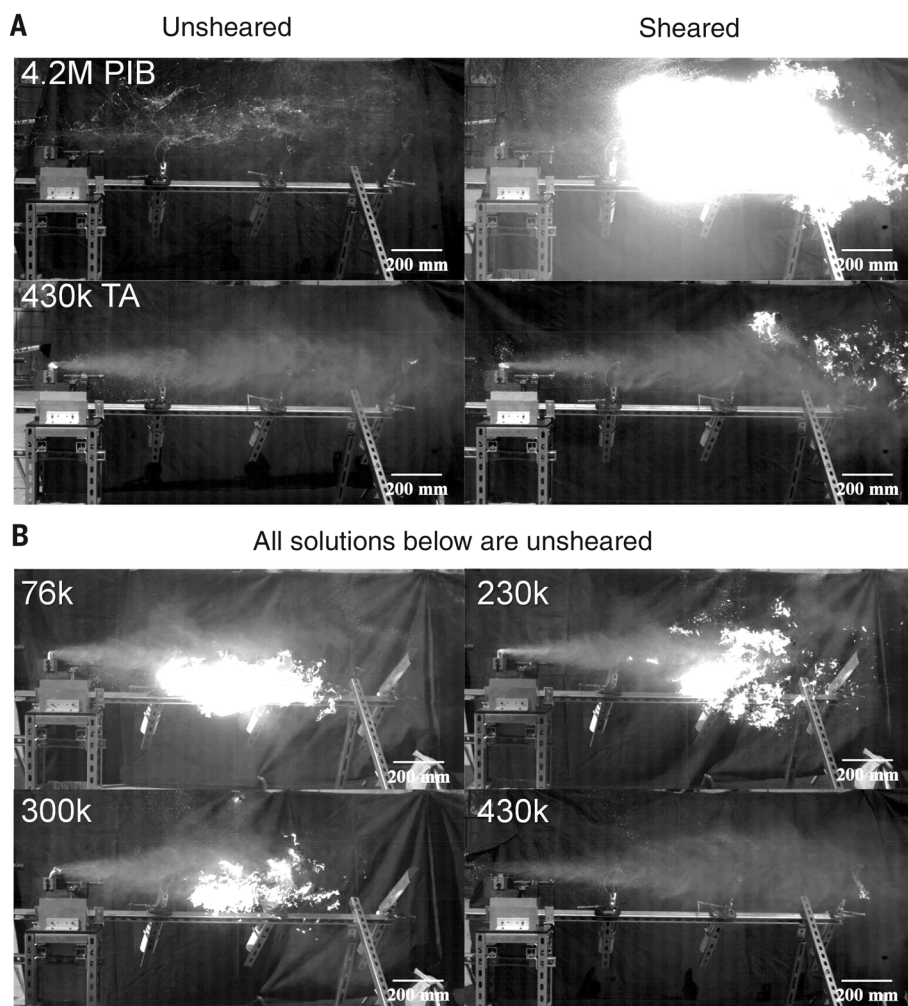


Fig. 4. Impact test in the presence of ignition sources (60 ms after impact, maximal flame propagation) for Jet-A solutions treated with 4.2M PIB or α,ω -di(di-isophthalic acid) polycyclooctadienes (TA). (A) Jet-A with 4.2M PIB (0.35 wt %) and Jet-A with 430k TA (0.3 wt %), “unsheared” and “sheared” as in Fig. 3. (B) Effect of TA molecular weight (76 to 430 kg/mol) in Jet-A at 0.5 wt % (unsheared).

(fig. S21A) show that, unlike ultralong PIB, LTPs retain their efficacy in mist control after repeated passage through a fuel pump. For untreated Jet-A fuel, the impact conditions generate a fine mist through which flames rapidly propagate into a hot fireball within 60 ms (movie S1). Polymer-treated fuel samples are tested in two forms: as prepared (“unsheared”) and after approximately 60 passes through a fuel pump (“sheared”) (fig. S18). Ultralong PIB (4200 kg/mol, 0.35 wt %) is known to confer mist control that prevents flame propagation (Fig. 4A, top left, and movie S2) (2); however, “sheared” PIB loses efficacy (Fig. 4A, top right, and movie S3). LTPs (TA, properties shown in fig. S22) provide mist control both before and after severe shearing (Fig. 4A, bottom, and movies S4 and S5), confirming their resistance to shear degradation (figs. S18C and S22B). The qualitative effects seen in still images at 60 ms (Fig. 4) are quantified by computing the average brightness of each frame (3000 images in 300 ms), which shows that both “unsheared” and “sheared” TA-treated fuels control misting

(fig. S21C). Moreover, the test also proves that the chain length of the telechelics plays a crucial role in mist control (Fig. 4B), consistent with the hypothesis that megasupramolecules are the active species conferring the observed effect.

In the absence of theory, it was not known whether individual chains with lengths below the threshold for shear degradation (1200 kg/mol for PCOD; fig. S18) and end-association strengths much weaker than a covalent bond (150 kT) could form megasupramolecules. Theory inspired us to test telechelics with the predicted end-association strength (16 to 18 kT) and chain lengths, which do form megasupramolecules even at low concentration. They cohere well enough to confer benefits typically associated with ultralong polymers, including mist control and drag reduction. These megasupramolecules reversibly dissociate under flow conditions that would break covalent bonds, allowing the individual LTPs to survive pumping and filtering, and allowing treated fuel to burn cleanly and efficiently in unmodified diesel engines.

REFERENCES AND NOTES

- G. H. McKinley, T. Sridhar, *Annu. Rev. Fluid Mech.* **34**, 375–415 (2002).
- K. K. Chao, C. A. Child, E. A. Grens II, M. C. Williams, *AIChE J.* **30**, 111–120 (1984).
- R. W. Paterson, F. H. Abernathy, *J. Fluid Mech.* **43**, 689–710 (1970).
- R. G. Larson, in *The Structure and Rheology of Complex Fluids* (Oxford Univ. Press, New York, 1999), pp. 132–142.
- H. Jacobson, W. H. Stockmayer, *J. Chem. Phys.* **18**, 1600–1606 (1950).
- M. R. Tant, K. A. Mauritz, G. L. Wilkes, in *Ionomers: Synthesis, Structure, Properties and Applications* (Blackie Academic and Professional, London, 1997), chap. 4.
- S. K. Yang, A. V. Ambade, M. Weck, *Chem. Soc. Rev.* **40**, 129–137 (2011).
- M. A. Winnik, A. Yekta, *Curr. Opin. Colloid Interface Sci.* **2**, 424–436 (1997).
- S. T. J. Peng, R. F. Landel, *J. Non-Newton. Fluid Mech.* **12**, 95–111 (1983).
- National Research Council, Committee on Aviation Fuels with Improved Fire Safety, *Aviation Fuels with Improved Fire Safety: A Proceedings* (National Academies Press, Washington, DC, 1997).
- R. L. A. David *et al.*, *Macromolecules* **42**, 1380–1391 (2009).
- A. M. Pedley, J. S. Higgins, D. G. Peiffer, A. R. Rennie, *Macromolecules* **23**, 2494–2500 (1990).
- J.-M. Lehn, *Science* **295**, 2400–2403 (2002).
- T. Aida, E. W. Meijer, S. I. Stupp, *Science* **335**, 813–817 (2012).
- A. K. Boal *et al.*, *Nature* **404**, 746–748 (2000).
- A. S. Tayi *et al.*, *Nature* **488**, 485–489 (2012).
- O. Ikkala, G. ten Brinke, *Science* **295**, 2407–2409 (2002).
- S.-L. Li, T. Xiao, C. Lin, L. Wang, *Chem. Soc. Rev.* **41**, 5950–5968 (2012).
- R. P. Sijbesma *et al.*, *Science* **278**, 1601–1604 (1997).
- Z.-R. Chen, J. P. Claverie, R. H. Grubbs, J. A. Kornfield, *Macromolecules* **28**, 2147–2154 (1995).
- K. F. Freed, *J. Chem. Phys.* **136**, 244904 (2012).
- T. F. A. de Greef, G. Ercolani, G. B. W. L. Ligthart, E. W. Meijer, R. P. Sijbesma, *J. Am. Chem. Soc.* **130**, 13755–13764 (2008).
- R. G. Petschek, P. Pfeuty, J. C. Wheeler, *Phys. Rev. A* **34**, 2391–2421 (1986).
- M. R. Nyden, S. I. Stoliarov, P. R. Westmoreland, Z. X. Guo, C. Jee, *Mater. Sci. Eng. A* **365**, 114–121 (2004).
- R. E. Goldstein, *J. Chem. Phys.* **84**, 3367–3378 (1986).
- J. Sartorius, H.-J. Schneider, *Chem. Eur. J.* **2**, 1446–1452 (1996).
- G. Gilli, P. Gilli, in *The Nature of the Hydrogen Bond: Outline of a Comprehensive Hydrogen Bond Theory* (Oxford Univ. Press, Oxford, 2009), pp. 147–192.
- M. A. Hillmyer, S. T. Nguyen, R. H. Grubbs, *Macromolecules* **30**, 718–721 (1997).
- S. Ji, T. R. Hoyer, C. W. Macosko, *Macromolecules* **37**, 5485–5489 (2004).
- A. Nickel *et al.*, *Top. Catal.* **55**, 518–523 (2012).

ACKNOWLEDGMENTS

Funding for this research was provided from U.S. Army TARDEC, FAA, and NASA (NAS7-03001) and the Gates Grubstake Fund. B.L. is grateful for support from the Schlumberger Foundation Faculty for the Future Program. We thank P. Arakelian (GALCIT) and T. Wynne (JPL) for assistance with the fuel impact tests; B. Hammouda (NIST) and L. He (ORNL) for assistance with SANS; T. Durbin, R. Russell, D. Pacocha, and K. Bumiller at UCR CE-CERT for assistance with engine tests; A. Meyer at Wyatt Technology and Caltech graduate student J. Kim for assistance with MALLS; and Caltech undergraduates S. Li and A. Guo for assistance with shear degradation tests and rheological measurements. A patent application (WO/2014/145920) based on some results reported here has been submitted.

SUPPLEMENTARY MATERIALS

www.sciencemag.org/content/350/6256/72/suppl/DC1
Materials and Methods
Figs. S1 to S22
Tables S1 to S5
Movies S1 to S5
References (31–40)

30 March 2015; accepted 30 July 2015
10.1126/science.aab0642

EARTH HISTORY

State shift in Deccan volcanism at the Cretaceous-Paleogene boundary, possibly induced by impact

Paul R. Renne,^{1,2*} Courtney J. Sprain,^{1,2} Mark A. Richards,² Stephen Self,² Łoż Vanderkluyzen,³ Kanchan Pande⁴

Bolide impact and flood volcanism compete as leading candidates for the cause of terminal-Cretaceous mass extinctions. High-precision $^{40}\text{Ar}/^{39}\text{Ar}$ data indicate that these two mechanisms may be genetically related, and neither can be considered in isolation. The existing Deccan Traps magmatic system underwent a state shift approximately coincident with the Chicxulub impact and the terminal-Cretaceous mass extinctions, after which ~70% of the Traps' total volume was extruded in more massive and more episodic eruptions. Initiation of this new regime occurred within ~50,000 years of the impact, which is consistent with transient effects of impact-induced seismic energy. Postextinction recovery of marine ecosystems was probably suppressed until after the accelerated volcanism waned.

The Deccan Traps are the most recent of several large ($>10^6 \text{ km}^3$) continental flood basalt provinces that are circumstantially implicated in mass extinctions (1, 2). The extent to which Deccan volcanism was a factor in the biotic crises that terminated the Mesozoic Era has been heavily debated, largely because the Chicxulub bolide impact provides a plausible mechanism for severe and abrupt environmental perturbations (3). The temporal coincidence between the impact and mass extinctions at the Cretaceous-Paleogene boundary (KPB) is well established (4) and implicates the bolide impact as a forcing mechanism. However, the possibility of a contributing role for volcanism, presumably through the discharge of climate-modifying gases, remains plausible in view of data showing that the immense flood basalt eruptions of the Deccan Traps spanned the KPB. A temporal correlation between other major flood volcanic events and extensive environmental transitions (1, 2) illustrates the potential for the Deccan Traps alone to have caused the KPB extinctions. We combined high-precision $^{40}\text{Ar}/^{39}\text{Ar}$ dating of the lavas with previously reported U/Pb dates (5) and lava volume estimates (6) to infer that the Chicxulub impact initiated a substantial acceleration of Deccan volcanism within ~50 thousand years (ky). This probably contributed to the extinctions and moderated subsequent recovery.

The general coincidence of the Deccan Traps with the KPB, evident in geochronologic and paleomagnetic data (7), is not established with sufficient precision or stratigraphic control to locate

the boundary within the lava stratigraphy. Limited constraints on the detailed history and tempo of volcanism obscure possible mechanisms that would relate the Deccan Traps to KPB phenomena, because these factors modulate volatile input to the atmosphere (8). The absence of reliable estimates of magma volume over time challenges models that suggest extrusion of the Traps in three discrete pulses (9, 10). The geochemically defined stratigraphy of Deccan Group volcanics in the best-studied region, the Western Ghats, is divided into formations composing the Kalsubai,

Lonavala, and Wai Subgroups, in ascending order. Each formation comprises multiple eruptive units. Paleomagnetic secular variation suggests that the eruptions were highly episodic, with a lower mean eruption frequency in the youngest and most widely distributed subgroup, the Wai (11, 12). Lavas with broadly contemporaneous ages and geochemical and isotopic affinities with the Wai Subgroup occur as far north as Rajasthan (13), as far northeast as the Mandla lobe (~1000 km from the Western Ghats escarpment) (14, 15), and as far east as Rajahmundry on the Bay of Bengal coast (16).

The Wai Subgroup contains numerous oxidized horizons ("red boles") between lava flows, interpreted as paleosols (17–19), which are consistent with the inference of a lower eruption frequency. Red boles are much less prevalent in the underlying Lonavala and Kalsubai Subgroups (11, 20), providing possible evidence for variable long-term eruption rates during the lifetime of the Deccan magma system.

A discontinuity in lava geochemistry, flow volumes, and feeder dike orientations occurs between the Lonavala and Wai Subgroups (6). This discontinuity coincides with geomorphic evidence of widespread fractures and an abrupt change in susceptibility to erosion, approximately at the contact between these subgroups (6). It also coincides with the transition to more episodic, albeit more voluminous, eruptions in the Wai Subgroup, as inferred from paleomagnetic secular variation and the frequency of red bole horizons. Existing age constraints are compatible with the hypothesis that the KPB coincides with the transition from the Lonavala Subgroup (Bushe Formation) to the Wai Subgroup (Poladpur Formation) (6).

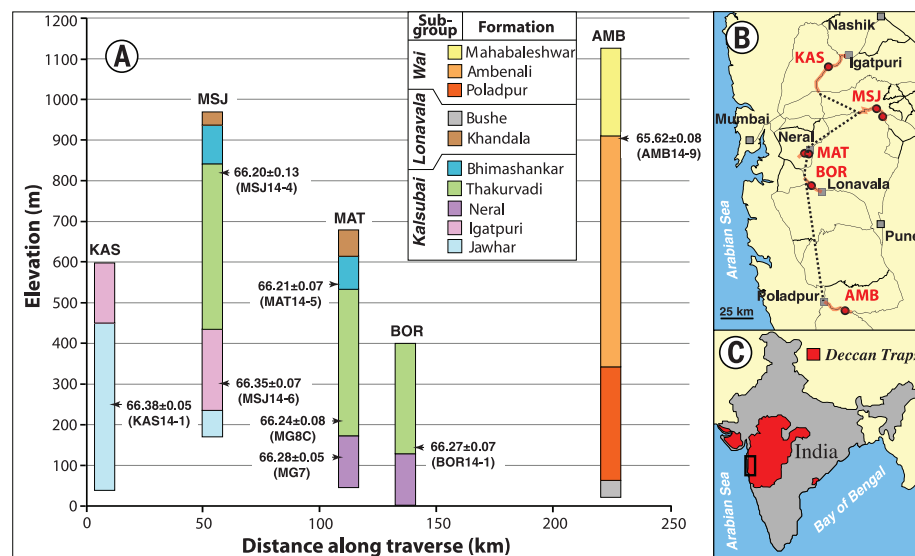


Fig. 1. Stratigraphic and geographic context of the samples. (A) Stratigraphic sections with dated horizons indicated, corresponding to the five traverses shown by red lines in (B). Ages (millions of years ago) are shown with uncertainties (SEM). Sample numbers for the dated horizons are given in parentheses. **(B)** Stratigraphy adapted from (11) for traverses KAS (Shahapur-Igatpuri section), MAT (Matheran-Neral section), BOR (Khopali-Khandala section), and AMB (Mahabaleshwar-Poladpur section). Stratigraphic data for the MSJ traverse (Malshej Ghat section) were acquired in this study. The dotted black line connects the bases of the traverses. The black rectangle in (C) shows the location of the area shown in (B).

¹Berkeley Geochronology Center, 2455 Ridge Road, Berkeley, CA 94709, USA. ²Department of Earth and Planetary Science, University of California-Berkeley, Berkeley, CA 94720, USA. ³Department of Biodiversity, Earth and Environmental Science, Drexel University, Philadelphia, PA 19104, USA. ⁴Department of Earth Sciences, Indian Institute of Technology Bombay, Powai, Mumbai 400 076, India.

*Corresponding author. E-mail: preenne@bgc.org

Available geochronologic data are not sufficiently precise to resolve age variations of less than 100 ky, with the exception of U/Pb zircon data (5). These data reveal protracted zircon age distributions, requiring subjective interpretation (7). Additionally, material suitable for U/Pb geochronology is reported only in rare bodies interpreted as magma segregation features and in red boles, which are sparse in both the Lonavala and Kalsubai Subgroups. These limitations restrict both the extent and the overall resolution of Deccan stratigraphy that can be determined from the U/Pb technique. Here, we report high-resolution $^{40}\text{Ar}/^{39}\text{Ar}$ dating of igneous plagioclase, which has an unambiguous genetic relationship to the host lavas and negligible retention of pre-eruptive radiogenic ^{40}Ar at basalt eruption temperatures $>1100^\circ\text{C}$. We used detailed stepwise heating, dense bracketing of samples with standards during neutron irradiation, and detailed characterization of the interfering nuclear reactions to obtain data of appropriate precision and accuracy to clarify the eruptive history of the Deccan Traps (7).

We obtained $^{40}\text{Ar}/^{39}\text{Ar}$ plateau ages (fig. S3) for one to four aliquots of samples from each formation in the Kalsubai Subgroup and from the Ambenali Formation of the Wai Subgroup, in multiple sections across the Western Ghats region (Fig. 1). Where formation assignments were ambiguous, we analyzed samples geochemically to confirm their placement in the chemical stratigraphy by which the formations are defined (21). Weighted mean plateau ages placed in a composite stratigraphic section (Fig. 2) are generally consistent with previously reported U/Pb zircon data (5), within uncertainties.

Based on a composite stratigraphic section (6), our data indicate rapid eruption of no less than

~70% of the Kalsubai Subgroup before the KPB, over an interval of 173 ± 84 ky, as defined by the age difference between our samples from the Jawhar and Bhimashankar Formations (Fig. 2). The thicknesses of individual Kalsubai and Lonavala Subgroup formations vary substantially throughout the province; thus, inferences about mean magma generation rates based on values from any one section may be misleading. More meaningful inferences can be drawn from best estimates of volume (weighted by subgroup areal extent) for each formation (6), which indicate a volume of $71 \times 10^3 \text{ km}^3$ for this time interval, corresponding to a mean magma generation rate of $\sim 0.4 \pm 0.2 \text{ km}^3/\text{year}$.

The KPB, dated at 66.043 ± 0.010 (without systematic sources) or ± 0.043 [with systematic sources (7)] million years ago (22), occurred less than 165 ± 68 ky after the emplacement of the Kalsubai Subgroup, within the time represented by the Khandala, Bushe, Poladpur, or possibly lower Ambenali Formations. The time interval between the eruption of the basal Bhimashankar and uppermost Ambenali Formations is 547 ± 241 ky, during which $\sim 300 \times 10^3 \text{ km}^3$ of lava was extruded at a mean rate of $\sim 0.6 \text{ km}^3/\text{year}$. We determined a magma generation rate for the Wai Subgroup from U/Pb zircon dates (5) in the upper Ambenali and mid-Mahabaleshwar Formations, finding that a volume of $111 \times 10^3 \text{ km}^3$ of lava was extruded at a mean rate of $0.9 \pm 0.3 \text{ km}^3/\text{year}$. The mean long-term eruption rate represented by the Wai Subgroup, where it is well constrained, appears to be approximately double the rate represented by the Kalsubai Subgroup.

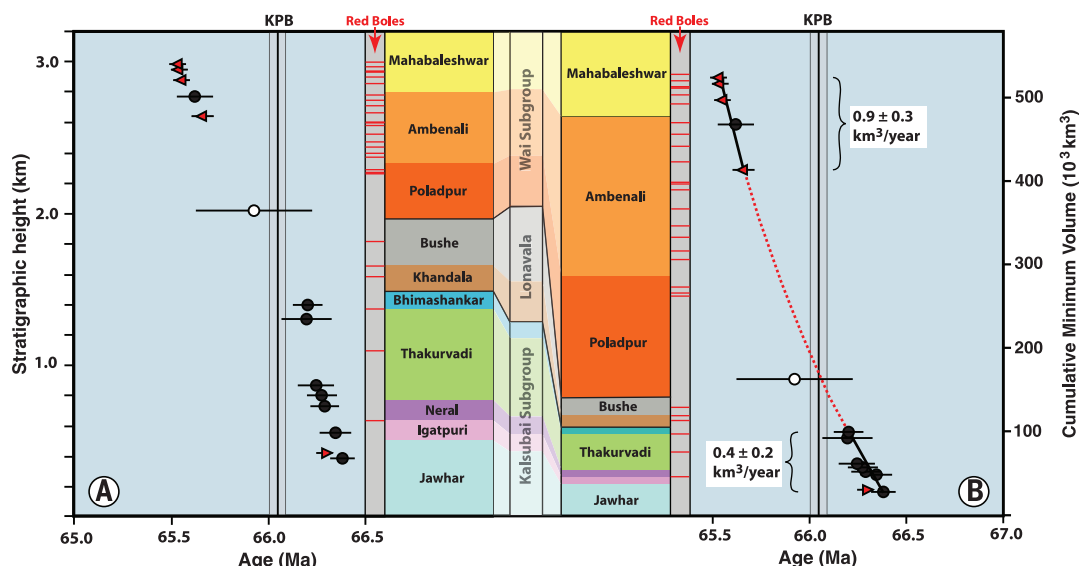
The increased mean magma production rate during the Wai Subgroup eruptions coincides with an abundance of red bole (weathering) horizons (Fig. 2), which first appear frequently in

the Ambenali Formation and persist into the Mahabaleshwar Formation. The cumulative time represented by red boles in the Western Ghats has been estimated to be on the order of 300 ky (11), most of which falls in the time interval represented by the Wai Subgroup. During the Wai Subgroup time interval, it appears that the mean eruption frequency decreased dramatically, whereas the lava volume per flow field (per single eruptive event) increased, so that the mean magma eruption rate approximately doubled. Alternatively, the increased abundance of red boles in the Wai Subgroup may reflect an increase in weathering rates due to climate change (greenhouse conditions) after the KPB.

The decrease in eruption frequency coincides generally with a transition from lava fields dominated by compound pahoehoe and rare a'a flows in the Kalsubai Subgroup (23) to lava fields dominated by thicker, laterally extensive, inflated pahoehoe sheet lobes in the Wai Subgroup (20, 24). The initiation of this transition appears to occur across the Lonavala Subgroup, with compound units absent in parts of the Khandala Formation but present in the Bushe Formation. In our study areas, sheet lobes begin to dominate near the base of the Wai Subgroup within the Poladpur Formation, where individual sheet lobes reach the greatest observed thickness of more than 60 m (20). The sparse occurrence of red boles in the Poladpur Formation suggests that the high eruption frequency continued until the time of the Ambenali Formation, at which point large eruptions became punctuated by longer repose intervals (represented by the red boles). During these repose intervals, occasional zircon-bearing, distally sourced silicic tephra apparently accumulated in developing paleosols (5).

Fig. 2. Eruptive history of the Western Ghats region.

(A) Composite stratigraphic thicknesses and (B) cumulative volumes, after (6), versus age for formations in the Western Ghats region. Included are (i) all $^{40}\text{Ar}/^{39}\text{Ar}$ plagioclase dates with uncertainties (SEM) of 300 ky or less, comprising data from this study (filled circles) and a previous study (open circles) (35), and (ii) previously reported U/Pb zircon dates (red triangles) (5). All ages are shown with 1σ uncertainties (bars), including from systematic sources. The apices of the triangles point in the direction of true age in the event of a possible bias in U/Pb ages (supplementary text). Sample positions are scaled from formation thicknesses in the sections sampled, as shown in Fig. 1A. Red boles are scaled from previous studies (11, 20) and our observations. New $^{40}\text{Ar}/^{39}\text{Ar}$ dates define the mean eruption rate represented by the Kalsubai Subgroup ($0.4 \pm 0.2 \text{ km}^3/\text{year}$); previously reported U/Pb zircon dates (5) define the mean eruption rate represented by part of the Wai Subgroup ($0.9 \pm 0.3 \text{ km}^3/\text{year}$). The dotted red curve shows a parabolic fit, representing possible continuous change in eruption rates between the time intervals of the Kalsubai and upper Wai Subgroups. The Panhala and Desur Formations, which overlie the Mahabaleshwar Formation with limited extents, are not shown. Ma, millions of years ago.



The transition from high-frequency, low-volume eruptions to low-frequency, high-volume eruptions suggests a fundamental change in the magma plumbing system. A state shift in the threshold properties of one or more magma chambers would have been required for the latter style of eruptions to occur. The Wai Subgroup lavas mark a sharp increase in mantle contributions relative to crustal contributions, are the least crustally contaminated of the entire Deccan Group (21, 25–27), and overlie Bushe Formation lavas that are the most crustally contaminated of the Deccan Group (21, 25, 26). This suggests a reduction in the magma-crust interface area, relative to magma volume, through an expansion of a deep-crustal magma chamber or a consolidation of multiple chambers; a shorter residence time of magma in the crust; or some combination of these factors.

A magma chamber expansion commencing with the emplacement of the Poladpur Formation, coupled with longer repose times indicated by the increased occurrence of red boles, would be associated with more extensive crystal fractionation (28). Wai Subgroup lavas are the most highly fractionated in the entire sequence (21, 25, 27). These and other independent lines of geochemical and tectonic evidence are all consistent with a sudden increase in magma flux from the Deccan mantle source (6). Larger flux rates would lead to larger magma chambers (presumably at Moho depths), longer time intervals to generate sufficient buoyancy to drive eruptions (via some combination of crystal fractionation and volatile exsolution), and hence larger and less frequent eruptions (29). We conclude that the Deccan magmatic system, at the source of the Western Ghats flood basalts and, by inference, the main portion of the Deccan Volcanic Province, underwent a fundamental transition upon initiation of the Wai Subgroup eruptions.

Straightforward interpolation of the age-volume data (Fig. 2B) suggests that this transition occurred within 50 ky of the Chicxulub impact and the KPB. This is an even closer temporal coincidence than indicated by previous analyses (6), which also suggested that strong seismic waves produced by the impact could have triggered increased volcanism. The close temporal coincidence of the impact and the accelerated volcanism makes it difficult to deconvolve the environmental perturbations attributable to each mechanism. The KPB extinctions probably resulted from the superposed effects of both phenomena.

The coincidence of widespread seismites at the Triassic-Jurassic boundary (30), correlated with the Central Atlantic Magmatic Province (31), may represent another example of seismic triggering of continental flood volcanism. The mechanisms by which seismic events trigger volcanic activity are not understood in detail (32), but they probably involve either a transient increase in the effective permeability of existing volcanic systems or, perhaps, induced volatile exsolution from supersaturated magma (33). These transient effects may not account for the subsequent episodic repetition of larger-volume, lower-frequency eruptions throughout the Wai Subgroup interval;

however, the repetition of such eruptions might reflect a state change toward longer recharge times due to magma chamber enlargement, perhaps combined with other episodic seismic disturbances (such as from large regional tectonic earthquakes). Eruptions that emplaced the volumetrically dominant formations of the Wai Subgroup continued for ~500 ky after the KPB, which is comparable with the time lag between the KPB and the initial stage of ecological recovery in marine ecosystems (34). The effects of the Wai Subgroup eruptions may have suppressed postextinction recovery until the final stages of the time interval represented by the Mahabaleshwar Formation.

REFERENCES AND NOTES

1. V. E. Courtillot, P. R. Renne, C. R. Geosci. **335**, 113–140 (2003).
2. P. B. Wignall, *Earth Sci. Rev.* **53**, 1–33 (2001).
3. P. Schulte et al., *Science* **327**, 1214–1218 (2010).
4. P. R. Renne et al., *Science* **339**, 684–687 (2013).
5. B. Schoene et al., *Science* **347**, 182–184 (2015).
6. M. A. Richards et al., *Geol. Soc. Am. Bull.* (2015).
7. Materials and methods are available as supplementary materials on Science Online.
8. S. Self, M. Widdowson, T. Thordarson, A. E. Jay, *Earth Planet. Sci. Lett.* **248**, 518–532 (2006).
9. A. L. Chenet, X. Quidelleur, F. Fluteau, V. Courtillot, S. Bajpai, *Earth Planet. Sci. Lett.* **263**, 1–15 (2007).
10. G. Keller et al., *Earth Planet. Sci. Lett.* **341–344**, 211–221 (2012).
11. A. L. Chenet et al., *J. Geophys. Res. Solid Earth* **114**, B06103 (2009).
12. A. L. Chenet, F. Fluteau, V. Courtillot, M. Gerard, K. V. Subbarao, *J. Geophys. Res. Solid Earth* **113**, B04101 (2008).
13. A. Sen et al., *J. Asian Earth Sci.* **59**, 127–140 (2012).
14. J. P. Shrivastava, R. A. Duncan, M. Kashyap, *Lithos* **224–225**, 214–224 (2015).
15. Z. X. Peng, J. J. Mahoney, P. R. Hooper, J. D. Macdougall, P. Krishnamurthy, *J. Geophys. Res. Solid Earth* **103**, 29843 (1998).
16. S. Self, A. E. Jay, M. Widdowson, L. P. Keszthelyi, *J. Volcanol. Geotherm. Res.* **172**, 3–19 (2008).
17. P. Ghosh, M. R. G. Sayeed, R. Islam, S. M. Hudekari, *Palaeogeogr. Palaeoclimatol. Palaeoecol.* **242**, 90–109 (2006).
18. J. P. Shrivastava, M. Ahmad, S. Srivastava, *J. Geol. Soc. India* **80**, 177–188 (2012).
19. M. Widdowson, J. N. Walsh, K. V. Subbarao, *Geol. Soc. Spec. Publ.* **120**, 269–281 (1997).

20. A. E. Jay, thesis, The Open University, Milton Keynes, UK (2005).
21. J. E. Beane, C. A. Turner, P. R. Hooper, K. V. Subbarao, J. N. Walsh, *Bull. Volcanol.* **48**, 61–83 (1986).
22. C. J. Sprain, P. R. Renne, G. P. Wilson, W. A. Clemens, *Geol. Soc. Am. Bull.* **127**, 393–409 (2015).
23. R. J. Brown, S. Blake, N. R. Bondre, V. M. Phadnis, S. Self, *Bull. Volcanol.* **73**, 737–752 (2011).
24. N. R. Bondre, R. A. Duraiswami, G. Dole, *Bull. Volcanol.* **66**, 29–45 (2004).
25. P. C. Lightfoot, C. J. Hawkesworth, C. W. Devey, N. W. Rogers, P. W. C. Van Calsteren, *J. Petrol.* **31**, 1165–1200 (1990).
26. Z. X. Peng, J. J. Mahoney, P. Hooper, C. Harris, J. E. Beane, *Geochim. Cosmochim. Acta* **58**, 267–288 (1994).
27. J. J. Mahoney et al., *Earth Planet. Sci. Lett.* **60**, 47–60 (1982).
28. C. J. Hawkesworth et al., *J. Petrol.* **41**, 991–1006 (2000).
29. L. Karlstrom, M. Richards, *J. Geophys. Res. Solid Earth* **116**, B08216 (2011).
30. M. J. Simms, *Geology* **31**, 557 (2003).
31. A. Marzoli et al., *Science* **284**, 616–618 (1999).
32. M. Manga, E. Brodsky, *Annu. Rev. Earth Planet. Sci.* **34**, 263–291 (2006).
33. R. J. Carey et al., *J. Geophys. Res. Solid Earth* **117**, B11202 (2012).
34. H. K. Coxall, S. D'Hondt, J. C. Zachos, *Geology* **34**, 297 (2006).
35. P. Hooper, M. Widdowson, S. Kelley, *Geology* **38**, 839–842 (2010).

ACKNOWLEDGMENTS

This work was funded by the Ann and Gordon Getty Foundation and by the Esper S. Larsen Fund of the University of California–Berkeley. C.J.S. was supported by a NSF Graduate Research Fellowship. L.V.'s participation was supported by NSF grant EAR-1250440. We thank W. Alvarez, S. Finnegan, C. Guns, R. Ickert, M. Manga, C. Marshall, A. Marzoli, R. Mundil, and H. Sheth for discussion; T. Becker and A. Jaouni for laboratory assistance; and H. Sheth for field assistance. Data are available in the supplementary materials.

SUPPLEMENTARY MATERIALS

www.sciencemag.org/content/350/6256/76/suppl/DC1
Materials and Methods
Supplementary Text
Figs. S1 to S4
Table S1
References (36–69)

8 June 2015; accepted 26 August 2015
10.1126/science.aac7549

WATER STRUCTURE

Ultrafast 2D IR spectroscopy of the excess proton in liquid water

Martin Thämer,¹ Luigi De Marco,^{1,2} Krupa Ramasesha,^{2,*}
Aritra Mandal,^{1,2} Andrei Tokmakoff^{1,†}

Despite decades of study, the structures adopted to accommodate an excess proton in water and the mechanism by which they interconvert remain elusive. We used ultrafast two-dimensional infrared (2D IR) spectroscopy to investigate protons in aqueous hydrochloric acid solutions. By exciting O–H stretching vibrations and detecting the spectral response throughout the mid-IR region, we observed the interaction between the stretching and bending vibrations characteristic of the flanking waters of the Zundel complex, $[\text{H}(\text{H}_2\text{O})_2]^+$, at 3200 and 1760 cm^{-1} , respectively. From time-dependent shifts of the stretch-bend cross peak, we determined a lower limit on the lifetime of this complex of 480 femtoseconds. These results suggest a key role for the Zundel complex in aqueous proton transfer.

Acid-base chemistry and most biological redox chemistry are governed by the transport of protons through water. Aqueous proton transfer is generally accepted to occur along hydrogen bonds through sequential hops of an excess proton from one solvating water mol-

ecule to the next. Although this widely accepted picture, known as the Grotthuss mechanism, captures the concept of long-range charge translocation without transport of a particular proton, numerous basic questions remain regarding the rapidly evolving structure of an aqueous proton (1).

Does the dominant structure resemble the Eigen complex, $\text{H}_3\text{O}(\text{H}_2\text{O})_3^+$ (a triply hydrated hydronium ion), or the Zundel complex, $\text{H}(\text{H}_2\text{O})_2^+$ (a proton that is equally shared between two water molecules)? What are the relative stabilities of these species? How do they interconvert during proton transport, and what role does the dynamics of solvating water molecules play in this process? Though these questions have been studied extensively via molecular dynamics (MD) simulations (1–4), experiments that entail visualizing time-dependent proton structures on femtosecond time scales have not been carried out. To address such questions, we performed ultrafast infrared (IR) spectroscopy experiments to observe the time-dependent vibrations associated with an excess proton within the fluctuating potential defined by its solvating water. Our experiments on hydrochloric acid solutions offer evidence for the presence of a metastable Zundel complex with a sufficiently long lifetime that it cannot only be a transition state between Eigen configurations.

A number of computational studies employing *ab initio* MD and empirical valence bond simulations have been performed to investigate the nature of the solvated proton. These studies have reached varying conclusions regarding the dominant structure of the solvated proton (Zundel or Eigen) and the proton-transport mechanism (2, 5–12). Several mechanisms have been described that involve the exchange of Zundel and/or Eigen complexes with varying degrees of distortion or delocalization. In part, these differing interpretations reflect the difficulty in classifying Zundel and Eigen species within a continuum of rapidly evolving hydrogen bond configurations. The variations of hydrogen bond lengths and angles between the two structures are small, and thermal fluctuations cause them to undergo rapid distortions (2). To gain insight into these processes and to help answer the questions presented above, experiments that can identify Zundel and Eigen configurations in the liquid phase and directly monitor the time evolution of these structures are required.

Aqueous proton configurations and their ultrafast interconversion give rise to broad overlapping spectral features in the linear IR absorption spectrum of strong acids. In addition to the O–H stretch absorption (3400 cm^{-1}) and the HOH bend vibration (1650 cm^{-1}) that arise from bulk-like water, the IR spectra of strong acids feature a broad absorption continuum that extends from the O–H stretching band to frequencies below 1000 cm^{-1} (Fig. 1) (13). This was originally explained by noting that the functional form of the potential of a proton shared by two oxygens could vary strongly between weakly anharmonic (for a proton bound to one of the water molecules) and double well (an

equally shared proton) and that the vibrational transitions associated with these potentials would span the entire continuum band (14). The continuum is not entirely featureless, however, but shows a “shoulder” on the high-frequency side of the H_2O bend (1760 cm^{-1}) and a broad absorption maximum at 1200 cm^{-1} (15).

Although a detailed experimental assignment correlating IR continuum frequencies to Eigen and Zundel structures in the liquid phase is missing, one may turn to gas-phase studies of protonated water clusters (16–18), MD simulations

(19–22), and *ab initio* calculations (23) for guidance. Gas-phase studies offer the ability to determine the vibrational spectra of well-defined Zundel and Eigen structures. Though it is unclear whether assignments of specific structures and vibrational modes from gas-phase studies will carry into the liquid phase, they provide insight into the correlated vibrational frequency shifts between different proton configurations. Based on the consistent observations across these studies, we propose the assignments shown in Fig. 1. Cluster studies (17, 20, 21) measure the O–H stretching vibrations

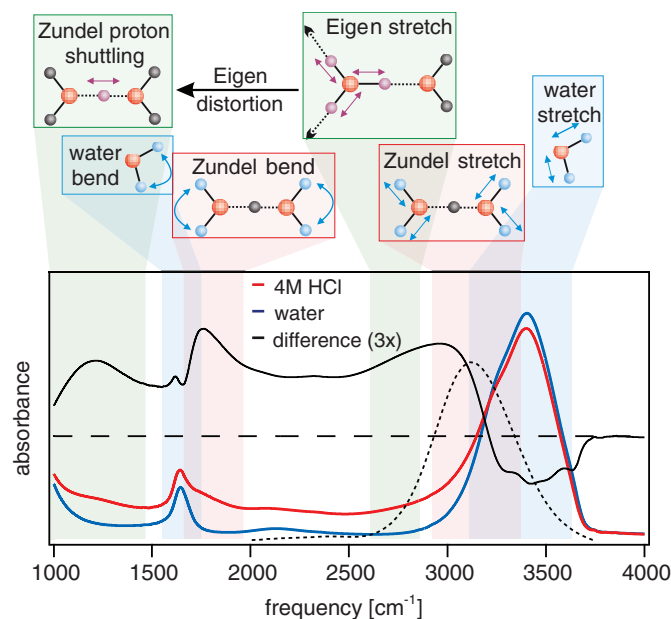


Fig. 1. Infrared spectra for water (blue trace) and 4 M HCl (red trace).

The black solid trace indicates the difference spectrum between 4 M HCl and water. The dashed trace represents the spectrum of the pump pulses used in the nonlinear experiments. Cartoons represent the proposed vibrational assignments of the different spectral features to vibrations of the solvated proton. The vibrations of the excess proton, bulk water, and flanking water molecules are shaded green, blue, and red, respectively. The horizontal dashed line is the zero line for the difference spectrum.

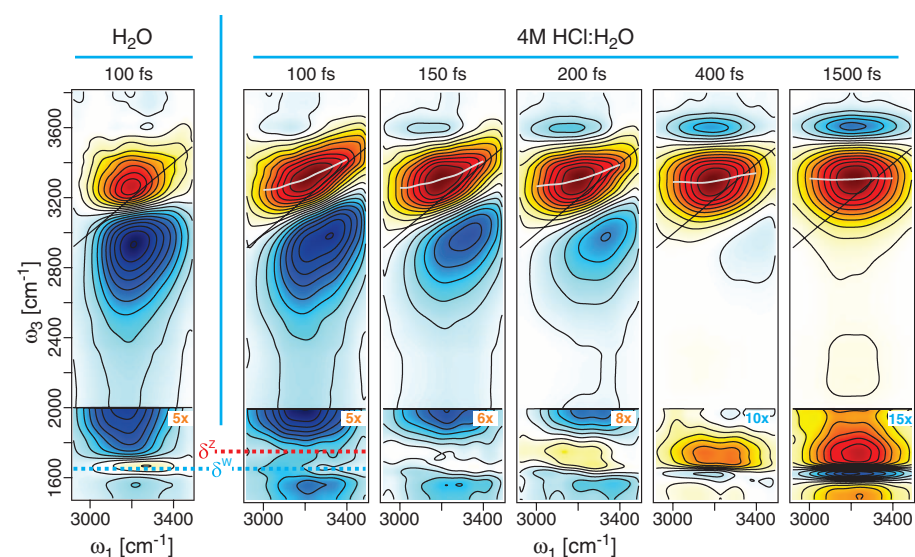


Fig. 2. Two-dimensional IR spectra of 4 M HCl in H_2O as a function of waiting time τ_2 . Bleaches are in red, induced absorptions in blue. The $\tau_2 = 100\text{ fs}$ spectrum of H_2O is shown for comparison. Center lines are depicted in white on the O–H stretch bleach. Detection frequencies corresponding to the Zundel bend and H_2O bend are labeled δ^Z and δ^W , respectively.

¹Department of Chemistry, Institute for Biophysical Dynamics, and James Franck Institute, The University of Chicago, Chicago, IL 60637, USA. ²Department of Chemistry, Massachusetts Institute of Technology, Cambridge, MA 02139, USA.

*Present address: Combustion Research Facility, Sandia National Laboratories, Livermore, CA 94550, USA. †Corresponding author. E-mail: tokmakoff@uchicago.edu

of the Eigen species' hydronium core at 2650 cm^{-1} , and MD simulations indicate that its breadth in the liquid spans several hundred wave numbers (19, 22). As one hydrogen bond of the three-coordinate Eigen complex is strengthened, a "special pair" is formed (10), shifting the structure toward the Zundel configuration. Consequently, the hydronium O–H stretching frequency of that hydrogen bond is red-shifted, whereas the frequency of the other two is blue-shifted. In the limiting case of a Zundel complex, the vibrational frequency of the shared proton is deeply red-shifted into the frequency range of the broad peak at 1200 cm^{-1} , whereas the flanking water molecules have a stretching frequency near 3200 cm^{-1} (17, 21, 22). Meanwhile, the feature at 1760 cm^{-1} has been associated with the bending vibration of the flanking waters of the Zundel complex (16–18, 22, 23). Given the strong anharmonicity of the system, these assignments are meant only as a simplified representation of more complex vibrations of mixed character. Even so, these assignments indicate that beneath the broad overlapping features there are characteristic frequencies associated with different structural motifs of the solvated proton (19, 21, 22).

With these assignments in mind, we performed ultrafast two-dimensional IR (2D IR) spectroscopy on 1 to 5 M hydrochloric acid solutions to spectroscopically characterize the protonated water species and their associated dynamics. In these experiments, O–H stretching vibrations were excited with a pair of 45-fs pulses that have a center frequency of 3150 cm^{-1} and a bandwidth of 400 cm^{-1} (Fig. 1, dashed trace). The center frequency was tuned to the red side of the O–H stretching band to preferentially excite strongly hydrogen-bonded water species that participate in proton hydration. The response to this excitation was subsequently probed with a sub-70-fs broadband pulse with a spectrum ranging from 1500 to 4000 cm^{-1} . 2D IR experiments measure the change in absorption at the detection frequency ω_3 after excitation at a frequency ω_1 and waiting a period of time τ_2 . The broad spectral bandwidth of the probe pulse makes it possible to study couplings between O–H stretch vibrations and different vibrational modes throughout the mid-IR region. Cross peaks in a 2D IR spectrum reveal correlations between features in the linear IR spectrum and provide a stringent test of vibrational assignments. From this analysis, we can

identify the presence of different solvation structures of the excess proton and follow their evolution on the femtosecond time scale.

The 2D IR spectra of 4 M HCl for several waiting times τ_2 are shown in Fig. 2. Comparison of the 2D IR spectra of HCl and H_2O for $\tau_2 = 100\text{ fs}$ reveals three common features that have been described previously for H_2O (24): (i) the bleach of the O–H stretch along the diagonal axis at $\omega_3 = 3200\text{ cm}^{-1}$ (red), (ii) an elongated induced absorption that tails from $\omega_3 = 3100$ to $<1500\text{ cm}^{-1}$ (blue), and (iii) a cross peak between the O–H stretch and bend vibrations at $(\omega_1, \omega_3) = (3300, 1650\text{ cm}^{-1})$. A notable difference between the spectra of pure water and the acid solutions is the diagonally elongated line shape of the O–H stretch peak for 4 M HCl. This feature is attributable to inhomogeneous broadening and reflects the strong hydrogen bonding interactions between the excess proton and water.

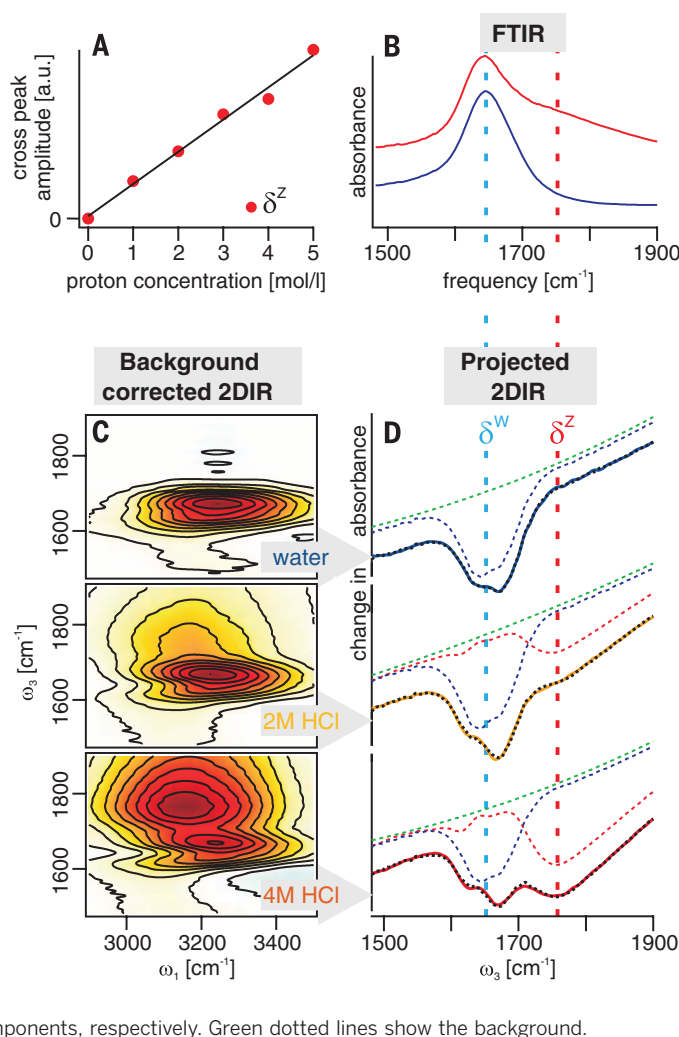
Of particular interest is a previously unobserved stretch-bend cross peak that appears at $\omega_3 = 1760\text{ cm}^{-1}$. This peak becomes more apparent in concentration-dependent 2D IR spectra when the smoothly varying background between $\omega_3 = 2000$ and 1500 cm^{-1} is subtracted (Fig. 3C). A projection onto ω_3 indicates that this peak corresponds to the Zundel bend transition observed in the linear IR spectrum (Fig. 3, B and D) and that it increases linearly with acid concentration (Fig. 3A).

Qualitatively, the dominant changes to the 2D IR spectra that occur with increasing waiting time can be divided into the rapid relaxation of the initial transient spectral features and the growth of a "long-time" spectrum that persists over the time scale of thermal diffusion. The desired structural and dynamical information of the liquid is encoded in the decaying spectral components, which have relaxation times between 80 and 765 fs, depending on both ω_1 and ω_3 . The long-time spectrum, which grows on a 675-fs time scale, is characterized by spectral changes in the detection dimension ω_3 that are similar to a linear difference spectrum due to a rise in temperature (see supplementary materials). This "hot ground state" (HGS) spectrum has been attributed to rapid nonadiabatic vibrational energy relaxation into strongly coupled low-frequency intermolecular modes, which shifts vibrational resonances in the same manner as a temperature increase (24–26). No obvious correlation between amplitude growth and waiting time was observed in the spectral region attributed to the O–H stretch vibrations of hydronium or the Eigen complex (2000 to 2800 cm^{-1}).

Additionally, the rapid loss of inhomogeneous broadening can be quantified by the decay of the center line slope (CLS) (27). The CLS decay time depends strongly on acid concentration, growing from 100 fs in neat water to 240 fs in 4 M HCl (see supplementary materials). Thus, irreversible vibrational relaxation of the initial O–H stretch excitation is substantially faster than the loss of initial O–H frequency memory. Because O–H frequency shifts require intermolecular structural changes, this is a clear indication of vibrationally non-adiabatic relaxation (24).

Fig. 3. Concentration dependence of 2D IR experiments.

(A) Amplitude of the Zundel stretch-bend cross peak as a function of proton concentration with linear fit. a.u., arbitrary units. (B) FTIR spectra of 4 M HCl (red) and water (blue) in the bending region identifying the bulk water bend (δ^W) and Zundel bend (δ^Z) frequencies. (C) 2D IR spectra for water, 2 M HCl, and 4 M HCl at $\tau_2 = 100\text{ fs}$ after subtraction of the background contribution. (D) Projection of 2D IR spectra (by integrating the spectra between $\omega_1 = 2900$ and 3500 cm^{-1}). Spectra for water (blue curve, top), 2 M HCl (yellow curve, middle), and 4 M HCl (red curve, bottom) are shown with corresponding fits from the spectral decomposition (black dotted lines). The blue and red dotted lines indicate the contribution of the δ^Z and δ^W components, respectively. Green dotted lines show the background.



To further analyze the stretch-bend cross peaks, we isolated the contributions of interest by performing a linear spectral decomposition of the stretch-bend cross-peak region ($\omega_3 < 1900\text{ cm}^{-1}$). Four distinct, physically meaningful components were needed to reconstruct the entirety of the data: (i) a stretch-bend cross peak at the frequency of the bulk water bend vibration, (ii) a stretch-bend cross peak arising from solvated protons, (iii) an HGS spectrum, and (iv) a sloping background. The procedure is explained in detail in the supplementary materials. Figure 3D illustrates the decomposition at $\tau_2 = 100\text{ fs}$ for different proton concentrations.

The results of the 2D IR spectral decomposition at $\tau_2 = 50$ and 600 fs are shown in Fig. 4A. The decomposition reveals the correlation between stretch and bend frequencies associated with the excess proton in water and separates this component from the overlapping stretch-bend cross peak of bulk H_2O . At the earliest waiting time, the peaks are clearly separated in excitation and detection frequency, with the proton stretch-bend cross peak at $(\omega_1, \omega_3) = (3185, 1760\text{ cm}^{-1})$ and the bulk H_2O stretch-bend cross peak at $(\omega_1, \omega_3) = (3260, 1650\text{ cm}^{-1})$.

The proton stretch-bend cross peak characterizes two coupled vibrational modes of the aqueous proton. Although the assignments of the features in the IR spectrum of HCl in Fig. 1 have varying degrees of uncertainty, the measurement of two correlated vibrational modes of the same molecular species provides considerably higher constraints. A projection of this cross peak onto the ω_1 and ω_3 axes presented on a common frequency

axis (Fig. 4B) provides an indication of the stretch and bend line shapes, as well as their overlap with the corresponding water vibrations. The observed frequencies for the proton correspond closely to the predicted stretching and bending vibrations of the Zundel complex (17, 22), providing evidence for the vibrational assignments and the presence of this complex. We use the term “Zundel” in a broad sense, to refer to a pair of vibrationally coupled water molecules flanking a shared proton. Additional computational investigations are needed to relate the vibrational frequencies to simulation parameters such as the proton-sharing parameter δ that characterizes the difference in distances between the excess proton and its two nearest oxygen atoms, as well as to differentiate symmetric Zundel configurations from strongly bound asymmetric special-pair configurations.

The presence of the Zundel complex in liquid water raises the question of its population among the protonated water complexes. In principle, our vibrational assignments indicate that we can spectrally separate the Zundel complex from bulk water in the bend region of the linear IR spectrum. The ratio of their peak amplitudes can then be used to determine a concentration if we know the ratio of the corresponding transition dipole moments (TDMs). In practice, this exercise is fraught with complications, such as how delocalization of the Zundel complex influences its apparent concentration and TDM, and uncertainty about the frequency of the Eigen bend. However, within certain approximations, such an estimate is still informative. The amplitude ratio of Zundel

bend to H_2O bend FTIR absorption peaks is $\sim 2:5$ in 4 M HCl. If we generously estimate the bend TDM for the Zundel species at a factor of 10 larger than that of the bulk water bend (28), the FTIR peak amplitudes result in a Zundel species concentration of 1.6 M, or 40% of the solvated protons. Because a more conservative estimate of the TDM would result in a larger Zundel concentration, we view 40% as the minimum fraction. This implies that the Zundel complex makes up a substantial, if not dominant, fraction of the protonated species in HCl solutions.

As illustrated by the grid lines marking the peak positions at $\tau_2 = 50$ and 600 fs (Fig. 4A), the Zundel stretch-bend cross peak blue-shifts along the excitation axis with increasing waiting time, asymptotically approaching the bulk water stretch excitation frequency. The shift reflects the growing probability of initially exciting the O–H stretch vibration of bulk water and detecting this excitation in the bending of a Zundel complex after waiting for a time τ_2 . A fit to the Zundel peak frequency in ω_1 as a function of τ_2 reveals that this shift occurs on a time scale of 480 fs (Fig. 4C).

The spectral shifting could originate from either proton transport or vibrational excitation transfer. In the former case, the initially excited H_2O accepts a proton, becoming a Zundel complex, whereas in the latter, only vibrational energy is transferred between the two species as a result of strong vibrational coupling between bulk water and the Zundel bend. Because both processes can contribute, the 480-fs time scale sets a lower bound for the exchange time between bulk water molecules and the Zundel complex. Vibrational energy transport and relaxation are important contributors to our data. Figure S6 in the supplementary materials illustrates the time-dependent amplitudes of components from the stretch-bend cross-peak decomposition, as well as the relaxation of the O–H stretch excited-state absorption. The excited O–H stretching vibrations evolve rapidly, exchanging energy among various modes on an 80-fs time scale. The resulting dissipation into intermolecular motions gives rise to the HGS signature, which grows on a time scale of 675 fs. The stretch-bend cross peaks decay on time scales of 410 fs for the Zundel complex and 765 fs for water. As a result, the observed shifting of the Zundel stretch-bend cross peak is likely dominated by the intermolecular vibrational energy transport, raising the possibility that the Zundel persistence time is markedly longer.

To draw further conclusions regarding the proton-transfer mechanism, we must distinguish between momentary configurations resulting from fast fluctuations and structures that are long-lived relative to the hydrogen bond dynamics of water. In the former case, the excess charge may be delocalized over multiple water molecules fluctuating about a mean position but not moving, on average; in the latter case, the charge is translocated, leaving no memory of its origin (3, 6). We refer to the latter case as proton transfer. In this work, we observe the Zundel complex through spectroscopic properties imposed by the

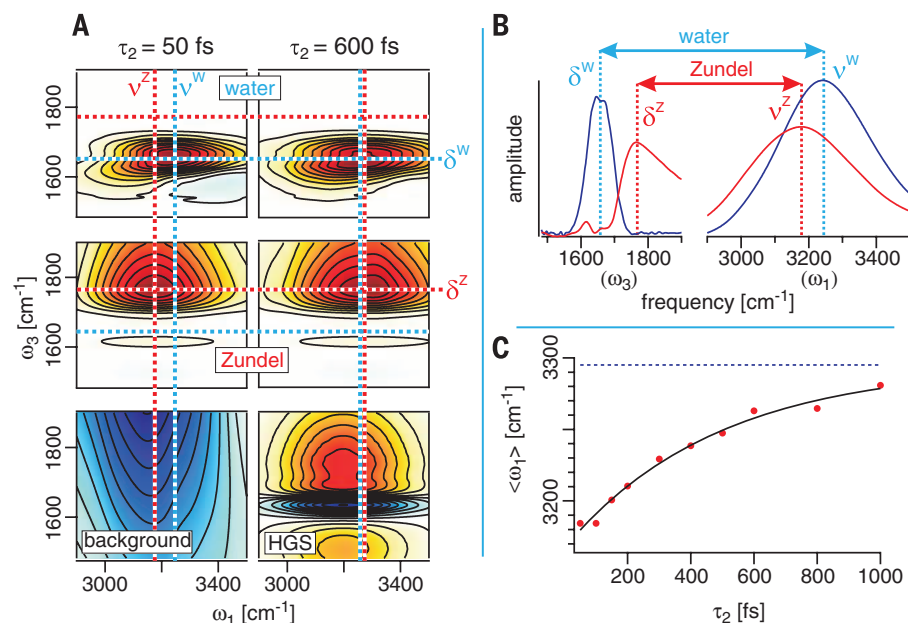


Fig. 4. Shape and time evolution of the stretch-bend cross peaks after decomposition. (A) Presentation of the three dominant components for 2D IR spectra of 4 M HCl for waiting times of $\tau_2 = 50$ and 600 fs. Grid lines illustrate the Zundel (red) and water (blue) peak frequencies. (B) Projections of the stretch-bend cross peaks onto one frequency axis: ω_1 for stretch (ν) and ω_3 for bend (δ). These bleach signals are inverted to present a positive spectrum. (C) Evolution of the peak frequency of the Zundel stretch-bend cross peak in ω_1 with increasing waiting time. The blue dotted line indicates the asymptotic value.

[H(H₂O)₂]⁺ core. Even if the excess charge could oscillate between more than two water molecules while the average charge position remains localized, the stretch-bend frequency correlation in the cross peak would be preserved. Therefore, the >480-fs persistence time for the Zundel configuration corresponds to long-range proton-transfer events. Earlier studies involving IR transient absorption experiments reported sub-100-fs exchange times between Eigen and Zundel species (29, 30). Questions about the role of vibrational energy transport aside, we believe that these experiments are reporting on localized proton fluctuations rather than long-range charge transport.

Because we did not observe the Eigen species in the experiments described here, we cannot draw conclusions regarding its stability or role in aqueous proton transfer. However, we note that no sign of vibrational excitation transfer was observed from the Zundel stretch into the region characteristic of Eigen configurations (2000 to 2800 cm⁻¹). A relatively long-lived Zundel complex represents an important part of the proton-transfer mechanism; this configuration is not merely a fleeting transition state traversed during an Eigen-to-Eigen proton transfer. In addition to Zundel-to-Zundel transport, exchange processes involving Zundel-to-Eigen transport are still consistent with our data. It is less clear how a barrierless Zundel-Eigen interconversion would be observed in our experiments. Deeper insight into the mechanism can be gained from ultrafast IR spectroscopy of the Eigen complex using excitation pulses in the window between 2000 and 2800 cm⁻¹, where the Eigen species or special-pair configurations are expected to absorb. Such experiments are planned for the future, as is investigation of the peak at 1200 cm⁻¹ in the acid continuum. Studies at lower concentrations are also needed to definitively evaluate the role of ion pairing in aqueous proton transfer (31, 32). Although many unanswered questions remain regarding the proton-transport mechanism in water, our findings place important constraints on the role of the Zundel complex in this process.

REFERENCES AND NOTES

1. N. Agmon, *Chem. Phys. Lett.* **244**, 456–462 (1995).
2. D. Marx, M. E. Tuckerman, J. Hutter, M. Parrinello, *Nature* **397**, 601–604 (1999).
3. D. Marx, *ChemPhysChem* **7**, 1848–1870 (2006).
4. P. L. Geissler, C. Dellago, D. Chandler, J. Hutter, M. Parrinello, *Science* **291**, 2121–2124 (2001).
5. H. Lapid, N. Agmon, M. K. Petersen, G. A. Voth, *J. Chem. Phys.* **122**, 014506 (2005).
6. M. Tuckerman, K. Laasonen, M. Sprik, M. Parrinello, *J. Phys. Chem.* **99**, 5749–5752 (1995).
7. R. Vuilleumier, D. Borgis, *Chem. Phys. Lett.* **284**, 71–77 (1998).
8. K. Ando, J. T. Hynes, *J. Phys. Chem. B* **101**, 10464–10478 (1997).
9. A. A. Kornyshev, A. M. Kuznetsov, E. Spohr, J. Ulstrup, *J. Phys. Chem. B* **107**, 3351–3366 (2003).
10. O. Markovitch et al., *J. Phys. Chem. B* **112**, 9456–9466 (2008).
11. T. C. Berkelbach, H. S. Lee, M. E. Tuckerman, *Phys. Rev. Lett.* **103**, 238302 (2009).
12. A. Hassanali, F. Giberti, J. Cuny, T. D. Kühne, M. Parrinello, *Proc. Natl. Acad. Sci. U.S.A.* **110**, 13723–13728 (2013).
13. G. Zundel, in *The Hydrogen Bond, Recent Developments in Theory and Experiments*, P. Schuster, G. Zundel, C. Sandorfy, Eds. (North Holland, Amsterdam, 1976), pp. 687–766.

14. R. Janoschek, E. G. Weidemann, G. Zundel, *J. Chem. Soc. Faraday Trans. 2* **69**, 505–520 (1973).
15. E. S. Stoyanov, I. V. Stoyanova, C. A. Reed, *J. Am. Chem. Soc.* **132**, 1484–1485 (2010).
16. K. R. Asmis et al., *Science* **299**, 1375–1377 (2003).
17. J. M. Headrick et al., *Science* **308**, 1765–1769 (2005).
18. T. L. Guasco, M. A. Johnson, A. B. McCoy, *J. Phys. Chem. A* **115**, 5847–5858 (2011).
19. J. Xu, Y. Zhang, G. A. Voth, *J. Phys. Chem. Lett.* **2**, 81–86 (2011).
20. M. Park, I. Shin, N. J. Singh, K. S. Kim, *J. Phys. Chem. A* **111**, 10692–10702 (2007).
21. J. Kim, U. W. Schmitt, J. A. Gruetzmacher, G. A. Voth, N. E. Scherer, *J. Chem. Phys.* **116**, 737–746 (2002).
22. W. Kulig, N. Agmon, *Nat. Chem.* **5**, 29–35 (2013).
23. O. Vendrell, F. Gatti, H. D. Meyer, *J. Chem. Phys.* **127**, 184303 (2007).
24. K. Ramasesha, L. De Marco, A. Mandal, A. Tokmakoff, *Nat. Chem.* **5**, 935–940 (2013).
25. E. T. J. Nibbering, T. Elsaesser, *Chem. Rev.* **104**, 1887–1914 (2004).
26. A. J. Lock, S. Woutersen, H. J. Bakker, *J. Phys. Chem. A* **105**, 1238–1243 (2001).
27. K. Kwak, S. Park, I. J. Finkelstein, M. D. Fayer, *J. Chem. Phys.* **127**, 124503 (2007).
28. L. Ojamäe, I. Shavitt, S. J. Singer, *Int. J. Quantum Chem.* **56**, 657–668 (1995).
29. S. Woutersen, H. J. Bakker, *Phys. Rev. Lett.* **96**, 138305 (2006).
30. W. Amir et al., *J. Chem. Phys.* **126**, 034511 (2007).
31. F. Wang, S. Izvekov, G. A. Voth, *J. Am. Chem. Soc.* **130**, 3120–3126 (2008).
32. M. D. Baer, J. L. Fulton, M. Balasubramanian, G. K. Schenter, C. J. Mundy, *J. Phys. Chem. B* **118**, 7211–7220 (2014).

ACKNOWLEDGMENTS

This work was supported by the U.S. Department of Energy (grants DE-SC0011456 and DE-SC0014305). M.T. thanks the Deutscher Akademischer Austauschdienst for a postdoctoral fellowship. L.D.M. thanks the Natural Sciences and Engineering Research Council of Canada for a scholarship.

SUPPLEMENTARY MATERIALS

www.sciencemag.org/content/350/6256/78/suppl/DC1
Materials and Methods
Supplementary Text
Figs. S1 to S6
References (33, 34)

20 April 2015; accepted 25 August 2015
10.1126/science.aab3908

MEMORY MECHANISMS

Multiple repressive mechanisms in the hippocampus during memory formation

Jun Cho,^{1,2*} Nam-Kyung Yu,^{2*} Jun-Hyeok Choi,² Su-Eon Sim,² SukJae Joshua Kang,² Chuljung Kwak,² Seung-Woo Lee,² Ji-il Kim,² Dong Il Choi,² V. Narry Kim,^{1,2†} Bong-Kiun Kaang^{2†}

Memory stabilization after learning requires translational and transcriptional regulations in the brain, yet the temporal molecular changes that occur after learning have not been explored at the genomic scale. We used ribosome profiling and RNA sequencing to quantify the translational status and transcript levels in the mouse hippocampus after contextual fear conditioning. We revealed three types of repressive regulations: translational suppression of ribosomal protein-coding genes in the hippocampus, learning-induced early translational repression of specific genes, and late persistent suppression of a subset of genes via inhibition of estrogen receptor 1 (ESR1/ERα) signaling. In behavioral analyses, overexpressing *Nr5n1*, one of the newly identified genes undergoing rapid translational repression, or activating ESR1 in the hippocampus impaired memory formation. Collectively, this study unveils the yet-unappreciated importance of gene repression mechanisms for memory formation.

Storing a persistent memory in the brain involves dynamic gene regulation. This is orchestrated by complex processes, including chromatin alteration and the activity of transcription factors (1), as well as translational controls by mammalian target of rapamycin (mTOR) (2), translation initiation or elongation factors (3, 4), and microRNAs (5). The importance of translational regulators for memory consolidation has been demonstrated by assessing the effect of genetic or pharmacological manipulation on behavioral phenotypes (6, 7). However, our

knowledge of the target genes controlled translationally during memory formation remains limited. One of the reasons has been the lack of high-throughput techniques to accurately measure the translation rate of endogenous genes in the brain (8). To date, temporal profiles of the transcriptome paired with the transcriptome throughout the memory consolidation period are not available, and it remains largely unknown which genes are controlled and how they are regulated during memory consolidation.

Ribosome profiling (RPF) allows sensitive and quantitative measurement of translation at the genomic scale (9–12). Deep sequencing of the ribosome-protected mRNA fragments (“ribosomal footprints”) yields quantitative information about the mRNAs undergoing translation. When normalized against the mRNA level, which can be

¹Center for RNA Research, Institute for Basic Science, Seoul 151-742, Korea. ²Department of Biological Sciences, College of Natural Sciences, Seoul National University, Seoul 151-747, Korea. *These authors contributed equally to this work. †Corresponding author. E-mail: narrykim@snu.ac.kr (V.N.K.); kaang@snu.ac.kr (B.K.K.)

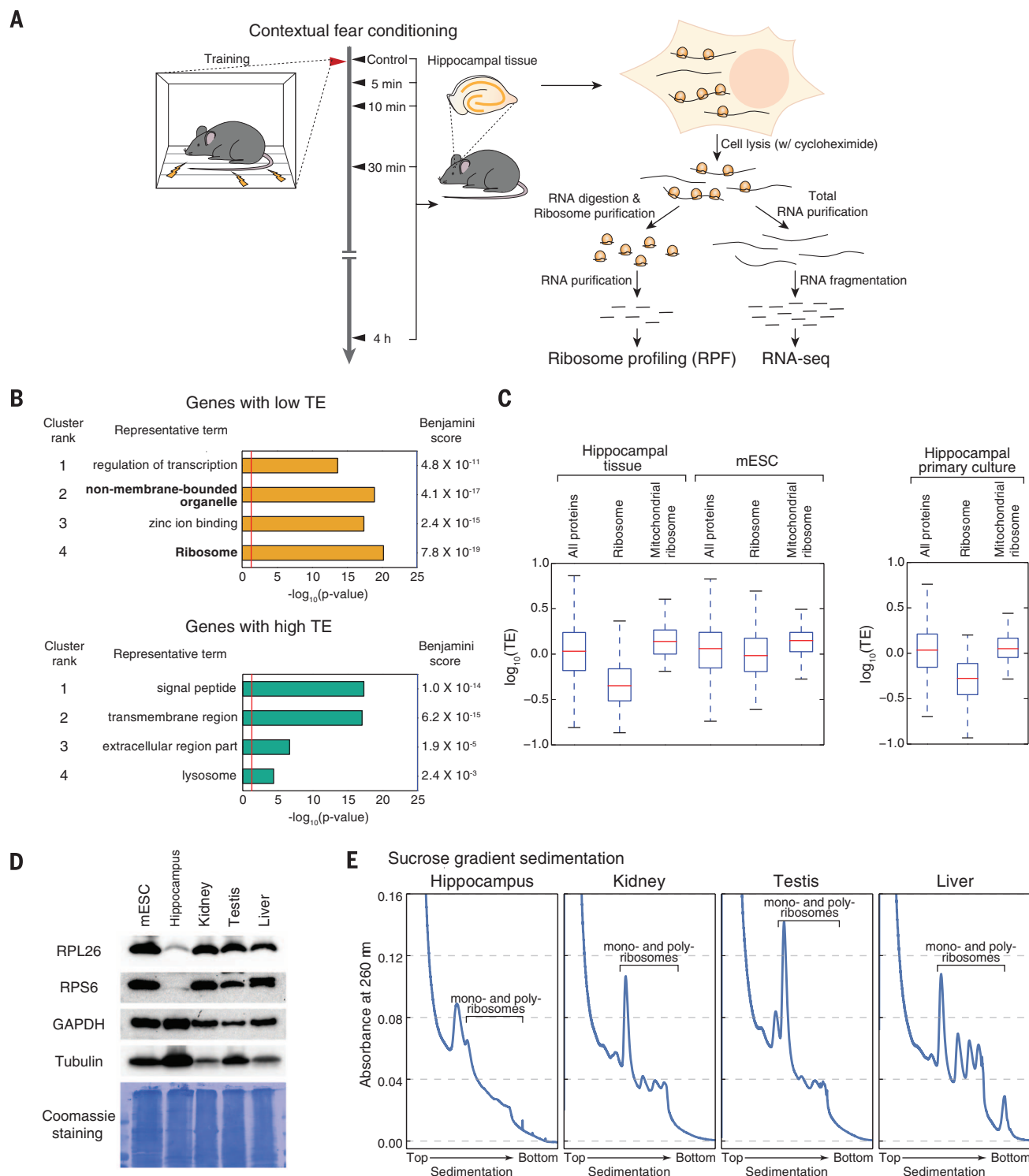


Fig. 1. Translational suppression of ribosomal protein-coding genes in the mouse hippocampus. (A) Workflow of RPF and RNA-seq from the mouse hippocampus after contextual fear conditioning. (B) The top four clusters of functional annotations associated with the genes that have low or high TE in the hippocampus. The top 1100 (10%) genes with high or low TE were selected for functional annotation analysis using the DAVID program (<http://david.abcc.ncifcrf.gov>). The “non-membrane-bounded organelle” also includes the ribosome. (C) Box plots showing the TEs of mRNAs that encode all

proteins, ribosomal proteins, or mitochondrial ribosomal proteins in hippocampal tissues and mESCs (left) and hippocampal primary culture (right). (D) Western blot analysis of mESCs and mouse tissues. RPL26 and RPS6 are components of the ribosome large and small subunit, respectively. Coomassie staining visualizes the amounts of loaded proteins (bottom). (E) Sucrose gradient sedimentation of mouse tissue lysates. Absorbance at 260 nm was recorded from the sedimented lysates to detect ribosome subunits, monosomes, and polyribosomes.

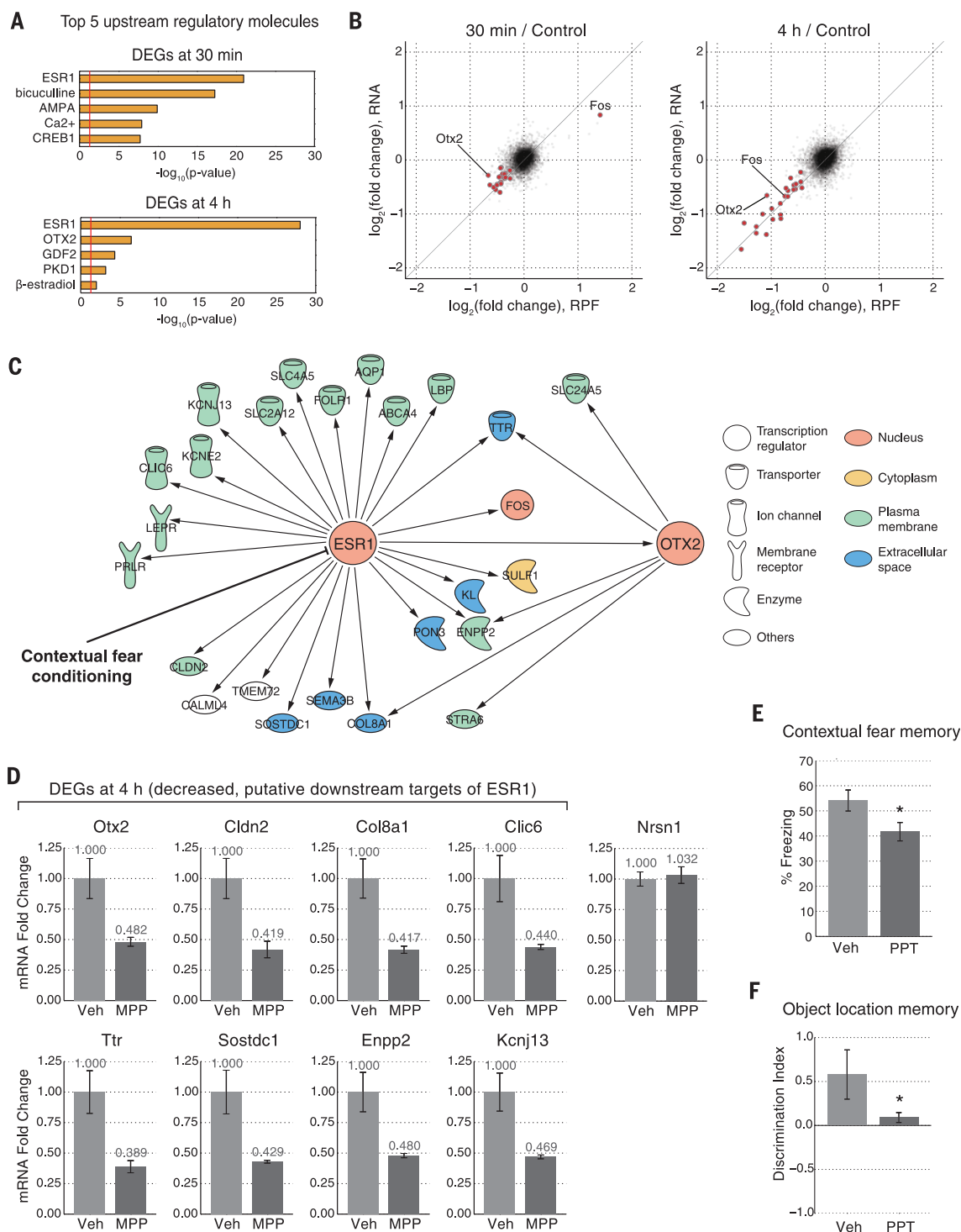


Fig. 2. Persistent transcript-level down-regulation after contextual fear conditioning via ESR1 inhibition. (A) Graphical demonstration of upstream regulators from the IPA for DEGs at 30 min and 4 hours. The y axis shows the identified regulators. The x axis displays the significance, which is $-\log_{10}(P \text{ value})$. (B) Scatter plots showing the fold changes of RPF (x axis) and RNA-seq (y axis) of all genes (gray) and the downstream genes of ESR1 (red) in 30-min (left) or 4-hour samples (right). (C) Graphical demonstration of the putative regulatory network of ESR1 and OTX2. Our data suggest that upon contextual fear conditioning, ESR1 signaling is suppressed, resulting in the marked decrease of the downstream genes at 4 hours after learning. (D) qRT-PCR of 8 DEGs in the hippocampal tissues of mice injected with MPP ($n = 4$)

or vehicle (veh; $n = 6$). The hippocampi were collected 3 hours after injection. The *Nrsn1* level was measured as a control. Data are shown as mean \pm standard error of the mean (SEM). (E and F) Contextual fear conditioning (E) or object location task (F) with ESR1 agonist administration into the hippocampus. One picogram of PPT, the ESR1 agonist, was bilaterally infused into the hippocampus through cannulae right after learning. (E) Contextual fear memory was assessed the next day by measuring the percentage of time that the mice spent freezing in fear (percentage time freezing). Unpaired t test, $*P = 0.0378$, $n = 12$ or 13 mice. (F) Object location memory tested 24 hours after sampling. Unpaired t test, $*P = 0.0115$, $n = 8$ or 9 mice. Data are shown as mean \pm SEM.

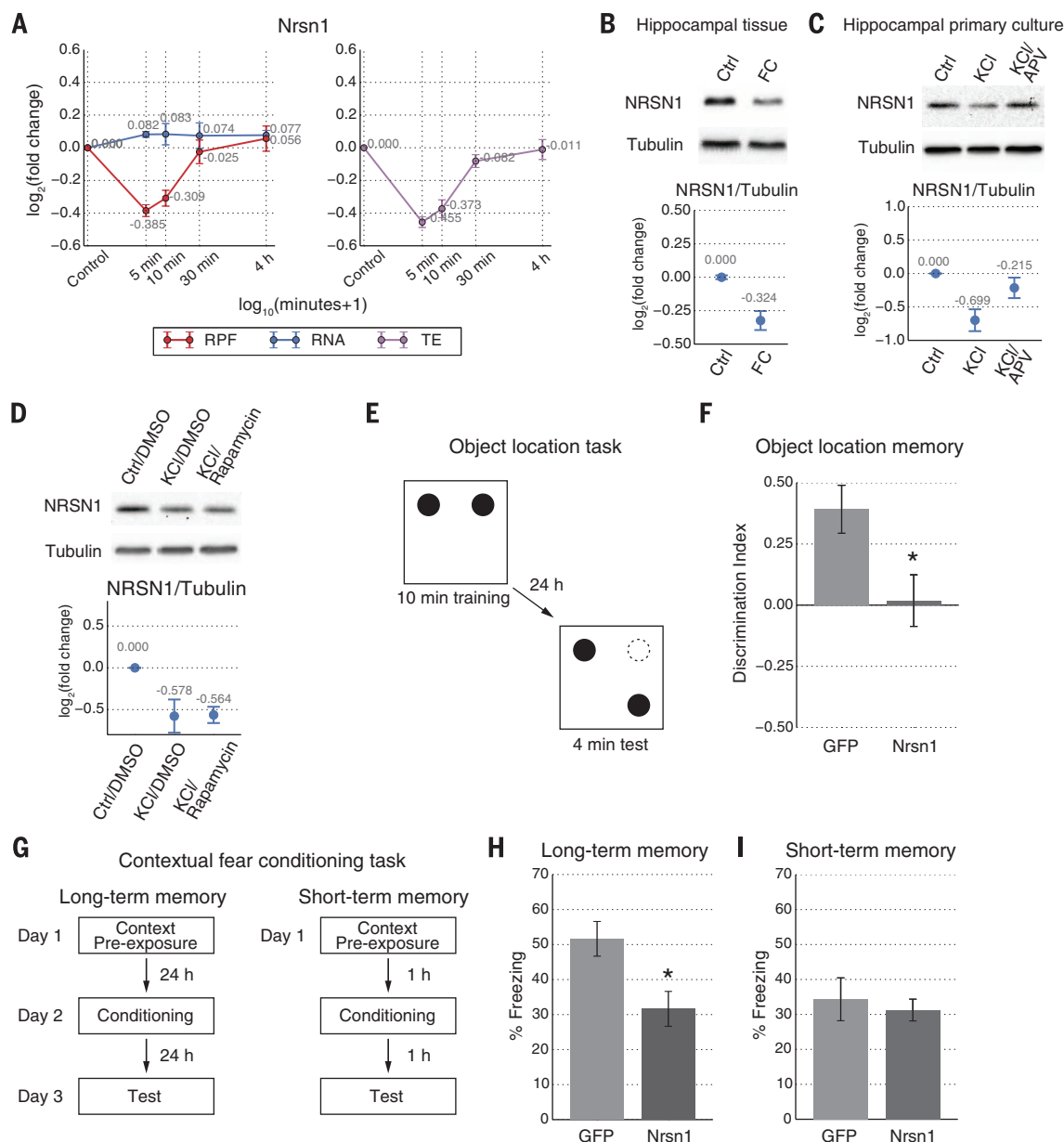


Fig. 3. Rapid translational repression of *Nrsn1* after conditioning. (A) Line plots showing the fold changes of RPF and RNA-seq (left) and in the TE (right) of *Nrsn1* after conditioning. The x axis (time) is in log scale. (B) Western blot and quantitative analyses on NRSN1 in hippocampal tissues from mice ($n = 4$ or 5) that underwent fear conditioning (FC) compared with home-cage controls (Ctrl). Unpaired t test, $**P$ value = 0.0055. (C) Western blot of NRSN1 in cultured neurons treated with KCl (40 mM) or KCl/APV (50 μ M). One-way analysis of variance (ANOVA), $F(2,15) = 8.393$, $**P = 0.0036$, post hoc Tukey's multiple comparison test, $**P < 0.01$ (Ctrl versus KCl), $*P < 0.05$ (KCl versus KCl/APV). (D) Western blot of NRSN1 in cultured neurons treated with KCl (40 mM) or KCl/rapamycin (200 nM). One-way ANOVA, $F(2,6) = 6.656$, $**P = 0.0300$, post hoc Tukey's multiple com-

parison test, $*P < 0.05$ (Ctrl/DMSO versus KCl/DMSO, Ctrl/DMSO versus KCl/rapamycin), $P > 0.05$ (KCl/DMSO versus KCl/rapamycin). (E) Schematic of the object location task, see also (13). (F) Object location memory of mice over-expressing *Nrsn1* or green fluorescent protein (GFP) ($n = 8$ or 9 mice). The discrimination index was calculated from the exploration time for each object [(displaced object – nondisplaced object)/(displaced object + nondisplaced object)]. Unpaired t test, $*P = 0.0202$. (G) Schematic of the contextual fear conditioning procedures, see also (13). (H and I) The percentage time freezing of mice over-expressing *Nrsn1* or GFP, showing the strength of contextual fear memory. Unpaired t test, $*P = 0.0148$, $n = 7$ mice per group for long-term memory (H) and $P = 0.6632$, $n = 6$ mice per group for short-term memory (I). All data are shown as mean \pm SEM.

measured by RNA sequencing (RNA-seq) in parallel, the translational efficiency (TE) of mRNAs from thousands of protein-coding genes can be determined simultaneously.

To map the comprehensive landscape of translome and transcriptome during memory formation, we used RPF and RNA-seq in the mouse

hippocampus after contextual fear conditioning (13) (Fig. 1A and fig. S1A). The hippocampi were collected from untrained mice (control) and from trained mice at 5, 10, and 30 min and 4 hours after conditioning. The qualities of our RPF libraries were confirmed by their enrichment in coding sequences (fig. S1B) and three-nucleotide peri-

odicity of the RPF reads (fig. S1C), two representative signatures of the in vivo movement of ribosomes in translation (9–12).

We first conducted functional annotation analysis using the Database for Annotation, Visualization and Integrated Discovery (DAVID) to learn about the global characteristics of hippocampal

translation (table S1 and Fig. 1B). The genes related to the translational machinery itself (i.e., the ribosome) were translationally suppressed in the hippocampus (Fig. 1, B and C, and fig. S2, A and C). Considering the importance of translational regulation, this specific suppression of translational machinery was unexpected. We observed similar suppression in cultured hippocampal neurons (Fig. 1C and fig. S2B) but not in the RPF data set from mouse embryonic stem cells (mESCs) (Fig. 1C and fig. S2C). The mRNA levels for ribosomal proteins were comparable in the hippocampus and mESCs (fig. S2D). Unlike cytoplasmic ribosomal protein genes, mitochondrial ribosomal protein genes did not show cell type-dependent differential regulation patterns (Fig. 1C). Western blotting demonstrated that the ribosomal protein levels (RPL26 and RPS6) were indeed much lower in the hippocampus than in mESCs and other tissues (Fig. 1D). We also estimated actively translating ribosomes by sucrose gradient sedimentation (9, 14). Polyribosomes were not clearly detected in the hippocampus, whereas they were readily observed in the kidney, testis, and liver (Fig. 1E). These data collectively indicate that ribosome biogenesis is suppressed translationally in the hippocampus and that overall translation activity is maintained at a low level as compared with that in other tissues.

To identify reproducible temporal changes of gene expression after contextual fear conditioning, we constructed three biologically independent replicates of the RPF and RNA-seq libraries. From these data, we determined differentially expressed genes (DEGs) by calculating the RPF read counts, which are values that provide better estimates of the ultimate protein output from individual genes than those of RNA-seq (15). DEGs at each time point were defined as the genes whose RPF counts altered significantly from those in untrained controls [\log_2 RPF fold changes above 0.35 or below -0.35, with a false discovery rate (FDR) of less than 0.1] (fig. S3, A to D, and table S2). We identified a total of 104 DEGs (fig. S3). The DEG groups of the 5- to 30-min time points showed only a few overlapping genes, indicating highly dynamic regulation across these time points (fig. S3, E and F).

At 5 min, DEGs showed either decrease (in 15 genes) or increase (in 10 genes) in RPF levels, mostly without significant alterations in RNA levels (14 of 15 decreased DEGs and 8 of 10 increased DEGs) (fig. S4A). Thus, the first wave of gene regulation after conditioning may be through translation rather than transcription. These changes became undetectable by 30 min in most cases (21 out of 22 translationally regulated DEGs at 5 min). Translationally regulated DEGs also appeared at 10 min (6 out of 8 decreased DEGs) (fig. S4B). At 10 and 30 min, the genes known as immediate early genes such as *Fos* and *Arc* were obviously induced at RNA and RPF levels (fig. S3, B, C, and E, and fig. S4, B and C), indicating that our data set is in accordance with previous studies of memory (7). Unlike DEGs at the early stage (5 to 10 min), most of the DEGs at 30 min and 4 hours showed concordant changes at mRNA and RPF levels (fig. S4, C and D), indicating that their

regulation is largely dependent on mRNA abundance rather than translational control at these later time points. Down-regulation rather than up-regulation became profoundly dominant over time (a decrease in 31 of 42 DEGs at 30 min and in 48 of 55 DEGs at 4 hours; fig. S3, C to F, and fig. S4, C and D). Most of the down-regulation found at 30 min appeared to continue through 4 hours (24 of 31 decreased DEGs at 30 min; fig. S3F). Our time-course study thus uncovered three major waves of alterations: an initial wave of transient translational regulation at around 5 to 10 min; a second wave of induction of immediate early genes at 10 to 30 min; and the suppression of genes through decrease of mRNA levels after 30 min, which continued through 4 hours.

It is generally believed that repressive gene regulation is relieved upon stimulus so as to allow the gene activation necessary for memory consolidation. Only a few cases are known for the repressive mechanisms that are triggered by learning and play an active role in forming a long-term memory (7, 16, 17). In our data set, however, two types of repressive events were markedly induced after learning.

We first looked into the transcript-level suppression. Whereas previous reports have shown that RNA and protein synthesis at 3 to 4 hours after learning are important for memory formation (18, 19), repressive gene regulation at this time point has not been investigated. To understand the mechanism of molecular changes at the late phase of memory formation, we performed ingenuity pathway analysis (IPA) (20) for the 4-hour DEGs (Fig. 2A, right; table S3; and supplementary text). Estrogen receptor 1 (ESR1/ER α) was identified as the most prominent upstream regulator (Fig. 2A; P value = 9.50×10^{-29} at 4 hours) and was predicted to be inhibited. Half of the decreased DEGs at 4 hours (24 of 48) were putative ESR1 downstream genes, and their down-regulation had already started to be seen at 30 min [Fig. 2, A (left) and B]. *Otx2*, one of the previously reported targets of ESR1 (21), markedly decreased at 30 min and 4 hours (Fig. 2B). OTX2 was also proposed as an upstream regulator of five down-regulated DEGs found at 4 hours (Fig. 2, A and C). Together, these results suggest that the ESR1/OTX2 axis may play a pivotal role in modulating gene-regulatory networks after learning (Fig. 2C and supplementary text).

To examine whether ESR1 inhibition indeed down-regulates these DEGs at 4 hours in the hippocampus, we subcutaneously administered the ESR1-specific antagonist methyl-piperidino-pyrazole (MPP) and conducted quantitative reverse transcription polymerase chain reaction (qRT-PCR) on hippocampal mRNAs. We observed marked decreases in *Otx2* and other putative ESR1 downstream targets after MPP treatment (Fig. 2D), indicating that these genes are under the control of ESR1 in the hippocampus. Furthermore, we assessed the importance of the ESR1 inhibition for memory formation by applying the ESR1-specific agonist 4,4',4''-(4-propyl-[1H]-pyrazole-1,3,5-triyl) trisphenol (PPT) into the hippocampus right after learning. Memory formation was significant-

ly impaired in PPT-injected mice as compared with vehicle-injected mice in two hippocampus-dependent tasks [contextual fear conditioning (Fig. 2E) and object location task (Fig. 2F)], suggesting that down-regulation of ESR1 signaling is important for memory formation.

Next, we examined the translational repression of specific genes soon after learning (within 10 min). *ATF4* is the only established gene undergoing translational repression during memory consolidation (4, 7). We could greatly expand the list of translationally repressed genes (14 DEGs at 5 min and 6 at 10 min). Among these genes, *Nrsn1* showed a clear decrease in TE at 5 to 10 min without a change in mRNA level (Fig. 3A). Our Western blot analysis also demonstrated that the Nrsn1 protein level in the hippocampus was significantly reduced after conditioning, as compared with that of untrained controls (Fig. 3B). Moreover, elevating neuronal activity in cultured hippocampal neurons resulted in a decrease of the Nrsn1 protein without affecting its mRNA level (Fig. 3C and fig. S5A). The *N*-methyl-D-aspartate receptor (NMDAR) (22) antagonist D-amino-phosphovalerate (D-APV) blocked this activity-dependent reduction of Nrsn1 protein (Fig. 3C). Activity-dependent translational suppression of the Kv1.1 channel depends on NMDAR and mTOR pathways (23). In contrast, *Nrsn1* down-regulation by neuronal activity was not affected by treatment with rapamycin, the mTOR inhibitor (Fig. 3D), suggesting that *Nrsn1* is controlled by a mechanism distinct from what controls Kv1.1. In addition to *Nrsn1*, *Mapk6*, another gene that was found to be translationally repressed in our analysis (fig. S5B), showed a significant decrease in protein level by neuronal activity (fig. S5C) without a change in mRNA level (fig. S5A). This was also NMDAR-dependent (fig. S5D) and mTOR-independent (fig. S5E). These results suggest the involvement of common upstream mechanisms in repression of 5 min DEGs including *Nrsn1* and *Mapk6*.

Some of these genes might be "memory suppressor genes" that need to be down-regulated for memory formation (24). Among the translationally repressed DEGs, we chose *Nrsn1* for further examination. *Nrsn1* encodes a neuron-specific membrane protein, which has been suggested to interact with tubulin and play a role in vesicle trafficking and neurite outgrowth (25, 26). Given that membrane trafficking (27) and microtubule dynamics (28) are essential processes that underlie memory storage, the regulation of *Nrsn1* expression might be relevant for learning and memory. To examine the functional role of *Nrsn1* in memory formation, we overexpressed *Nrsn1* in the mouse hippocampus using adeno-associated virus (fig. S5F). *Nrsn1*-overexpressing mice showed deficits in long-term memory formation in an object location task (Fig. 3, E and F) and contextual fear conditioning (Fig. 3, G and H). In contrast, short-term memory tested 1 hour after the conditioning was intact (Fig. 3I), supporting the idea that *Nrsn1* specifically interferes with the memory consolidation process without affecting the acquisition or expression of contextual fear memory. Thus, *Nrsn1*

may act as a suppressor of long-term memory formation, suggesting the physiological significance of its down-regulation after learning (24). In addition, we examined whether *Nr5n1* might regulate the 4-hour DEGs by overexpressing *Nr5n1* in cultured hippocampal neurons. The expression of these genes was not changed significantly by *Nr5n1* overexpression, suggesting that *Nr5n1* and the ESRI/OTX2 axis may operate independently (fig. S5G).

In addition to uncovering interesting repressive pathways, our quantitative data will provide a valuable resource for future studies of the regulation of numerous individual protein-coding genes in the hippocampus (tables S2 and S4). We could also examine long noncoding RNAs (lncRNAs); among the 886 lncRNAs detected, 13 lncRNAs showed significant changes ($FDR < 0.1$, \log_2 fold change >0.35 or <-0.35) for at least one time point (fig. S6, table S5, and supplementary text).

The integrative analysis of transcriptome and translome in mouse hippocampal tissue after contextual fear conditioning has uncovered numerous gene-regulatory events during memory formation in vivo. In particular, our study illustrates the potential importance of negative gene regulation in learning and memory.

REFERENCES AND NOTES

- C. M. Alberini, E. R. Kandel, *Cold Spring Harbor Perspect. Biol.* **7**, a021741 (2015).
- C. A. Hoeffer, E. Klann, *Trends Neurosci.* **33**, 67–75 (2010).
- M. Costa-Mattioli, W. S. Sossin, E. Klann, N. Sonenberg, *Neuron* **61**, 10–26 (2009).
- E. Santini, T. N. Huynh, E. Klann, *Prog. Mol. Biol. Transl. Sci.* **122**, 131–167 (2014).
- W. Wang, E. J. Kwon, L.-H. Tsai, *Learn. Mem.* **19**, 359–368 (2012).
- P. K. Dash, S. A. Orsi, A. N. Moore, *J. Neurosci.* **26**, 8048–8056 (2006).
- M. Costa-Mattioli et al., *Nature* **436**, 1166–1173 (2005).
- R. R. Kitchen, J. S. Rozowsky, M. B. Gerstein, A. C. Nairn, *Nat. Neurosci.* **17**, 1491–1499 (2014).
- J. Cho et al., *Cell* **151**, 765–777 (2012).
- H. Guo, N. T. Ingolia, J. S. Weissman, D. P. Bartel, *Nature* **466**, 835–840 (2010).
- N. T. Ingolia, S. Ghaemmaghami, J. R. Newman, J. S. Weissman, *Science* **324**, 218–223 (2009).
- N. T. Ingolia, L. F. Lareau, J. S. Weissman, *Cell* **147**, 789–802 (2011).
- Materials and methods are available as supplementary materials on Science Online.
- N. Kondrashov et al., *Cell* **145**, 383–397 (2011).
- A. Battle et al., *Science* **347**, 664–667 (2015).
- C. A. Miller, J. D. Sweatt, *Neuron* **53**, 857–869 (2007).
- B. G. Dias et al., *Neuron* **83**, 906–918 (2014).
- R. Bourtochouladze et al., *Learn. Mem.* **5**, 365–374 (1998).
- L. M. Igaz, M. R. Vianna, J. H. Medina, I. Izquierdo, *J. Neurosci.* **22**, 6781–6789 (2002).
- A. Krämer, J. Green, J. Pollard Jr., S. Tugendreich, *Bioinformatics* **30**, 523–530 (2014).
- X. Han et al., *J. Neurosci.* **33**, 2671–2683 (2013).
- T. Bliss, G. L. Collingridge, *Mol. Brain* **6**, 5 (2013).
- K. F. Raab-Graham, P. C. Haddick, Y. N. Jan, L. Y. Jan, *Science* **314**, 144–148 (2006).
- T. Abel, K. C. Martin, D. Bartsch, E. R. Kandel, *Science* **279**, 338–341 (1998).
- M. Araki, S. Taketani, *Dev. Neurosci.* **3**, 111–136 (2009).
- M. Ida, H. Suzuki, N. Mori, S. Taketani, M. Araki, *Neurosci. Res.* **50**, 199–208 (2004).
- M. J. Kennedy, M. D. Ehlers, *Annu. Rev. Neurosci.* **29**, 325–362 (2006).
- J. Jaworski et al., *Neuron* **61**, 85–100 (2009).

ACKNOWLEDGMENTS

We thank H. Chang, S.-C. Kwon, J. Park, Y. Choi, and J.-E. Park of the V. Narry Kim lab and H. K. Choe for helpful discussion of data analysis; and Y. Kim of the same lab for critical commentary on the manuscript. V.N.K. was supported by grant IBS-R008-D1 from the Institute for Basic Science from the Ministry of Science, Information, Communication and Technology and Future Planning of Korea. B.-K.K. was supported by the National Honor Scientist Program (2012R1A3A1050385) from the National Research Foundation of the Ministry of Science, Information, Communication and Technology. J.-i.K. was supported by the Pohang Iron and Steel Company (POSCO) Tae Joon (TJ) Park Foundation. High-throughput sequencing data have been deposited in the National

Center for Biotechnology Information Gene Expression Omnibus (GEO) database with accession number GSE72064.

SUPPLEMENTARY MATERIALS

www.sciencemag.org/content/350/6256/82/suppl/DC1
Materials and Methods
Figs. S1 to S6
Tables S1 to S5
References (29–46)

4 June 2015; accepted 4 September 2015
10.1126/science.aac7368

CLOUDS

Holographic measurements of inhomogeneous cloud mixing at the centimeter scale

Matthew J. Beals,¹ Jacob P. Fugal,^{2,3} Raymond A. Shaw,^{1,4,*} Jiang Lu,⁴ Scott M. Spuler,⁵ Jeffrey L. Stith⁵

Optical properties and precipitation efficiency of atmospheric clouds are largely determined by turbulent mixing with their environment. When cloud liquid water is reduced upon mixing, droplets may evaporate uniformly across the population or, in the other extreme, a subset of droplets may evaporate completely, leaving the remaining drops unaffected. Here, we use airborne holographic imaging to visualize the spatial structure and droplet size distribution at the smallest turbulent scales, thereby observing their response to entrainment and mixing with clear air. The measurements reveal that turbulent clouds are inhomogeneous, with sharp transitions between cloud and clear air properties persisting to dissipative scales (<1 centimeter). The local droplet size distribution fluctuates strongly in number density but with a nearly unchanging mean droplet diameter.

Clouds consist of only $\sim 10^{-6}$ volume fraction of liquid water; yet this trace amount is crucial to the formation of precipitation and the transport of enthalpy, electromagnetic energy in both optical and thermal infrared bands, and even entropy within the atmosphere (*1–3*). To a large extent, the challenge of representing clouds in coarse-resolution weather and climate models is to capture the details of how turbulence transports and dilutes cloud water through mixing with their environment (*4*). Mass and energy conservation allows precise calculation of the final liquid water content after a cloud is diluted with clear, subsaturated environmental air. Liquid water content, however, scales as $w_l \sim n\bar{d}^3$, where n is the droplet number density and \bar{d} is the droplet diameter; due to complex turbulent interactions between droplets and the water vapor and temperature fields, it is by no means obvious to what extent reduction in w_l results from relative changes in n

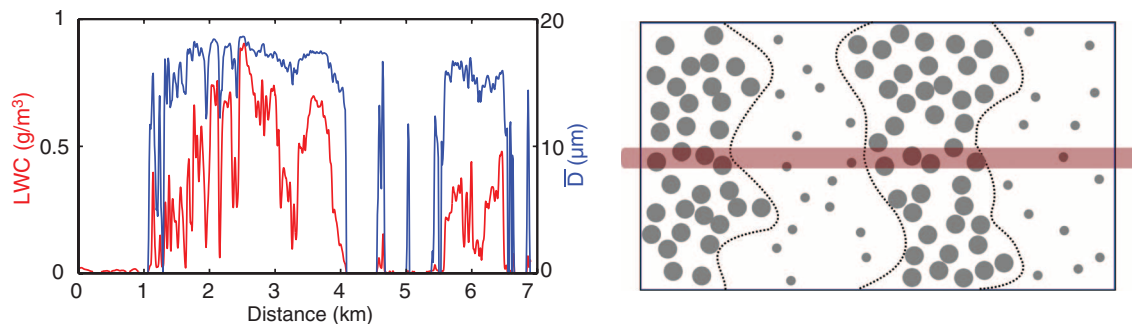
and \bar{d}^3 and how the answer may depend on the size of the averaging volume. For example, do droplets evaporate by uniformly reducing their size across the population, leaving n largely unchanged except through simple dilution, or, in the other extreme, does a subset of droplets evaporate completely, leaving the others in the volume unchanged, i.e., \bar{d}^3 constant? These two limiting processes, proposed by Baker and Latham more than 30 years ago, are referred to, respectively, as homogeneous and extremely inhomogeneous mixing (*5, 6*).

As simple as the posed question sounds, it has been the source of controversy for several decades and has set a high bar for measurements of cloud particle size distributions. At its most basic level, the question is related to the sharpness of cloud boundaries and how droplet size and number density vary along those edges. More specifically, in situ cloud measurements have required averaging over long distances compared to the turbulent scales of a cloud boundary (*7–12*), thereby relying on the questionable assumption of ergodicity when translating to an ensemble view in theoretical or computational models (see the supplementary text) (*13, 14*). In this work, we overcame the large-scale spatial averaging problem by using an airborne digital in-line holographic system that images the three-dimensional (3D) structure within

¹Atmospheric Sciences Program, Michigan Technological University, Houghton, MI 49931, USA. ²Institute for Atmospheric Physics, Johannes Gutenberg University Mainz, 55128 Mainz, Germany. ³Aerosol and Cloud Physics Group, Max Planck Institute for Chemistry, 55128 Mainz, Germany. ⁴Department of Physics, Michigan Technological University, Houghton, MI 49931, USA. ⁵National Center for Atmospheric Research, Boulder, CO 80307, USA.

*Corresponding author. E-mail: rashaw@mtu.edu

Fig. 1. Relative constancy of cloud droplet diameter during entrainment and mixing and its possible bias from sampling and averaging. (Left) Fluctuations in liquid water content w_l and mean droplet diameter \bar{d} in a cumulus cloud, as sampled by an airborne droplet-counting instrument (DMT Cloud Droplet Probe). Data were obtained during the IDEAS project in November 2011, from the NSF/NCAR C130 (15). The data have a resolution (spatial averaging scale for droplet-by-droplet counting) of 20 m. Cloud liquid water content (red curve) varies widely between $w_l = 0$ and nearly 1 g m^{-3} , but mean droplet diameter (blue curve) is seemingly binary, jumping suddenly between $\bar{d} = 0$ and $\sim 16 \mu\text{m}$. (Right) A



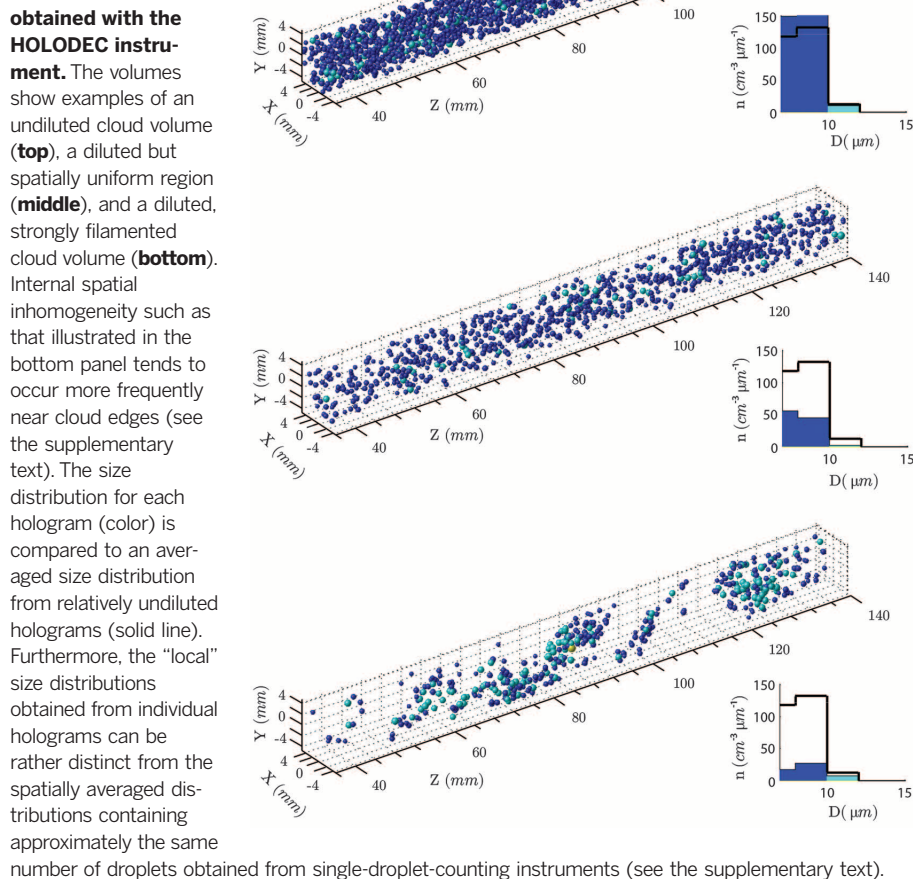
schematic view, not to scale, of droplets sampled by a single droplet detector (i.e., droplets intersected by the thin, red volume). The behavior observed in the top panel could be an artifact of instrument averaging over cloudy and clear regions within the 20 m needed to count enough droplets to estimate \bar{d} . The sampled number density n accurately accounts for the dilute regions, but the \bar{d} is strongly biased toward the value in the undiluted cloud regions.

$\sim 15\text{-cm}^3$ cloud volumes and provides size distributions of the $\sim 10^3$ droplets contained therein (15–17). The approach allows us to probe the response of cloud droplets to turbulent mixing down to the smallest scales where kinetic energy is dissipated by viscosity (~ 1 to 10 mm). Essentially, it allows us to visualize the sharpness of cloud edges and the changes in droplet diameter near those edges without ambiguities introduced through spatial averaging.

The response to reduction in w_l within $n - d$ space is of more than just academic interest because large-scale cloud properties like colloidal stability (18) and optical thickness (19) depend sensitively on both n and d . The magnitude and longevity of the problem are illustrated by Blyth (20), who in a review of the state of the field 20 years ago went so far as to speculate that without entrainment and turbulent mixing “many problems in cloud physics would have been more-or-less solved.” As a specific example, it is arguable that the microphysical response to entrainment directly influences the albedo response of the planet to aerosol perturbations (21). Jeffery (22) provided a scaling argument to demonstrate the importance of mixing for the shortwave optical depth τ , which, because the droplets are large compared to the wavelength, scales as $\tau \sim nd^2$. The response of τ to reduction in cloud liquid water content $w_l \sim nd^3$ by evaporation can be expressed as a susceptibility $S_\tau = \partial \ln \tau / \partial \ln w_l$. In the homogeneous limit where $(\partial / \partial w_l)_h \sim (\partial / \partial d^3)_N$, this results in $(S_\tau)_h = 2/3$, and in the extremely inhomogeneous limit where $(\partial / \partial w_l)_i \sim (\partial / \partial N)_d$, the susceptibility is $(S_\tau)_i = 1$. These are comparable to other indirect effect susceptibilities (see the supplementary text) (23) and suggest that the nature of mixing, and its representation in models, has a leading-order effect on the optical properties of clouds. Thermal infrared properties may be even more strongly influenced because of the absorption near cloud edge, where the imprint of mixing is most prominent (19).

Figure 1 (left panel) illustrates typical empirical evidence supporting the notion of inhomogeneous

Fig. 2. Centimeter-scale measurements of cloud droplet spatial distributions and corresponding size distributions obtained with the HOLODEC instrument. The volumes show examples of an undiluted cloud volume (top), a diluted but spatially uniform region (middle), and a diluted, strongly filamented cloud volume (bottom). Internal spatial inhomogeneity such as that illustrated in the bottom panel tends to occur more frequently near cloud edges (see the supplementary text). The size distribution for each hologram (color) is compared to an averaged size distribution from relatively undiluted holograms (solid line). Furthermore, the “local” size distributions obtained from individual holograms can be rather distinct from the spatially averaged distributions containing approximately the same



mixing at the macro scale, with w_l varying nearly continuously between zero and the maximum for the undiluted cumulus cloud, but with \bar{d} jumping sharply from zero to a nearly constant value. The implication is that cloud dilution occurs

primarily through reductions in the number density n . The lingering question, however, is whether this is rather an artifact of the measurement method, by which individual droplets are counted and sized as they cross a narrowly

Fig. 3. Mean cubic drop-let diameter \bar{d}^3 versus cloud droplet number density n , measured with digital holography in two convective clouds. Each point

corresponds to a “local” \bar{d}^3 and n obtained from individual, $\sim 15\text{-cm}^3$ holograms. The clouds were sampled in **(top)** November 2011 from the NSF/NCAR C130 and **(bottom)** September 2012 from the University of Wyoming King Air research group (15). Mean diameter and number density are normalized by the least-diluted cloud values \bar{d}_0^3 and n_0 , such that an undiluted cloud sample would lie at the position (1,1). The curved

dashed line is the theoretical prediction for homogeneous mixing, and the horizontal solid line is the prediction for the extremely inhomogeneous mixing limit. The homogeneous mixing line is calculated based on measurements of temperature and water vapor concentration in the environment outside the cloud and in undiluted regions of cloud (15). For that calculation, total water content (vapor plus liquid) and liquid-water potential temperature are assumed to be conserved scalars during mixing (9, 28). For both clouds, the holograms display $\bar{d}^3/\bar{d}_0^3 \approx 1$, confirming that inhomogeneous mixing persists down to centimeter scales, the dissipative scale of turbulence. The points in the second example do show a tendency to drop away from the inhomogeneous mixing line at maximum dilution, and this may be evidence for mixing with preconditioned air—e.g., a subsiding shell (30). For example, the points in the bottom panel are bounded by a homogeneous mixing line consistent with a mixture of approximately 10% environmental air and 90% saturated cloud air.

focused laser beam. To obtain a statistically robust estimate of the mean diameter, between 10 and 100 m of flight path must be traversed. Figure 1 (right panel) depicts the resulting dilemma: Suppose at cloud edge, there are filaments of undiluted cloud and homogeneously mixed cloud, in which droplet diameter has decreased in proportion with the mass fraction of entrained clear, dry air. The averaging instrument obtains an accurate measure of the reduction in n due to entrainment and mixing but measures a \bar{d} that is strongly biased toward the value in the undiluted cloud (i.e., the great majority of droplets sampled are from undiluted cloud regions). It therefore remains unknown at what scale inhomogeneous mixing actually occurs or to what extent homogeneous mixing is masked by instrument sampling artifacts. To a large degree, this measurement challenge has motivated important new developments in cloud physics instrumentation over the course of at least two decades: for example, the use of high-speed optical counters that reveal the fine-scale spatial statistics of clouds (8–10, 24–26) or optical methods for estimating droplet effective radius and liquid water content on 10-cm scales (27, 28). Most of these measurements have indicated a prevalence of inhomogeneous mixing. As pointed out by Burnet and Brenguier (9), however, these advances have still left the

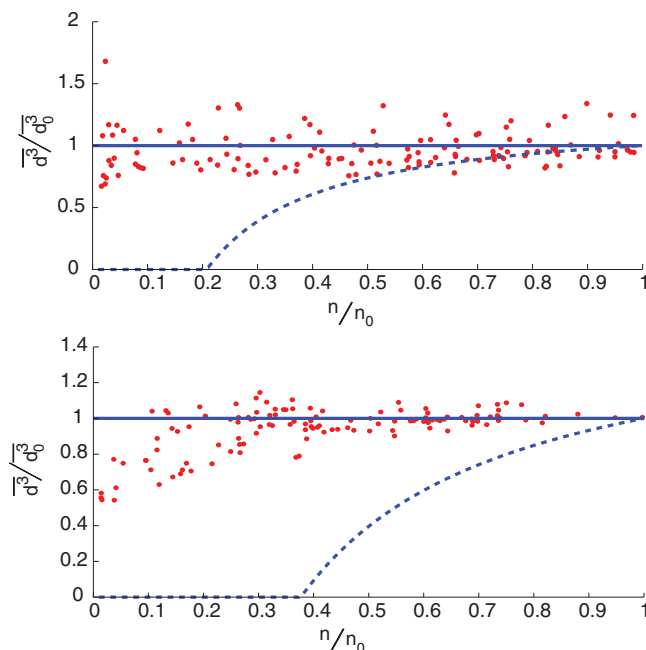
fundamental ambiguity as to whether the apparently inhomogeneous signature is real or an artifact of instrument averaging. The problem calls for an instrument capable not only of measuring locations of droplets on small scales but also of directly measuring the full droplet size distribution on those same scales.

We have developed an approach based on holographic imaging of cloud droplets within discrete volumes, which allows us to overcome the need for spatial averaging and the associated assumptions regarding statistical homogeneity and ergodicity (see the supplementary text). Individual in-line holograms encode the size and 3D position of an ensemble of hydrometeors in a localized volume illuminated by coherent light. That information is later extracted through digital reconstruction. The Holographic Detector for Clouds (HOLODEC) is an airborne instrument that takes snapshot holograms of all resolved particles in an approximately 15-cm^3 volume (15–17). The important result is that holography allows statistically robust cloud droplet size distributions to be determined for each hologram (or even for subvolumes within a hologram). The sampling strategy is in contrast to that of single-particle light-scattering techniques, which often require averaging over 10 to 100 m to build up a similar number of droplets for a statistically

robust estimate of the size distribution. Digital holography provides a well-defined sample volume with particle size and 3D position recorded without coincidence effects. Thus, HOLODEC provides accurate (both in terms of single droplet measurement and in terms of statistical sampling) droplet size distributions representative of “local” (i.e., centimeter-scale), microphysical conditions relevant to diffusion growth and mixing.

We have used the HOLODEC instrument to investigate the variability of liquid water content and droplet size distribution on centimeter scales relevant to microphysical response to turbulent mixing. The data used in this study come from convective clouds sampled during two stages of the Instrument Development and Education in Airborne Science (IDEAS) field project (15). Figure 1 (left panel) is taken from a single cloud pass during IDEAS-2012 and illustrates the highly variable conditions on 20-m scales and above. Other cloud passes from both field projects exhibit qualitatively similar behavior. The holograms recorded provide an unprecedented view of the 3D distributions of cloud droplets at centimeter-to-micrometer scales within the cloud and the size distributions that result from droplets sampled on that scale. Figure 2 shows sample volumes typical for undilute (top) and dilute (middle and bottom) cloud regions. The dilute holograms are sometimes observed to be homogeneous in their spatial structure (middle) but sometimes are quite striking in their filamentary structure (bottom). The corresponding size distributions suggest that large drops remain within the clustered holograms, whereas more uniform evaporation has occurred within the homogeneous volumes. The filamented holograms provide direct and striking evidence for the persistence of sharp edges down to centimeter scales, consistent with turbulent scaling arguments (6, 11). For the observed turbulent conditions in these clouds, a transition scale below which homogeneous mixing should predominate is predicted to be on the order of several centimeters (10).

The spatial distributions in Fig. 2 suggest that highly inhomogeneous mixing exists, so we consider to what extent this pervades the cloud. In Fig. 3, we look at the centimeter-scale size distributions across the entire two-cloud traverses by plotting the two variables contributing to liquid water content, n and \bar{d}^3 (7, 9). Each point on the plot represents n and \bar{d}^3 derived from counting and sizing droplets in a single hologram—i.e., in a $\sim 15\text{-cm}^3$ volume with maximum dimension ~ 10 cm. The values are normalized by the corresponding averages of the 10 holograms with the highest droplet number density (i.e., n_0 and \bar{d}_0^3), such that undiluted cloud is assumed to lie at the point (1,1). Two theoretical curves are shown on the plot: the horizontal (solid) line at $\bar{d}^3/\bar{d}_0^3 = 1$ represents extremely inhomogeneous mixing—i.e., as clear air is entrained, a subset of droplets is completely evaporated, leaving the remaining droplet diameters unchanged. The curved (dashed) line represents homogeneous mixing, in which all



droplets are assumed to evaporate in a uniformly and thoroughly mixed volume. Results from passes through the two clouds previously described are shown to illustrate that the trends are quite general. The data points in both examples show striking agreement with the inhomogeneous hypothesis, confirming for the first time from direct measurements of the droplet size distribution in localized volumes that clouds indeed have sharp edges down to centimeter scales. Apparently, even when the edges, which represent the signature of transient mixing events, eventually diffuse away, they do so after sufficient evaporation occurs that the majority of remaining droplets have relatively undisturbed diameter.

The holographic measurements show that turbulent clouds are inhomogeneous, with sharp transitions between cloud and clear-air properties persisting to dissipative scales (1 to 10 mm). As a result, the droplet size distribution fluctuates strongly in number density but with a nearly unchanging mean droplet diameter, down to the smallest turbulent scales. This 3D view of the cloud structure has several implications, including motivation for including the effects of microphysical mixing in subgrid-scale representation of entrainment in cloud models (13, 14, 29). This in turn will influence the modeled optical and dynamical cloud properties, along with their role in weather and climate (see the supplementary text). For example, the predominance of inhomogeneous mixing suggests that the optical depth susceptibility $S_\tau = \partial \ln \tau / \partial \ln w_l$ is closest to its maximum possible value of 1. The observations also add further plausibility to the hypothesis that mixing and the resulting evaporation can lead ultimately to enhanced droplet growth (18): Inhomogeneous response to mixing leaves droplets of the same diameter as in the undiluted regions of cloud but with considerably reduced competition for excess water vapor. Perhaps, however, the qualitative picture of clouds having sharp edges down to the centimeter scale is the most vivid impression to be taken from the work.

REFERENCES AND NOTES

1. G. Feingold, I. Koren, H. Wang, H. Xue, W. A. Brewer, *Nature* **466**, 849–852 (2010).
2. B. Stevens, S. Bony, *Science* **340**, 1053–1054 (2013).
3. P. R. Bannon, *J. Atmos. Sci.* **59**, 1967–1982 (2002).
4. E. Bodenschatz, S. P. Malinowski, R. A. Shaw, F. Stratmann, *Science* **327**, 970–971 (2010).
5. M. B. Baker, R. G. Corbin, J. Latham, *Q. J. R. Meteorol. Soc.* **106**, 581–598 (1980).
6. M. B. Baker, R. E. Breidenthal, T. W. Choularton, J. Latham, *J. Atmos. Sci.* **41**, 299–304 (1984).
7. J. B. Jensen, P. H. Austin, M. B. Baker, A. M. Blyth, *J. Atmos. Sci.* **42**, 173–192 (1985).
8. I. R. Paluch, D. G. Baumgardner, *J. Atmos. Sci.* **46**, 261–278 (1989).
9. F. Burnet, J.-L. Brenguier, *J. Atmos. Sci.* **64**, 1995–2011 (2007).
10. K. Lehmann, H. Siebert, R. A. Shaw, *J. Atmos. Sci.* **66**, 3641–3659 (2009).
11. C. Lu, Y. Liu, S. Niu, *J. Geophys. Res.* **116**, D20207 (2011).
12. C. Lu, Y. Liu, S. Niu, S. Endo, *J. Geophys. Res.* **119**, (2014).
13. S. K. Krueger, C.-W. Su, P. A. McMurtry, *J. Atmos. Sci.* **54**, 2697–2712 (1997).
14. W. W. Grabowski, *J. Atmos. Sci.* **64**, 3666–3680 (2007).
15. Materials and methods are available as supplementary materials on Science Online.

16. J. P. Fugal, R. A. Shaw, *Atmos. Meas. Tech.* **2**, 259–271 (2009).
17. S. M. Spuler, J. Fugal, *Appl. Opt.* **50**, 1405–1412 (2011).
18. W. A. Cooper, S. G. Lasher-Trapp, A. M. Blyth, *J. Atmos. Sci.* **70**, 1727–1743 (2013).
19. F. Chosson, J.-L. Brenguier, L. Schüller, *J. Atmos. Sci.* **64**, 2670–2682 (2007).
20. A. M. Blyth, *J. Appl. Meteorol.* **32**, 626–641 (1993).
21. W. W. Grabowski, *J. Clim.* **19**, 4664–4682 (2006).
22. C. A. Jeffery, *J. Geophys. Res.* **112** (D24), D24S21 (2007).
23. G. Feingold, W. L. Eberhard, D. E. Veron, M. Previdi, *Geophys. Res. Lett.* **30**, 1287 (2003).
24. D. Baumgardner, B. Baker, K. Weaver, *J. Atmos. Ocean. Technol.* **10**, 557–565 (1993).
25. B. A. Baker, *J. Atmos. Sci.* **49**, 387–404 (1992).
26. J.-L. Brenguier, *J. Appl. Meteorol.* **32**, 783–793 (1993).
27. A. Davis, A. Marshak, H. Gerber, W. Wiscombe, *J. Geophys. Res.* **104**, 6123–6144 (1999).
28. H. E. Gerber, G. M. Frick, J. B. Jensen, J. G. Hudson, *J. Meteorol. Soc. Jpn.* **86A**, 87–106 (2008).
29. C. Lu, S. Niu, Y. Liu, A. M. Vogelmann, *Geophys. Res. Lett.* **40**, 2333–2338 (2013).
30. T. Heus, H. J. J. Jonker, *J. Atmos. Sci.* **65**, 1003–1018 (2008).

ACKNOWLEDGMENTS

We thank J. French and the aircraft staff for assistance with the instrument deployment on the University of Wyoming King Air research group. We thank the staff of the National Center for Atmospheric Research (NCAR) Earth Observing Laboratory for assistance with the instrument deployment on the NSF/NCAR C130. This project was supported by U.S. National Science Foundation grant AGS-1026123, by the U.S. Department of Energy as part of the Atmospheric Radiation Measurement Climate Research Facility, and by a NASA Earth and Space Science Fellowship. NCAR is sponsored by the U.S. National Science Foundation. Data are available according to instructions in the supplementary materials on Science Online.

SUPPLEMENTARY MATERIALS

www.sciencemag.org/content/350/6256/87/suppl/DC1
Materials and Methods
Supplementary Text
Figs. S1 to S10
References (31–69)

11 March 2015; accepted 28 August 2015
10.1126/science.aab0751

PALEOECOLOGY

Community stability and selective extinction during the Permian-Triassic mass extinction

Peter D. Roopnarine^{1*} and Kenneth D. Angielczyk²

The fossil record contains exemplars of extreme biodiversity crises. Here, we examined the stability of terrestrial paleocommunities from South Africa during Earth's most severe mass extinction, the Permian-Triassic. We show that stability depended critically on functional diversity and patterns of guild interaction, regardless of species richness. Paleocommunities exhibited less transient instability—relative to model communities with alternative community organization—and significantly greater probabilities of being locally stable during the mass extinction. Functional patterns that have evolved during an ecosystem's history support significantly more stable communities than hypothetical alternatives.

Accelerating rates of extinction will have negative impacts on Earth's ecosystems and human well-being (1), but they have no modern precedents, and ecosystem responses are uncertain (2). The Earth's history, however, has recorded episodes of extreme biodiversity loss. Here, we use the most severe of those events, the Permian-Triassic mass extinction (PTME), to examine how the short-term stability of ecological communities may vary as their functional structures are altered by extinction. We modeled paleocommunity stability as local stability (3), and transient dynamics after perturbation (4). Both measures describe paleocommunity dynamics when species populations are perturbed. Paleocommunity structures were determined by species richnesses, species partitioning among functional groups or trophic guilds, and the distribution of

interspecific trophic interactions (Fig. 1A). We examined the relationships between these parameters and stability by comparing paleocommunity food webs to hypothetical alternatives, wherein species richness, the number of trophic interactions, and average interaction strength were held constant as we varied patterns of functional partitioning and trophic interaction distributions (Fig. 1, B to F). We thus characterized paleocommunity stability before, during, and after the mass extinction.

We assembled paleocommunity data for the Middle Permian to Middle Triassic terrestrial ecosystems of the Beaufort Group in the Karoo Basin of South Africa (5) (Fig. 2). Only four tetrapod genera of over 50 are known to have crossed the Permian-Triassic boundary (PTB) (6–8), and richness remained low in the Early Triassic (9). Our paleocommunities include the Permian *Pristerognathus*, *Tropidostoma*, *Cistecephalus*, and *Dicynodon* assemblage zones, and the Triassic *Lystrosaurus* and *Cynognathus* assemblage zones (table S1). We used a two-pulsed extinction (10) to reconstruct three communities from the *Dicynodon*

¹Institute for Biodiversity Science and Sustainability, California Academy of Sciences, 55 Music Concourse Drive, San Francisco, CA 94118, USA. ²Integrative Research Center, Field Museum of Natural History, Chicago, IL 60605, USA.
*Corresponding author. E-mail: proopnarine@calacademy.org

assemblage zone (DAZ): (i) a Phase 0 (Ph0) community comprising all taxa that occurred within the DAZ; (ii) a Phase 1 (Ph1) survivor community

that spanned the lower part of the extinction interval; and (iii) a Phase 2 (Ph2) survivor community comprising taxa that became extinct just

before the PTB or survived into the Early Triassic. We refer to Ph1 and Ph2 throughout as mass extinction intervals, and all other paleocommunities, including Ph0, as intervals of background extinction.

Species were partitioned among guilds according to trophic ecology and body size (11) (Fig. 1A). Amniotes were divided into ten guilds, with herbivores feeding on a single producer guild, while faunivores preyed on amniote herbivores and faunivores up to two size classes larger and smaller than themselves, with the smallest two faunivore guilds also preying on arthropods (tables S2 and S3). Temnospondyl guilds preyed on temnospondyl and amniote guilds up to two size classes larger and smaller than themselves, as well as fish, insects, and aquatic invertebrates. Fish fed on aquatic producers, insects, aquatic invertebrates, and temnospondyls. Insects were divided into herbivorous, omnivorous, and predatory guilds (5). Few noninsect invertebrates are known from the Beaufort Group, but our data include molluscs, myriapods, and conchostracans. Plant species were not treated individually because taxonomic resolution is currently insufficient. We instead assume that producer species behaved neutrally with respect to competition and herbivory, and so we aggregated them into four guilds: aquatic microphytes, aquatic macrophytes, terrestrial production accessible to insects and amniotes, and terrestrial production available to insects only (arboreal amniotes were absent from the Beaufort Group).

Although paleontological data lack details of biotic interactions that are available for modern species, paleotrophic interactions can be inferred from predatory traces, preserved gut contents (12), functional morphological interpretations, body size relationships, and habitat (13). These define partitions of paleocommunity species richness (S) into a fixed number of trophic guilds, as well as a pattern of functional organization or interactions among guilds. Thus, of all food web topologies possible given S (14), only a subset would be consistent with paleocommunity data (15) (Fig. 1B). We constrained this subset further by assuming a hyperbolic decay distribution

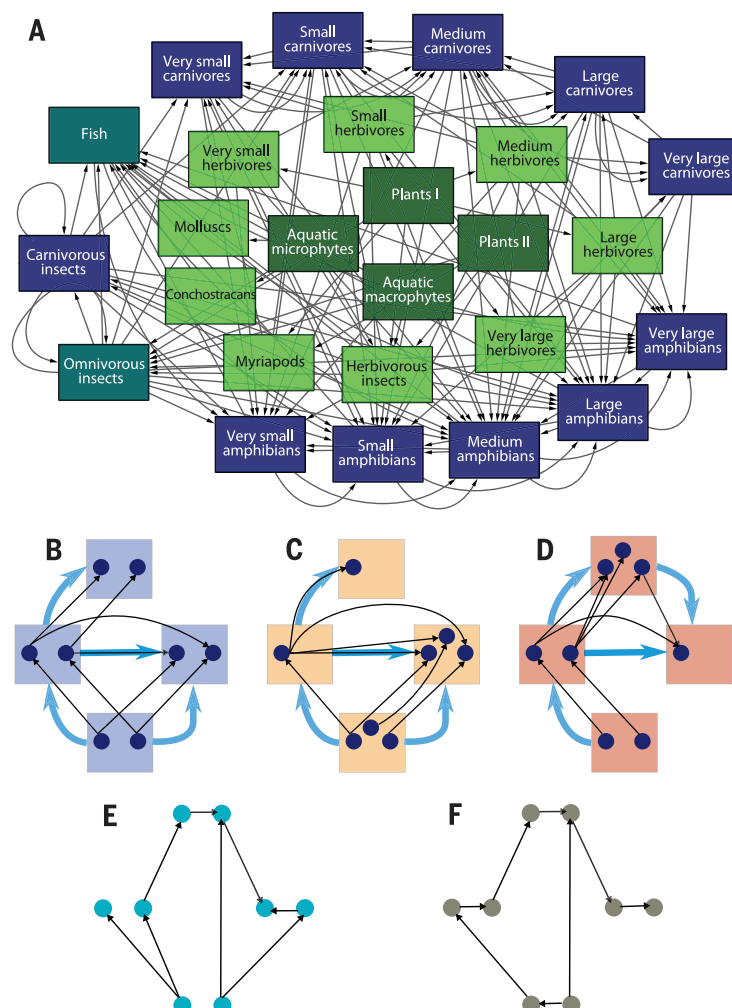
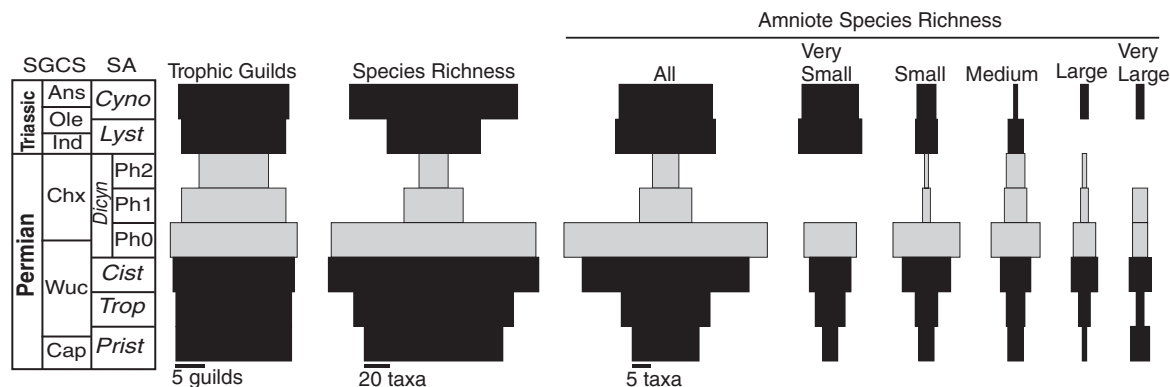


Fig. 1. Guild interactions and alternative models. (A) Beaufort Group food web. Guild richnesses are listed in table S2. (B to F) Food web models: (B) Example paleocommunity web, with four guilds and two species per guild. Blue arrows, guild interactions; black arrows, species interactions. (C to F) Alternative models of community organization.

Fig. 2. Beaufort Group paleocommunity compositions.

(Right) Gray bars represent the extinction stages; missing bars indicate that richness was zero. Total amniote species are subdivided by body size. (Left) Correlations between Beaufort Group assemblage zones and the geological time scale. The subdivisions of the *Dicynodon* assemblage zone, illustrated as of equal length, were of unequal durations (10). Stratigraphic units: Ans, Anisian; Cap, Capitanian; Chx, Changhsingian; Ind, Induan; Ole, Olenekian; Wuc, Wuchiapingian. Assemblage zones: *Cist*, *Cistecephalus*; *Cyno*, *Cynognathus*; *Dicyn*, *Dicynodon*; *Lyst*, *Lystrosaurus* assemblage zone; *Prist*, *Pristerognathus*; *Trop*, *Tropidostoma*.



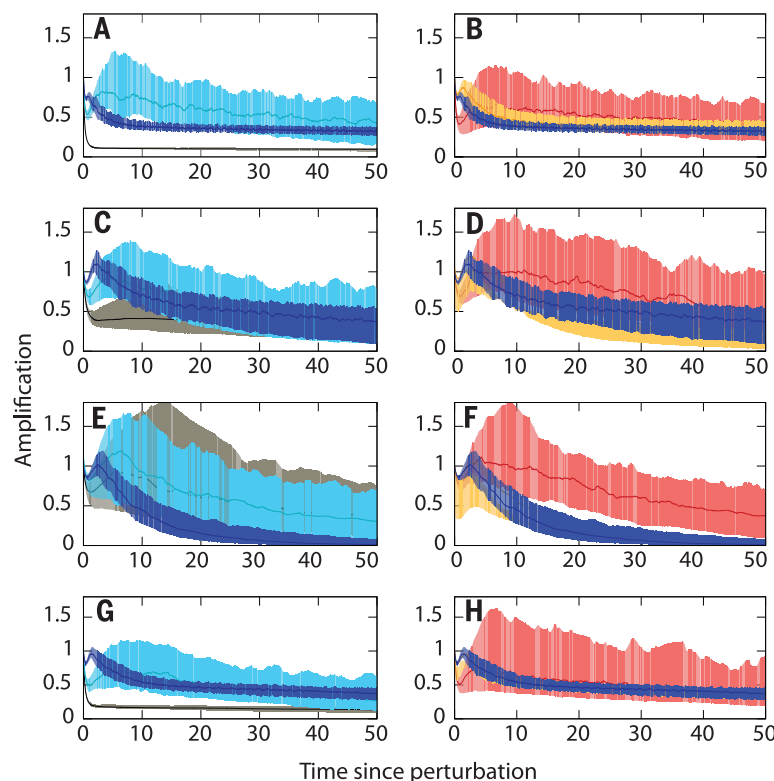


Fig. 3. Paleocommunities and alternative model transient dynamics. (A and B) DAZ Ph0; (C and D) Ph1; (E and F) Ph2; (G and H) LAZ (see text for explanation). Colors correspond to models illustrated in Fig. 1, B to F; deep blue are paleocommunity results. Lines represent median of 100 simulations per model, and filled envelopes are 25th and 75th percentiles.

for the number of prey species per consumer species (5, 16), with more species being relatively specialized, and the distribution's heavy tail representing fewer, relatively generalized consumers. Finally, we sampled food webs from the constrained subset, describing species interactions with generalized Lotka-Volterra (LV) functions, and each food web as a $S \times S$ matrix of interspecific interactions. Time-averaging and incomplete preservation limit measurement of the number of biotic interactions and their strengths, so we parameterized interaction number with stochastic draws of the number of prey per consumer from the hyperbolic distribution, as well as corresponding interaction coefficients from uniform distributions (5). Positive off-diagonal elements represent predation, and negative elements represent the impacts of predatory species. Diagonal terms describe population growth in the absence of interspecific interactions and are always negative in our models. Each paleocommunity's matrices are therefore of statistically similar connectance and average interaction strength.

We formulated a series of alternative food web models, each one relaxing a constraint on topology, to understand how changing functional organization would have affected paleocommunity stability during the PTME (Fig. 1, C to F). Each model expands the subset of food webs to include webs that are inconsistent with some

aspect of the paleocommunity. For example, the first model retains species richness, as well as guild structure, but randomizes species assignments to consumer guilds (Fig. 1C). Subsequent models randomize interactions and species assignments to consumer guilds (holding guild number constant) (Fig. 1D); or remove guild structure altogether but retain the interaction distribution (Fig. 1E); or assign trophic interactions randomly, yielding short-tailed Poisson distributions (Fig. 1F) (17).

Paleocommunity and model stabilities were assessed as the proportion of stochastically generated webs that are locally stable and the transient instability of each web. Local stability is a mathematically simplified but tractable measure of stability given typical community complexity, with a community in equilibrium returning to equilibrium after a minor perturbation. The simplification restricts local stability analysis to minor perturbations but is, nonetheless, a useful first approximation (3). We measured local stability as the real (noncomplex) part of the dominant eigenvalue of a LV matrix. Negative eigenvalues indicate that any perturbation will decline asymptotically to zero, whereas webs with positive eigenvalues do not return to equilibrium. At least 100 LV matrices were generated stochastically for each model and paleocommunity.

No matrices of the background extinction paleocommunities, or their alternative models, were

locally stable. This is consistent with the negative relationship between the probability of local stability, and species richness, density of interspecific interactions, and average interaction strength (17). S ranged from 71 to 140 for those paleocommunities. The fractions of locally stable webs do increase for Ph1 and Ph2, to 25% and 84%, respectively, as S declined to 43 and 19, respectively. The increase is not a function of declining richness but, instead, of functional organization, because, whereas holding S and functional organization constant but partitioning species randomly (Fig. 1C) yielded frequencies of 56% and 88% in Ph1 and Ph2, respectively, frequencies were significantly lower when functional organization was also randomized (Fig. 1D); 2% and 24%, respectively [Ph1: $\chi^2(df = 2, n = 400) = 74.78, P < 0.0001$; Ph2: $\chi^2(df = 2, n = 400) = 134.86, P < 0.0001$]. Removing guild compartmentalization (Fig. 1E) also reduces the frequencies significantly, to 0% and 41% for Ph1 and Ph2, respectively [$\chi^2(df = 1, n = 300) = 30, P < 0.0001$; $\chi^2(df = 1, n = 300) = 58.33, P < 0.0001$, respectively]. Poisson-distributed models (Fig. 1F) yielded no locally stable webs. Real patterns of functional organization therefore promoted significantly greater probabilities of yielding locally stable food webs during the PTME, regardless of how species were partitioned.

Multispecies models generally amplify perturbations and return to equilibrium nonmonotonically. Such transient short-lived instability is common in real communities (18) and contributes to dynamics when perturbations are frequent, as would be expected during the PTME. We therefore measured three transient responses to perturbation: reactivity, maximum amplification, and the timing of maximum amplification (4, 5). Reactivity is the instantaneous rate of displacement in response to perturbation. The dynamics of the displacement yield the maximum amplification during the return to equilibrium. We measured locally stable matrices only, using a Monte Carlo optimization approach to ensure local stability (5) even if a stochastically generated matrix was not initially stable.

Paleocommunities were significantly more reactive than alternative models (e.g., Ph0, $F_{4,497} = 1119.07, P < 0.0001$) (table S4), and reactivity decreases from the most structured model to the least (Fig. 1, C to F). Almost all background extinction paleocommunities amplify perturbations to a significantly lesser degree, and earlier in time, than do models with alternative guild structure or hyperbolically distributed interactions, although Poisson-distributed webs are least amplified (e.g., Ph0, Kruskal-Wallis $H = 97.734, df = 4, P = 0.0001$) (Fig. 3, A and B). Species responses to perturbation would thus be significantly dampened in paleocommunities relative to alternatively structured communities. The mass extinction Ph1 paleocommunity is no more amplified than alternative models ($H = 136.385, df = 4, P = 0.0001$) (Fig. 3, C and D), except the Poisson model, which remains the most stable. During Ph2, paleocommunity perturbations

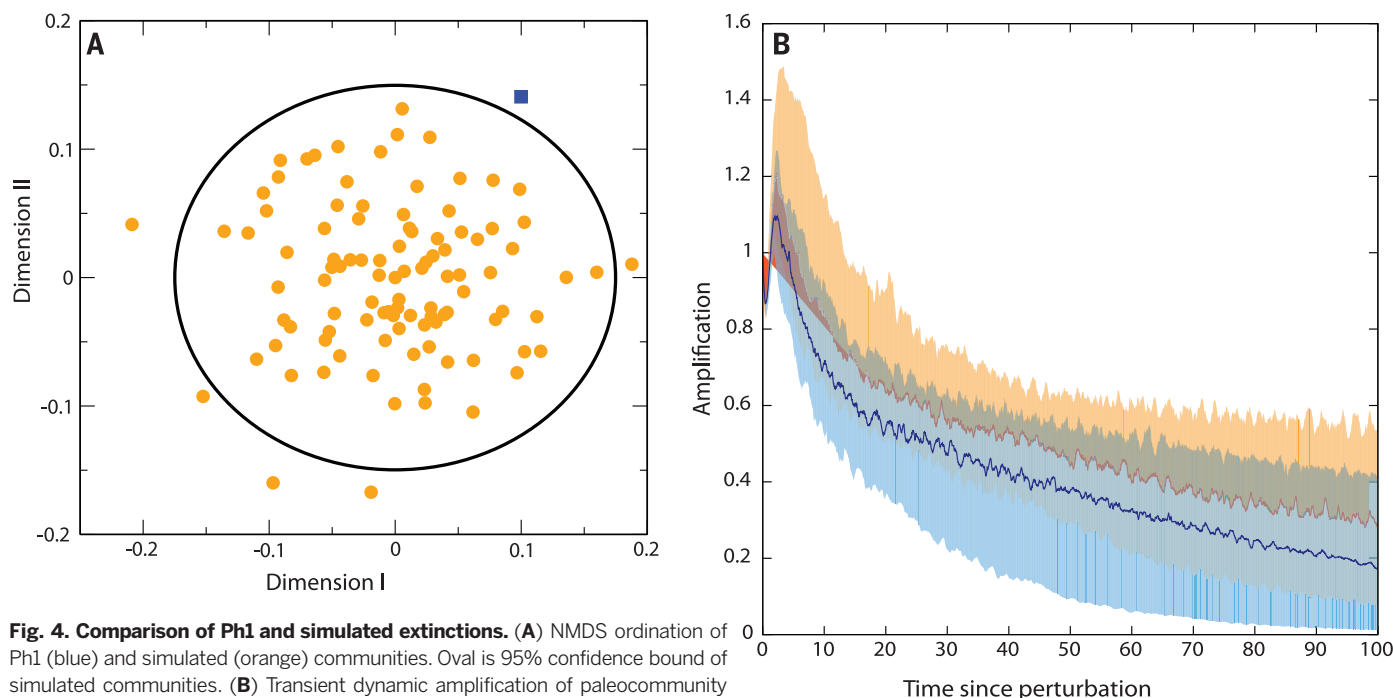


Fig. 4. Comparison of Ph1 and simulated extinctions. (A) NMDS ordination of Ph1 (blue) and simulated (orange) communities. Oval is 95% confidence bound of simulated communities. (B) Transient dynamic amplification of paleocommunity and simulated communities.

are amplified significantly less than those of the functionally altered models ($H = 32.613$, $df = 2$, $P = 0.0001$) (Fig. 3F), but there is no longer any distinction based on interaction distributions ($H = 2.176$, $df = 2$, $P = 0.1402$) (Fig. 3E). Paleocommunities during the PTME were therefore as stable or significantly more stable than models with alternative functional organization. The Early Triassic *Lystrosaurus* assemblage zone (LAZ) paleocommunity, in the aftermath of the PTME, is indistinguishable from the guild-randomized and hyperbolic interaction distribution models ($H = 3.759$, $df = 3$, $P = 0.2887$) (Fig. 3, F and G) but differs significantly from the Poisson-distributed model ($H = 53.455$, $df = 1$, $P = 0.0001$) (Fig. 2F). This paleocommunity was therefore no more stable than the randomized models, an observation consistent with LAZ's inferred hypersensitivity to simulated disruptions of primary productivity (11). By the Middle Triassic, though, the *Cynognathus* assemblage zone community exhibited dynamics similar to those of the premass extinction communities (table S4).

The increased frequencies of locally stable paleocommunities and greater transient stability of the Ph1 and Ph2 paleocommunities, compared with alternative models, suggests that the extinctions were not random. We tested this by comparing the Ph1 paleocommunity to simulated communities produced by applying the Ph1 extinction randomly to the Ph0 paleocommunity. The simulated communities differed significantly in composition from the Ph1 community [non-metric multidimensional scaling (NMDS) Bray-Curtis dissimilarity, $n = 100$, Hotelling's $T^2 = 10.355$, $P = 0.0076$] (Fig. 4A). The average probability of producing any single simulated community by random extinction, although exceedingly

small ($P = 1.19 \times 10^{-29}$, $n = 100$), is significantly larger than the probability of producing the Ph1 paleocommunity itself ($P = 1.61 \times 10^{-34}$) (χ^2 test, $P < 0.001$) (5). The bias stems from a significantly elevated frequency of extinction of small-bodied amniotes, in contrast to medium and very large amniotes (Fisher's exact test, $P = 0.016$) (Fig. 2). Furthermore, although the proportion of locally stable simulated communities does not differ from that of the Ph1 community (19%, Fisher's exact test, $P = 0.308$), they are significantly more reactive ($F_{1,199} = 869.9$, $P < 0.0001$) and have greater values of maximum amplification ($H = 10.426$, $P = 0.0012$). Biased extinction therefore produced a Ph1 community more stable than expected had extinctions been unbiased. There is no evidence of bias, however, in the Ph2 extinction.

Communities before the PTME therefore exhibited less transient instability than alternative model communities because of their functional organization. During the PTME, communities biased by the selective extinction of small-bodied amniotes during Ph1 exhibited no more, and in some cases less, transient instability than alternative models and were more likely to be locally stable. Community stability and its maintenance were, therefore, defining features of this Permian-Triassic ecosystem.

REFERENCES AND NOTES

- G. M. Mace et al., *Glob. Environ. Change* **28**, 289–297 (2014).
- A. D. Barnosky et al., *Nature* **486**, 52–58 (2012).
- S. L. Pimm, *Food Webs* (Univ. of Chicago Press, Chicago, ed. 1, 1982).
- M. G. Neubert, H. Caswell, *Ecology* **78**, 653–665 (1997).

- Materials and methods are available as supplementary materials on Science Online.
- J. Botha, R. M. H. Smith, *Lethaia* **40**, 125–137 (2007).
- A. K. Huttenlocker, C. A. Sidor, R. M. H. Smith, *J. Vertebr. Paleontol.* **31**, 405–421 (2011).
- A. K. Huttenlocker, J. Botha-Brink, *Peer J.* **2**, e325 (2014).
- J. Fröbisch, in *Early Evolutionary History of the Synapsida*, C. F. Kammerer, K. D. Angielczyk, J. Fröbisch, Eds. (Springer, Dordrecht, Netherlands, 2014), pp. 305–319.
- R. M. H. Smith, J. Botha-Brink, *Palaeogeogr. Palaeoclimatol. Palaeoecol.* **396**, 99–118 (2014).
- P. D. Roopnarine, K. D. Angielczyk, S. C. Wang, R. Hertog, *Proc. Biol. Sci.* **274**, 2077–2086 (2007).
- J. A. Dunne, C. C. Labandeira, R. J. Williams, *Proc. R. Soc. London Ser. B* **281**, 20133280 (2014).
- P. D. Roopnarine, in *The Paleontological Society Papers*, vol. 15, *Conservation Paleobiology*, G. Dietl, K. Flessa, Eds. (The Paleontological Society, Boulder, CO, 2009), pp. 195–220.
- S. Levin, *Fragile Dominion* (Helix Books, Perseus Publishers, Cambridge, MA, 2007).
- P. D. Roopnarine, in *The Paleontological Society Papers*, vol. 16, *Quantitative Methods in Paleobiology*, J. Alroy, G. Hunt, Eds. (The Paleontological Society, Boulder, CO, 2010), pp. 143–161.
- R. J. Williams, *Theor. Ecol.* **3**, 45–52 (2010).
- R. M. May, *Stability and Complexity in Model Ecosystems* (Princeton Univ. Press, Princeton, NJ, 1973).
- A. Verdy, H. Caswell, *Bull. Math. Biol.* **70**, 1634–1659 (2008).

ACKNOWLEDGMENTS

Data are available in the supplementary materials. We thank two anonymous reviewers for comments. This work was supported by NSF Earth Life Transitions Grant 1336986 (to P.D.R., K.D.A., and C. Sidor).

SUPPLEMENTARY MATERIALS

www.sciencemag.org/content/350/6256/90/suppl/DC1
Materials and Methods
Tables S1 to S4
References (19–36)

16 March 2015; accepted 18 August 2015
10.1126/science.aab1371

NEURODEVELOPMENT

Somatic mutation in single human neurons tracks developmental and transcriptional history

Michael A. Lodato,^{1*} Mollie B. Woodworth,^{1*} Semin Lee,^{2*} Gilad D. Evrony,¹ Bhaven K. Mehta,¹ Amir Karger,³ Soohyun Lee,² Thomas W. Chittenden,^{3,4†} Alissa M. D'Gama,¹ Xuyu Cai,^{1‡} Lovelace J. Luquette,² Eunjung Lee,^{2,5} Peter J. Park,^{2,5§} Christopher A. Walsh^{1§}

Neurons live for decades in a postmitotic state, their genomes susceptible to DNA damage. Here we survey the landscape of somatic single-nucleotide variants (SNVs) in the human brain. We identified thousands of somatic SNVs by single-cell sequencing of 36 neurons from the cerebral cortex of three normal individuals. Unlike germline and cancer SNVs, which are often caused by errors in DNA replication, neuronal mutations appear to reflect damage during active transcription. Somatic mutations create nested lineage trees, allowing them to be dated relative to developmental landmarks and revealing a polyclonal architecture of the human cerebral cortex. Thus, somatic mutations in the brain represent a durable and ongoing record of neuronal life history, from development through postmitotic function.

Ongoing random mutation of DNA ensures that no two cells in an individual are genetically identical (1). Some of these “somatic” mutations cause cancer or, when they occur in progenitors in the developing human brain, neurological diseases such as epilepsy and developmental brain malformations (2). Whereas mature neurons can survive for the life of the individual, DNA is buffeted by mutagens such as oxygen free radicals, electromagnetic radiation, and endogenous transposable elements. These forces have the potential to induce somatic mutations throughout the life of a neuron, and they may contribute to normal aging and neurodegenerative disease (3). High-throughput sequencing of DNA isolated from thousands of cells from “bulk” tissue, although useful, is unable to detect mutations present in one or small numbers of cells, and determining whether mutations exist together within one cell requires single-cell analyses (4, 5). Although previous analyses of single neurons in the human brain have demonstrated occasional somatic copy-number variants (6, 7) and L1 retrotransposon insertions (8, 9), SNVs are a major source of germline and cancer variation (10, 11), and likely represent a more substantial source of the overall somatic mutation burden in neurons.

To investigate rates and patterns of somatic SNVs, we analyzed high-coverage (~40×) whole-genome sequencing (WGS) data from 36 single neurons from postmortem brain tissue of three neurotypical individuals: a 15-year-old female (UMB4638), a 17-year-old male (UMB1465) (8), and a 42-year-old female (UMB4643) (sources designated brains A, B, and C, respectively). Using fluorescence-activated nuclear sorting (FANS), we purified single NeuN⁺ cortical neuronal nuclei from the prefrontal cortex of postmortem human brain tissue; we then amplified the DNA by multiple-displacement amplification (MDA) (7) (Fig. 1A). We subjected this amplified DNA to high-throughput sequencing, achieving ≥10× average coverage per neuron at 82 to 87% of loci (table S1). After analysis of overall quality (8), false-positive and false-negative variant calls, allelic balance, and locus/allele dropout (figs. S1 and S2; supplementary text), we used these single-cell MDA WGS data to identify somatic mutations, focusing on SNVs.

We identified single-cell SNV candidates by means of three established mutation-calling algorithms (see materials and methods), thereby defining a conservative list of somatic SNVs as those identified by all three callers in at least one single neuron but absent from DNA isolated from bulk tissue (e.g., heart) from the same individual (Fig. 1B). These “triple-called” SNVs were confirmed by Sanger sequencing at a very high rate (92%) in the single-cell DNA sample from which they were identified (table S2 and fig. S3). Single neurons from the three brains averaged 1685 to 1793 triple-called SNVs (Table 1, Fig. 1D, table S3, and fig. S4). Across all neurons, we observed a mean of 8.3% allelic dropout (loss of one allele of a heterozygous locus) and 3.3% locus dropout (fig. S1). With an estimated 23% false-discovery rate, our results suggest that each neuron from these individuals may have contained 1458 to 1580 somatic

SNVs. Additional model-based analyses resulted in a similar range of SNVs identified (fig. S5; supplementary text). These rates of mutation per neuron are consistent with single-cell sequencing of other normal cell types (12) but are lower than somatic SNV rates in normal skin cells, which are exposed to damaging ultraviolet light (13), and in several tumor types (11, 12, 14).

The molecular profile of neural SNVs is quite distinct from cancer and germline mutations, and reveals mutagenic forces that affect a neuron during its life. Cancer and germline mutation rates correlate with DNA replication (15, 16), with late-replicating DNA more susceptible to mutation, and they negatively correlate with transcription (15, 17). In contrast, single-neuron SNVs did not correlate with replication timing (fig. S6 and table S4) and were enriched in coding exons (Fig. 2A) with a strand bias (purine-purine transitions enriched on the nontemplate strand), as expected for transcription-associated mutations (18, 19) (Fig. 2B and fig. S7). We also observed a signature of methylated cytosine (meC) to thymine (T) transitions (fig. S8), which can occur as a result of replication-independent deamination of meC, in single-neuron SNVs. Taken together, these data demonstrate that replication-independent mutational mechanisms generate more SNVs than does replication in human neurons, which are postmitotic and live long, transcriptionally active lives.

Integration of our SNV data with gene expression in the prefrontal cortex from public databases (20) revealed that highly expressed genes (in particular, those in the third quartiles) were enriched for single-neuron SNVs with statistical significance (Fig. 2D, fig. S9, and table S5), and, unlike mutations in cancers (such as glioblastoma multiforme), single-neuron SNVs correlated with chromatin markers of transcription (21) from fetal brain (Fig. 2C and table S6). Neural-related gene sets were enriched for somatic SNVs (Fig. 2E, fig. S10, and table S7), and single neurons harbored heterozygous coding SNVs in genes that, when a single copy is mutated in the germline, confer a high risk of neurological disease (table S8). For example, *SCN1A* (seizure disorder) (22) and *SLC12A2* (schizophrenia) (23) both contained coding mutations in neurons from brain B (Fig. 2F and table S8). Thus, genes active in human neurons and critical for their function are vulnerable to somatic mutation, and even the normal brain contains individual neurons with disruptive mutations.

Mutations shared by multiple neurons, which must necessarily have arisen during development, revealed surprising lineage relationships in the human brain. We genotyped shared somatic variants in brain B, including 15 SNVs (table S9), a TG-dinucleotide expansion on chromosome 4 (see materials and methods), and two L1 retrotransposon insertions (7, 8), in 210 amplified single-neuron genomes isolated from the same region of cortex as the original 16 cells from brain B; 136 of 226 (60%) single-neuron genomes contained at least one clonal SNV (fig. S11), and the results suggested serial mutations over the course of development. For example, three SNVs showed

¹Division of Genetics and Genomics, Manton Center for Orphan Disease, and Howard Hughes Medical Institute, Boston Children's Hospital, Boston, MA, USA; Departments of Neurology and Pediatrics, Harvard Medical School, Boston, MA, USA; and Broad Institute of MIT and Harvard, Cambridge, MA, USA. ²Department of Biomedical Informatics, Harvard Medical School, Boston, MA, USA. ³Research Computing, Harvard Medical School, Boston, MA, USA. ⁴Complex Biological Systems Alliance, North Andover, MA, USA. ⁵Division of Genetics, Brigham and Women's Hospital, Boston, MA, USA. *These authors contributed equally to this work. †Present address: WuXi NextCODE, Cambridge, MA, USA. ‡Present address: Illumina Inc., San Diego, CA, USA. §Corresponding author. E-mail: peter_park@harvard.edu (P.J.P.); christopher.walsh@childrens.harvard.edu (C.A.W.)

distinct mosaic profiles: SNV C1 was present in 23% (51/226) of the neurons tested (suggesting that it occurred early in development), C8 was present only in three of these 51 neurons, and C10 only in two of this set of three, neurons 2 and 77 (Fig. 3A and fig. S11). SNVs identified mutually exclusive sets of neurons such that, for example, cells marked by variants discovered in neurons 39 and 47 never contained SNVs present in neurons 6 and 18, 2 and 77, or 3 and 12 (except one anomalous cell; fig. S11). These data placed 9/16 sequenced cells, and 60% (136/226) of analyzed cortical neurons, into four separate clades (pink, green, blue, and purple in Fig. 3A), which suggests that at least five distinct clades—the

four marked, plus at least one additional unmarked clade—gave rise to the 226 neurons in this sample.

Genotyping DNA samples from across the brain, using ultradeep sequencing of a targeted panel of clonal somatic SNVs, showed that although some SNVs were present at low mosaic fractions (up to 4% of cells) only in restricted regions of frontal cortex, all four major clades dispersed across the cortex at surprisingly low levels of mosaicism (green clade, 0.2 to 2%; blue clade, 0.5 to 6%; purple clade, 1 to 7%; pink clade, 18 to 32%) (Fig. 3B, fig. S12, and table S10). For example, SNVs C8 and C10 were restricted to <3% of cells in the middle frontal gyrus surrounding the site of sequencing,

whereas C1 marked deeper branches of this same clade and was found throughout the cortex in 7 to 26% of cells, as well as in the cerebellum and spinal cord (Fig. 3B). Analysis of non-brain tissue of individual B showed that variants present in >5 to 10% of his brain cells were generally detected widely outside the brain, in tissues derived from endoderm, ectoderm, and mesoderm (Fig. 3C, fig. S13, and table S10), which suggests that these SNVs arose before the three germ layers segregated at gastrulation, yet still marked a minority of neurons.

Our data demonstrate that individual clones intermingle widely in the human cortex and that neurons from a given cortical region constitute

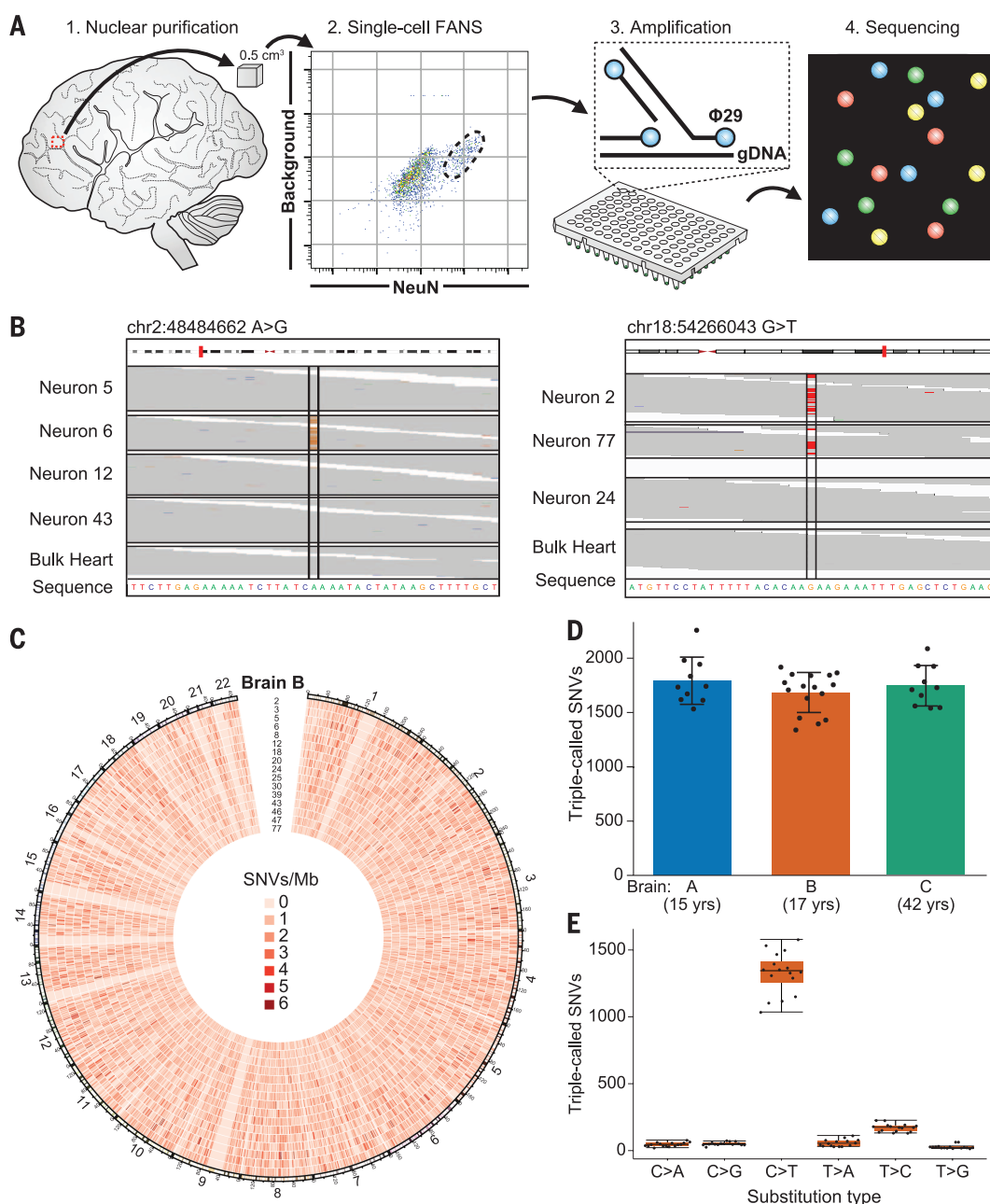


Fig. 1. Somatic SNVs are detected by single-neuron whole-genome sequencing.

(A) Schematic of approach. Nuclei are isolated from a 0.5-cm³ piece of frozen post-mortem tissue by fluorescence-activated nuclear sorting (FANS), and DNA is amplified by Φ 29 polymerase-mediated multiple-displacement amplification (MDA) and subjected to whole-genome sequencing (WGS). (B) Sample sequencing alignment tracks from brain B. One SNV is called uniquely in one sample (left), and one is shared between neurons 2 and 77 but absent from other single cells and heart (right). (C) Circos plot of SNV rate per megabase in brain B across human autosomes demonstrates that somatic mutations are distributed broadly. (D) SNVs per neuron are tightly correlated within each individual. (E) Most single-neuron SNVs in brain B are C>T transitions. Error bars in (D) and (E) denote SD; data points from individual neurons are spread horizontally for visibility.

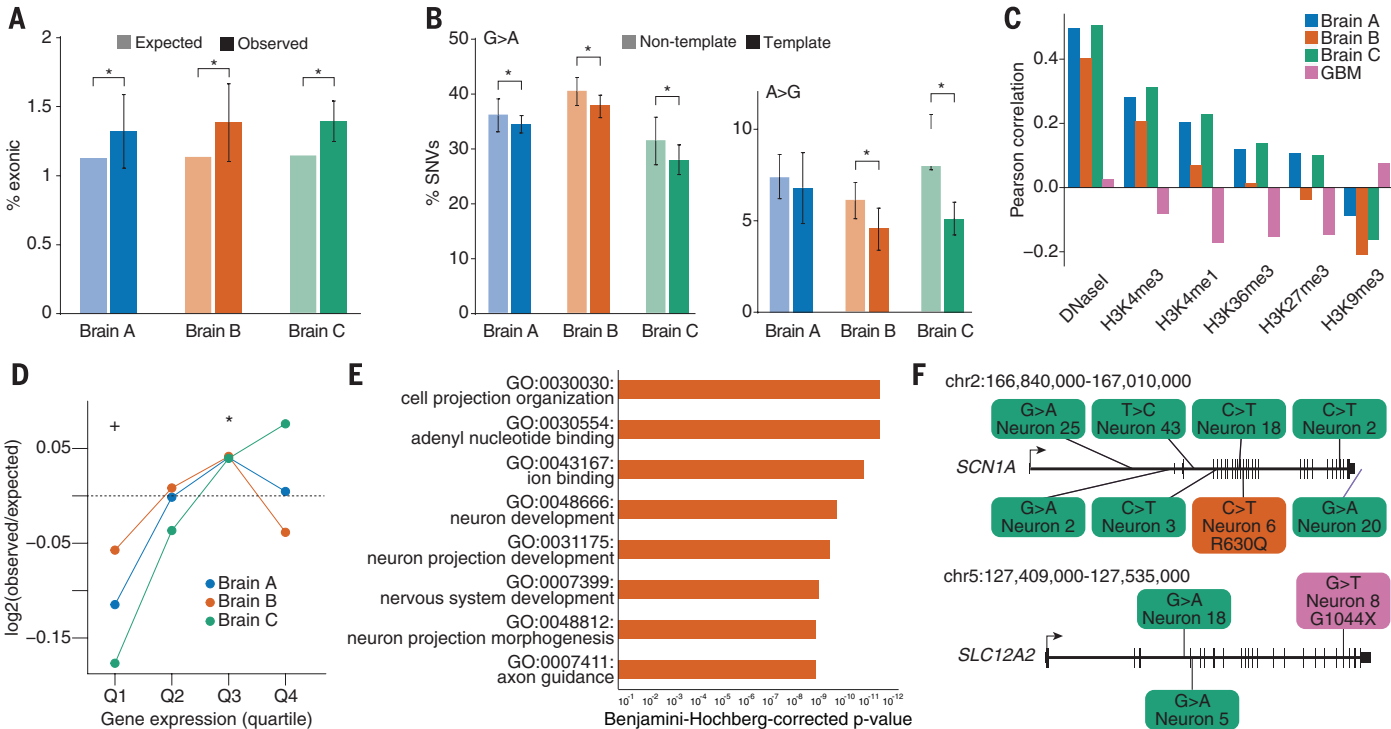


Fig. 2. Somatic SNVs occur at loci that are expressed in the brain and associated with nervous system function and disease. (A) Coding exons are enriched for somatic SNVs. $^*P < 0.05$, combined binomial test, Bonferroni-corrected. (B) SNVs in transcribed regions display a strand bias, suggesting that transcriptional damage influences the somatic SNV rate. $^*P < 0.05$, analysis of variance with Sidak's correction for multiple testing. Error bars in (A) and (B) denote SD. (C) Single-neuron SNVs correlate with epigenetic marks of transcription in the fetal brain and are depleted in heterochromatin, in opposition to the pattern observed in glioblastoma multiforme (GBM) SNVs. (D) Single-neuron SNVs occur in genes expressed in the cerebral cortex. Genes

in the lowest expression quartile were significantly depleted, and those in the third quartile were significantly enriched, for single-neuron SNVs. $^*P < 0.05$, $+P < 0.05$, Fisher combined one-tailed Poisson P value for enrichment and depletion of SNVs, respectively. (E) Gene ontology categories associated with nervous system development and function are enriched for mutated genes across single neurons from brain B. (F) Examples of genes implicated in human disease that were mutated in single brain B neurons (for full list, see table S8). Green SNVs occurred in introns or downstream of the coding region, the orange SNV occurred in an exon and induced a missense mutation, and the magenta SNV is a nonsense mutation.

Table 1. SNVs found in 36 single human cortical neurons isolated from three normal individuals.						
SNV	Brain A (n = 10)		Brain B (n = 16)		Brain C (n = 10)	
	Count	Percentage	Count	Percentage	Count	Percentage
Coding	23.7	1.3%	23.4	1.4%	24.4	1.4%
Silent	8.3	0.5%	7.1	0.4%	6.2	0.4%
Missense	14.1	0.8%	14.4	0.9%	16.8	1.0%
Truncating	1.3	0.1%	1.8	0.1%	1.3	0.1%
Noncoding	254.3	14.2%	243.5	14.5%	243.4	13.9%
Untranslated region	22.0	1.2%	21.0	1.2%	26.5	1.5%
Noncoding RNA	232.3	13.0%	222.5	13.2%	216.9	12.4%
Intronic	710.0	39.5%	660.1	39.2%	693.6	39.7%
Splice	0.3	0.0%	0.4	0.0%	0.6	0.0%
Other intronic	709.7	39.5%	659.7	39.2%	693.0	39.7%
Intergenic	805.0	44.9%	757.6	45.0%	785.5	45.0%
Mean	1793.0		1685.0		1747.0	

no fewer than five distinct clades of cells that trace their lineage back to separate mutation-marked pluripotent founder cells in the pre-gastrulation embryo. A given cortical neuron marked by SNV C1, for example, shares a more

recent common cellular ancestor with a cardiomyocyte marked by this same somatic mutation than it does with approximately 75% of neighboring cortical neurons, with which no clonal connection is evident as far back as gastrulation. To

confirm this polyclonal derivation, we dissected three consecutive 300- μ m coronal sections from Brodmann area (BA) 40 and axially divided these sections into three regions, each 8 mm wide (Fig. 3D). Each region contained contributions from at least three, and usually four, of the major clades identified by single-neuron sequencing. Our data suggest that although late divisions of cortical progenitors likely generate neurons within a relatively restricted cortical zone (24, 25), a given anatomical column of cortex (26) derives from overlapping, intermingled clones from at least four, and likely more, developmental lineages (fig. S14).

Our results show that each human cortical neuron has a profoundly distinctive genome, harboring as many as 1458 to 1580 somatic SNVs, in addition to large CNVs and occasional retroelement insertions, as previously reported (5–8). These estimates are likely to improve with better sequencing and amplification methods as well as more samples. Similar SNV rates were seen at ages 15, 17, and 42, but whether older age is associated with increased SNV rates remains to be explored. These SNVs display signatures of mutagenic processes, such as transcription-associated DNA damage and a preponderance of meC>T

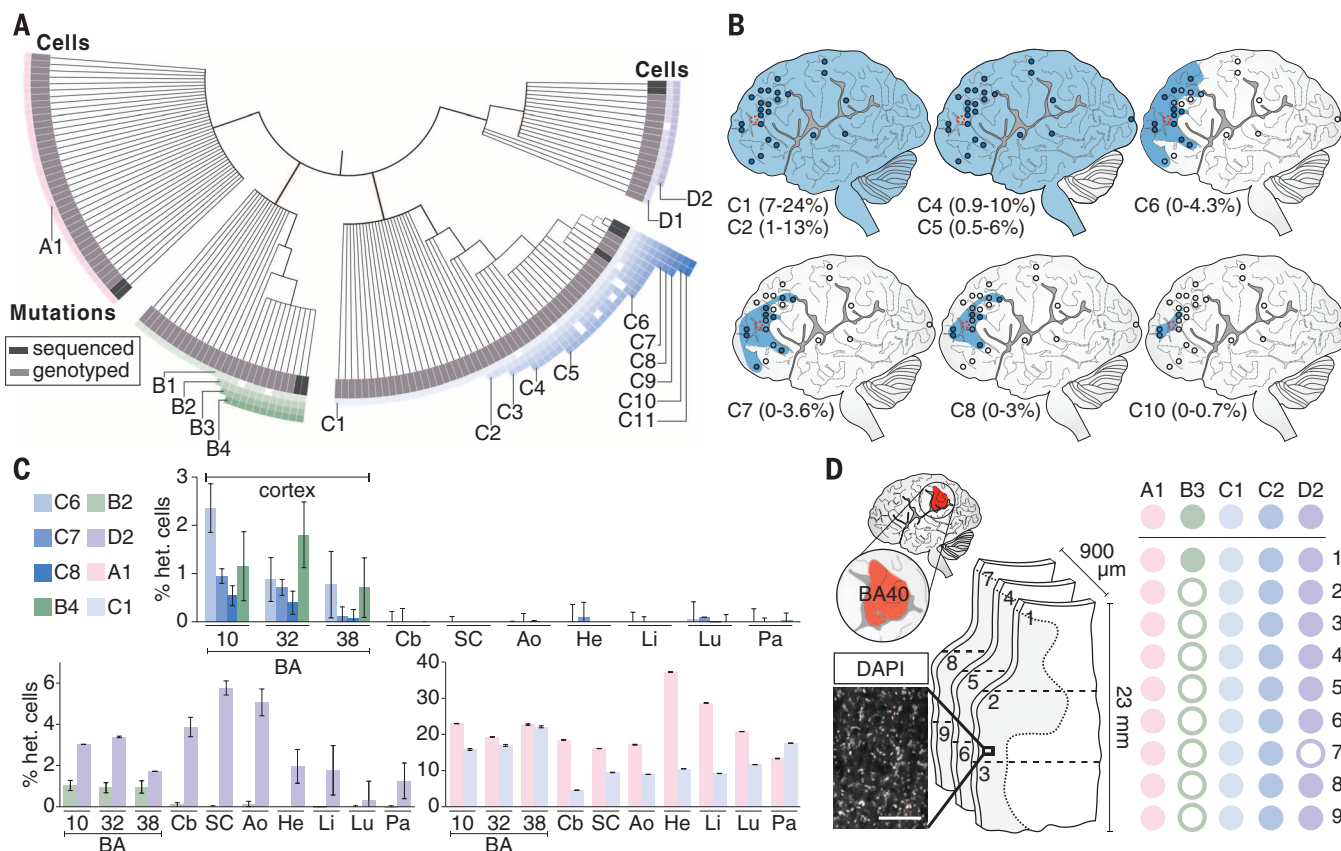


Fig. 3. Somatic mutations are shared between multiple neurons and demonstrate lineage relationships. (A) Lineage map of 136 human cortical neurons from brain B derived from 18 clonal somatic mutations, including SNVs, long interspersed nuclear element (LINE) insertions, and a TG-dinucleotide expansion. Neurons are placed into four distinct nested clades (pink, green, blue, purple) defined by one or more independent mutations. Cells are ordered within clades according to the presence of multiple somatic mutations. A few cells in each clade fail to manifest individual SNVs shared by other cells of the same clade (indicated by open squares), likely representing incomplete amplification (fig. S2). Dark gray boxes represent cells analyzed by WGS; light gray represents cells analyzed by Sanger-based genotyping. Genomic locations of somatic mutations are given in fig. S11. (B) Ultra-deep sequencing of mutated loci across the cortex of brain B. Clonal SNVs from a single clade are progressively regionally restricted to frontal cortex and become progressively rarer in bulk tissue, reflecting their later origin during development and neurogenesis. Blue circle,

mutation present; empty circle, mutation absent; blue shading, likely spatial distribution of mutation. Percentage range of heterozygous cells is indicated for each SNV. (C) Ultra-deep sequencing of mutated loci across the brain and body. Some variants are brain-specific (top) and others are shared across germ layers (bottom). Samples sequenced are prefrontal cortex [Brodmann area (BA) 10/BA46], cingulate cortex (BA32/BA8), temporal cortex (BA38), cerebellum (Cb), spinal cord (SC), aorta (Ao), heart (He), liver (Li), lung (Lu), and pancreas (Pa). (D) Genotyping shared variants in small sections of human cortex. Left: 4',6-diamidino-2-phenylindole (DAPI) stain of segment of representative section; scale bar, 200 μ m. Center: Three consecutive 300- μ m coronal sections from BA40 (red, upper left) were dissected into three axial regions each (1 to 9). Right: Genotyping results for dissected sections. Solid circles denote presence of mutation in indicated sample; open circles denote absence. Mutations with high allele fractions are present in all or virtually all regions, whereas only the least prevalent somatic variant (present in <0.5% of cells) is present in one region but not most regions.

deamination. SNVs in coding regions of genes involved in nervous system development and mature neuronal function suggest a “use it and lose it” scenario, in which the very genes used for the function of a neuron are those most likely to be damaged during its life.

Our work demonstrates that somatic mutations can be used to reconstruct the developmental lineage of neurons, suggesting a potential “population genetics” of brain cells and representing a durable record of the series of cell divisions that gives rise to the human brain. This clonal mosaicism in the brain, an organ with exquisite arealization of function, may buffer the brain against deleterious clonal mutations that inevitably arise during development (2). Somatic mutations are also likely to modify the penetrance of germline neurological mutations to generate var-

iable phenotypic effects of germline mutations in different family members, or even between identical twins.

REFERENCES AND NOTES

- S. A. Frank, *Proc. Natl. Acad. Sci. U.S.A.* **107** (suppl. 1), 1725–1730 (2010).
- A. Poduri, G. D. Evrony, X. Cai, C. A. Walsh, *Science* **341**, 1237–1240 (2013).
- S. De, *Trends Genet.* **27**, 217–223 (2011).
- J. P. Dumanski, A. Piotrowski, *Methods Mol. Biol.* **838**, 249–272 (2011).
- S. Behjati et al., *Nature* **513**, 422–425 (2014).
- M. J. McConnell et al., *Science* **342**, 632–637 (2013).
- X. Cai et al., *Cell Reports* **8**, 1280–1289 (2014).
- G. D. Evrony et al., *Cell* **151**, 483–496 (2012).
- G. D. Evrony et al., *Neuron* **85**, 49–59 (2015).
- G. R. Abecasis et al., *Nature* **467**, 1061–1073 (2010).
- C. W. Brennan et al., *Cell* **155**, 462–477 (2013).
- X. Xu et al., *Cell* **148**, 886–895 (2012).
- I. Martincorena et al., *Science* **348**, 880–886 (2015).
- G. Guo et al., *Nat. Genet.* **45**, 1459–1463 (2013).
- M. S. Lawrence et al., *Nature* **499**, 214–218 (2013).
- J. A. Stamatoiyannopoulos et al., *Nat. Genet.* **41**, 393–395 (2009).
- A. Hodgkinson, A. Eyre-Walker, *Nat. Rev. Genet.* **12**, 756–766 (2011).
- P. Green, B. Ewing, W. Miller, P. J. Thomas, E. D. Green, *Nat. Genet.* **33**, 514–517 (2003).
- P. Polak, P. F. Arndt, *Genome Res.* **18**, 1216–1223 (2008).
- J. A. Miller et al., *Nature* **508**, 199–206 (2014).
- A. Kundaje et al., *Nature* **518**, 317–330 (2015).
- R. Parihar, S. Ganesh, *J. Hum. Genet.* **58**, 573–580 (2013).
- Y. Morita et al., *J. Neurosci.* **34**, 4929–4940 (2014).

24. P. Gao et al., *Cell* **159**, 775–788 (2014).
 25. C. B. Reid, I. Liang, C. Walsh, *Neuron* **15**, 299–310 (1995).
 26. D. R. Kornack, P. Rakic, *Neuron* **15**, 311–321 (1995).

ACKNOWLEDGMENTS

We thank A. Rozzo, R. S. Hill, H. Lehmann, and W. Paoletta for assistance; J. Macklis and N. Sestan for helpful comments on the manuscript; the Dana-Farber Cancer Institute Hematologic Neoplasia Flow Cytometry Core; and the Research Computing group at Harvard Medical School for computing resources, including the Orchestra computing cluster (partially provided through National Center for Research Resources grant 1S1ORR028832-01). Human tissue was obtained from the NIH NeuroBioBank at the University of Maryland. We thank R. Johnson

of the NeuroBioBank for assistance with tissues, and we thank the donors and their families for their invaluable donations for the advancement of scientific understanding. Figure 3A was illustrated by K. Probst (Xavier Studio). Supported by National Institute on Aging grant T32 AG000222 (M.A.L.), the Leonard and Isabelle Goldenson Research Fellowship (M.B.W.), National Institute of General Medical Sciences (NIGMS) grant T32 GM007753 and the Louis Lange III Scholarship in Translational Research (G.D.E.), NIGMS grants T32 GM007753 and T32 GM007226 (A.M.D.), the Eleanor and Miles Shore Fellowship (E.L.), National Institute of Mental Health grant P50 MH106933 (P.J.P.), and National Institute of Neurological Disorders and Stroke grants R01 NS032457, R01 NS079277, and U01 MH106883 and the Manton Center for Orphan Disease Research (C.A.W.). C.A.W. is a Distinguished Investigator

of the Paul G. Allen Family Foundation and an Investigator of the Howard Hughes Medical Institute. Supplement contains additional data. Sequencing data have been deposited in the NCBI SRA under accession numbers SRP041470 and SRP061939.

SUPPLEMENTARY MATERIALS

www.sciencemag.org/content/350/6256/94/suppl/DC1
 Figs. S1 to S14
 Tables S1 to S10
 Materials and Methods
 References (27–55)

22 March 2015; accepted 3 August 2015
 10.1126/science.aab1785

INJURY RECOVERY

Function of the nucleus accumbens in motor control during recovery after spinal cord injury

Masahiro Sawada,^{1,2} Kenji Kato,^{1,3} Takeharu Kunieda,² Nobuhiro Mikuni,⁴ Susumu Miyamoto,² Hirotaka Onoe,⁵ Tadashi Isa,^{1,3} Yukio Nishimura^{1,3,6*}

Motivation facilitates recovery after neuronal damage, but its mechanism is elusive. It is generally thought that the nucleus accumbens (NAc) regulates motivation-driven effort but is not involved in the direct control of movement. Using causality analysis, we identified the flow of activity from the NAc to the sensorimotor cortex (SMC) during the recovery of dexterous finger movements after spinal cord injury at the cervical level in macaque monkeys. Furthermore, reversible pharmacological inactivation of the NAc during the early recovery period diminished high-frequency oscillatory activity in the SMC, which was accompanied by a transient deficit of amelioration in finger dexterity obtained by rehabilitation. These results demonstrate that during recovery after spinal damage, the NAc up-regulates the high-frequency activity of the SMC and is directly involved in the control of finger movements.

Motivation enhances and depression impedes functional recovery after neuronal damages (1, 2). However, the mechanism underlying this psychological effect on recovery remains obscure. The nucleus accumbens (NAc) plays a critical role in processing motivation to obtain reward (3–6). A large fraction of neurons in the NAc reflects the availability of a reward and the vigor of a subsequent approach to a target (7). However, the NAc is not thought to be directly involved in the control of motor functions such as finger dexterity. It has been reported that the NAc controls locomotion (8, 9); however, it might be through the regulation of vigor (10–12). On the other hand,

in functional brain imaging studies in nonhuman primates, the activity of the NAc during a reach-and-grasp task was increased in association with the primary motor cortex (M1) during recovery from a partial spinal cord injury (SCI), which had not been observed before the injury (13, 14). These studies suggest that the interaction between the NAc and M1 plays a pivotal role in the recovery of finger dexterity. However, the causal relationship between the neural activities of M1 and the NAc and functional recovery remains obscure. In this study, we investigated the interaction between the neuronal activities of the NAc and M1.

After sufficient training on a reach-and-grasp task (Fig. 1A), four macaque monkeys were subjected to SCI, which was limited to the C4/5 level of the lateral corticospinal tract (Fig. 1B and fig. S3). Finger dexterity was immediately impaired in the three monkeys who had relatively large lesions (monkeys M, T, and R; Fig. 1B and fig. S3). Consistent with recent lesion studies (15–17), recovery of the precision grip exceeded 90% within 100 days in monkeys whose finger dexterity was impaired immediately after SCI. “Early-stage” recovery was defined as the period from SCI to the time point at which the success

rate reached 100% for 2 successive days. “Late-stage” recovery was defined as the period after which the grip success rate remained repeatedly at 100% (Figs. 1B and 3B and movie S1). Finger dexterity was not markedly impaired in monkey D, presumably because the SCI was comparatively small (fig. S3).

To evaluate the potential of the NAc to motivate recovery, we determined the relationship between NAc and M1 activity during the two stages of behavioral recovery and compared with the pre-SCI stage. We examined oscillatory activity of the two regions while the monkey performed a reach-and-grasp task requiring dexterous finger movements at various time points before and after SCI in two monkeys [monkeys T and R, in which we conducted simultaneous recordings of electrocorticography (ECoG) in the sensorimotor cortex (SMC) and local field potentials (LFPs) in the NAc (Fig. 1C)]. During the early-stage and late-stage recovery, time-frequency analysis of M1 activity showed long-lasting high-frequency gamma activity (115 to 400 Hz) through the period of reach-and-grasp movements, as compared with that observed before SCI (Fig. 1D, upper row and E). The high-frequency component of the NAc at the early stage appeared to have reached the similar level as the pre-SCI level (Fig. 1D, lower row and F). On the other hand, the low-frequency component in the NAc during the early recovery stage showed significant decrease during reaching and grasping (Fig. 1F). We successively employed Granger causality analysis (GCA) (18–20) to evaluate the directionality of interactions between M1 and NAc activity in the two monkeys. GCA demonstrated an increased signal flow from the NAc to M1 in the high-gamma band (115 to 400 Hz) during early-stage recovery (Fig. 2A, upper middle). In the late-stage recovery, the signal flow from the NAc to M1 was diminished (Fig. 2A, upper right). Compared with observations before SCI or during late-stage recovery, the signal flow from the NAc to the global SMC was much stronger (Fig. 2C).

Despite these analyses, it remained unclear whether the NAc is a critical modulator of SMC activity. We therefore injected muscimol at various time points before and after SCI to induce a temporary unilateral blockade of the NAc in the contralesional hemisphere. We tested the effects of NAc inactivation on finger dexterity in all four monkeys and on SMC brain activity in three

¹Department of Developmental Physiology, National Institute for Physiological Sciences, Okazaki 444-8585, Japan.

²Department of Neurosurgery, Graduate School of Medicine, Kyoto University, Kyoto 606-8507, Japan. ³Department of Physiological Sciences, School of Life Science, The Graduate University for Advanced Studies, SOKENDAI, Hayama 240-0193, Japan. ⁴Department of Neurosurgery, Sapporo Medical University, Sapporo 060-8543, Japan. ⁵Division of Bio-Function Dynamics Imaging, RIKEN Center for Life Science Technologies, Kobe 650-0047, Japan. ⁶Precursory Research for Embryonic Science and Technology, Japan Science and Technology Agency, Tokyo 102-0076, Japan.

*Corresponding author. E-mail: yukio@nips.ac.jp

Fig. 1. Time course of recovery of finger dexterity and brain activity. (A) Reach and grasp. **(B)** The time course of precision grip success rate in monkey R. Black arrowheads indicate the days corresponding to the recordings shown in (D). The black area in the inset indicates the site of the spinal cord lesion. The percentage value beside the spinal cord illustration shows the proportion of the tissue that was lesioned. **(C)** Schematic drawing of simultaneous recording of SMC-ECoG and NAc-LFP. **(D)** Time-frequencygram of M1 (upper panels) and NAc (lower panels) activities in monkey R. Time 0, grasp onset; green arrowheads, reach onset; red arrowheads, grasp end. Each panel is the average of 30 trials. **(E)** Population data of mean power change compared with baseline period (–1.5 to –1.0 s from grasp onset) in M1 while the monkeys were grasping (0 to 0.5 s from grasp onset). *n*: The number of simultaneous recording sessions consisted of 30 trials across two monkeys (T and R) at each stage. Shading indicates the standard error of the mean (SEM). Blue points at the top of the graph: $P < 0.05$, one-way analysis of variance. See the methods. **(F)** Same as (E) but in the NAc.

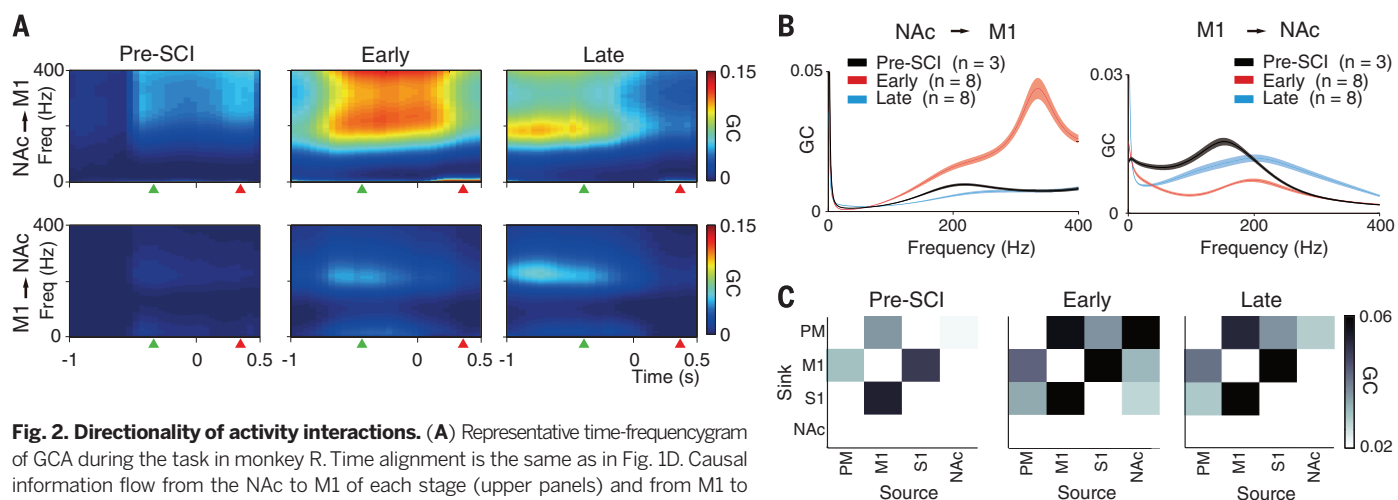
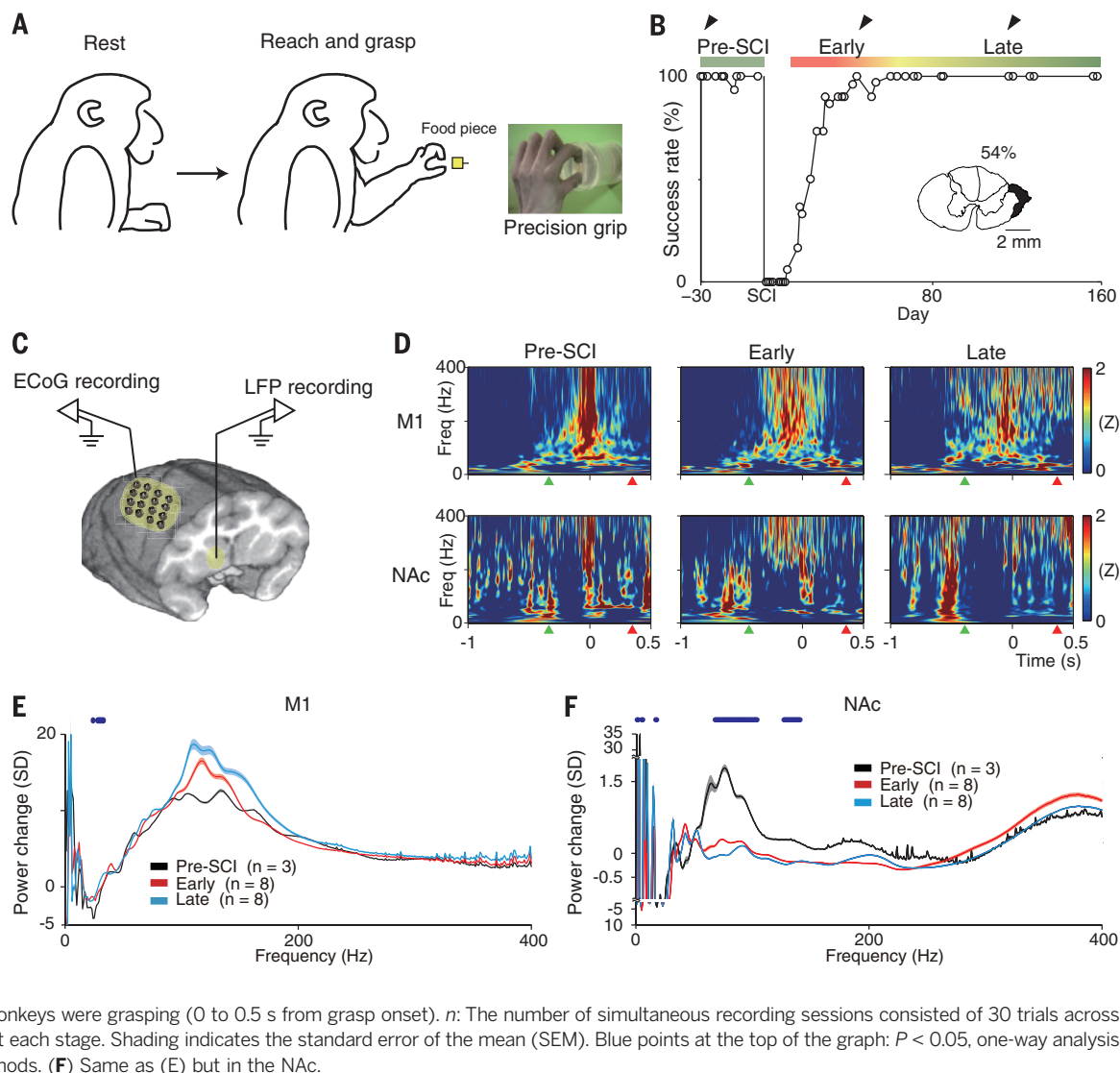
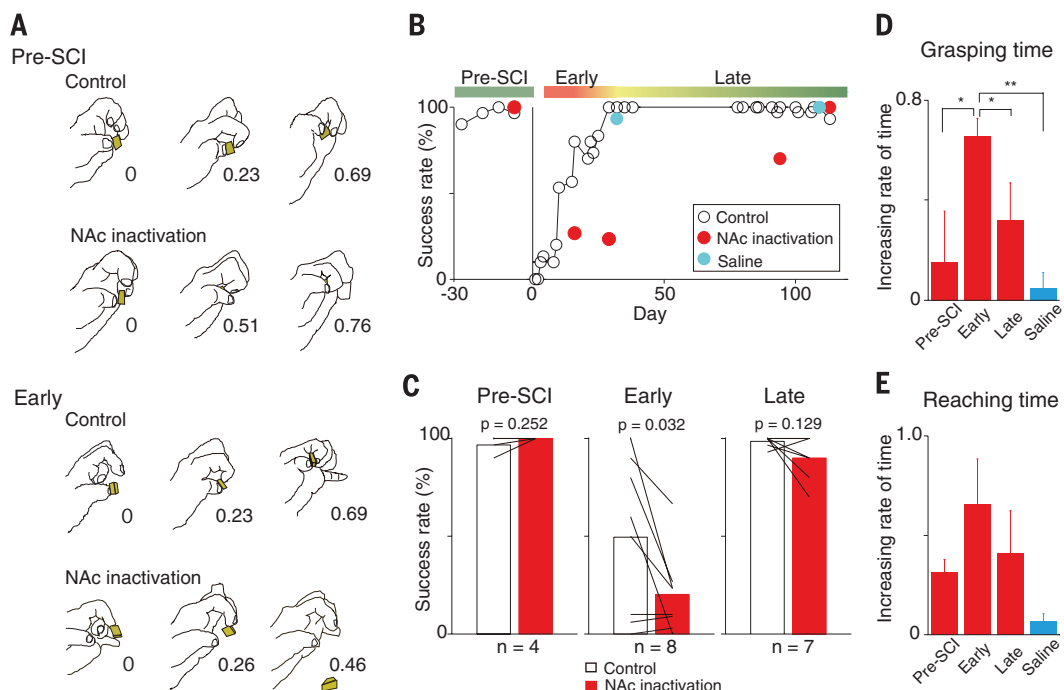


Fig. 2. Directionality of activity interactions. (A) Representative time-frequencygram of GCA during the task in monkey R. Time alignment is the same as in Fig. 1D. Causal information flow from the NAc to M1 of each stage (upper panels) and from M1 to the NAc (lower panels) is shown. **(B)** GCA population data from the NAc to M1 (left panel) and from M1 to the NAc (right panel) during the task, obtained across all recordings in two monkeys (T and R). The number means the total number of experimental days across the two monkeys. Shading indicates the SEM. **(C)** GCA networks. The x and y axes are the source and sink of information, respectively.

Fig. 3. Temporal inactivation of the NAc caused additional impairment of dexterous finger control. (A) Retrieval of a piece of food before (control) and during muscimol inactivation of the NAc (NAc inactivation) in monkey M before (pre-SCI) and 29 days after SCI (early), respectively. The time (in seconds) elapsed after the first panel is indicated below subsequent panels. (B) Success rate of precision grip before NAc inactivation (open circles) and after NAc inactivation (red circles) in monkey M. The light blue circles indicate results after a control injection of saline into the NAc (saline). (C) Population data collected across all monkeys reveals the impairment of finger dexterity after SCI (monkeys M, T, and R) (paired *t* test). (D) Increase in the mean grasping time caused by muscimol inactivation or after saline injections into the NAc at each experimental stage across monkeys M, T, and R. Error bars indicate the SEM. See the methods for statistical analysis. (E) Increase in mean reaching time. There was a trend of increase during the early stage, but due to the limited number of animals and intrinsic variability, no statistical significance was reached.



monkeys (monkeys M, T, and R; see the methods in the supplementary materials). In the three monkeys with SCI-induced impaired finger dexterity, NAc inactivation exacerbated the grasping deficits during the early recovery stage (Fig. 3, A to C, and movie S2). The same manipulation caused no remarkable deficit during either the pre-SCI period (Fig. 3, A to C, and movie S3) or the late recovery stage (Fig. 3, B and C, and movie S4). Importantly, despite their additional early-stage motor impairment, the monkeys' intention to obtain food was undiminished. During the inactivation, monkeys would try to pick up a piece of food they had dropped and could retrieve it using the contralesional hand (fig. S6A and movie S5). Accompanying the impaired precision grip success rate of monkeys M, T, and R, their movement time for grasping was also prolonged only during the early stage in all these animals (Fig. 3D). NAc inactivation tended to prolong the reaching time, but due to the limited number of animals and intrinsic variability, no statistical significance was reached (Fig. 3E). After SCI, reaching was relatively unaffected after NAc inactivation, presumably because the pathways involved in the control of reaching [via corticopropriospinal (17, 21) and corticoreticulospinal tracts (22)] mostly remained intact. Furthermore, inactivation of the ipsilesional NAc caused no additional effect on the lesion-affected finger dexterity (fig. S6B). Similarly, NAc inactivation had no obvious effect on finger dexterity before or after SCI in the monkey D, who had no clear impairment in finger dexterity after SCI (fig. S3).

In the three monkeys with lesion-impaired grasping (M, T, and R), we explored changes in M1 activity induced by NAc inactivation (Fig. 4A). Before the SCI, no change in cortical activity was observed after NAc inactivation ("pre-SCI" in the left column of Fig. 4B, in Fig. 4D, and in the left column of fig. S4, A and B). However, during the early stage of recovery, NAc inactivation attenuated high-frequency gamma activity (115 to 400 Hz), whereas lower-frequency gamma activity (50 to 100 Hz) tended to be enhanced ("early" in the middle column of Fig. 4B, in Fig. 4D, and in the middle column of fig. S4, A and B). This result was consistent with the fact that the gamma band in the NAc decreased during early-stage recovery. During late-stage recovery, NAc inactivation had no clear effect on the SMC-ECOG signals ("late" in the right column of Fig. 4B, in Fig. 4D, and in the right column of fig. S4, A and B). These results accompanied the finding that finger dexterity was also unaffected by NAc inactivation during the late stage of recovery.

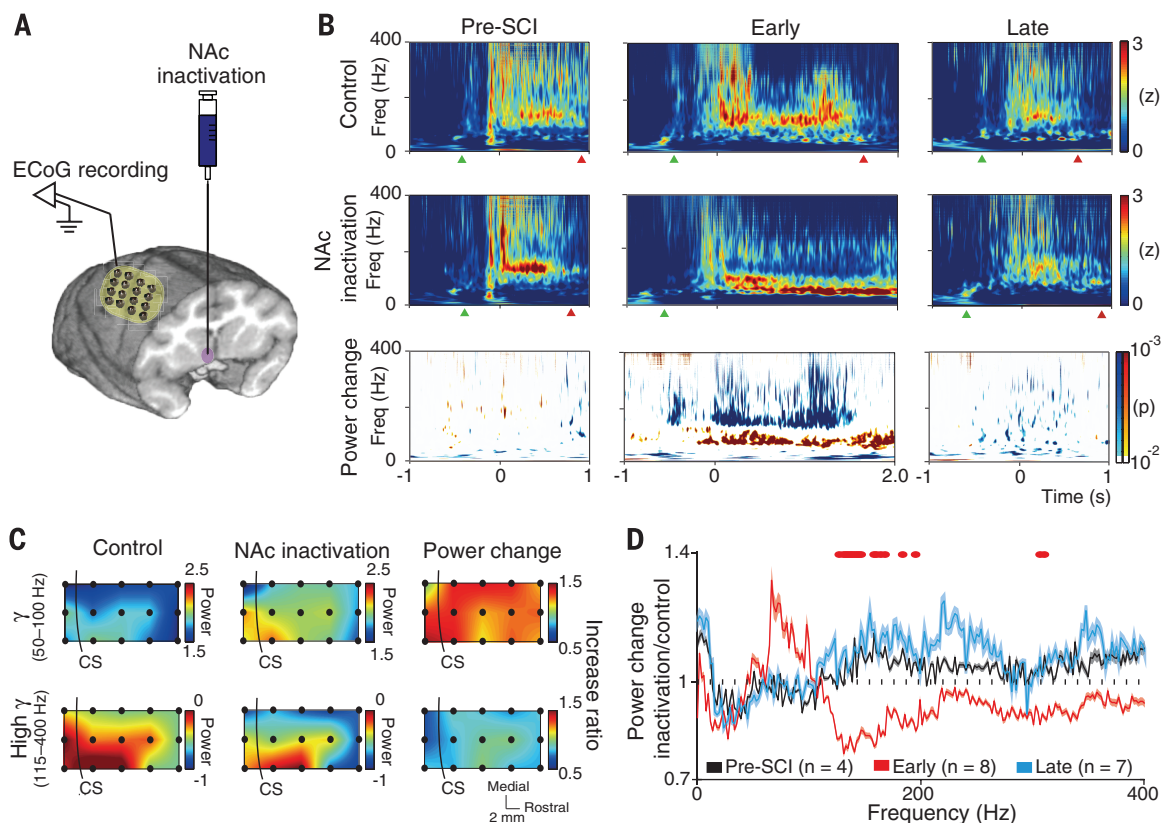
It is widely accepted that high-gamma-band activity reflects synchronized firing of a neural population near the electrode (23, 24). Our finding that the disappearance of high-gamma activity (115 to 400 Hz) occurred in association with disturbed finger dexterity suggests that the high-frequency oscillatory activity of M1, which was interrupted by NAc inactivation, played a critical role in the control of dexterous finger movements during recovery. Additionally, we observed that this oscillatory modulation occurred across all areas of the SMC, including the premotor cortex, M1, and the primary somatosensory cortex.

Before NAc inactivation, both high-frequency gamma (115 to 400 Hz) and lower-frequency gamma (50 to 100 Hz) bands were observed in the dorsolateral SMC (Fig. 4C and fig. S5, A and B). However, after NAc inactivation, the reduction in high-frequency gamma power and the increase in lower-frequency gamma power occurred on all of the electrodes in the SMC (Fig. 4B and fig. S5, A and B).

In this study, we demonstrated that NAc inactivation produced severe deficits in finger movement during the early-stage recovery. This suggests that the NAc makes a direct contribution to motor performance during the early-stage recovery after SCI. This conclusion is supported by the finding that NAc inactivation significantly suppressed high-frequency oscillatory activity in the SMC. Other investigations have shown that the NAc plays a pivotal role in maintaining the motivation to obtain reward when required to expend more effort (4–6). Indeed, rats with NAc lesions switched to choosing low-value rewards at low costs, rather than choose high-value/high-cost rewards (4). In our study, possibly several planning and/or executing centers, including the motor cortex, require a higher level of activity for the execution of the same movement after SCI. This idea might be similar to what has been described by Brodal as "mental energy" in his self-observation after stroke (25). Therefore, during the early stage of recovery, the monkeys would have to exert more motivational effort to achieve the precision grip. When the recovery was almost complete, such extra effort would no longer be necessary. The pathways

Fig. 4. NAc inactivation disrupted cortical activity during the early-stage recovery.

(A) Schematic drawing of recording of SMC-ECoG during NAc inactivation. (B) Time-frequencygram of brain activity of the contralesional M1 while monkey M performed the grasp task before (upper row) and during (middle row) NAc inactivation. Time alignment in the map is the same as in Fig. 1D. The lower row indicates the power change in M1 activity caused by NAc inactivation. Blue and red areas indicate statistically inactivated and activated components, respectively. (C) Topographical mapping of the intensity of gamma and high-gamma activity before and during inactivation in monkey M during the early stage (left and middle columns). Each dot on the maps indicates each electrocorticographic electrode. The right column indicates the mapping of power changes in gamma and high-gamma activity. CS, central sulcus. (D) Population data showing NAc inactivation-induced mean changes in power and SEM (shading) for each frequency across all electrodes in three monkeys. The number means the total number of experimental days across the three monkeys. Red points at the top of the graph: $P < 0.05$, post-hoc test between early and pre-SCI. See the methods.



from the NAc to the SMC remain unclear. However, it has been shown that the NAc provides multisynaptic (minimally disynaptic) projection to all the body-part representations in M1, presumably through the basal forebrain cholinergic neurons (26–28). On the other hand, there exists a pathway from the ventral tegmental area, which receives dense inputs from the NAc, to the SMC (29).

Because the motor recovery after the same SCI was shown to be training-dependent (30), it would be reasonable to suggest from the present results that the NAc contributes to recovery after SCI. Our findings suggest that the NAc could be a critical target for therapeutic interventions that aim to enhance the motivation of patients with SCIs and thereby promote their recovery. This idea may apply to a broad range of neurological disorders, including stroke, traumatic brain injuries, etc.

REFERENCES AND NOTES

1. E. Chemerinski, R. G. Robinson, J. T. Kosier, *Stroke* **32**, 113–117 (2001).
2. S. K. Saxena, T. P. Ng, G. Koh, D. Yong, N. P. Fong, *Acta Neurol. Scand.* **115**, 339–346 (2007).
3. E. S. Chantal, E. P. Richard, *Behav. Brain Res.* **61**, 9–21 (1994).
4. R. N. Cardinal, D. R. Pennicott, C. L. Sugathapala, T. W. Robbins, B. J. Everitt, *Science* **292**, 2499–2501 (2001).
5. R. N. Cardinal, J. A. Parkinson, J. Hall, B. J. Everitt, *Neurosci. Biobehav. Rev.* **26**, 321–352 (2002).
6. J. D. Salamone, M. Correa, A. Farrar, S. M. Mingote, *Psychopharmacology (Berlin)* **191**, 461–482 (2007).
7. V. B. McGinty, S. Lardeux, S. A. Taha, J. J. Kim, S. M. Nicola, *Neuron* **78**, 910–922 (2013).
8. L. E. Annett, R. M. Ridley, S. J. Gamble, H. F. Baker, *Psychopharmacology (Berlin)* **99**, 222–229 (1989).
9. S. Ikemoto, B. M. Witkin, *Synapse* **47**, 117–122 (2003).
10. M. Amalric, G. F. Koob, *Neuroscience* **7**, 2129–2134 (1987).
11. V. J. Brown, E. M. Bowman, *Eur. J. Neurosci.* **7**, 2479–2485 (1995).
12. C. Gierter, I. Bohn, W. Hauber, *Behav. Pharmacol.* **15**, 55–63 (2004).
13. Y. Nishimura *et al.*, *Science* **318**, 1150–1155 (2007).
14. Y. Nishimura *et al.*, *PLOS ONE* **6**, e24854 (2011).
15. S. Sasaki *et al.*, *J. Neurophysiol.* **92**, 3142–3147 (2004).
16. Y. Nishimura, Y. Morichika, T. Isa, *Brain* **132**, 709–721 (2009).
17. B. Alstermark, T. Isa, *Annu. Rev. Neurosci.* **35**, 559–578 (2012).
18. A. Brovelli *et al.*, *Proc. Natl. Acad. Sci. U.S.A.* **101**, 9849–9854 (2004).
19. C. Bernasconi, P. König, *Biol. Cybern.* **81**, 199–210 (1999).
20. W. Hesse, E. Möller, M. Arnold, B. Schack, *J. Neurosci. Methods* **124**, 27–44 (2003).
21. M. Kinoshita *et al.*, *Nature* **487**, 235–238 (2012).
22. D. G. Lawrence, H. G. Kuypers, *Brain* **91**, 1–14 (1968).
23. R. Supratim *et al.*, *J. Neurosci.* **45**, 11526–11536 (2008).
24. E. C. Leuthardt, G. Schalk, J. R. Wolpaw, J. G. Ojemann, D. W. Moran, *J. Neural Eng.* **1**, 63–71 (2004).
25. A. Brodal, *Brain* **96**, 675–694 (1973).
26. S. Miyachi *et al.*, *J. Neurosci.* **25**, 2547–2556 (2005).
27. S. Miyachi *et al.*, *Neurosci. Res.* **56**, 300–308 (2006).
28. S. N. Haber, B. Knutson, *Neuropsychopharmacology* **35**, 4–26 (2010).
29. A. Jonas *et al.*, *J. Neurosci.* **7**, 2481–2487 (2011).
30. Y. Sugiyama *et al.*, *J. Neurophysiol.* **109**, 2853–2865 (2013).

ACKNOWLEDGMENTS

We thank P. Redgrave for comments on the manuscript and Y. Itani, N. Takahashi, M. Togawa, and K. Isa for technical help. The monkeys used in this study were provided by the National Institute of Natural Sciences through the National Bio-resource Project of the Ministry of Education, Culture, Sports, Science and Technology of Japan (MEXT). This work was supported by grants from the “Brain Machine Interface Development” and performed under the Strategic Research Program for Brain Sciences from MEXT and the Japan Agency for Medical Research and Development to Y.N., a Grant-in-Aid for Scientific Research on Innovative Areas “Adaptive circuit shift” to T.I. (Project no. 26112008) and H.O. (26112003), and a Grant-in-Aid for Scientific Research from MEXT to H.O. [KAKENHI (B) no. 24300196 and (A) no.15H01819]. All data are stored at the Department of Developmental Physiology at the National Institutes for Physiological Sciences, Okazaki, Japan.

SUPPLEMENTARY MATERIALS

www.sciencemag.org/content/350/6256/98/suppl/DC1
Materials and Methods
Figs. S1 to S6
References (31–38)
Movies S1 to S5

25 April 2015; accepted 4 September 2015
10.1126/science.aab3825

NEUROTRANSMISSION

Aldehyde dehydrogenase 1a1 mediates a GABA synthesis pathway in midbrain dopaminergic neurons

Jae-Ick Kim,¹ Subhashree Ganesan,¹ Sarah X. Luo,^{2,3} Yu-Wei Wu,¹ Esther Park,¹ Eric J. Huang,^{2,3,4} Lu Chen,¹ Jun B. Ding^{1,5*}

Midbrain dopamine neurons are an essential component of the basal ganglia circuitry, playing key roles in the control of fine movement and reward. Recently, it has been demonstrated that γ -aminobutyric acid (GABA), the chief inhibitory neurotransmitter, is co-released by dopamine neurons. Here, we show that GABA co-release in dopamine neurons does not use the conventional GABA-synthesizing enzymes, glutamate decarboxylases GAD65 and GAD67. Our experiments reveal an evolutionarily conserved GABA synthesis pathway mediated by aldehyde dehydrogenase 1a1 (ALDH1a1). Moreover, GABA co-release is modulated by ethanol (EtOH) at concentrations seen in blood alcohol after binge drinking, and diminished ALDH1a1 leads to enhanced alcohol consumption and preference. These findings provide insights into the functional role of GABA co-release in midbrain dopamine neurons, which may be essential for reward-based behavior and addiction.

Midbrain dopamine (DA) neurons are important for fine-movement control, motivation, and reward-based learning (1, 2). Dysfunction of dopaminergic systems leads to movement disorders, such as Parkinson's disease, and various forms of addiction and drug abuse (3, 4). DA is the primary neurotransmitter released by DA neurons, and activation of DA receptors in postsynaptic neurons can modulate neuronal excitability and circuit output. It has recently been shown that GABA is copackaged with DA in midbrain DA neurons by the vesicular monoamine transporter 2 and is subsequently co-released in the striatum (5), where it provides direct and potent inhibition to postsynaptic striatal projection neurons through activation of GABA type A (GABA_A) receptors.

In the mammalian central nervous system (CNS), GABA biosynthesis is mediated by two glutamate decarboxylases (GAD65 and GAD67, 65- and 67-kD isoforms, respectively). Expression of either isoform of GAD has traditionally been used to identify GABAergic neurons in the CNS. To identify which subset of midbrain DA neurons is capable of GABA synthesis, we examined GAD expression in DA neurons by coupling immunohistochemistry for tyrosine hydroxylase (TH), the rate-limiting enzyme in DA synthesis, with in situ hybridization for *Gad1* or *Gad2* (which encode GAD67 and GAD65, respectively). Only a

small percentage of midbrain DA neurons express *Gad* in the substantia nigra pars compacta (SNc, ~9%) (Fig. 1, A to K) and the ventral tegmental area (VTA, ~15%) (fig. S1) (6, 7).

An individual DA neuron can extend elaborate axonal arbors covering large portions of the striatum (8). Consequently, even though GAD is expressed in only a small subset of DA neurons, it is possible that GAD-expressing neurons can drive sustained GABA co-release throughout the striatum. We thus asked whether GAD is required for GABAergic transmission in the striatum by recording alterations in dopaminergic inhibitory postsynaptic currents (IPSCs) in spiny projection neurons (SPNs) that resulted from pharmacological inhibition or conditional genetic deletion of GAD. The striatum comprises two parallel output pathways arising from distinct groups of "direct" and "indirect" pathway GABAergic SPNs (dSPNs and iSPNs, respectively) that differ in their expression of postsynaptic DA receptors coupled with heterotrimeric guanine nucleotide-binding protein. SPNs also send collateral inhibitory projections within the striatum. As SPNs express GAD and are considered conventional GABAergic neurons, we used striatal collateral inhibition as an internal control for our experiments. We expressed channelrhodopsin 2 (ChR2) in iSPNs by crossing A2A-Cre mice (in which Cre recombinase is selectively expressed in iSPNs but not in midbrain DA neurons) with transgenic mice containing a conditional floxed allele of ChR2 in the *Rosa26* locus (Ai32 mice). Progeny from this cross were bred to *Drd1a*-tdTomato-expressing transgenic mice carrying a bacterial artificial chromosome transgene that selectively labels dSPNs. We then performed whole-cell voltage-clamp recordings in dSPNs in brain slices of dorsal striatum prepared from A2A-Cre;Ai32; *Drd1a*-tdTomato mice, in which ChR2 is selec-

tively expressed in A2A adenosine receptor-expressing iSPNs and tdTomato expression is restricted to dopamine 1 (D1) receptor-expressing dSPNs. Optogenetic stimulation of iSPN axons with brief pulses (0.5 ms) of blue light (450 nm) reliably evoked IPSCs in dSPNs. Optogenetically evoked IPSCs (oIPSCs) recorded in dSPNs were significantly attenuated by GAD inhibitor 3-mercaptopropionic acid (3-MPA, 500 μ M) (Fig. 1L), which confirmed that local collateral inhibitory transmission arising from iSPNs is dependent on GAD function. We next selectively deleted GAD in iSPNs (9), using *Gad1* and *Gad2* double conditional knockout mice (A2A-Cre;*Gad1*^{fl/fl};*Gad2*^{fl/fl}). When recording oIPSCs from dSPNs in A2A-Cre;*Gad1*^{fl/fl};*Gad2*^{fl/fl};Ai32;*Drd1a*-tdTomato mice, we found that genetic deletion of both GADs in iSPNs abolished nearly all of the oIPSCs recorded in dSPNs. These data confirmed that GAD-mediated GABA synthesis is necessary for conventional GABAergic transmission within the striatum (Fig. 1L).

To test whether GAD is required for functional GABA co-release by midbrain DA neurons, whose axon terminals project onto SPNs, we used DAT-Cre;Ai32 mice to selectively express ChR2 in DA neurons (5, 10) and recorded oIPSCs and oEPSCs in postsynaptic dorsal striatum SPNs. Monosynaptic oIPSCs and oEPSCs can be abolished by GABA_A and glutamate-receptor blockers, respectively (fig. S2). To our surprise, neither incubating brain slices with 3-MPA (Fig. 1, M and N) nor genetically deleting both GAD isoforms in midbrain DA neurons using DAT-Cre;Ai32;*Gad1*^{fl/fl};*Gad2*^{fl/fl} mice (Fig. 1, O and P) significantly altered the amplitudes of oIPSCs and oEPSCs in SPNs, which indicated that midbrain DA neuron GABA co-release does not require canonical GAD-mediated GABA synthesis. GABA co-release from DA neurons was observed in recordings obtained throughout the striatum, in both dorsal and ventral regions. Notably, the oIPSCs recorded in dorsal striatum SPNs were significantly larger than those recorded from SPNs in the nucleus accumbens (Nac). Within Nac, oIPSC and oEPSC amplitudes were not significantly different between SPNs in the core or medial shell, and, as with oIPSCs recorded in dorsal striatum, oIPSCs recorded in the Nac were not blocked by application of 3-MPA (fig. S3). Recent work has suggested that DA can directly activate postsynaptic GABA_A receptors (11). To exclude this possibility and test whether dopaminergic oIPSCs were caused by direct activation of GABA_A receptors by DA, we locally applied DA and GABA onto individual SPNs and recorded IPSCs. Direct application of DA did not evoke IPSCs, whereas GABA successfully evoked IPSCs in the same SPN, which indicated that DA was not likely to be activating GABA_A receptors directly in our cells. This idea was further supported by application of the DA transporter (DAT) blocker GBRI2935, which elevates extracellular DA concentrations and similarly did not affect oIPSC amplitudes in the striatum (fig. S4). Together, these data suggest that dopaminergic oIPSCs were not caused by direct activation of GABA_A receptors by DA.

¹Department of Neurosurgery, Stanford University School of Medicine, Palo Alto, CA 94304, USA. ²Department of Pathology, University of California San Francisco, San Francisco, CA 94143, USA. ³Neuroscience Graduate Program, University of California San Francisco, San Francisco, CA 94143, USA. ⁴Pathology Service 113B, San Francisco VA Medical Center, San Francisco, CA 94121, USA. ⁵Department of Neurology and Neurological Sciences, Stanford University School of Medicine, Palo Alto, CA 94304, USA.

*Corresponding author. E-mail: dingjun@stanford.edu

In plants, GABA can be synthesized from putrescine (12) by the enzymes diamine oxidase (DAO) and aldehyde dehydrogenase (ALDH) (fig. S5A) (13, 14). GABA production through this alternative evolutionarily conserved pathway also exists in *Xenopus* tadpole (15) and mammalian cells (16–19). Glial cells can also use putrescine to produce GABA during retinal early development (18, 20). We tested whether ALDH-mediated alternative GABA synthesis drives GABA production in midbrain DA neurons. ALDH1a1 is the most abundant form of cytosolic ALDH (21, 22) and is highly expressed in the ventral midbrain, including the region delineating the SNc (23) (for *Aldh1a1* mRNA) (24). We first examined ALDH expression in midbrain DA neurons by double immunostaining for ALDH1a1 and TH. ALDH1a1 is indeed highly expressed in a subset of DA neurons, colocalizing with TH in the SNc and VTA (Fig. 2, A to C, and fig. S5B). To examine subcellular localization of ALDH1a1, we injected an adeno-associated virus (AAV) carrying green fluorescent protein (GFP)-tagged ALDH1a1 into the

midbrain and examined GFP expression in the striatum. We found that GFP strongly colocalizes with TH within axons in the dorsal striatum (Fig. 2D), which suggested that ALDH1a1 is highly abundant in dopaminergic terminals (fig. S5, C to F). We then tested the involvement of ALDH1a1 in GABA synthesis in these neurons by blocking its activity with the ALDH inhibitors 4-(diethylamino)-benzaldehyde (DEAB, 10 μ M), or disulfiram (10 μ M). To ensure that intracellular GABA levels were sufficiently depleted, we pretreated brain slices from DAT-Cre;Ai32 mice with artificial cerebrospinal fluid (ACSF) containing these blockers for 2 to 4 hours (a paradigm similar to our pharmacological treatment with 3-MPA targeting conventional GABA synthesis in SPNs). Treatment with both 4,4'-bis-(diethylamino)-benzophenone (DEAB) and disulfiram dramatically reduced oIPSC amplitude in SPNs after DA axon stimulation (Fig. 2, E and F, and fig. S6, A and B). We also recorded oEPSCs in the same SPNs by stimulating DA fibers. Notably, this treatment did not affect the peak amplitude of oEPSCs (Fig.

2, E and F, and fig. S6, A and B), which suggested that these blockers do not prevent global neurotransmitter release, but rather selectively impair GABA co-release.

If GABA were indeed converted from putrescine, blocking DAO would also reduce GABA production. We thus used DAO blockers [aminoguanidine (AG), 100 μ M, or amiloride, 10 μ M] and examined the effect of each treatment on oIPSCs, using the same paradigm as above. Both AG and amiloride significantly and selectively reduced oIPSC amplitude in SPNs, with no effect on oEPSC amplitude (Fig. 2, G and H, and fig. S6, C and D) or on conventional GABAergic transmission (fig. S7). Notably, ALDH1a1 is known to be important for the synthesis of retinoic acid (RA) (25) and breakdown of the DA metabolite 3,4-dihydroxyphenylacetaldehyde to 3,4-dihydroxyphenylacetic acid (26). It is possible, then, that deletion of ALDH1a1 may lead to RA deficiency and a concomitant increase in extracellular DA concentration, both of which may have effects on synaptic transmission. Application of exogenous

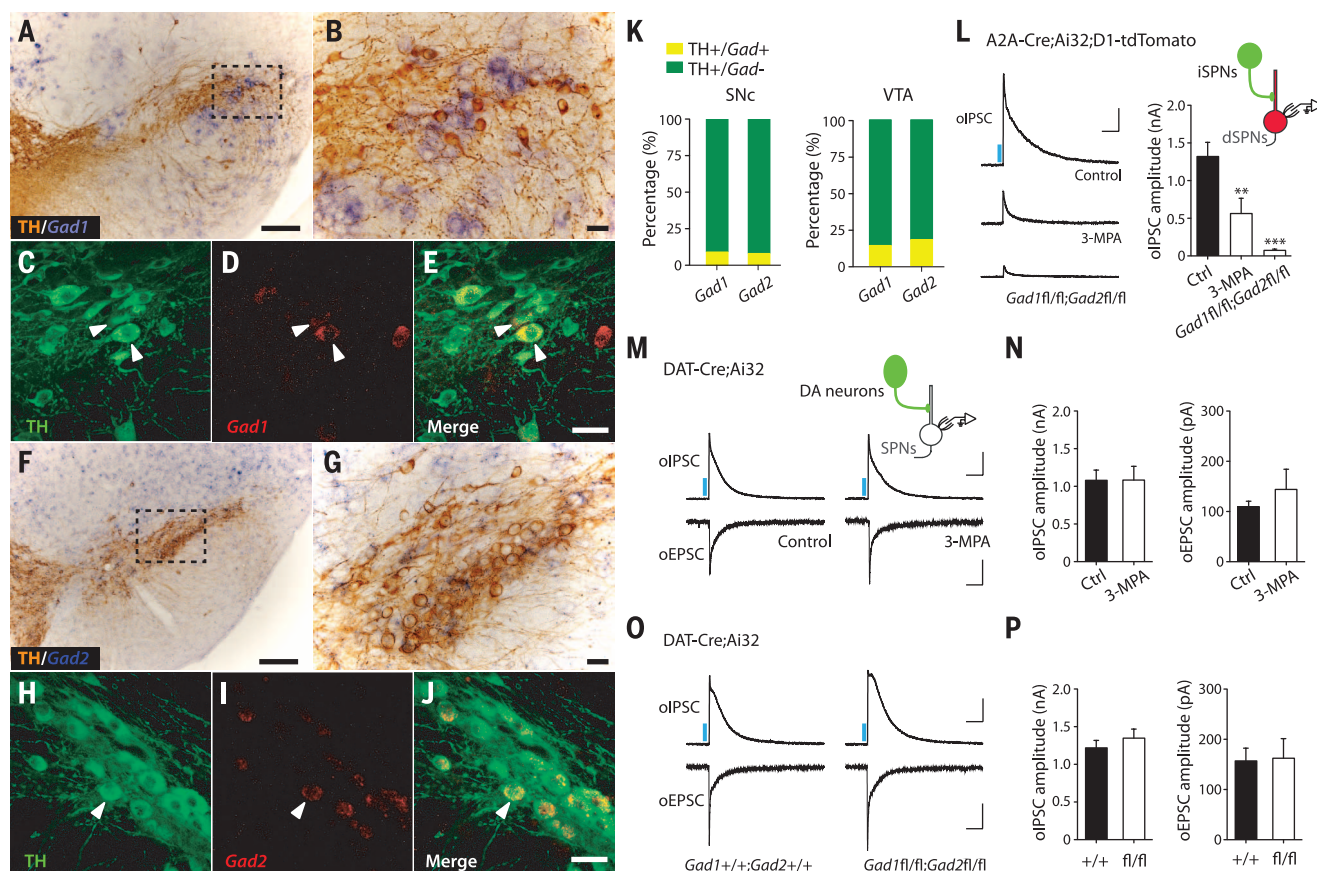


Fig. 1. GABA co-release by midbrain DA neurons does not require GAD.

(A to J) Expression of *Gad1* and *Gad2* mRNA in DA neurons of the SNc. Immunolabeled TH-positive dopaminergic neurons (brown) combined with chromogenic in situ hybridization (ISH) for *Gad1* (A and B) and *Gad2* (F and G) mRNA. Confocal fluorescence images of ISH for *Gad1* (D) and *Gad2* (I) mRNA (red) combined with TH immunostaining (green) (C) to (E) and (H) to (J) show limited expression of *Gad* in TH⁺ cells. (K) Quantification of TH/*Gad* colocalization in SNc (left) and VTA (right). (L) (Left) Representative oIPSC traces in control (top); 3-MPA-treated (500 μ M) (middle); and *Gad1*^{fl/fl};*Gad2*^{fl/fl}

(bottom) A2A-Cre;Ai32;Drd1a-tdTomato mice. (Right) Summary statistics for oIPSC recordings. Representative traces (M) and summary statistics (N) for oIPSC and oEPSC recorded from DAT-Cre;Ai32 mice treated with ACSF (control) and 3-MPA, respectively. Representative traces (O) and summary statistics (P) for oIPSC and oEPSC recorded from DAT-Cre;Ai32;*Gad1*^{+/+};*Gad2*^{+/+} and DAT-Cre;Ai32;*Gad1*^{fl/fl};*Gad2*^{fl/fl} mice. Blue bar indicates 450-nm light stimulation. Scale bars: 200 μ m for (A) and (F), 50 μ m for (B) to (E) and (G) to (J); current of 400 pA and time of 100 ms for oIPSC and 50 pA and 100 ms for oEPSC. Error bars indicate means \pm SEM. ***P* < 0.01, ****P* < 0.001.

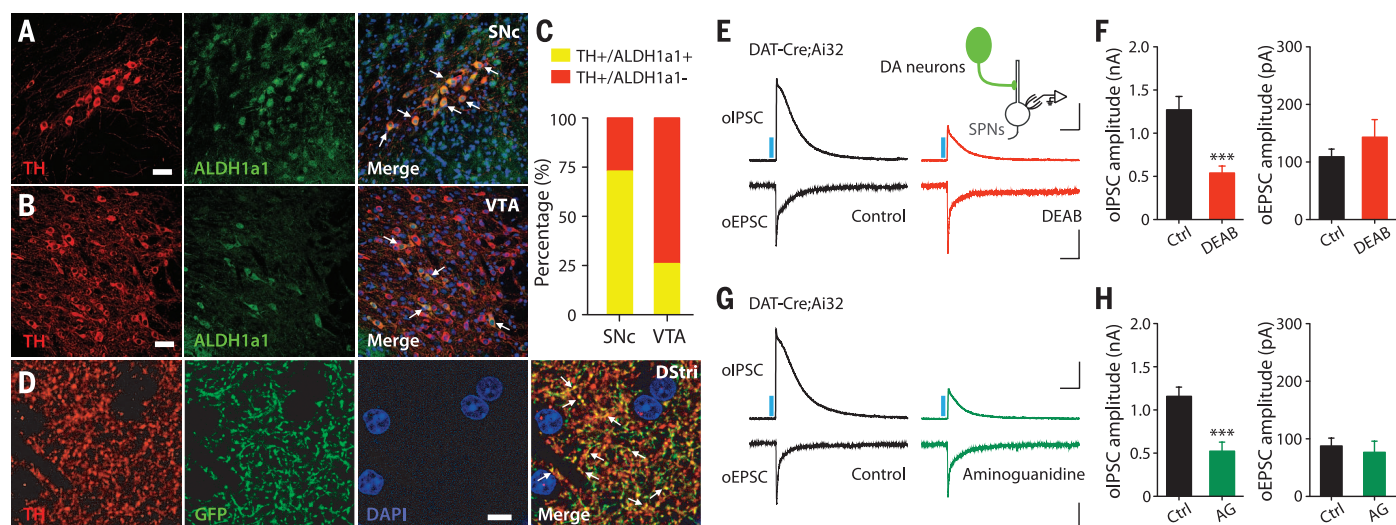
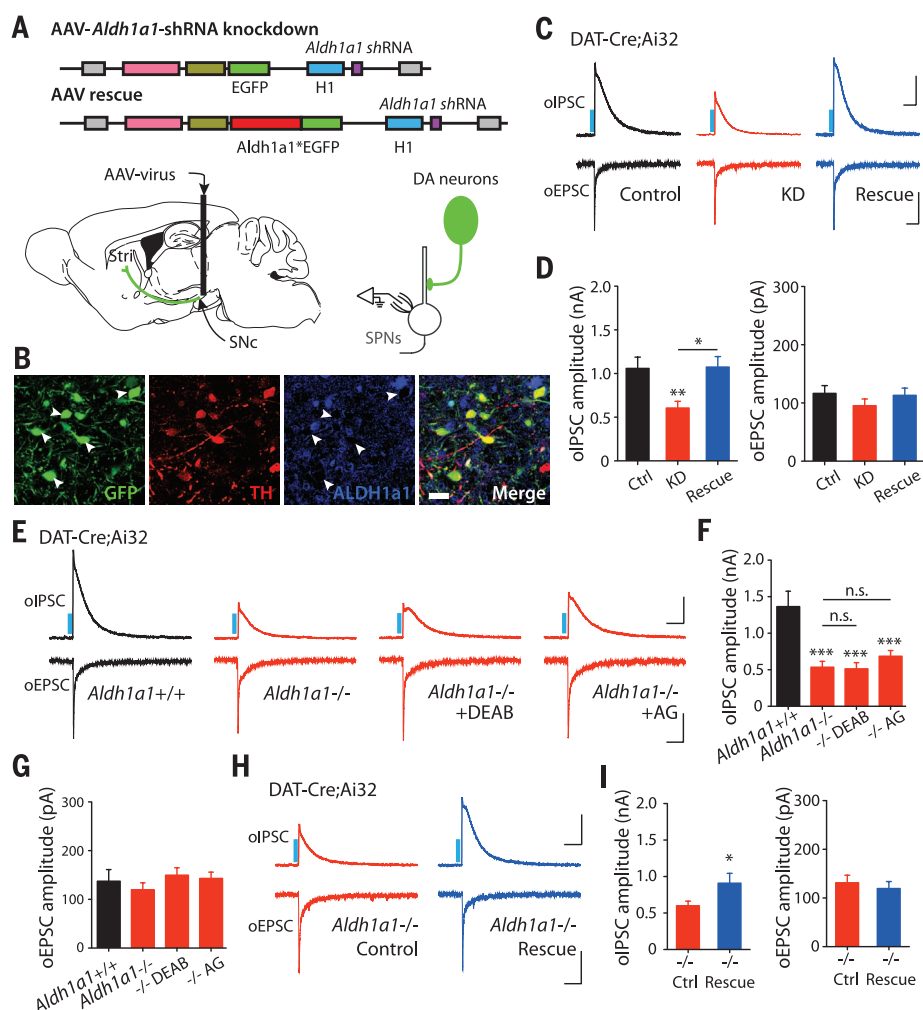


Fig. 2. ALDH1a1-mediated noncanonical GABA synthesis in DA neurons. (A and B) Confocal images depicting double immunostaining for TH (left, red) and ALDH1a1 (middle, green) in SNc (A) and VTA (B). Scale bar, 40 μ m. (C) Quantification of ALDH1a1 expression in TH⁺ DA neurons in SNc and VTA. (D) Confocal images depicting double immunostaining for TH (red), ALDH1a1-GFP (green), and 4',6'-diamidino-2-phenylindole (DAPI) (blue) in the dorsal striatum (DStr). Scale bar, 10 μ m. Representative oIPSC and oEPSC traces

(E) and summary statistics (F) recorded from DAT-Cre;Ai32 mice treated with ACSF (control, left) and DEAB (10 μ M, right). Representative oIPSC and oEPSC traces (G) and summary statistics (H) recorded from DAT-Cre;Ai32 mice treated with ACSF (control, left) and AG (100 μ M, right). Blue bar indicates 450-nm light stimulation. Scale bars: 400 pA and 100 ms for oIPSC and 50 pA and 100 ms for oEPSC. Error bars indicate means \pm SEM. *** P < 0.001. The arrows in (A), (B), and (D) highlight the colocalization of TH and ALDH1a1.

Fig. 3. *Aldh1a1* knockdown and genetic deletion reduce dopaminergic oIPSCs and are rescued by *Aldh1a1* overexpression.

(A) Schematic illustration depicting viral shRNA constructs (*Aldh1a1*^{*} indicates an shRNA-resistant WT *Aldh1a1*) and experimental configuration. Stri, striatum. (B) Confocal image showing expression of shRNA (green) in TH⁺ (red) neurons. Arrowheads indicate absence of ALDH1a1 (blue) in GFP⁺/TH⁺ neurons. Scale bar, 20 μ m. Representative oIPSC and oEPSC traces (C) and summary statistics (D) in DAT-Cre;Ai32 mice injected with *Aldh1a1* knockdown and rescue viruses. Representative oIPSC and oEPSC traces (E) and summary statistics for oIPSC (F) and oEPSC (G) in *Aldh1a1*^{+/+};DAT-Cre;Ai32 or *Aldh1a1*^{-/-};DAT-Cre;Ai32 mice, or loss-of-function mice treated with DEAB (10 μ M) or AG (100 μ M). Representative oIPSC and oEPSC traces (H) and summary statistics (I) recorded from *Aldh1a1*^{-/-};DAT-Cre;Ai32 mice injected with control and rescue viruses. Blue bar indicates 450-nm light stimulation. Scale bars: 400 pA and 100 ms for oIPSC and 50 pA and 100 ms for oEPSC. Error bars indicate means \pm SEM. * P < 0.05, ** P < 0.01, *** P < 0.001.



RA and a D2 receptor antagonist (sulpiride), however, did not prevent observed reduction of oIPSCs in SPNs and had no effect on oEPSCs, which suggested that these other ALDH1a1-mediated functions are not important for GABA co-release (fig. S8).

To selectively manipulate ALDH1a1 expression in midbrain DA neurons, we injected an AAV-expressing short hairpin RNA (shRNA) targeted against *Aldh1a1* into the ventral midbrain of DAT-Cre;Ai32 mice to reduce the supply of the gene or [knockdown (KD)] and so reduce *Aldh1a1* expression (Fig. 3, A and B, and fig. S9). *Aldh1a1* KD in the midbrain significantly reduced oIPSC amplitude in SPNs (Fig. 3, C and D), an effect that was fully rescued by simultaneous expression of an shRNA-resistant wild-type (WT) *Aldh1a1* (*Aldh1a1**) (Fig. 3, C and D). Notably, *Aldh1a1* KD and rescue had no effect on oEPSCs recorded in the same neurons. These data suggest that presynaptic expression of ALDH1a1 in DA neurons is critical for GABA synthesis and co-release.

We next asked whether genetic deletion of ALDH1a1 can selectively diminish GABA corelease by midbrain DA neurons (27). We recorded oIPSCs and oEPSCs in SPNs from the dorsal striatum of *Aldh1a1*^{-/-};DAT-Cre;Ai32 transgenic mice and *Aldh1a1*^{+/-} littermate controls. Dopaminergic oIPSCs were strongly attenuated in *Aldh1a1*^{-/-} mice, whereas oEPSCs were unaffected (Fig. 3, E to G). Because ALDH1a1 is the final enzyme in the conversion process leading to GABA synthesis, the pharmacological effects of DAO and ALDH blockers should be occluded by *Aldh1a1* deletion. We treated brain slices from *Aldh1a1*^{-/-};

DAT-Cre;Ai32 with DAO and ALDH blockers and found that DAO and ALDH blockers did not further reduce oIPSC amplitude in SPNs in *Aldh1a1*^{-/-} mice (Fig. 3, E to G). As an additional control, we examined oIPSCs in *Aldh1a1*^{-/-};A2A-Cre;Ai32;Drd1a-tdTomato mice resulting from collateral intrastratial inhibition and confirmed that conventional GABA transmission is not affected in mutant mice (fig. S10). Last, we tested whether elevated expression of *Aldh1a1* could rescue the reduction of dopaminergic IPSCs observed in SPNs in *Aldh1a1*^{-/-} mice. To achieve this, we injected AAV-rescue constructs into the midbrain of *Aldh1a1*^{-/-};DAT-Cre;Ai32 mice and subsequently recorded oIPSCs in SPNs. Overexpression of *Aldh1a1* fully rescued the dopaminergic oIPSCs in SPNs without affecting oEPSCs (Fig. 3, H and I). GABA transporters also contribute to the accumulation of presynaptic GABA in midbrain DA neurons (fig. S11). Taken together, our data suggest that ALDH1a1-mediated alternative GABA synthesis supports functional GABAergic transmission by DA neurons.

Mutations of *aldh1a1* have been linked to alcoholism in human populations (28, 29), which suggests that GABA co-release by DA neurons may be altered by drug abuse. Given the involvement of the dopaminergic system and dorsal striatum in enhanced alcohol consumption, preference, and addiction (30–32), we examined GABA co-release in mice exposed to repeated in vivo administration and withdrawal of EtOH, a behavioral paradigm approximating binge drinking episodes in humans. Intoxicating levels of EtOH were administered (2 g/kg EtOH, 20%,

intraperitoneal injection) daily for seven consecutive days (32). Two to 4 hours after the final EtOH injection, we prepared striatal brain slices from DAT-Cre;Ai32 mice and recorded oIPSCs in SPNs. We found that repeated in vivo administration of EtOH significantly decreased oIPSC, but not oEPSC, amplitude recorded in SPNs (Fig. 4, A and B). We then tested whether a direct EtOH treatment can affect GABA co-release in brain slices. To mimic blood alcohol levels after binge drinking, we pretreated striatal brain slices for 2 to 4 hours (paradigm comparable to our previous pharmacological manipulations) with EtOH at concentrations comparable to blood alcohol levels during binge-drinking episodes (17 to 50 mM). Prolonged, but not acute, treatment with 17 to 50 mM EtOH significantly decreased the oIPSCs amplitude recorded in SPNs after DA axon stimulation (Fig. 4, C and D). The same EtOH treatments did not affect oEPSC amplitude or that of oIPSCs recorded from dSPNs in A2A-Cre;Ai32;Drd1a-tdTomato mice (fig. S12). Reduction of GABA co-release was not observed in *Aldh1a1*^{-/-} mice (fig. S13), which suggested that EtOH modulation is dependent on ALDH1a1. Our results indicate that GABA co-release is attenuated by EtOH at blood alcohol concentrations similar to those measured after binge drinking. As excessive alcohol drinking enhances the inclination for alcohol drinking behavior (33), we used the home cage continuous two-bottle-choice test to evaluate behavioral consequences of ALDH1a1 deletion on EtOH intake (34). Basal locomotion, as assessed by an open-field test, remains intact in

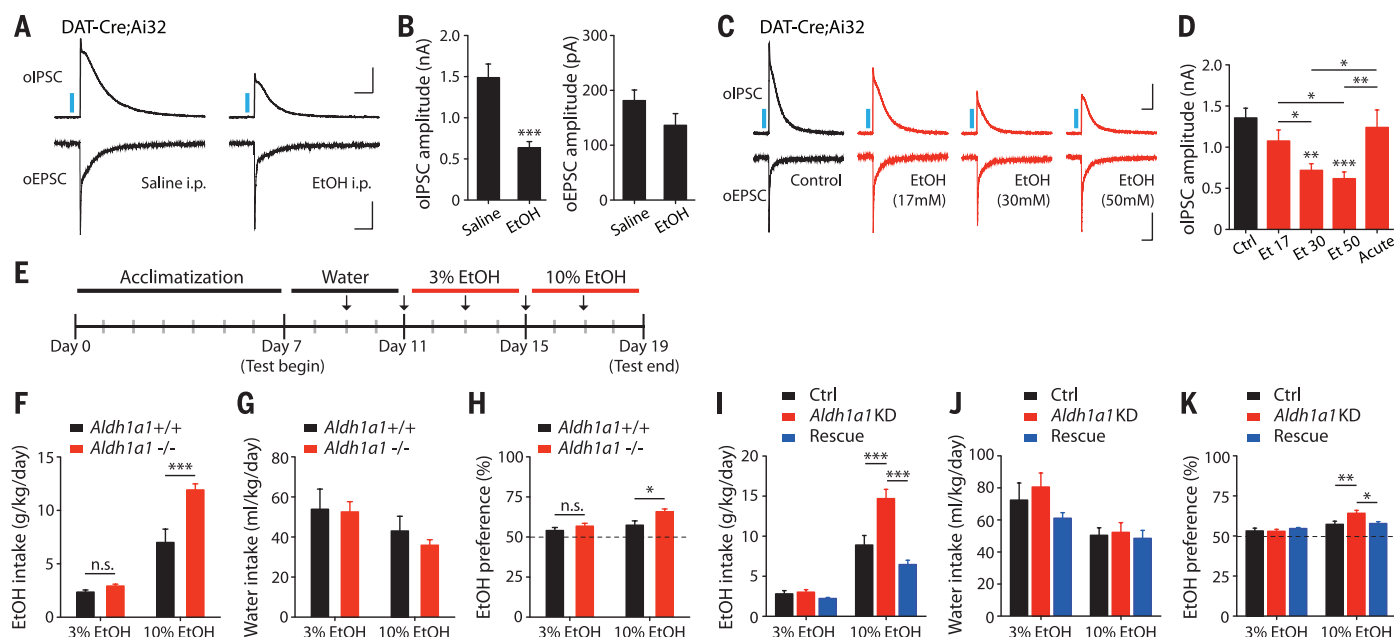


Fig. 4. Altered GABA co-release in conditions related to alcohol binge drinking. Representative oIPSC and oEPSC traces (A) and summary statistics (B) in DAT-Cre;Ai32 mice in control or after repeated in vivo administration of EtOH. Representative oIPSC and oEPSC traces (C) and summary statistics (D) in DAT-Cre;Ai32 mice in control mice or mice treated with EtOH (17 to 50 mM). (E) Schematic illustration depicting the timeline of the two-bottle-choice behav-

ioral assay. (F) Quantification of average daily EtOH intake, (G) average daily water intake, and (H) average EtOH preference. (I) Quantification of average daily EtOH intake in *Aldh1a1* KD or *Aldh1a1* overexpression mice. (J) Average daily water intake. (K) Average EtOH preference. Blue bar indicates 450-nm light stimulation. Scale bars: 400 pA and 100 ms for oIPSC and 50 pA and 100 ms for oEPSC. Error bars indicate means \pm SEM. * P < 0.05, ** P < 0.01, *** P < 0.001.

Aldh1a1^{-/-} mice (fig. S14). When given continuous access to EtOH, *Aldh1a1*^{-/-} mice significantly increased their intake of and preference for EtOH, with no significant difference in daily water intake, compared with WT littermates (Fig. 4, E to H). To more conclusively demonstrate that loss of ALDH1a1 specifically in midbrain neurons is responsible for enhanced EtOH consumption, we injected an AAV-expressing *Aldh1a1*-shRNA into the ventral midbrain of WT mice to knockdown *Aldh1a1* expression (fig. S9). *Aldh1a1* KD in the midbrain recapitulated the behavioral phenotype in which increased intake of and preference for EtOH is observed in *Aldh1a1*^{-/-} mice. This behavioral effect was fully rescued by simultaneous expression of an shRNA-resistant WT *Aldh1a1** (Fig. 4, I to K). Together, our studies suggest that diminished GABA co-release may serve as a potential determinant for enhanced alcohol consumption and preference.

Midbrain DA neurons are known to act through slow neuromodulatory mechanisms. However, GABA co-release in DA neurons demonstrates a rapid and potent inhibitory control used by DA neurons. A variety of neuronal subtypes can co-release multiple neurotransmitters in different neural circuits (35–37). How an individual neuron releases and regulates multiple neurotransmitters remains unclear. We found that DA neurons use an alternative GABA synthesis pathway to support functional GABAergic neurotransmission. Co-released GABA can permit very local inhibition of dendritic excitability, a key mechanism controlling synaptic plasticity. Moreover, as this pathway is evolutionarily conserved and given the widespread expression of ALDH1 in a variety of cell types—including cells of the retina (19, 20) and hippocampus (21), and a subset of SPNs (fig. S5), our findings suggest that GABA alternative synthesis may represent a more fundamental mechanism used by broader classes of GABAergic neurons.

The dorsal striatum plays important roles in the transitioning from initial voluntary drug use to habitual, and ultimately compulsive, drug abuse (30, 38, 39). The GABAergic synapse has also been the focus of extensive study for its role in the behavioral consequences of EtOH exposure. In particular, it has been suggested that acute and chronic EtOH exposure modulate GABAergic release and synaptic GABA_A receptors through pre- and postsynaptic mechanisms, respectively (40). Our studies indicate that EtOH attenuates GABA co-release by inhibiting GABA biosynthesis at concentrations similar to those after binge-drinking alcohol, which provides an additional mechanism through which EtOH exposure can modulate the activity of GABAergic synapses. Diminished GABA co-release and ALDH1a1 activity may directly contribute to enhancement of alcohol intake and preference behavior, reminiscent of humans with *Aldh1a1* mutations. In evaluating genetic factors associated with risk of alcohol abuse then, we will likely need to consider pre- and postsynaptic components that converge on the GABAergic system. Together, our data indicate that GABA co-release, in addition

to DA, may serve an essential function in the regulation of the development of addictive behaviors.

REFERENCES AND NOTES

- W. Schultz, *Annu. Rev. Neurosci.* **30**, 259–288 (2007).
- N. X. Tritsch, B. L. Sabatini, *Neuron* **76**, 33–50 (2012).
- B. T. Chen, F. W. Hopf, A. Bonci, *Ann. N. Y. Acad. Sci.* **1187**, 129–139 (2010).
- P. Redgrave et al., *Nat. Rev. Neurosci.* **11**, 760–772 (2010).
- N. X. Tritsch, J. B. Ding, B. L. Sabatini, *Nature* **490**, 262–266 (2012).
- T. González-Hernández, P. Barroso-Chinea, A. Acevedo, E. Salido, M. Rodríguez, *Eur. J. Neurosci.* **13**, 57–67 (2001).
- N. X. Tritsch, W. J. Oh, C. Gu, B. L. Sabatini, *eLife* **3**, e01936 (2014).
- W. Matsuda et al., *J. Neurosci.* **29**, 444–453 (2009).
- C. L. Heusner, L. R. Beutler, C. R. Houser, R. D. Palmiter, *Genesis* **46**, 357–367 (2008).
- S. Lammel et al., *Neuron* **85**, 429–438 (2015).
- P. Hoerbel, T. A. Lindsley, M. W. Fleck, *J. Neurosci.* **35**, 3525–3536 (2015).
- K. Williams, *Cell. Signal.* **9**, 1–13 (1997).
- S. G. Xing, Y. B. Jun, Z. W. Hau, L. Y. Liang, *Plant Physiol. Biochem.* **45**, 560–566 (2007).
- B. J. Shelp et al., *Plant Sci.* **193–194**, 130–135 (2012).
- M. R. Bell, J. A. Belarde, H. F. Johnson, C. D. Aizenman, *Nat. Neurosci.* **14**, 505–512 (2011).
- E. B. Sequerra, P. Gardino, C. Hedin-Pereira, F. G. de Mello, *Neuroscience* **146**, 489–493 (2007).
- T. Noto et al., *Pharmacol. Biochem. Behav.* **25**, 411–414 (1986).
- E. N. Yamasaki, V. D. Barbosa, F. G. De Mello, J. N. Hókoc, *Int. J. Dev. Neurosci.* **17**, 201–213 (1999).
- J. Laschet, T. Grisar, M. Bureau, D. Guillaume, *Neuroscience* **48**, 151–157 (1992).
- B. A. Barres, W. J. Koroshetz, K. J. Swartz, L. L. Chun, D. P. Corey, *Neuron* **4**, 507–524 (1990).
- J. Aoto, C. I. Nam, M. M. Poon, P. Ting, L. Chen, *Neuron* **60**, 308–320 (2008).
- G. Liu et al., *J. Clin. Invest.* **124**, 3032–3046 (2014).
- P. McCaffery, U. C. Dräger, *Proc. Natl. Acad. Sci. U.S.A.* **91**, 7772–7776 (1994).
- Allen Brain Atlas, <http://mouse.brain-map.org/gene/show/11455>.
- V. Vasilou, A. Pappa, D. R. Petersen, *Chem. Biol. Interact.* **129**, 1–19 (2000).
- D. S. Goldstein et al., *J. Neurochem.* **126**, 591–603 (2013).
- X. Fan et al., *Mol. Cell. Biol.* **23**, 4637–4648 (2003).
- R. Sherva et al., *Alcohol. Clin. Exp. Res.* **33**, 848–857 (2009).
- J. Liu et al., *Alcohol. Clin. Exp. Res.* **35**, 304–316 (2011).
- B. J. Everitt, T. W. Robbins, *Nat. Neurosci.* **8**, 1481–1489 (2005).
- G. Chen et al., *Alcohol. Clin. Exp. Res.* **35**, 1739–1748 (2011).
- J. Wang et al., *J. Neurosci.* **32**, 15124–15132 (2012).
- L. E. O'Dell, A. J. Roberts, R. T. Smith, G. F. Koob, *Alcohol. Clin. Exp. Res.* **28**, 1676–1682 (2004).
- S. Ben Hamida et al., *J. Neurosci.* **33**, 14369–14378 (2013).
- T. S. Hnasko et al., *Neuron* **65**, 643–656 (2010).
- D. H. Root et al., *Nat. Neurosci.* **17**, 1543–1551 (2014).
- S. J. Shabel, C. D. Proulx, J. Piriz, R. Malinow, *Science* **345**, 1494–1498 (2014).
- D. M. Lovinger, *Neuropharmacology* **58**, 951–961 (2010).
- C. M. Pennartz et al., *J. Neurosci.* **29**, 12831–12838 (2009).
- J. L. Weiner, C. F. Valenzuela, *Pharmacol. Ther.* **111**, 533–554 (2006).

ACKNOWLEDGMENTS

The authors thank A. Du and Y. Liu for technical assistance; D. Ron for suggestions on using the two-bottle-choice behavior test; and T. Sudhof, G. Panagiotakos, W. Wei, Z. Khaliq, and members of the Ding laboratory for helpful discussions. Supported by grants from the National Institute of Neurological Disorders and Stroke, NIH, NS075136, NS091144 (J.B.D.), the Klingenstein Foundation (J.B.D.), and National Institute of Mental Health, NIH, MH086403 (L.C.) and MH091193 (L.C.). The authors declare no conflicts of interest. All primary electrophysiological and immunohistochemical data are archived on a server in the Department of Neurosurgery at Stanford University School of Medicine.

SUPPLEMENTARY MATERIALS

www.sciencemag.org/content/350/6256/102/suppl/DC1

Materials and Methods

Figs. S1 to S14

Table S1

References (41–51)

29 April 2015; accepted 25 August 2015

10.1126/science.aac4690

STRUCTURAL BIOLOGY

Crystal structure of the metazoan Nup62•Nup58•Nup54 nucleoporin complex

Hema Chug, Sergei Trakhanov, Bastian B. Hülsmann, Tino Pleiner, Dirk Görlich*

Nuclear pore complexes (NPCs) conduct nucleocytoplasmic transport and gain transport selectivity through nucleoporin FG domains. Here, we report a structural analysis of the FG Nup62•58•54 complex, which is a crucial component of the transport system. It comprises a ≈13 nanometer-long trimerization interface with an unusual 2W3F coil, a canonical heterotrimeric coiled coil, and a kink that enforces a compact six-helix bundle. Nup54 also contains a ferredoxin-like domain. We further identified a heterotrimeric Nup93-binding module for NPC anchorage. The quaternary structure alternations in the Nup62 complex, which were previously proposed to trigger a general gating of the NPC, are incompatible with the trimer structure. We suggest that the highly elongated Nup62 complex projects barrier-forming FG repeats far into the central NPC channel, supporting a barrier that guards the entire cross section.

Nuclear pore complexes (NPCs) are embedded into the nuclear envelope and built from nucleoporins (Nups). They conduct nucleocytoplasmic transport in order to supply the cell nucleus with proteins and the cytoplasm with ribosomes, mRNA, and tRNAs. The

NPC framework is of eightfold rotational symmetry and assembled from the Nup155•Nup35•Nup93•Nup188/205 complex, as well as the

Department of Cellular Logistics, Max Planck Institute for Biophysical Chemistry, Göttingen, Germany.

*Corresponding author. E-mail: goerlich@mpibpc.mpg.de

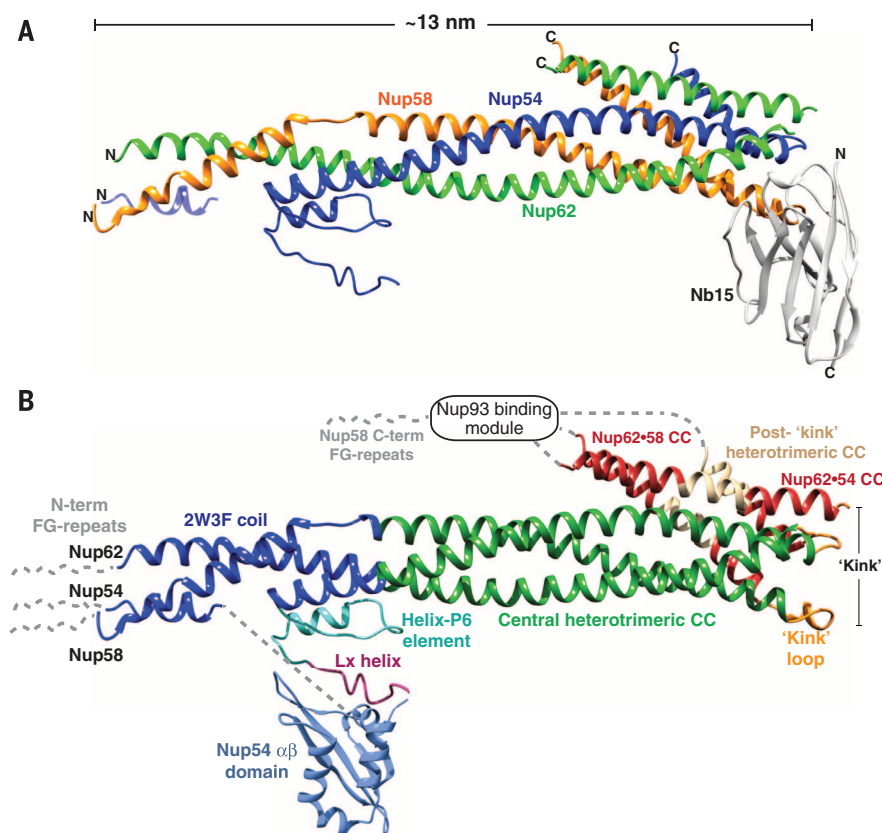


Fig. 1. Architecture of the *Xenopus* Nup62•58•54 complex. (A) Crystal structure of the xNup62•58•54 complex with nanobody Nb15 bound, comprising Nup62³⁵⁸⁻⁴⁸⁵, Nup58²⁸³⁻⁴⁰⁶, and Nup54³¹⁵⁻⁴⁵⁰. Coloring is by chains. Light blue region in Nup54 was built only as poly(Ala). (B) Overall architecture of the Nup62•58•54 complex, combining crystal structures from (A) and of the Nup54²¹⁴⁻³¹⁴ αβ domain detailed below. Coloring is according to the indicated structural modules. Dashed lines denote unresolved segments: the disordered FG repeat domains, a region in Nup54 preceding the αβ domain, and the C-terminal Nup93-binding module. CC, coiled coil.

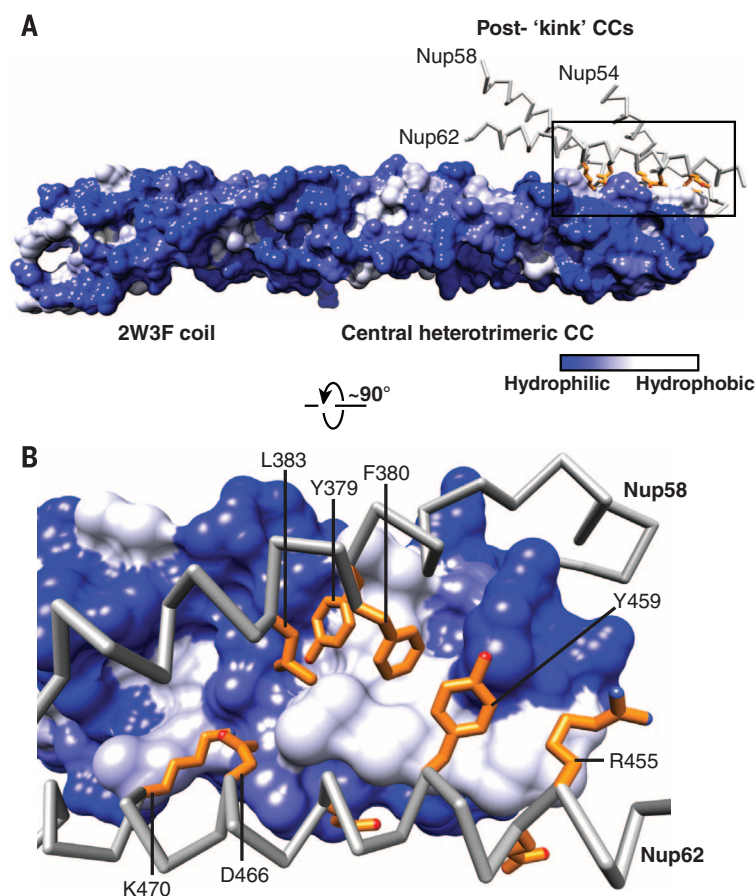


Fig. 2. Structure of the “kink” region. (A) The “kink” in the Nup62•58•54 complex is stabilized by extensive hydrophobic packing, mainly between the Nup54 pre-kink helix and the Nup58 and Nup62 post-kink helices. “Pre-kink structures” (2W3F and coiled coils) are rendered in surface representation, with blue indicating hydrophilic and white hydrophobic regions. “Post-kink CCs” are shown as gray C_α traces, with residues involved in hydrophobic packing depicted as orange sticks. Most of these residues are highly conserved from fungi to vertebrates (fig. S1). (B) Magnified view of boxed region in (A), rotated as indicated. The Nup54 post-kink helix is omitted for clarity.

nine-membered Y complex [reviewed in (1–3)]. These core components contact integral membrane proteins, confer peripheral membrane interaction, and anchor FG Nups, which contain Phe-Gly (FG) repeat domains that bind shuttling nuclear transport receptors (NTRs) in transit.

NPCs grant free passage to small molecules but become increasingly restrictive as the size of the diffusing species approaches or exceeds a limit of ~ 30 kD in mass or 5 nm in diameter (4). This property is critical for keeping nuclear and cytoplasmic contents separate. NTRs, however, are not bound by this size limit. They mediate facilitated NPC passage and ferry cargoes up to the size of newly assembled ribosomal subunits (~ 25 nm in diameter) between the two compartments. Facilitated translocation is usually completed within 10 ms (5). NPCs can conduct ~ 1000 facilitated translocation events or a mass flow of ~ 100 MD per pore per second (6), which further implies that NPCs can translocate numerous species in parallel.

Interactions between NTRs and FG repeats are essential for facilitated translocation.

The metazoan FG Nup62•58•54 (Nup62) complex (7–9) is anchored by Nup93 at the pore and is critical for NPC function. It contributes a considerable share of the total FG-repeat mass, and its depletion severely impairs the ability of *Xenopus* NPCs to accumulate cargoes against a concentration gradient (7, 10). Likewise, all subunits of its yeast Nsp1•Nup49•Nup57 counterpart are essential for viability (11–15).

There are two main views as to how FG repeats confer transport selectivity. In the first, FG domains themselves form the actual permeability barrier, which is then selectively traversed by NTR•cargo complexes (6, 16).

In a second series of models (17–20), FG repeats do not function as barrier-forming units but instead operate as “sensors” in a general gating mechanism, where the Nup62•58•54 complex forms an additional ring scaffold that restricts the pas-

sage of macromolecules but widens upon NTR-binding to FG domains of either Nup54, 58, or 62. These models were based on crystal structures of small coiled-coil fragments from one or two subunits of the heterotrimeric complex and assume that the different observed interactions between these fragments and their oligomerization into higher-order assemblies indeed represent transport intermediates.

Our starting point for structural analysis was a larger *Xenopus* Nup62 complex lacking only the intrinsically disordered FG repeats. This “complex 1” comprises residues Nup54^{146–535}, Nup58^{267–490}, and Nup62^{342–547} and efficiently assembles into NPCs (10). It includes all predicted coiled coils and a large preceding region in Nup54 (residues 146 to 356), whose amino acid composition and strong sequence conservation are also predictive of a globular fold (fig. S1).

Recombinant protein expression in *Escherichia coli* showed that individual subunits as well as

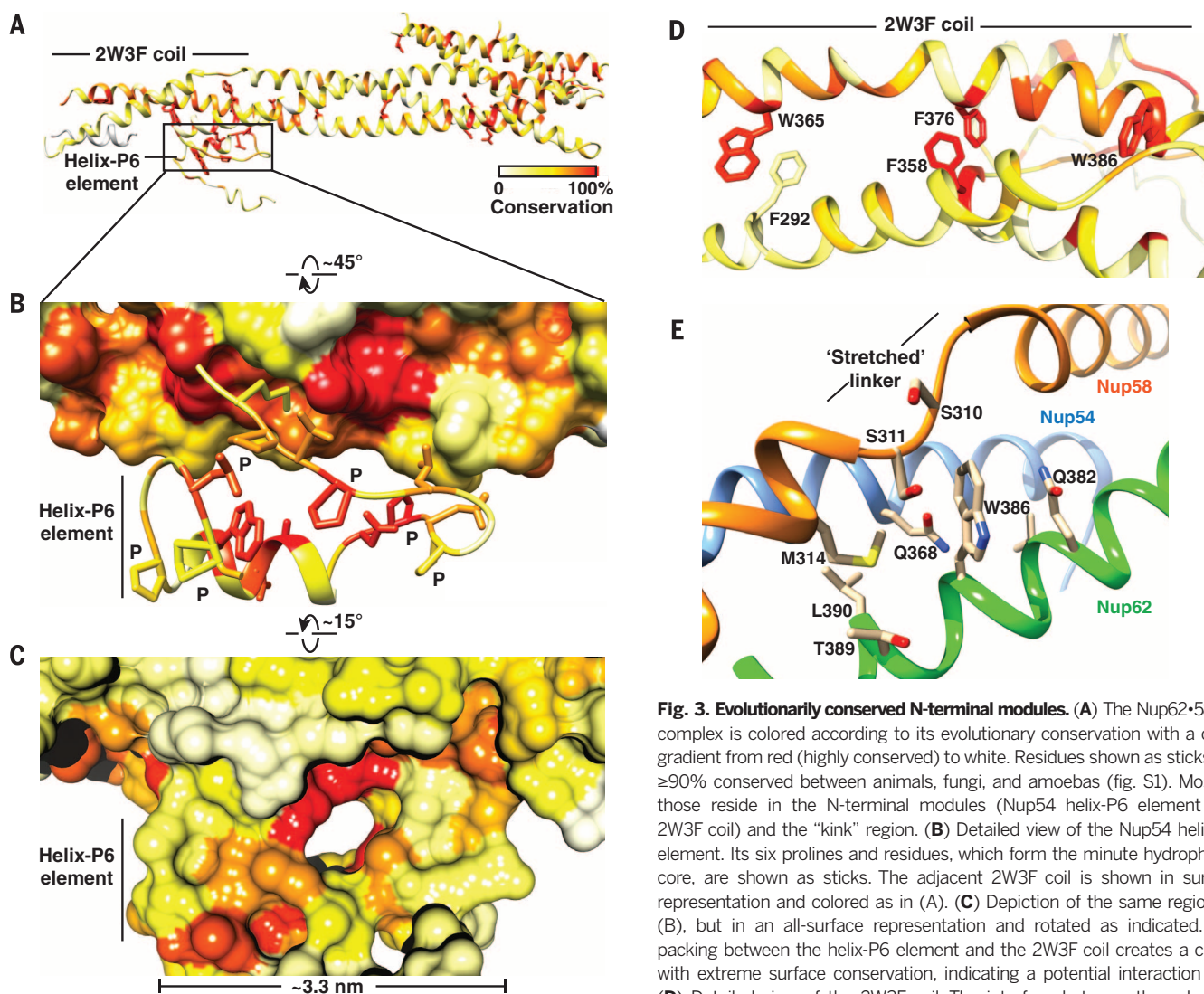


Fig. 3. Evolutionarily conserved N-terminal modules. (A) The Nup62•58•54 complex is colored according to its evolutionary conservation with a color gradient from red (highly conserved) to white. Residues shown as sticks are $\geq 90\%$ conserved between animals, fungi, and amoebas (fig. S1). Most of those reside in the N-terminal modules (Nup54 helix-P6 element and 2W3F coil) and the “kink” region. (B) Detailed view of the Nup54 helix-P6 element. Its six prolines and residues, which form the minute hydrophobic core, are shown as sticks. The adjacent 2W3F coil is shown in surface representation and colored as in (A). (C) Depiction of the same region as (B), but in an all-surface representation and rotated as indicated. The packing between the helix-P6 element and the 2W3F coil creates a cavity with extreme surface conservation, indicating a potential interaction site. (D) Detailed view of the 2W3F coil. The interface between these helices

includes conserved aromatic residues (shown as sticks) that are prohibited in canonical coiled coils. (E) Close-up of the highly unusual Nup62^{W386}, which is partially solvent-exposed and forced to pack against hydrophilic residues, namely, Ser³¹⁰ and Ser³¹¹ from the “Nup58 stretched linker” and Nup54^{Q368}. The extreme conservation of this arrangement suggests a docking site for other nucleoporins.

subunit pairs are highly prone to form inclusion bodies. Coexpression of all three subunits, however, yielded a soluble 1:1:1 stoichiometric complex that showed no signs of self-association (figs. S2 and S3). Complex 1 crystallized when bound to Nb15, a nanobody (21) specific for the heterotrimer (fig. S4). However, the resulting crystals diffracted to only ~ 7 Å (table S1).

While optimizing the Nup62•58•54 complex for improved crystal packing, we observed that its interaction with Nup93 requires C-terminal regions of all three subunits (figs. S5 and S6). Deleting the heterotrimeric Nup93-binding module led to complex 16, whose cocrystals with Nb15 diffracted to 2.9 Å (fig. S7 and table S1). We solved the structure with experimental phases obtained by single-wavelength anomalous diffraction (22) from selenomethionine-substituted or europium (III)-derivatized crystals (table S2).

A central element of the structure is a long, parallel heterotrimeric coiled coil formed by Nup62, Nup58, and Nup54. Given that so far only pairwise Nup62•54 and Nup58•54 interactions had been considered (15, 18, 23, 24), this was unexpected. On the C-terminal side, the heterotrimeric coiled coil is followed by a sharp kink and by a post-kink coiled-coil structure, which includes short Nup62•54 dimeric, Nup62•58•54 trimeric, and Nup62•58 dimeric segments (Fig. 1 and fig. S8). On the N-terminal side, the central coiled coil loosens and the heterotrimeric coil structure gets interrupted to engage in interactions with further N-terminal parts of Nup54 (see below).

The central coiled coil conforms to a heptad-repeat arrangement (25) in which hydrophobic “a” and “d” residues pack inside the hydrophobic core of the heterotrimer while most polar residues remain solvent-exposed. Two Nup62 “a” positions, however, are occupied by the highly conserved

glutamines Nup62^{Q411} and Nup62^{Q425}. They form buried H-bonds to the strategically positioned threonines Nup54^{T396} and Nup58^{T349}, which also correspond to normally hydrophobic “a” or “d” positions. Such hydrophilic contact layers counteract off-target and off-register interactions of the respective heptad motifs (26) and thus confer specificity to the heterotrimerization. Consistent with these glutamines pointing into the coiled coil’s hydrophobic core, we found that bacterially expressed Nup62^{Q411R} and Nup62^{Q425R} mutants failed to assemble a trimeric Nup62 complex (fig. S9). The central coiled coil is further stabilized by numerous intra- and interchain salt bridges in solvent-exposed regions.

The “kink” folds the second coiled-coil structure, in a nearly antiparallel fashion, back onto the first one and thereby generates a six-helix bundle structure. The kink is stabilized by a network of highly conserved hydrophobic and hydrophilic contacts, which together bury a large interface of ~ 940 Å². The hydrophobic packing expands the hydrophobic interiors of the two coiled coils to a common hydrophobic core, resulting in a “CC₃-kink-CC” fold (Fig. 2). We expect no flexibility at this six-helix bundle arrangement.

Nb15 recognizes the Nup62•58•54 trimer but neither individual subunits nor subunit pairs (fig. S4). This specificity is explained by the structure: Nb15 recognizes the peculiar CC₃-kink-CC fold of the Nup62 complex, which requires all three subunits to interact (Fig. 1 and fig. S10). Nb15 also recognizes the endogenous Nup62•58•54 complex from *Xenopus* egg extracts (fig. S11), indicating that the native complex conforms to our structural model.

The human Nup62 complex differs from the *Xenopus* complex by a Nup62^{S438L} exchange. The leucine (L413) in human Nup62 sterically

excludes Nb15 binding. The converse L→S exchange restored the nanobody interaction (fig. S10), indicating that the mammalian and *Xenopus* Nup62•58•54 complexes share the same architecture.

The central heterotrimeric coiled coil comprises ~ 7.5 heptad repeats. The helices of all three subunits extend N-terminally much further but continue their interactions with each other in a noncanonical manner: Nup58 skips one helical turn and thus provides two helix segments joined by a stretched linker. Nup54 contributes two shorter helix segments with a large gap in between. The interhelix packing is also unusual in that it involves residues that are normally strongly disfavored in coiled-coil interfaces (25): namely, two tryptophans (Nup62^{W365} and Nup62^{W386}) and three phenylalanines (Nup54^{F358}, Nup62^{F376}, and Nup58^{F292}). Given their extreme evolutionary conservation (Fig. 3 and figs. S1 and S12), we refer to this structural element as a “2W3F coil”. Perhaps the most notable feature of this element is the positioning of the highly conserved Nup62^{W386}. It is clamped between Nup54^{Q368}, Nup62^{Q382}, and the stretched interhelix linker of Nup58 but presents the nitrogen-containing side of its indole moiety to the solvent. An essential role of the 2W3F coil is suggested by earlier genetic evidence in *Saccharomyces cerevisiae* (27), where Nsp1^{W644C} and Nsp1^{L640S} mutations (equivalent to xNup62^{W365} and xNup62^{W386}, respectively) caused severe growth defects, temperature sensitivity, and impaired mRNA export. Additionally, a partial deletion of Nsp1 corresponding to the Nup62 2W3F coil caused lethality without compromising the assembly of the Nsp1•Nup49•Nup57 complex.

The two Nup54 helical segments of the 2W3F coil are separated by a long sequence, which was only partially resolved in the crystal structure.

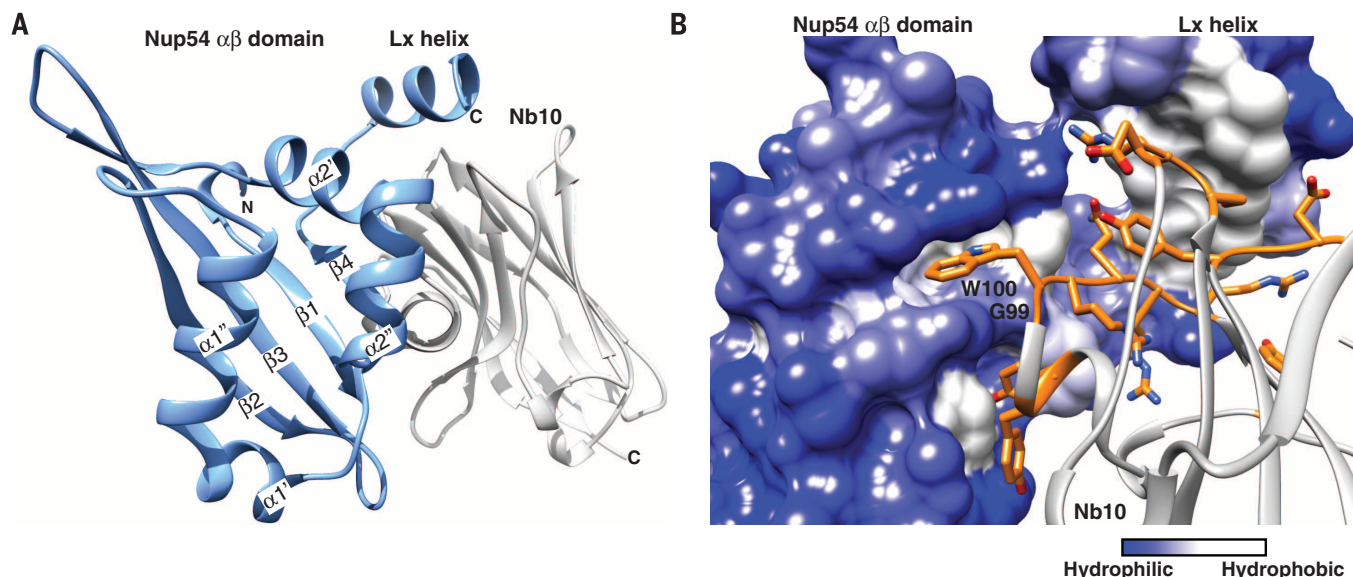


Fig. 4. Structure of the Nup54 $\alpha\beta$ domain. (A) Structure of the Nup54^{214–314} $\alpha\beta$ domain bound to Nb10. Secondary-structure elements of the ferredoxin-like $\alpha\beta$ domain are indicated. It differs from canonical ferredoxin folds mainly by kinks in the α helices. Here, the Lx helix adopts a different conformation than in the crystals of the Nup62•58•54•Nb15 complex. (B) Details of the nanobody Nb10 interaction with the Nup54 $\alpha\beta$ domain. The $\alpha\beta$ domain is shown in surface representation and colored by hydrophobicity. Nb10 is shown as gray ribbon, and its three complementarity-determining regions are highlighted in orange. Residues involved in the interaction are shown as orange sticks. Tryptophan Nb10^{W100} docks into a deep hydrophobic pocket of the Nup54 $\alpha\beta$ domain.

The resolved part of this sequence contains a highly conserved helix with a back-folded proline-rich stretch, the “helix-P6 element” (Fig. 3 and fig. S8).

Most anti-Nup62 complex nanobodies recognized a region that remained unresolved in the crystals (fig. S4), and as nanobodies favor folded epitopes, this hinted at additional globular domain(s). We mapped the immune-dominant domain, expressed it, formed a complex with nanobody Nb10, and obtained crystals that diffracted to 1.55 Å. As the structure revealed a ferredoxin-like fold with a $\beta\alpha\beta\beta\alpha\beta$ topology (Fig. 4), we will refer to it as the “Nup54 $\alpha\beta$ domain.” The presence of kinks in the α helices and extended loops between the structural elements, however, places this domain into a new family of ferredoxin-like folds. This ferredoxin-like Nup54 $\alpha\beta$ domain is unique to metazoans (fig. S1) and might relate to their open mitosis. Nb10 interacts with this domain mainly through hydrophobic interactions, where a tryptophan of Nb10 (W^{100}) docks into a deep hydrophobic pocket on the surface of the Nup54 $\alpha\beta$ domain. The region following the globular domain folds into an amphipathic helix (1 \times helix) and packs against Nb10 through its hydrophobic surface.

Although there is agreement about the importance of the Nup62•58•54 complex, there has been controversy about the way it functions. On the basis of different interaction modes observed in the structures of a Nup58 fragment [Protein Data Bank (PDB) 2OSZ] and of Nup58•Nup54 (PDB 3T98), as well as Nup62•Nup54 (PDB 3T97) fragment pairs, a Nup62 complex-mediated general gating mechanism has been proposed (17–19). The different interaction modes represent, according to this model, rearrangements in the Nup62 complex, which occur upon NTR-binding to FG domains, and bring about “constriction” or “dilation” of the NPC central channel. A structure comparison (fig. S13) shows, however, that all proposed “ring-cycle” intermediates are prohibited in the context of the properly assembled Nup62•58•54 heterotrimer.

The interactions described by the PDB 2OSZ, 3T97, and 3T98 structures have been characterized as inherently unstable, and this instability was considered crucial for facilitating transport-relevant structural transitions in the Nup62 complex (17–19). Knowing the heterotrimeric structure, it appears, however, more likely that the observed instability was due to the lack of cognate interaction partners. Indeed, the heterotrimeric complex resists thermal denaturation up to 46°C (fig. S7), which is 16°C higher than the upper temperature limit tolerated by *Xenopus laevis*. Likewise, earlier reports (7, 8) emphasized the extraordinary stability of the native Nup62 complex that resists not only very high salt but also harsh detergents and at least 2 M urea. Moreover, in the mixing experiments with differently tagged trimeric complexes,

we detected no exchange between the subunits, even when the incubation was extended to hours at room temperature. Thus, considering that NPC passage of cargo molecules occurs in milliseconds (5), it is unlikely that any alternations occur in the quaternary structure of the Nup62 complex that could possibly be relevant for facilitated translocation.

For transport selectivity, preventing the passage of unwanted material is as important as allowing NTR•cargo species to pass. This is straightforward to explain by an adaptive barrier that seals around a translocating species, particularly because cohesive FG domains readily assemble such self-sealing barriers in the form of FG hydrogels (28, 29).

In contrast, a general gating mechanism as an obligatory part of individual translocation cycles is a rather problematic concept: NPCs in steady state are essentially saturated with NTRs and translocate in parallel many NTR molecules in both directions. A “general gate” would therefore stand open at all times and consequently fail as a barrier. Structural changes in architectural NPC elements might, however, be relevant when exceptionally large cargoes pass or NPCs adjust to changes in the overall transport load. In consequence of attenuated transport, certain rearrangements near the central NPC channel have indeed been observed (30).

So far, it has been known that the Nup62 complex is anchored by Nup93 at the NPC and that it interacts through its four FG domains with NTRs in transit. We have now identified several elements, whose extreme evolutionary conservation suggests them to be additional interaction sites with other nucleoporins or even with certain NTR•cargo complexes that pass the pore. These elements include the Nup62^{W386} patch of the 2W3F coil, the helix-P6 element, and the Nup54 $\alpha\beta$ domain, as well as another highly conserved region in Nup54 (residues 149 to 210) that remained unresolved in our analysis.

Our structure also revealed the Nup62 complex to be a particularly elongated (~13 nm) and rigid entity, which is flanked by the C-terminal Nup93-binding module and N-terminal FG domains. This arrangement is highly conserved. Yet it is a valid question why these FG domains are not directly anchored to the NPC scaffold. One possibility is that the Nup62 complex multiplies the number of anchored FG domains. Moreover, it might project its barrier-forming FG domains far into the central NPC channel and thus help to guard the otherwise perhaps weakest region of the channel's cross section. Compared to a central channel that is more narrow to begin with, this arrangement could have a crucial advantage: namely, that an elastically anchored Nup62 complex would allow for concerted long-range movements of the connected FG domains—for example, to give way for very large cargoes.

REFERENCES AND NOTES

1. E. Grossman, O. Medalia, M. Zwerg, *Annu Rev Biophys* **41**, 557–584 (2012).
2. E. Hurt, M. Beck, *Curr. Opin. Cell Biol.* **34**, 31–38 (2015).
3. S. Bilokapic, T. U. Schwartz, *Curr. Opin. Cell Biol.* **24**, 86–91 (2012).
4. D. Mohr, S. Frey, T. Fischer, T. Güttler, D. Görlich, *EMBO J.* **28**, 2541–2553 (2009).
5. W. Yang, J. Gelles, S. M. Musser, *Proc. Natl. Acad. Sci. U.S.A.* **101**, 12887–12892 (2004).
6. K. Ribbeck, D. Görlich, *EMBO J.* **20**, 1320–1330 (2001).
7. D. R. Finlay, E. Meier, P. Bradley, J. Horecka, D. J. Forbes, *J. Cell Biol.* **114**, 169–183 (1991).
8. K. Kita, S. Omata, T. Horigome, *J. Biochem.* **113**, 377–382 (1993).
9. T. Guan *et al.*, *Mol. Biol. Cell* **6**, 1591–1603 (1995).
10. B. B. Hülsmann, A. A. Labokha, D. Görlich, *Cell* **150**, 738–751 (2012).
11. E. C. Hurt, *EMBO J.* **7**, 4323–4334 (1988).
12. S. R. Wente, M. P. Rout, G. Blobel, *J. Cell Biol.* **119**, 705–723 (1992).
13. P. Grandi, V. Doye, E. C. Hurt, *EMBO J.* **12**, 3061–3071 (1993).
14. P. Grandi, N. Schlaich, H. Tekotte, E. C. Hurt, *EMBO J.* **14**, 76–87 (1995).
15. N. L. Schlaich, M. Häner, A. Lustig, U. Aebi, E. C. Hurt, *Mol. Biol. Cell* **8**, 33–46 (1997).
16. S. S. Patel, B. J. Belmont, J. M. Sante, M. F. Rexach, *Cell* **129**, 83–96 (2007).
17. I. Melčák, A. Hoelz, G. Blobel, *Science* **315**, 1729–1732 (2007).
18. S. R. Solmaz, R. Chauhan, G. Blobel, I. Melčák, *Cell* **147**, 590–602 (2011).
19. S. R. Solmaz, G. Blobel, I. Melčák, *Proc. Natl. Acad. Sci. U.S.A.* **110**, 5858–5863 (2013).
20. J. Koh, G. Blobel, *Cell* **161**, 1361–1373 (2015).
21. S. Muyldermans, *Annu. Rev. Biochem.* **82**, 775–797 (2013).
22. T. R. Schneider, G. M. Sheldrick, *Acta Crystallogr. D Biol. Crystallogr.* **58**, 1772–1779 (2002).
23. F. Buss, M. Stewart, *J. Cell Biol.* **128**, 251–261 (1995).
24. A. Ulrich, J. R. Partridge, T. U. Schwartz, *Mol. Biol. Cell* **25**, 1484–1492 (2014).
25. D. N. Woolfson, T. Alber, *Protein Sci.* **4**, 1596–1607 (1995).
26. A. N. Lupas, M. Gruber, *Adv. Protein Chem.* **70**, 37–38 (2005).
27. S. M. Bailer, C. Balduf, E. Hurt, *Mol. Cell Biol.* **21**, 7944–7955 (2001).
28. S. Frey, D. Görlich, *EMBO J.* **28**, 2554–2567 (2009).
29. H. B. Schmidt, D. Görlich, *eLife* **4**, e04251 (2015).
30. M. Eibauer *et al.*, *Nat. Commun.* **6**, 7532 (2015).

ACKNOWLEDGMENTS

We thank the crystallization facility of our institute for providing the robotic screening infrastructure; the team at the synchrotron facility of the Paul Scherrer Institute, Switzerland, for assistance in diffraction data acquisition; the VIB Nanobody Service Facility (Vrije Universiteit Brussel) for providing coding sequences for anti-Nup62 complex nanobodies; U. Steuerwald for support in crystallization; K. Gencalp for helping with MALS; R. Rees, J. Krull, and J. Schünemann for excellent technical help; M. Aksu and K. Gencalp for critical reading of the manuscript; and the Max-Planck-Gesellschaft and the Deutsche Forschungsgemeinschaft (SFB 860) for funding this work. Coordinates and structure factor files have been submitted to the Protein Data Bank (PDB) and are available under the accession codes 5C3L (Nup62•58•54 complex bound to Nb15) and 5C2U (Nup54 $\alpha\beta$ domain bound to Nb10).

SUPPLEMENTARY MATERIALS

www.sciencemag.org/content/350/6256/106/suppl/DC1
Materials and Methods
Tables S1 and S2
Figs. S1 to S13
References (31–41)

5 June 2015; accepted 6 August 2015
Published online 20 August 2015
10.1126/science.aac7420



CRITICAL FAILURES HIDE IN EVERY WESTERN WORKFLOW

**YOU WOULDN'T CLIMB
A MOUNTAIN WITHOUT
COMPLETE CONFIDENCE
IN YOUR TOOLS.**

Protect your proteins the same way.

Overcome sample degradation, fragile gels and unpredictable antibodies with Sigma-Aldrich's dedicated technical support and suite of Western Blot products.

Find out more.

sigma-aldrich.com/westernblot

ACS **axial**

CREATED FOR
**MORE
EFFICIENT
BONDING**

**CONNECT WITH THE SCIENTIFIC
COMMUNITY & ACS PUBLICATIONS
AT ACS AXIAL**

Introducing *ACS Axial*, a new blog from ACS Publications. Don't miss out on the latest ideas, insights, and advice for authors, researchers, librarians, and the global scientific community.

Go to axial.acs.org now

axial.acs.org



ACS Publications
Most Trusted. Most Cited. Most Read.

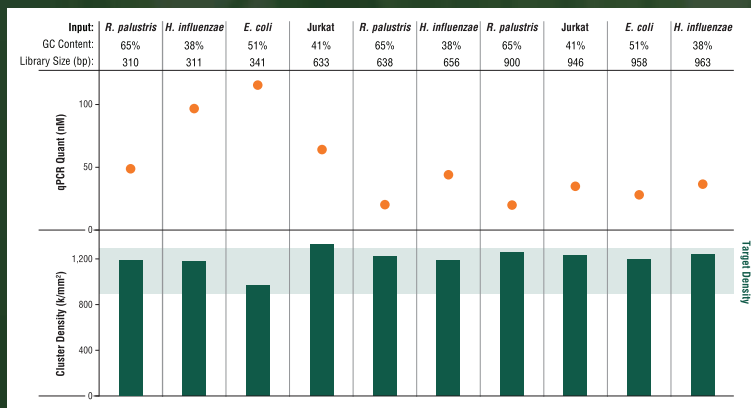
Count on it.

Introducing the NEBNext[®] Library Quant Kit for Illumina[®]

Accurate quantitation of next generation sequencing libraries is essential for maximizing sequencing data output and quality. The NEBNext Library Quant Kit for Illumina is a qPCR-based method that delivers higher consistency and reproducibility of quantitation than other currently available methods. With optimized kit components and a more convenient protocol, you can count on your quantitation values, every time.

To learn more and request a sample,
visit www.neb.com/E7630

With the NEBNext Library Quant Kit, optimal cluster density is achieved from quantitated libraries with a broad range of library size and GC content.



Libraries of 310–963 bp from the indicated sources were quantitated using the NEBNext Library Quant Kit, then diluted to 8 pM and loaded onto a MiSeq[®] (v2 chemistry; MCS v2.4.1.3). Library concentrations ranged from 7–120 nM, and resulting raw cluster density for all libraries was 965–1300 k/mm² (ave. = 1199). Optimal cluster density was achieved using concentrations determined by the NEBNext Library Quant Kit for all library sizes.

EPIGENETICS: DISCOVERY THROUGH VALIDATION

692

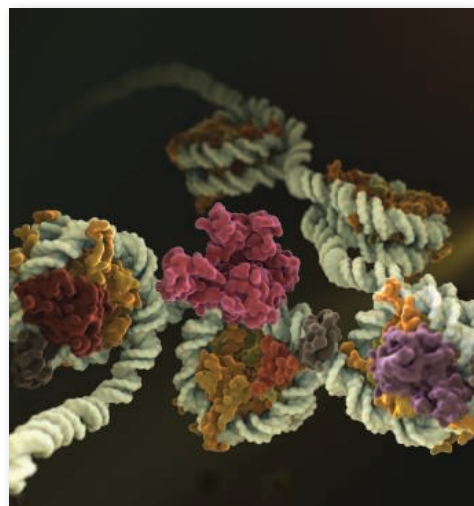
CST antibodies for epigenetic-related targets, including histone modifications, epigenetic regulators, and general transcription factors.

226

CST antibodies validated for ChIP according to ENCODE* Consortium guidelines.

Validated Tools for Discovery:

- » SimpleChIP® Kits to facilitate Chromatin IP from cells and tissue.
- » PTMScan® Kits and Services to enable MS-based discovery of methylated and acetylated proteins.
- » Most ChIP-validated antibodies approved for additional applications like IHC, Flow, IF and WB.



Molecular model of chromatin.

Learn more at: www.cellsignal.com/epigeneticdiscovery

*Landt S.G. et al. (2012) *Genome Res.* 22, 1813–1831.



Reliable Quantification

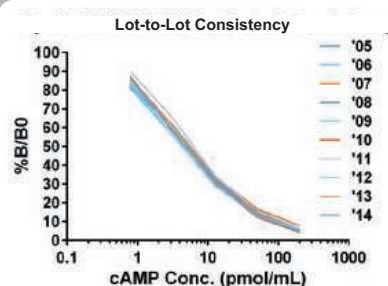
High-Sensitivity Screening Assays

Rapidly and reliably quantify second messengers with high-sensitivity assays

As our understanding of neurodegenerative disease origins increases, so does the need for innovative, high-quality screening assays for identifying potential therapeutics. Enzo's expertise in labeling & detection and assay development provide a unique collection of innovative research tools to monitor neural signaling networks.

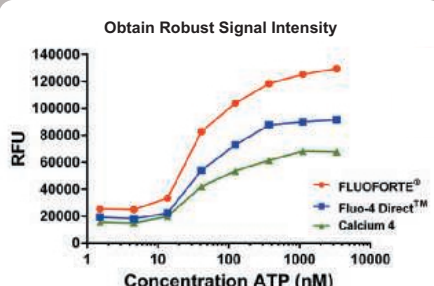
cAMP/cGMP ELISAs

Most sensitive and reliable ELISA kits for detection of cAMP/cGMP



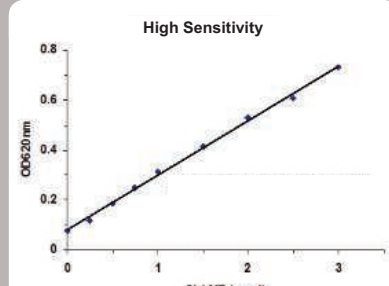
FLUOFORTE® Calcium Assays

Brighter, more robust fluorescent calcium mobilization assays



Cyclic Nucleotide Phosphodiesterase Assay

Unique colorimetric assay used to screen inhibitors and modulators of cyclic nucleotide PDE activity



Issues with your tissues? Process all your slides in a SNAP for streamlined IHC.

Variability – it's the challenge you face in traditional immunohistochemistry (IHC) experiments. If you're handling slides manually, using pip pens, pipetting, dipping and pouring, you risk slide-to-slide process variability, which may affect your results.

Experience a controlled vacuum force that removes solutions evenly from all your slides at once – in seconds.

Experience minimal slide handling, with blocking, washing, antibody and staining solutions contacting your tissues in self-contained reservoirs.

The SNAP i.d.® 2.0 system has been delighting Western blot users for years. Now we've applied its power to IHC.



Enhance your research with
the SNAP i.d.® 2.0 system.
www.emdmillipore.com/IHC

EMD Millipore is a division of Merck KGaA, Darmstadt, Germany

EMD Millipore, the M logo and SNAP i.d. are registered trademarks of Merck KGaA, Darmstadt, Germany.
© 2014 EMD Millipore Corporation, Billerica, MA USA. All rights reserved. BS GEN-14-10289-EX 07/2014

eppendorf
& Science
PRIZE FOR
NEURO
BIOLOGY

Congratulations
to Shigeki Watanabe, Ph.D.
University of Utah
& Charité - Universitäts-
medizin Berlin



And the Winner Is...

Eppendorf & Science Prize for Neurobiology

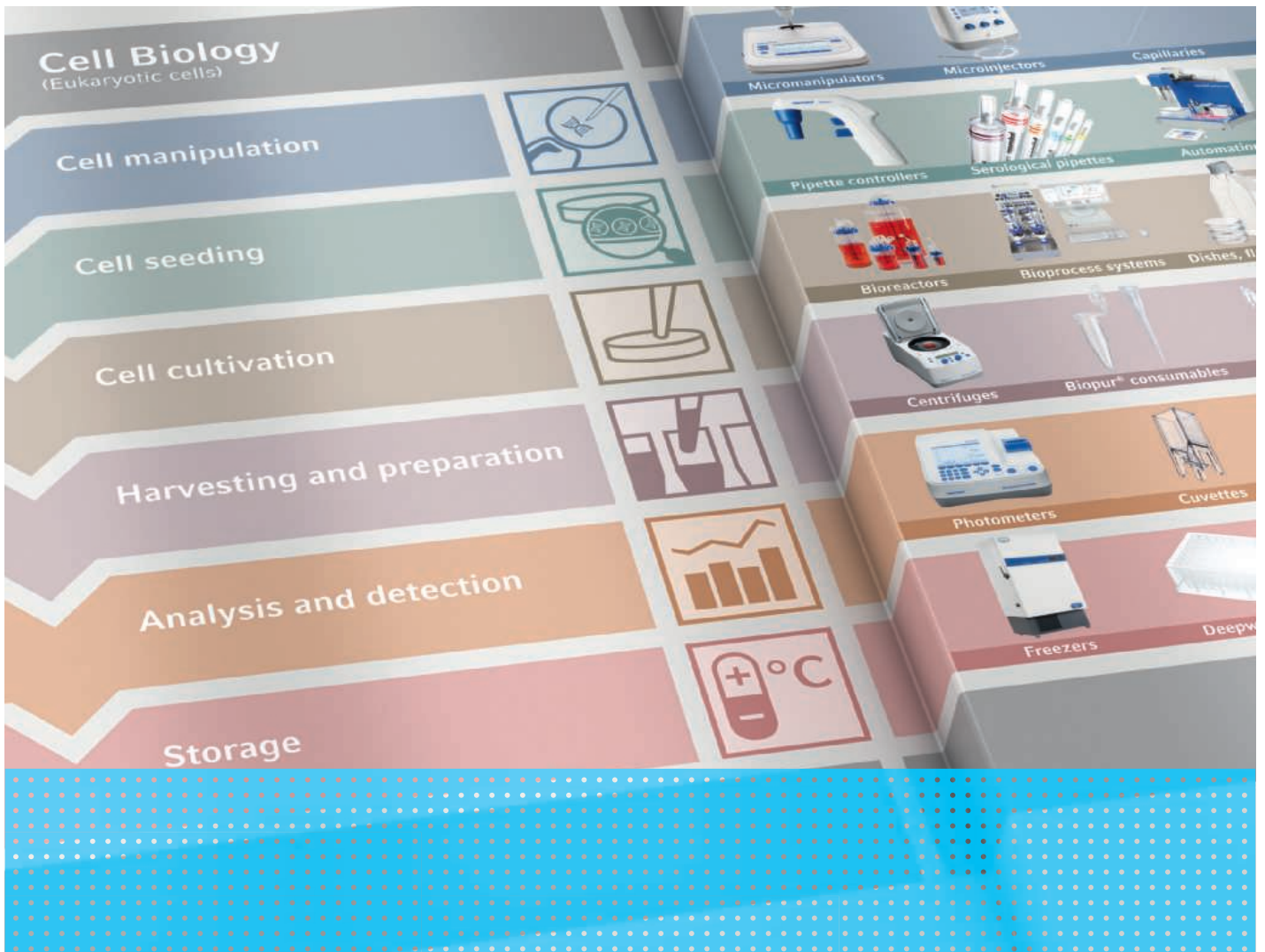
Congratulations to Shigeki Watanabe on winning the 2015 Eppendorf & Science Prize for his work on synaptic vesicle endocytosis. Dr. Watanabe has developed two novel techniques in electron microscopy that allow visualization of protein and membrane dynamics at synapses at a millisecond temporal resolution. Using these techniques, he has discovered an ultrafast mechanism that removes synaptic vesicle components rapidly from the plasma membrane following exocytosis and further demonstrated that synaptic vesicles are regenerated from endosomes.

The annual US\$25,000 Eppendorf & Science Prize for Neurobiology honors scientists, like Dr. Watanabe, for their outstanding contributions to neurobiological research. Shigeki Watanabe is the 14th recipient of this international award. He will be presented with the Prize at a ceremony held during the week of the 2015 Annual Meeting of the Society for Neuroscience in Chicago.

You Could be Next Year's Winner.

If you are 35 years of age or younger and currently performing neurobiological research, you could be next to win the 2016 Prize. Deadline for entries is June 15, 2016.

Learn more at: www.eppendorf.com/prize



Being in Process

Visit us at the BIOTECHNICA 2015
Hall 9, Booth F13

Eppendorf—Your workflow-oriented system supplier

As a workflow oriented provider of lab equipment, Eppendorf offers instruments, consumables, and accessories that perfectly fit your processes in the lab and thus to your daily lab work. Our comprehensive solutions are engineered with smart innovations to simplify or even eliminate cumbersome lab work.

- > Flexible solutions to prepare, handle, and analyse your samples and cells
- > System supplier of a broad portfolio for a wide variety of different applications
- > Accompanying maintenance and service contracts are available

www.eppendorf.com/workflows

Eppendorf® and the Eppendorf logo are registered trademarks of Eppendorf AG, Hamburg, Germany. All rights reserved, including graphics and images. Copyright © 2015 by Eppendorf AG.

AACR Annual Meeting

American Association
for Cancer Research

2016 • NEW ORLEANS

APRIL 16-20, 2016
ERNEST N. MORIAL
CONVENTION CENTER
NEW ORLEANS, LA

For more information visit
www.AACR.org/AACR2016

Delivering
Cures
Through
**Cancer
Science**

Join us in New Orleans

for the best cancer science and medicine meeting in the world...
the AACR Annual Meeting 2016!

You are invited to stretch your boundaries, form collaborations, attend sessions outside of your own area of expertise, and learn how to apply exciting new concepts, tools, and techniques to your own research.

Get your fill of ground-breaking cancer science each day, and then enjoy the great sounds, food, and culture that is New Orleans.

If you can only attend one cancer science meeting this year, the AACR's Annual Meeting is it!

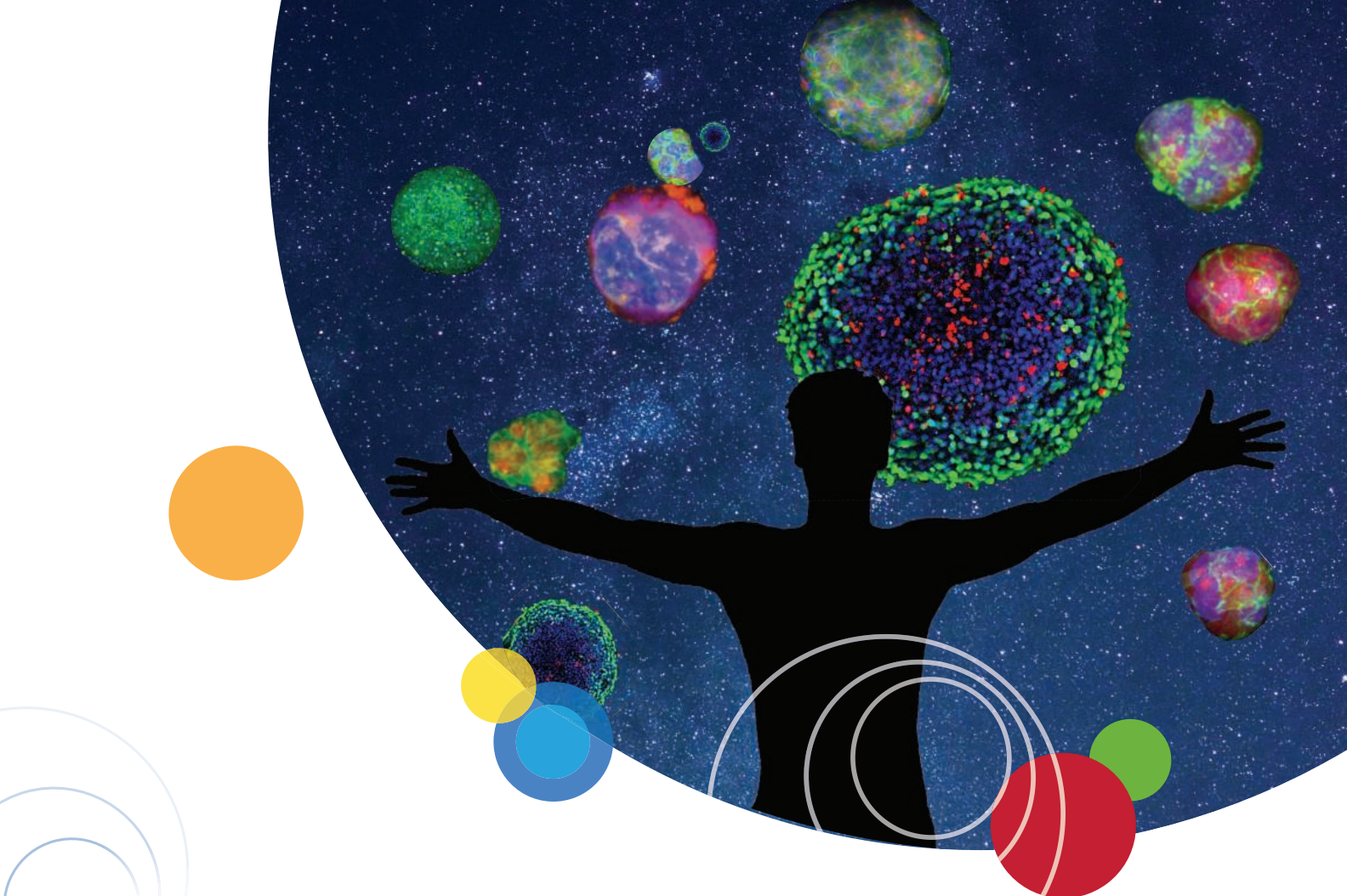
Submit your abstract by **December 1, 2015!**

Be sure to register early to take advantage of reduced rates!

Become a Member!

Join the AACR and enjoy substantially reduced registration rates, the privilege of sponsoring an abstract for the Annual Meeting and Special Conferences, funding and award opportunities, and much more.

We look forward to seeing you in New Orleans!



Explore the new dimension

The confocal system for your complex biology

Explore the complexities of biology faster, easier and with better results. With our new ImageXpress® Micro Confocal High-Content Imaging System, you can run 3D cellular assays with confocal results—at a speed you'd only expect from widefield screening. Freely select an optical geometry from crisp confocal and whole-well widefield options to get easily quantified images and statistically relevant data. Built on the reliable, field-proven ImageXpress Micro platform, the ImageXpress Micro Confocal system is our most versatile yet.

Discover more.

moleculardevices.com/complexbiology



ImageXpress® Micro Confocal system



Unleash your brilliance™

For Research Use Only. Not for use in diagnostic procedures.
© 2015 Molecular Devices, LLC. All Rights Reserved. The trademarks mentioned herein are the property of Molecular Devices, LLC or their respective owners.

How it works...

PNAS Submission & Editorial Review



Submissions are accepted from researchers all over the world.

Authors do not need to have a connection to an NAS member to publish in PNAS.

PNAS is committed to transparency in its editorial review process.

FAQs for authors explaining the review process are available at www.pnas.org/site/authors/authorfaq.xhtml.



>75%

More than 75% of published papers are submitted directly to PNAS—

not contributed by NAS members.

All articles are evaluated solely on their scientific merit by peers—

not by staff editors. Accepted papers must be of exceptional scientific importance and intelligible to a broad scientific audience.



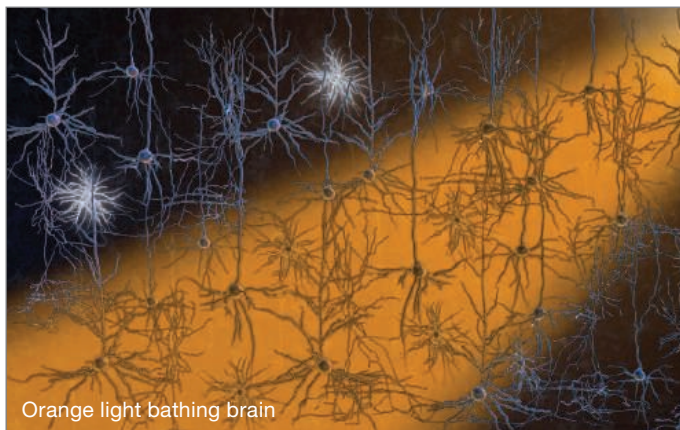
PNAS uses a three-tier review process.

An NAS member makes the final decision for every paper

- 1 Editorial Board Member**—from one of the 31 NAS disciplines. A full list of Editorial Board members and their disciplines is available at www.pnas.org/misc/masthead.xhtml.
- 2 NAS Member Editor**—professional scientists and active researchers.
- 3 Independent Peer Reviewers**—recognized subject experts.

PNAS

www.pnas.org



Orange light bathing brain

Neurophysiology charges ahead

At first glance, animal nervous systems seem to defy understanding. Even a “simple” animal such as a fly has over 100,000 neurons that can fire in billions of possible combinations, driving precise, nuanced responses to complex environmental stimuli. Nonetheless, evolution has given brains a few features that make them tantalizingly easy to study—at least in theory. **By Alan Dove**

Neurons primarily operate electrically, a fact neuroscientists have exploited for decades. Using tiny wire electrodes or capillary tubes, researchers can measure current and voltage changes in isolated cells or living animals. Simple electronic hardware can then amplify and record the signals. The brain is also relatively isolated from the body and composed of cell types found nowhere else. That means investigators can genetically engineer animals’ nervous systems with exquisite precision.

Though both the electrophysiological and genetic approaches to neuroscience have been popular for years, recent advances in both fields are now spawning a new generation of techniques. The developments range from gradual but persistent progress in electrode design to automated surgery systems and novel genetic engineering strategies. Taken together, the new methods may soon let many more researchers incorporate advanced neurophysiology analyses into their work.

Getting wired

The most common way to measure electrical changes in neurons is to stick metal electrodes into brain slices in a petri dish, or directly into the brains of living animals, methods investigators have used for over 50 years. For nearly as long, researchers like David Farb, professor of pharmacology

at **Boston University School of Medicine** in Boston, Massachusetts, have steadily expanded the capabilities of these methods. “When I first started in electrophysiology we used vacuum tube amplifiers,” says Farb. At that time, he explains that “an investigator might spend a day and get a recording from one cell, and maybe the next day nothing worked, so it was ... very slow.”

After a long series of refinements, Farb and his colleagues can now measure activity in entire brain regions while an animal engages in natural behaviors. The work is still tedious, though.

For each experiment, Farb’s lab builds a multilayered apparatus. First, they bundle four electrodes into a device they call a “tetrode,” which is about the diameter of a human hair. Companies such as **Thomas Recording** in Giessen, Germany and **Tucker-Davis Technologies** in Alachua, Florida sell prebuilt tetrodes and related equipment, but researchers without the resources to purchase this type of equipment often build their own. Farb explains that he has a small shop full of undergraduate students building the single-use tetrodes continuously, “because we can’t afford to buy them.”

Whether they buy or build the tetrodes, though, using them requires patience and sophisticated surgical skill. Two to three dozen tetrodes attach to a top section called a “head stage,” which holds a set of microdrives, mounts that hold and position the tetrodes. The microdrives contain tiny screws that the researcher advances a short distance each day, to avoid damaging the brain tissue. The process slowly moves the tetrodes into the desired brain region of a rat or other animal.

For those who can work with them, though, the multiplexed electrodes can yield troves of data. Farb’s lab has traced networks of “place cells” to show how animals navigate in different environments, findings that have helped illuminate everything from the fundamental mechanisms of learning to the pathogenesis of Alzheimer’s disease.

Unfortunately, electrode analyses in conscious animals have been traditionally restricted to nonhuman primates and occasionally rats, as mice were too small to accommodate the field’s standard equipment. Joshua Dudman, a group leader at the Howard Hughes Medical Institute’s (HHMI) **Janelia Research Campus** in Ashburn, Virginia, wanted to change that. “I actually went and talked to my late grandfather, who was a mechanical engineer who designed carburetors, [and] we kind of bounced some ideas off each other” says Dudman.

Armed with a cocktail napkin drawing and some additional advice from Robert Wurtz, a distinguished scientist at the National Institutes of Health’s (NIH) **National Eye Institute** in Bethesda, Maryland who developed similar systems for monkeys, Dudman began building a standardized system for probing mouse brains. His team used a 3D printer to create mounting brackets that hold the electrodes and restrain the animal’s head. Working with another group at Janelia Research **continued>**

Upcoming Features

Single Cell Technologies—Nov. 6 ■ Cell Sorting Technologies—Dec. 4 ■ Automated Sample Preparation—Jan. 15



Patch clamping uses a tiny microcapillary tube to track fluctuations in a single neuron's ion channels.

Campus, they then refined an older design for silicon chip-based electrode arrays. The result was the rodent in vitro/ in vivo electrophysiology targeting system (RIVETS). As the name implies, RIVETS allows a single, standardized set of components to be used for studies in live animals or brain slices. It also permits simultaneous imaging with two-photon microscopy.

Besides the 3D printed parts, RIVETS also uses off-the-shelf equipment that most neurobiology labs should already have. "One of the big issues is how do you integrate it with all these other pieces of equipment. If we want to position something precisely, we don't really want to remake micro-manipulators, since there are many excellent companies making really high-end stuff," says Dudman. A micromanipulator is a precisely machined device usually built to attach to a microscope stage, with joysticks or handles that allow a researcher to move tiny components such as electrodes into specific positions.

Scientists can download the 3D printing files and other information from Dudman's website, and use micromanipulators from companies such as **Scientifica** in East Sussex, United Kingdom, or **Sutter Instrument** in Novato, California. Dudman adds that Scientifica recently bought a nonexclusive license to sell packaged RIVETS systems for researchers who prefer a commercially supported product.

Dudman isn't the only one trying to build a better mouse cap. "The main innovation that we made in my lab was to make ultralight but still ultrastable versions of chronic electrophysiology implants," says Christopher Moore, associate professor of neuroscience at **Brown University** in Providence, Rhode Island.

The light weight was crucial in allowing the team to study mouse brains. "The revolution in genetic engineering and in vivo systems in mammals has been a huge boon, but it's all come in mice, and mice are little guys," says Moore. He explains that with the new arrays, "now you can do the physiology you used to only be able to do in rats and monkeys but in a prep that's so much better tolerated by the mice."

Plumbing the mind

Whether used in vitro or in vivo, wire electrodes generally measure electrical changes among groups of neurons. A complementary technique, patch clamping, uses a tiny microcapillary tube to track fluctuations in a single neuron's ion channels.

For those new to the patch clamp technique, the first step should be a review of basic electronics. "Doing patch clamp work, ultimately you're treating a neuron like an electrical device, and understanding how electrical devices work and how those principles apply within a biological context is, I think, of the utmost importance," says Michael Markham, assistant professor of biology at the **University of Oklahoma** in Norman, Oklahoma. Markham maintains a free software package called "Electrophysiology of the Neuron" to aid that process.

Among other electrical challenges, Markham points out that the further a capillary goes into an animal's brain, the higher its inherent resistance and capacitance. That means deeper probes have less bandwidth than shallower ones.

Inserting capillaries into a live animal's brain for patch clamp experiments also entails a tricky operation, requiring exceptional care and surgical skill. Edward Boyden, leader of the synthetic neurobiology group at the **Massachusetts Institute of Technology (MIT)** Media Lab in Cambridge, Massachusetts, decided to turn the job over to a robot. "We discovered an algorithm that ... allows you to patch clamp neurons, and also allows for automation in a computer. It doesn't require human intuition," says Boyden.

Boyden's group uses the algorithm to drive a robot, which slowly inserts a patch clamp capillary into the desired region of an animal's brain until it detects an increase in electrical resistance, indicating that the capillary has encountered a neuron. The robot can then attach the capillary, and not only measure ion channel activation in the neuron but also extract cytoplasmic material for biochemical analysis.

After publishing the technique, the researchers also created a company, **Neuromatic Devices**, which now sells automated patch clamp equipment to make it easier for others to duplicate the technique. Boyden anticipates automating other aspects of neurophysiology in live animals, too. "What we think we've stumbled across is an area that one might call 'in vivo robotics,' where we could deploy a wide variety of technologies to automate and make turnkey these kinds of processes," he says.

Meanwhile, Moore's team is trying to make wire electrode physiology more accessible. Jakob Voigts, a graduate student in Moore's lab, built a collection of standard electrophysiology equipment available under an open source license. The project, called **Open Ephys**, allows researchers to assemble a sophisticated set of neurophysiology gear from a few thousand dollars' worth of parts. An online support community helps debug any problems that arise.

Bright ideas

Besides making it easier to measure neuronal activity, Boyden also helped pioneer new ways to activate neurons experimentally. The innovation grew out of his frustration with traditional pharmacological and electrical stimulation methods, neither of which is especially precise. "You couldn't



Featured Participants

**Boston University
School of Medicine**
www.bumc.bu.edu

Brown University
www.brown.edu

**Central Michigan
University**
www.cmich.edu

**HHMI Janelia Research
Campus**
www.janelia.org

**Massachusetts Institute
of Technology**
www.mit.edu

**NIH National Eye
Institute**
www.nei.nih.gov

Neuromatic Devices
www.neuromaticdevices.com

Open Ephys
www.open-ephys.org

Scientifica
www.scientifica.uk.com

Sutter Instrument
www.sutter.com

Thomas Recording
www.thomasrecording.com

Tucker Davis Technologies
www.tdt.com

University of Oklahoma
www.ou.edu

just activate a specific set of neurons,” says Boyden.

While searching the literature, he and his colleagues found a tantalizing lead. “We were brainstorming in the Spring of 2000, and we stumbled across some papers on so-called microbial opsins,” Boyden explains. The team was especially intrigued by photosensitive opsins, which open ion channels in the microbial cell membrane in response to light. When the investigators genetically modified animal neurons to express one of these proteins, the neurons started to fire in response to pulses of light. Since then, Boyden’s group and others have steadily improved the technology, called “optogenetics,” which is now a standard tool for probing neurophysiology in live animals as well as brain slices.

The latest developments in optogenetics include channel proteins sensitive to red light, which can penetrate deeper into brain tissue, and a photosensitive chloride channel that can inhibit neurons in response to light instead of stimulating them. Clever mouse genetic techniques also allow scientists to restrict the photosensitive channels’ expression to very specific brain regions. Combining the techniques, researchers can now shine light through an intact mouse skull and either activate or inhibit target neuronal populations with exquisite precision. “The tools have really started to get very routine in usage,” says Boyden.

Optical tricks can extend the optogenetic possibilities even further. For example, researchers can now project multiphoton holograms into animal brains to activate single neurons. “You can really try to dial in the complex three-dimensional configuration of neural coding, and that would then allow for very specific hypotheses of neural codes to be tested,” Boyden explains.

Optogenetics also combines well with electrophysiology. One major challenge in traditional wire-electrode placement has been figuring out where the electrode is in the animal’s brain. With optogenetics, investigators can now be certain.

“You can tell pretty well when you flash the light whether the neuron you’ve isolated with your metal electrode is [the right type],” says Brown’s Moore.

Moore’s lab has even figured out how to combine optogenetics with another favorite tool of neuroscientists: functional MRI (fMRI). By revealing changes in blood flow throughout the brain, fMRI gives an overview of the response to a stimulus. Optogenetics can now provide very precise stimuli. “It allows you to stimulate a specific cell type in a specific spot, let’s say in the hand representation of the neocortex; then you can use fMRI to say, ‘Where else in the brain is activated when I stimulate just that cell type in just that spot?’” says Moore, adding, “That’s an amazingly powerful thing to know.”

Despite its advantages, optogenetics still has some drawbacks. For the most accurate activation of cells, researchers still have to insert fiber optics into a mouse’s brain through the skull. Ute Hochgeschwender, associate professor of neuroscience at **Central Michigan University** in Mount Pleasant, Michigan, is working on a different strategy. “A way to get around that would be if instead of using a physical fiber, if you can use basically a light source which is also biological,” says Hochgeschwender.

Hochgeschwender and her colleagues fused luciferase proteins from fireflies with light-sensitive opsins and fluorescent protein domains. The resulting luminopsins open their ion channels in response to light, emit light when provided with the appropriate luciferase substrate, and glow when examined under a fluorescent microscope. Researchers can activate the targeted neurons either by shining light on them or giving the animal an injection of the luciferase substrate, while the fluorescent tag reveals which cells are expressing the protein. “Any opsin, any optogenetic element developed, we can give the additional dimension of being chemically accessible,” says Hochgeschwender.

In the latest iteration of the technology, Moore and Hochgeschwender are collaborating to build a system using luciferase enzymes that are also calcium sensitive, requiring both the substrate and a calcium ion to illuminate. Firing causes an influx of calcium into the neuronal cytoplasm, so “you can think about a system where actually neuronal activity turns on the light in the presence of substrate,” Hochgeschwender explains.

Researchers can then identify the luminescent cells, even through an intact skull. Hochgeschwender envisions a strategy where a scientist could determine which mice were expressing the protein in the right cells before performing an experiment, eliminating those with inappropriate expression patterns and substantially reducing the number of animals required for an experiment.

Whether they use wire electrodes or bioluminescent enzymes, though, scientists working with the new generation of techniques are palpably excited about the deluge of recent advances. As Farb says, “Now I feel like this kid, where we’re getting results and I’m just like ‘Wow, I can’t believe this, I never thought of this, I never imagined it.’”

Alan Dove is a science writer and editor based in Massachusetts.

DOI: 10.1126/science.opms.p1500098

Big Image Data Solution

New microscopy technologies, such as light sheet fluorescence microscopy (LSFM) or clearing methods, allow the imaging of large samples at high resolution or high frame rates. Handling, processing, and analyzing these multiterabyte data sets has become increasingly difficult for scientists in fields such as developmental biology and neuroscience. New tools are needed to overcome these challenges. Therefore, Zeiss has teamed up with Arivis AG to offer complete solutions from initial image acquisition to final results. Arivis Vision4D is a modular software for handling multidimensional (3D+) images of nearly unlimited size. Users can easily import images generated with microscope systems such as Zeiss Lightsheet Z.1, and comfortably stitch and align single images into large comprehensive image stacks. This enables easy assessment and efficient analysis of high resolution brain-mapping experiments or long-term observation of developmental processes in embryos, for example. Zeiss is offering an integrated package worldwide, consisting of Arivis Vision4D software and certified high-performance computer hardware.

Zeiss

For info: +49-3641-64-3949
www.zeiss.com

Wireless Transmitter/Receiver

The MOVE wireless system is a solution that replaces the existing cables connecting the electrodes and amplifier in electroencephalography (EEG) systems with wireless-based communication. This solution allows the subject to move freely and makes it very suitable for use with a brain-computer interface, neurofeedback, and motor learning. Paradigms that cannot be used with standard cabled EEG systems can now be incorporated into day-to-day research, and normal experiments will become more convenient for the participants. The small, lightweight transmitter box and receiver can be used with virtually any existing amplifier/electrode combination. The transmitter amplifies and digitizes the incoming raw analog signal and sends it to the receiver, where the digital data is converted back to analog. If the data is not received properly, the receiver unit will send a transistor-transistor logic (TTL) pulse marker to the amplifier, and a marker is sent when stable and reliable data reception resumes.

Brain Vision

For info: 877-334-4674
www.brainvision.com



PET/SPECT/CT System

A proprietary gridless positron emission tomography (PET) detector architecture makes the Albira Si the most advanced preclinical PET system on the market. It delivers submillimeter spatial resolution across the full radial field of view (FOV), increasing the high-resolution FOV by an order of magnitude, as compared to traditional PET systems. This capability, combined with high count-rate performance and high PET sensitivity, makes Albira Si the preferred system for dynamic and gated PET in vivo studies. The Albira Si offers all the benefits of integration with single-photon emission tomography (SPECT) and computed tomography (CT). The microCT provides anatomical reference images and attenuation corrections for PET and SPECT imaging. In addition, the Albira Si is compatible with Bruker's multimodal animal beds for cross-platform magnetic resonance imaging (MRI) and optical molecular imaging. Also, the new BioSpec 3T PET/MRI further combines the Albira Si's PET detector technology with superior MRI soft-tissue contrast.

Bruker

For info: +49-(0)-721-5161-6500
www.bruker.com

FRAP Imaging Platform

Enabling the easy addition of photomanipulation techniques to imaging platforms, Olympus has launched a new cellFRAP deck system for the popular "open source concept" IX83 and IX73 microscopes. cellFRAP is designed with researchers in mind, providing highly accurate and flexible live-cell photomanipulation with various evaluation options for data presentation needs. Unlike conventional, widefield-based fluorescence recovery after photobleaching (FRAP) systems, Olympus' cellFRAP employs a diffraction-limited laser spot for high-intensity and precise positioning of the bleaching region across the full field of view (FOV). This ensures that photomanipulation reaches every point in the FOV without needing to move the sample. The system's excellent spot quality allows full flexibility in the position and shape of the bleaching region, and enables control of the bleaching area with extreme accuracy. Driven by the Olympus real-time controller, the cellFRAP system achieves an unrivaled short switchover time of only 200 μ s between bleach and postbleach acquisition, ensuring detection of the most valuable initial sample response after stimulation.

Olympus

For info: +49-(0)-40-23773-5913
www.olympus-lifescience.com

Neurophysiological Data Analysis Package

NeuroExplorer v5.017 is now available with significant improvements/additions, including enabling maximum benefit when working with and saving neural data files greater than 2 GB, and a new "Find Oscillations" analysis, which identifies episodes of oscillatory activity in the specified frequency band in recorded analog signals. NeuroExplorer is a neurophysiological data analysis package that supports sophisticated analyses and generates a professional presentation of

the results. Researchers require the ability to analyze, manipulate, and save such data in huge files. NeuroExplorer launched its new .NEX5 file format last year to meet the industry's growing data demands. This most recent release, v5.017, leverages the increased flexibility of the .NEX5 format not only to analyze and save files greater than 2 GB, but also to save unlimited metadata for the whole file and for every file variable in JavaScript Object Notation (JSON) format.

Plexon

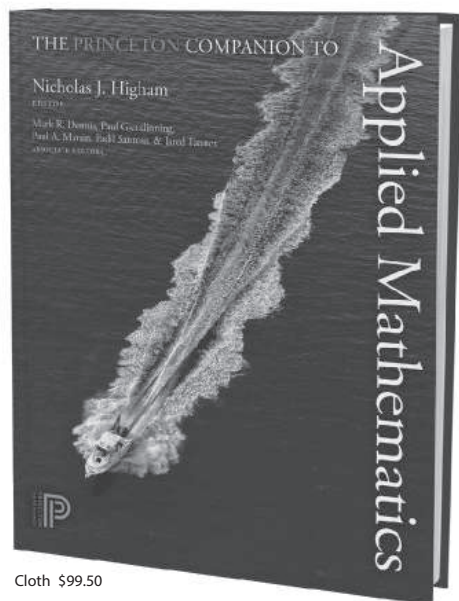
For info: 214-369-4957
www.plexon.com

Electronically submit your new product description or product literature information! Go to www.sciencemag.org/products/newproducts.dtl for more information.

Newly offered instrumentation, apparatus, and laboratory materials of interest to researchers in all disciplines in academic, industrial, and governmental organizations are featured in this space. Emphasis is given to purpose, chief characteristics, and availability of products and materials. Endorsement by Science or AAAS of any products or materials mentioned is not implied. Additional information may be obtained from the manufacturer or supplier.

“Monumental and comprehensive. . . . An instant classic.”

—Steven Strogatz, Cornell University



Cloth \$99.50

The Princeton Companion to Applied Mathematics

Edited by Nicholas J. Higham

*Mark R. Dennis, Paul Glendinning, Paul A. Martin, Fadil Santosa
& Jared Tanner, associate editors*

“The treasures [in the *Princeton Companion to Applied Mathematics*] go on and on. . . . PCAM shows us that applied mathematics is vast and it is confident. We see here a discipline engaged in every corner of the human enterprise, from cosmology to the spread of infectious diseases, from pattern formation to aircraft design, from financial portfolio optimization to the ranking of movie preferences.” —**Lloyd N. Trefethen, *SIAM Review***

- Features nearly 200 entries organized thematically and written by an international team of distinguished contributors
- Presents the major ideas and branches of applied mathematics in a clear and accessible way
- Explains important mathematical concepts, methods, equations, and applications
- Explores the connections between applied mathematics and other disciplines



Also available:

The Princeton Companion to Mathematics

Edited by Timothy Gowers

June Barrow-Green and Imre Leader, associate editors

Cloth \$99.50



PRINCETON UNIVERSITY PRESS

press.princeton.edu

AAAS Travels



MADAGASCAR

August 20–September 4, 2016
See the Annular Solar Eclipse Sept. 1, 2016!



Explore the unique heritage of this enchanting land including the Annular Solar Eclipse. Madagascar is home to thousands of unique species including lemurs and reptiles, flowering plants, palms, and many birds. This is an exceptional opportunity to become acquainted with Madagascar and experience the Annular Solar Eclipse in 2016! \$4,995 pp + air

For a detailed brochure, call (800) 252-4910
All prices are per person twin share + air



BETCHART EXPEDITIONS INC.
17050 Montebello Rd, Cupertino, CA 95014
Email: AAASInfo@betchartexpeditions.com
www.betchartexpeditions.com

ELECTROPHYSIOLOGY SYSTEMS

Bundled Configurations

NEW



Sutter Instrument is now offering several systems or “Big Kits” that include dual manipulators and either manipulator stands and scope translator or a large moving stage.

FEATURES

- Discounted pricing offers savings and value
- Classic electrophysiology design – single system configuration
- 2 manipulators with each bundled system
- Easy toggle selection of active component
- Single ROE controls manipulators and components
- Manipulator, stage and translator features retained
- Compatible with a wide range of imaging software platforms

SUTTER INSTRUMENT

PHONE: 415.883.0128 | FAX: 415.883.0572
EMAIL: INFO@SUTTER.COM | WWW.SUTTER.COM

The 2016 Keystone Symposia Neurobiology Conferences

Biology of Down Syndrome: Impacts Across the Biomedical Spectrum

Scientific Organizers: Victor Tybulewicz, Elizabeth Fisher, Thomas Blumenthal and Jeanne Lawrence

January 24–27, 2016

Hilton Santa Fe Historic Plaza Hotel | Santa Fe, New Mexico | USA

www.keystonesymposia.org/16A4

Deadlines: Discounted Abstract/Scholarship – Sep 24, 2015; Abstract – Oct 26, 2015; Discounted Registration – Nov 20, 2015

Traumatic Brain Injury: Clinical, Pathological and Translational Mechanisms

Scientific Organizers: Ann C. McKee, Ramon Diaz-Arrastia and Lee E. Goldstein

joint with **Axons: From Cell Biology to Pathology**

Scientific Organizers: Giampietro Schiavo, Bruce D. Carter and Rejji Kuruvilla

January 24–27, 2016

Eldorado Hotel & Spa | Santa Fe, New Mexico | USA

www.keystonesymposia.org/16J3 | www.keystonesymposia.org/16J4

Deadlines: Discounted Abstract/Scholarship – Sep 24, 2015; Abstract – Oct 27, 2015; Discounted Registration – Nov 23, 2015

Neurological Disorders of Intracellular Trafficking

Scientific Organizers: Dennis Drayna and Bettina Winckler

January 31–February 4, 2016

Keystone Resort | Keystone, Colorado | USA

www.keystonesymposia.org/16A7

Deadlines: Discounted Abstract/Scholarship – Sep 30, 2015; Abstract – Nov 2, 2015; Discounted Registration – Dec 1, 2015

State of the Brain

Scientific Organizers: Terrence J. Sejnowski and Sten Grillner

May 22–26, 2016

Alpbach Congress Centrum | Alpbach | Austria

www.keystonesymposia.org/16R1

Deadlines: Discounted Abstract/Scholarship – Jan 21, 2016; Abstract – Feb 23, 2016; Discounted Registration – Mar 22, 2016

Common Mechanisms of Neurodegeneration

Scientific Organizers: Bradley T. Hyman, Adriano M. Aguzzi and Ricardo E. Dolmetsch

joint with **Microglia in the Brain**

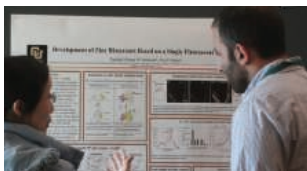
Scientific Organizers: Beth Stevens and Richard M. Ransohoff

June 12–16, 2016

Keystone Resort | Keystone, Colorado | USA

www.keystonesymposia.org/16Z3 | www.keystonesymposia.org/16Z4

Deadlines: Discounted Abstract/Scholarship – Feb 11, 2016; Abstract – Mar 10, 2016; Discounted Registration – Apr 12, 2016



Submit an abstract to participate fully in the conference via poster presentation and possible selection for a short talk. Scholarships are available for graduate students and postdoctoral fellows. For full details on these and other related conferences, please visit www.keystonesymposia.org/neuro.

KEYSTONE SYMPOSIATM
on Molecular and Cellular Biology
Accelerating Life Science Discovery

PO Box 1630 | Silverthorne, CO 80498 | 800-253-0685 | 970-262-1230

WHY WORRY ABOUT CROSS-REACTIVITY?

Introducing Superclonal secondary antibodies,
a breakthrough technology designed to
eliminate cross-reactivity

The results are in, and the images are stunning. Our completely new category of secondary antibodies uses recombinant technology to offer accurate and precise detection of primary antibodies for bright, clear images. Thermo Scientific™ Superclonal™ Secondary Antibodies — a precisely better antibody.

See the difference at thermofisher.com/superclonal

ThermoFisher
SCIENTIFIC



There's only one **Science**

Science Careers Advertising

For full advertising details, go to ScienceCareers.org and click For Employers, or call one of our representatives.

Tracy Holmes

Worldwide Associate Director
Science Careers
Phone: +44 (0) 1223 326525

THE AMERICAS

E-mail: advertise@sciencecareers.org

Fax: +1 (202) 289 6742

Tina Burks

Phone: +1 (202) 326 6577

Nancy Toema

Phone: +1 (202) 326 6578

Online Job Posting Questions

Phone: +1 (202) 312 6375

EUROPE / INDIA / AUSTRALIA / NEW ZEALAND / REST OF WORLD

E-mail: ads@science-int.co.uk

Fax: +44 (0) 1223 326532

Sarah Lelarge

Phone: +44 (0) 1223 326527

Kelly Grace

Phone: +44 (0) 1223 326528

Online Job Posting Questions

Phone: +44 (0) 1223 326528

JAPAN

Katsuyoshi Fukamizu (Tokyo)

E-mail: kfukamizu@aaas.org

Phone: +81 3 3219 5777

Hiroyuki Mashiki (Kyoto)

E-mail: hmashiki@aaas.org

Phone: +81 75 823 1109

CHINA / KOREA / SINGAPORE / TAIWAN / THAILAND

Ruolei Wu

Phone: +86 186 0082 9345

E-mail: rwu@aaas.org

All ads submitted for publication must comply with applicable U.S. and non-U.S. laws. *Science* reserves the right to refuse any advertisement at its sole discretion for any reason, including without limitation for offensive language or inappropriate content, and all advertising is subject to publisher approval. *Science* encourages our readers to alert us to any ads that they feel may be discriminatory or offensive.

ScienceCareers

FROM THE JOURNAL SCIENCE AAAS

ScienceCareers.org

2015 Annual Top Employers in Biotech & Pharma



Special Career Feature: October 30, 2015

Reserve your ad by October 13 to guarantee space.

Ads accepted until October 26 if space is still available.

For recruitment in science, there's only one **Science**

WHO IS NO. 1 THIS YEAR?

Science publishes the results of its 14th annual Top Employers Survey on October 30. *Science* has a long history of providing a forum for scientists to express their opinions about the biotech and pharma industry.

Recruit or brand your organization and reach both ACTIVE and PASSIVE job seekers. Here's how:

1. Scientists in the biotech/pharma community eagerly anticipate the results of this survey every year. By announcing your openings in this special feature, your reach goes beyond active job seekers to those involved in the field, targeting elusive passive job seekers at the same time.
2. Your association with this issue tells prospective recruits that you are among the best. You have a unique opportunity to brand your company as a leader. Reach the scientists that your competitors are reaching and promote your advantages.

**Start building your pipeline
today with *Science*.**



SCIENCECAREERS.ORG

**Science
Careers**
AAAS

To book your ad: advertise@sciencecareers.org

The Americas
202-326-6582

Japan
+81-3-3219-5777

Europe/RoW
+44(0)1223-326500

China/Korea/Singapore/Taiwan
+86-186-0082-9345



Mountain in Anhui Province

Science and technology in Central China

In central China, a science renaissance is happening. Away from the hectic coastal cities, scientists and entrepreneurs have found new opportunities in ancient cities, such as Xi'an, Zhengzhou, and Wuhan. This region also receives abundant funding for research and education, but the cost of living is lower than in the big cities. In recent years, universities in central China have been producing high-quality research and forging collaborations in key disciplines, such as hydraulic engineering, aerospace technology, and translational medicine. New urban centers, built using sustainable designs and high-tech infrastructure, are popping up and attracting investments from Chinese as well as global firms. As a result, this region is becoming a new hub for researchers and tech companies to launch exciting projects in science and engineering. **By Wayne Peng**

Central China is less known to the West than the major coastal metropolises like Beijing and Shanghai; however, this has not always been the case. The entry point for Western goods and ideas shifted from inland China to the coast in the 12th century. Prior to this, the capitals of successive Chinese dynasties were to be found inland and were considered by many to be amongst the largest cities in the world. At the peak of the Tang dynasty, around 750 CE, more than a million people lived in Chang'an (present day Xi'an)—where trade with Europe and central Asia began via the Silk Road.

Today, as the coastal cities approach developmental saturation, Chinese policy makers, scientists, and entrepreneurs are taking a fresh look at the inland region's rich cultural and natural resources. Central China is a loosely defined geographical area that usually includes the provinces of Shanxi, Shaanxi, Henan, and Hubei, but can also refer to the Anhui, Hunan, and Jiangxi provinces. At the northern end, ancient cities dot the banks of the Yellow River and its major tributaries—a region that is considered the cradle of Chinese

civilization. The Yangtze River runs along the southern border, serving as an artery for transportation and providing hydraulic resources.

Here, we highlight the region's rise in scientific research and education, as well as the push to recruit more talent and attract technology investments. The examples highlighted here showcase the renaissance of central China and the new opportunities in this "old" region.

Strengthening international collaborations

Zhou Chuangbing became president of Nanchang University in 2013 after spearheading science and technology affairs at Wuhan University in Hubei province for more than a decade. As a leading expert on rock mechanics and hydraulic engineering in China, Zhou has dedicated his career to improving the safety and environmental sustainability of hydraulic engineering projects. "China leads the world in many hydraulic engineering achievements," says Zhou. Perhaps the best known example is the Three Gorges Project, the largest hydropower station in the world, which is only a few hundred miles west of Nanchang on the Yangtze River.

Zhou's engineering philosophy is "safety always comes first." He adds, "We need to protect the ecological habitats at the site of any major hydraulic engineering project." Safety and sustainability are relatively new concepts in the booming Chinese economy. These concepts exemplify the pioneering, future-driven vision that Zhou has brought with him to Nanchang University, which is famous in China for research on the science and manufacturing of light-emitting diodes, food science and engineering, and medicine.

Desiring to build upon Nanchang's strengths, Zhou sees a need to internationalize the university's scientific research and education. He explains that central China's location can sometimes hinder the recruitment of top talent directly from abroad; however, he encourages young faculty members to seek opportunities to collaborate with researchers outside of China and to spend time overseas to learn how critical thinking is carried out. Zhou hopes that this type of exposure will improve Nanchang's scientists' abilities to formulate quality research questions. "When [our faculty members] come back after a period of training abroad, they become much better scientists," says Zhou. With a strong push for international collaboration, Zhou hopes to elevate the academic profile of Nanchang University by helping its existing students and faculty members succeed in education and research.

Facilitating large-scale projects

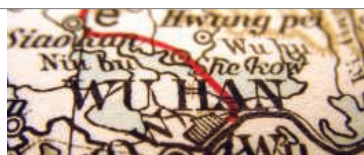
Further up the Yangtze River, in Wuhan, **Lu Youming** is building a new brain research institute at Huazhong University of Science and Technology (HUST) Tongji Medical College. When Lu was first nominated for the Chinese government's highly selective Thousand Talents Program in 2008, he was running a lab at Louisiana State University Health Sciences Center in New Orleans. By that time, Lu had already established himself as a key contributor to the field of neuroscience, particularly in glutamate receptor research; however, he wanted to make a greater impact and thought there were two ways to do so: find something that will change clinical practice **continued >**

Upcoming Features

Faculty—October 9 ■ Top Employers Survey—October 30 ■ Cell Biology Careers—December 4



Building at Huazhong University of Science and Technology



Lu Youming

or make a discovery that is important enough to alter the textbooks.

Lu's research on death-associated protein kinase 1 (DAK1) had already been making strides toward the clinic for stroke management. He wanted to further investigate some fundamental scientific questions, but the work would require large-scale 'omics studies. It's a big challenge to fund such endeavors in the United States, Lu points out, adding that "even five R01 research grants cannot support the functional genomic work necessary to answer the key questions in neuroscience, such as the specific function of a gene expressed in individual brain cells." Science funding is different in China, Lu explains. "What takes a nationwide collaboration to accomplish in the United States can be supported by a handful of projects funded by the central government or the provincial authorities in the region."

In 2011, after touring a dozen major universities around China, Lu settled down at HUST and began building a brain research center. Instead of joining the crowded research hubs in Beijing or Shanghai, Lu believed he could make a larger difference by tapping into the local resources in Wuhan at HUST. Lu's team has already generated 16,000 knockout mouse lines in a systematic attempt to dissect out the function of genes expressed in the brain, and a new research building is already underway (scheduled for completion in 2016) to house this vast resource. Lu has also secured 170 million yuan (US\$26 million) in funding to recruit top research talent, mainly through the government's Thousand Young Talents Program. "In two years," predicts Lu, "there will be more Thousand Young Talents Program scholars in Wuhan than in Shanghai."

Funding and resources are not an issue for doing scientific research in China. The real challenge is "to be able to identify and study important questions [that are at the forefront] of science," says Lu. For young scientists starting a career in China, Lu has two important pieces of advice: be willing to change and improve the research environment and do not single-mindedly focus on publishing papers. He encourages young scientists at his institute to spend more time on innovative thinking and to avoid chasing hot topics or doing incremental experiments. For scientists looking to relocate to China, Lu suggests visiting prospective institutes multiple times to really understand the environment and the support offered, because every institute in China has a unique culture.

Finding coastal connections

By building connections with the more established coastal

region, Xi'an-based Northwestern Polytechnical University (NPU) hopes to boost its status via an expansion at Research & Development Institute in Shenzhen (R&DIS) in Guangdong Province under the guidance of Dean **Shang Peng**.

The economic reforms of the 1980s in China led to conditions that limited growth in the technology sector in "special economy zones" like Shenzhen. Though private investments and the entrepreneurial spirit were plentiful in Shenzhen, its economy was almost entirely based on manufactured exports, with little focus on technology and innovation. To ensure the city's long-term success, the Shenzhen municipal government began inviting universities to bring technology, higher-education curricula, and scholars to the area. In 1999, NPU and other major Chinese universities began setting up satellite campuses, such as R&DIS, in Shenzhen. NPU has long been a leader in aerospace science and engineering education in China and thus made these fields the focus of R&DIS. In return, NPU gained access to venture capital-backed tech transfer resources and the entrepreneurial know-how in Shenzhen.

Last year, NPU received an empty plot of land within a designated high-tech zone, prompting the university to expand R&DIS into a full-fledged research and development center. Shang is now tasked with the major expansion. He already has a track record of success after having built the School of Life Science and a key laboratory at the NPU from scratch. With a background in biomedical engineering and pharmacology, Shang joined NPU 10 years ago to construct the school at a university that specialized mainly in airplanes and rockets. Over the past decade, research in extreme-environment biology, gravitational biology, and aerospace medicine, such as bone metabolism during space flight, has flourished under Shang's guidance.

At the newly expanded R&DIS, "apart from focus on the research and development of unmanned aerial vehicles for civil use, human health research will be another new major focus," explains Shang. NPU will build a 28-story research facility with 50,000 square meters of floor space on the new plot. Establishing this coastal connection with Shenzhen is "good for NPU in terms of recruitment, technology transfer, industrialization, and internationalization," says Shang, but it is mutually beneficial in that central China in turn "helps recruit high-level talent and supplies educational resources to the coast." In addition, he sees new concepts—such as entrepreneurship, teamwork, resilience to failure, and service-oriented operations—and access to venture capital flowing back to Xi'an, which further elevates the academic profile of NPU.

Building a "sponge city"

Xianyang, the ancient capital of the Qin dynasty, is a small city west of Xi'an. Against this historical backdrop, contemporary urban planning concepts are being used to build five new cities between Xi'an and Xianyang—collectively called the "Xixian New Area"—to accommodate the growing population and attract technology investments to the region. The arid climate and archaeological sites present unique challenges for new development in this area.

One such place, the Fengxi New City, is designed as a 143-square-kilometer high-tech park and an urban service center. "We have taken the latest urban development concepts to plan Fengxi New City from scratch," says **Kang Zhenfeng**, deputy director of the managing committee for Fengxi New City. The city plan is plotted with parks and green belts at the center to avoid the type of concentric sprawl **continued>**



暨南大學
JINAN UNIVERSITY

百年暨大，誠聘英才
攜手暨大，共創未來

Associate Professor/ Professor Jinan University, Guangzhou, China

Job description

The Guangdong-Hongkong-Macau Institute of CNS regeneration (GHMICR) at Jinan University, Guangzhou, China (<http://ghmicr.jnu.edu.cn>) is recruiting young leading neuroscientists who use innovative approaches to investigate problems from molecular and cellular level to systems in neuroscience related to neural protection and regeneration. Successful candidates will be expected to develop thriving, well-funded research programs and to contribute to graduate education. Positions will be for a three-year period with extensions to long-term positions pending performance. Jinan University will provide attractive annual salary (300 to 1500 thousand RMB), start-up fund, housing allowance and others based on your records. The general information can be found at the website (Chinese): <http://personal.jnu.edu.cn/>.

Qualifications

Successful candidates must have a PhD degree or equivalent and display high potential based on publications. The successful candidates are expected to develop projects independently.

Application

The recruitment is available for a long term until enough candidates are selected. Please send electronic application including a statement of interest, full CV, a brief description of research goals and accomplishments, a summary of current and past grant support, names of 3 references, and representative reprints of 3~4 original reports to:

Prof. Libing Zhou, Associate director
GHM Institute of CNS Regeneration, Jinan University,
Huangpu Avenue W. 601, Guangzhou, P. R. China, 510632
Email: tlibingzh@jnu.edu.cn, Tel: (+86) 20-85228362

High-level Talents Online Job Fair 2015



The second action of 2015

will be held on October 18th, from 7AM to 24PM
in Shanghai

Recruitment requirements:

Scholars and doctors with working position and
graduating doctors domestic and overseas

Please send your curriculum vitae to:

acabridge@gmail.com
chisa.add@gmail.com
chisa_yang@163.com

For more information, please check the following web sites

<http://www.edu.cn/cv>
http://www.chisa.edu.cn/zt/yczt/network_video/index.html



南京工業大學
NANJING UNIVERSITY
OF TECHNOLOGY

海外領軍人才招聘

Overseas Talents Recruitment

Nanjing Tech University, with a history of more than one hundred years, is a multidisciplinary university with a particular strength in engineering.

Aiming at excellence and innovation, Nanjing Tech University is set to become a first-class research university with a global vision. We are now seeking outstanding academic and research leaders in the following and related fields: Basic disciplines from within the Physical Sciences; Cutting edge disciplines from within the Life Sciences; Applied disciplines from within the Information Sciences; Humanities represented by Management Science.

Applicants should have a Ph.D. with at least 3-years research experience from leading universities or institutes. Candidates should demonstrate an internationally recognized research record and outstanding achievements. Successful candidates are expected to develop vigorous research programs and lead an independent research team. Successful candidates will be provided with a competitive relocation fee and salary package, generous start-up funds and spacious laboratories.

Interested candidates should visit <http://rczyb.njtech.edu.cn> for application details.

Phone: Ms. Wang +86-25-58139148.

E-mail: job@njtech.edu.cn



上海交通大學
SHANGHAI JIAO TONG UNIVERSITY

Multiple Faculty Positions in Ultrafast Sciences / Electron Microscopy Shanghai Jiao Tong University, Shanghai, China

Shanghai Jiao Tong University is establishing a world-class research Center for Ultrafast Sciences in physics, chemistry, materials and biology with integration of both experimental and theoretical efforts. The Center will provide state-of-the-art ultrafast laser spectroscopy, electron diffraction and microscopy, and excellent multi-disciplinary environment for cutting-edge research.

The Center invites applications for a number of open-rank faculty positions to begin in the fall of 2016 (or earlier). Applicants should have a Ph.D. degree, preferably with postdoctoral experience in a closely related field, and a strong record of research accomplishments. Previous experience in electron microscopy and ultrafast sciences is favorable. The successful candidates will be expected to develop world-class research programs and teach classes at both undergraduate and graduate levels. The University will provide attractive annual salary, start-up fund, housing allowance and other benefits.

All applicants should send a cover letter, a curriculum vitae with a publication list, a research proposal (3-4 pages) and a statement of teaching interest in a single pdf file by Dec. 01, 2015 to Xiaoyan Li, Shanghai Jiao Tong University, Shanghai 200240, China through e-mail to: ultrafast@sjtu.edu.cn. Please also arrange three reference letters to be sent directly to the above e-mail address. Applications after the deadline could be reviewed until the positions are filled.

<http://join.sjtu.edu.cn/>

“We have designed a ‘sponge city’ [Fengxi New City] that uniquely fits the climate of northern China, with an underground reservoir and an extensive network of collection ducts to save rainwater for the dry season.”
– Kang Zhenfeng



Nanchang City



Shanxi Lanterns

Featured Participants

Fengxi New City
www.fcfx.gov.cn/fxzw/
[Chinese]

Huazhong University of Science and Technology
english.hust.edu.cn

Nanchang University
www.ncu.edu.cn/language/english.html

Research & Development Institute in Shenzhen, Northwestern Polytechnical University
www.nwpu.edu.cn [Chinese]

Tongji Hospital
english.tjh.com.cn

Zhengzhou National High-Tech Incubator
www.zzjkq.gov.cn [Chinese]

found in Beijing and many other Chinese cities that are plagued by traffic and air pollution. Other innovative concepts have been adapted to facilitate ecological preservation, green-energy use, and rainwater conservation. The latter is particularly important in northern China because of the uneven rainfall between the rainy and dry seasons. “We have designed a ‘sponge city’ that uniquely fits the climate of northern China, with an underground reservoir and an extensive network of collection ducts to save rainwater for the dry season,” says Kang. With a high-tech city in mind, the planners of Fengxi New City have laid a network of conduits for electrical and data cables underneath the roads, eliminating the need to dig in the future.

“Fengxi New City strives to lead in China in terms of urban planning,” says Kang, and the innovations have already created a very attractive environment for the type of high-tech companies intended for the area, such as Microsoft and China Telecom. Fengxi is offering comprehensive packages to attract more tech companies, especially those in the areas of cloud computing and big data. It also partners with universities in nearby Xi’an to further strengthen the pool of highly skilled labor in information technology. “Sponge city” is not just a literal design that balances rainfall between seasons, but also a vivid metaphor for the area’s ability to absorb investments and talent from other regions of China and all over the world.

Incubating high-tech startups

Technology recruitment is also taking place in other ancient cities within central China. In Zhengzhou, **Ma Gencan**, director of the National High-Tech Incubator in the Zhengzhou National Economic and Technological Development Zone (ZNETDZ), has set his 2015 priority as talent recruitment. Despite ZNETDZ’s success, “the challenge in front of us is a shortage of talent and resources for science education,” he says.

Since its inception in 1993, ZNETDZ has successfully

established the city as a pivotal distribution hub for goods to all major Chinese markets by taking advantage of its central location and extensive network of railroads, highways, and airlines that all converge in the area. In 2013, a cargo train began running from Zhengzhou through western China, Kazakhstan, Russia, Belarus, and Poland to Hamburg, Germany. This train moves Chinese exports to Europe and returns with automobiles and other goods for the growing Chinese consumer market. The train has cut the transportation time for European goods coming in from several weeks to 15 days and has greatly enhanced safety. As a result, Zhengzhou is now the largest automobile manufacturing and distribution center in China.

The High-Tech Incubator within ZNETDZ was established in 1998 to offer policy, funding, and consulting services to (the now over 500) startups and to help them commercialize nascent technology products. Focusing on three key areas—sustainability technology, information technology, and health care—and armed with funding support from the provincial government, Ma is actively recruiting top tech experts from abroad and other regions in China. “More importantly, the region needs to keep local talent from migrating out,” he says. Recruiting and retaining talent is more critical than ever as technology investments begin to come back to the region and demand more support from the local talent pool.

It may be true that, by many objective measures, central China still lags behind other regions in terms of scientific research, science education, and technological investments. However, with its rich culture, abundant labor force, and central location between major cities, central China is poised to become a new center of scientific capital and technological innovation in the near future.

Wayne Peng is a writer based in New York, NY, USA.

DOI: 10.1126/science.opms.r1500158

Science Careers

Cernet

“《科学》职业”已经与Cernet/赛尔互联开展合作。中国大陆的高校可以直接联系Cernet/赛尔互联进行国际人才招聘。



请访问

Sciencecareers.org/CER
点得联系信息。

中国大陆高校以外的 招聘广告，或者
高校 的其它业务，请与国 际合作、
出版副总监吴若蕾联系：

+86-186 0082 9345 | rwu@aaas.org

Science



Postdoctoral Fellow/Staff Scientist

Chinese National Clinical Research Center for Metabolic Diseases at Rui-Jin Hospital in the heart of downtown Shanghai is a large complex including the Shanghai Institute of Endocrine and Metabolic Diseases and the Department of Endocrine and Metabolic Diseases. The center is pioneering both basic and translational science, housing research teams dedicated to studying endocrine tumors, diabetes, and obesity, among other areas. It is to become the most important clinical and research center in the field of endocrine and metabolic diseases in China.

The center is currently seeking a full time Postdoctoral Fellow or Staff Scientist to carry out basic and translational research in the fields of endocrine and metabolic diseases.

Applicants should have a Ph.D., MD., or equivalent degree. Curriculum vitae containing a summary of past research accomplishments, a statement of research interests and names of references should be submitted via email to:
Dr. Yan Xu, xuyanrr@aliyun.com.





FACULTY POSITION NEUROBIOLOGY

The Department of Neurobiology and Anatomy at The University of Texas Medical School at Houston invites applications for a tenure-track appointment in the broad area of circuit neuroscience. We particularly encourage applications from candidates who employ novel computational or experimental techniques including electrophysiology, imaging, and viral approaches to record, manipulate, and analyze in vivo neuronal activity. Applications at both junior and senior levels will be considered, with rank dependent on experience and qualifications. We are located within the Texas Medical Center and its very rich and collaborative neuroscience community including Baylor College of Medicine, Rice University and the University of Houston.

Individuals will be expected to develop a strong, independent research program and contribute to our departmental teaching mission. Interested applicants should submit electronically their curriculum vitae, a statement of their research and teaching interests, and the names of four references through our online application system at <https://jobs.uth.tmc.edu/applicants/Central?quickFind=106100>. The position will remain open until a suitable candidate is identified.

EOE/M/F/Disabled/Vet.



School of Medicine

Two open-rank tenure-track positions in Neuroscience

The Department of Pharmacology of the Creighton University School of Medicine invites applications for two tenure-track positions at the Assistant, Associate or Full Professor level. We are seeking applicants in the broad area of cellular and molecular neuroscience that complement and expand our ongoing basic, clinical and translational neuroscience research on campus. This recruitment is a component of Creighton University's strategic plan commitment to the expansion of its neuroscience research and education programs. Areas of research strength at Creighton University include epilepsy, autism, prion diseases, neurogenesis, glutamate receptor physiology, GPCR signaling, auditory and autonomic systems, and neuroimmunology. Researchers utilizing innovative cellular imaging, optogenetic and whole-animal experimental techniques are particularly encouraged to apply. Applicants at the Assistant Professor level are expected to develop a competitive research program that attracts significant extramural funding. Candidates for Associate or Full Professor level are expected to have a proven track record of extramurally funded research. Incoming faculty are expected to participate in teaching in the undergraduate neuroscience, health profession and/or graduate programs. Successful candidates will receive competitive salary, benefits, start-up package, laboratory space, access to core facilities and collaborative opportunities. The positions are available starting January, 2016.

Candidates must possess a PhD and/or MD and appropriate postdoctoral training. To apply please send a Cover Letter, Curriculum Vitae, Research Statement and contact information for at least three references to **Dr. Shashank Dravid** (shashankdravid@creighton.edu), Chair Search Committee. Applications received before **November 30th, 2015** will receive full consideration.

EOE/AA



Learn more and conduct your job search the easy way.

- Search thousands of job postings
- Create job alerts based on your criteria
- Get career advice from our Career Forum experts
- Download career advice articles and webinars
- Complete an individual development plan at "myIDP"

Target your job search using relevant resources on **ScienceCareers.org**.

ScienceCareers

FROM THE JOURNAL SCIENCE AAAS

Yale SCHOOL OF MEDICINE



Department of Neurobiology

New Haven, CT 06520-8001

<http://medicine.yale.edu/neurobiology/index.aspx>



MULTIPLE FACULTY POSITIONS

As part of a significant expansion, the Department of Neurobiology at Yale University seeks to hire several scientists who work in one or more of the following areas:

- **Molecular, cellular, and genetic approaches to study the development and function of the nervous system and its dysfunction in disease.**
- **Neuronal or circuit-level analysis, including computational approaches, to understand behavior and cognition in health and disease.**

Candidates employing any model organism, from invertebrates to non-human primates, are welcome to apply. Emphasis will be placed on recruiting at the level of Assistant Professor, but outstanding applicants at Associate Professor level will also be considered. We seek candidates with an exceptional track record, potential for outstanding future achievements, and a wish to participate in a dynamic and growing neuroscience community at Yale that includes the Kavli Institute for Neuroscience at Yale, the Program in Cellular Neuroscience, Neurodegeneration and Repair (CNNR) and the Swartz Center at Yale. Candidates are expected to develop a productive and innovative research program and to participate actively in graduate and medical education.

Candidates must hold a Ph.D., M.D., or equivalent degree. Please send a cover letter, curriculum vitae, up to 3 representative publications, a research plan (strictly limited to 2 pages), and arrange for submission of 3 letters of recommendation. All application materials should be sent **electronically** to **Pietro De Camilli** at the following e-mail address: neuro.search@yale.edu. Applications will be reviewed as they are received, but full consideration will be given to applications received by **November 15, 2015**.

Yale is an Affirmative Action Equal Opportunity Employer. Yale values diversity among its students, faculty, and staff. Women, persons with disabilities, protected veterans, and underrepresented minorities are encouraged to apply.



Assistant, Associate, or Full Professor of Neuroscience Department of Neuroscience and Regenerative Medicine

Georgia Regents University (GRU) is accepting applications for an Assistant, Associate, or Full Professor position (tenure-track or tenured) in the Department of Neuroscience and Regenerative Medicine. Candidates should have a PhD or MD; postdoctoral experience; interests in neural development, synaptic plasticity, or disorders of the central or peripheral nervous systems; and a strong record of research accomplishments. Faculty members are expected to establish or have cutting edge research programs and participate in teaching medical and graduate students. Appointment to an endowed chair may be possible for senior, highly qualified individuals. GRU is a state supported academic medical center located in a historic city with outstanding recreational and lifestyle opportunities.

Apply online at <http://www.gru.edu/jobs/university/>. Reference job opening ID: **00004987**. Submit a CV, statement of current/future research interests, and contact information for three references to: Dr. Darrell Brann, c/o Deenie Cerasuolo (dcerasu@gru.edu). Applications will be received until the position is filled.

GRU is an EEO/AA/Equal Access Employer.



McGOVERN INSTITUTE
FOR BRAIN RESEARCH AT MIT

Call for Nominations: Scolnick Prize in Neuroscience

The McGovern Institute for Brain Research is accepting nominations for the 13th annual Edward M. Scolnick Prize in Neuroscience. The Prize recognizes an outstanding discovery or significant advance in the field of neuroscience. The prize is \$125,000. The recipient presents a public lecture at MIT, hosted by the McGovern Institute and followed by a dinner in Spring 2016.

Nomination Deadline: **December 15, 2015**

Nomination procedures: Candidates for the award must be nominated by individuals affiliated with universities, hospitals, medical schools, or research institutes, with a background in neuroscience. Self-nomination is not permitted. Each nomination should include: • A biosketch or CV of the nominee; • A letter of nomination with a summary and analysis of the major contributions of the nominee to the field of neuroscience. • Up to two representative reprints will be accepted.

Selection Procedure: • Members of the selection committee and faculty affiliated with MIT are not eligible. • Announcement of the award recipient will be made in January 2016 • Recipient must attend all events to be awarded the prize.

Past Scolnick Prize Recipients:

- 2004: Dr. Masakazu Konishi, California Institute of Technology
- 2005: Dr. Judith L. Rapoport, National Institutes of Mental Health/NIH
- 2006: Dr. Michael E. Greenberg, Children's Hospital/HMS
- 2007: Dr. David Julius, University of California, San Francisco
- 2008: Dr. Michael Davis, Emory University School of Medicine, Atlanta
- 2009: Dr. Jeremy Nathans, Johns Hopkins University
- 2010: Drs. Lily and Yuh-Nung Jan, UCSF
- 2011: Dr. Bruce McEwen, The Rockefeller University
- 2012: Dr. Roger Nicoll, University of California, San Francisco
- 2013: Dr. Thomas Jessell, HHMI, Columbia University Medical Center
- 2014: Dr. Huda Zoghbi, HHMI, Baylor College of Medicine
- 2015: Dr. Charles Gilbert, The Rockefeller University

Send nomination packet to: gwolf@mit.edu or Attn: **Scolnick Prize Nomination, McGovern Institute for Brain Research, Massachusetts Institute of Technology, 77 Massachusetts Avenue 46-3160, Cambridge, MA 02139.**

For more information: <http://mcgovern.mit.edu>



Join Germany's international research community



© DAAD/Volker Lohmeier

Discover the opportunities that Germany offers:

- First-class doctoral training
- Excellent career opportunities in research and industry
- Attractive funding programmes for international researchers

Visit us at
Neuroscience 2015

McCormick Place, Chicago, IL, USA

17 – 21 October 2015
Booth Number: 2033



Find us on Facebook:
facebook.com/
Research.in.Germany



Follow us on Twitter:
twitter.com/
ResearchGermany



AN INITIATIVE OF THE
Federal Ministry
of Education
and Research

Research in
Germany



Land of Ideas

www.research-in-germany.org



Director, Institute of Neurobiology in Old San Juan University of Puerto Rico Medical Sciences Campus

The University of Puerto Rico Medical Sciences Campus is seeking a Director for the Institute of Neurobiology, an interdepartmental, interdisciplinary research facility with a long and rich history of research excellence. Established in 1967 by the prominent neurophysiologist Dr. Jose del Castillo, the Institute is located in the heart of the culturally vibrant historical center of Old San Juan, and serves as a flagship for neuroscience research in the Caribbean and beyond. Its members carry out basic research into the fundamental mechanisms underlying nervous system function and development, with particular, but not exclusive, focus on environmental neuroscience, neuroethology and neural plasticity. The Director is responsible for the administration and leadership of the Institute's research efforts, and the professional development of its faculty. The faculty at the Institute of Neurobiology receive strong institutional support from the University of Puerto Rico, and are funded by NIH and NSF research programs. The Director will supervise two federally funded programs: a Center of Biomedical Research Excellence (COBRE-NIGMS) focused on neural plasticity, and a Center of Research Excellence in Science and Technology (CREST- NSF) dedicated to the new field of environmental neuroscience.

The Director should qualify for a faculty appointment at the level of full professor. The appointment carries an administrative stipend and substantial resources for research and faculty hiring. Strong administrative and leadership capabilities, a record of superior research and grant support, and excellent communication skills are essential for the position.

Applicants must apply online at <http://academicjobsonline.org/ajo> and include a letter of application explaining how they meet the required and desired qualifications; curriculum vitae; and the names and email addresses of three references. Applicants should ensure that their last name as part of each uploaded file name. Cover letters should be addressed to Dr. Emma Fernández-Repollet, Chair of the Search Committee for the Director of the Institute of Neurobiology. Applications must be received by **December 1, 2015** to receive full consideration.

For general information about the Institute of Neurobiology, see the website at <http://www.neuro.upr.edu/>, or contact Dr. Emma Fernández-Repollet, Chair of the Search Committee for the Director of the Institute of Neurobiology, at neurosearch.rcm@upr.edu.

UPR-MSU is an Equal Opportunity/Affirmative Action Employer.



University of California, Santa Barbara Assistant Professor in Neuroscience

The College of Letters and Science at UCSB invites applications for a tenure-track Assistant Professor position in neuroscience, with the expected start date of July 1, 2016. This position is for applicants applying state-of-the-art experimental approaches that address animal behaviors and cellular circuitry in either conventional or nonconventional model organisms.

This position is part of the University of California, Santa Barbara's expansion in neuroscience, capitalizing on our existing strengths in engineering, physics, molecular, cellular & developmental biology, psychological & brain sciences, materials research, photonics, computer science, and evolutionary biology. The specific departmental affiliation will be determined based on the candidate's specific research interests.

Two other positions at UCSB are being advertised simultaneously, as part of our campus-wide commitment to interdisciplinary collaborative research that alters the future of neuroscience. One is in the College of Engineering (working at the cusp between neuroscience and engineering, including computer science, material science and instrumentation) and one in the Department of Psychological and Brain Sciences (in vision science/visual neuroscience).

Candidates may hold postdoctoral (or equivalent) appointments, although applicants currently holding the rank of Assistant Professor (or equivalent) are also welcome to apply. Applicants should have outstanding records of research accomplishment and will be expected to establish highly creative research programs. A commitment to teaching at the undergraduate and graduate levels is also important. The Department is especially interested in candidates who can contribute to the diversity and excellence of the academic community through research, teaching and service.

Applicants should submit a statement of past and future research interests, a curriculum vitae, and arrange for three letters of recommendation to be submitted directly to <https://recruit.ap.ucsb.edu/apply/JPF00553>. Applications are due **November 5, 2015** for primary consideration, but applications will be accepted until the position is filled. Questions can be emailed to queenan@brain.ucsb.edu.

The University of California is an Equal Opportunity/Affirmative Action Employer and all qualified applicants will receive consideration for employment without regard to race, color, religion, sex, sexual orientation, gender identity, national origin, disability status, protected veteran status, or any other characteristic protected by law.



Department of Health and Human Services
National Institutes of Health
National Institute of Neurological Disorders and Stroke
Director of the Extramural Office of Translational Research
National Institute of Neurological Disorders and Stroke
National Institutes of Health

Recent advances in neuroscience have created unprecedented opportunities to develop effective new treatments for the many disorders that affect the nervous system. The National Institute of Neurological Disorders and Stroke (NINDS) is at the forefront of efforts to translate discoveries in basic research into therapeutic interventions for neurological disease. NINDS seeks a Director of its Office of Translational Research, to lead the development of new therapies and oversee ongoing translational programs centered on biologics, small molecules and devices. The Director will report directly to and advise the NINDS Director on translational programs. The Director will represent the Office of Translational Research at an executive level within NINDS and on the growing trans-NIH and trans-agency translational programs. Programs within the Office of Translational Research include a variety of high-risk, milestone-driven projects that pursue different approaches to therapeutics development. The person recruited for this position will have a major say in what approaches are prioritized.

The Director will also work with the NINDS Office of Clinical Research to transition promising therapies into initial studies in patients, work closely with the extramural research community, build partnerships with nonprofit research organizations and companies, and set priorities for the Institute's grants to small businesses (SBIR and STTR). The successful candidate for this position will have an international reputation for accomplishments in translational neuroscience research, and have demonstrated skills, knowledge, and experience in therapeutic development, project management, technology transfer, and public-private partnerships. Consistent with the required qualifications, the individual will be appointed as a Science Executive in Title 42.

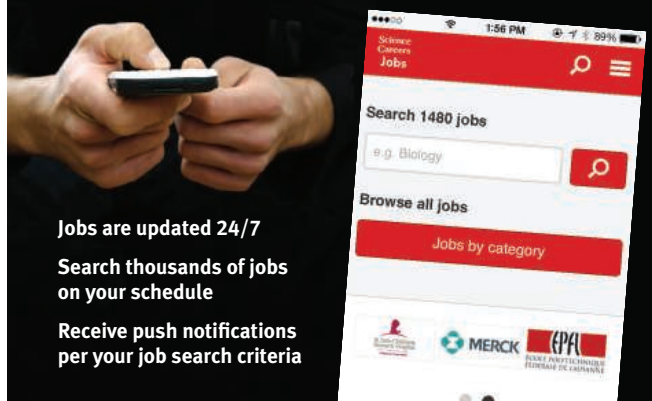
Applications for this position should be sent to: **Dr. Walter Koroshetz, Director, NINDS, c/o Joanne Pomponio, Building 31 Room 8A52 NIH, Bethesda, MD 20892.** Evaluation of applications will begin on **November 1, 2015.** The NINDS is one of the Institutes of the National Institutes of Health, a component of the Department of Health and Human Services.



HHS and NIH are Equal Opportunity Employers.



Download the Science Careers jobs app from Science



Jobs are updated 24/7
Search thousands of jobs on your schedule
Receive push notifications per your job search criteria

Get a job on the go.

Search worldwide for thousands of scientific jobs in academia, industry, and government. The application process is seamless, linking you directly to job postings from your customized push notifications.



Scan this code to download app or visit apps.sciencemag.org for information.

Science Careers | AAAS
FROM THE JOURNAL SCIENCE

ScienceCareers.org

Neuroscience Post-doctoral Programme

Linköping University is one of Sweden's six large universities, currently enrolling 27,000 students. The Centre for Systems Neurobiology involves some 50 independent research groups, from the Faculty of Medicine and the Faculty of Science and Engineering, as well as the University Hospital.

The Centre for Systems Neurobiology is now seeking Postdoctoral Fellows (2+2 years) within several neuroscience research areas: Addiction, Animal Behavior, Electrophysiology and Circuits, Neuroimaging, Neurodegeneration, Neuroendocrinology, Neurodevelopment, Pain, Psychiatry, and Sensory Systems.

li.u LINKÖPING UNIVERSITY

For more details regarding the Centre, the different research labs involved in the programme, and to submit a letter-of-intent please go to: www.hu.liu.se/neuro. For information regarding the university and the region, please go to: www.hu.liu.se, www.liu.se, www.eastsweden.com.

myIDP: A career plan customized for you, by you.



For your career in science, there's only one **Science**



**Recommended by
leading professional
societies and the NIH**

Features in myIDP include:

- Exercises to help you examine your skills, interests, and values.
- A list of 20 scientific career paths with a prediction of which ones best fit your skills and interests.
- A tool for setting strategic goals for the coming year, with optional reminders to keep you on track.
- Articles and resources to guide you through the process.
- Options to save materials online and print them for further review and discussion.
- Ability to select which portion of your IDP you wish to share with advisors, mentors, or others.
- A certificate of completion for users that finish myIDP.

Visit the website and start planning today!
myIDP.sciencecareers.org

ScienceCareers In partnership with:



Open Faculty Positions

The **Okinawa Institute of Science and Technology** [OIST] Graduate University (www.oist.jp) invites applications for at least 7 new faculty members. Research areas include **Biology, Chemistry, Computer Science, Ecology and Environmental Science, Marine Science, Mathematics, Neuroscience, and Physics**. Appointments will be made as Tenure Track Assistant Professor, Tenured Associate Professor, and Tenured Professor. This is part of a plan to hire 50 new faculty members by 2023.

We seek applicants with outstanding scholarship, creativity, and interdisciplinary interests. Successful candidates will be offered research resources and competitive salaries. Further information and instructions for submitting applications online may be accessed at <https://groups.oist.jp/facultypositions>

Application Deadline: 15th November, 2015

OIST is a new, English-language graduate university offering a world-class research environment and has an international research community with faculty, students and staff from over 50 countries. The campus is located on a beautiful, subtropical island in Okinawa, Japan.

OIST Graduate University is an equal opportunity educator and employer committed to increasing the diversity of its faculty, students and staff by having proactive policies in place. We provide a family-friendly working environment, including a bilingual child development center on campus. Applications from women and other underrepresented groups are strongly encouraged. See <https://groups.oist.jp/ged>

Inquiries should be directed to Professor Ken Peach, Dean of Faculty Affairs, faculty-recruiting@oist.jp



UAB SCHOOL OF MEDICINE

Knowledge that will change your world

The University of Alabama at Birmingham

POSTDOCTORAL FELLOW Division of Pulmonary, Allergy & Critical Care Medicine

Postdoctoral Fellow position is open to investigate acquired (non-genetic) defects in CFTR biology in COPD-related chronic bronchitis and to test CFTR therapeutics in vivo. This project is supported by a recently funded R01 and involves the study of mucus clearance defects in a novel ferret model of COPD using innovative lung function measures, real-time optical coherence tomography (μ OCT) imaging of ciliated epithelium and electrophysiological assays in vivo. Our work has been featured in the *New England Journal of Medicine*, *Science*, and the *AJRCCM*, among others.

The ideal candidate will be innovative and have a high level of self-motivation and commitment to pursuing an independent research effort upon completion of the fellowship. Candidate will have access to exceptional research infrastructure, experienced colleagues, funding, mentorship and work in a laboratory with successful track record of transitioning basic scientists. The successful candidate will have a Ph.D. or an equivalent degree in physiology/pharmacology/pathology/toxicology, experience with molecular lung physiology, membrane biology, preclinical animal models, physiologic assays, cellular imaging and electrophysiology. The position requires designing and performing experiments, writing manuscripts for publications and assisting with preparation of grant proposals.

Applicants should submit their CV and three references to Steven M. Rowe, M.D., M.S.P.H., Professor and Director, Cystic Fibrosis Research Center, University of Alabama at Birmingham, Birmingham, Alabama 35294. E-mail: smrowe@uab.edu

UAB is an Equal Opportunity/Affirmative Action Employer committed to fostering a diverse, equitable and family-friendly environment in which all faculty and staff can excel and achieve work/life balance irrespective of race, national origin, age, genetic or family medical history, gender, faith, gender identity and expression as well as sexual orientation. UAB also encourages applications from individuals with disabilities and veterans.



NATURAL SCIENCES & MATHEMATICS

Department of Biological Sciences Assistant Professor – Cell Biology

The Division of Natural Sciences and Mathematics at the University of Denver has been expanding our Molecular Life Sciences Initiative with 14 tenure-track hires in recent years. The Department of Biological Sciences invites applicants for two tenure track faculty positions at the Assistant Professor level to begin September 1, 2016. We are seeking candidates with research interests in cell biology that include but are not limited to the study of intracellular signaling and trafficking, intermolecular interactions, and cell physiology. Individuals applying advanced fluorescence imaging or other biophysical approaches are encouraged to apply. The successful candidate will have a Ph.D. and post-doctoral experience in an appropriate field, will develop an extramurally funded research program, will supervise Ph.D. and M.S. students and undergraduate research projects and will teach undergraduate and graduate courses in area of expertise. All candidates must submit their application through <https://dujobs.silkroad.com> Information on Departmental programs can be found at <http://www.du.edu/nsm/departments/biologicalsciences/> Successful applicants will also be eligible to participate in the interdepartmental Molecular and Cellular Biophysics Ph.D. program <http://www.du.edu/nsm/departments/molecularandcellular/index.html>.

The online application should include: a curriculum vitae, and separate statements of research interests and teaching philosophy and two recent publications. In addition, at least three recommenders should email letters of reference to: Cell Biology Faculty Search Committee, University of Denver, Department of Biological Sciences at biology.rec@du.edu. The review of applications will begin **November 15, 2015** and continue until the position is filled. Contact Schuyler Van Engelenburg at schuyler.vanengelenburg@du.edu if you have questions regarding the search.

The University of Denver is committed to enhancing the diversity of its faculty and staff and encourages applications from women, minorities, members of the LGBT community, people with disabilities and veterans. The University is an Equal Opportunity/Affirmative Action Employer.

POSITIONS OPEN



Interdisciplinary Position:

Research Microbiologist/Molecular Biologist
0401 GS-12/13

Salary Range: \$75,136 to \$116,149 per year
Announcement closes: October 30, 2015

The USDA Western Human Nutrition Research Center, located on the campus of the University of California, Davis, is recruiting a research scientist to conduct research on the effect of diet, dietary patterns or specific nutrients on the intestinal microbiota and the relationship of that microbiota to appropriate functioning of the immune system for maintaining health. The microbiologist filling this position will work as part of a team including nutritionists and immunologists. The Center focuses on human nutrition studies but also uses animal models as appropriate to a given research question relating to human nutrition. This is a competitive, permanent appointment and U.S. citizenship is required. For further details about this position and how to apply go to website: www.USAJobs.gov vacancy announcement number ARS-ARS-D15W-0485 or use the direct link: <https://www.usajobs.gov/GetJob/ViewDetails/415916800>. For questions about the position contact Charles B. Stephensen, Research Leader, Immunity and Disease Prevention Research Unit, Western Human Nutrition Research Center, e-mail: Charles.Stephensen@ars.usda.gov.

ARS is an Equal Opportunity Employer and Provider.

LECTURER POSITION

The Department of Chemistry and Biochemistry in the College of Science at Utah State University invites applications for a **LECTURER POSITION** beginning Fall 2016. Applicants will preferably have already obtained a Ph.D. in Chemistry or Biochemistry. Applicants with an MS degree in Chemistry or Biochemistry and significant university level teaching experience may also be considered. Teaching duties will include teaching general chemistry courses and their associated laboratories during the academic year. Ability to teach introductory organic chemistry and biochemistry courses, as well as a GOB (General/Organic/Biochemistry) introductory chemistry sequence, is highly desirable. Experience with online and electronic course delivery is also desired. Application information can be found on-line at website: <http://jobs.usu.edu> (REQ ID F1500085). Evaluation of applications will begin October 26, 2015 and will continue until the position is filled. For further information please visit our website at <http://www.chem.usu.edu>. Utah State University is an Equal Opportunity/Affirmative Action Employer committed to assembling a diverse faculty. Women and members of minority groups are strongly encouraged to apply.

PROFESSOR OF PRACTICE Ecology and Evolutionary Biology

The Department of Ecology and Evolutionary Biology, Tulane University, invites applications for one full-time, non-tenure-track Professor of Practice beginning fall 2016. Candidates must hold a Ph.D. in biological sciences and have teaching experience at college level, preferably with experience in active learning. We seek an individual with expertise in ecology, evolution and organismal biology as well as commitment to excellence in undergraduate education and scholarship of teaching and learning. For more details about the position, department, search and applications, see website: <http://tulane.edu/sse/ceb/positions>. Apply to website: <http://apply.interfolio.com/32032>. Review of applications will begin November 15 2015, and the search will remain open until the position is filled. Tulane is an Equal Opportunity Employer/Male/Female/Veteran/Disabled Employer.

POSITIONS OPEN



Department of Biology Assistant Professorship Tenure Track position

California State University, Northridge, seeks a Plant Evolutionary Biologist to become a **TENURE-TRACK ASSISTANT PROFESSOR** of Biology. Applicants research should address evolutionary questions in plant biology, with a preferable focus on molecular systematics. Applicants must have a Ph.D. and postdoctoral experience. Teaching will include Evolutionary Biology, Flowering Plants, and/or an upper division course developed by the applicant. The successful candidate is expected to develop a vigorous research program involving undergraduate and M.S. students, aggressively seek extramural funding, demonstrate teaching excellence, and provide effective instruction to students of diverse backgrounds in a multicultural setting.

For more information and application procedure visit website: <http://www.csun.edu/science-mathematics/biology/jobs>. Screening application will begin on **November 1, 2015**.

California State University, Northridge is an Equal Opportunity Employer committed to excellence through diversity.

Structural Biology Assistant Professor

The Roy J. Carver Department of Biochemistry, Biophysics and Molecular Biology at Iowa State University in Ames, IA has embarked on a transformational expansion of its structural biology research enterprise through a large philanthropic gift from the Roy J. Carver Charitable Trust. This major research initiative in Biomolecular Structure includes long-term investment in new instrumentation, endowed funds for graduate student training, and a series of new faculty hires working at the forefront of any aspect of structural biology.

As part of the faculty positions associated with this initiative, and as part of the interdisciplinary effort across the Iowa State University campus to expand structural biology research, the Department seeks a new tenure-track Assistant Professor to establish a vibrant, externally funded research program of international prominence and participate in graduate and undergraduate teaching.

Applicants should have a Ph.D. or equivalent degree, and research accomplishments indicative of the ability to establish an independent research program of national prominence.

To view the entire vacancy #500159 and apply, create an electronic application at website: www.iastatejobs.com

To guarantee consideration, the applications must be received by **December 7, 2015**.

Iowa State University is an Equal Opportunity/Affirmative Action Employer. All qualified applicants will receive consideration for employment without regard to race, color, religion, sex, national origin, disability, or protected Vets status.

FACULTY POSITIONS


Virginia Commonwealth University. The Department of Biomedical Engineering at Virginia Commonwealth University invites applications for faculty positions at all ranks in with research experience in one of the following areas: rehabilitation engineering, biomedical instrumentation, biomedical signal processing, cell and molecular bioengineering, regenerative medicine, computational biomedical engineering, nanotechnology, biomechanics, biomaterials, or drug delivery systems. Biomedical Engineering at Virginia Commonwealth University offers the B.S., M.S. and Ph.D. degrees and collaborates closely with clinicians and biomedical scientists on the VCU Medical Center campus of the university in downtown Richmond, Virginia. The School of Engineering is undergoing a period of rapid expansion and will double the number of its faculty over the next five years. For further details on this position, please visit website:

<https://www.vcujobs.com/postings/46720>.

Virginia Commonwealth University is an Equal Opportunity/Affirmative Action Employer. Women, minorities, veterans, and persons with disabilities are encouraged to apply.

Advance your career
with expert advice from
Science Careers.



 **Download Free Career
Advice Booklets!**

ScienceCareers.org/booklets

Featured Topics:

- Networking
- Industry or Academia
- Job Searching
- Non-Bench Careers
- And More



Science Careers

FROM THE JOURNAL SCIENCE 



AAAS is here – helping scientists achieve career success.

Every month, over 400,000 students and scientists visit ScienceCareers.org in search of the information, advice, and opportunities they need to take the next step in their careers.

A complete career resource, free to the public, *Science Careers* offers hundreds of career development articles, webinars and downloadable booklets filled with practical advice, a community forum providing answers to career questions, and thousands of job listings in academia, government, and industry. As a AAAS member, your dues help AAAS make this service available to the scientific community. If you're not a member, join us. Together we can make a difference.

To learn more, visit
aaas.org/plusyou/sciencecareers



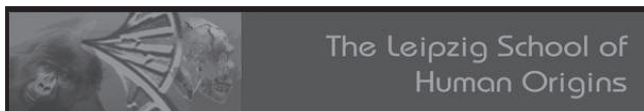
UCLA

Microbiology, Immunology and Molecular Genetics Tenure-Track Faculty Position

The Department of Microbiology, Immunology and Molecular Genetics at the David Geffen School of Medicine at University of California Los Angeles invites applications for a TENURE-TRACK faculty position at the Assistant or Associate level. Outstanding Ph.D., M.D. or equivalent candidates with postdoctoral experience working in the areas of immunology, virology, microbial pathogenesis or microbial genomics are invited to apply. Successful candidates are expected to develop an innovative research program and join a highly interactive group of scientists within the Department of Microbiology, Immunology and Molecular Genetics (<http://www.mimg.ucla.edu>). The candidate will benefit from a collaborative research community spanning the basic and clinical sciences from the Schools of Medicine and Engineering, College of Letters and Science, California NanoSystems Institute, Jonsson Comprehensive Cancer Center, and the UCLA Institute of Stem Cell Biology and Medicine. This tenure-track position includes a guaranteed salary, a highly competitive start-up package and laboratory space in a state-of-the-art research facility. Eligible individuals will also receive the Shaper Family Career Development Chair.

Applications will be screened beginning **November 1, 2015**. For full consideration applicants are encouraged to apply before the closing date of the search, December 15, 2015. Applicants should submit full curriculum vitae and a 2-page summary describing their current research program and future directions, a brief statement on teaching experience, and contact information for three references. Applicants with a history of commitment to mentoring undergraduate minorities are encouraged to apply and should indicate their experience in a cover letter. All applications are to be submitted through UC Recruit (<https://recruit.apo.ucla.edu/apply>) Job number JPF01584. Inquiries, but not application material, should be directed to: **Matt Clouston**, mclouston@mednet.ucla.edu, **Assistant to Chair, Faculty Search Committee, Department of Microbiology, Immunology and Molecular Genetics, University of California, Los Angeles, 1602 Molecular Science Building, Box 951489, Los Angeles, CA 90095-1489.**

The University of California is an Equal Opportunity/Affirmative Action Employer. All qualified applicants will receive consideration for employment without regard to race, color, religion, sex, national origin, disability, age or protected veteran status. For the complete University of California nondiscrimination and affirmative action policy see: UC Nondiscrimination & Affirmative Action Policy



The Leipzig School of Human Origins

- An International Max Planck Research School -

by

The University of Leipzig

and

The Max Planck Institute for Evolutionary
Anthropology

The **Leipzig School of Human Origins** offers a unique interdisciplinary graduate program to study the evolutionary history of humans and great apes. Graduate students are accepted into one of the following areas, but are encouraged to take part in courses and seminars from all three disciplines:

Comparative and Molecular Primatology

**Evolutionary and Functional Genomics, Ancient DNA,
Molecular Anthropology and Genome Bioinformatics**

**Human Paleontology, Prehistoric Archaeology
and Archaeological Science**

The language of the school is English. Visit www.leipzig.de for information on living in Leipzig, Germany, in the center of Europe.

For project and application details go to
www.leipzig-school.eva.mpg.de

or contact us at:

e-mail: leipzig-school@eva.mpg.de

phone: ++49 (0) 341 3550-0

fax ++49 (0) 341 3550-119

Application deadline: December 01, 2015



Tenure-Track Faculty Position (Assistant/Associate/Full Professor) Department of Genetics, Yale University School of Medicine



The Department of Genetics at Yale University School of Medicine invites applications for junior or senior tenure-track faculty positions. The search is open to investigators from all areas of biological and biomedical research. However, we are particularly interested in applicants focused on Functional Genomics, Computational Biology and Statistical Genetics. Applications from investigators working on the interface of these areas with developmental biology and experimental genetics will also be strongly considered. The rank of the appointment will be commensurate with experience.

The Department of Genetics comprises an exceptional group of 22 primary basic science faculty with research interests including fundamental aspects of genetics, genomics and epigenetics, with investigation of model systems including fly, worm, fish, frog and mouse, as well as humans. To this end, the Department has established a highly productive next generation DNA sequencing center (Yale Center for Genome Analysis) that is producing extremely rich genetic and functional genomic datasets in a broad range of biological systems.

Applications should be received by **November 15, 2015** and should include: Cover Letter, Curriculum vitae, a description of previous research (1 page), a concise statement of research plans (up to 2 pages), and 3 letters of reference. Applications and letters of reference should be sent to the attention of Richard Lifton, Chair, Department of Genetics. A single PDF file named: Lastname_firstname_mentorlastname.pdf should be uploaded in the application website <http://apply.interfolio.com/31893>. Questions should be sent to genetics.admin@yale.edu.

Yale University is an Affirmative Action/Equal Opportunity Employer and welcomes applications from women, persons with disabilities, protected veterans, and members of minority groups.

By Elisabeth Pain

After the bombs

As the flow of Syrians seeking refuge from their war-torn country turned into a flood, *Science Careers* spoke to a Syrian computer scientist who was able to reach Europe before it became overwhelmed with refugees in despair. She described her professional life before the war and her efforts to rebuild her career and ensure a future for her family. Her identity is undisclosed for security reasons. This interview has been edited for clarity and brevity.

Q: What was your career like before the conflict?

A: My career was evolving slowly because of the way the academic system was in Syria. It's not that the system was discriminatory against women; it's just that it was not helpful for most people. There was favoritism regarding access to resources, based on sectarian or political reasons. We were supposed to do research but didn't have the means to do so.

Still, with perseverance, I fulfilled part of a dream. As a professor, I was not satisfied with the way Syrian students were being taught, and so I was trying to put in place a program to improve teaching at my university. But, in March 2011, just as the program was taking shape, the conflict started and everything else was stopped.

Q: How have you seen the conflict evolve?

A: At the beginning, my colleagues and I were freely discussing the pro-democracy protests and government response. However, within a few months, we started to see people getting arrested and tortured—including students on campus. So I stopped discussing my opinions openly.

Still, as the civil war took hold of the country, not risking your life became impossible. The year I left, just before the students' final exams, there was a big explosion near my office. Had I been at work, I would have been killed. The next day, I had very few students in class, and I could see in their eyes how lost they felt. But, with time, people in Syria have realized they aren't safe at home either, and students and professors keep going to universities.

Q: How did you leave Syria?

A: Back in 2012, it was still relatively easy, as the numbers of refugees sharply increased only later. My husband, children, and I first traveled to a neighboring country, where my husband moved his small business. It was



*Syrian professor refugees
“need opportunities to
rebuild their ... lives.”*

going rather well, but we didn't feel safe there in the long run.

To help my family get to a more secure country, I applied—to no avail—for any open university position I could find in the Gulf states. Then, one day on Facebook, I discovered a U.S. funding program for hosting threatened scholars, called the Institute of International Education's Scholar Rescue Fund (IIE-SRF). I applied and got a fellowship. Meanwhile, my husband was able to obtain a work visa for Europe, and the rest of the family followed him. Nevertheless, it took me 10 months, and help from IIE-SRF and the Scholars at Risk Network, to finally secure a visiting position to take up my fellowship.

Q: What are your immediate aspirations?

A: I am planning to extend my 1-year fellowship to move to a new institution and expand my network, with the hope of securing a stable job in the end.

Meanwhile, I have also been trying to find opportunities in refugee education. Gaining access to universities in host countries is difficult for Syrian students because of money issues, language barriers, and laws. But we can imagine a lot of solutions and, with time, I think I will be able to make a contribution. And maybe then I will be ... not happy—it is impossible for us Syrians to feel happy as we hear about all the tragic events afflicting our people—but somewhat relieved.

Finally, I would like to raise awareness that Syrian professors can bring interesting backgrounds and great value to their host countries and institutions. They need opportunities to rebuild their personal and professional lives, as I am trying to do now. ■

Elisabeth Pain is Science Careers contributing editor for Europe. For more on life and careers, visit sciencecareers.org. Send your story to SciCareerEditor@aaas.org.